

Investigation of Using Fibre Bragg Grating Sensing Technology for Thermal Condition Monitoring In Electric Machinery

A thesis submitted to The University of Manchester for the degree of
Doctor of Philosophy
in the Faculty of Science and Engineering

2019

Anees Mohammed

School of Electrical and Electronic Engineering
Power and Energy Division

TABLE OF CONTENTS

TABLE OF CONTENTS	2
LIST OF FIGURES	5
LIST OF TABLES	12
LIST OF ACRONYMS	14
ABSTRACT	16
DECLARATION	17
COPYRIGHT STATEMENT	18
ACKNOWLEDGEMENTS	19
CHAPTER 1: INTRODUCTION	20
1.1 Introduction	20
1.2 LVEMs developments	21
1.3 LVEMs thermal issues	22
1.4 Thermal condition monitoring issues	25
1.5 Problem statement	26
1.6 Objectives	27
1.7 Contribution of the research	28
1.8 Structure of the thesis	29
1.9 List of publications	33
1.9.1 Papers published/submitted as result of this research	33
1.9.2 Publications produced during this PhD study not in the research focus of thesis work	34
CHAPTER 2: LITERATURE REVIEW	36
2.1 Introduction	36
2.2 LVEM failure modes and condition monitoring review	36
2.2.1 Classification of LVEMs failures and their root causes	36
2.2.2 LVEMs condition monitoring systems	42
2.2.3 Thermal condition monitoring	45
2.3 Fibre Bragg Grating Sensing Technology (FBGST)	52

2.3.1	<i>FBGS structure</i>	53
2.3.2	<i>Fabrication of a FBGS</i>	54
2.3.3	<i>FBGS interrogation</i>	58
2.3.4	<i>FBGS sensing principles</i>	60
2.3.5	<i>Advantages and disadvantages of FBGST</i>	66
2.3.6	<i>Review of FBG sensing application for EMs</i>	69
2.4	<i>Summary</i>	77
CHAPTER 3: SIMULATION AND EXPERIMENTAL SETUP DESCRIPTION		79
3.1	<i>Introduction</i>	79
3.2	<i>Thermal models description</i>	79
3.2.1	<i>Thermal models development using Motor-CAD</i>	80
3.3	<i>Experimental setup description</i>	89
3.3.1	<i>FBG thermal sensing system</i>	90
3.3.2	<i>Thermal calibration test-rig</i>	100
3.3.3	<i>Prototype wound coil test system</i>	101
3.3.4	<i>FBG embedded LVEMs test-rigs</i>	104
3.3.5	<i>Other equipment used in experimental research</i>	119
3.4	<i>Summary</i>	121
CHAPTER 4: CALIBRATION, CHARACTERISATION AND PERFORMANCE ASSESSMENT OF RANDOM WOUND COIL EMBEDDED IN-SITU FBG THERMAL SENSING SYSTEM		122
4.1	<i>Introduction</i>	122
4.2	<i>Paper 1: In-situ FBG sensing system installation, characterisation and performance evaluation for hot spot monitoring in electric machinery random wound components</i>	124
4.3	<i>Paper 2: FBG thermal sensing features for hot spot monitoring in random wound electric machine coils</i>	155
CHAPTER 5: ON-LINE LOW VOLTAGE STATOR WINDING INTERNAL TEMPERATURE MONITORING USING IN-SITU FBG THERMAL SENSING SYSTEM		177
5.1	<i>Introduction</i>	177
5.2	<i>Paper 1: Stator Winding Internal Thermal Monitoring and Analysis Using in-situ FBG Sensing Technology</i>	178
5.3	<i>Paper 2: Multiplexing FBG Thermal Sensing in Stator Windings Interior for Distributed Thermal Monitoring in In-service Electric Machines</i>	204
CHAPTER 6: WINDING FAULT DETECTION AND DIAGNOSIS BASED ON FAULT INDUCED THERMAL SIGNATURE MONITORING		225
6.1	<i>Introduction</i>	225

6.2	<i>Paper 1: Stator Winding Fault Thermal Signature Monitoring and Analysis by in-situ FBG Sensors</i>	<i>226</i>
6.3	<i>Paper 2: FBG Thermal Sensing Ring Scheme for Stator Winding Condition Monitoring in PMSMs.....</i>	<i>251</i>
CHAPTER 7: FBG SENSING APPLICATION FOR ELECTRIC MACHINERY ROTARY COMPONENTS CONDITION MONITORING.....		275
7.1	<i>Introduction.....</i>	<i>275</i>
7.2	<i>Paper 1: A Feasibility Study of Simultaneous Thermal and Mechanical Fibre Optic Sensing for Electric Motor Rotary Components Condition Monitoring .</i>	<i>277</i>
CHAPTER 8: CONCLUSIONS AND RECOMMENDATION FOR FUTURE RESEARCH ...		293
8.1	<i>Conclusions.....</i>	<i>293</i>
8.2	<i>Thesis contribution summary</i>	<i>296</i>
8.3	<i>Recommendation for future research</i>	<i>296</i>
REFERENCES.....		299

LIST OF FIGURES

CHAPTER 2:	36
Fig 2.1: Illustration of the winding structure in random wound LVEMs.....	37
Fig 2.2: Types of short circuit faults in a random wound winding	39
Fig 2.3: Stator winding failures in a slot and an end-winding section [67]	39
Fig 2.4: Core failure due to stator winding electrical faults [71, 72]	40
Fig 2.5: Rotor failures in induction machines: a) squirrel cage rotor, b) wound rotor [74]	41
Fig 2.6: Bearing failures damage in rotating electric machines [77, 78]	41
Fig 2.7: Conventional condition monitoring system structure	44
Fig 2.8: Thermal monitoring approaches for LVEMs.....	47
Fig 2.9: Fibre Bragg grating sensor structure	54
Fig 2.10: A schematic diagram of the two-beam interference configuration [124]	55
Fig 2.11: A schematic diagram of the phase-mask technique [127]	56
Fig 2.12: Modified phase-mask technique [121].....	56
Fig 2.13: A typical reflected wavelength spectrum of a standard FBGS [121]	57
Fig 2.14: Schematic principle diagram of the WDM interrogation technique [135]	60
Fig 2.15: Working principle of FBGS [137]	61
Fig 2.16: Operating principle of the FBG array sensor [137]	62
Fig 2.17: FBG temperature sensor operating principle [137]	63
Fig 2.18: FBG temperature sensor operating principle [137]	64
Fig 2.19: FBG strain sensor operating principle [137].....	64
Fig 2.20: Embedded FBG sensing system in a low voltage induction machine [165]...	70
Fig 2.21: Fibre routing along the stator slots for winding temperature measurements [146]	71
Fig 2.22: Distributed thermal sensing based FBG sensing technology in a large generator [167]	72
Fig 2.23: Implementation of FBGSs on a large hydroelectric power plant in Brazil [164]	72
Fig 2.24: FBG heads installation on magnet rotor structure [146].....	73

Fig 2.25: Placing a FBG strain sensor in the stator core tooth between core lamination [172]	75
Fig 2.26: Stator teeth mechanical excitation measurement using a FBG strain sensor [46]	75
Fig 2.27: a) Strain measurement in stator teeth, b) torque measurements in rotor shaft.	76
CHAPTER 3:	79
Fig 3.1: Disassembled motor and dimensions measurement for Motor-CAD model inputs	80
Fig 3.2: IM model in Motor-CAD.....	82
Fig 3.3: Interface window for materials setting	82
Fig 3.4: Thermal network model of test IM determined by Motor-CAD	83
Fig 3.5: Integrating the slot layer model in the lumped network model	84
Fig 3.6: Slot and rotor bars models by the 2D-FE.....	85
Fig 3.7: Optimized Motor-CAD model results for the DC test.....	87
Fig 3.8 : 3D components model of the PMSM in Motor-CAD.....	88
Fig 3.9: Thermal network and 2D-FE model for the PMSM in Motor-CAD	89
Fig 3.10: FBG thermal sensor design: diagram (top) and photograph (bottom)	91
Fig 3.11: Preparing procedure of the packaged FBG temperature sensor.....	92
Fig 3.12 : Preparing non-metallic packaging capillaries for sensing fibre insertion.....	93
Fig 3.13: FBGS probes design sketch for order	93
Fig 3.14 : Supplied FBG single and array probes	94
Fig 3.15: SmartScan interrogator unit [136]	95
Fig 3.16: SmartSoft instrumentation window interface	96
Fig 3.17: Slotting of the wavelength spectrum.....	98
Fig 3.18: Enhanced acquisition – Sensors tab.....	99
Fig 3.19: Fibre optic rotary joint model MJXA-FAP-155-28-FA.....	99
Fig 3.20: Experimental system for FBG sensor calibration tests	101
Fig 3.21: Prototype random wound test coil ant its manufacture.....	102
Fig 3.22: Test coil embedded in different housing structures	102
Fig 3.23: The embedded FBG sensor positions in the prototype coil structures.....	103
Fig 3.24: Test DC power supplies	104
Fig 3.25: A side view photographs of the examined IM	105
Fig 3.26: Layout connection of the healthy stator windings.....	106
Fig 3.27: Modified IM stator windings	106

Fig 3.28 : FBG temperature sensors positions in the tested IM	109
Fig 3.29: Photographs of rewinding process of the examined motor.....	110
Fig 3.30: Experimental test rig of the embedded IM	112
Fig 3.31: PMSM side view	112
Fig 3.32: PM synchronous motor original winding	113
Fig 3.33: PMSM original winding configuration	114
Fig 3.34: Healthy phase A winding configuration	114
Fig 3.35: Modified PMSM winding configuration	115
Fig 3.36: Capillary positions in the PMSM.....	116
Fig 3.37: PEEK capillaries position in the slot centre.....	117
Fig 3.38: Photographs of re-winding process of the PMSM.....	118
Fig 3.39: Experimental test rig layout of the embedded PMSM.....	119
Fig 3.40: Thermal camera type FLIR TG-165 [188].....	120
Fig 3.41: Testo 450i anemometer.....	120
CHAPTER 4:.....	122
PAPER 1:.....	124
Fig. 1: Operating principle of the FBG array sensor.....	127
Fig. 2: FBG thermal sensors design for in-situ thermal monitoring	129
Fig. 3: Examined prototype coil systems embedded with FBG temperature sensors design.....	130
Fig. 4: Experimental system setup for calibration and characterisation.....	131
Fig. 5: Experimental system setup for in-situ FBG performance assessment.....	131
Fig. 6: Calibration characteristics of the packaged FBG array sensor heads.....	133
Fig. 7: (a) Motorette structure, (b) showing embedded sensor position.....	133
Fig. 8: FBG Peek and TC thermal cycle measurements.....	134
Fig. 9: (a) FBG Peek and TC thermal response measurement, (b) FBG Peek and TC static thermal.....	135
Fig.10: FBG sensor placement within the test motorette geometry.....	135
Fig.11: Motorette coil thermal measurements.....	136
Fig.12: Bragg wavelength shift under different temperature change rates.....	137
Fig.13: FBG temperature sensors performance under thermal cycle.....	138
Fig.14: Stator core embedded FBG enabled test coil.....	139
Fig.15: Thermal measurement for a continuous thermal cycle.....	140
Fig.16: Thermal measurements for an intermittent periodic thermal cycle.....	141

Fig.17:	External thermal excitation measurements effects.....	142
Fig.18:	FBG sensing system wavelengths - temperature characteristics.....	143
Fig.19:	(a) FBGS measured temperature sensitivity; (b) FBGE measured temperature sensitivity.....	143
Fig.20:	Single-coil test system.....	144
Fig.21:	FBG array thermal measurements in steady state conditions.....	145
Fig.22:	FBG array thermal measurements in transient conditions.....	146
Fig.23:	Illustration of external coil use for localised high thermal stress.....	147
Fig.24:	Thermal measurements under non-uniform thermal stress.....	147
Fig.25:	Thermal images under non-uniform thermal stress.....	148
Fig.26:	Multi-coil test system.....	148
Fig.27:	Measured dynamic temperature by the in-situ FBG array sensor under even thermal excitation.....	150
Fig.28:	FBG array thermal measurements in transient conditions.....	150
Fig.29:	Measured dynamic temperature by the in-situ FBG array sensor under uneven thermal stress.....	152
Fig.30:	Thermal images of the tested multi-coil system.....	152
PAPER 2:		155
Fig. 1:	Test coil design, manufacture and the IEEE motorette rig	158
Fig. 2:	FBG thermal sensor design for hot spot temperature monitoring	159
Fig. 3:	Possible error margins for coil embedded FBG sensor measurements.....	160
Fig. 4:	FBG sensor pre-embedment calibration process.....	161
Fig. 5:	Measured Bragg wavelength for a single FBG head.....	162
Fig. 6:	In-situ measurement error using EFC and PEFC calibration curves for motorette coils.....	163
Fig. 7:	Embedded stator slots cross-sections with FBG temperature sensor.....	163
Fig. 8:	In-situ measurement error using CEFC and PEFC calibration curves for stator core embedded coils.....	164
Fig. 9:	Random wound test coil embedded with an FBG array.....	165
Fig.10:	Experimental system setup for vibration sensitivity test.....	166
Fig.11:	Test coil embedded FBG array sensor in-situ thermal hot spot measurements under mechanical excitation.....	167
Fig.12:	Hot spot temperature at 50 Hz for a thermally excited coil.....	168
Fig.13:	Measured temperature at 50 Hz with a 1.5 mm pk-pk displacement.....	168
Fig.14:	Thermal FEA model of the FBG sensor package.....	170

Fig.15:	Simulated transient thermal response of different package FBGs.....	171
Fig.16:	In-situ temperature rise measurements for thermal transient tests.....	174
CHAPTER 5:.....		177
PAPER 1:.....		178
Fig. 1:	Thermal limits for insulation classes A, B, C and F [14].....	179
Fig. 2:	Stator slot thermal model.....	183
Fig. 3:	Predicted steady-state temperature gradient of the slot section.....	184
Fig. 4:	Predicted axial thermal gradient in the test motor.....	185
Fig. 5:	FBG sensor for in-situ hot spot temperature monitoring.....	189
Fig. 6:	Experimental system for FBG sensor calibration tests.....	189
Fig. 7:	Sensor calibration test data.....	190
Fig. 8:	Temperature sensor positions in the tested motor.....	192
Fig. 9:	Experimental test rig for TEFC on-line temperature monitoring.....	192
Fig.10:	Stator winding temperature measured by in situ FBG and TC sensors during running duty cycle S1 operation: (a) no-load .(b) full-load.....	194
Fig.11:	Measured S1 duty cycle steady-state temperature rise versus load.....	195
Fig.12:	Temperature gradients measured within the slot area.....	196
Fig.13:	Measured temperature under intermittent duty cycle S3.....	198
Fig.14:	Measured temperature under continuous operation duty cycle S6.....	199
PAPER 2:.....		204
Fig. 1:	Reported cases of deteriorated cooling system capability in TEFC machines operating in paper machine and pulp industries [14,15].....	208
Fig. 2:	FBG array for distributed radial thermal sensing in TEFC-IM.....	209
Fig. 3:	Schematic diagram of the experimental test rig.....	210
Fig. 4:	Measured radial temperature distribution for different load conditions.....	211
Fig. 5:	Measured temperatures at 50Hz and 100% load.....	213
Fig. 6:	Measured temperatures and phase currents at 50Hz in 100% load.....	213
Fig. 7:	Measured air velocity along the axial length of the TEFC-IM.....	214
Fig. 8:	Test motor with coated upper frame.....	214
Fig. 9:	Measured radial temperature in coated frame tests.....	215
Fig.10:	Measured temperature rise in coated frame tests.....	216
Fig.11:	Emulated cooling air blockage areas.....	217
Fig.12:	Measured hot spot temperature during uneven frame cooling.....	217
Fig.13:	Examined TEFC-IM cowling obstruction scenarios.....	219

Fig.14:	Thermal measurements under obstructed air inlets.....	219
Fig.15:	Thermal images before and during 100% cowling air inlets obstruction.....	219
Fig.16:	Examined torque-speed characteristics in constant V/f control.....	221
Fig.17:	Measured temperature-rise distribution at different frequency.....	222
Fig.18:	Measured radial average temperature distribution at different supply frequency.....	216
CHAPTER 6:		225
PAPER 1:		226
Fig. 1:	IM stator winding under inter-turn fault.....	230
Fig. 2:	A winding coil with inter-turn fault.....	230
Fig. 3:	Modified stator phase for winding ITSCF emulation.....	234
Fig. 4:	Test motor thermal sensor positions. (a) FBG sensor locations in slot sections (b) FBG locations in end-winding sections.....	235
Fig. 5:	Experimental test rig setup.....	236
Fig. 6:	Measured temperature rise profiles under ITSCF condition.....	239
Fig. 7:	Measured fault induced temperature rise in steady-state conditions.....	239
Fig. 8:	Measured currents in healthy and faulty turns, induced voltage in shorted turns.....	240
Fig. 9:	Fault induced heat loss, shorted turn current and resistance variation with load, 10 turns shorted fault.....	242
Fig.10:	ITSCF temperature measurement in steady state conditions.....	243
Fig.11:	Measured MCSA ITSCF signature.....	244
Fig.12:	FBG-AF measurements for different operating frequencies.....	245
Fig.13:	Thermal measurements in dynamic conditions, 5 turns shorted fault.....	247
Fig.14:	Measured temperature profile under fault propagation.....	248
PAPER 2:		251
Fig. 1:	A simple schematic diagram of three-phase stator winding highlighting different overheating scenarios.....	255
Fig. 2:	PMSM stator winding configuration.....	257
Fig. 3:	Three phase coil-ends arrangement in DE-winding.....	257
Fig. 4:	2D-TSR design and location in the examined PMSM windings.....	258
Fig. 5:	Modified phase B winding configuration.....	259
Fig. 6:	Test-rig setup.....	260
Fig. 7:	Thermal web measurements at rated speed and different load conditions....	261

Fig. 8:	Thermal web measurements at different speed/load conditions.....	263
Fig. 9:	2D-TSR induced thermal patterns for ITSCF diagnosis.....	264
Fig.10:	Thermal web measurements at different fault locations.....	265
Fig.11:	Fault induced thermal signature behaviour at different load levels.....	268
Fig.12:	Fault induced thermal signature behaviour at different speeds.....	269
Fig.13:	Measured shorted turns induced voltage and current in coil5-C under different speed condition.....	269
Fig.14:	Fault induced thermal signature behaviour at different speed/load.....	270
Fig.15:	Dynamic performance assessment of the 2D-TSR in comparison with FBG slot.....	271
Fig.16:	End-winding thermal visualisation using 2D representative model.....	272
CHAPTER 7:		275
PAPER 1:		277
Fig. 1:	Bearing instrumentation with FBG sensing system.....	282
Fig. 2:	Rotor instrumentation with FBG sensing system.....	283
Fig. 3:	Embedded FBG sensors thermal calibration.....	284
Fig. 4:	Test-rig setup.....	285
Fig. 5:	Measured bearing temperature by FBG-B under different load condition...	286
Fig. 6:	End-cap obtained thermal images.....	286
Fig. 7:	Analysis of mechanical operating conditions related information.....	287
Fig. 8:	FFT spectrum of thermal steady-state dynamic measurement.....	289
Fig. 9:	Measured bearing temperature by FBG-B under different load condition...	290
Fig.10:	FBG array analysis of mechanical operating conditions related information @ 100% load.....	290
Fig.11:	FFT spectrum of array thermal steady-state dynamic measurements @ 100 load.....	291

LIST OF TABLES

CHAPTER 2:	36
Table 2.1: reliability surveys on electrical machine	42
CHAPTER 3:	79
Table 3.1 : Dimensions and properties of PEEK capillary [181]	91
Table 3.2: FBG sensor specifications	94
Table 3.3: SmartScan interrogator specifications [136]	95
Table 3.4: SmartScan multiple scan rate[136]	97
Table 3.5: MJXA-FAP-155-28-FA specifications	100
Table 3.6: IM data specification	105
Table 3.7: Investigated inter-turn fault severity	107
Table 3.8: PMSM specifications	113
CHAPTER 4:	122
PAPER 1:	124
Table. I: Calculated fit curve parameters	133
PAPER 2:	155
Table. I: Tested capillaries thermal properties	170
CHAPTER 5:	177
PAPER 1:	178
Table. I: Test motor specification	183
CHAPTER 6:	225
PAPER 1:	226
Table. I: Heat loss calculation in healthy and faulty coils	231
Table II: Heat calculation in the slot section	234
Table. III: Test Motor specification	234
Table IV: Investigated inter-turn fault severity	235
Table V: Shorted turns current and heat loss components for all fault cases	242
PAPER 2:	251
Table. I: PMSM Motor specification	256

CHAPTER 7:	275
PAPER 1:	277
Table. I: Test motor specification.....	281

LIST OF ACRONYMS

2D-FE	Two Dimensional Finite Element
2D-TSR	Two Dimensional Thermal Sensing Ring
AC	Alternating Current
APC	Angled Physical Contact
AWG	American Wire Gauge
CEFT	Core Embedded Fit Curve
CM	Condition Monitoring
CMS	Condition Monitoring System
DAQ	Data Acquisition
DC	Direct Current
DE	Drive End-winding
EFC	Embedded FBG Fit Curve
EM	Electric Machine
EMF	Electromotive Force
EMI	Electromagnetic Interference
FBG	Fibre Bragg Grating
FBGAS	Fibre Bragg Grating Array Sensor
FBGS	Fibre Bragg Grating Sensor
FBGST	Fibre Bragg Grating Sensing Technology
FC	Fibre Connector
FE	Finite Element
FEA	Finite Element Analysis
FFT	Fast Fourier Transform
FL	Full-Load
FORJ	Fibre Optic Rotary Joint
FS	Full-Speed
FWHM	Full Width Half Maximum

HL	Half-Load
HS	Half-Speed
IEC	International Electrotechnical Commission
IM	Induction Machine
ITSCF	Inter-turn Short Circuit Fault
LS	Low-Speed
LV	Low Voltage
LVEM	Low Voltage Electric Machine
MCSA	Machine Current Signature Analysis
MEA	More Electric Aircraft
MMF	Magnetomotive Force
NDE	Non-drive End-winding
NEMA	National Electric Manufacturers Association
NL	No-Load
PC	Personal Computer
PEEK	Polyetheretherketon
PEFT	Pre-embedment Fit Curve
PM	Permanent Magnet
PMDC	Permanent Magnet Direct Current Motor
PMSM	Permanent Magnets Synchronous Machine
RTD	Resistance Temperature Detector
SMF	Single Mode Optical Fibre
TC	Thermocouple
TEFC	Totally Enclosed Fan-Cooled Motor
TSD	Temperature Standard Deviation
UV	Ultraviolet
VI	Virtual Instrument
WDM	Wavelength-Division Multiplexing
WSD	Wavelength Standard Deviation

ABSTRACT

This thesis reports an investigation of the design, development, implementation and use of in-situ thermal sensing systems utilising Fibre Bragg Grating Sensing Technology (FBGST) for low voltage electric machine (LVEM) thermal condition monitoring applications. The thesis first investigated the key design and operational features of the in-situ FBG temperature sensor for thermal hot spot monitoring in stand-alone prototype random wound components. Vital sensing aspects such as the sensor characterisation, packaging material choice, in-situ calibration requirements, use of multiplexing for distributed sensing, the installation procedure and the thermal measurement sensitivity to machine vibration were investigated. The reported findings enable a much improved understanding of the performance implications of embedded FBG sensor design features and the attainable in-situ hot spot thermal monitoring performance in random wound coils. It is shown that reliable, improved fidelity information on the coil's thermal status can be obtained from application of wound coil embedded FBG thermal sensing systems.

The thesis then reported the use and performance evaluation of the devised in-situ FBG temperature sensor in operational LVEMs. Different in-situ FBG thermal sensing configurations were designed and embedded into two standard LVEM topologies: an induction machine and a permanent-magnet synchronous machine. The in-situ system's on-line thermal monitoring performance was experimentally examined under different thermal conditions, ranging from typical healthy continuous and periodic running duty cycles, to deteriorated cooling system and winding fault conditions. It was demonstrated that the presented scheme has the potential to provide competent on-line measurement of critical machine thermal hot spots that are largely beyond effective reach of conventional thermal monitoring solutions. In addition, the ability of the proposed system to enable fault diagnosis through identification of fault induced localised thermal signature is also reported. The results demonstrate the capability of unambiguous recognition of inter-turn faults, including a single shorted turn, and diagnosis of fault severity, location and fault critical-thermal operating conditions. Finally, the winding thermal and electrical characteristics at inter-turn fault onset were investigated, enabling advanced understanding of fault thermal signature manifestation in a wide range of operating conditions.

The thesis also investigated the use of the FBGST multi-physical sensing feature for extracting simultaneous thermal and mechanical information of rotary components for condition monitoring purposes. It is shown that a single FBG embedded in a bearing or rotor structure can enable simultaneous understanding of component's thermal and mechanical operating conditions, and thus improved understanding of their health status.

DECLARATION

No portion of the work referred to in this dissertation has been submitted in support application for another degree or qualification for other university or other institute of learning.

COPYRIGHT STATEMENT

- i. The author of this thesis (including any appendices and/or schedules to this thesis) owns certain copyright or related rights in it (the “Copyright”) and s/he has given The University of Manchester certain rights to use such Copyright, including for administrative purposes.
- ii. Copies of this thesis, either in full or in extracts and whether in hard or electronic copy, may be made only in accordance with the Copyright, Designs and Patents Act 1988 (as amended) and regulations issued under it or, where appropriate, in accordance with licensing agreements which the University has from time to time. This page must form part of any such copies made.
- iii. The ownership of certain Copyright, patents, designs, trademarks and other intellectual property (the “Intellectual Property”) and any reproductions of copyright works in the thesis, for example graphs and tables (“Reproductions”), which may be described in this thesis, may not be owned by the author and may be owned by third parties. Such Intellectual Property and Reproductions cannot and must not be made available for use without the prior written permission of the owner(s) of the relevant Intellectual Property and/or Reproductions.
- iv. Further information on the conditions under which disclosure, publication and commercialisation of this thesis, the Copyright and any Intellectual Property and/or Reproductions described in it may take place is available in the University IP Policy (see <http://documents.manchester.ac.uk/DocuInfo.aspx?DocID=24420>), in any relevant Thesis restriction declarations deposited in the University Library, The University Library’s regulations (see <http://www.library.manchester.ac.uk/about/regulations/>) and in The University’s policy on Presentation of Theses.

ACKNOWLEDGEMENTS

My colossal gratitude goes to the Almighty Allah for giving me the opportunity, health and strength to pursue the PhD.

I would like to express my sincere gratitude to my supervisor Dr Siniša Djurović for his continuous support and invaluable guidance, motivation and patience. His supervision helped me in all the time of research and in particular writing of this thesis.

Many thanks, to the academic staff, research associates and PhD students in the Power Conversion Group at The University of Manchester for their support and friendship. I must thank Dr. Paul Tuohy, Ignacio Melecio and Jonathan Hunte for their help in proofreading some of my thesis chapters.

I would like to acknowledge the Libyan Ministry of Higher Education and Scientific Research for their financial support.

Finally, I would like to thank my parents, my wife and children, my brothers and sisters, who were my source of power during my PhD. My research would have been impossible without their support, especially at the beginning of my PhD when it was dark due to my health issues; their love was my light to continue.

Chapter 1: *Introduction*

1.1 Introduction

In recent years, the research activity in condition monitoring systems (CMSs) for electric machines (EMs) in general, and for low voltage electric machines (LVEMs) in particular, has experienced remarkable development [1-4]. This is largely due to the much intensified use of electric machinery in existing but also in many novel and critical industrial applications [5-8]. The health condition of the utilised EMs is often of vital importance for the overall system process, as it directly affects its integrity and indirectly its financial viability. EM performance, reliability and availability are thus key for modern industrial applications. Research to develop new techniques for rotating EM health monitoring and to enable reliable and early fault diagnosis are thus of considerable importance [1, 3, 9-11].

One of the important aspects of EM condition monitoring is thermal monitoring, since thermal stress is one of main contributors to failure, as well as performance and lifetime reduction [10, 12-16]. The existing thermal monitoring techniques are limited in effective provision of machine full thermal status, including critical, device embedded, hot spots and distributed sensing; further limitations exist with these where monitoring reliability and safety are concerned [17-20]. An alternative thermal monitoring technique is provided by recent advances in Fibre Bragg Grating Sensing Technology (FBGST). The features of FBGST such as size, electric and electromagnetic immunity, flexibility and capability of distributed sensing make it an attractive solution for effective in-situ and distributed thermal monitoring in EMs, and has the potential to overcome the limitations of existing thermal monitoring techniques.

The main aim of this PhD research is to investigate the potential use of FBGST for improved thermal monitoring in LVEMs. To this end this research first examines the FBGST sensing application aspects in LVEMs (i.e. in-situ sensor design, installation, characterisation and calibration), as this is a novel application in LVEMs that has not been fully investigated and understood. The second part of this research focuses on investigating the utilisation of this technology for healthy and faulty thermal condition monitoring in LVEMs.

1.2 LVEMs developments

LVEMs are no longer considered as simple motors, generators and pumps employed in conventional industrial applications. In recent decades, there has been a considerable development in LVEM manufacture and operation, including new designs, materials, topologies and operating and control techniques [21, 22]. Consequently, the use of these machines has been extended beyond that of conventional applications. With the new ‘more electric’ industry trends, modern LVEMs are being incorporated in the core of several novel and safety-critical energy conversion systems such as those in air and ground transportation and wind energy industries [5, 6, 21, 23].

In the aircraft industry, the more electric aircraft (MEA) trend has promoted the use of a considerable number of LVEMs, including induction, permanent-magnet and reluctance machines, ranging from 1-50 kW, in a single modern civil aircraft. These LVEMs perform and enable high precision and safety critical functions such as flight control, landing systems and fuel pumping [5]. Electric vehicle manufacture is another novel industry largely underpinned by the development of high efficiency and reliability LVEMs. Different LVEM topologies are currently used in commercial electric vehicles available in the market [6]. In wind power generation, LVEMs are found at the core of most modern wind turbine systems: in addition to the MW size electric generator that is the vital element of these systems, they employ a number of smaller power rating LV motors, such as those used in yaw and pitch drive systems [8, 23].

In modern industrial applications, aspects such as safety, reliability, efficiency and automation are highly demanded and present key areas for consideration in system design. This in turn imposes increased requirements for safety, reliability and efficient performance of the LVEMs used in these applications [8, 24]. Ineffective LVEM performance can adversely affect overall system performance; furthermore, failures in these machines do not solely cause expensive repairs, but can also cause expensive loss of production such as in high power off-shore wind turbine systems, or even potential loss of life, such as in modern aircrafts and electric ground vehicles. LVEMs are complex and interconnected multi-physical systems that include electric, magnetic, thermal and mechanical structural features. This imposes constraints and limitations during their operating life, to ensure avoidance of machine exposure to high electrical, mechanical and thermal stresses, which directly affect their performance and integrity [10, 11]. The availability of CMS that monitor critical LVEM operational parameters on-line is essential

for enabling a reliable understanding of machine operational integrity and insuring its proper functioning [25].

Conventional EM CMSs are based on continuous monitoring of vital electrical, thermal and mechanical parameters and perform processing techniques to extract diagnostic indices that carry information on the machine operational status. The common commercially available monitoring techniques that have received significant research attention are vibration, thermal and electric/magnetic signals analysis [26-29]. Here thermal monitoring of LVEM components is of particular importance, as thermal stresses in these machines are considered a major contributor to their lifetime and performance reduction [12, 14, 15, 17, 30, 31]. The following section will address the thermal issues in LVEMs and highlight its significance.

1.3 LVEMs thermal issues

The output power of an EM is limited by the allowable current that can flow in the machine winding conductors. This current is limited by the permissible operating temperature of the windings insulation system. Operating at temperatures close or above the permissible winding insulation rated temperature can thermally stresses the insulation material and hence significantly reduces its life time. Therefore, a general trend is to apply overly conservative safety margins by over sizing, or to employ a higher insulation system class and/or cooling system design. However, with the demand for high power density machines that are small size and light weight for modern applications the over sizing/over rating safety methods become very challenging to apply [32].

The insulation system is thus very important in EMs. It is generally highly required for it to provide high dielectric strength with good thermal properties. However, from the perspective of insulation material performance this requirement is challenging [22]. Typically, in most materials the electrical and thermal properties are directly proportional; materials with good electrical properties also have good thermal properties. In modern EMs, the insulation materials deliver high dielectric strength properties but possess relatively weak thermal and mechanical properties. Elevated temperature can thus lead to insulation degradation and hence insulation breakdown [1].

The heat generated in EMs is due to the induced electrical, magnetic and mechanical losses dissipated to the surroundings. Electrical loss (i.e. copper loss) generally contributes the highest percentage of machine total loss. However, its magnitude is temperature dependant [33], as change in the windings temperature results in a change of its electrical

resistance (temperature rise of 50 °C above ambient increases the resistance by 20 %) and thus copper loss, assuming constant current. This means that operating at higher temperatures can lead to undesirable increased losses and the corresponding excess heat exposes machine components to detrimental thermal stresses [33].

Modern EMs are generally integrated with power electronics and control systems (electrical drives) for enabling adequate machine performance in different operating modes. Integrated control systems generally use the machine electric and magnetic parameters, some of which are temperature dependent. Therefore, for accurate and reliable performance of these control systems under different operating conditions, real time correction of control parameters related to the operating temperature state is highly required [12, 34].

Permanent-magnet EMs are a key enabling topology for many novel industrial applications. The performance of permanent-magnet machines largely depends on the embedded magnets' performance. The magnet's characteristics are affected by the operating temperature; their performance generally degrades with temperature increase leading to complete demagnetisation at high temperature, as can be caused by operating conditions such as overloading or a fault condition such as winding faults. To ensure reliable and effective operation of permanent-magnet EMs preventing magnet demagnetisation due to temperature, the magnet temperature must be kept at safe temperature value [35].

Cooling systems are very important for EMs. These act to accelerate the process of dissipating the heat induced within the machine structure to the surrounding ambient and to ensure the machine components' temperatures are maintained below permissible thermal limits. Cooling systems can fail or suffer a performance degradation resulting in significant overheating of machine components [36]. In modern wind turbine generators for example, rated powers are gradually nearing the 10 MW rated power boundary – the losses in a standard 8 MW permanent magnet generator at 98% efficiency are ≈ 160 kW. Failure to efficiently remove such heat losses can cause significant damage [37].

Rotary bearings are key machine components. Bearing temperatures need to be maintained below a prescribed level as these can be prone to failure due to high operating temperatures [38]. In general, bearing temperatures can be internally elevated due to improper installation, fatigue or lubrication degradation. Normally, a bearing produces a relatively small amount of heat during operation. However, its temperature is related to

thermal conditions in other machine components such as stator windings and the rotor. A temperature rise in these can thus results in a bearing temperature rise [26].

Electrical and mechanical failures in EMs generate heat in the internal faulty components. The resultant thermal excitation can be harmful not only for the failing component but also to surrounding healthy components, e.g. the damage that can occur to the core due to winding faults [39]. The level of fault induced heat and its propagation rate depends on the type of fault. In electrical failures such as winding faults, this is relatively high and fast. Conversely, for mechanical faults it is relatively low and slow [34]. Most importantly, if the fault thermal features can be appropriately measured they can be used for fault diagnosis [39].

In summary, it is evident that overheating in LVEMs can cause component degradation, life time reduction, and failures, and that increased thermal levels can be a sign of a developing fault. Furthermore, the performance of LVEMs is directly affected by their thermal status. Therefore, thermal monitoring is a fundamental requirement for modern LVEMs protection, and reliable and effective performance. This is particularly pertinent where the thermal conditions of the machine's most critical components to thermal stress are concerned.

Windings are the most critical component in EMs where thermal stress effects are concerned, as their insulation integrity is temperature dependant. Winding failures have been reported to be one of the most frequent failure event in LVEMs, and their diagnosis remains a challenging task, in particular at an incipient fault stage [10]. Windings have the highest temperature rise level and the fastest thermal time constant among all machine components and are the major contributor to net heat induced within a machine. Therefore, windings can reach their permissible temperature before other machine components. The winding temperature affects the thermal status of all other machine components, and elevated windings temperature will cause elevated temperatures in other machine parts. In a faulty condition, windings induce a significant amount of heat with a relatively fast propagation rate, which can cause catastrophic damage to the machine components.

Therefore, thermal monitoring of EMs is largely based on stator winding temperature monitoring, as this presents a key parameter for machine protection and performance. In addition to the stator winding, the thermal condition monitoring of the rotor structure including bearings is also important for ensuring machine reliability and effective performance.

1.4 Thermal condition monitoring issues

The current practice for monitoring winding thermal conditions is based on employing embedded thermal sensors or temperature estimation techniques [20]. The latter are generally established using a thermal model-based or a parameter-based temperature estimator [19, 31, 40]. Evaluating winding temperature using a parameter-based temperature estimator is achieved by estimating on-line the winding electrical resistance and hence its temperature [40]. However this cannot provide a full thermal image of the winding nor its hot spots, and yields only the average winding temperature, whilst also being limited in accurate tracking of thermal change during fast transient conditions [41]. Winding temperature monitoring using thermal model-based estimators such as finite element (FE) or lumped network models, can provide detailed information about thermal gradients and hot spots. However, thermal models impose considerable constraints: the FE models are computationally demanding and therefore not effective in on-line applications, whilst lumped network thermal models impose complexity in appropriate evaluation of model parameters including parameter dependency on thermal conditions [19, 40].

Winding temperature gradient and hot spot monitoring using conventional sensing techniques such as thermocouples (TCs) or resistance temperature detectors (RTDs) can be limited for safety critical applications, primarily due to inherent use of electrically conductive material in the sensor structure. This poses a risk to the winding and the sensing system integrity. Insulating these sensors with appropriate packaging can minimise this risk. This however considerably increases the sensor structure size, which can be impractical where the machine geometries of interest for monitoring, such as the slot areas, are concerned [25, 42]. In addition, their intrinsic low electromagnetic interference (EMI) immunity and low resistance to harsh environmental conditions do not favour their long term deployment in EMs. Another reason for conventional thermal sensing systems not being preferred for distributed sensing applications due to their limiting connection, installation and acquisition requirements.

The existing thermal monitoring techniques limitations are further highlighted when applied for rotor structure thermal monitoring. This is due to the limited access to the rotor structure and hence, its electrical parameters for temperature based estimation techniques [15]. While embedding thermal sensors in rotors presents a considerable challenge such as the complexity of installation and wiring, and the data transmission between the rotor and a stationary external sensing platform is non-trivial [13].

1.5 Problem statement

As highlighted in previous sections, thermal monitoring is imperative for enabling effective protection and performance of LVEMs. This is particularly pertinent in the light of rising demand for efficient and reliable LVEMs for future industrial and transport applications. Thermal monitoring of LVEM's hot spot can enable increase awareness of their operational thermal status and thus, enhancing machine thermal management and performance. Targeted hot spots monitoring could also allow prevention of any degradation process acceleration and hence, life time reduction of components most susceptible to thermal stress. Moreover, localised hot spots monitoring could provide improved fidelity indication of fault and be used for its diagnosis and prognosis.

The existing thermal monitoring techniques are limited in safe and accurate monitoring of the highest temperature points in LVEMs. This is particularly valid where the winding internal thermal conditions are concerned, as these are invariably the points of highest temperature within a machine. The temperature estimation techniques only provide the average temperature of the stator winding. While conventional sensors can provide information on localised temperatures, they impose significant constraints for safe and practical measurements of winding internal temperature. Another limitation of existing techniques is their practical inability to provide a full thermal picture of the winding distributed temperatures and limitations in enabling effective monitoring of rotor structure temperatures.

A thermal sensing alternative is therefore proposed in this thesis by recent advances in fibre-optic FBGST, whose inherent EMI immunity, robustness, multiplexing, flexibility and size make it an attractive candidate for facilitating operative solutions for machine component embedded thermal monitoring [43]. The interest in applying FBGST in EMs has been reported in very recent literature [44-49]. While promising, the FBG potential for thermal condition monitoring in LVEMs has not been fully explored nor understood. The currently reported studies mainly focus on large form wound winding structures [43, 50] and non-direct contact winding [49, 51] temperature monitoring in LVEMs, and do not consider coil embedded hot spot locations that are of critical interest. Moreover, the proposed FBG temperature sensor design includes metallic packaging, which is not appropriate for inherently electric and electromagnetic environment such as that in a machine winding.

This PhD research examines the application of FBGST to provide advanced thermal monitoring and diagnostics in LVEMs. This study aims to develop in-situ distributed thermal sensing system that enables effective real time tracking of windings internal and rotor structure temperatures. This aim imposes a number of research challenges: the first is the multidisciplinary requirement for this research, requiring additional scientific backgrounds to that in electric machinery operation and condition monitoring, such as photonics, sensing and heat transfer analysis. The development of a new EM sensing application based on an unstandardised technology such as FBGST for new applications such as internal machine structure monitoring requires a careful consideration of the important sensing aspects, such as sensor design, characterisation, calibration and installation due to the imposed constraints by targeted sensing locations and environments. This requires a wide investigation before sensing performance examination in operational devices is undertaken.

1.6 Objectives

To accomplish the aim of proposed research the following set of objectives have been defined:

- Investigate and understand the key operational and design aspects of FBGST including their fabrication, integration and sensing principles, and conduct a literature review of existing FBGST applications for EMs. This will help understand the features of FBGST and opportunities for the targeted sensing application in this research.
- Develop an in-situ thermal sensor based on FBGST aimed at enabling hot spot monitoring in a random wound coil structure; and ensure the sensor design satisfies the current carrying coil application requirements, e.g. is dielectric, electromagnetically passive and physically flexible and small in size. Finally, examine the possibility of designing a distributed thermal sensing network interior to the coil structure.
- Develop laboratory test-rig facilities utilising prototype random wound coil systems to examine and improve the performance and efficacy of the developed in-situ thermal sensors for on-line monitoring of coil internal thermal conditions.
- Investigate the performance implications of the installation procedure, characterisation, calibration and in-situ sensing performance of a wound coil embedded FBG thermal sensor as precursor to enabling further development of embedded sensing applications within operational devices.

- Research and understand hot spots and hence, the optimal thermal sensing placement in conventional LVEMs by developing conventional thermal models using a commercial EM's thermal model software package. Another important purpose of the developed thermal models is to enhance the understating of conventional LVEM heat transfer and thermal behaviour in healthy and faulty conditions, as well as to enable cross-correlation with obtained experimental results.
- Design and develop laboratory test-rig facilities to enable a full investigation of the developed in-situ FBG thermal sensing system performance in conventional LVEMs, and investigate its potential for providing on-line thermal monitoring in healthy and faulty operating conditions. To this end an induction machine and a permanent-magnet low voltage machines will be examined, and their stators re-wound to enable installation of the developed FBG sensing scheme, as well as the emulation of a variety of stator winding fault scenarios.
- Conduct an experimental investigation of the feasibility of using the proposed in-situ FBG sensing system for on-line hot spots monitoring in operational LVEMs using the embedded random wound machines with FBG sensing system. The thermal behaviour of the stator windings and the in-situ FBG sensing system performance will be studied and evaluated under different operating conditions including different loads, thermal cycles and supply conditions (grid/inverter connected).
- Perform experimental studies to investigate the potential use of in-situ FBG temperature sensors for stator winding fault diagnostics based on in-situ thermal signature monitoring. The investigation will include scenarios of short circuit faults in both tested machine topologies.
- Investigate the use of FBGST for LVEM rotary component sensing applications. A proof of principle investigation will also be conducted to ascertain the feasibility of FBG enabled simultaneous in-situ thermal and mechanical sensing in rotary components of operational LVEMs for condition monitoring purposes.

1.7 Contribution of the research

The main contributions of this research are summarised in the following points:

- A novel in-situ thermal sensor for single and/or distributed hot spots monitoring within random wound current carrying coils is reported in this work. The thermal sensor design is based on FBGST. The in-situ thermal sensor is small in size, non-conductive and EMI immune.

- A detailed insight into the installation and calibration procedures requirements, and characterisation of the proposed in-situ FBG thermal sensor is provided. Furthermore, an evaluation of its in-situ sensing performance on a stand-alone prototype coil test systems is reported, as a precursor to enabling further development of embedded sensing applications within operational devices.
- A new on-line internal distributed temperature measurement in low voltage random wound stator windings based FBGST is reported. The proposed technique enables real-time monitoring of stator winding hot spot temperatures, which is extremely challenging to achieve at the same efficacy levels with conventional thermal monitoring techniques. Analysis of the thermal behaviours of the examined machines based on the obtained in-situ FBG thermal measurements is also reported.
- A new technique for on-line detection of winding faults in random wound electric machines based on winding in-situ thermal signature monitoring using coil embedded FBG temperature sensors is reported. This technique can provide reliable diagnosis of winding faults at early stages (i.e. a single turn short), as well as fault severity diagnosis and identification of the fault location in windings. Unlike leading winding fault diagnostic techniques reported in the literature, the method developed in this research does not require complex real time processing of monitored signals to achieve diagnosis.
- This thesis reports an analysis of the EM stator winding thermal and electrical characteristics at the onset of inter-turn faults with a view to enhancing their usage for fault diagnostic purposes. The analysis enables understanding of the fault induced thermal signature behaviour and thus the determination of fault critical thermal operating conditions. Furthermore, it enables better correlation of electrical and thermal characteristics of winding fault and therefore enables development of improved multi-source fault diagnostics.
- The thesis also reports a feasibility study of on-line thermal and mechanical health condition monitoring of bearing and rotor structures of conventional low voltage induction machine design based rotor in-situ FBGST application.

1.8 Structure of the thesis

This thesis has been formatted and written up on the basis of the Journal Format Thesis approved by the School of Electrical and Electronic Engineering and permitted by The University of Manchester [52]. The journal format thesis allows writing chapters in the thesis in a format suitable for publication. These chapters can include published

contributions during PhD research, in press contributions and submitted or ready for submission contributions. Therefore, this thesis includes four main chapters (**Chapter 4 to Chapter 7**) written in peer-reviewed paper format; each chapter consists of two papers, with the exception of the last chapter, which contains a single paper. Each chapter will contain an introduction section that details the purpose and the structure of the chapter, and explains the connection between chapter contributions and the overall thesis contribution. The introduction also clarifies the contribution of the other authors to the papers. Generally, the papers in the paper-style chapters include two authors. The second author is the supervisor of this PhD who contributed to the conception of the presented ideas in a supervisory role.

The papers presented in **Chapter 4 to Chapter 7** are formatted based on the template for IEEE Transactions/Journals publications, with the exception of the font size and one column format presentation to maintain consistency with the thesis margins. The thesis also includes other chapters (**Chapter 2 and Chapter 3**) to enhance the overall research understanding by providing insight on the research background, the techniques used and the description of the developed test-rigs and simulation.

The journal format style of this thesis incorporates publication-style chapters and thus inherently led to some duplication in the texts, figures, tables and equations. This is because the written up publication-style chapters have self-contained components that can overlap with other section of the thesis. However, this repetition enhances the readability, as each chapter in the thesis can be read independently.

Following the introduction chapter, the thesis is organised as follows:

Chapter 2 is a literature review chapter; it is divided into two main sections:

Section one: reviews LVEMs' common failure modes and their root cause, with a particular focus on temperature as main a contributor to failure. It also provides an overview of LVEMs' most common condition monitoring systems. The final part of this section presents a literature review on LVEM thermal condition monitoring, discussing the need for thermal monitoring in LVEMs and identifies the existing thermal monitoring techniques features and limitations.

Section two: presents an overview of FBGST including the FBG sensor structure, fabrication, interrogation and sensing principles. The advantages and disadvantages of FBGST in general, and for electric machine sensing applications in particular, are also

presented and discussed. Finally, a literature review on FBGST applications for rotating electric machines is reported.

Some of the **Chapter 2** contents will be summarised in the papers' introduction and theoretical background sections of the main chapters (**Chapter 4 to Chapter 7**) to help understanding the research problem and background relevant to each paper.

Chapter 3 describes the simulation and experimental test-rigs setup development for this PhD research. This chapter is also divided into two main sections:

Section one: describes and explains the development of thermal models for the two examined machine topologies using a commercial software package (Motor-CAD). The Motor-CAD thermal model package concept, the models development and tuning procedure are explained.

Section two: demonstrates and explains the developed test-rigs setup and tools used in the research including: 1) the FBG sensing system (i.e. sensors packaging and design, interrogation and software package); 2) the calibration and characterisation test-rig setup; 3) the prototypes random wound coil system rigs; 4) the test-rig layouts, construction, operation and design features of two embedded LVEM topologies with FBGST; 5) and, test-rig setup for rotor structure FBG sensing applications.

Although complete details of experimental test-rigs are provided in this chapter, the paper style chapters (**Chapters 4 to 7**) also include sub-sections on experimental setup that repeat some of key relevant information.

Chapter 4 investigates embedment and calibration methodologies, characterisation and performance assessment of the in-situ FBG temperature sensor for internal distributed thermal monitoring in random wound components. This chapter reports a series of experiments undertaken on prototype random wound coil systems embedded with FBG temperature sensors. The target application in this chapter is to provide an insight into the performance implications of the installation procedure of a wound coil embedded FBG thermal sensor and an assessment of its in-situ sensing performance and features considering the physical features of the electrical machine environment; this enables the application of these sensors in operating LVEMs later in this research. This chapter consists of two papers. The first paper is a collection of contributions published in three *IEEE conferences* [48, 53, 54], and one *Elsevier journal* [55]. The contents of the second paper have been published in a leading IEEE journal on sensing technology (*IEEE Sensors*) [56].

Chapter 5 reports the use of in-situ FBG thermal sensing for on-line distributed thermal monitoring of stator winding internal temperature in random wound LVEMs. This chapter aims to investigate the capability and performance of the proposed and examined in-situ FBG sensor in **Chapter 4** for thermal monitoring in operational LVEMs. The chapter is formed by two papers. The contents of the first paper has been published in *IEEE Transactions on Energy Conversion* [17]. In this paper, the reported scheme is evaluated on induction machine design operated in grid supplied conditions under dynamic thermal cycles defined by the relevant IEC standard. The thermal sensing performance was cross-correlated with a thermal model developed in **Chapter 3** and conventional electrical thermal sensors. In the second paper, the multiplexing feature of FBG sensing technology was investigated to create a distributed thermal sensing network for internal monitoring and evaluation of stator winding temperature [*not submitted*]. The proposed distributed in-situ FBG sensing system was used to evaluate the examined induction machine performance under degraded cooling system capability.

Chapter 6 is structured of two papers, which report studies to examine the potential of using the in-situ FBG sensing system for on-line diagnoses of winding faults in LVEMs based on winding in-situ thermal signature monitoring. The first paper has been published in *IEEE Transactions on Industrial Electronics* [57]. The paper reports a series of experimental tests on an inverter driven induction machine embedded with targeted in-situ FBG sensors. The diagnostic potential of the in-situ monitored inter-turn fault thermal signature was examined in steady-state and in transient operating conditions with a particular focus on the critical, incipient fault stages. In the second paper, the proposed technique was considerably optimised to enable entire stator winding system monitoring and diagnostics. The optimised in-situ sensing design for winding fault diagnosis was examined on a fault tolerant winding permanent-magnet machine design [*not submitted*].

Chapter 7 comprises of a paper that reports a feasibility study on simultaneous thermal and mechanical sensing in rotary components of LVEMs using FBGST. The performance of the FBG sensing system was evaluated under different operating conditions [*submitted to IEEE International Electric Machine & Drive Conference, IEMDC2019*].

Chapter 8 will provide conclusions of the thesis and suggestions for future work directions.

1.9 List of publications

1.9.1 Papers published/submitted as result of this research

Journals:

1. **A. Mohammed** and S. Djurović, "FBG Thermal Sensing Features for Hot Spot Monitoring in Random Wound Electric Machine Coils," in *IEEE Sensors Journal*, vol. 17, no. 10, pp. 3058-3067, May15, 2017.
2. **A. Mohammed** and Siniša Djurović, "A study of distributed embedded thermal monitoring in electric coils based on FBG sensor multiplexing," *Elsevier Microprocessors and Microsystems*, vol. 62, pp. 102-109, March 2018.
3. **A. Mohammed** and S. Djurović, "Stator Winding Internal Thermal Monitoring and Analysis Using In-Situ FBG Sensing Technology," in *IEEE Transactions on Energy Conversion*, vol. 33, no. 3, pp. 1508-1518, Sept. 2018.
4. **A. Mohammed**, J. I. Melecio and S. Djurovic, "Stator Winding Fault Thermal Signature Monitoring and Analysis by in situ FBG sensors," in *IEEE Transactions on Industrial Electronics*, 2019.
5. **A. Mohammed** and S. Djurovic, "Multiplexing FBG Thermal Sensing in Stator Windings Interior for Distributed Thermal Monitoring in In-service Electric Machines," submitted to *IET Electric Power Applications*, 2019.

Conferences:

1. **A. Mohammad** and S. Djurović, "Evaluation of fiber-optic sensing performance for embedded thermal monitoring of electric machinery wound components," 2016 *IEEE 5th Mediterranean Conference on Embedded Computing (MECO)*, Bar, 2016, pp. 72-76.
2. **A. Mohammed**, S. Djurović, A. C. Smith and K. Tshiloz, "FBG sensing for hot spot thermal monitoring in electric machinery random wound components," *IEEE XXII International Conference on Electrical Machines (ICEM)*, Lausanne, 2016, pp. 2266-2272.
3. **A. Mohammed** and S. Djurović, "FBG array sensor use for distributed internal thermal monitoring in low voltage random wound coils," *IEEE 6th Mediterranean Conference on Embedded Computing (MECO)*, Bar, 2017, pp. 1-4.
4. **A. Mohammed** and S. Djurović, "A Feasibility Study of Embedded FBG Thermal Sensing Use for Monitoring Electrical Fault Induced Thermal Excitation in Random Wound Coils," *9th IET international Conference on Power Electronics, Machines and Drives (PEMD)*, 2018.
5. **A. Mohammed**, and S. Djurović. "A Feasibility Study of Simultaneous Thermal and Mechanical Fibre Optic Sensing for Electric Motor Rotary Components

Condition Monitoring." Submitted to *IEEE International Electric Machines and Drives Conference (IEMDC)*, 2019.

1.9.2 Publications produced during this PhD study not in the research focus of thesis work

During the PhD research period, the research was involved in related studies that resulted in following contributions.

Journals

1. D. Zappalá, N. Sarma, S. Djurović, J. Crabtree, **A. Mohammad**, P. Tavner, "Electrical & Mechanical Diagnostic Indicators of Wind Turbine Induction Generator Rotor Faults, " *In Renewable Energy*, vol. 131, 2019.
2. **A. Mohammed**, J. I. Melecio and S. Djurovic, "Open Circuit Fault Detection in Stranded PMSM Windings Using Embedded FBG Thermal Sensors," in *IEEE Sensors Journal*, 2019.

Conferences

1. K. Tshiloz, A. C. Smith, **A. Mohammed**, S. Djurović and T. Feehally, "Real-time insulation lifetime monitoring for motor windings," *2016 XXII International Conference on Electrical Machines (ICEM)*, Lausanne, 2016, pp. 2335-2340.
2. N. Sarma, **A. Mohammed**, J. I. Melecio, K. Tshiloz and S. Djurović, "An experimental study of winding fault induced slot harmonic effects in the cage rotor induction machine stator current," *8th IET International Conference on Power Electronics, Machines and Drives (PEMD 2016)*, Glasgow, 2016, pp. 1-6.
3. **A. Mohammed**, N. Sarma and S. Djurović, "Fibre optic monitoring of induction machine frame strain as a diagnostic tool," *2017 IEEE International Electric Machines and Drives Conference (IEMDC)*, Miami, FL, 2017, pp. 1-7.
4. J. I. Melecio, **A. Mohammed** and S. Djurović, "Towards embedded intelligence enabled autonomous condition monitoring systems for AC motor drives," *IEEE 7th Mediterranean Conference on Embedded Computing (MECO)*, Budv, 2018.
5. M. Heggo, **A. Mohammed**, J. Melecio, K. Kabbabe, P. Tuohy, S. Watson and S. Djurović, "Evaluation and mitigation of offshore HVDC valve hall magnetic field impact on inspection quadcopter propulsion motors," in press *EERA DeepWind'2018, 15th Deep Sea Offshore Wind R&D Conference*, 16 – 18 January 2019, Trondheim, Norway.
6. Juan I Melecio, **A. Mohammad** and S. Djurović, "3D-printed rapid prototype rigs for surface mount PM rotor controlled segment magnetisation and assembly," submitted to *IEEE International Electric Machines and Drives Conference (IEMDC)*, 2019.

7. A. Stetco, **A. Mohammed**, S. Djurović and G. Nenadic "Deep learning for wind turbine operational state prediction: towards feature-less condition monitoring," submitted to *25th ACM Sigkdd Conference on Knowledge Discovery and Data Mining, 2019*.

Chapter 2: *Literature Review*

2.1 Introduction

The literature review is divided into two main sections: 1) review on LVEMs failure modes, condition monitoring and thermal monitoring techniques; and 2) review on FBGST and its recent applications for LVEMs.

2.2 LVEM failure modes and condition monitoring review

LVEMs are subjected to undesirable stresses on their structures while in service, which affects their performance and increases the risk of premature failures [4]. These faults, generally, lead to unscheduled downtime, loss of production, catastrophic damage and hence, have associated high maintenance costs [23, 42, 58, 59]. As a consequence, different CM approaches have been reported, developed and integrated in modern LVEM applications to predict pending failure. Thermal monitoring is one of fundamental LVEM monitoring techniques used for fault diagnosis and to enhance reliability and performance, as thermal conditions are a key operational factor for EMs. This section provides an overview on LVEMs failure modes and their root causes, with a particular focus on temperature as the main contributor to failure and as fault indicator. The section also reviews the available condition monitoring systems for LVEMs and in particular their thermal monitoring techniques.

2.2.1 Classification of LVEMs failures and their root causes

The failure modes in LVEMs can be broadly classified into three categories: electrical, mechanical and other failures. This classification is largely based on the machine components physical structure [1]. The main causes of LVEM failures are the stresses imposed on their structure during operating life, i.e. thermal, mechanical, electrical and environmental stresses. These invariably cause machine component degradation and lead to component breakdown [26, 60].

2.2.1.1 Electrical failures

Electrical failures include the stator and rotor related electrical failures, which will be explained in the following sub-sections.

A. Stator-related failures

The stator in an EM is an important component; it forms a large portion of the overall structure of the machine. In LVEMs the stator winding compromise random wound coils that are made of insulated copper wire. These coils are placed and distributed in the stator core slots, which are insulated from the core by the ground slot wall insulation (slot liner). One slot can contain a collection of individual conductors of one or two coil sides for either the same phase or two different phases. The coil sides are insulated from each other by a coil separator, as shown in Fig 2.1.a [33]. The random wound coils ends are firmly combined to form the end-winding portions in the machine drive and non-drive ends (see Fig 2.1.b). The winding is impregnated to increase rigidity against mechanical stresses due to magnetic forces and vibration, and to enhance heat dissipation [22].

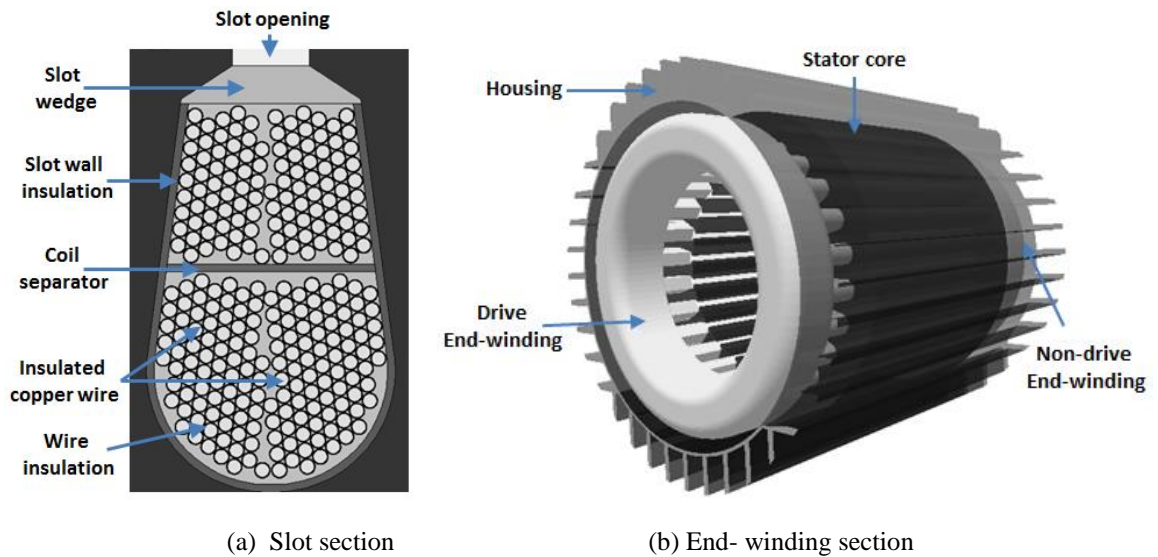


Fig 2.1: Illustration of the winding structure in random wound LVEMs

1. Insulation failure

Random wound windings are structurally complicated and their integrity is highly dependent on the insulation integrity. Stator windings are subjected to different stresses while they are in service, e.g. thermal stress caused by thermal cycling or overheating, mechanical stress due to vibration, and electrical stress induced by voltage spikes in inverter-driven topologies [61]. The insulation system integrity and lifetime are largely affected by the aforementioned stresses, and it has been reported that insulation breakdown is one of most common failure modes in LVEMs [10, 58]. An insulation system failure usually results in unscheduled downtime and irreversible damage to the machine's components. Therefore, a diagnostic and prognostic determination of the insulation degradation in its early stages is important.

Among all stress which the winding insulation system is exposed to, thermal stress is considered as the main contributor to insulation degradation. The mechanism of reducing insulation lifetime due to thermal stress is known as the thermal aging process. A generally accepted criterion is that insulation lifetime is reduced by 50% with exposure to each 10 °C increase above the permissible insulation operating temperature [61]. The insulation system used in an LVEMs is classified by standards such as NEMA [62], which are based on the maximum allowable operating temperature whilst in service. The insulation maximum permissible temperature is recognised as the sum of the ambient temperature (max 40 °C), the permissible temperature rise above ambient temperature and the hot spot allowance temperature. The hot spot allowance is to ensure a thermal safety margin for winding hot spots that may be difficult to measure or estimate [17]. Therefore, it is necessary to monitor the winding temperature, especially the hot spots, to ensure the operating temperature is below the insulation thermal limit.

2. Stator winding faults

Stator winding faults are typically a consequence of the windings' insulation system breakdown. The complex nature of the random wound winding structure and the stresses imposed on its insulation system significantly increase the risk of winding faults. Two types of fault scenarios may generally occur in random wound windings: open circuit faults or short circuit faults [16]. An open circuit fault is a complete loss of one or more of the machine phases or a strand in a stranded winding configuration. Open circuit faults can generally be caused by improper connections or as a consequence of a short circuit fault [63].

The winding short circuit fault can be classified as: inter-turn fault, phase-to-phase fault or a phase-to-ground fault, as shown in Fig 2.2. The latter two fault types generally result from a propagated inter-turn fault. A short circuit fault starts with an insulation breakdown between two adjacent turns of the same coil in the slot or end-winding sections, which gives rise to a turn-to-turn short circuit fault [64]. This fault generates high circulating current, which flows in the shorted turns, resulting in localised high temperature spots. The resulting inter-turn fault induced thermal excitation degrades the insulation of neighbouring healthy turns and hence, more turns are gradually involved in the fault. This further propagates through the coil and the damage can eventually reach the coil separator or the slot wall insulation, ultimately causing either phase-to-phase and/or phase-to-ground faults. These faults are more serious and can cause permanent damage to the machine's components relatively quickly [65]. Fig 2.3 shows photos of LVEM stator winding faults

in their final stage. Detecting winding short circuit faults at the incipient stages of an inter-turn fault is important to prevent catastrophic damage to the machine [66]. Diagnosis of inter-turn faults at the incipient stage remains a challenging task in EM fault diagnostics [3, 10].

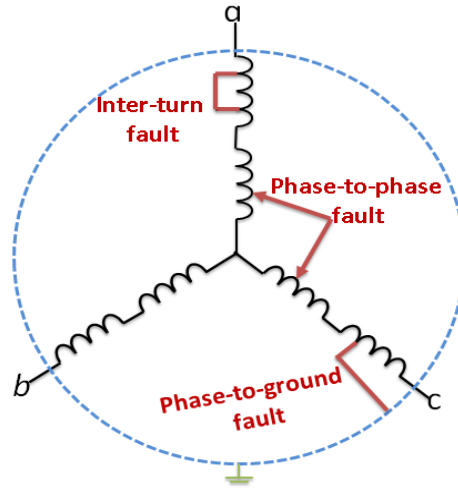


Fig 2.2: Types of short circuit faults in a random wound winding



Fig 2.3: Stator winding failures in a slot and an end-winding section [67]

There is minimal data available on the transition time of fault propagation from the instant of an inter-turn fault (i.e. a few turns involved) occurrence to the instant of winding breakdown failure. There are many factors that can effect this transition period such as machine design, rating and operating conditions [61]. It can generally be concluded that estimating the propagation time of winding short circuit faults is a challenging task; it has been reported that this time can vary from seconds, to hours [68, 69], or even days and months [70]. However, the excessive heat induced by a winding short circuit fault can be considered the main factor that affects this transition. Knowing the temperature in the faulty part of the winding can not only be used for fault detection, but also to assist in estimating the time to reach critical insulation breakdown temperatures of the adjacent healthy turns, which is a crucial aspect in determining the time available for corrective action to be applied.

3. Core failure

The stator core in EMs has two major functions: 1) it provides the path for the magnetic field and 2) it houses the electrical windings. Generally, the core is built of thin insulated steel laminations, which are stacked together to minimise the core losses. Failures in the stator core generally lead to loss of production, long shutdown periods and high maintenance costs [39]. The causes and failure modes of stator cores in large and small size machines have been reviewed in literature [1, 39, 61]. For LVEMs, it can be summarised that the core integrity is largely affected by overheating, which may result in degrading the core inter-laminar insulation and/or melting the core. The high temperature generated in case of winding faults, for example, can cause localised damage to the core. Fig 2.4 shows photos of a damaged stator core due to overheating.

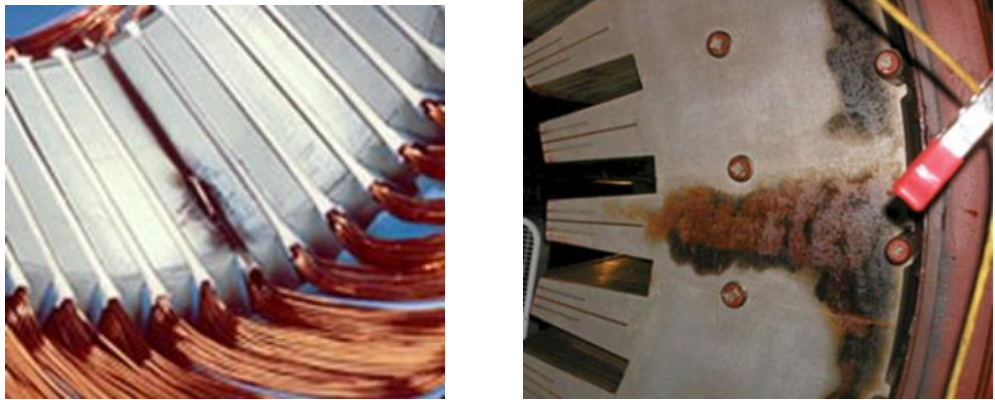


Fig 2.4: Core failure due to stator winding electrical faults [71, 72]

B. Rotor-related failures

The rotor structure in LVEMs is different from one machine topology to another. Hence, the failure modes and their root causes also differ from one rotor topology to another. For example, broken rotor bars are the most common failures in cage rotor machines, and insulation and slip rings failures are the most common in wound rotor machines [1]. In permanent-magnet machines the rotor failures predominantly arise due to magnet demagnetisation.

A common cause of failure in rotors is thermal stress. Overheating can cause cracks in squirrel cage rotor bars and can also lead to insulation integrity degradation in wound rotors, leading to catastrophic damage of the rotor structure [16], as shown in Fig 2.5. High temperatures such as those caused by overloading or winding faults can eventually lead to rotor magnets demagnetisation in permanent-magnet machines [73]. Rotor structure temperature must be maintained below the operating permissible temperature to prevent breakdowns.



Fig 2.5: Rotor failures in induction machines: a) squirrel cage rotor, b) wound rotor [74]

2.2.1.2 Mechanical failures

Mechanical failures include failures in machine mechanical components such as bearings and shafts.

While bearings are generally robust components made of solid metal, bearing failures are one of the most common failure modes among all machines' electrical/mechanical failures. There are different types of bearings used in EMs, with rolling element bearings being most common [1, 38]. Early bearing failures are usually attributed to defective design or to improper installation or lubrication. Mechanical and thermal stresses such as high vibration levels or high temperature dissipated from the winding are generally the main causes of bearing failures [26]. Mechanical faults such as eccentricity or shaft bending can also cause bearing failures [11, 75]. Fig 2.6 shows photos of bearing failures. Bearing faults increase machine vibration and noise. The initial symptoms appear as low level vibrations, which increase as the fault propagates. Bearing faults also cause a temperature rise in the bearing structure. Therefore vibration and temperature monitoring is crucial for bearing health monitoring [11].

Shaft faults are rare and their propagation takes a relatively long time to reach the breakdown stage. Some common shaft faults are shaft bending and torsion. The root causes of shaft failures include: over loading, fatigue, high temperature and corrosion. [60, 76].



Fig 2.6: Bearing failures damage in rotating electric machines [77, 78]

2.2.1.3 Failure statistics in EMs

EMs reliability and service lifetime have been an area of research interest both in industry and academia with a number of EM reliability surveys reported. Table 2.1 summarises the key reported reliability surveys on various EMs (rated at > 50hp and with supply in the range of 0-15kV) integrated into several industrial applications. Table 2.1 is based on a recent report in the IEEE gold book, which summaries the work conducted by an IEEE work group (1983-1985 and 1973-1974) and compares it with other surveys [58]. Additionally, a collection of reliability surveys summarised by P. Tavner in his recent book [1] is also included. The faults are classified to represent the most commonly failed components in EMs. The percentage of machine failures classified by component, presented in Table 2.1, shows that the largest percentages of failed components are the bearing and stator windings. These statistics clearly highlighting the need for reliable and improved bearing and winding diagnostic reliability.

Table 2.1: reliability surveys on electrical machine

Fault type	Reported surveys				
	IEEE Group 1985 [79]	EPRI 1986 [80]	Thorsen 1995 [81]	IEEE std 493 2007 [58]	Papers IEEE [1]
Bearing	40%	41%	42%	44%	21%
Stator winding	37%	36%	13%	26%	35%
Rotor	10%	9%	8%	4%	44%
Other	12%	14%	38%	27%	-

2.2.2 LVEMs condition monitoring systems

2.2.2.1 Overview

On-line monitoring of EMs operational parameters has significant potential to ensure reliable, effective, safe and consistent operation during service life and thus, help meet modern EMs applications requirements [82]. Consequently, the development of CMSs and techniques for EMs have received increase attention by the industry, as well as academia.

A CMS is a process undertaking continuous assessment of EM health whilst in service, with the capability of detecting machine faults at the incipient stages, before a catastrophic failure occurs [1]. This highlights the difference and the importance of CMSs over conventional protection systems. Generally, protection systems act after a fault has occurred and is in its final stages, when, usually, the machine is damaged considerably and

repair or replacement is required [1]. However, CMSs have the potential to prevent this, and thus, reduce downtime and maintenance costs [83]. Apart from the aforementioned features of CMSs, these can also provide other supplementary features such as enhancing the machine's performance and efficiency by better understanding the operating limits of the machine. The data provided by CMSs can be also used to understand failure root causes.

Fig 2.7 illustrates the common structure of a conventional CMS that includes several stages. The sensing stage is the measuring of the targeted physical quantities using suitable transducers. There are a number of conventional sensors used for EMs monitoring such as RTDs for thermal measurement; accelerometers for vibration; and, voltage/current probes for electrical signal measurements. The transducers output is generally an analogue electrical voltage that is converted into digital data using suitable data-acquisition instruments, which represents the second stage. The acquisition device conversion and data transmission frequency should be high [1].

In the third stage, the measured, sampled and transmitted signals are analysed using a suitable processing technique to timely extract specific fault related features that enable derivation of diagnostic decisions [84]. The processing technique depends on various factors such as the type of monitored signal (i.e. electrical, mechanical, thermal) and the operating condition (i.e. stationary or non-stationary). Common processing techniques are time averaging, Fast Fourier Transform, wavelet methods. Once the signals are processed, the fault related features are extracted (generally, these features are identified in advance) – this is a key part of the overall diagnostic process whose efficacy is directly reliant on the reliability of the proposed diagnostic technique and associated fault features. Pre-set thresholds levels of the identified fault features are then compared with on-line measurements a decision is then made when the measured features levels are higher than the pre-set values.

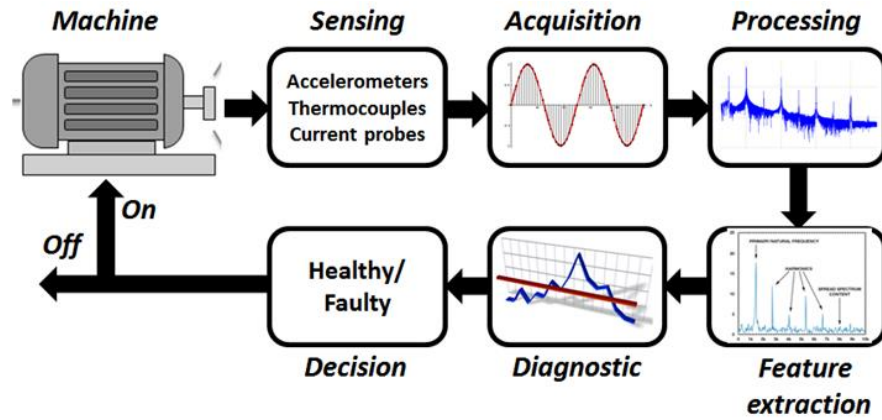


Fig 2.7: Conventional condition monitoring system structure

2.2.2.2 LVEM condition monitoring techniques

CM techniques for rotating EMs have been developed and applied in industry for some time. This research focuses on on-line monitoring techniques and specifically on developing a reliable and effective thermal monitoring tool for on-line thermal monitoring of random wound LVEMs. Therefore, the following sections provide a background on the common existing on-line thermal monitoring techniques for LVEMs. This is paralleled by a brief background on other common monitoring techniques such as, vibration monitoring and electrical signal monitoring.

A. Electrical signal monitoring

Various CM methods based on measuring and analysing machine electrical and/or electromagnetic quantities such as currents, voltages, instantaneous power, air-gap flux and machine electromagnetic torque have been investigated and reported in literature [29, 85-87]. The driving argument for these techniques is that, generally, no extra sensors are required, as these parameters are already measured or estimated in modern drive systems (for protection and control purposes). The resulting CM methods are thus generally classified as non-invasive [82]. However, electrical signal monitoring techniques are still under investigation and development; their deployment in industry has seen limited use as there are considerable challenges in fidelity and reliability of diagnosis these provide [3].

Machine Current Signature Analysis (MCSA) has been widely investigated for diagnosis of a variety of electrical [88] and mechanical faults [82]. The three phase stator currents have been analysed to detect faults using different processing techniques such as Park's vector [89], zero and negative sequence components [90], fast Fourier transform [91] and wavelet [92]. Initially, MCSA was investigated for stator windings electrical faults and the investigation subsequently extended to examine its use for other type of faults such as broken rotor bars [93], eccentricity [29] and bearing faults [82].

Generally, on-line monitoring based on electrical and/or electromagnetic quantities have shown limitations in reliably diagnosing faults, due to predominantly high sensitivity to variations in the operating conditions [94] but also to challenges in defining reliable fault indices [3]. For instance, minor load variations, supply voltage unbalance and inherent asymmetry can significantly affect the detection performance of these methods. In addition, distinguishing between faults and identifying the fault severity are other drawbacks which arise when these techniques are applied. To overcome these drawbacks advanced processing techniques are needed which in turn complicates the implementation of these techniques [17, 95].

B. Vibration monitoring

EMs vibrate even during healthy operating conditions; this is due to the nature of their structure and operation [96]. The radial forces induced due to the airgap magnetic field and the mechanical forces induced due to the nature of rotary movement of the rotor are the main contributors to machine vibration. These electromagnetic/mechanical forces contain information on the machine condition. Therefore, monitoring and analysing machine vibration can provide an indication about the health of the machine.

Commercial CMSs for EM diagnostics are largely based on vibration signal analysis, since it is well understood for key modes of mechanical fault analysis and has been in practice for a long time. Vibration techniques have been proven to be effective for the diagnosis of mechanical machine and drivetrain faults such as bearing failures, gears, shaft misalignment and rotor related failures [97, 98]. Recently, it has also been examined for machine electrical fault diagnostics [99]. However, vibration analysis based diagnostics come at a penalty of not being fully effective in identifying the entire array of possible failure modes such as, diagnosis of electrical fault and mechanical faults at low speed conditions, for example [100, 101].

2.2.3 Thermal condition monitoring

2.2.3.1 The need for thermal monitoring

The thermal issues in EMs and the need for thermal monitoring were discussed in Chapter 1, Section 1.3. In summary, LVEMs are designed to operate within a permissible temperature range that is defined by the thermal limits of machine's components. However, there are conditions under which the machine operating temperature is elevated above the permissible level, as a result of undesirable increases in machine's losses or degradation of the heat dissipation process. Examples of these conditions are: transient and

running over loading, unbalanced supply, high ambient temperature, degraded cooling capability and fault conditions [102].

Overheating is one of the main root causes of LVEM failure modes. Elevated temperature can degrade and eventually lead to breakdown of the machine key components such as the rotor, core, bearings and windings. The winding insulation system is the most vulnerable component to overheating, since the winding temperature is the highest and its temperature limit is usually reached before those of other machine components. Therefore, thermal monitoring of the windings in particular, in addition to, other components (i.e rotor and bearings) in LVEMs is valuable and can be critical for ensuring reliable operation and extended machine life.

EM thermal monitoring is not solely limited to thermal protection; knowing in-service machine temperature would also enable its more effective exploitation, since controlled overloads or identification of overly conservative ratings can be achieved. The thermal time constant in EMs is considerably higher than the electrical time constant, allowing controlled high current densities to be applied for a limited time to produce higher power in controlled overloads. This can be effectively achieved with online thermal monitoring to ensure winding temperature is kept within permissible limits [18]. Another potential application of thermal monitoring is machine control performance improvement through online correction of temperature dependent control parameters: here on-line tracking of the winding temperature enables online correction of its resistance value for the controller.

Fault diagnostics and prognostics are other important aspects of thermal monitoring. Electrical and mechanical faults in EMs manifest themselves as heat; therefore, measuring the fault induced thermal signature can enable timely fault diagnostics. For prognostics, temperature is an important parameter for remaining life time estimation of machine insulation systems [12, 18].

2.2.3.2 Thermal monitoring techniques

Fig 2.8 provides a general summary of existing thermal monitoring techniques for LVEMs. In general there are two approaches to LVEM temperature monitoring: direct temperature measurements or temperature estimation techniques [12, 20, 37, 40, 103-105].

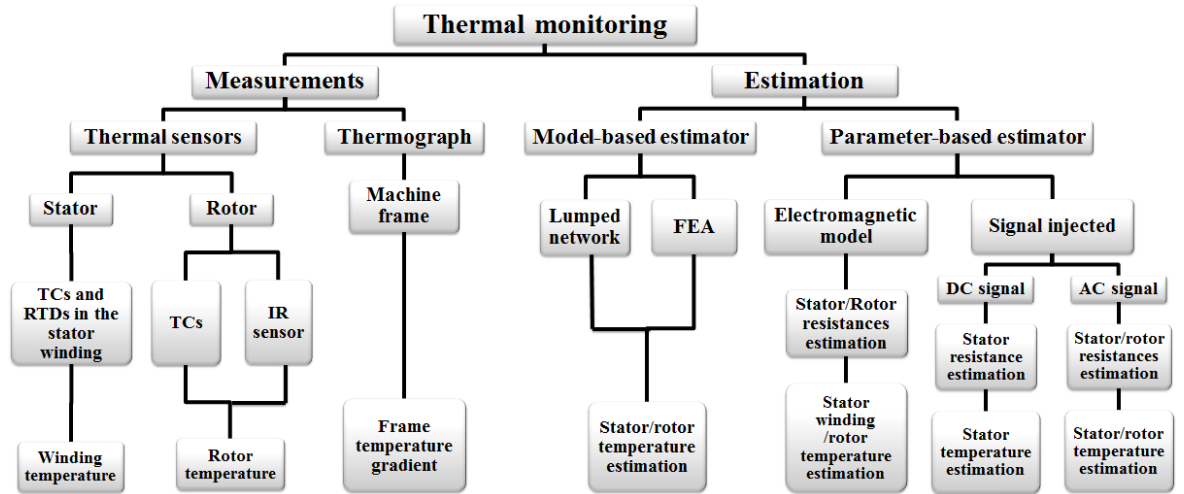


Fig 2.8: Thermal monitoring approaches for LVEMs

A. Stator winding thermal monitoring

Stator winding temperature monitoring is fundamental to EMs overall thermal monitoring. Winding temperature monitoring can be achieved by direct measurement or an estimation technique, as described below.

1. Thermal monitoring-based measurements (Direct)

a) Embedded thermal sensors

Thermal monitoring based on embedded thermal sensors generally provides the most reliable thermal protection and monitoring approaches [10, 61]. Thermal sensors such as RTDs and TCs are commonly installed in the machine during manufacturing to monitor the winding temperature, at locations which are inaccessible when the machine is in service [106]. The relevant EM standards such as IEC 60034-1-2010 [106] and IEEE std-112-2004 [107] identify placement positions for detecting thermal elements, which are generally advised to be installed in or as close to the highest temperature point that is likely to occur in the machine windings [106, 107].

Embedded thermal sensors should be distributed within the stator windings [106]. For the slot section, the sensors are usually installed between the coil side and the slot wall/wedge or between coils sides in double layer windings [107]. However, IEC 60034-1 specifies the sensing element to be located in the top of the slot between the coil surface and the slot wedge as the preferred sensing location. In this position the sensor can monitor the winding thermal status more closely than positioned at the slot bottom or side, which is largely affected by core temperature. For the end windings, the sensing points are installed between adjacent coil sides, in close contact with the surface of the coils [106].

The available conventional thermal sensors impose some limitations in thermal monitoring of EMs:

- The structure of conventional thermal sensors (e.g. TC and RTD) is inherently conductive, which prevents them from being installed in direct contact with the most active thermal component in a machine (current carrying coils). This raises a concern about the safety and the integrity of the winding-sensor proximity, as any direct contact between the windings and the sensor structures can cause a short circuit, which may damage the windings and/or the sensors [1, 17].
- Due to their inherent conductivity, these sensors must be appropriately insulated for embedding into a winding structure. This can minimise the short circuit risk. However, this results in a considerable increase in sensor structure bulk/dimensions, which can be impractical for thermal sensing in slot areas that are of key importance, as the slot geometry and winding fill factor limit the space available [1, 108].
- These sensors are sensitive to electromagnetic interference (EMI) and their measurement scale is within the range of μV to mV , which increases the potential of erroneous measurements [106, 109].
- Conventional thermal sensors are not the preferred choice for distributed thermal sensing in EMs, due to the installation difficulties with wiring leads and size [13]. Each sensor also requires its own acquisition channel, which increases the total system cost.
- These sensors are not particularly suited to harsh environments, which largely reduces their effective lifetime. In addition to, they are not preferred choice for an explosion hazardous environment such as in flooded fuel pumps used in the modern aircraft industry [110]

The aforementioned limitations highlight the fact that the conventional thermal sensors are not best suited to deliver the desired functionality targets for future safety critical EMs applications.

b) Infrared thermography

Thermography is another technique recently reported for thermal monitoring. Thermal cameras were used to monitor machine frames in order to observe thermal hot spots induced by winding faults or bearing faults [111-113]. Thermography is a non-contact thermal monitoring technique, so it can be applied to different machine topologies and ratings with a thermal measurement range up to 1000 °C. However, this technique is not

effective for detecting the incipient stages of a fault occurring inside the machine structure, as the thermal camera can only monitor the machine surface thermal conditions and thus, provides limited thermal data about key EM components. In addition, high resolution thermal cameras are costly and their performance can be greatly affected by the surrounding environment [28].

2. Thermal monitoring-based estimation

a) Thermal model-based estimator

A thermal model-based estimator is the process of machine components temperature prediction by analytically solving linear or non-linear thermal differential equations. There are two types of thermal models developed for rotating EMs: the lumped network thermal model and the finite element thermal model [105].

The lumped thermal model requires comprehensive knowledge of a machine's physical dimensions and construction materials; calculating multiple parameters of the thermal model and different heat sources is inherently complex. The model can be sufficiently complex to include temperatures of all machine components in steady state and transient conditions [15, 17]. While this model can provide a sufficient picture of the thermal status of the machine it can however also be inaccurate and unreliable. The model thermal parameters (which are assumed to be constant) assume constant thermal conditions, which may not be the case in practice [61]. Therefore, for an accurate model a few thermal sensors are required to correct and tune the model parameters making this thermal estimator inherently reliant on sensing quality [105, 114].

A finite element model is used to analyse heat transfer modes in modern EMs. Like the lumped model, FE models require information on machine physical dimensions and construction materials. FE models are highly accurate and can provide a good representation of the temperature gradient within the machine components and identify hot spots. However, the time required to compute the thermal profile of these models is too long, rendering them ineffective for on-line thermal monitoring. These models are more favourable at the machine design stage for assessing and resolving design issues [12, 114].

b) Parameter-based estimator

This thermal monitoring technique is based on estimating the machine's stator and/or rotor resistances to predict their temperatures, according to the relationship between the winding electrical resistance and the winding temperature [106]:

$$\frac{R_x - R_0}{R_0} = \alpha (T_x - T_0) \quad 2.1$$

from which the temperature can be calculated as [102]:

$$T_x = \frac{R_x - R_0}{R_0 \alpha} + T_0 \quad 2.2$$

where R_x is the winding electrical resistance (Ω) at winding temperature T_x ($^{\circ}\text{C}$) and R_0 is the winding electrical resistance (Ω) at T_0 ($^{\circ}\text{C}$) (The latter values can be obtained experimentally or from the machine nameplate). α is the winding material thermal coefficient of resistivity (for copper windings, $\alpha \approx 0.004/^{\circ}\text{C}$). This thermal monitoring technique has an important advantage over the thermal model based estimator, as it is less complex and can provide temperature estimation under varying thermal conditions. However, the resistance based estimator technique only provides the average winding temperature, which can be ineffective for thermal protection and detection of localized heat induced at the outset of a fault or abnormal conditions. Furthermore, this estimator has performance limitations when applied on a machine with a low winding resistance or when connections and joints contribute a significant portion to the total winding resistances [106]. The temperature based resistance estimator can be achieved by two approaches as follows:

1) Model-based estimator

Initially, the resistance estimation based model approach was developed and reported in literature for either improving control performance [115] or sensorless speed estimation [116] in induction machines. However, later work reported the use of resistance estimation for thermal monitoring [102, 104]. A model-based estimator is a software based method that requires measurements for model inputs and predetermined model parameters. Therefore, its accuracy depends on the measurement accuracy and the model's parameter accuracy [114]. Furthermore, it suffers from accurately tracking the resistance variation during fast transient conditions and a wideband speed range. A minor error in the resistance estimation can result in a large error in the calculated temperature [102].

2) Signal injection-based estimator

In this method, an AC or a DC signal is injected into the machine winding to measure its electrical resistance and hence, its temperature. The injection of the external signal requires an external circuit installed in series with the machine winding. Therefore, this method is considered invasive [13]. The external circuit injects a current into the winding and measures the voltage; the phase resistance is then determined from the injected current

and the measured voltage. The winding temperature can then be estimated based on this resistance. The advantage of this technique is that the estimated temperature does not depend on the machine thermal parameters so its accuracy is not affected by the variation of the thermal conditions [31]. However, the estimated temperature is the average winding temperature, so it cannot provide thermal information related to hot spots induced due to abnormal operation. The injected current can also cause an undesirable pulsating torque, which affects the overall performance of the machine [114].

B. Rotor thermal monitoring

Rotor temperature monitoring in EMs is important for their effective protection and performance. Operating under overheating conditions can result in catastrophic failure of the rotor structure including bearing, shaft, cage/rotor winding (for induction machines) and/or demagnetisation (for permanent-magnet machines). An overheating condition can damage the rotor relatively fast, and can be difficult to protect against when based on stator thermal protection or monitoring techniques [16].

The rotor temperature can be estimated using estimator based-thermal model or estimator based- machine parameters. Thermal models are capable of accurately predicting the rotor average temperature [105, 117]. However, the average temperature cannot reflect the entire thermal status of the rotor. Furthermore, these models require precise thermal parameters and machine losses, which are challenging to obtain [15]. Estimator based-machine parameters suffer from accuracy of estimation, particularly during transient conditions. Monitoring the rotor temperature using thermal sensors can provide sufficient data for the thermal status of the rotor. However, placing thermal sensors in the rotor of an electric machine is challenging and not usually done. The challenges arise due to rotary movement and the associated complexities of installation due to centrifugal forces, wiring problems and data transmission between the rotating sensors and their conditioning units [15, 118].

C. Bearing thermal monitoring

Bearing temperature monitoring is a traditional method of monitoring bearing health, since bearing failures such as lubrication degradation or bearing fatigue induces extra heat within the bearing, which results in bearing temperature rise. On the other hand, elevated bearing temperature caused by external factors such as elevated temperature in the stator winding, transient loading and high speed operation can cause damage to the bearing structure [38]. Therefore, standards such as IEEE 481 for motors used in the petroleum and

chemical industry specify 45 °C as the maximum allowable temperature for motor bearings [26]. Bearing temperature monitoring can ensure bearing protection from high temperatures and simultaneously provide useful information about bearing integrity [58].

Generally, bearing temperature monitoring is achieved by embedding thermal sensors in the bearing or by portable thermal cameras [111]. The main drawback of bearing thermal monitoring is that when a temperature rise is detected in the bearing structure, further investigation is required to ensure the detected temperature rise is exclusive to the bearing and not influenced by other machine operational factors [38].

2.2.3.3 Thermal protection

Commercially, there are number of EM thermal protection devices available such as fuses, thermal circuit breakers, overload relays and microprocessor embedded thermal models [102]. These devices are considered cost effective thermal protection tools, and are mainly used for thermal overload protection. The performance of these devices is limited and unreliable due to their incapability to follow accurately the thermal characteristics of EMs. These devices use a fixed thermal time constant, which largely results in either false tripping or thermal underestimation [61, 119]. Furthermore, thermal devices based on current measurements are not effective for protecting the machine under deteriorated cooling capability or undesirable heat induced by operating conditions such as a supply unbalance or high ambient temperatures.

Thermal protection based microprocessor embedded thermal models can be improved by further sophistication of the model algorithm, which can provide improved accuracy temperature estimation and hence, protection of the machine under different thermal conditions [120]. However, the algorithm cannot be used as a general standard because its model parameters are machine design and geometry specific. Furthermore, these models are also not effective for protection under cooling system failure. Therefore, at least one temperature sensor is required to be installed in a machine for this protection scenario [61].

2.3 Fibre Bragg Grating Sensing Technology (FBGST)

The term Fibre Bragg Grating (FBG) describes the fundamental operating principles of this sensing technology: the word fibre defines the structure and the operating media of this technology whereas Bragg stands for Bragg's law, which forms the basis of the sensing concept; finally, the word grating describes the induced permanent physical change in an optical fibre core that forms the FBG structure.

The history of FBGST started in the late 1970's. It was discovered a few years later after the invention of fibre optic technology [121]. In 1978, the Canadian Communications Research Centre reported the first formation of grating phenomenon in an optical fibre core. The phenomenon appeared after a continued exposure of the fibre core to argon-ion laser radiation for a period of time, and unexpectedly, the transmitted light through the optical core gradually decayed and was reflected back, which was explained due to the grating formation [122]. However, the milestone of FBG formation was reported later, in 1989, by a research group at United Technology Research Centre in the USA; where a permanent FBG was directly inscribed in an optical fibre core using a coherent interference patterns of ultraviolet (UV) light [123].

The Fibre Bragg Grating Sensor (FBGS) is the most popular sensor in the fibre optic sensing family. FBGSs have created their own market and have been commercially available since the early 2000's. In the beginning, FBGs were mainly used as a wavelength filter in the communications industry where fibre optic technology is well-known [124]. However, the FBG technology has recently drawn the attention of sensing engineers, since FBGSs unique features such as small size, EMI immunity, high sensitivity, distributed and multi-physic sensing capability, and harsh environmental resistance make them a promising sensing solution for a wide range of applications. Consequently, the number of developed FBGST based techniques for modern sensing applications have considerably increased in recent years [125, 126].

The aim of this section is to provide an overview of the FBGST. The FBGS structure is explained in Section 2.3.1 and FBGS fabrication and interrogation are described in Sections 2.3.2 and 2.3.3, respectively. Section 2.3.4 presents the FBGST sensing principles. The advantages and disadvantages of FBGST are discussed in Section 2.3.5. The last section (Section 2.3.6) reports a literature review of the applications of FBGST in rotating electric machinery.

2.3.1 FBGS structure

A FBGS is a short segment imprinted into a core of a single-mode optical fibre (SMF) [127]. It is formed longitudinally on the optical fibre core, in which a modulated periodic refractive index is formed in a SMF core when exposed to an interference pattern of UV light [124].

Fig 2.9 illustrates the FBGS structure imprinted in a SMF. A conventional SMF consists of a cylindrical glass core with a diameter ranging between 4 to 9 μm . The core is

surrounded with a cladding glass layer of 125 μm in diameter. The function of the cladding layer is to maintain that the light propagates only inside the fibre core. This is achieved by doping the core with other materials such as germanium, to produce a core with a higher refractive index (core n_0) than the cladding (cladding n_1) [124, 125]. The top layer of the SMF is the coating layer, which is generally made of acrylate or polyimide to protect the fibre.

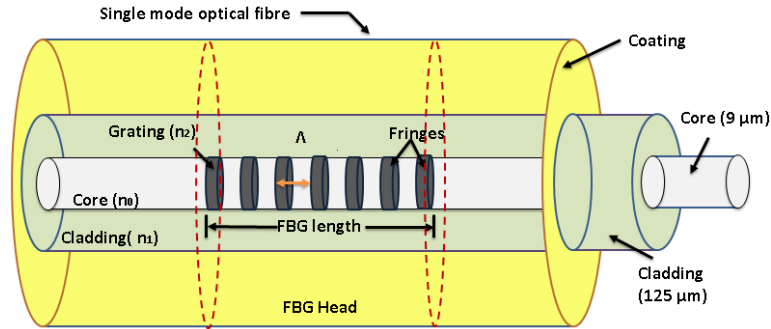


Fig 2.9: Fibre Bragg Grating sensor structure

The FBGS length that outlines the sensing area on the SMF core can generally vary between 3 to 20 mm [127]. This length is determined by the number of grating fringes and the distance between them (grating period Λ), as shown in Fig 2.9. The number of grating fringes can be up to several thousand, with the grating period in the hundreds of nanometres [121]. The number of gratings and the distance between them determine the FBG reflected light characteristics, which will be discussed in the following section. The grating area has a higher refractive index (grating n_2) than the core due to the fabrication process.

There are different types of FBG structures such as uniform grating, chirped grating and superstructure grating FBGs [128]. However, in this research, the uniform FBG structure type is only used, as shown in Fig 2.9, since it has a simple structure and fabrication process, and is generally considered the most suitable grating structure for sensing applications [129].

2.3.2 Fabrication of a FBGS

This section describes the common techniques used to fabricate a standard FBGS and discusses the fabrication requirement parameters. The fabrication of a FBGS is the process applied to an optic fibre to induce periodical permanent modulated reflective indexes in a segment of the fibre core [128]. The fabrication has been continually researched since the first grating formation discovery. As a result, great success in commercialising the fabrication process has been achieved [127]. The developed fabrication techniques

consider the sensing market requirements such as production flexibility, measurement range, low production cost and high physical and optical quality.

2.3.2.1 Fabrication techniques

The common method of inscribing Bragg gratings in a short segment of a fibre's core is achieved by using a coherent interference pattern of UV light imposed on the fibre. There are two approaches of inscribing an FBGS using an external coherent interference pattern of UV light:

1. Two-beam interferometer technique

The two-beam interferometer technique is the first practical method of externally fabricating a FBGS in SMF. It was reported by Meltz in 1989 [123]. Meltz used an ultraviolet laser light source divided into two beams by a beam splitter. Both beams are absorbed and reflected using two side mirrors, as shown in Fig 2.10. The reflected light from the mirror produces coherence interference UV beams focused on a section of SMF to be inscribed. This technique is also known as the transverse holographic technique, since the fibre's cladding is transparent to the ultraviolet light whereas the fibre's core is highly absorbent to ultraviolet light [130]. The advantage of this technique is that FBGSs with specific Bragg wavelengths (λ_B) can be obtained. This is achieved by varying the grating period (Λ) of the fabricated FBGSs by tuning the angle (φ) between the split UV beams and the perpendicular axis of the fibre core, which is expressed as [127]:

$$\Lambda = \lambda_{uv} / \varphi , \quad 2.3$$

where: Λ is the FBGS's grating period, λ_{uv} is the wavelength of the UV light, and φ is the tuneable angle. The disadvantage of this technique is the difficulty of accurately aligning the split UV beams on the inscribing area [121].

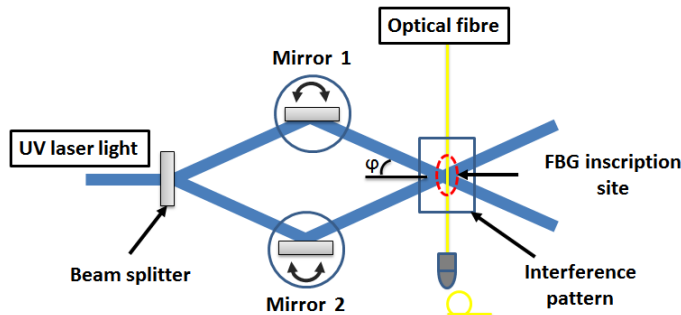


Fig 2.10: A schematic diagram of the two-beam interference configuration [124]

2. Phase mask technique

Several years later, in 1993, Hill [131] reported a new technique for FBGS fabrication. The reported fabricating technique is based on a phase mask made from transparent

material such as silica glass. The phase mask consists of etched square wave shapes, as illustrated in Fig 2.11. The phase mask is almost placed in contact with the optic fibre and when the UV light beam is incident to the phase mask, it will produce coherent interference pattern beams, which in turn modulate the fibre's core refractive index [131]. The disadvantage of this method is that for each Bragg wavelength, a separate phase mask is required.

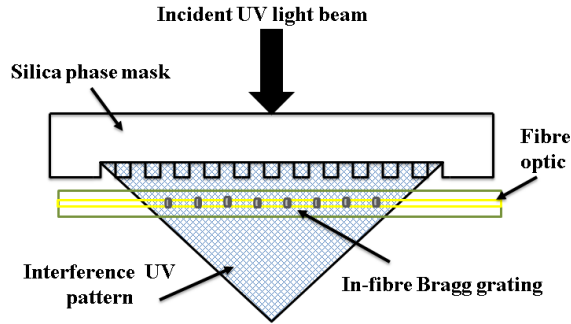


Fig 2.11: A schematic diagram of the phase-mask technique [127]

An alternative configuration to the phase mask technique was reported in 1996 by Dockney [127]. The modified version of the phase mask technique is shown in Fig 2.12. Dockney added two tuning factors to the phase mask technique to extend the selection of the Bragg wavelength region of the inscribed FBGs. The first tuning factor was achieved by increasing the distance between the phase mask and the optic fibre, and adding two mirrors to control the angle of the interferences beams. The second tuning factor was achieved by adding a moving lance between the phase mask UV laser source, so the UV light wavelengths incipient to the phase mask could be tuned [121]. Nowadays, most FBG sensors are fabricated using the phase mask technique. It is simpler and more practical, and the method can be computerised, which increases the production rate.

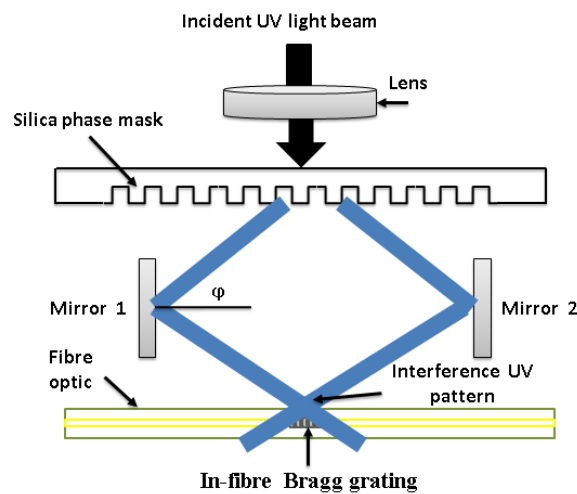


Fig 2.12: Modified phase-mask technique [121]

2.3.2.2 Fabrication tuning parameters

The fabrication of FBGSs requires a consideration of the key fabrication parameters such as FBG central wavelength λ_B , FBGS length, FBGS bandwidth and reflectivity [121], since these parameters are interconnected and affect each other. More importantly, they determine the spectrum characteristics of the FBG reflected light. In addition, these parameters are generally important for the user and need to be consistent with its sensing application and the interrogation unit. Other specifications such as the type of the fibre, coating and connectors are also important. These fabrication specifications will be discussed in Chapter 3, Section 3.3.1, as part of the FBGS design section.

Fabrication parameters characterise the FBG reflected spectrum, as illustrated by the reflected wavelength spectrum of a standard FBGS in Fig 2.13. The central wavelength (i.e Bragg wavelength λ_B) is the calculated peak mid-point of the reflected wavelength spectra. The FBGS bandwidth is determined by the full width at half maximum (FWHM), which is the reflected spectra width at 50% or -3 dB from the maximum peak point of the reflection spectra. The reflectivity is the percentage of light intensity reflected by the FBGS. Another fabrication parameter that indirectly affects the FBG reflected spectrum is the FBG head length [132]. The FBGS length is directly related to the FBGS structure parameters, grating number and grating spacing, which affect the FBGs bandwidth and reflectivity.

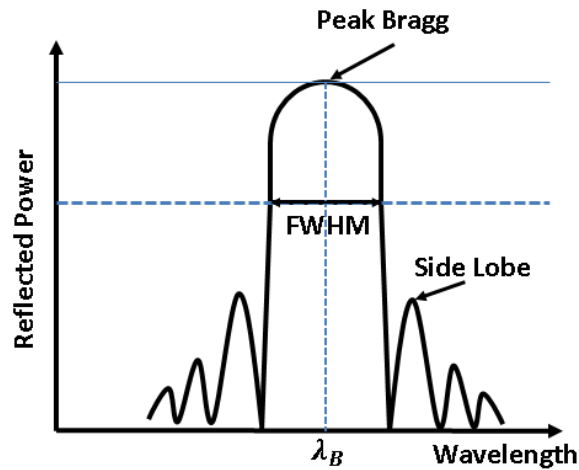


Fig 2.13: A typical reflected wavelength spectrum of a standard FBGS [121]

Generally, the fabrication process starts by identifying the FBG head length and the reflected spectrum central wavelength. To fabricate a FBGS with a specific central wavelength, this wavelength has to meet the Bragg condition, which can be calculated as [124]:

$$\lambda_B = 2 \Lambda n_{eff} , \quad 2.4$$

Where n_{eff} is the effective refractive index. From Eq. 2.4, Λ and n_{eff} are important parameters to determine λ_B . The effective refractive index varies inconsiderably during the fabrication process and hence, it does not have a large impact on λ_B . Thus, to meet the Bragg conditions, Λ must be half of the specified λ_B , which is calculated as:

$$\Lambda = \frac{\lambda_B}{2 n_{eff}}, \quad 2.5$$

Λ is directly proportional to the FBGS length and inversely proportional to the number of imprinted gratings. With an identified FBGs length, central wavelength λ_B and hence, determined Λ , the required number of gratings can be calculated as:

$$Ng = \frac{\text{Grating length (Gl)}}{\text{Grating period } (\Lambda)} \quad 2.6$$

However, the number of gratings have a direct impact on the reflected spectrum bandwidth and reflectivity. The FBG bandwidth (FWHM) is a function of the grating number and hence, length. Typically, the bandwidth is 0.05 - 0.3 nm for FBGS length ranging from 3 - 20 mm [121, 128]. The FWHM can be varied in a limited range by the exposed UV pulses intensity. The FBG bandwidth is an important parameter for multiplexing, which will be explained in Section 2.3.4. The reflectivity is the intensity of the light reflected by a FBGS, which is also affected by the number of gratings. One FBG head can consist of thousands of gratings. Each grating reflects $\approx 0.01 - 0.1$ % of the reflected light and all the reflections add coherently to build up the reflected narrow wavelength spectrum [127, 128]. Therefore, longer FBGSs will have more gratings and hence, higher reflectivity.

2.3.3 FBGS interrogation

To use an FBG head imprinted in SMF as a sensor, an interrogation mechanism that sends light to the grating head, then receives and monitors the reflected Bragg wavelength is essential. An interrogation mechanism should distinguish minor shifts in the reflected Bragg wavelength of the FBG head, and thus register any change in the physical quantity observed by the head. This is an important feature, in particular for sensing in condition monitoring applications [129]. A direct method of interrogating an FBG head is by using an optical spectrum analyser. It is a simple technique, as an external broadband optical source is used to illuminate the fiber and the reflected light is directed and monitored by the optical power analyser. However, the optical analyser is relatively expensive and large

in size and thus, remains a laboratory based technique inappropriate for industrial environments [121].

A number of interrogation schemes have been reported in literature [127, 133]. However, the reported interrogation techniques are complicated and costly with non-multiplexed capability. Therefore, they have not been successfully commercialised for real time applications [134, 135]. An ideal interrogator should provide a number of specifications such as high resolution, accuracy within the range of pico-meters, multiplexing sensing capability, and finally, their cost should be competitive with instrument systems used for conventional electric sensors [127]. The next section presents a successfully commercialised interrogation technique in the FBG sensing market. This technique is the basis of the interrogator unit used in this research.

2.3.3.1 Wavelength-division multiplexing

In the wavelength-division multiplexing technique (WDM), many FBGSs combined in SMF or distributed on a number of SMFs can be simultaneously monitored [135]. Fig 2.14 illustrates the schematic principle of the WDM interrogation technique. A broadband light source is used to illuminate the interrogated FBGSs. Typically, the broadband light source bandwidth has a range of ≈ 40 to 80 nm. A standard FBGS reflected spectrum bandwidth is typically ≈ 0.3 nm, as discussed in the previous section. Considering a 2 nm bandwidth for a λ_B shift due to strain or temperature, a simultaneous interrogation of a maximum of 40 FBGSs imprinted in SMF and illuminated with a 80 nm broadband light source can be achieved [124, 135].

In the WDM technique, a scan generator is used to tune the bandwidth of the broadband light source by using a light filter. The light bandwidth injected into the fibres can be tuned to a narrow bandwidth that can also be swept back and forth across the broadband light source window, as shown in Fig 2.14. Narrowing the light bandwidth when accessible (i.e small number of FBGS are interrogated) accelerates the light scan rate performed by the photodetector and the processor and hence, an accelerating acquisition rate [136]. However, reducing the light source bandwidth results in less FBGSs being interrogated. A coupler network is used to inject the light bandwidth into a number of fibre channels. The coupler network enables interrogation of FBGSs with the same λ_B connected to different channels. In addition, the total number of FBGSs interrogated by one channel can be multiplied by the number of total channels [121].

The reflected light back from the FBGSs are detected using a photodetector. The reflected light spectrums are then transmitted to the processor, which processes the spectrums and performs calculations to identify the Bragg wavelength peaks in each spectrum.

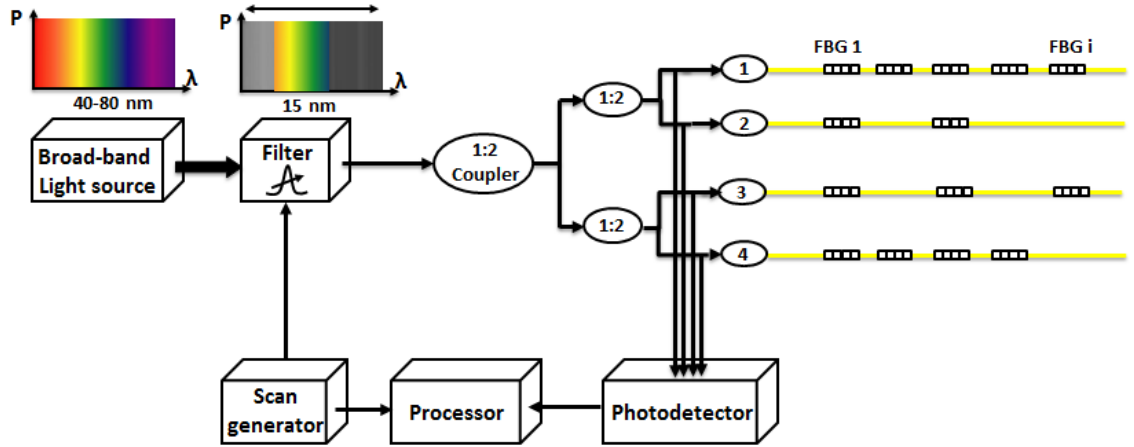


Fig 2.14: Schematic principle diagram of the WDM interrogation technique [135]

2.3.4 FBGS sensing principles

The fabrication and interrogation of FBGSs imprinted in SMF has been presented and discussed in the previous sections. In this section, the sensing concept of FBGSs will be demonstrated and discussed.

Fig 2.15 illustrates the operating principle of a FBGS. In principle, a FBGS operates as a light filter and its filtering concept is based on Bragg reflection theory. When an optical fibre imprinted with a FBG head is illuminated by a broadband light source (see Fig 2.15.a), the light is normally travelling through the fibre until it reaches the FBG head (see Fig 2.15.b). At this instance, a particular wavelength of the incident light is reflected back by the FBG head (the wavelength that meets the Bragg condition). All other light wavelengths are transmitted through the FBG head without being effected, as illustrated in Fig 2.15.c. The reflected Bragg wavelength alters with the variation of the FBGS structure parameters (grating period Λ and refractive index n_{eff} , see Eq. 2.4) when it is exposed to external mechanical and/or thermal excitations. The λ_B shift due to mechanical and/or thermal excitation will be explained further in the following text.

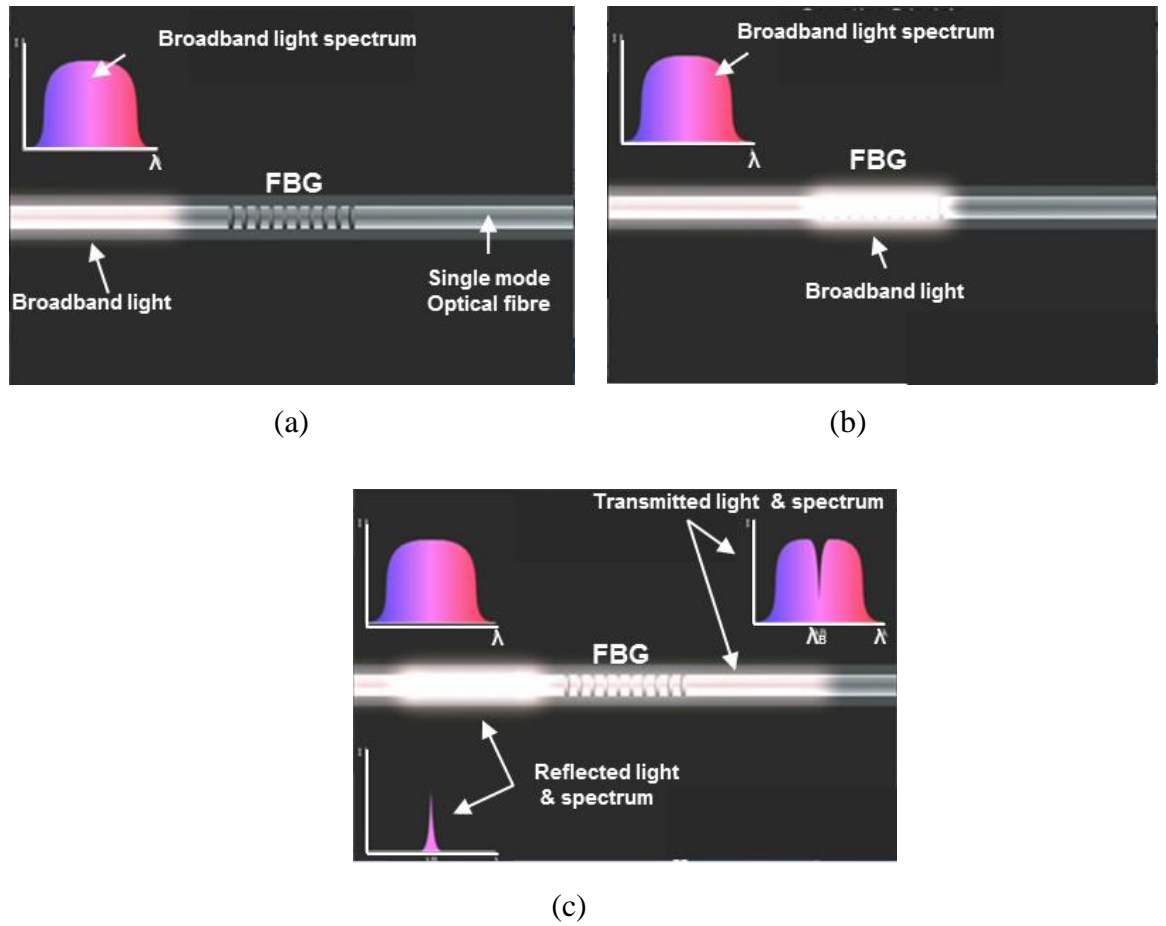


Fig 2.15: Working principle of FBGS [137]

Combining the advanced interrogation techniques that include multiplexing capability with the ability of imprinting a number of FBG heads in a SMF, FBGST provides an important feature for distributed sensing applications. Several FBGSs in a SMF can be interrogated, as these sensors can be fabricated with different Bragg wavelengths to prevent wavelength spectra overlapping [138]. A single optical fibre with several FBG heads is known as an FBG array sensor (FBGAS). Fig 2.16 illustrates the working theory of an FBGAS: the array is illuminated with broadband light and particular wavelengths are reflected by each FBG sensing head. Each FBG head reflects a specific light spectrum matching its designed Bragg wavelength [139], as illustrated in Fig 2.16.a. The array can be designed to measure a single physical quantity such as temperature, in which all the FBG heads work as temperature sensors, or as multi physical sensors where different FBG heads work to measure different physical quantities such as temperature, strain, pressure and force (see Fig 2.16.b).

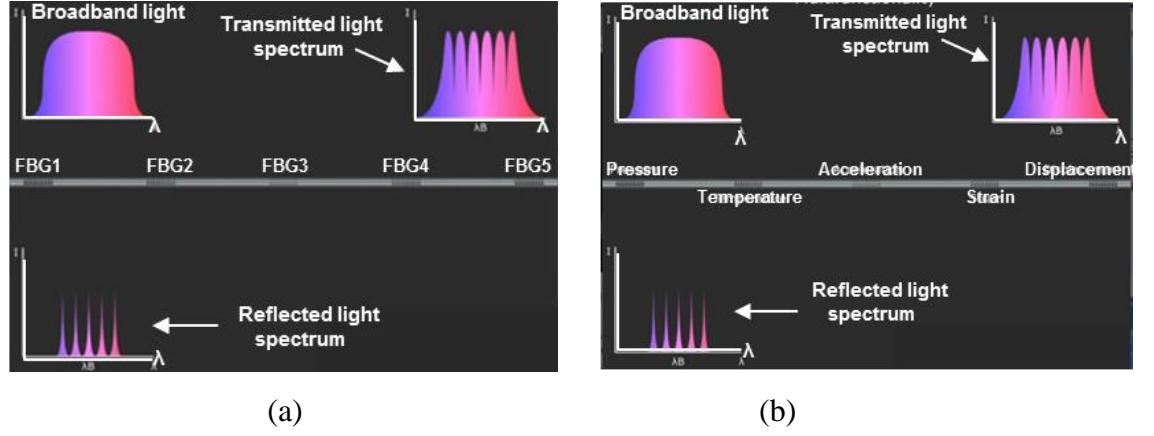


Fig 2.16: Operating principle of the FBG array sensor [137]

The reflected λ_B varies as a function of the FBGS structure parameters (grating period and refractive index). These parameters alter with the change in strain and/or temperature exposed to the FBGS [140]. Therefore, monitoring the variations of the reflected λ_B enables the sensing capability to be achieved. The reflected λ_B relative rate of change due to changes in the FBG structure parameters can be defined in terms of the acting thermal and/or mechanical excitation as [127]:

$$\frac{\Delta\lambda_B}{\lambda_B} = \overbrace{2 \left(\Lambda \frac{dn_{eff}}{d\varepsilon} + n_{eff} \frac{d\Lambda}{d\varepsilon} \right) \Delta\varepsilon}^A + \overbrace{2 \left(\Lambda \frac{dn_{eff}}{dT} + n_{eff} \frac{d\Lambda}{dT} \right) \Delta T}^B, \quad 2.7$$

where: $\Delta\lambda_B$ is the shift in the Bragg wavelength, λ_B is the base Bragg wavelength, ε is the strain and T is the temperature. The term A in Eq. 2.7 signifies the Bragg wavelength shift caused by elastic-optic effect due to strain. Term B in Eq. 2.7 describes the Bragg wavelength variation due to thermo-optic and thermal expansion effects caused by temperature variation [48, 125]. Eq. 2.7 can be simplified and rewritten as:

$$\frac{\Delta\lambda_B}{\lambda_B} = k_\varepsilon \Delta\varepsilon + k_T \Delta T, \quad 2.8$$

where: k_ε and k_T are the FBGS sensitivity factors to strain and temperature, respectively.

2.3.4.1 FBGS temperature sensing dependency

When a FBGS structure is subjected to temperature variation, the reflected λ_B is shifted and corresponds to the subjected temperature variation, as illustrated in Fig 2.18. The temperature response of λ_B is due to the optical fibre temperature dependency effects. The first effect is due to the change in the grating spacing (Λ), which is caused by the induced longitudinal thermal expansion in the optical fibre. The second cause is the thermo-optic effect, which is due to the dependency of the effective refractive index n_{eff} on

temperature. Assuming no mechanical excitation exists and the FBG head is exposed only to thermal excitation, the first part of Eq. 2.8 can be ignored and the variation in λ_B due to temperature expressed as [138]:

$$\Delta\lambda_B \setminus \lambda_B = k_T \Delta T = (\alpha + \xi)\Delta T, \quad 2.9$$

where: α represents the longitudinal thermal expansion coefficient and ξ is the thermo-optic coefficient. In a standard optical fibre made of silica, α is $\approx 0.55 \times 10^{-6} / ^\circ\text{C}$ and ξ is $\approx 6.9 \times 10^{-6} / ^\circ\text{C}$ [138]. The thermal expansion coefficient of optical fibres is very minor. Thus, the shift in λ_B when a FBGS is subjected to thermal excitation largely depends on the change in n_{eff} . However, the thermal expansion coefficient effect can be used to enhance the FBGS temperature sensitivity. This can be achieved when a FBG temperature sensor is packaged with a material that has a high thermal expansion coefficient; in this case α in Eq. 2.9 is the packaging material thermal expansion coefficient [141].

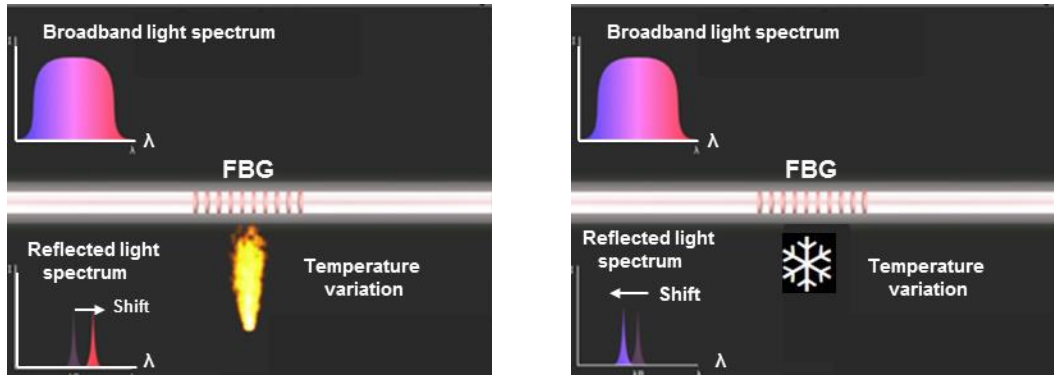


Fig 2.17: FBG temperature sensor operating principle [137]

The temperature sensitivity of a standard FBGS with $\lambda_B \approx 1550$ nm can be estimated from Eq. 2.9. For 1 $^\circ\text{C}$ of temperature change, the temperature sensitivity can be ≈ 10 -14 pm/ $^\circ\text{C}$. [142]. The temperature measurements range of FBGS is limited by the fibre type, coating and packaging (in case of packaged FBGSs). Generally, fibres with an acrylate coating can operate within a -20 to 80 $^\circ\text{C}$ temperature range, and fibres with a polyamide coating can operate within a -50 to 300 $^\circ\text{C}$ temperature range [136]. However, the use of FBG thermal sensors for high temperature measurements, above 600 $^\circ\text{C}$, has also been recently reported in literature [143, 144].

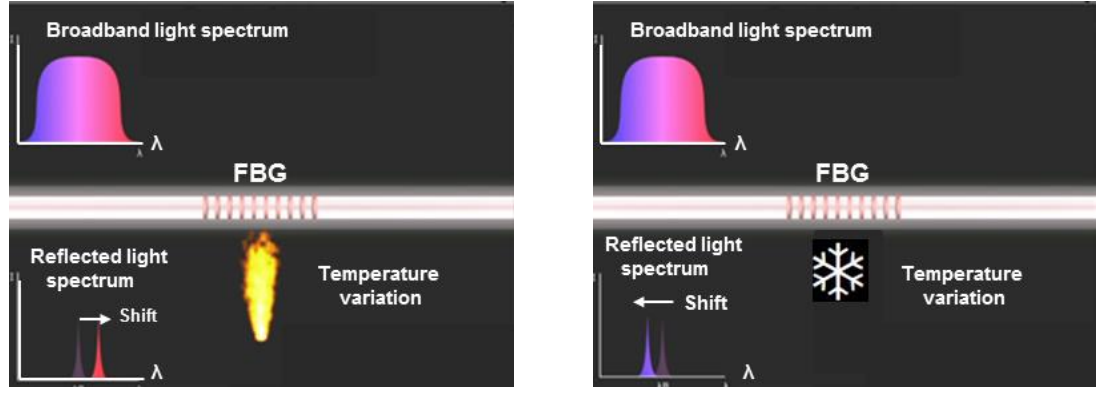


Fig 2.18: FBG temperature sensor operating principle [137]

2.3.4.2 FBGS strain sensing dependency

An FBG strain sensor is based on monitoring the λ_B shift due to an applied strain. The shift in λ_B is due to the change in the grating spacing Λ (elongation of the optical fibre) and the change in n_{eff} (fiber photo-elastic effect) [125, 138]. Fig 2.19 shows the reflected λ_B shift and the change in the grating spacing (expansion or contraction) of FBGS when it is subjected to external strain. Assuming constant temperature, the variation in λ_B due to strain can be expressed as [127]:

$$\Delta\lambda_B \setminus \lambda_B = k_\epsilon \Delta\epsilon = (1 - P_e)\Delta\epsilon, \quad 2.10$$

where $\Delta\epsilon$ is the axial strain and P_e is the photo-elastic coefficient of the fibre, which can be calculated as [127]:

$$P_e = \left(\frac{n_{eff}^2}{2} \right) [P_{12} - \nu (P_{11} + P_{12})] \approx 0.22 \quad 2.11$$

P_{11} and P_{12} are the strain optic tensor coefficients and ν is the Poisson's ratio. From Eq. 2.10 and Eq. 2.11, the FBGS strain sensitivity for a standard fiber optic with $\lambda_B \approx 1500$ nm is ≈ 1.2 pm/ μ strain [136]. FBGSs can measure strain up to ± 10000 μ strain [124].

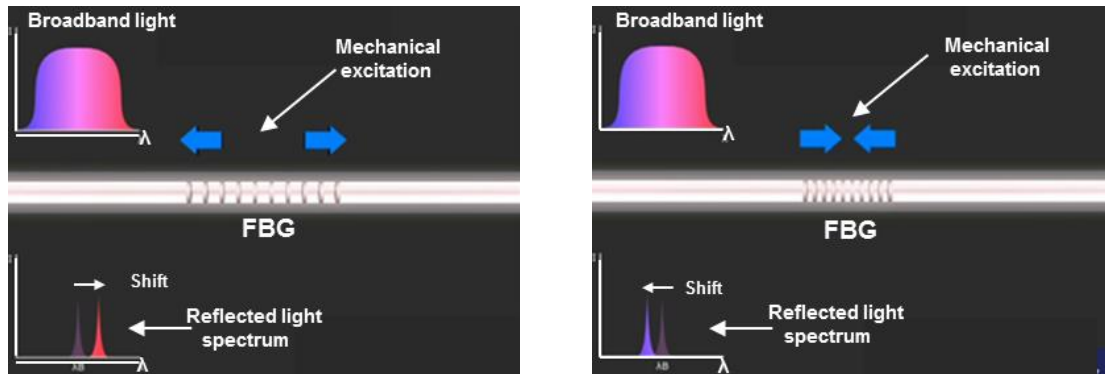


Fig 2.19: FBG strain sensor operating principle [137]

2.3.4.3 Temperature-strain cross-sensitivity in FBGSs

As previously discussed, the displacement in the reflected λ_B of FBGSs can be induced due to any change in the strain or the temperature the sensor is exposed to. Eq. 2.8 clearly illustrates the cross-sensitivity between the strain and temperature on a FBGS output. Therefore, precise measurements of strain and/or temperature individually or simultaneously can only be attained if the discrimination between the effects of strain and temperature on the reflected light spectrum is achieved [124].

For exclusive temperature measurement, an FBGS must be isolated against external mechanical excitation; this can be achieved with appropriate packaging design. However, extreme care must be taken when packaging a FBG temperature sensor, as the sensor accuracy and sensitivity can be strongly influenced by the packaging design [142, 145].

Various techniques for strain measurement using FBGSs have been reported. A straightforward method involves an additional FBG temperature sensor (i.e. an FBGS protected from mechanical excitation) to correct the strain measurements obtained from the FBG strain sensor. The additional FBGS should be placed in the same thermal environment of the active FBG strain sensor. The error induced in the strain measurement due to temperature variation effect can be corrected on-line by subtracting the measured wavelength shift of the FBG temperature reference sensor from the measured wavelength shift of the FBG strain sensor, as follows:

$$\frac{\Delta\lambda_{B-corrected}}{\lambda_{B\epsilon}} = \frac{\Delta\lambda_{B\epsilon}}{\lambda_{B\epsilon}} - \frac{\Delta\lambda_{BT}}{\lambda_{BT}}, \quad 2.12$$

where $\Delta\lambda_{B\epsilon}$ is the induced wavelength shift in the active strain sensor and $\Delta\lambda_{BT}$ is the induced shift in the additional temperature sensor. This method usually gives accurate measurements but the total cost of the sensing system is increased because of the need for an additional sensor [124].

2.3.4.4 FBG multi-physical sensing

An FBG head is inherently sensitive to variations in strain and/or temperature, as described previously. However, an FBG head can be used to develop transducers that are able to sense other physical quantities such as: stress, pressure, force, magnetic field, electrical field, voltage, current, acceleration and displacement [124, 127, 138, 146-149]. This can be achieved with appropriate coatings and packaging designs of the FBGSs. The multi-physical sensing capability of FBGST is very interesting. However, it is out of the scope of this thesis, since this research is mainly focused on investigating the thermal

sensing features of FBGSs to be used as a thermal sensing tool for on-line thermal monitoring applications in electric machines.

2.3.5 Advantages and disadvantages of FBGST

FBGST has many inherent advantages when compared with other conventional electrical sensing technologies or with other optical fibre sensing families. The features of FBGST make it a strong candidate and attractive sensing solution for many industrial applications. EMs is among one of the applications that can benefit from this technology; FBGST can overcome the limitations of conventional sensing solutions and can improve the sensing performance. In this section, the general advantages and disadvantages of FBGST are discussed, with particular focus on FBGS' features for developing improved sensing solutions for rotating electric machinery applications.

2.3.5.1 The Advantages of FBGSs

- 1) **Size:** An FBGS is a modified segment in a conventional single mode optic fibre core and thus, its size is about $\approx 125 \mu\text{m}$ in diameter and typically a few millimeters in length [135]. An FBGSs size and its light weight make it an appropriate sensing solution for embedding in hard to reach locations with low mass impact [150]. The size and weight are important features for modern EMs, where the machine's weight and size are critical for some applications such as aerospace and transport in general. With this feature, FBGSs can provide unparalleled opportunity for in-situ thermal and mechanical monitoring of the internal structures of EM components.
- 2) **Uniquely self-coded:** Each FBGS is coded by its central Bragg wavelength λ_B [135]. This reduces the confusion between measurements and the complexity of sensor labeling.
- 3) **Multiplexing:** A number of FBG heads can be inscribed into a single optic fibre (FBG array) and can be simultaneously interrogated. Moreover, a number of FBG arrays containing multiple sensing points can be simultaneously interrogated using a multi-channel interrogator unit. This feature is important from a sensing point of view, as it can significantly reduce the sensing system size, wiring problems and also installation difficulties [130, 151]. Most importantly, with a multiplexing feature, a distributed sensing system can be easily achieved. A single fibre can contain theoretically a high number of sensing points resulting in a sensing array, which routed through a machine structure can be achieved to provide useful real time monitoring data.

- 4) **Electromagnetic/electrical immunity:** FBGS structure is electrically non-conductive (dielectric) and completely immune to electrical and electromagnetic interference. This advantage makes FBGSs a strong candidate for embedded sensing solutions in confined high electrical and electromagnetic environments where conventional sensors would fail or have measurement issues. This feature allows the FBGSs to be safely and reliably embedded in direct contact with active electric and/or electromagnetic components (i.e stator windings, stator core and magnets) in EMs [121, 152].
- 5) **Multi-physics sensing:** Transducer based FBGST can be developed to sense several physical quantities such as: stress, force, magnetic field, electrical field, voltage, current and displacement [124, 127, 138, 146-149]. Combining the multi-physics sensing capability with multiplexing capability, an all-in-one sensing system designed for EMs can be achieved, where monitored parameters such as temperature, vibration, forces and magnetic field are key for EMs health assessment. This can significantly reduce the requirements for the monitoring system size and hence, cost.
- 6) **Working in harsh conditions:** FBGSs are capable of operating and surviving in harsh environments (i.e corrosion and high pressure). Furthermore, an FBGS is a passive sensor (i.e no current or voltage is required to operate the sensor), so it provides safe operation in hazardous and explosive environments [121, 150].
- 7) **Distance sensing:** FBGSs can be located several kilometers from the interrogation unit. This is because an optic fibre is an efficient single carrier, where other electrical sensors require amplification for remote sensing. This feature is important in applications where EMs are far away from their operating and control units [121].
- 8) **High sensitivity:** An FBGS is highly sensitive to strain and temperature with ≈ 1.2 pm/ μ strain and ≈ 10 -14 pm/ $^{\circ}$ C sensitivity coefficient, respectively [127, 136].
- 9) **Long-term stability:** FBGSs can offer robust and long lifetime solutions. These sensors are commercially certified for a minimum 25 years lifetime in the telecommunications industry according to the Telcordia programme (based on a number of tests such as temperature cycling, high temperature storage and humidity testing, etc.) [136, 153].
- 10) **Rotary sensing:** FBGSs can be installed in rotating components such as rotors in EMs. This can be achieved by coupling spinning FBG heads with interrogation units through a fibre-optic rotary joint (FORJ) device [47, 154]. This is an important

advantage for electric machinery applications, where sensing of rotor parameters was avoided due to signal transition difficulties, implementation problems and reliability.

2.3.5.2 The disadvantages of FBGST

- 1) **Standard:** To date there is no specified standard for FBG sensing applications.
- 2) **Cross-sensitivity:** Simultaneous and exclusive measurements of strain and/or temperature require additional compensation work, which increases the complexity and the cost of the system [155]. In sensing application for EMs, this challenge would be further highlighted, since EMs are natural sources of thermal and mechanical excitation and thus, exclusive or simultaneous measurements are not straightforward to achieve.
- 3) **Installation:** FBGSs are fragile and easy to break. Therefore, careful handling and installation is required [156].
- 4) **Weak market:** FBGST is still limited in terms of market size. This is mainly due to it being a relatively new technology and still unknown [150].
- 5) **Cost:** FBGSs are reasonably inexpensive sensors but their interrogation system is relatively costly, currently costing in the order of thousands of UK pounds depending on the performance requirements [124].

From an industry prospective, the current technology cost can be considered a limitation. However, FBGST is not a mature technology yet, it is still under development and thus, its cost is expected to reduce. The inherently multi-physical and multiplexing nature of FBG sensing systems has the potential to provide a sizeable and considerable reduction of the overall monitoring system size and cost. In addition, FBG sensing features can provide a number of attractive monitoring and performance improvements in EMs that would be challenging to deliver by alternative sensing or design approaches. Despite its current relatively high cost, this sensing technology has already found use in aerospace [157] applications and in wind turbines [158] where its features have contributed to the development of more effective condition monitoring systems.

It is known that cost and market are associated with demand and manufacturing competition. A recent report on the global FBGS market up to 2017 shows a rapid growth rate of the technology in the market place [126]. Recently, FBGST has found real applications and has been practically integrated into a number of important applications

where the technology feature are vital such as aerospace, oil and gas industries, and also medical and energy industries [126, 136, 159]. In addition the demand for research activities on FBG application techniques is reflected by the considerable increase in publications number about FBGST in different areas. [126] also shows an increase in the number of the technology manufacturers around the world. The manufacturing competition now is not only based on FBGST developers such as Micron Optics [159], FBGS [160] and Smart Fibers Limited [136], it also recently includes world known companies in sensing and instrumentation such as HBM [137] and National Instruments [161].

2.3.6 Review of FBG sensing application for EMs

The interest in utilising FBGST for rotating electric machine sensing applications commenced early last decade. However, the majority of advanced application studies are reported within the last five years period and the number is expected to show gradual growth in the coming years [150]. The following sections report a review on the most important studies of FBGST applications in EMs available in current literature. The literature is divided into sub-sections based on the sensing parameters classification: thermal sensing, mechanical sensing, rotor sensing and other sensing. The literature includes laboratory-based and field-based publications, which were mostly conducted by a limited number of research groups around the world due to specific requirements for multi domain expertise in optic sensing and electrical machines.

2.3.6.1 Thermal sensing applications

Thermal sensing and monitoring of EMs based on FBG thermal sensing technology has already received attention in a number of studies [43, 49, 51, 162-166]. The features of a FBG temperature sensor such as small size, non-conductive, EMI immunity and multiplexing make it a strong candidate to provide a thermal measurement solution for EM most susceptible components to thermal stress such as the stator windings and rotor structure.

For LVEM thermal sensing applications based on FBGST, which is of direct interest to this research, there are a few studies recently reported in literature. These studies are mainly reported by two research groups. The first group is from The Federal University of Technology in Brazil. This group has reported a few studies on FBG thermal sensing for LVEMs [51, 162, 165]. In [162] the research group reported the first feasibility study on using FBG thermal sensing for LVEM. A 3.7 kW, three-phase, induction motor was embedded with eight FBG thermal sensors located above the slot wedges in the slot

openings of eight different slots, as shown in Fig 2.20a. The FBG temperature sensors were located above the slot's wedges in the slot openings of eight different slots. In order to eliminate the mechanical excitation effects upon the FBGs thermal measurements, the FBG heads were encapsulated within a steel tube with both ends glued (see Fig 2.20b). The performance of the proposed sensing system was used to monitor the stator temperature distribution under healthy conditions. The FBG embedded 3.7 kW induction motor has been used for different studies by this group. In [51], the FBG sensing system was used to measure the temperature rise in the stator due to mechanical and core losses and in [165], the thermal sensing system was used to validate the thermal model result.

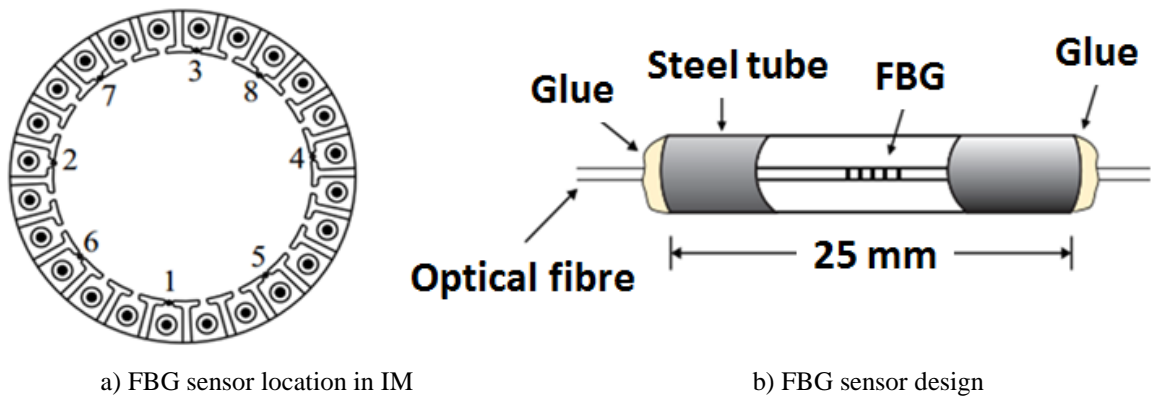


Fig 2.20: Embedded FBG sensing system in a low voltage induction machine [165]

The second research group is from Nottingham University and City University of London. This group investigated the use of FBGST for multi-parameter monitoring in LVEMs. The outcomes of their research have been recently reported in two publications [49, 146]. [146] reported a feasibility study of multi-parameters monitoring such as temperature, strain, speed and torque in a permanent-magnet motor. For a thermal sensing solution, two FBG arrays consisting of 12 FBGSs per each array were looped axially across the slot openings. The examined motor consisted of 12 slots and hence, each slot opening in the stator contained two FBGSs, as shown in Fig 2.21. The paper only showed the initially obtained results from the proposed system network. No information was provided about the methods of instrumentation, material used for bounding packaging of the FBGSs and the compensation method for the thermal mechanical excitation effects.

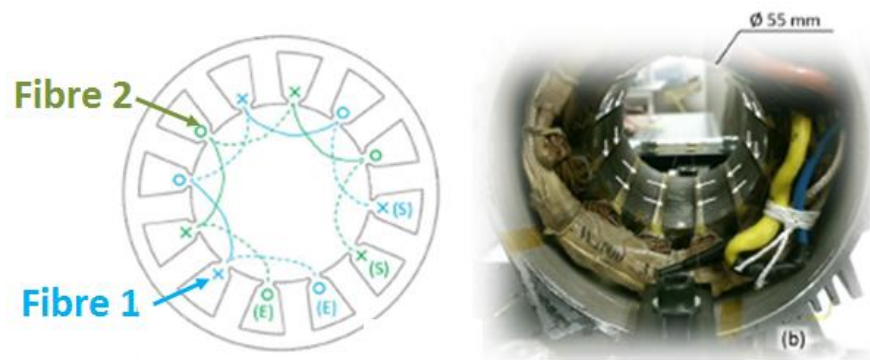


Fig 2.21: Fibre routing along the stator slots for winding temperature measurements [146]

For large scale EMs, the interest in FBG sensing application commenced earlier than for LVEMs. The first practical attempt to use FBG temperature sensors in EMs was for a large power generator reported in Germany in 2002, by Siemens [43]. The work was reported as the world's first realisation of thermal measurements of stator windings in a large power generator, since a number of FBG sensors were directly attached to the stator winding copper bars. The reported work demonstrated on-line dynamic thermal measurements of stator copper bars under normal operation. However, instability in the thermal measurements was reported, which was concluded due to the installation methodology (no information was included on the sensors design and packaging).

Nine years later, in 2011, [156] reported the first quasi-distributed thermal measurements of stator windings inner temperature of a large power generator in China. The study included an investigation about embedding techniques and methods. In this work a stainless steel tube with an inner diameter of 0.5 mm and outer diameter of 1.5 mm was used to package the FBG heads. The conductor length of the examined generator was ≈ 3 m. A 12 FBG heads and were embedded in a small groove in the conductor bar top surface.

In 2012, extended work by Siemens was reported in [167]. Six FBG arrays containing a large number of FBG heads were installed on six stator winding copper bars in a large turbo generator. Each FBG array sensor was fixed on a strip of 1.5 mm thickness made of insulation material. The strip was then fixed on the bar surface, as illustrated in Fig 2.22. The embedded bars were then taped with mica glass fibre and inserted into a stator slot. The in-situ thermal sensing design was tested in service for five years under normal operation and its performance compared with a conventional, resistance detector based, thermal sensing system [168]. The paper concluded that there were no problems reported with the implemented FBG sensing system in such a harsh environment during the examined five year period.

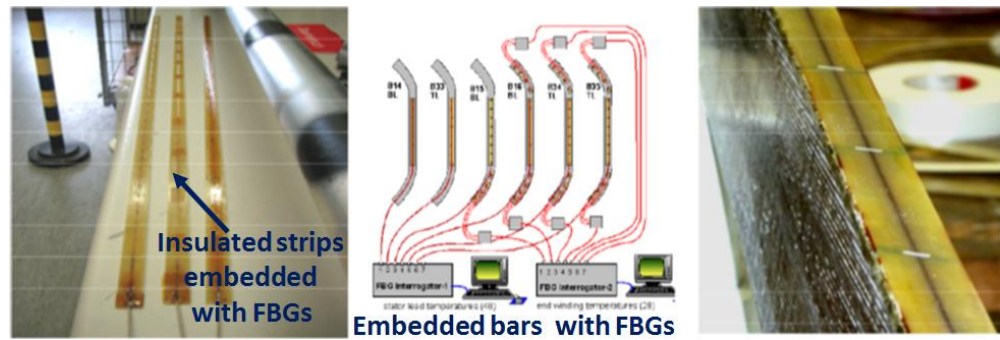


Fig 2.22: Distributed thermal sensing based FBG sensing technology in a large generator [167]

Another work using FBG temperature sensors for large generators thermal monitoring was reported by Federal University of Technology research group [50, 163, 164, 169]. In [164], the stator surface temperature of a high power synchronous generator was monitored using FBGSs. Six FBG thermal sensors were placed into small grooves between the stator surface insulation and the rotor poles, as shown in Fig 2.23. The sensing system performance was examined after the generator was returned to service. The generator stator thermal measurements were monitored under transient start-up and normal operating conditions. This work was reported as the first temperature measurement of a hydroelectric plant generator in South America.



Fig 2.23: Implementation of FBGSs on a large hydroelectric power plant in Brazil [164]

It is important to highlight that the available literature on FBGSs use for thermal monitoring in EMs is limited and almost exclusively focused on applications in large generators, with significant slot geometries and a form wound winding configuration. The existing reports on LVEMs application only assess the general potential of FBGST for thermal monitoring internal to the machine structure and do not consider EMs relevant standards for sensing requirement and placement. In the reported studies the FBGSs were embedded in the slot openings, a location which does not directly reflect the stator winding temperature that is of critical interest in low voltage machinery. EMs relevant standards such as IEC 60034-1-2010 [106] and IEEE std-112-2004 [107] identify placement positions for detecting thermal elements to be within the slot and end-windings structures; these locations are not considered by the reported studies.

In addition, the FBG thermal sensor packaging designs used in the reported studies utilise conductive materials such as stainless steel and aluminium, which can impose operational challenges in EM applications. Furthermore, there is no sufficient information on sensor design, packaging, installation and calibration techniques, which can impose significant limitations in efficacy of thermal monitoring in low voltage machinery. For example, the reported sensing utilises surface bonded metallic packaging in a strong magnetic field environment and is therefore susceptible to undesirable mechanical and thermal stress that may cause inaccurate readings and sensor displacement.

2.3.6.2 Rotary element sensing applications

FBGST offers a new capability of multi-physical sensing in EM rotating parts including the rotor conductors, magnets, shaft and core. In principle, a number of FBGSs can be installed and distributed on the rotor structure. The communication between the sensors and an interrogator unit can be achieved through a FORJ. The rotary joint optic-mechanical component enables continuous transmission of optic light between rotating and stationary parts [170].

For LVEM rotary sensing application, recent work was reported in [146] as a feasibility study on temperature measurements of rotor's magnets in a low voltage permanent-magnet motor. The work was part of a study on multi-sensing application of FBGST for EMs. A number of FBGS heads were installed on the rotor structure, as shown in Fig 2.24. The FBGs mounted on the rotor were driven using a FORJ, which allowed for sensing heads interrogation during rotary movement. The reported work only showed one graph demonstrating the feasibility of the sensing system. However, no information is provided about the FORJ adaption, sensing installation/design and measurements reliability and interpretation.

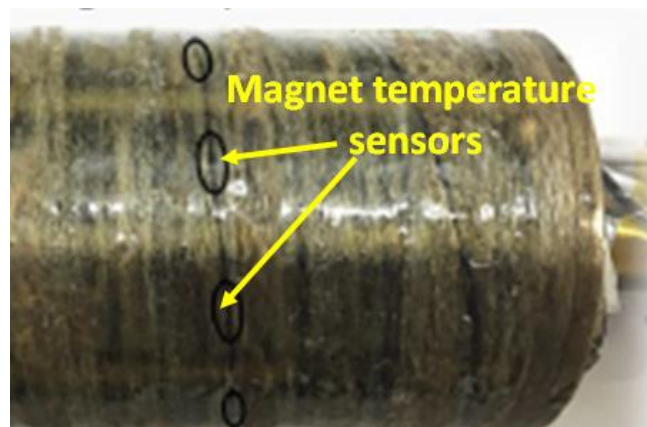


Fig 2.24: FBG heads installation on magnet rotor structure [146]

For large scale EMs [152] also reported a feasibility study of embedding an FBG distributed sensing system in the rotor of a 75 MVA hydro generator. A multi-channel FORJ was used to interrogate large number of FBGSs distributed on four single mode optical fibers. The obtained thermal measurements from the embedded FBG sensing system were compared with thermal predictions obtained by electrical-thermal software modelling. The work concluded that FBGSs can provide a safe and effective tool for monitoring field windings in large hydro generators. However, more work is required for developing an appropriate sensor design and installation procedure.

[166] investigated FBGS design for temperature monitoring of rotor field windings in a large hydro generator. The paper investigated the influence of the mechanical-thermal excitation on the developed metallic packaged FBG temperature sensor. In large generators, for example, the variation in temperature can cause thermal expansion in the components embedded with the FBGSs, which may affect the sensors performance. The proposed FBGS design was built of three layers: a thermal adhesive layer to keep the sensor attached to the rotor structure and resist centrifugal forces while rotating, sensor packaging to eliminate external mechanical stress, and a silicon layer to reduce the effect of the cooling air around the sensor. The work concluded that thermal-mechanical effects on the FBG assembly can cause errors in the measurements.

The available literature suggests that the rotary sensing application in EMs and in particular LVEMs has not been adequately researched. The reported work shows the feasibility of this and addressed some of the challenges. More research is required for understanding FBGST application in EMs rotary parts. Aspects such as: 1) FORJ adaption for machine applications, 2) FBG installation, characterisation and calibration: 3) sensors performance over a wide range of operating conditions; and 4) interpretation of the measured data for condition monitoring applications.

2.3.6.3 Mechanical sensing applications

For mechanical sensing (strain measurements) in EMs, which is another important feature of FBGST, a few studies were recently reported in literature [46, 171-173].

[172] is a US patent that reported three different embedded configurations of a FBG chain in the stator core of an EMs. The embedded FBGSs operated as strain sensors that aimed to measure the dynamic deformation that occurred on the stator lamina surface due to electromagnetic forces. The reported work exploits the small size and EMI immunity features of FBGSs to be placed in between stator core laminations where other sensors are

extremely challenging to place. The FBGSs were attached to the surface of one stacked lamination in the tooth section that contained micro meter grooves made by laser cutting, as shown in Fig 2.25. The measured deformation can be related to the magnetic field, forces and torque. The patent only reported the embedding configuration and no experimental results were presented.

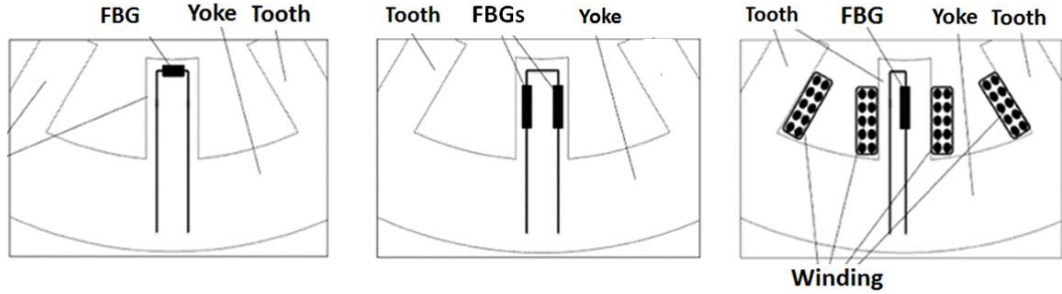


Fig 2.25: Placing a FBG strain sensor in the stator core tooth between core lamination [172]

In [46] and [173], the deformation in the stator teeth of two- and four-pole induction motors due to the magnetic forces, as the interaction between the stator and the rotor, was measured using FBG strain sensors. The sensors were instrumented between two teeth and 120 mechanical degrees apart, as shown in Fig 2.26. The measured dynamic strain

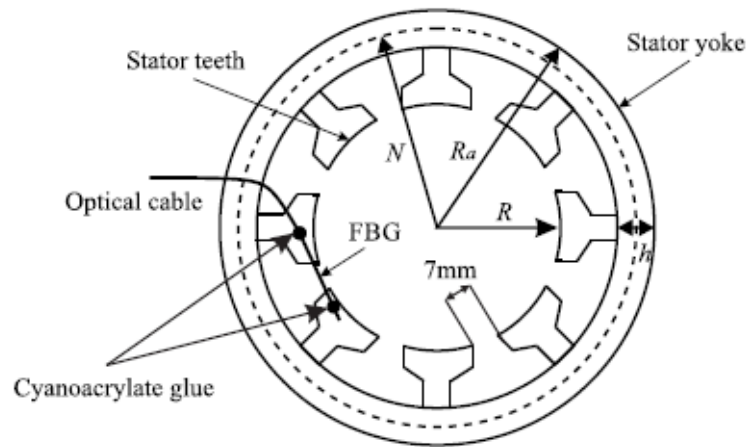


Fig 2.26: Stator teeth mechanical excitation measurement using a FBG strain sensor [46]

performed by the FBGSs were analysed using a fast Fourier transformer to detect rotor mechanical faults such as broken rotor bars and static and dynamic eccentricity defects. The reported results of the strain spectrums clearly showed frequency components in the spectrum that identified the faults in the examined motors.

[49] reported the use of FBGST for measuring physical quantities such as vibration, torque, rotor speed and position in permanent-magnet motor. In the proposed work, the FBG array contained 12 FBGSs were circumferentially attached to the stator core in a way that each FBG head was positioned between two adjacent stator teeth, as shown in Fig

2.27. These FBGSs were used to measure the strain induced in the stator teeth, then using appropriate data processing and algorithms, parameters such as vibration, rotor speed and position were obtained. For torque measurement, two FBGSs were attached to the shaft with a 90° angle between them and 45° from the shaft rotating axis, as shown in Fig 2.27b. In this configuration, the difference between the two FBG reflection peak wavelengths was used as a measurement of torque.

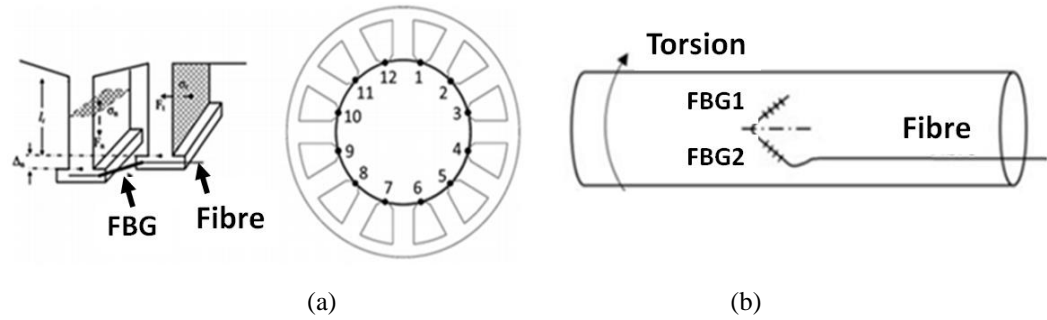


Fig 2.27: a) Strain measurement in stator teeth, b) torque measurements in rotor shaft

2.3.6.4 Other sensing applications

The development of vibration sensors based FBGST for EMs condition monitoring have also been reported in recent literature [45, 174-177]. For high voltage EMs, vibration transducers based-FBGST were developed and examined to measure end-windings vibration [177], whilst for LVEMs, frame mounted FBG vibration transducers were examined [45].

A proof of principle for an electric field sensor design based on FBGST used in high voltage EMs was demonstrated in [44]. The sensing concept was established on the electrostriction phenomenon of the fibre silica core, which appears when a FBG head is placed in parallel with an electric field higher than 1kV. Electrostriction phenomenon causes variation in the refractive index of the bare FBGS and hence a Bragg wavelength shift. The developed sensor was examined in a prototype laboratory test rig representative of copper bars of a large electric generator. The reported results demonstrated the feasibility of sensing high electric fields using FBGST.

A magnetic field sensor based on FBGST was developed and proposed in [178]. The magnetic field sensor design was based on packaging the FBG head with material sensitive to magnetic fields, which has a linear deformation response when it is exposed to magnetic field variation. The deformation is transmitted to the FBGS as strain, which results in a linear Bragg wavelength shift with magnetic field variation. The sensor was placed in a ventilation duct facing the rotor poles of the field winding. The results clearly

demonstrated the capability of the FBG magnetic field sensor to measure the magnetic field induced by the rotor.

2.4 Summary

This chapter provided the research background by conducting a review on the important and relevant research aspects. The review covers the most dominant failure modes in LVEMs and highlighted their association with temperature as a failure root causes and failure indicator. This chapter also reviewed LVEM's condition monitoring systems. The review was divided into three main sections: a condition monitoring system description section, the existing commercial monitoring techniques review section (excluding thermal monitoring) and an in-depth review section on thermal monitoring techniques. Since FBGST is the drive key of this PhD research, a large portion of the provided background was conducted on this technology. The FBGST review included the key sensing aspects of this technology such as FBG structure, fabrication, interrogation and sensing principles. FBGST advantages and disadvantages in general and in particular for EMs applications were also reviewed. The last part of the chapter focused on providing a literature survey on the recent FBGST applications in rotating EMs.

In summary, LVEMs are integrated in the core process of novel, safety critical energy conversion system applications such as those in aerospace, electric vehicle and offshore wind industries. LVEM's reliability and availability are thus a key in ensuring the ambitious operational efficacy targets for these applications are met. However, LVEMs are prone to failure due stresses acting on their structure while they are in service. Therefore, on-line condition monitoring system with the potential of fault diagnostics in incipient fault stages is of utmost important to enable a reliable understanding of LVEM operational integrity and insuring its proper functioning.

Thermal stress is one of the main contributors to the machine failures, and in particular to the dominant failure modes, windings and bearing faults. In addition, LVEM's thermal status is important factor that effect their performance and lifetime. Therefore, on-line thermal monitoring is fundamental for LVEM's protection and the enhancement of their performance, reliability and availability. The exiting thermal monitoring techniques have some limitations in their attempt to achieve the reliable, effective and safe thermal monitoring of LVEMs, especially hot spot monitoring, which are the points of concern. Therefore, the development of effective thermal monitoring techniques that can enable

increased awareness of operational thermal status, enhanced thermal management and effective fault diagnosis is of utmost important.

FBG is a new thermal sensing technology that recently received great attention in the sensing research field. FBGST have significant benefits over conventional sensors such as size, inherently non-conductive, immunity to electromagnetic interferences, multiplexing and multi-sensing capability, distance sensing with high sensing response and stability. FBGST features make it an attractive sensing solution for EMs sensing thermal applications to overcome the limitation of the existing thermal monitoring techniques.

FBG embedded sensing application for EMs, however, would not be a straightforward application. There are number of technical and practical challenges that need to be considered. Thermal-mechanical cross-sensitivity aspect in FBGST imposes design constraints for sensing in EMs, since thermal and mechanical excitations are naturally and simultaneously induced in an EM structure. Therefore, for exclusive or simultaneous thermal and/or mechanical measurements an appropriate sensor design is required. Another design constraint can be raised due to the fact that FBGs are made of glass, thus appropriate packaging and installing techniques are highly required. FBGSs are delicate sensors and their measurement performance and reliability can be largely affected by sensor design, packaging, installation and calibration, which increase the challenges of embedding this sensing technology in EMs.

Recent literature demonstrates the feasibility of LVEMs embedded with FBGST for thermal sensing. However, the reported sensor designs, positioning, and installation techniques can impose significant limitations in efficacy of thermal monitoring in LVEMs; the reported sensing solutions were not positioned according to standards and were largely away from critical thermal hot spots. The reported work utilised surface bonded metallic packaging in a strong magnetic and electrical field environment, which limited their effectiveness. The embedding positions in the reported work were largely chosen to avoid some the complexities in the above challenges.

Embedded FBG sensing for LVEM on-line thermal monitoring, and in particular the winding internal thermal monitoring for healthy conditions and also for fault diagnosis condition has not been researched. Therefore, this research aims to develop embedded FBG sensing system for internal thermal monitoring in random wound components. The developed system will consider the mentioned challenges.

Chapter 3: *Simulation and Experimental Setup Description*

3.1 Introduction

This chapter demonstrates and describes the developed simulation and experimental test-rig setup for this research; it aims to provide more details than those presented in the peer reviewed paper format chapters (**Chapters 4-7**). This chapter includes two main sections: the thermal models section and the experimental test-rigs section. Section 1 presents the development of the LVEM thermal models using a commercial software package. Section 2 demonstrates and explains the built test-rigs and the associated tools for the experimental work conducted throughout the research.

3.2 Thermal models description

Thermal models of two examined LVEM topologies were developed using a commercial software package (Motor-CAD). The aim of the thermal models was to identify the highest temperature points in the investigated LVEMs under different operating conditions. Identifying hot spots locations and manifestation was deemed crucial for this research; it enables the development of understanding of optimal in-situ thermal sensing placement and hence, the appropriate sensing design requirements for the FBG sensing system. The thermal models enhanced the understanding of the test machines' thermal behaviour and the associated heat transfer modes, which is key for understanding and interpretation of the practical thermal measurements. The established thermal models were also used for planning the experimental tests in advance by identifying the required thermal equilibrium time for each of the test conditions, as well as identifying thermal safe margins for each test and validating the obtained thermal measurements.

Motor-CAD is a specialist software package for electromagnetic and thermal modelling for EMs [179]. For thermal modelling, the model package is based upon the 3D lumped network model technique, which is integrated with a 2D-finite element thermal model (2D-FE). Motor-CAD does not require the user to identify complicated thermal model parameters such as those associated with forced and natural convention heat transfer modes in EMs, which are out of the scope of this research. Motor-CAD reduces the complexity by

automatically determining the required thermal model parameters based on solving the appropriate formulae for a given machine design and specification (e.g. frame shape, cooling system, etc.) [179]. However, an accurate model in Motor-CAD requires precise settings for a considerable range of parameters, as will be explained in the following sub-sections.

3.2.1 Thermal models development using Motor-CAD

Motor-CAD thermal models were developed for the two machine designs examined in this research: one for a 0.55 kW squirrel cage induction machine (IM) and the other for a 5.5 kW permanent-magnet synchronous machine (PMSM). Full details of the test machines are provided in Section 3.3.4 of this chapter. The developed FBG thermal sensing systems were embedded in these machines to evaluate sensing performance in operational LVEMs, and investigate their potential use for on-line thermal monitoring under healthy and faulty conditions.

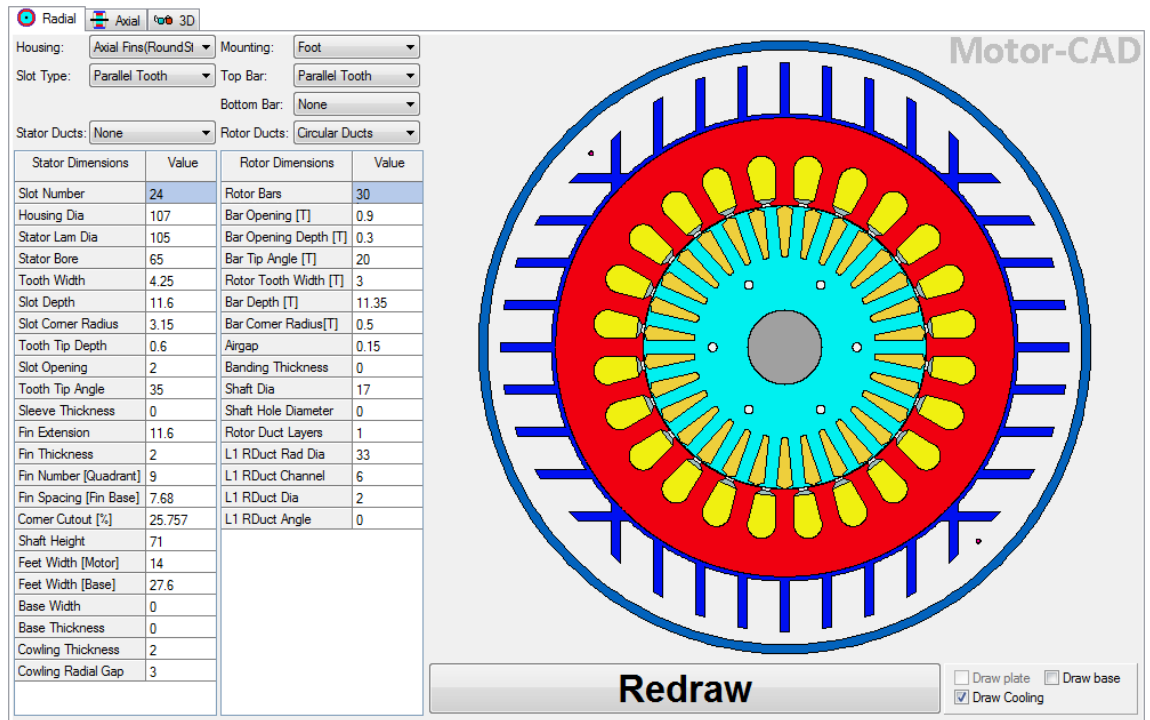
3.2.1.1 IM thermal model development

In order to develop a thermal model in Motor-CAD, a set of detailed machine dimensions are required. Certain dimensions are difficult to obtain from the manufacturer, since they are considered commercially sensitive. To overcome this challenge, a machine identical to the one tested was fully disassembled and its component dimensions measured, as shown in Fig 3.1.

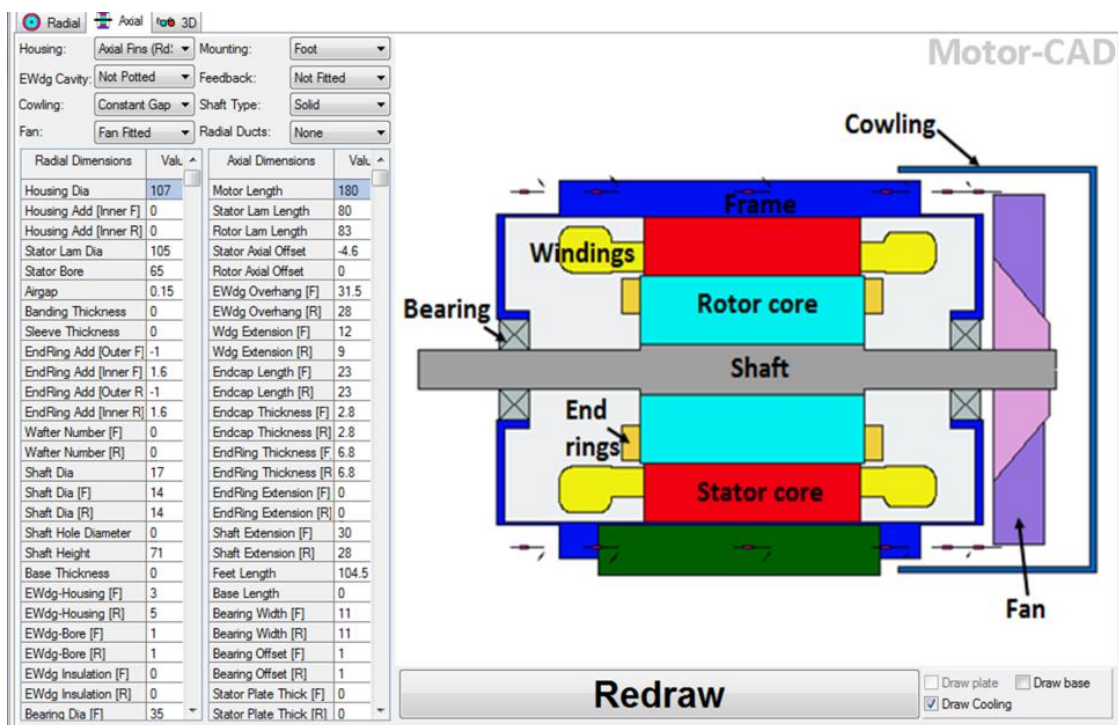


Fig 3.1: Disassembled motor and dimensions measurement for Motor-CAD model inputs

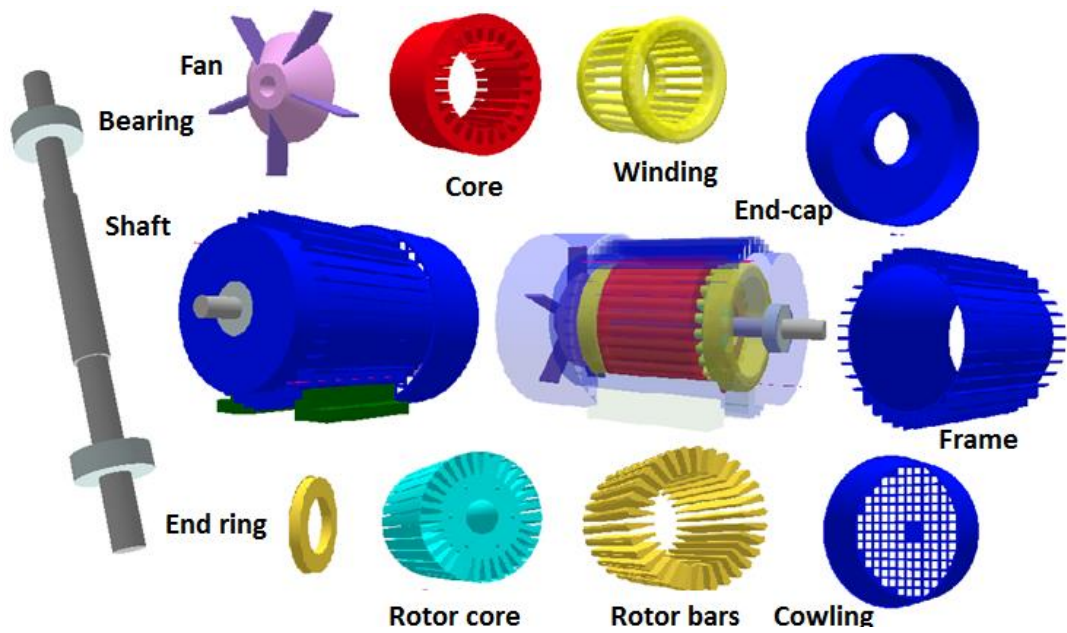
The measurements were taken based on the IM axial and radial dimensions specified by Motor-CAD. For illustration purpose, the measured dimensions and the modelled radial and axial cross sections of the test IM are shown in Fig 3.2 a and b, while the 3D models of the IM components are shown in Fig 3.2 c.



(a) Radial cross-section of the IM in Motor-CAD model



(b) Axial cross-section of the IM in Motor-CAD model









(c) IM 3D components models in Motor-CAD

Fig 3.2: IM model in Motor-CAD

Once the geometric model was completed, settings for different thermal model aspects based on the machine design and specification were required. These settings were input through a number of interface windows for each model thermal aspect (e.g. material, cooling design, heat transfer calculation, losses, etc.). For illustration, Fig 3.3 shows the interface window for the materials settings. Some of the parameter settings required execution of experimental tests, e.g. tests to measure the air flow velocity along the axial length of the machine frame at different speed conditions, and tests to determine the machine core and mechanical losses (specified by the IEEE 112 standard [107]).

Geometry Winding Input Data Temperatures Output Data Transient Graph Sensitivity Scripting									
Cooling Losses Materials Interfaces Radiation Natural Convection Blown Over End Space Duty Cycle Settings Material database									
Component	Material from Database	Thermal Conductivity	Specific Heat	Density	Weight Internal	Weight Multiplier	Weight Addition	Weight Total	Notes
Units		W/m/C	J/kg/C	kg/m ³	kg		kg	kg	
Housing [Active]		180	1000	2950	0.2719	1	0	0.2719	
Housing [Front]		180	1000	2950	0.1074	1	0	0.1074	
Housing [Rear]		180	1000	2950	0.07614	1	0	0.07614	
Housing [Total]					0.4555			0.4555	
Endcap [Front]		180	1000	2950	0.0952	1	0	0.0952	
Endcap [Rear]		180	1000	2950	0.0952	1	0	0.0952	
Stator Lam (Back Iron)		28	650	7800	1.543	1	0	1.543	
Inter Lam (Back Iron)		0.02723	1007	1.127	6.895E-06	1	0	6.895E-06	
Stator Lam (Tooth)		28	650	7800	0.8323	1	0	0.8323	
Inter Lam (Tooth)		0.02723	1007	1.127	3.719E-06	1	0	3.719E-06	
Stator Lamination					2.375			2.375	
Winding [Active]		401	400	8933	0.3686	1	0	0.3686	
Winding [Front End-Wdg]		401	400	8933	0.1728	1	0	0.1728	
Winding [Rear End-Wdg]		401	400	8933	0.1728	1	0	0.1728	
Winding [Total]					0.7142			0.7142	
Wire Ins. [Active]		0.21	1000	1400	0.01272	1	0	0.01272	
Wire Ins. [Front End-Wdg]		0.21	1000	1400	0.006157	1	0	0.006157	
Wire Ins. [Rear End-Wdg]		0.21	1000	1400	0.004995	1	0	0.004995	
Wire Ins. [Total]					0.02387			0.02387	
Impreg. [Active]		0.2	1700	1400	0.01921	1	0	0.01921	
Impreg. [Front End-Wdg]		0.2	1700	1400	0.02773	1	0	0.02773	
Impreg. [Rear End-Wdg]		0.2	1700	1400	0.02284	1	0	0.02284	
Impreg. [Total]					0.06977			0.06977	
Slot Wedge		0.21	1000	700	0.004192	1	0	0.004192	
Slot Liner		0.21	1000	700	0.0002619	1	0	0.0002619	
Rotor Lam (Back Iron)		30	550	7650	0.6777	1	0	0.6777	
Rot Inter Lam (Back Iron)		0.02723	1007	1.127	3.088E-06	1	0	3.088E-06	
Rotor Lam (Tooth)		30	550	7650	0.6754	1	0	0.6754	

Fig 3.3: Interface window for materials setting

The final model thermal network constructed by Motor-CAD from the entered data and model setup is shown in Fig 3.4. The thermal network consists of thermal resistances (conduction thermal resistance , convection thermal resistance , radiation thermal resistance , interface thermal resistance ), the power loss source , thermal nodes  and the thermal capacitances. The components are colour coded to match those shown in the radial and axial cross-sections (see Fig 3.2). The values of the thermal components are automatically determined and updated by Motor-CAD for each operating condition. For example, the values of the conventional resistances between the housing and ambient are air flow velocity dependent and thus, their values largely change with the change of cooling capability. In addition, some of the loss components are temperature and/or speed dependant (winding losses are temperature dependent, windage and iron losses are speed dependant). However, network components that change with operating conditions require suitable set-up in the model to avoid errors in the model derived temperatures. The generated thermal network model is used to perform steady-state and transient node temperature solutions by solving appropriate heat transfer equations for each defined node.

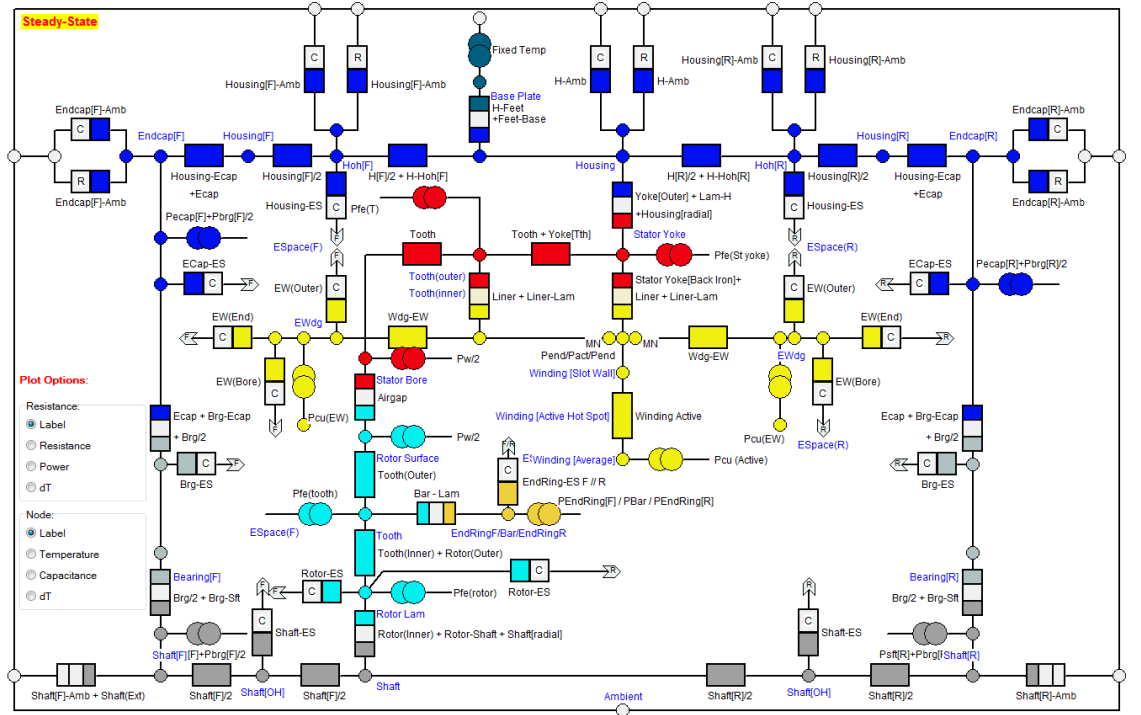


Fig 3.4: Thermal network model of test IM determined by Motor-CAD

As the interest of this research is winding hot spots monitoring, the winding's thermal model is important in this context. In general, detailed thermal modelling of random wound stator winding in LVEMs is challenging due to the arbitrary nature of the winding structure in the slot and end-winding sections. For example, accurately modelling the

enamelled wires distribution within the slot geometry and the end-winding section with estimating the impregnation quality in the winding is extremely challenging. In this research, a winding layer model integrated with the lumped network model was used. The winding layer model replaces the single node representing the winding with a number of multiple nodes to describe the temperature gradient of the winding. The winding layer model is only applied to the slot section, while the end-windings are represented by one node per each end-winding section. This is because the end-windings have a more random nature and are thus simply modelled as one thermal component [179].

The layered model divides the slot section into a number of parallel layers, as illustrated in Fig 3.5.a. Each layer represents a percentage of the materials, i.e copper, wire insulation, impregnation, air and slot liner, in the slot. The sum of cross-sectional areas related to one material (i.e copper) is equal to its actual cross-sectional area in the slot. Fig 3.5.b shows the integrated layered slot model in the lumped network circuit. The layers are represented in the network model by nodes, which are connected by a set of thermal resistances determined by the layer dimensions and material properties. The boundary node of the slot layer model is connected to the tooth and yoke core nodes. The nodes temperatures represent the temperature gradient within the slot. The rear and front end-windings are represented by a node each, and both are connected to the mid node in the layered model. The copper loss in the slot is distributed across individual nodes based on the associated layer volume.

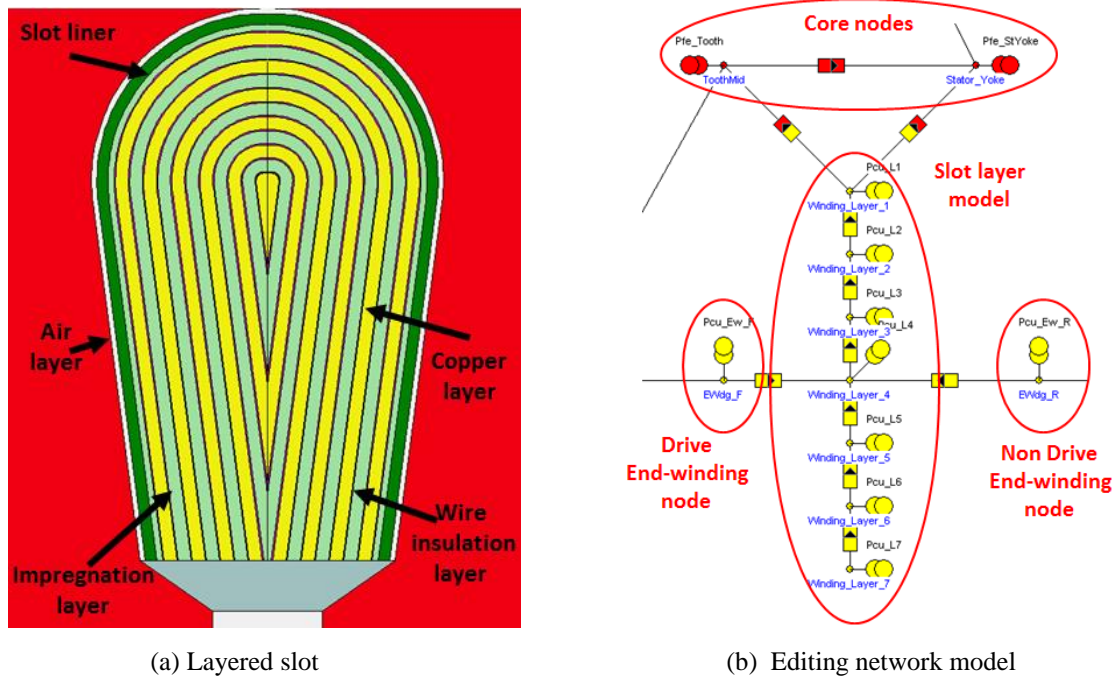
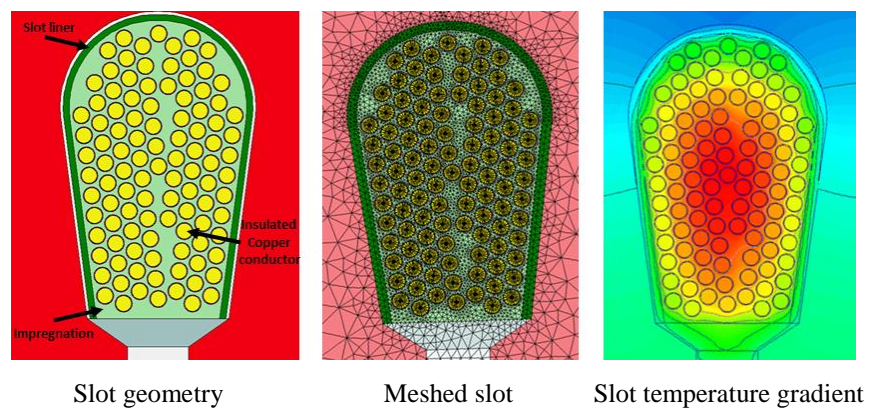
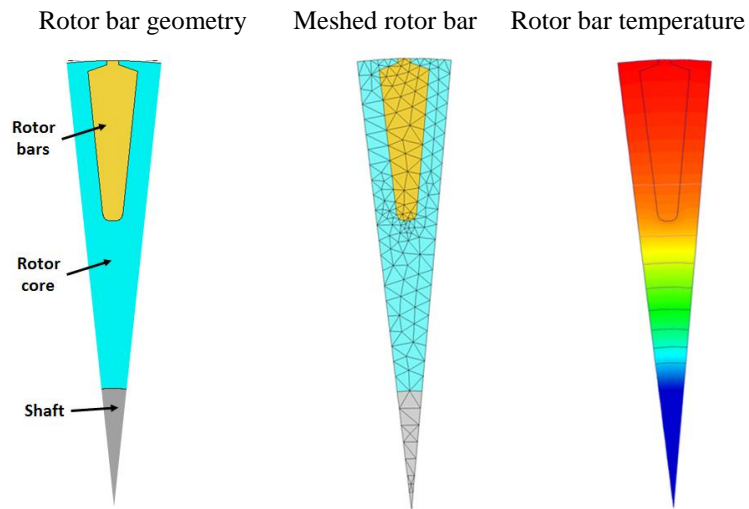


Fig 3.5: Integrating the slot layer model in the lumped network model

For more accurate winding temperature and thermal gradient prediction, Motor-CAD has a 2D-finite element (2D-FE) model integrated with the 3D lumped network model. The 2D-FE model only performs conduction heat transfer analysis; it can provide more details of the temperature gradient of various components in the machine, which can lead to identifying their hotspot [179]. FE models are unable to solve convection and radiation heat transfer mode, thus, the boundary condition temperature of the 2D-FE are provided by the lumped network model. The losses considered by the 2D-FE are the losses entered for the thermal network mode; however, it only considers the relevant losses of the part analysed by the FE model tool. Fig 3.6 shows the slot and rotor bars 2D-FE model of the modelled IM.



(a) Slot section model in 2D-FE



(b) Rotor bar section model in 2D-FE

Fig 3.6: Slot and rotor bars models by the 2D-FE

3.2.1.2 Model tuning

For accurate temperatures prediction, the developed model was tuned and validated. Motor-CAD has a built-in sensitivity analysis tool; this tool is designed for machine designers to optimise their designs. The sensitivity tool allows the user to vary single or

multiple model parameters (i.e. geometry parameters), to observe their impact on thermal, electrical and magnetic characteristics of the developed design. The sensitivity analysis tool was used in this research for tuning the developed models to enable temperature predictions close to the measured temperatures.

Model tuning using the sensitivity analysis tool was achieved by performing a number of experimental tests to obtain temperature measurements of the examined machine components under different conditions. Tests were performed such as DC test, locked rotor test, prime mover test, and different loading tests. The temperatures of the stator windings slot/end sections; core, rotor and frame were recorded during the performed tests using a set of installed thermal sensors and a thermal camera. The measured temperatures and the model initial predicted temperatures under similar conditions were set in the sensitivity analysis tool and the temperature difference between them for each component was determined. To reduce the error between measured and predicted temperatures some of the model's parameters were specified to be varied by the sensitivity tool, as explained. The model parameters were identified with their minimum and maximum variation range and their step of change. The sensitivity tool ran an iteration algorithm to find the optimal specified parameters values that provide the closest match between the predicted and measured temperatures.

A set of parameters were chosen to be modified using the sensitivity analysis tool, which were practically difficult to measure or to estimate and they can affect the model accuracy, in particular the winding temperature prediction. For winding temperature tuning the varied parameters are the impregnation quality (largely determines the winding thermal conductivity), the gap between the slot liner and slot wall (determines the conduction heat between the winding and core), and the core and frame inner bore interface gap (determines the transfer of heat from the core to frame). A variation range was set for each parameter. The impregnation quality, was set to vary from 0.4 to 0.7 (0.5 means 50 % is impregnation and 50 % is air in the winding). The variation of impregnation quality changes the impregnation layers thermal conductivity and hence, the determined thermal resistances (in the layered winding model). The stator laminations to housing interface gap was varied between 0.0 and 0.09 based on values determined in [180]. These values determine the thermal resistance between the core and frame (0.0 means perfect contact between surfaces and thus, zero resistance). The interference gap between the slot liner and slot wall was set between 0 to 0.2 mm. This value was set based on visual inspection of the examined IM.

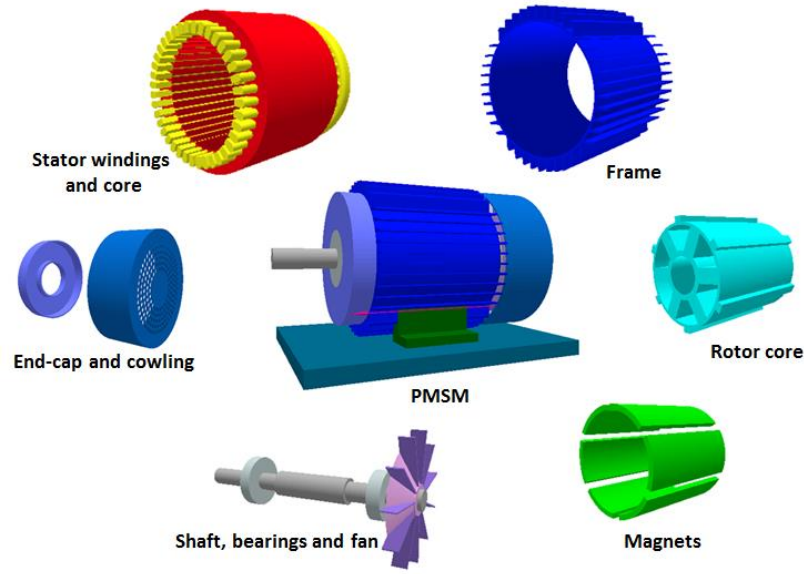
For illustration, Fig 3.7 shows the model predicted temperatures after tuning analysis, measured temperature and their temperature difference for the performed DC test [180]. The DC test was performed by applying DC power to the stator three phase windings while the rotor was at standstill. Under such test conditions, the only loss component in the machine is the winding DC loss, which can thus be directly determined. To ensure an equal DC current flow in the three-phase stator winding and thus ensure equal copper loss, the three-phase stator windings were connected in series and supplied by a single current controlled DC power supply; this was enabled by ensuring access is available to both ends of each phase winding. The heat transfer modes involved in this test are the heat conduction from the windings to the frame and natural convection from the frame to ambient. The test enables calibration of the conduction heat transfer path between the windings and the frame. To setup the model to simulate the laboratory DC test, the only loss that was set in the model was the copper loss. The cooling system model was set to natural convection, since this is the case when the rotor speed is zero in the examined motor design. After tuning, the model predicted temperatures showed good agreement to the measured values. For the winding average temperature, the temperature difference was less than 1 °C.

Legend	Graph	Motor-CAD Temperature	Validation Temperature	Difference	Percentage Difference	
	<input type="checkbox"/>	C	C	C	%	
Ambient	<input type="checkbox"/>	40				
Housing [Active]	<input checked="" type="checkbox"/>	74.046	80	-5.954	-7.442	
Housing OH [Front]	<input type="checkbox"/>	73.070				
Housing [Front]	<input type="checkbox"/>	73.029				
Endcap [Front]	<input type="checkbox"/>	72.588				
Housing OH [Rear]	<input type="checkbox"/>	73.59				
Housing [Rear]	<input type="checkbox"/>	73.304				
Endcap [Rear]	<input type="checkbox"/>	72.707				
Stator Back Iron	<input type="checkbox"/>	82.212	82	0.212	0.259	
Stator Surface	<input checked="" type="checkbox"/>	84.121	82	2.121	2.587	
Rotor Surface	<input type="checkbox"/>	82.814				
Rotor Tooth	<input type="checkbox"/>	82.814				
Rotor Back Iron	<input checked="" type="checkbox"/>	82.657	85	-2.343	-2.756	
Shaft [Active]	<input type="checkbox"/>	82.076				
Shaft [Front]	<input checked="" type="checkbox"/>	76.345	79	-2.655	-3.361	
Shaft [Rear]	<input type="checkbox"/>	64.864				
EWdg_Rear_R (C2)	<input type="checkbox"/>	95.734				
EWdg_R (Average) (C2)	<input checked="" type="checkbox"/>	96.17	100	-3.83	-3.830	
SlotCentre (C2)	<input type="checkbox"/>	87.100				
Liner (C2)	<input type="checkbox"/>	90.113				
Wdg_inner_C (C2)	<input type="checkbox"/>	95.148				
Wdg_F (C2)	<input type="checkbox"/>	95.839				
Wdg_R (C2)	<input type="checkbox"/>	95.463				
Wdg (Average) (C2)	<input type="checkbox"/>	94.835				
Stator Tooth (C2)	<input type="checkbox"/>	84.183				
Winding (Average)	<input checked="" type="checkbox"/>	94.905	95	-0.095	-0.100	

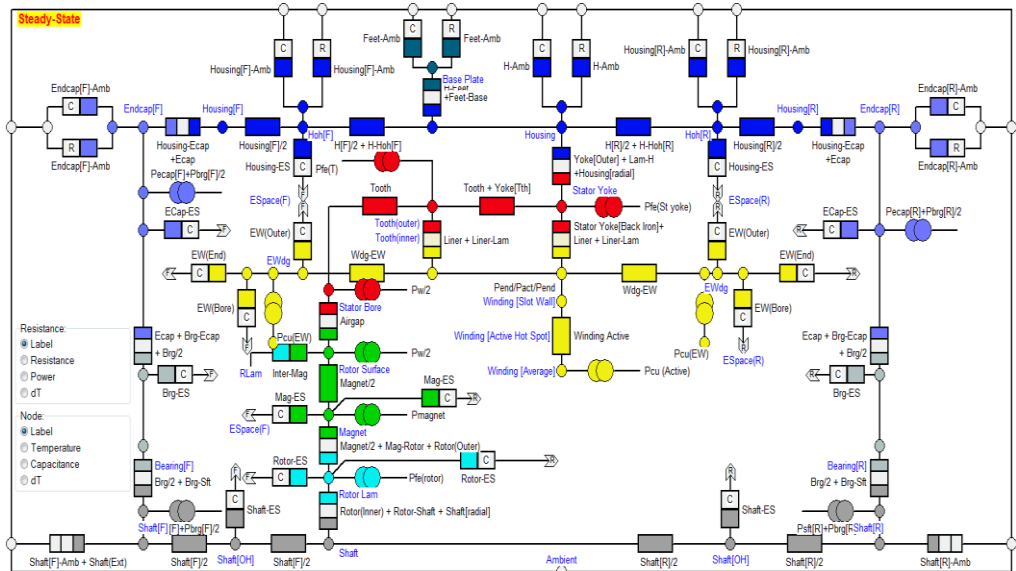
Fig 3.7: Tuned Motor-CAD model results for the DC test

3.2.1.3 PMSM thermal model development

The lumped network and FE thermal models for the 5.5 kW PMSM were also developed and tuned in Motor-CAD following the same procedure as that followed for the IM model. However, unlike with the IM model, where the required geometry and specifications were taken from an identical disassembled machine, here the model required geometries and specifications were determined during the PMSM rewinding process. Fig 3.8a shows the 3D plots of the modelled machine components and Fig 3.8b shows the determined PMSM lumped thermal network. Fig 3.9 shows the slot and rotor FE model sections of the examined PMSM.



(a) 3D components model of the PMSM



(a) Thermal network model determined by Motor-CAD

Fig 3.8 : 3D components model and the thermal network of the PMSM in Motor-CAD

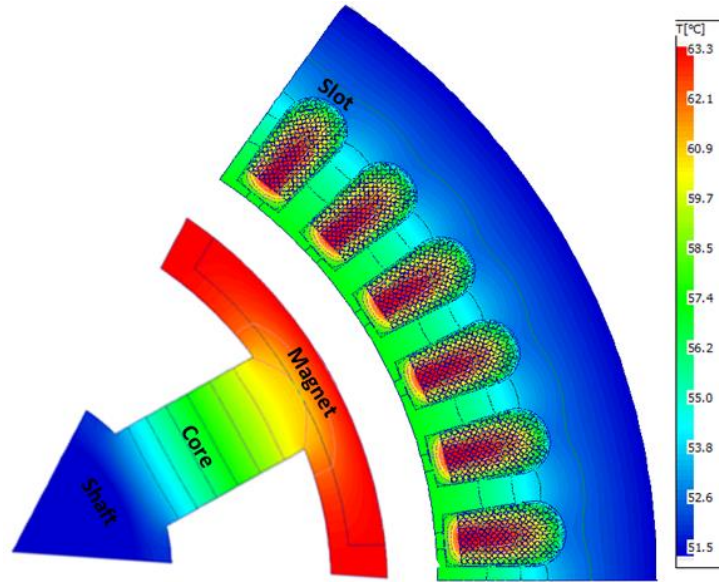


Fig 3.9: 2D-FE model for the PMSM in Motor-CAD

3.3 Experimental setup description

The main goal of this PhD research was to investigate the potential use of FBGST for reliable and effective thermal condition monitoring of LVEMs. The investigation was conducted in stages based on extensive experimental work that was required to achieve the research goal. In the first stage, the important sensing aspects of FBGST such as in-situ sensing design, distributed sensing, calibration, characterisation and installation for embedding thermal sensing applications in LVEMs were investigated. Then, in the second stage, the in-situ sensing performance of the FBG sensing system developed in the first stage was evaluated in operational LVEMs. The last stage investigated the potential use of in-situ FBG sensing system for condition monitoring under healthy and faulty conditions. To this end, it was necessary to develop different experimental test-rig setups that aligned with each stage of research development.

The FBG thermal sensing system and the experimental test-rigs developed and used in this PhD research are described and discussed in this section as follows: 1) first the FBG sensing system is presented and discussed including: in-situ thermal sensor design and specification, packaging, procurement, interrogation and measurement software; 2) the test system developed for FBG sensors calibration and characterisation is then presented and explained; 3) the developed prototype coil systems used as a test vehicle for understanding the performance implications of the sensing aspects of a wound coil embedded FBG thermal sensor are then described; 4) the test-rig layouts, construction, operation and design features of two machine topologies embedded with FBG thermal sensing system for healthy and faulty condition thermal monitoring are explained.

3.3.1 FBG thermal sensing system

This section describes the FBG thermal sensing system, including the developed in-situ FBG temperature sensors for thermal monitoring in LVEMs and the commercial interrogation system used in this PhD research.

3.3.1.1 FBG temperature sensor design and packaging

The key target sensing application in this research is the interior monitoring of a stator random wound coil structure, in direct proximity to the coil thermal hot spot. The primary design constraints of the thermal sensing system arising from its application within a current carrying coil are: 1) the desirability for the sensing element to be dielectric; 2) possess EMI immunity; 3) have the capability to be placed in the centre of the coil structure, implanted between individual current carrying conductors; and 4) be capable to function in and withstand the thermal environment characteristic of winding elements in conventional EM designs [48, 56]. The FBG head itself can act as a thermal sensing element that satisfies the above design requirements. However, the fibre it is imprinted on is fragile and requires suitable packaging to ensure its mechanical integrity. In addition, the packaging plays an important role in enabling exclusively thermal measurements, as it isolates the FBG head from external mechanical excitation and thus eliminates the cross-sensitivity effect in the shifted Bragg wavelength due to temperature and strain, as explained in Chapter 2, Section 2.3.4.3 [48, 56].

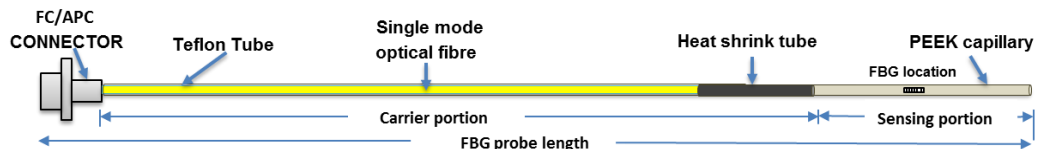
To satisfy sensor design requirements, a Polyetheretherketon (PEEK) capillary was proposed in this research to package the FBG sensing heads. PEEK was chosen due to its mechanical and dielectric properties that are deemed suitable for the operating environment found in conventional EMs [48]. PEEK has replaced stainless steel in applications such as aerospace, due to its high degree of hardness combined with flexibility and extreme resistance to harsh environments [181]. A PEEK capillary can protect the FBG head from external mechanical excitation in an EM application and hence, ensure wavelength shifts only occur due to thermal excitation. Furthermore, its flexibility makes it an attractive packaging material for distributed FBG thermal sensing embedded in wound coils, as the sensor package can readily conform to the coil shape. PEEK also has good dielectric properties. It has been proposed as an insulation material for EM applications (e.g. copper wire insulated with PEEK, slot liner made of PEEK) [182].

The dimensions and properties of PEEK capillaries used in this research are shown in Table 3.1. Capillary dimensions were selected to provide a close match to the 0.56 and/or 0.6 mm diameter size of the test coil's copper wire and therefore, facilitate easier

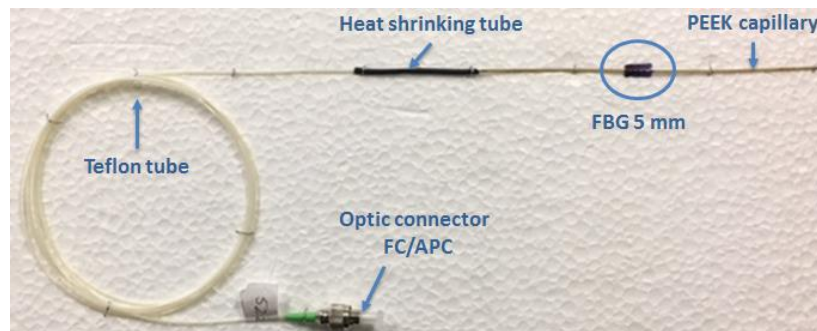
placement. These dimensions also allowed a large area of contact between the sensor PEEK package and the surrounding copper wire to help achieve a more effective thermal sensing performance of the FBG sensor embedded within the random wound coil structure. A narrow capillary wall of 0.1 mm was used, which is desirable to enhance the sensor response time by reducing the packaging thermal resistance [48, 53].

Table 3.1 : Dimensions and properties of PEEK capillary [181]

Fig 3.10 shows the schematic diagram and a photograph of an example of a single in-situ packaged FBG thermal sensing element (the probe contains a single FBG head). The same design is applied for an array FBG thermal (the probe with multiple FBG heads). For the purpose of this research, the total length of an individual FBG probe ranges from 1.5 m for a single FBG probe to 3 m for an array FBG probe. The FBG probe can be divided into two portions; the sensing portion and the non-sensing portion. The sensing portion is the single/multiple FBG head/heads that are contained by the PEEK capillary, as shown in Fig 3.10. The length of this section is identified by the length of the capillary which is chosen



(a) Schematic diagram



(b) Photograph of FBG packaged temperature sensor

Fig 3.10: FBG thermal sensor design: diagram (top) and photograph (bottom)

to match the length of the targeted coil/windings area. The non-sensing portion is the remaining length of the optical cable and the probe connector. This part of the optic cable is protected by a Teflon tube in this work. The connection between the packaging of the two parts is maintained by a heat shrinking tube.

The embedment procedure of the packaged FBG temperature probe within a random wound coil/windings structure implies that the packaging capillary has to first be installed within the monitored coil/winding structure during the winding process, and the FBGs

inserted in the packaging after the winding process is completed. More details of the embedding methodology are presented in Sections 3.3.3 and 3.3.4. A preparation stage for the FBG thermal probe is required before embedding it into the monitored coil/windings. In this stage, the fibre containing the FBG head and the packaging capillary goes through the preparation procedure to ensure appropriate sensor dimensions for the targeted coil/windings structure. Careful measurements are taken to get the correct length of the capillary packaging required and to identify the sensing areas on the surface of the PEEK capillary for careful positioning of the sensing head in the targeted location within the monitored coil. The PEEK capillaries are carefully cut to obtain clear and smooth end openings. Fig 3.11 illustrates the preparation procedure of an in-situ FBG temperature sensor (the pictures were taken through the lens of a laboratory magnifying light).

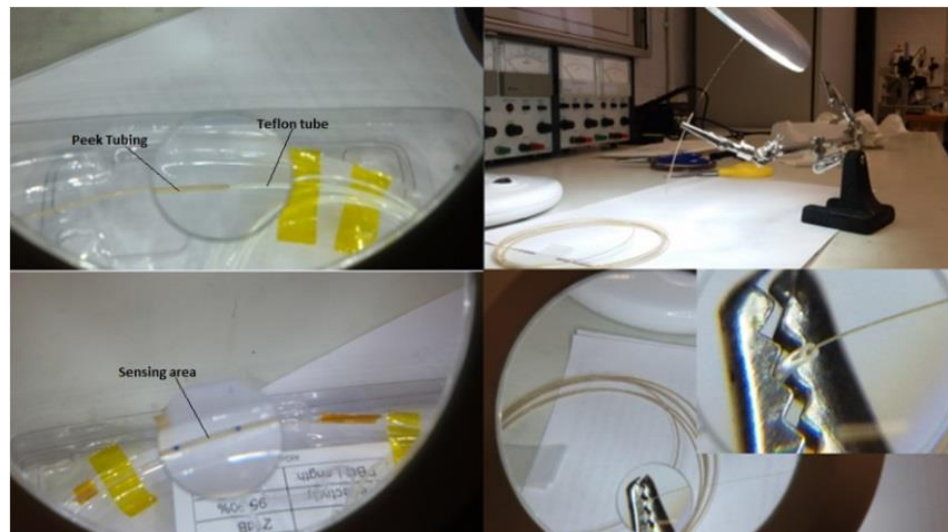


Fig 3.11: Preparing procedure of the packaged FBG temperature sensor

The use of other non-metallic and metallic capillaries was also examined in this research for assessing the influence of different packaging materials on in-situ thermal measurement performance. The dimensions of these capillaries were identical to the PEEK capillary dimensions provided in Table 3.1. The preparation procedure for the development of the FBG sensor packaged within these capillaries was closely similar to that described for the PEEK capillaries. Cutting the fine metallic capillaries to the required length, however, posed a challenge: a diamond cutter was therefore used for the purpose of cutting the metallic capillaries. Nevertheless, this produced sharp and unclear opening ends, which can potentially damage the optical fibre during installation, as shown in Fig 3.12 (a). To resolve this problem, the capillaries opening ends were carefully scraped away with sand paper. The final finishing of the capillary cutting is shown in Fig 3.12 (b).

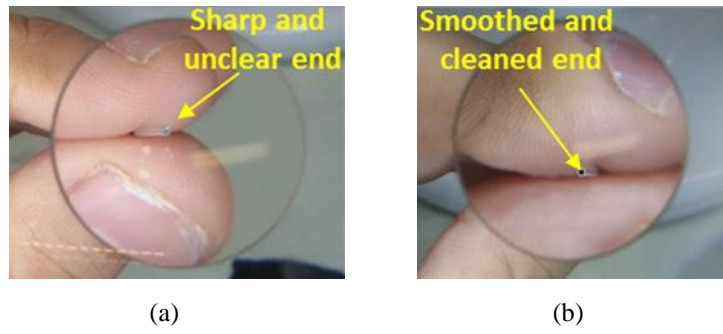


Fig 3.12 : Preparing non-metallic packaging capillaries for sensing fibre insertion

3.3.1.2 FBG sensing specification and procurement

For the purpose of this research, a number of FBG single and array sensors were ordered from manufacturers that specialise in the production of FBG fibres. FBGSs are not off-the-shelf products. To order an FBG single/array sensor, the key design and specifications of the sensor must be clearly identified (i.e. wavelength centre, wavelength range, FBG head length, number of heads, fibre type, connector type, etc.) by the end user and provided to the manufacturer. The first step is to identify the sensor structure and dimensions; this includes the number of FBG heads, their dimensions, positions on the fibre and the distance between them. This information mainly depends on the type of application and the dimensions of the monitored structure, which requires accurate physical dimensions. A final sketch of the designed FBG sensor fibre has to be provided to the manufacturer. Fig 3.13 shows designs of a single (a) and array (b) FBG sensors to be ordered.

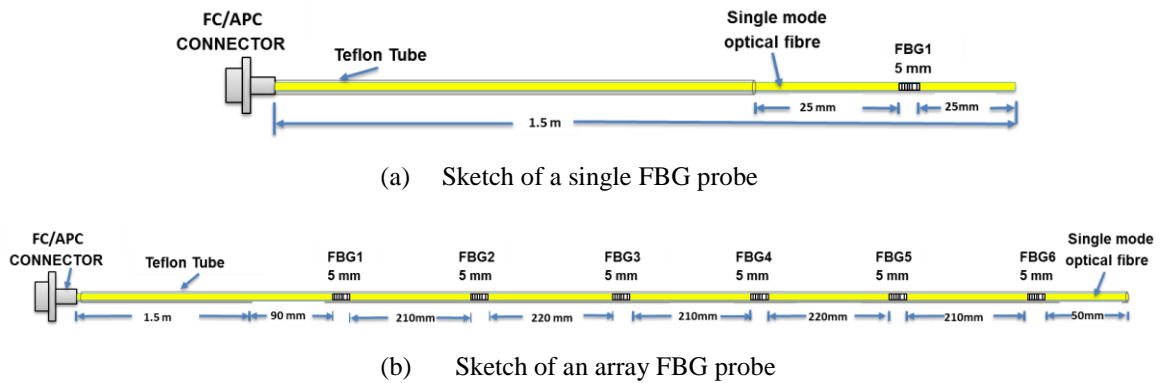


Fig 3.13: FBGS probes design sketch for order

Once the sensor structure and dimensions are identified, the sensor's specifications need to be identified such as the centre wavelength range, the fibre and coating type, and the probe connector type. Table 3.2 presents some specifications that were provided to the manufacturer for the sensors used in this research. The FBGs centre wavelength range is identified based on the interrogator unit broadband light source range. The type of fibre used in this investigation was a single mode Polyimide SMF-28e fibre. The Polyimide

fibre was chosen because it can withstand continuous temperatures of up to 300 °C [183]. It is also available as a standard SMF or bend-insensitive SMF. The latter type is preferred for this application since it is designed for small a bending radius and lower bending loss. The fibre is recoated with a layer of Polyamide to enhance it mechanical strength. The connector type used in this work was FC/APC, which is consistent with the interrogator unit; this connector type is recognised as the preferred choice for FBG sensing due to low return losses.

Table 3.2: FBG sensor specifications

FBGs centre wavelengths	nm	1528 - 1568
FBG length	mm	5
Refractivity	%	> 80 %
Bandwidth	nm	< 0.3
Connector type	--	FC/APC
Fiber Length	m	≈ specified on drawing
Fibre type	--	Polyimide SMF-28e (standard – bend sensitive)
Recoating	--	Polyimide
Strain range	μϵ	± max Standard designed
Temperature range	°C	Up to 250°C

Fig 3.14 shows some samples of FBG sensors ordered during this research. The FBG sensors were ordered from two FBGST manufacturers: Smart Fibres based in the UK [136] and AtGrating technologies based in China [184].



(a) Single FBG



(b) Array FBG with 2 FBG heads

Fig 3.14 : Supplied FBG single and array probes

3.3.1.3 Interrogation

Fig 3.15a shows the commercial SmartScan 04 interrogator unit used in this research. It is manufactured by Smart Fibres, who develop measurement systems based on FBGST. The SmartScan 04 unit is a compact and robust interrogator with a high resolution (< 1pm wavelength shift) and a maximum sampling frequency of 25 kHz for dynamic measurement of FBG sensors [136]. The interrogator specifications are provided in Table 3.3. Fig 3.15b illustrates the general system diagram of the SmartScan interrogator; it is based on the wavelength division multiplexing technique (more information on WDM is

provided in Chapter 2, Section 2.3.3.1). The SmartScan has four channels presented by the FC/APC connectors and labelled as CH1, CH2, CH3 and CH4 in Fig 3.15a. The interrogator communicates with the interrogated FBG sensors through these channels via sending and receiving light. Each channel is capable of running simultaneously up to 16 FBGs imprinted in a single strand of single mode optic fibre. The data acquired by the SmartScan are transmitted to a computer for processing through a RJ45 connector. There is an optional data logging connector to connect a USB memory device (for large data sets).

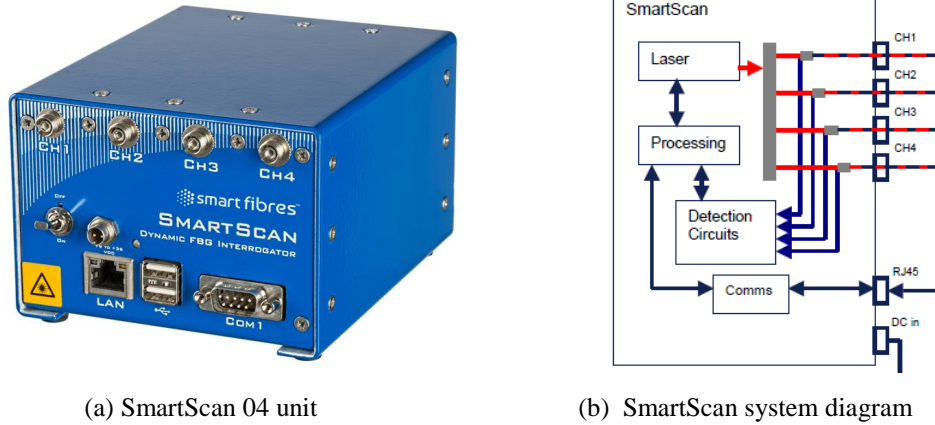


Fig 3.15: SmartScan interrogator unit [136]

Table 3.3: SmartScan interrogator specifications [136]

Specifications	
Wavelength Range	40 nm (1528 – 1568 nm)
Number of Optical Channels	4
Maximum Number of Sensors/Channel	16
Scan Frequency (all sensors simultaneously)	2.5 kHz
Maximum Scan Frequency (with reduced wavelength range)	25 kHz
Bragg Grating Full Width Half Maximum (FWHM)	Minimum > 0.2 nm, > 0.5 nm recommended
Wavelength Stability	< 5 pm over operating temperature range, +/- 20 pm over 25 years
resolution	< 1 pm
Optical Connector	FC/APC
Operating Temperature	-15 to +55°C
Dimensions	140 x 115 x 85 mm
Data Connector	RJ45 standard

3.3.1.4 SmartSoft

SmartSoft is a software package designed by Smart Fibres that is supplied with the SmartScan interrogator unit to operate the device; it is a LabVIEW based software routine with a customised interface window. SmartSoft enables setting-up the interrogator and the connected FBGs and processing the acquired data to achieve different sensing requirements through a number of interface windows, which contain a range of settings to setup the interrogation system and the interrogated FBGs [136]. For demonstration, the

following paragraphs and figures explain the setting up and data acquisition from an FBG array sensor contains four FBG heads.

First, the FBG array probe is connected to CH1 in the SmartScan via the FC/APC connector. The SmartScan is connected to a computer that runs SmartSoft to initialise the SmartScan and allow communication between the SmartScan and the array probe. Fig 3.16 shows the instrumentation setup window in SmartSoft that was used to setup the connected FBGs, the data acquisition system and the processing system.

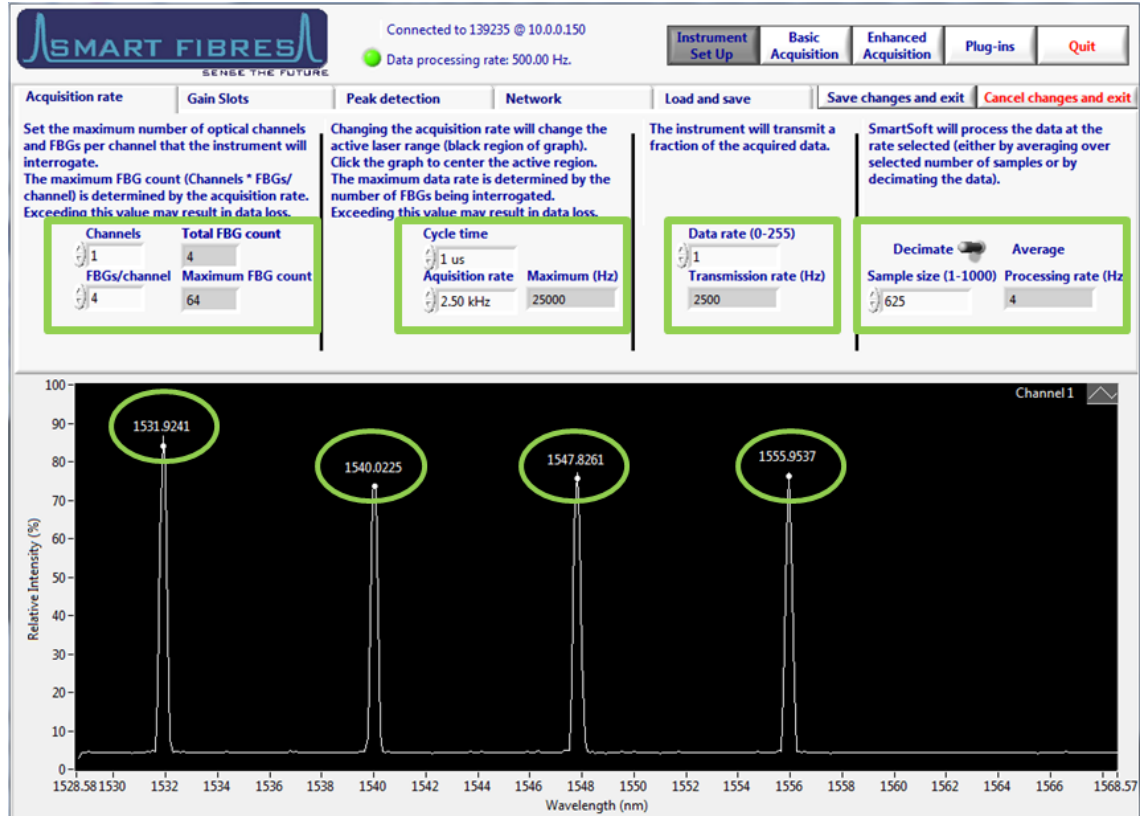


Fig 3.16: SmartSoft instrumentation window interface

The SmartScan acquisition rate can be adjusted based on the number of the activated optical channels and the number of FBGs per channel, which is set to a desired value within specification (first green box from the left in Fig 3.16). This configuration enables the active light wavelength range sent to the optical fibre containing the FBG sensors to be adjusted, which in turn enables tuning of the scan cycle time (second green box from the left in Fig 3.16). The cycle time is the time required to complete one scan of the light sent to the FBGs and received by the detector circuit. For example, a single FBG probe with λ_B at 1550 nm can be only illuminated with a maximum light range of 3 nm to operate as a thermal sensor. Therefore, activating 3 nm range of the broadband light source (1548.5 – 1551.5 nm) will reduce the cycle time required to scan this light range (3 nm) compared to the time required to scan 40 nm of the whole light range of the broadband source. Table

3.4 shows the possible scan rates with the associated activated light ranges for SmartScan [136].

Table 3.4: SmartScan multiple scan rate[136]

Scan rate kHz	Activated bandwidth nm
2.5	40
5	20
10	10
20	5
25	4

The rate of processing the data by the SmartSoft can be adjusted; this can be achieved by either changing the transmission rate (the rate of transmitting the data from the SmartScan to the PC) or by changing the processing sampling size (third and fourth green box from the left in Fig 3.16, respectively). Usually, all of the acquired data are transmitted to the PC for processing. However, it may be desirable to slow the transmission rate on a slow network connection or because the host PC cannot process the data fast enough [136]. The processing sampling size can be set with a number x , which will result in every x^{th} transmitted data point being processed [136]. In Fig 3.16 the lower window shows the reflected light spectrum from CH1, which only shows the activated channel in this case. It can be seen there are four peaks with numbers displayed at their respective tops highlighted by green circles. Each peak represents the reflected λ_B from one FBG in the FBG array sensor. The numbers are the determined peak λ_B for each FBG head by SmartSoft.

Another important setting feature provided by SmartSoft is the wavelength gain slot. This feature enables each FBG to operate within an individual wavelength window to prevent measurement interference. Moreover, in each slot the peak intensity can be amplified (this is applicable for FBGs with low reflectivity); however, care must be taken so the FBG peak does not saturate. Fig 3.17 shows the slotting of the CH1 wavelength spectrum to four windows i.e. one window per FBG head. The slot boundaries are defined by the yellow lines and were set using SmartSoft. The gain slot feature can be applied to all interrogator channels; this is an important feature when there are large numbers of FBGs connected to each channel.

Once the FBGs, the acquisition and processing systems are setup, the sensor measurement type and unit can be set and the real-time measurements can be viewed and

recorded. For measurements (i.e. strain or temperature) other than the measured reflected wavelength, a number of coefficients are required to perform the conversion from the measured wavelength shift to the measured physical quantity. These coefficients are typically obtained by calibration tests, as detailed in Section 3.3.2. Fig 3.18 shows the final setting of the FBG sensor array. The left table displays the available FBG sensors per channel that correspond to the settings made in the instrumentation setup window. The right hand table shows the configured sensors that can be monitored on-line and recorded. The first four arrows represent the instantaneous monitored peak λ_B for each FBG and the last four arrows represent the measured temperature based on the entered coefficients for the wavelength shift-temperature conversion. These data can be graphically presented on-line using the ‘Charts’ tab.

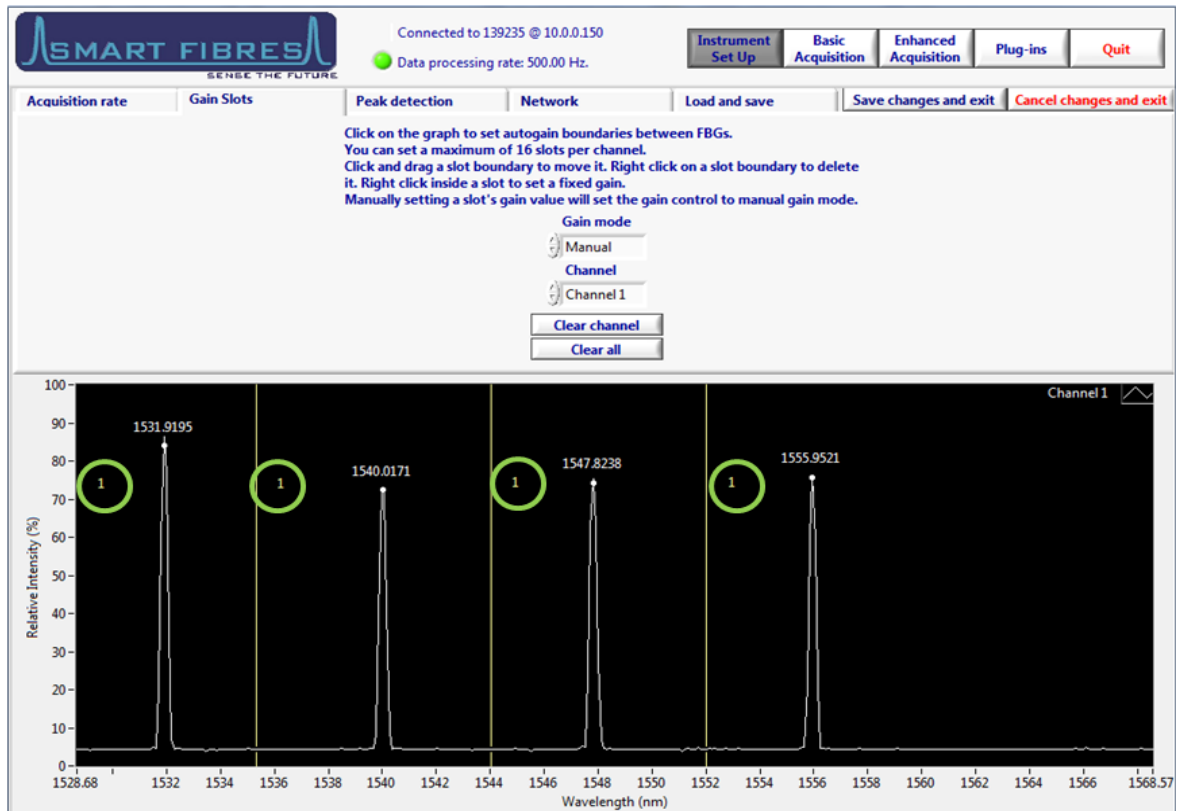


Fig 3.17: Slotting of the wavelength spectrum

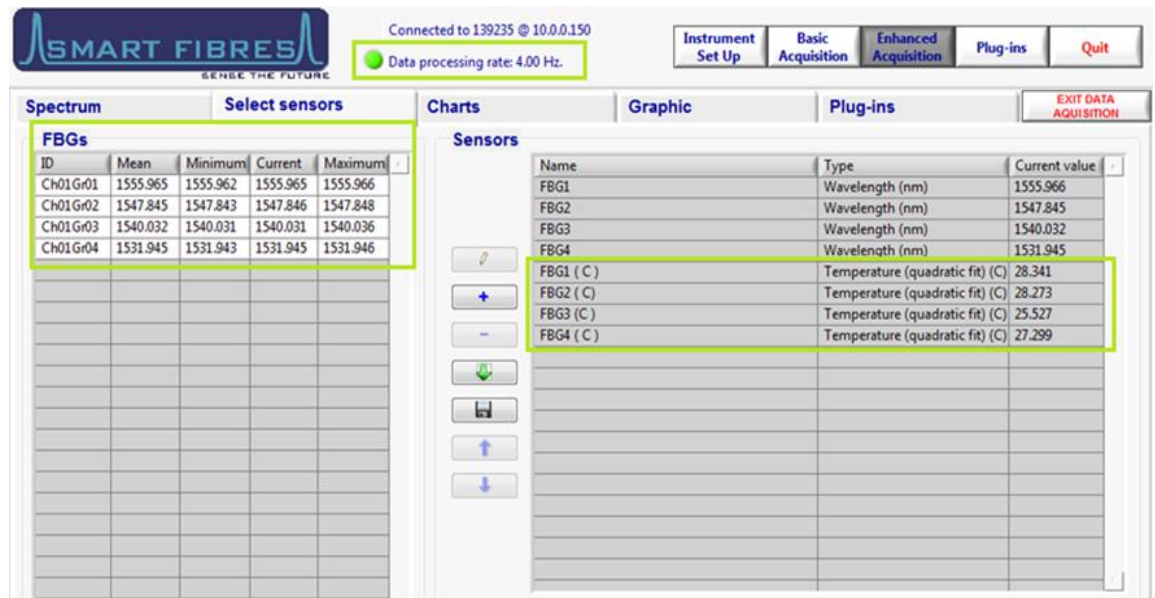


Fig 3.18: Enhanced acquisition – Sensors tab

3.3.1.5 Fibre optic rotary joint (FORJ)

For the purpose of investigating the use of FBGST for rotary components sensing applications, a fibre optic rotary joint model (MJXA-FAP-155-28-FA) manufactured by Princetel was adapted to the examined machine geometry to enable communication between rotating in-situ installed FBGs and the stationary interrogator unit. Fig 3.19 shows the FORJ structure and Table 3.5 shows its specifications. The FORJ consist of two parts, stator and rotor, which are mechanically-optically linked; it is compact and light with very low return loss performance. The maximum operating speed of the applied joint model is 2000 rpm, which is suitable for commercial LVEM applications examined in this work; the operating speed of FORJs can generally be designed to be much higher [185].

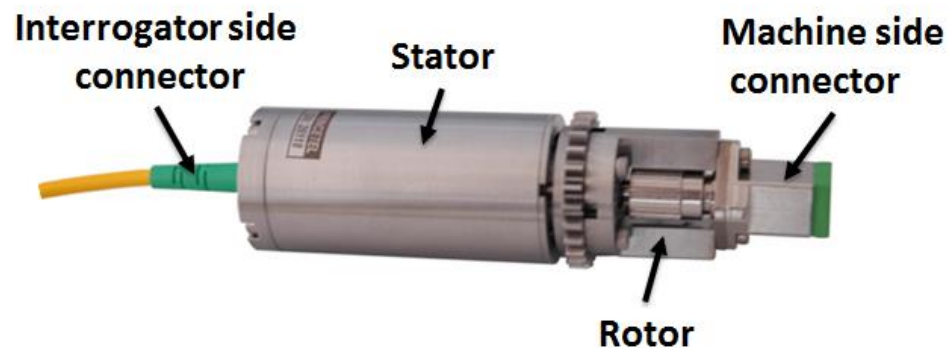


Fig 3.19: Fibre optic rotary joint model MJXA-FAP-155-28-FA

Table 3.5: MJXA-FAP-155-28-FA specifications

Specifications	
Wavelength range	650-1650 nm
Insertion loss	<2 dB (typical: <0.5 dB)
Return loss (SM)	>40 dB (typical: 45 dB, 23 °C), >55 dB (MJXA)
Maximum speed	2,000 rpm
Start up torque	<0.01 Nm
Working temperature	-40 to 85 °C
Housing material	Stainless steel
Fiber types	Single mode
Connector types	FC/APC
Dimensions	28 mm dia x 680 mm length
Weight	10 g
Estimated life cycle	>500 million revolutions

3.3.2 Thermal calibration test-rig

To obtain temperature readings from the reflected λ_B of the FBG sensors, a thermal calibration test is required. This thermal calibration test helps to determine the optimal temperature-wavelength fit curve for each FBG. In this test, the FBGs to be calibrated are exposed to controlled, steady-state thermal excitation levels and their reflected λ_B s are monitored and recorded for each thermal level. The FBG under calibration could be a single/array, unpackaged (free FBG heads)/packaged and embedded/free within coil/machine structure.

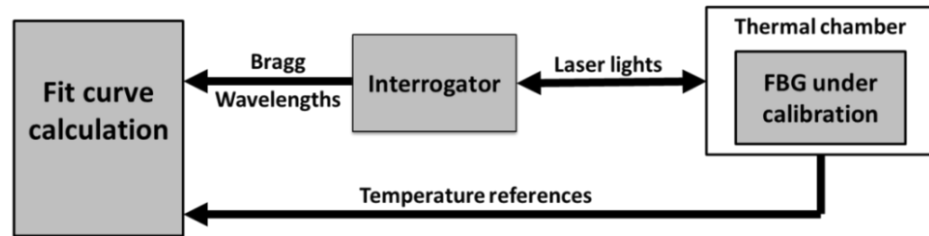
To achieve the required controlled thermal excitation, a controlled industrial thermal chamber (type Lenton WHT6/30) with temperature control accuracy of ± 0.5 °C and a maximum temperature of 500 °C was used. The temperature references were read by the chamber proprietary thermal sensors and for correct temperature verification, a type K thermocouple sensor conditioned by K-type thermometer (FLUKE t3000 FC) was placed inside the chamber in close proximity to the FBG sensors under calibration. Fig 3.20 shows the industrial thermal chamber and a general schematic diagram for the calibration test.

The thermal calibration tests were performed by first placing the FBG sensor in the thermal chamber and then exposing it to incremental set point temperatures up to the rated temperature of the targeted coil/machine for embedding. The temperature is regulated by the chamber controller in the tests in a rising sequence of 10 °C steps, which was deemed sufficient to achieve satisfactory characterisation of the sensor behaviour. At each step the temperature was held constant for a sufficient period to ensure the thermal equilibrium is achieved before thermal measurements were taken. The FBG reflected wavelength and the chamber temperature were recorded at each evaluated thermal equilibrium set point in the

investigated temperature range. The recorded data was then used to calculate the temperature-wavelength conversion fit curve. The polynomial quadratic fit curve was the fit curve used in this research as based on undertaking a comparison study of different curve fit models, i.e. linear fit, 2nd, 3rd and 4th order polynomial fits, it was found to be the most appropriate fit for the FBG thermal sensors in this type of application[186].



(a) Commercial thermal test chamber



(b) Schematic diagram of thermal calibration test setup

Fig 3.20: Experimental system for FBG sensor calibration tests

3.3.3 Prototype wound coil test system

The proposed FBG thermal sensing system design was extensively examined using prototype coils, which provided an optimal test platform to examine sensing performance before embedding the sensors and investigating their performance in operational LVEMs. This intermediate stage aimed to understand and evaluate the in-situ FBG thermal sensing system performance, calibration, and characterisation. It also provided insight into the performance implications of the installation procedure of a wound coil embedded FBG thermal sensor, as a step to enable further development of FBG embedded thermal sensing applications. The prototype coil systems were designed to replicate a standard low power stator winding design of LVEMs [53, 56].

3.3.3.1 Test prototypes coil system design

The prototype coil was a multi-turn random wound coil, which was manufactured on a purpose made coil bobbin using a winding rig. The coil bobbin was designed to fit into the winding rig and could be easily dismantled to facilitate the removal of the wound coil and its placement into the targeted housing on a desired test rig without damaging the coil

insulation and the embedded in-situ FBG sensor. Fig 3.21 shows the test random wound coil and its manufacture [56].

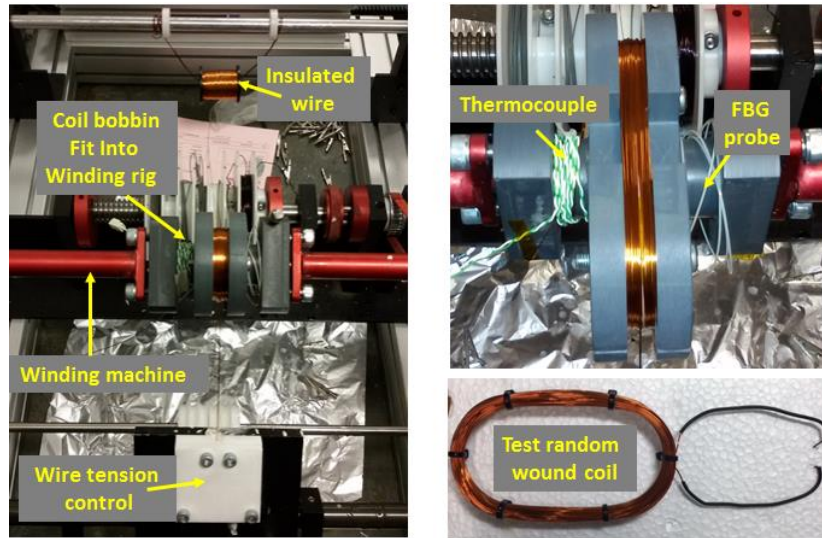


Fig 3.21: Prototype random wound test coil ant its manufacture

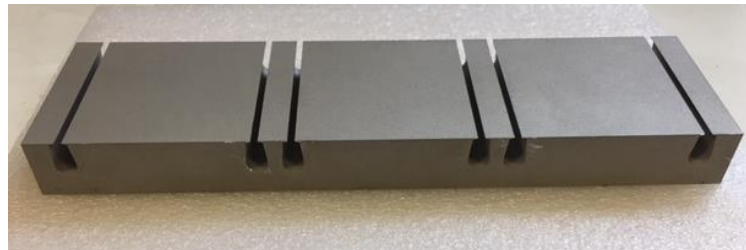
The prototype coils were largely housed in slot assemblies (i.e. motorettes) designed according to relevant IEEE standards [95]. However, for research purposes the prototype coils were also embedded in a commercial low voltage motor core structure and a purpose made steel core structure. Fig 3.22 shows the housing for the prototype random wound coil, an IEEE slot assembly (see Fig 3.22.a), a commercial low voltage motor core structure (see Fig 3.22.b) and a multi slot steel core structure (see Fig 3.22.c).



(a) IEEE motorette slot assemble



(b) Prototype low voltage core structure



(c) Multi slot steel core structure

Fig 3.22: Test coil embedded in different housing structures

3.3.3.2 In-situ FBG sensor installation in the prototype coil systems

To ensure the FBG temperature sensors were positioned in the targeted hot spot sensing points (the interior of the prototype coils structure) the following procedure was applied: the packaging capillary was first embedded within the coil structure; it is not instrumented with the FBG sensor at this stage. For the IEEE motorette coil system, this was achieved by winding half of the coil turns, fitting the capillary and then winding the rest of the coil. Once the coil was completed and mounted on the IEEE motorette frame, the FBG sensing fibre was loosely inserted into the capillary. The embedded sensor's positioning is illustrated in the IEEE motorette coil cross section sketch in Fig 3.23a.

For the prototype coils embedded in the prototype stator core or in the purpose-built steel core, the placement of the FBG sensor in the targeted point was achieved by first winding the full coil with the required number of turns using the bobbin and the winding rig. Then, half of the coil turns were inserted into the relevant slot and then fitting the packaging capillary in the coil centre. Once this was completed the remainder of the coil was inserted. The FBG sensing fibre was then inserted into the capillary to form an operation in-situ FBG thermal sensor. Fig 3.23b and c illustrate the embedded sensor locations in the cross-section of the stator core and the built core. This process enables in-situ hot spot sensing and offers an advantage of avoiding the undesirable exposure of the fragile sensing fibre to mechanical stress during the winding process [109].

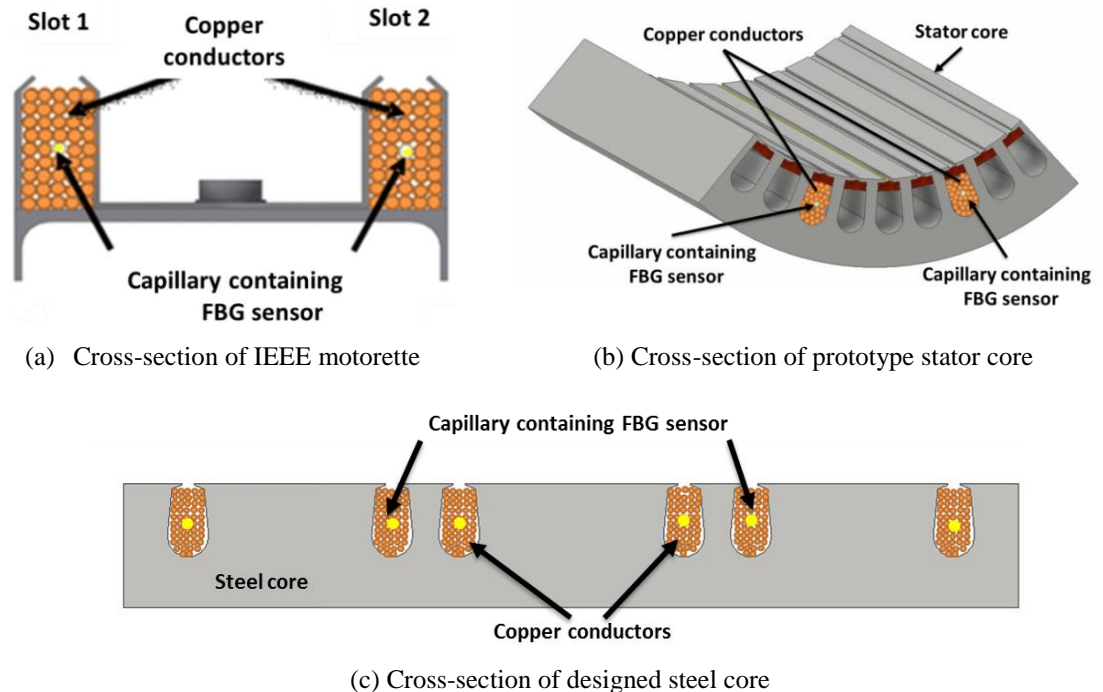


Fig 3.23: The embedded FBG sensor positions in the prototype coil structures

For testing, the desired thermal excitation conditions applied to the prototype coils embedded with FBG temperature sensors were experimentally achieved by two methods: 1) by exposing the test coils system to external controlled thermal excitation using the controlled thermal chamber or 2) energizing the prototype coils with a controlled DC current to induce internal thermal excitation. The choice of the thermal excitation method is based on the investigated case study. For the external thermal excitation, the thermal chamber used in the calibration test was used here as well, with the FBG embedded coil system placed into the chamber. For the internal thermal excitation, a programmable DC power supplies (type SorensenSGI100/50D, rated at 50A/100V) or (TTi CPX series rated at 20A/60V) was used. Fig 3.24 shows photographs of the used DC power supplies. The higher rated Sorensen DC power supply was used to apply a fast thermal variation by applying a high DC current for a pre-determined time. The output DC power was controlled to specific applied current profiles and hence, specific thermal excitation profiles in real-time by controlling the DC power supply using LabVIEW code.

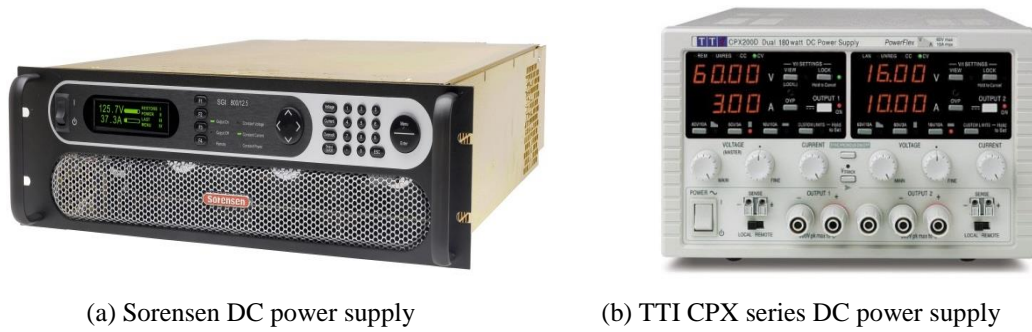


Fig 3.24: Test DC power supplies

3.3.4 FBG embedded LVEMs test-rigs

To investigate the performance of the proposed in-situ FBG thermal sensing system for on-line thermal condition monitoring of LVEMs under healthy and faulty conditions, two LVEM test rigs based on two different conventional LVEMs were developed. The examined machine topologies are the IM and PMSM that are thermally modelled using Motor-CAD. The following sections explain the operational details of individual test-rigs.

3.3.4.1 IM test rig

The examined IM was a 0.55 kW, 4-pole, three-phase, totally enclosed fan cooled-squirrel cage induction machine manufactured by TEC Electrical Motor based on IEC standards [187]. Photographs of the examined machine side view are shown in Fig 3.25 and its data specifications are given in Table 3.6. For the purpose of embedding the in-situ FBG thermal sensing system in the target positions (interior of the machine stator winding)

and to allow emulation of stator winding faults, the IM stator winding was stripped and rewound. The machine original/modified winding's configurations, the embedded FBG thermal sensors design, locations, the installation methodology and the test-rig layout setup are demonstrated and explained in the following sections.



Fig 3.25: A side view photographs of the examined IM

Table 3.6: IM data specification

Motor Data	
Rated Power / Voltage / Current	0.55 kW / 400 V / 1.6A
Frequency	50 Hz
Efficiency	66 %, IE1
Rated speed	1380 rpm
Power factor	0.75
Pole number	4
Cooling method	IC 41
Slot number stator / rotor	24 / 30
Insulation class	F
Temperature rise class	B
Duty cycle type rating	S1
Design standard	IEC- 60034

A. Original IM stator winding configuration

Fig 3.26 illustrates the layout connections of the original IM stator winding. The original winding design and layout information were not available from the manufacturer. Therefore, the original winding design was reverse engineered during removal. It was found that the stator was constructed of a concentric single layer winding, with six groups of coils distributed over 24 slots. Each phase had two groups connected in series and each group consisted of two coils. The total number of turns per coil was 105 turns wound with AWG 24 (0.564 mm) insulated copper wire. In this concentric winding, the inner coil of each group had a coil-span of 5 and the outer coil has coil-span of 7 (as seen in Fig 3.26).

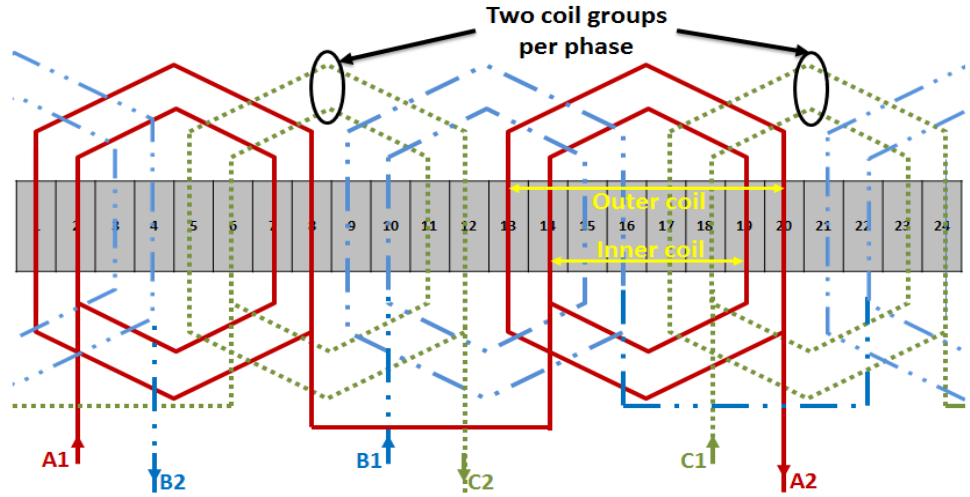
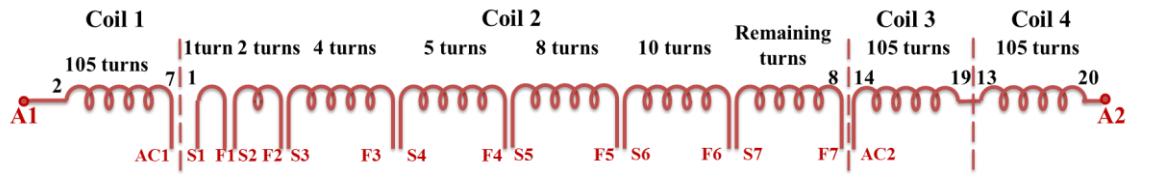


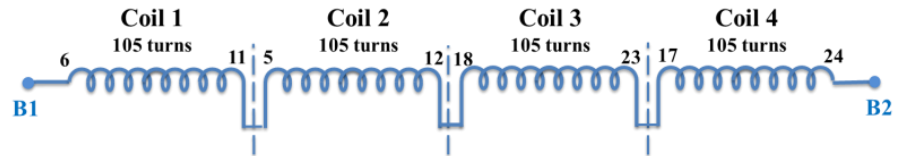
Fig 3.26: Layout connection of the healthy stator windings

B. Modified stator winding configuration for fault emulation

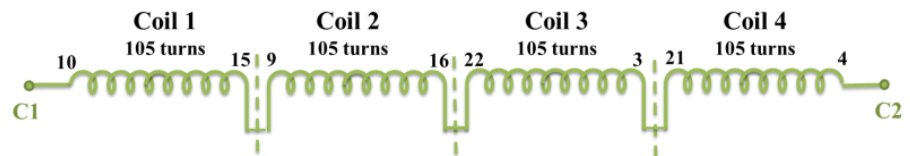
The original stator winding discussed in the previous section was modified to enable emulation of different fault scenarios and severities in the examined IM stator winding. This was done for a single turn fault to multiple turn faults, and involved tapping specific turns in the rewind winding. The modified three-phase stator winding configuration including tapplings is illustrated in Fig 3.27. The modification was applied to phase A, where the desired number of turns were tapped to enable practical emulation of a winding fault scenario, as shown in Fig 3.27.a. The other two phases (B and C) remained unmodified (see Fig 3.27 b and c).



(a) Phase A modified winding



(b) Phase B modified winding



(c) Phase C modified winding

Fig 3.27: Modified IM stator windings

The fault location was arbitrarily chosen to be in coil 2 of phase A. The tapped turns were determined to induce inter-turn short circuit fault with different fault severities in phase A. Table 3.7 represents the possible number of induced shorted turns and their corresponding fault severity percentages with the required tapping connections. The severities are defined as the ratio of the turns shorted to the effective turn per phase. The maximum inter-turn fault severity in a single coil is 2.38 % (i.e. 10 turns shorted). This is because this research focuses on detection/diagnosis of the incipient stages of winding faults using FBGST, since they are very challenging to detect and diagnose with conventional condition monitoring techniques.

Table 3.7: Investigated inter-turn fault severity

Connection	No. faulted turns	Fault severity % per phase	Connection	No. faulted turns	Fault severity % per phase
S1 – F1	1	0.238	S1 – F3	7	1.66
S2 – F2	2	0.476	S5 – F5	8	1.9
S1 – F2	3	0.714	S3 – F4	9	2.14
S3 – F3	4	0.95	S6 – F6	10	2.38
S4 – F4	5	1.19	S1 – F7	105/one coil	25
S2 – F3	6	1.42	AC2 – A2	210/two coils	50

C. In-situ FBG thermal sensors locations

The installation of the in-situ FBG thermal sensors in the examined IM stator winding was established by first embedding the PEEK capillaries packaging within the winding structure in the targeted slot/end-winding positions during the rewinding process. When the rewinding and impregnation processes were completed, the FBG sensors were inserted into the desired positions. This procedure offers an advantage of avoiding the undesirable exposure of the fragile sensing fibre to mechanical stress during the rewinding process. Another key practical advantage is that the sensing fibre is made accessible for replacement, reposition or re-calibration, which is not the case with conventional temperature sensors [109]. From a research and practical usage point of view, this process enables reuse of FBG sensors/sensing fibres and enables flexible embedment of FBG sensors in positions of interest without having to embed all the FBG sensors during the rewind process. The in-situ FBG thermal sensing system embedded in the IM stator winding was designed to enable distributed thermal sensing for on-line winding internal temperature monitoring. The thermal sensing points allow the measurement of hot spots in the entire winding structure, including slot and end-winding sections.

For the slot section, two aspects of internal sensing location were considered in the sensor design: the sensor axial and radial positions. The radial position requirements dictated a sensor placement in the cross-sectional centre point of the slot section between the copper conductors, where a thermal hot spot is located. This is achieved by appropriate PEEK packaging of the FBG sensor and the methodology of installation (discussed in the next section). Regarding the axial sensing position, the in-situ thermal sensor for slot radial sensing requirements was also designed to enable arbitrary sensor positioning in the slot axial length. To this end the packaging capillary length was designed to be closely similar to the winding axial length; this enabled the packaging capillary to house the entire fibre section containing the FBG sensing head that was implanted in the winding slot region, starting from the non-drive end-winding through to the slot section to drive end-winding, as illustrated in Fig 3.28a. This design allows for positioning of the FBG sensing head at any desired point along the axial length of the winding slot section. This is a very important design feature for machines topologies with large thermal gradients in the axial direction. For machine end-windings, the PEEK packaging was laying between end-windings coils ends in the targeted sensing points. This sensing design enables practical monitoring of the internal temperature of different winding sections (i.e. slot and end winding hot spots). Combined with the multiplexing feature of FBG sensors this design can allow different distributed thermal configurations to be established.

To this end, six PEEK capillaries were embedded between the copper conductors in the slot centre of six different slots, each two slots containing a different phase winding (two capillaries fitted per phase, as illustrated in Fig 3.28.b). For phase A, one capillary was embedded in a healthy slot (slot contains a healthy coil side) and one in a faulty slot (slot contains a faulty coil side). The six PEEK capillaries were extended along the winding axial length and pitched by 4 slots to enable a uniform thermal sensing distribution within the examined motor winding structure. Two PEEK capillaries were embedded in the drive end end-winding section and non-drive end winding section, as shown in Fig 3.28c. To benchmark the in-situ FBG sensing thermal system performance a set of type K thermocouples were also embedded in the stator winding, as shown in Fig 3.28.b and c. These thermocouples were distributed as follows: two TCs were embedded in the end-winding section (one in the drive end-winding and one the non-drive end-winding) to validate the obtained results by the FBG embedded in the same positions. Another two TCs were embedded between the coil's surface and the slot's wall insulation, one in the bottom of the slot and the other in the top of the slot under the slot wedge. The TCs positions were

chosen in accordance with IEC 60034-1 standard [106]. Another two TCs were inserted in holes machined for this purpose, of 1.5 mm diameter and 10 mm depth, one in the core back and one in the tooth where the faulty coil was placed for thermal model tuning.

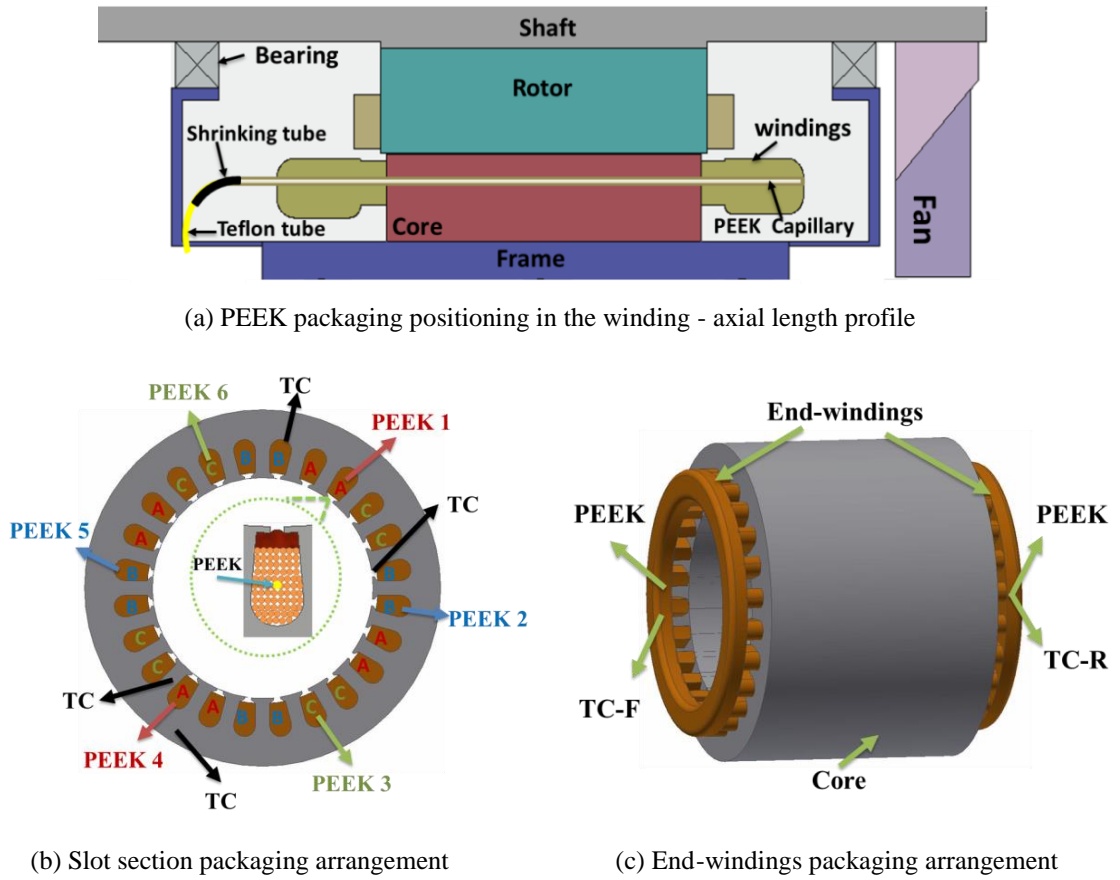


Fig 3.28 : FBG temperature sensors positions in the tested IM

D. Description of rewinding process

The rewinding process commenced by stripping out the original winding. Once the stripping process was completed new slot liners were placed in the core slots (see photo 1 in Fig 3.29). The stator coils were wound to establish the six winding groups required to form the three-phase windings – here each winding group comprises two concentrically wound coils (refer to Fig 3.26 winding diagram and photo 2 showing a single winding group). The coils targeted for embedment with FBG thermal sensors are divided by a strip tied around half of the total turns number to enable placement of the FBG sensor in the desired point at a later stage. The winding group containing the faulty coil (i.e. the coil with tapped turns) was rewound with a specific tapping to enable emulation of fault scenarios of interest (as discussed in Section 3.3.4.1.B). The tappings leads to the connection box were protected by insulated tubes (see Fig 3.29, photo 6) to enhance their mechanical integrity and insulate them from each other, since they would be carrying high current under fault conditions experiments.

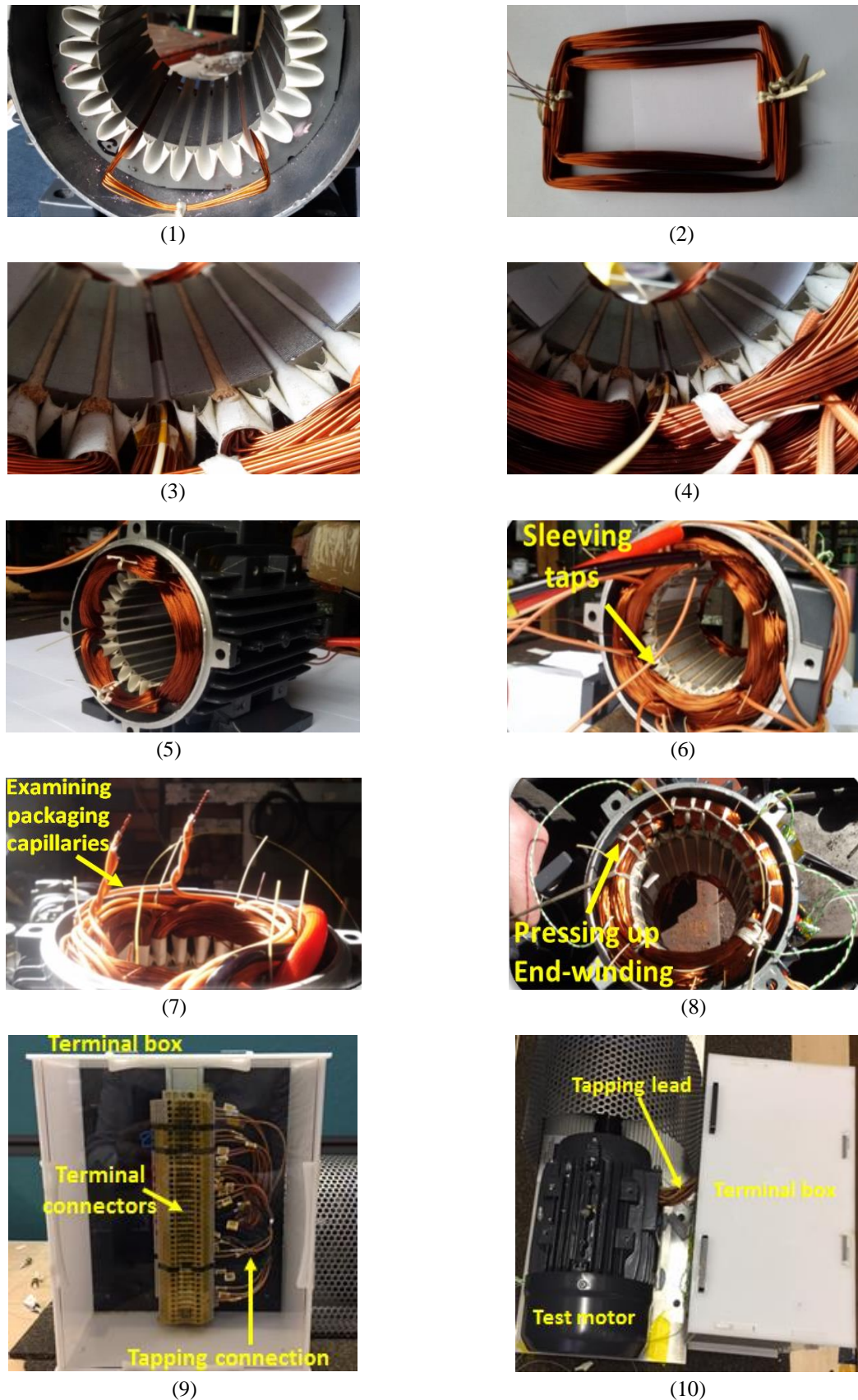


Fig 3.29: Photographs of rewinding process of the examined motor

The packaging capillaries were prepared, as discussed in section 3.3.1.1. To ensure they were approximately positioned in the slot centre, half of the relevant coil section was inserted in its respective slot winding position first, and then the packaging capillary fitted

in the coil centre location. The remainder of the coil was then wound in (see Fig 3.29, photos 3 and 4). Once the coils were inserted in the relevant slots, the integrity of the PEEK capillaries was examined before, during and after pressing in the end-windings (see Fig 3.29, photo 7 and 8). To impregnate the embedded winding, the ends of the capillaries were sealed to prevent ingress of impregnation fluid. The windings were then impregnated (dip impregnation) and placed in a thermal oven to cure at 120 °C for 60 mins. Once the winding impregnation was completed, the capillary ends were unsealed and examined. A connection box was designed and the tappings were connected to allow practical emulation of healthy and faulty conditions (see Fig 3.29, photos 9 and 10). The tapping leads and their connections will inevitably give rise to a relative increase in the resistance of the tapped phase (phase A) in healthy conditions, and act as a short circuit current limiter in the fault condition (inherently introducing additional resistance into the short circuit current path). Some resistance increase is unavoidable with this approach, however, to keep its influence as low as possible care has been taken to keep the tapped leads' length at minimum.

E. Test rig layout

Fig 3.30 illustrates the experimental test rig setup for examining the IM embedded with the proposed in-situ FBG thermal sensing system. The prototype FBG embedded IM was coupled to a 0.75 kW permanent-magnet DC load machine whose armature current was regulated using a controllable resistive load bank. For the purpose of this research, the IM was driven via the grid or a commercial drive. For grid connected experiments, the IM stator winding was connected to the grid via a variac. For inverter driven operation experiments, the motor was supplied by a commercial three-phase (SDD890 parker) AC drive and operated under open-loop (V/f) control mode.

The IM voltages, currents and power values were monitored using a power analyser (Norma D6000). However, for dynamic measurements of the phase currents and voltages, a set of sensors and platforms were used: 1) LEM-LA25 Hall effect current transducers

whose output was connected to a NI 9205 DAQ module and conditioned via a LabView VI routine. These were used to measure the IM phase currents. LeCroy CP150 current probes and LeCroy ADP300 voltage probes connected to a LeCroy 434 digital oscilloscope were also used to measure currents and voltages in the shorted turn circuit. The FBG temperature sensors were illuminated and monitored using the SmartScan04 interrogator and the associated software package (SmartSoft) described in Section 3.3.1.3. The thermocouples outputs were acquired and conditioned by a thermocouple input module NI

9211 DAQ connected to a NI Compact 9178 DAQ and conditioned using a LabView VI routine.

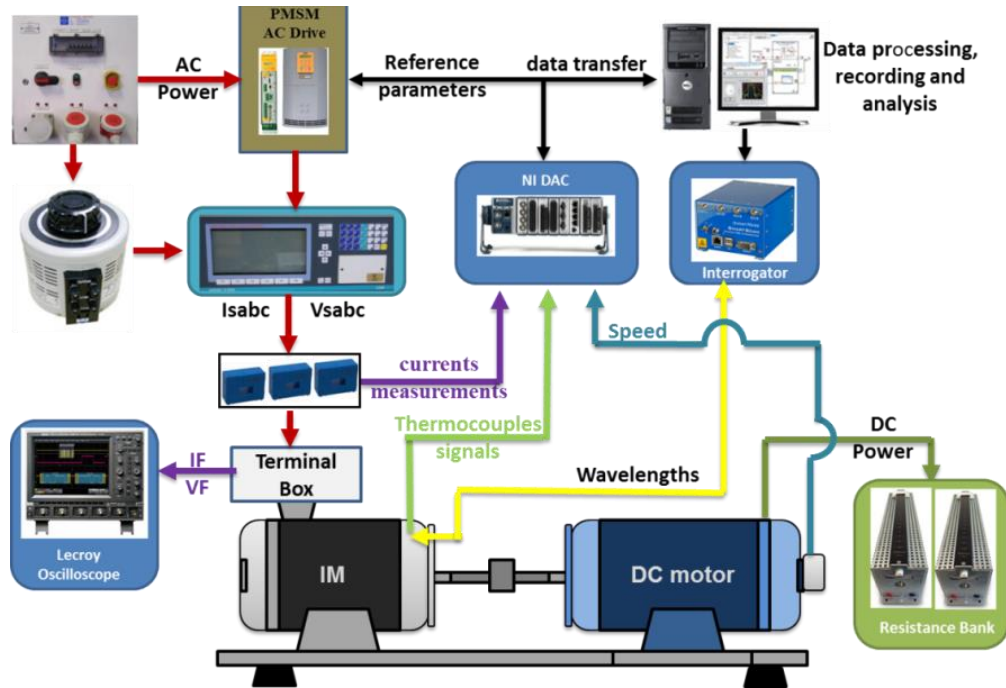


Fig 3.30: Experimental test rig of the embedded IM

3.3.4.2 PMSM topology test rig

The examined PMSM was a 5.5 kW, 6-pole, three-phase PMSM, manufactured by LAFERT, based on IEC-60034 standards. Fig 3.31 shows a side view photograph of the PMSM while Table 3.8 gives its data specifications. The PMSM stator winding was rewound to enable embedding the in-situ FBG thermal sensors in target positions and to allow emulation of stator winding faults, following the same principles as those applied in development of the IM test prototype.



Fig 3.31: PMSM side view

Table 3.8: PMSM specifications

PMSM Data	Type:	HP51141500
Rated Power / Voltage / Current/ Frequency		5.5 kW / 400 V / 11.5A / 75 Hz
Rated speed		1500 rpm
Torque		35 Nm
Pole number/ Rotor configuration		6 / Surface mounted magnet
Slot number stator		39
Insulation class / Temperature rise class		F / B
Duty cycle type rating		S1
Design standard		IEC 60034

A. Healthy stator winding configuration

The PMSM original stator winding design was determined during the rewind process; photos of the original winding are shown in Fig 3.32. Fig 3.33 shows the schematic diagram of the determined original winding configuration. It was found that the stator winding consisted of 18 coils in total, distributed over 36 slots. Three empty slots, shown in Fig 3.33 (8, 19 and 30), were found to be present in the original stator winding design, as can be noted in Fig 3.32. Each phase winding comprised six coils connected in series and wound by six parallel strands of 23.5 AWG (0.5994 mm) copper wire. Each coil of the six coils forming one phase was built up of six parallel coils of 23 turns, giving 138 total turns for the entire coil. For clarification, Fig 3.34 shows the schematic diagram of phase A in the examined stator three-phase winding: it can be seen that phase A consists of six parallel paths (P1 - P6) and each path consists of six coils with 23 turns. The main six coils of the phase are highlighted in the Fig. 3.33 with an orange dashed line square. The phase winding coils are also differently pitched, having either a six or a seven slot pitch: this is shown in Fig 3.33, and denoted in Fig. 3.33 by showing the number of the slots containing coil sides. The winding configurations of phases B and C were identical to that of phase A.



Fig 3.32: PM synchronous motor original winding

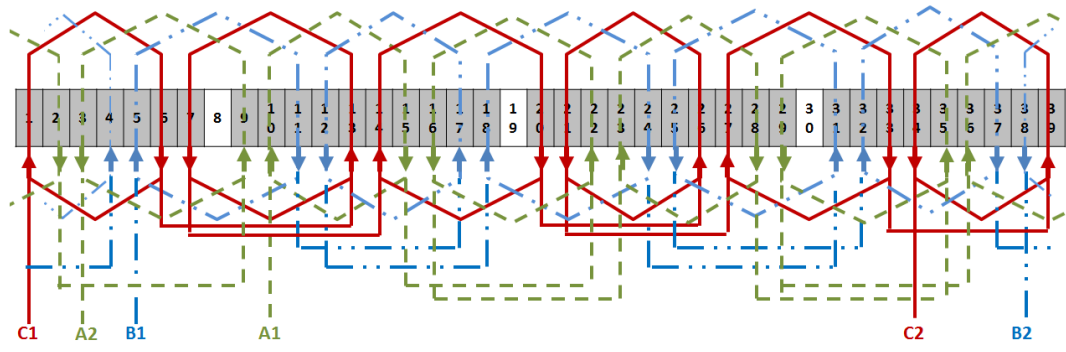


Fig 3.33: PMSM original winding configuration

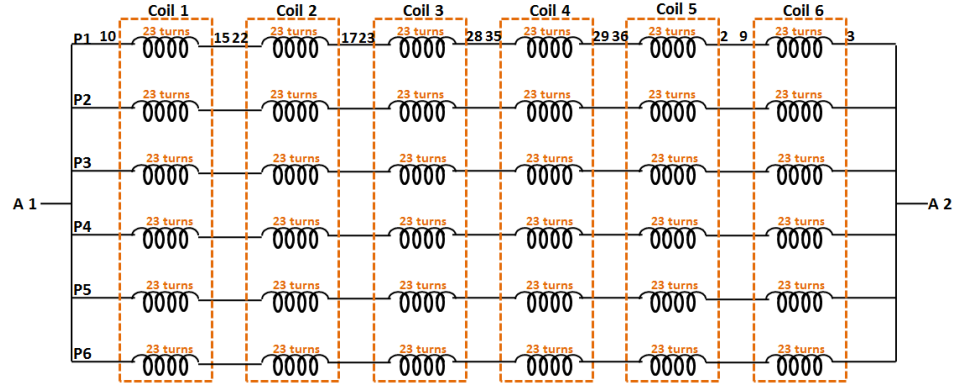


Fig 3.34: Healthy phase A winding configuration

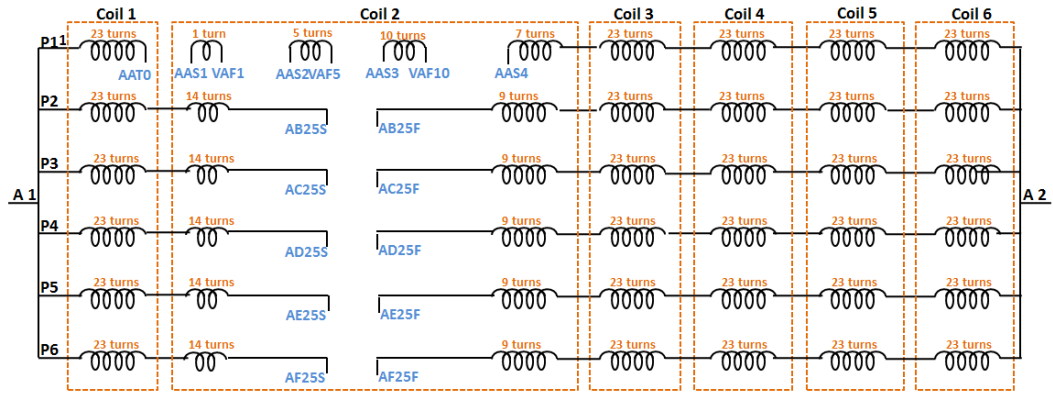
B. Modified stator winding configuration for fault emulation

The stator winding was modified to enable experimental emulation of electrical faults using the tapping technique similar to that applied to the IM. This PMSM winding configuration is more complicated than that previously described for the test IM. It has a number of parallel and series coils connected in each phase, which can lead to different short circuit scenarios, such as short circuit fault between turns of one path or between turns of parallel paths in a single coil. Thus, this winding arrangement was considered for emulating different fault type and severity. To this end, all three-phase windings of the PMSM were modified. The purpose of this was to have physically different fault locations and severity within the examined winding structure for investigating the diagnostic performance and capability of the proposed in-situ FBG sensing system with optimised sensing design for winding fault detection and diagnostics.

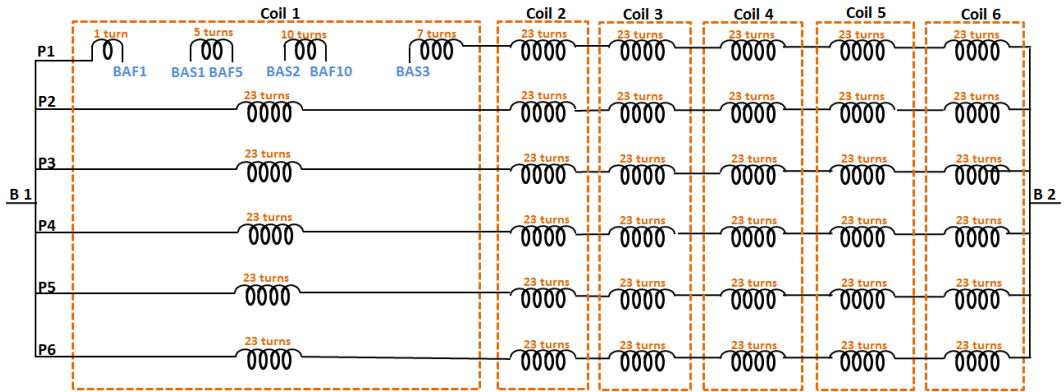
For phase A, the designed tapplings allow to emulate short circuit faults including a turn-to-turn fault, a series turn fault. Fig 3.35a illustrates the modified phase A winding and the designed tapplings. For the inter-turn fault scenarios, the second coil of the phase A was modified with tapplings as follows: the first path turns (P1) were split into different tapped turn numbers to allow 2, 5 and 10 turn short circuit fault connections. In addition, the rest of the paths (P2 to P6) were also tapped in the second coil to allow emulation of a short

circuit fault between parallel paths in the same coil and to enable emulation of an open circuit fault in phase A, ranging from one path open circuit to a full phase open circuit.

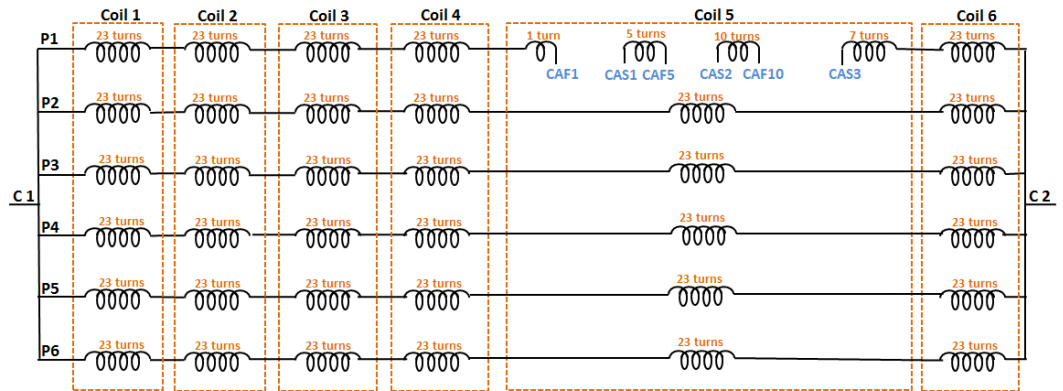
Phases B and C were also modified by tappings to allow emulation of inter-turn short circuit faults with 2, 5 and 10 shorted turns such as designed for phase A. However, the tapped locations were different for each phase. In phase B the first coil was the modified coil, while in phase C the fifth coil was modified. This modification enabled inducing identical fault scenarios in different phases and at different locations in the examined winding. Fig 3.35b and c illustrate the modified phase B and C windings.



(a) Modified phase A in PMSM



(b) Modified phase B in PMSM



(c) Modified phase C in PMSM

Fig 3.35: Modified PMSM winding configuration

C. In-situ FBG thermal sensor locations

Comparable to the IM, the PMSM was embedded with a set of PEEK capillaries during the rewinding process to allow later installation of different sensing configurations for distributed thermal monitoring of stator winding internal temperatures. Three PEEK capillaries were embedded in the slot section centre of three different slots with capillary lengths extended along the axial length of the winding structure for distributed axial thermal sensing. Each PEEK capillary was placed in a slot that housed a tapped coil side (faulty coil), one capillary per phase, as shown in Fig 3.36.a. In the end-windings, two PEEK capillaries were embedded between coil ends in the drive end side. One packaging capillary was placed between coils ends of phase A and phase B, the second packaging capillary was placed between coils ends of phase B and phase C. The packaging PEEK length was equal to the circumference length of the end-winding. Fig 3.36.b illustrates the embedded capillaries positions in end winding section. This design allowed for distributed thermal sensing for healthy and faulty conditions based on the multiplexing feature of FBG sensor embedded in machine end-windings.

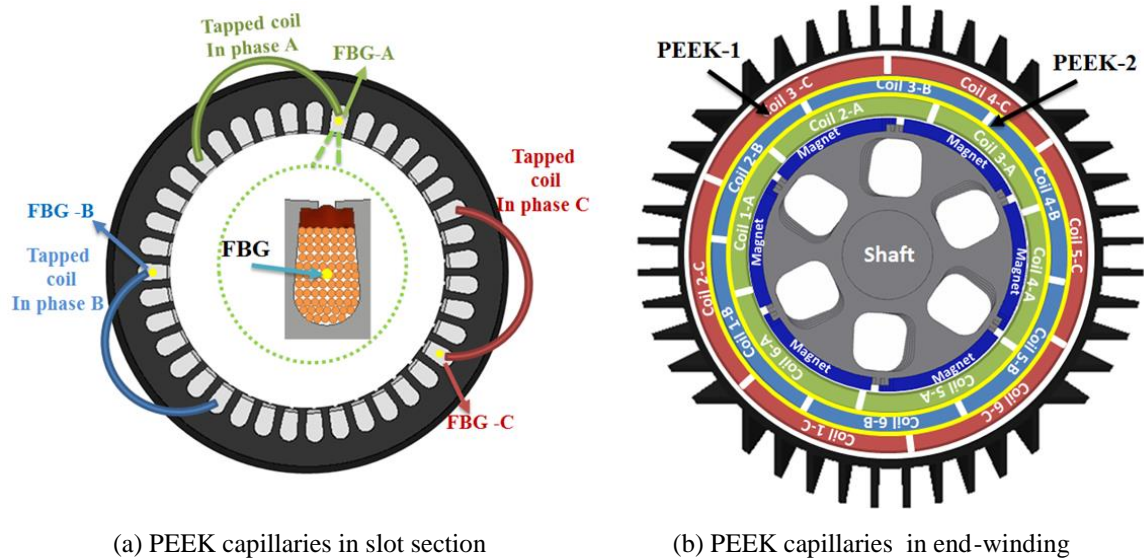


Fig 3.36: Capillary positions in the PMSM

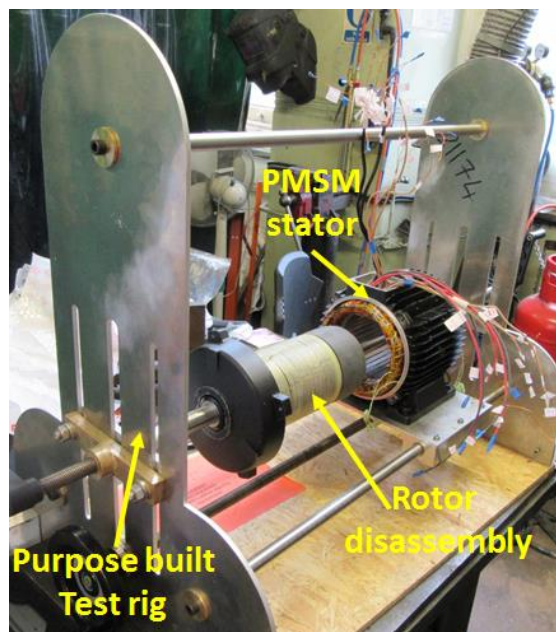
At a later stage of the research, the PMSM was rewound for a second time for other purpose of research. The positions of the FBG sensors embedded in the slot center in the first rewind were investigated. Fig 3.37 shows photographs of the PEEK capillary positions within the slots during the stripping out process. It can be seen that the capillaries are located in close vicinity of the slot center position.



Fig 3.37: PEEK capillaries position in the slot centre

D. Description of the rewinding process

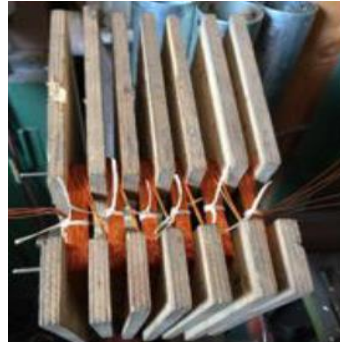
In general, the process of rewinding and embedding the FBG packaging into the PMSM was similar to that applied for the test IM. However, disassembling the stator and rotor parts for rewinding purposes required careful disassembly of the rotor, since the rotor contains magnets. The magnet induced forces can cause damage to the stator core or to the magnets if the rotor pulls to one side of the stator during the rotor pullout process. These forces can also lead to injuries if not seriously considered. To this end, a specially designed rig for permanent magnet rotor assembly and disassembly was designed and manufactured, (see Fig 3.38, photos 1). The developed tool allowed for safe disassembling and reassembling of the PM rotor during the rewinding and sensor embedment procedures. Fig 3.38 also shows photos that were taken during the PMSM rewind process. The tap leads from the stator winding were assembled and connected in a purpose built box with appropriate terminal connectors. The terminal box was located above the PMSM and safely isolates the electrical connections from the operators during experiments.



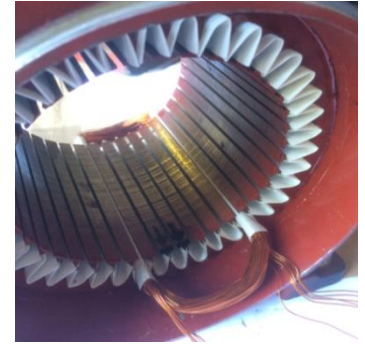
(1) Magnet rotor assemble and reassemble tool



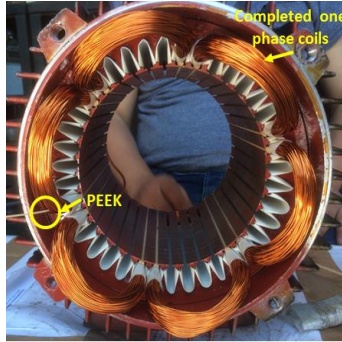
(2) Striped winding



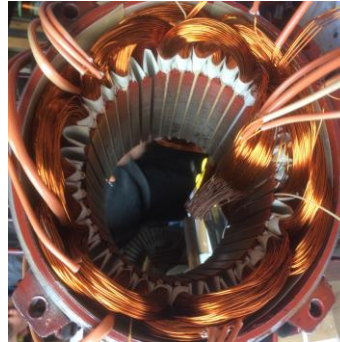
(3) Rewound coils makign up one phase



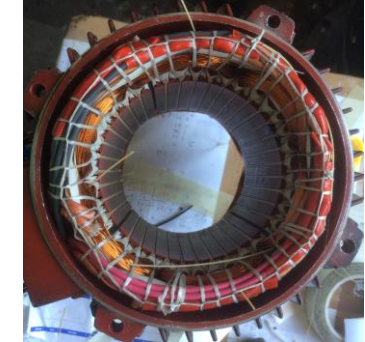
(4) Coil insertion



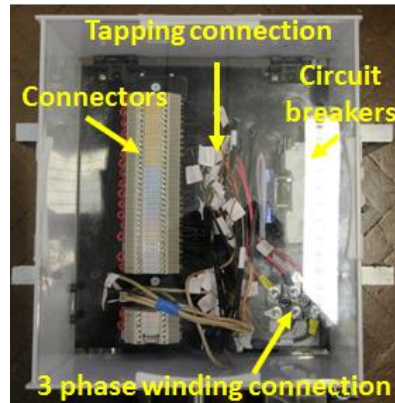
(5) PEEK embedment



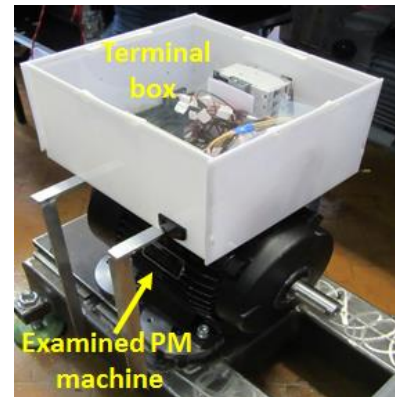
(6) Phase C coils insertion



(7) Drive end-winding



(8) Connection box



(9) Rewound PMSM

Fig 3.38: Photographs of re-winding process of the PMSM

E. Test rig setup layout

The PMSM test rig was developed in parallel with another PhD research project on PMSM condition monitoring using embedded control signals. The developed test rig layout is illustrated in Fig 3.39. The embedded PMSM was coupled to a 15.5 kW DC machine, whose speed/torque characteristics was controlled by a 15.5 kW Parker/Eurotherm drive (DC 590SSD). The PMSM were connected to a 7.5 kW 890SSD AC drive system from Parker drive, which was automated via the DSE Lite software provided by the manufacturer. The DSE Lite contains a pre-programmed algorithm to run the PMSM, which requires careful definition of a large number of parameters. The communication between the AC drive and the PMSM and its control was part of the

parallel PhD research. For this research, the PMSM was operated in closed loop control with feedback information (rotor speed/position) provided by a resolver fitted to the machine.

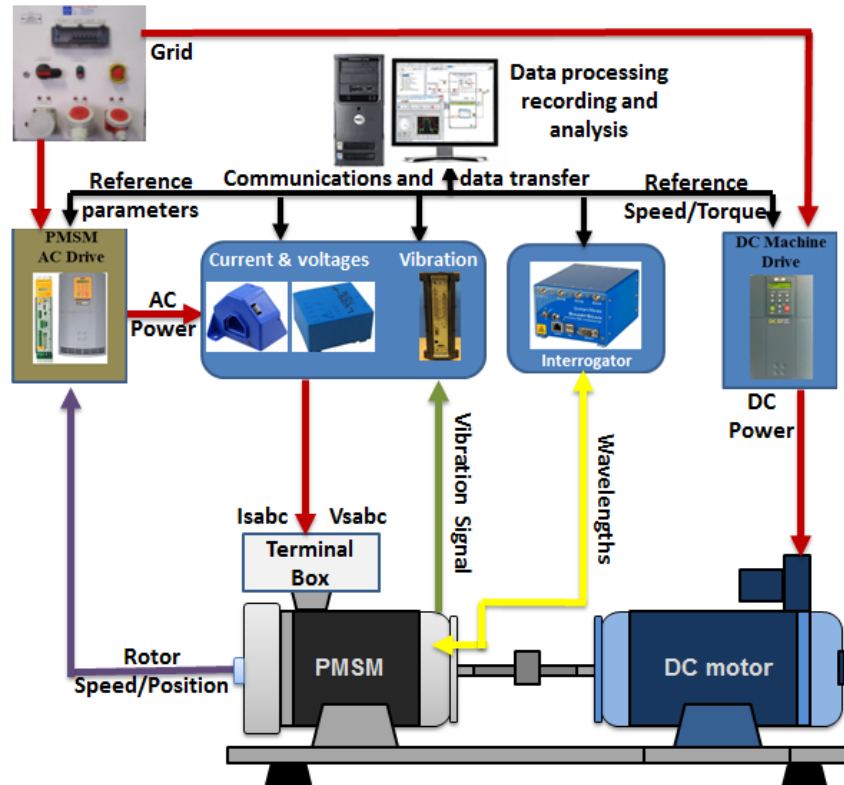


Fig 3.39: Experimental test rig layout of the embedded PMSM

For the measurements, the 890SSD drive and its managed DSE Lite software enabled monitoring of the PMSM RMSs (currents, voltages, power, speed and frequency). However, for the purpose of condition monitoring investigation, additional commercial sensing platforms were installed: 1) LEM currents probes (LA 205-S LEM) connected to a NI DAQ platform and conditioned via LabVIEW code were set to preform real-time measurements of the examined PMSM three-phase currents.

3.3.5 Other equipment used in experimental research

3.3.5.1 Thermal camera

A thermal camera, type FLIR TG-165, was also used during this research. Fig 3.40 shows the used thermal camera. The FLIR TG-165 was used to monitor the stand alone coils surfaces and the examined machine frames when appropriate. A thermal camera is an important thermal measurement tool for monitoring temperature gradient and can identify hot spots in structure surfaces. The used FLIR TG-165 is factory calibrated to provide the best possible thermal images. However, the accuracy of the temperature measurements obtained by thermal camera can be affected by the emissivity. Emissivity is a measure of

how well a material surface radiates infrared energy. Its value is between 0.0 and 1.0 where a surface with 1.0 emissivity is considered a perfect radiator. The used thermal camera enables change of the emissivity setting from 0.4 - 0.98. In this study, the thermal camera was largely used to inspect surface temperature differences (hot spots) rather than actual temperature distribution.



Fig 3.40: Thermal camera type FLIR TG-165 [188]

3.3.5.2 Anemometers

To measure the air speed flows between machine frame fins for the thermal model and some experimental tests a Testo 405i anemometer was used, as shown in Fig 3.41. The anemometer was connected to a smartphone via the Testo Smart Probes APP. The APP allows for static and dynamic measurements and recording.



Fig 3.41: Testo 405i anemometer

3.4 Summary

This chapter provided a detailed description of the different test-rig systems, including the FBG sensing system and the additional tools, used to conduct experimental research in this PhD study. The chapter also described the development of two thermal models using Motor-CAD for the two examined LVEMs in this research.

Chapter 4: Calibration, Characterisation and Performance Assessment of Random Wound Coil Embedded In-situ FBG Thermal Sensing System

4.1 Introduction

FBG thermal sensing is a novel sensing technology in EM sensing applications. Its application for in-situ thermal sensing in wound components such as those in LVEMs while promising remains largely unexplored. Standalone FBGs are sensitive devices; their performance can be significantly affected by usage aspects such as sensor packaging, calibration and installation methods. Effective use of these devices for coil embedded thermal monitoring therefore requires a full understanding of key design constraints and a careful consideration of the aforementioned aspects.

To this end, this chapter presents a series of experimental studies conducted on prototype coil systems as initial step towards embedding FBG sensing technology in the interior of the random wound coil structure of LVEMs for hot spot thermal monitoring. The underlying purpose of the reported work is twofold: to establish an understanding of performance implications of the sensor installation procedure into a wound coil, and to evaluate its in-situ sensing performance and characterisation in operating conditions representative of those encountered in an actual LVEMs. Attaining this understanding is a precursor to enabling further development of embedded sensing applications within operational EMs.

The chapter consists of two papers written up in paper-style format. The second author contribution to both papers is performing a technical and academic writing review and technical guidance during this work.

Paper 1: the content of this paper is a collection of published contributions in a number of *IEEE conferences* [48, 53, 54] and one *Elsevier journal* [55]. The main contributions of these papers are:

- A novel small size, dielectric and EMI immune FBG temperature sensor design aimed at electric coil in-situ thermal monitoring is proposed.

- The application potential of the proposed in-situ FBG thermal sensor for hot spot thermal monitoring in random wound coils is examined and validated in a range of experiments.
- The use of the proposed in-situ FBG thermal sensing system for distributed internal thermal monitoring in random wound coils based on FBG multiplexing is examined and validated.
- In-depth analysis of installation, calibration and characterisation of random wound coil embedded in-situ FBG temperature sensor.

Paper 2: The content of this paper has been published in a leading sensing journal *IEEE Sensor Journal* [56]. The main contribution of this paper is:

- An investigation and identification of key design and operational features of embedded FBG sensing for thermal hot spot in-situ monitoring in random wound coils of LVEMs. The investigation was conducted by examining three vital application aspects of coil embedded FBG hot spot monitoring.

4.2 Paper 1:

In-situ FBG Temperature Sensor Installation, Characterisation and Performance Evaluation for Hot Spots Monitoring in Electric Machinery Random Wound Components

A. Mohammed, *Student Member, IEEE*, S. Djurović, *Member, IEEE*

Abstract—This study investigates the application of fibre optic sensing based Fibre Bragg Grating (FBG) sensors for thermal hot spot temperature monitoring of random wound electric coils. The paper presents the design, installation, in-situ characterisation and performance details of a thermal sensor used for enabling real-time internal thermal monitoring of wound coil structure, in close proximity to the thermal hot spot location. The paper first examines the design of an embedded in-situ FBG thermal probe aimed at single thermal point sensing in wound coils internal structure. Then the multiplexing property of FBG sensing technology is examined to achieve a multipoint, distributed thermal monitoring design in arbitrary points within the coil structure. A series of thermal monitoring experiments are undertaken on prototype test coil systems embedded with FBG temperature sensors under a range of controlled static and dynamic thermal conditions. The findings demonstrate the feasibility of applying FBG thermal sensing technology for effective thermal monitoring within wound electrical components. It is shown that reliable, improved fidelity information on the coil's thermal status can be obtained from embedded in-situ FBG thermal sensors when compared to conventional thermal monitoring solutions.

Index Terms—Fibre Bragg Grating thermal sensor, in-situ sensing, embedded distributed sensing, random wound coils, thermal hot spot monitoring.

I. INTRODUCTION

RANDOM wound coils are an essential component of most low voltage electric machinery in modern industrial systems [1]. The effective use of electrical machines utilising random wound coils is limited by their sensitivity to electro-thermal stresses their coils are exposed to during operation. The coil thermal overloads are of particular concern in this respect as they generally result in lower efficacy of machine use and its lifetime reduction, and in extreme cases can result in insulation breakdown and catastrophic machine failure [2]. This can be caused by excessive current levels in coil conductors but also by other reasons such as a failure in the integrated cooling system or a coil electrical

fault, where localised hot spots are induced in the coil structure leading to insulation breakdown. The prospect of effective on-line thermal monitoring of the coil structure and its hotspots in particular is therefore attractive; it could enable improved thermal protection of operating machinery by improved understanding of machine operational status. In addition, such monitoring capability could be used to enable recognition of early stages of coil degradation process, enabling remedial action to be undertaken before a catastrophic fault occurs [3].

The current practice for monitoring the thermal conditions based sensing solution of wound components in electric machinery is predominantly based on utilising conventional thermal sensors such as a thermocouple (TC) or resistance temperature detector (RTD). These are however generally impeded in providing hot spot thermal measurement in current carrying wound components due to inherent use of electrically conductive material in their structures as well as susceptibility to EMI effects [3,4]. In addition the RTDs and TCs are not a preferable choice for distributed thermal sensing applications due to the length and volume of their wiring leads [5]. An alternative is provided by the latest advances in fibre-optic sensing technology, whose characteristic EMI immunity, robustness, multiplexing flexibility and size make it a strong candidate to deliver the required operative solutions for wound components embedded thermal monitoring [6].

The utilisation of Fibre Bragg Grating sensors in electric machinery monitoring has already received attention in a number of studies, ranging from frame vibration sensing to stator core and coil surface thermal monitoring [7-14]. The available literature on FBG use for wound component thermal monitoring is however almost exclusively focused on applications in large generators [12-14], with significant slot geometries and a form wound winding configuration. The existing reports on low and medium power machinery application of FBGs assess the general potential for thermal monitoring internal to machine structure and do not consider coil embedded hot spot locations [15]. In addition, the FBG thermal sensor packaging designs used in reported studies utilise conductive materials such as stainless steel and aluminium which can impose operational challenges in electrical machinery applications.

This paper reports an experimental examination of an in-situ FBG temperature sensing system enabled hot spot thermal monitoring in a prototype random wound coil system such as those used in electric machines. Different structures of random wound coil systems are used: the test coils are wound of class F or H insulated copper wire to represent designs commonly used in conventional low voltage electric machines [15]. The in-situ FBG

thermal sensor package is made of dielectric material for enhanced immunity in this work. The sensor design, the procedure of sensor installation into a random wound coil structure for single and distributed thermal sensing points, its calibration and characterisation are presented. The sensing system performance was examined in a range of steady-state and transient thermal experiments performed by externally controlled thermal excitation using a thermal chamber and internally controlled thermal excitation by applying controlled DC power. The FBG sensor hot spot thermal measurements are benchmarked in tests with those obtained from conventional TC sensors placed in close proximity or thermal measurements taken by thermal camera. The underlying aim of this work is to assess the attainable hot spot thermal monitoring performance of an FBG thermal sensor embedded in the structure of a current carrying random wound coil.

This paper is organised as follows, Section II provides a brief description on FBG sensing principles, followed by the test system description in Section III that includes the in-situ FBG thermal sensor design, installation and the used random wound coil system structures. Section IV contains the experimental results and discussion and is divided into four main sub-sections. Sub-section IV. A presents the in-situ FBG sensing system calibration, while sub-section IV. B reports the in-situ sensor performance examination in external controlled thermal environment using a thermal chamber. Sub-section IV. C presents the second stage of this study, which examines the proposed in-situ sensing system performance in a current carrying coil environment. Sub-section IV. D reports the design of an embedded array FBG sensing system aimed at facilitating real-time distributed internal thermal conditions monitoring in wound coils of electric machines.

II. FIBRE BRAGG GRATING SENSING PRINCIPLES

FBGs are periodic gratings on the optical fibre core that result in a periodic modulation of its refractive index when exposed to an interference pattern of laser light. The wavelengths reflected by the FBG structure will alter with the variation in the strain and/or temperature it is exposed to. With appropriate design, this phenomenon enables the grating fibre to be utilised as a mechanical or a thermal sensor. The FBG centre wavelength is given as [16]:

$$\lambda_B = 2 \Lambda n_{eff} \quad (1)$$

where: λ_B is the Bragg (i.e. centre) wavelength, Λ is the grating period (i.e. the spacing between successive gratings) and n_{eff} is the effective fibre core refractive index. Any change in the fibre temperature and/or strain will give rise to a change of n_{eff} and Λ , and

consequently result in an alteration of the reflected wavelength. The reflected Bragg wavelength relative rate of change can be defined in terms of the existing thermal and/or mechanical excitation as [17]:

$$\Delta\lambda_B = \overbrace{2\lambda_B \left(\lambda \frac{dn_{eff}}{d\varepsilon} + n_{eff} \frac{d\lambda}{d\varepsilon} \right)}^A \Delta\varepsilon + \overbrace{2\lambda_B \left(\lambda \frac{dn_{eff}}{dT} + n_{eff} \frac{d\lambda}{dT} \right)}^B \Delta T \quad (2)$$

where: ε is strain and T is temperature. The term A in (2) represents the Bragg wavelength shift caused by the strain induced elastic-optic effect. The term B describes the temperature change induced wavelength shift that arises due to thermo-optic and thermal expansion effects [11]. The reflected wavelength change due to temperature change can be expressed in terms of the fibre thermal characteristics as [18]:

$$\Delta\lambda_B = \lambda_B (\alpha + \xi) \Delta T \quad (3)$$

where: α is the fibre thermal expansion coefficient ($\approx 0.55 \times 10^{-6}/^\circ\text{C}$) and ξ is the fibre thermo-optic coefficient ($\approx 6-9 \times 10^{-6}/^\circ\text{C}$) [11]. For a standard bare FBG with the Bragg wavelength of 1550 nm operating at ambient temperature the fibre thermal sensitivity can be evaluated to be $\approx 10-14$ pm/ $^\circ\text{C}$. FBG technology is particularly suitable for distributed sensing applications, where a single optical fibre can be used to contain a range of FBG sensing heads, with each head coded with a specific Bragg wavelength and acting as a separate sensor. This structure, known as an FBG array sensor, can provide attractive solutions for random wound coil embedded multi-point thermal sensing, where a single fibre optic probe could be applied to provide distributed sensing within the monitored coil structure. Fig .1 illustrates the operating concept of an FBG array sensor: the array is illuminated with broadband light and particular wavelengths reflected by each FBG sensing head. Each FBG reflects a specific light spectrum matching its designed Bragg wavelength. The process of fibre light excitation and examination of the reflected spectrum for Bragg wavelengths is managed by an interrogator device.

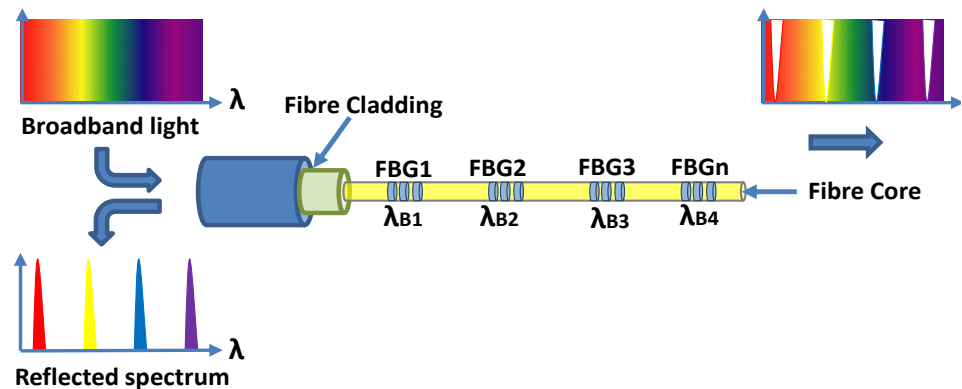


Fig. 1: Operating principle of the FBG array sensor

III. TEST SYSTEM DESCRIPTION

A. FBG sensor design for in-situ thermal monitoring

The bare FBG is extremely fragile and requires suitable packaging to ensure its mechanical integrity and isolate it from mechanical excitation, i.e. mitigate as much as possible the cross-sensitivity of shifted Bragg wavelength due to temperature and strain. To achieve this, Polyetheretherketon (PEEK) capillary is used in this work to package the FBG sensing heads due to its dielectric and mechanical properties; the thermal conductivity of PEEK is 0.173 W/m.k and it can withstand operating temperatures in excess of $\approx 250^{\circ}\text{C}$.

The FBG sensing configuration investigated in this paper is designed to enable single and distributed thermal sensing points for hot spot thermal monitoring within single\multi random wound coil structure. In this study a number of single and array FBG temperature probes were used. The FBGs heads were imprinted in bend insensitive polyimide optic fibre with double polyimide coating. The FBG heads length is 5 mm with Bragg wavelengths distributed in a bandwidth of 1529-60 nm and average reflectivity and bandwidth of 88 % and 0.36 nm, respectively. The single FBG probes were designed to be located as single thermal sensing point at the centre of the coil slot and/or end-winding sections. While the array FBG probes were designed to create thermal sensing network for distributed hot spot monitoring in single and multiple coils system.

Fig. 2 shows the schematic diagrams of the packaged sensing elements used in this study. The total length of individual FBG probes is ≈ 1.5 m. The fibre probe can be divided into two portions: sensing portion (i.e section contains the FBG heads and embedded within the coil structure) and the rest of the fibre portion. The sensing portion is packaged using PEEK capillaries. The inner and outer diameter dimensions of the utilised PEEK capillary were chosen as 0.6 mm and 0.8 mm, respectively, resulting in wall thickness of 0.1 mm. This was to provide a relatively close match to the 0.56 diameter size of the test coil's copper wire and therefore facilitate easier placement and more effective thermal sensing performance of the sensor package within the random wound test coil structure. In addition, the cross sectional area of the FBG array sensor has a negligible effect on the coil packing factor when compared to conventional TC or RTD thermal sensors. The remainder of the optic cable is tubed in Teflon for protective purposes.

The single FBG probes consist of one 5 mm FBG head as illustrated in Fig. 2a. While the first FBG array, illustrated in Fig. 2b, consists of four FBG heads with the sensing region length of ≈ 30 cm defined by the length of the PEEK capillary containing the

sensing heads. This sensor was used for distributed internal thermal sensing within a single random wound coil structure. A second FBG array design consisting of six FBG heads distributed in ≈ 120 cm sensing area, shown in Fig. 2c. was designed for distributed internal thermal sensing within multi random wound coil structure.

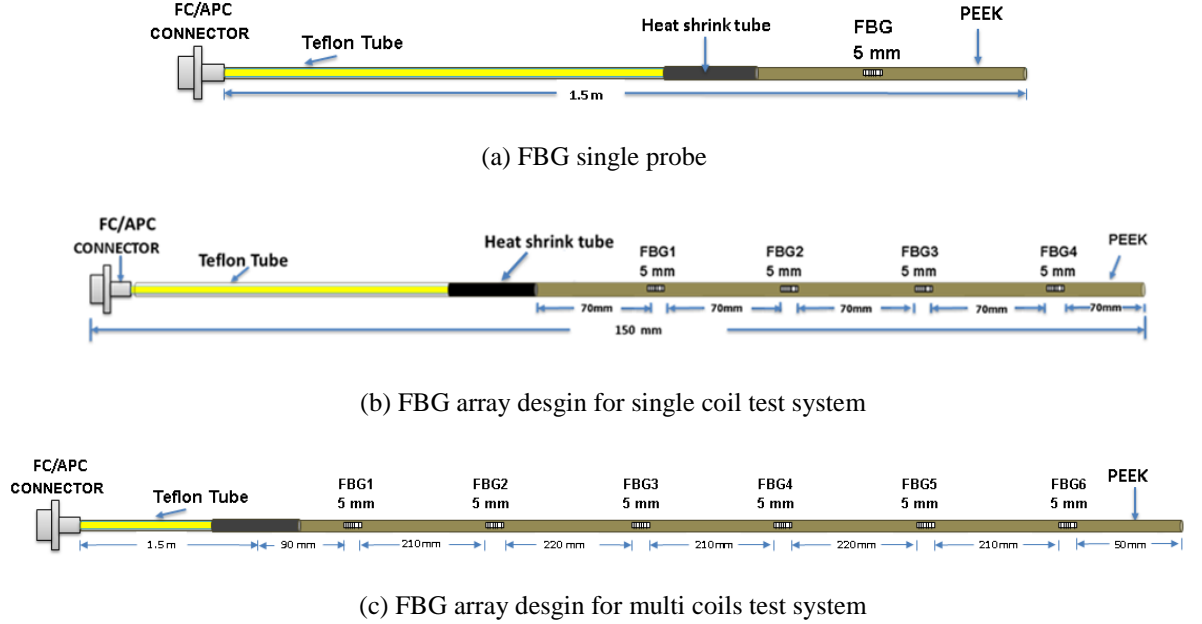


Fig. 2: FBG thermal sensors design for in-situ thermal monitoring

B. Test coil system design

This study undertakes experimental tests on prototype coil systems embedded with FBG temperature sensors designs put forward in section III. A. The proposed in-situ FBG sensing system was examined in different prototype coil system designs. Fig. 3 illustrates the used coil systems in this research. The first random wound test coil geometry, illustrated in Fig 3a, is designed according to IEEE standards for test procedures to evaluate insulating materials for random-wound AC electric machinery [15]. The motorette is wound on a winding machine with a number of series connected turns of class F or H enamelled copper wire. The IEEE motorette is representative of EM's stator winding structure and was used in this study as the main test system to enable understanding of the in-situ FBG sensor's embedment procedure, characteristics and on-line performance. The second coil system is a prototype coil wound into a stator core of a commercial machine design, as shown in Fig. 3b. This tests system was used to investigate the FBG sensing system's installation methodology impact on its measurement performance in a typical machine winding setting; this could be ignored in the IEEE motorette tests due to motorette test system's more controlled FBG instrumentation process. The last coil system is a multi-coil structure mounted on a purpose made core design. The purpose of this test system is to

evaluate the proposed in-situ thermal sensing multiplexing feature use for distributed internal thermal monitoring in multi-coil systems such as those that would be encountered in practical electric machine windings. The prototype coils were embedded with in-situ FBG and TC sensors to enable performance cross-correlation. The sensors positions and installation for each coil system are discussed in the corresponding sub-sections of the experimental work result and discussion section IV.

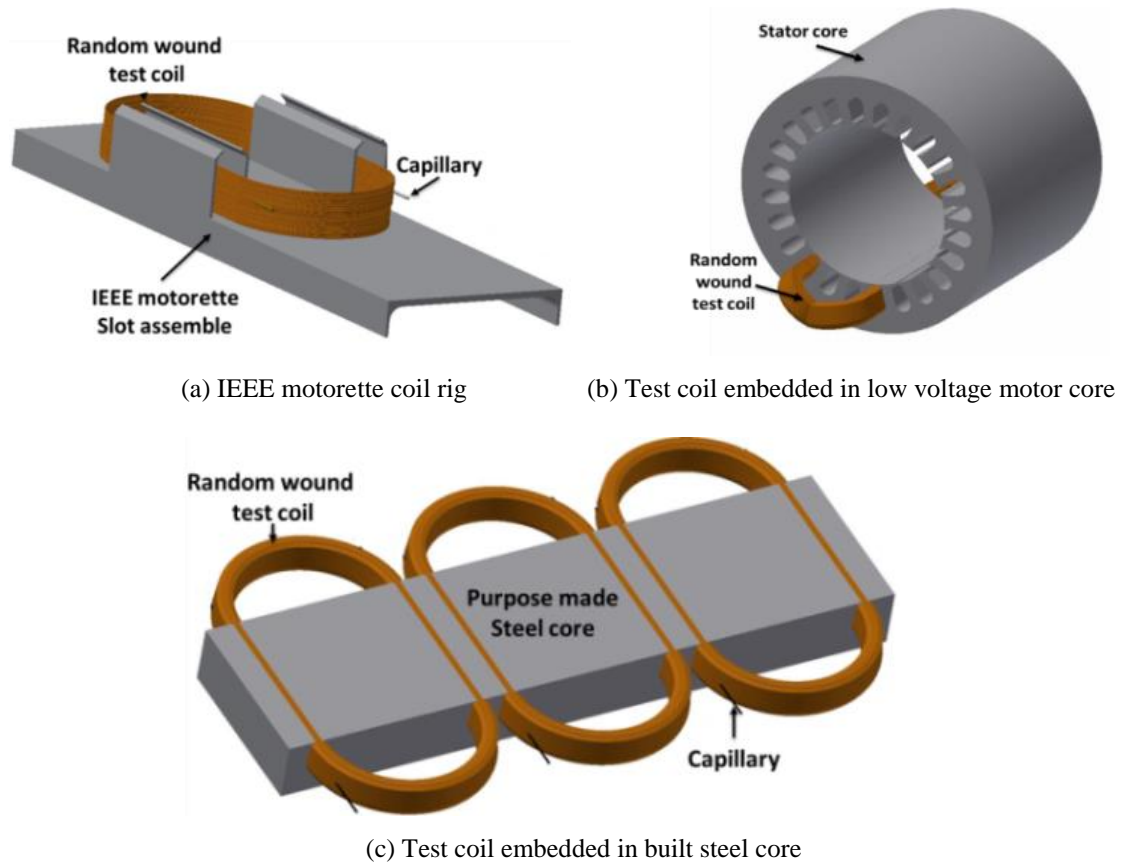


Fig. 3: Examined prototype coil systems embedded with FBG temperature sensors designs

C. Experimental test system

Two experimental system setups were developed for this study: the first was used for calibration and characterisation study while the second system setup was developed for the in-situ performance assessment.

A schematic illustration of the experimental arrangement used for FBG sensors calibration and characterisation is shown in Fig. 4. The calibration and characterisation experimental setup was used to obtain the wavelength-temperature calibration fit curve for each FBG sensor and to characterise the FBG sensors before and after packaging and embedment (i.e. base wavelength shift and sensor temperature sensitive variation due to packaging and embedment). The calibration and characterisation of the FBG sensing system was achieved by utilising a controlled thermal chamber, which isolated the

free/packaged/embedded FBG sensors and exposed them to a desired, controlled steady-state thermal excitation level. The reference temperature within the thermal chamber was monitored by the chamber in-built thermal sensors and an additional FLUKE K type thermometer placed inside the chamber and used for temperature measurement control.

Fig. 5 shows the experimental test system utilised for on-line performance assessment of the in-situ FBG thermal sensing system under a variety of thermal conditions representative of electric machine operation. This requires a practical emulation of a range of uniform and uneven stationary/transient thermal conditions including dynamic thermal cycling. To achieve this a programmable DC power supplies were used to inject the desired current level into the prototype coil under test. The coil current was measured synchronously with temperature using a LEM 55-P current transducer.

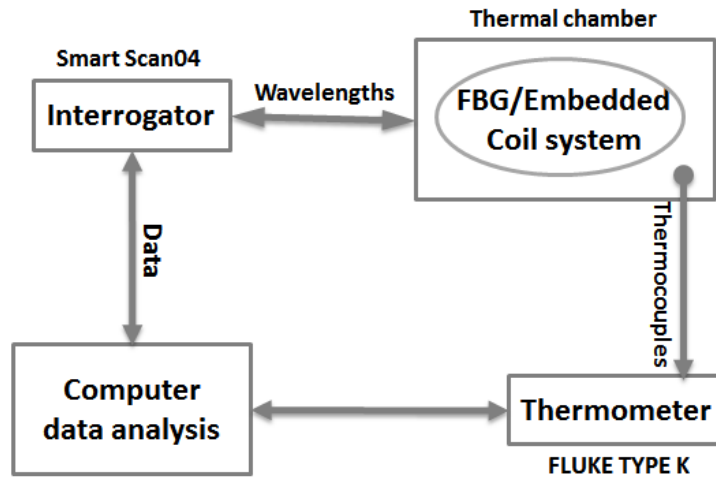


Fig. 4: Experimental system setup for calibration and characterisation

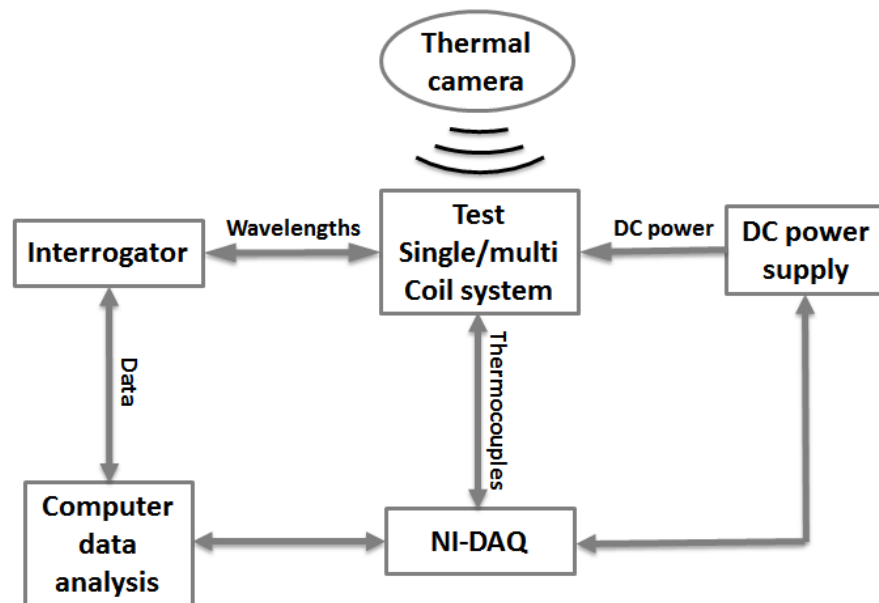


Fig. 5: Experimental system setup for in-situ FBG performance assessment

A commercial SmartScan 04 interrogator system was used to illuminate the FBG probes sensor and enable dynamic measurement of reflected wavelengths [19]. The interrogator was connected to a personal computer running LabVIEW code to record and analyse the measured data. The TCs outputs are conditioned by an NI DAQ interfaced with a personal computer executing an appropriate LabVIEW VI routine. A thermal camera (type FLIR TG-165) was used to cross-correlate the coil distributed thermal measurements obtained by the FBG array sensing system with those captured on the coil surfaces. Thermal cameras are an important thermal monitoring technique for temperature gradients and identifying hot spots on structure surface.

IV. EXPERIMENTAL RESULTS AND DISCUSSION

A. *In-situ FBG thermal sensor calibration*

The interpretation of the measured reflected peak wavelengths from each FBG head to respective temperature reading requires a calibration test, which yields a temperature-wavelength fit curve for each individual FBG head [20]. The calibration tests were carried out using a commercial thermal chamber.

The prototype coil systems embedded with FBG single/array sensors were placed in the thermal chamber and exposed to a range of pre-defined static thermal stress. The sensors were calibrated in the thermal range of ≈ 40 to ≈ 150 °C or 170 °C in a rising sequence of ≈ 10 °C steps, to match the thermal rating of the examined class F and H insulated coils, respectively. Measurements were taken at every examined thermal steady-state once the thermal equilibrium was achieved. For illustration purpose Fig. 6 shows the data recorded during the calibration test of the FBG array containing 4 FBG heads (embedded in the single-coil test system of class H insulation system); the corresponding calculated parameters of the second order polynomial ($Y = B_2 X^2 + B_1 X + \text{intercept}$) fit curves for each FBG head are listed in Table I. The table also includes the calculated standard error for each parameter and the calculated correction coefficient for each FBG head. The four FBG heads are seen to show good linearity with a correction factor coefficient higher than 0.999. From the conducted calibration tests, the average temperature sensitivity of the used FBGs was calculated to be ≈ 11 pm/°C with temperature resolution of ≈ 0.1 °C determined by the interrogator wavelength shift resolution. The FBG interrogator system accuracy is $\approx \pm 1$ pm, which largely determined by the accuracy of the embedded algorithm hardware that enables wavelength shift tracking. The other calibrated FBG array was found to manifest a closely similar performance.

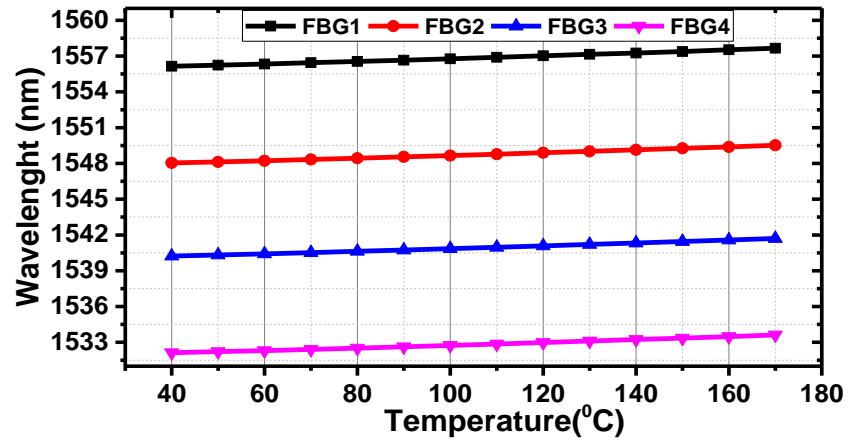


Fig. 6: Calibration characteristics of the packaged FBG array sensor heads

TABLE I
CALCULATED FIT CURVE PARAMETERS

FBG (Wavelength base)	Intercept		B1		B2		Statistics
	Value	Standard Error	Value	Standard Error	Value	Standard Error	
FBG1 (1555.859)	1555.771	0.0137	0.00855	2.85E-04	1.50E-05	1.34E-06	0.99978
FBG2 (1547.742)	1547.669	0.0112	0.00851	2.34E-04	1.41E-05	1.10E-06	0.99985
FBG3 (1539.957)	1539.852	0.0101	0.00871	2.11E-04	1.30E-05	9.90E-07	0.99988
FBG4 (1531.849)	1531.768	0.0131	0.00808	2.72E-04	1.67E-05	1.28E-06	0.9998

B. In-situ FBG temperature sensor performance in externally controlled thermal environment

The aim of this test is to evaluate the in-situ sensing performance and cross correlate its performance with a conventional TC sensor in a controlled thermal environment. To this end, a single FBG probe was embedded in an IEEE motorette coil; the sensor package is embedded in the center of a prototype motorette as shown in Fig. 7a. The motorette consists of a total of 80 turns of class F enamelled copper wire. In order to position the thermal sensing package in the coil center, 40 turns were wound first before placing the FBG package in the center of the coil and completing the winding of the remaining 40 turns. This procedure enabled the sensing package to be situated in the close proximity to

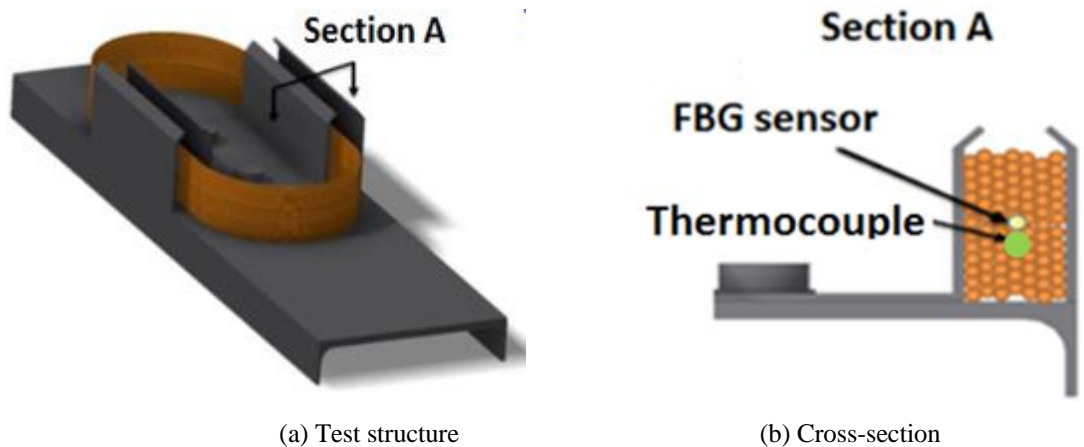


Fig. 7: (a) Motorette structure, (b) showing embedded sensor position

the motorette center and monitor its thermal hot spot. In order to enable the FBG sensor performance benchmarking against that of a known thermal sensing technology a TC (type K) was placed next to the FBG package during the winding process, as illustrated in Fig. 7b.

The thermal monitoring performance of the motorette embedded packaged FBG sensor was evaluated in dynamic tests in the thermal chamber. The motorette was exposed to three thermal cycles from $\approx 20\text{ }^{\circ}\text{C}$ to $\approx 150\text{ }^{\circ}\text{C}$. Fig. 8 shows the obtained experimental results for the synchronously recorded FBG sensor and TC temperature measurements. To enable the assessment of steady-state thermal monitoring performance the chamber temperature was initially controlled to match the ambient temperature ($\approx 20\text{ }^{\circ}\text{C}$) for the duration of 100 sec before initiating thermal cycling for ≈ 30 minutes. The applied thermal cycle is random in nature to represent arbitrary field operating conditions. The measured data show a good agreement between the temperature profiles recorded by the FBG and the TC sensors. The packaged FBG shows good repeatability with no significant evidence of hysteresis at this range of temperature and dynamic change rate [20].

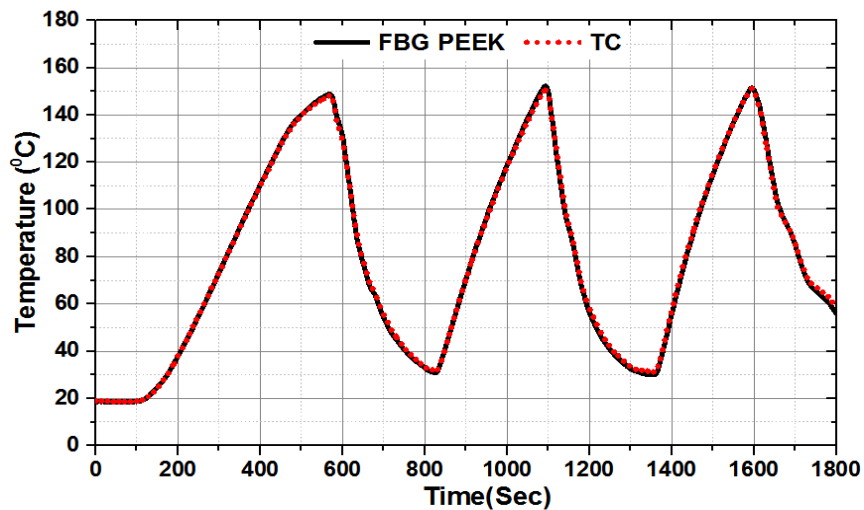


Fig. 8: FBG Peek and TC thermal cycle measurements

The embedded FBG sensors response time is compared with that of the adjacent TC in a detailed view of the temperature change measured during the performed thermal cycle, shown in Fig. 9a. For the investigated thermal cycle dynamics the FBG is seen to deliver a closely identical response time to the TC. A detailed view of the thermal measurements taken during the initial steady-state thermal conditions is shown in Fig. 9b to provide a comparison of TC and FBG steady-state performance. The results show that the TC and FBG recorded data are in close agreement with the maximum deviation between the measurements of $\approx 0.4\text{ }^{\circ}\text{C}$ and maximum deviation during cycle time of $\approx 1.5\text{ }^{\circ}\text{C}$.

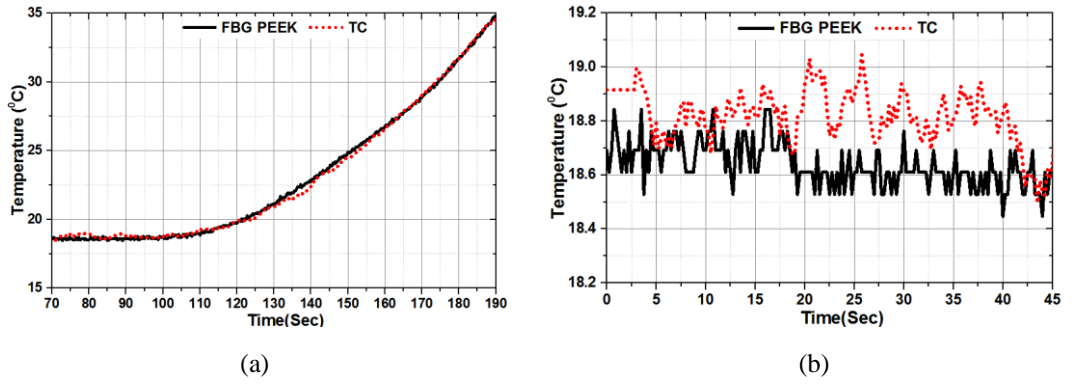


Fig. 9: (a) FBG Peek and TC thermal response measurement, (b) FBG Peek and TC static thermal

C. In-situ FBG temperature sensor performance in current carrying coil

In this section the performance evaluation of the proposed in-situ FBG sensing system was taken a step further by including sensing points in the coil end-winding portion. The sensors were used to monitor the thermal hot spot in a current carrying coil.

1) Motorette coil embedded FBG thermal monitoring

This section presents the thermal hot spot monitoring results obtained from FBG sensors placed within the current carrying motorette coil. The FBG sensors thermal monitoring performance was evaluated by a number of dynamic thermal cycle tests based on the international standard for rating and performance of rotating machines, IEC 60034-1 [21]. Fig. 10 shows the sensing elements positions within the tested motorette coil. The section A graph in Fig. 10 shows a detailed cross sectional view of the motorette slot section, clearly identifying the FBG thermal sensor position at the centre of the coil (FBGS). Similarly, the section B detailed view in Fig. 10 illustrates the cross section of the end-winding part of the prototype motorette, including the position of the FBG sensor installed in this area (FBGE). For the purpose of performance assessment of the embedded FBG thermal sensors with respect to a known conventional thermal sensing technology and its placement limitations,

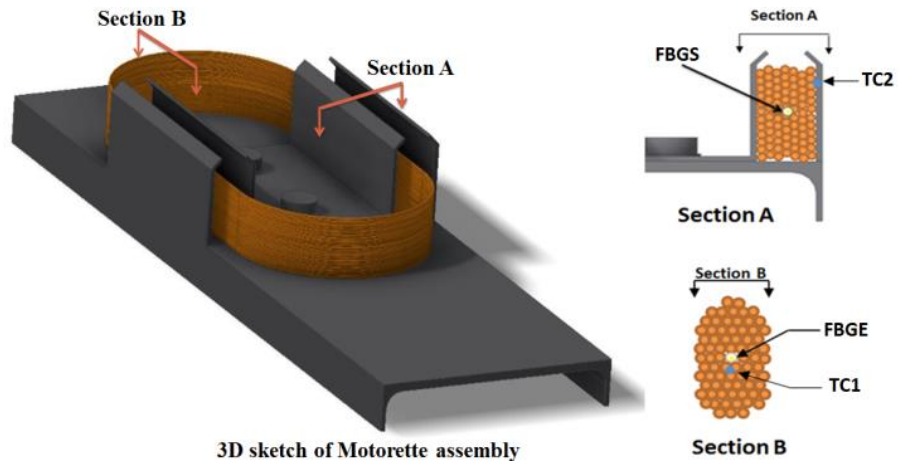


Fig. 10: FBG sensor placement within the test motorette geometry

TC sensors were installed in the vicinity of the motorette embedded FBG thermal packages, as shown in Fig. 10. TC2 was attached to the coil slot section outer surface to assess the thermal monitoring improvement potential that can be obtained from sensing in a point in the centre of the coil structure. For direct comparison of FBG versus conventional sensing performance in hot spot monitoring, TC1 was placed next to FBGE. The embedded motorette was placed in the thermal chamber to calibrate both the FBG sensors as discussed in section III. A.

A continuous running duty cycle S1 test was first performed by injecting a DC current of 2 A in the motorette coil. This current magnitude was found in tests to provide non-destructive thermal levels, that are representative of wound component thermal conditions experienced in practical systems but are below the temperature rating (155 °C) of the used class F insulation wire. The total S1 cycle test duration is 1500 sec as shown in Fig. 11. The measured data clearly show a close agreement of temperature measurements between FBGS and FBGE and TC1. This is due to the fact these are exposed to same thermal environments in the centre of the current carrying motorette coil. The temperature readings respectively obtained from FBGS, FBGE and TC1 after the coil thermal equilibrium for the applied current level is reached, are 117.50 °C, 116.96 °C and 116.76 °C, as illustrated by the detailed view inset in Fig. 11. The thermal reading obtained from the coil surface mounted TC2 however reports a slightly lower thermal level; this is expected as the thermal sensing point on the surface of the coil is affected by the surrounding ambient temperature and the temperature gradient between the coil centre temperature and that on the coil surface. The reported experimental data clearly illustrate the significance of effective thermal sensing placement and the strong potential of FBG sensors to deliver operative solutions for coil embedded hot spot monitoring.

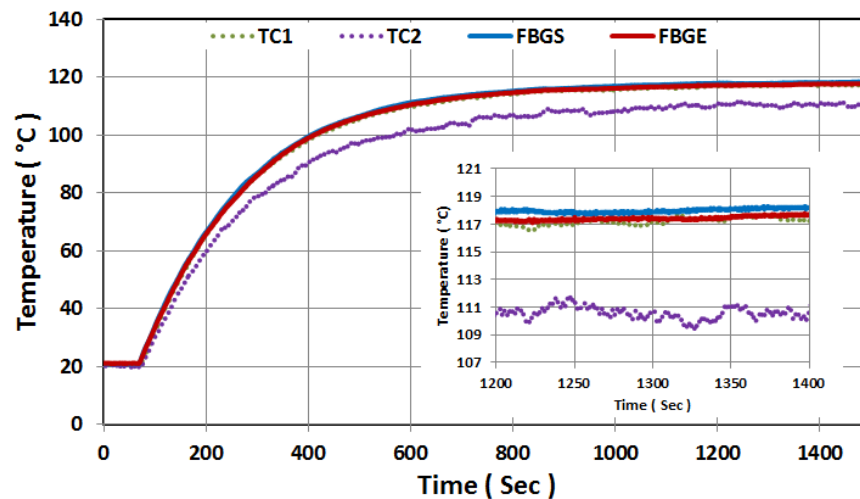


Fig. 11: Motorette coil thermal measurements

An FBG thermal sensor is temperature transducer that measures temperature from the monitored reflected Bragg wavelength shift. An investigation of how the monitored wavelength behaves under dynamic thermal conditions is important in assessing the potential of coil embedded FBG sensing for on-line condition monitoring, where reliable tracking of transient thermal processes that may originate from winding degradation is essential. For this purpose, a test was undertaken on the motorette coil during which four successive thermal transients having equal duration of 300 sec but with different, increasing thermal change rate ranging from $\approx 1 - 8$ °C/min were induced in the coil by appropriate control of the injected current. The corresponding monitored wavelength shifts for FBGS and FBGE plotted against the temperature rise measured by TC1 are shown in Fig. 12. The measured profiles clearly show that the monitored Bragg wavelength shift of both FBGS and FBGE reliably follow the temperature rise profiles under all examined temperature change rates. This suggests that coil embedded FBG thermal sensing has a good potential for delivering effective on-line thermal monitoring under transient thermal conditions.

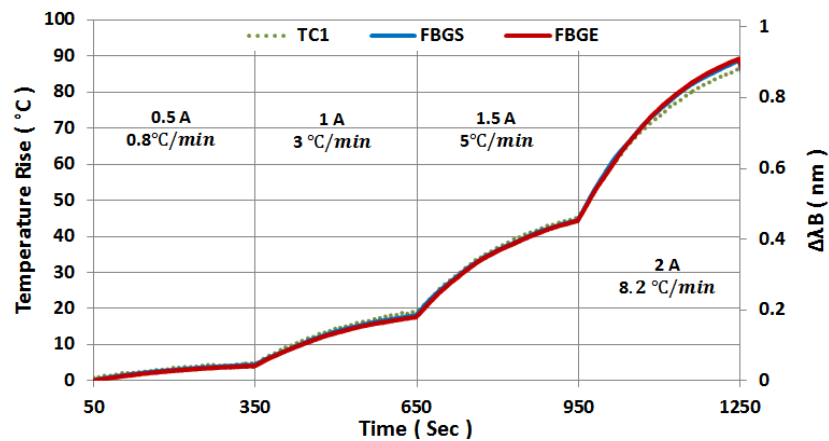


Fig. 12: Bragg wavelength shift under different temperature change rates

The dynamic thermal monitoring performance of the FBG sensing system was assessed and benchmarked against a conventional thermal sensor in an intermittent periodic duty cycle S3 test, performed through appropriate modulation of the coil current. A sequence of identical thermal cycles was applied by regular switching of the DC current level from a constant 2 A to zero. The cyclic duration factor was chosen to be 60 % with cycle duration of 5 min to induce a fast dynamic thermal profile that is within the thermal rating of the coil. The measured data are shown in Fig. 13. The thermal profiles recorded by the FBG and TC sensors in the motorette coil hot spots are in close agreement, with a maximum temperature difference between FBG sensors of 1.1 °C and between the FBG sensors and TC1 of 1.6 °C. The TC2 measurement deviates from the hot spot thermal measurements,

with a temperature difference between TC2 and TC1 of $\approx 11\text{ }^{\circ}\text{C}$ and $\approx 3\text{ }^{\circ}\text{C}$ for the highest and the lowest thermal levels in the considered cycle. This can be explained by the nature of the heat transfer mechanism within the coil, as the radial conduction heat transfer in the coil cross section area is faster than the natural convection heat transfer from its surface

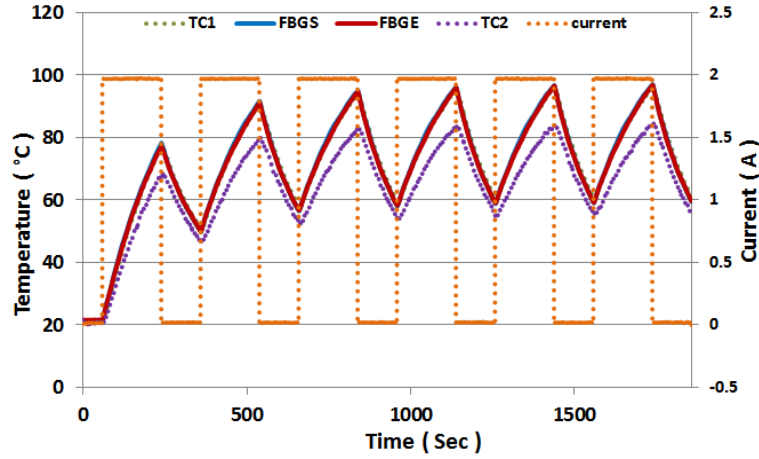


Fig. 13: FBG temperature sensors performance under thermal cycle

during energised time, thus creating a large temperature gradient. During the cooling period no heat is generated within the coil and its surface dissipates the heat induced during the energised period. No similar effects can be observed in other thermal measurements taken in this experiment which further demonstrates the inherent advantages provided by thermal monitoring in the coil hot spot points. The reported performance of embedded FBGs shows good repeatability with no significant evidence of hysteresis at this range of temperature and dynamic change rate.

2) Stator coil embedded FBG thermal monitoring

In order to enable the embedded FBG thermal monitoring evaluation in a current carrying coil wound into an AC machine stator geometry, the test coil design procedure described in previous text was replicated and wound into a stator core of a commercial induction machine design, as shown in Fig. 14 including photographs of the laboratory test system. This procedure enables the assessment of the FBG sensing system's performance, installation methodology and its requirements in a typical electric machine winding setting. For this purpose, the stator windings of the test stator geometry were removed and a single coil rewound with conductor dimensions based on the removed winding design. The test coil was wound into the core structure by first inserting one side of the coil into the appropriate slot and wedging it in place. A half of the other side of the coil was then inserted into the correct slot and kept in place to enable the installation of the FBG sensing package in the coil slot and end winding areas centre positions. After this was completed,

the remaining turns were placed over the sensors to complete the core installed FBG enabled test coil. Once the fully wound coil was in place slot wedges were inserted to compress the coil conductors and enhance the thermal contact between them and the sensor package surface.

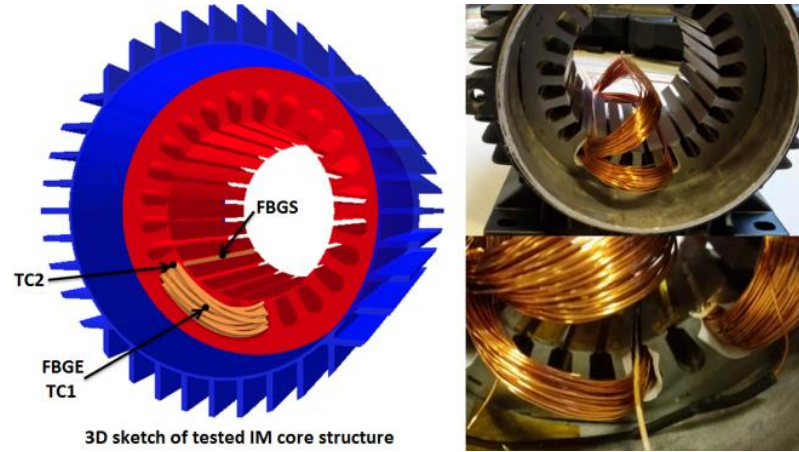


Fig. 14: Stator core embedded FBG enabled test coil

The FBG sensor placement within the prototype coil is identical to that examined for the motorette coil in Fig. 10. The FBG sensing elements positioning in the close proximity of the coil centre is ensured by bracing the sensor package to the initially inserted coil half using Kapton tape. To enable FBG sensors performance validation TCs were installed in the test coil in identical positions to those used in the stand-alone coil; TC1 was placed in the centre of the end-winding portion next to FBGE and TC2 was inserted between the coil surface and the slot insulation wall. The performance of embedded FBG thermal sensing in a current carrying coil wound into the stator core is investigated in this section building on the analysis presented in IV.C.1.

To evaluate the sensing performance at steady-state thermal conditions a continuous duty cycle S1 is applied on the coil by passing constant DC current through it. Before the cycle start the test coil ambient temperature was recorded for 1 min, a detailed view of which is shown in Fig. 15a. It can be seen that both FBGs and TCs show a close reading of ambient temperature, with a measurement difference of less than 1 °C. The measured thermal data obtained for the test cycle S1 is shown in Fig. 15b. A detailed view of the recorded thermal measurements once the steady-state temperature is reached is shown in Fig. 15c. Due to thermal characteristics of the stator core and frame structure the measured total cycle time is ≈ 2 hours. The thermal traces obtained from FBGE and TC1 sensors located in the end winding hot spot show an almost identical temperature reading throughout the examined cycle duration. However, a comparison of thermal readings obtained from FBGS and TC2 shows a constant temperature difference of ≈ 3 °C during cycle time. This largely arises

from the temperature gradient between the coil centre and its surface, in addition to the fact that the TC2 thermal reading is affected by the stator core temperature. More importantly, a clear difference can be observed between the thermal measurements obtained by FBGS and FBGE, measured at $\approx 6^\circ\text{C}$. This is also confirmed by the TC1 and TC2 thermal readings after accounting for the temperature difference due to the sensor placement.

It should be noted that the used FBG heads are packaged separately and imprinted in separate optic cables to ensure no packaging cross effects can exist. The observed thermal readings difference can be explained by the different thermal environments that the two embedded FBG sensors are exposed to. The induced heat in the slot portion is dissipated by conduction through the slot liner to the stator core and the machine frame, which constitute a considerable thermal structure in comparison to the test coil and therefore significantly assist the heat dissipation process in the coil slot section area in the utilised experimental arrangement. In addition to axial heat conduction towards the slot section, the end winding thermal energy is largely dissipated by means of natural convection which is inherently considerably slower than the heat dissipation process in the slot portion. The results in Fig. 15 clearly demonstrate the advantages of in-situ winding temperature sensing.

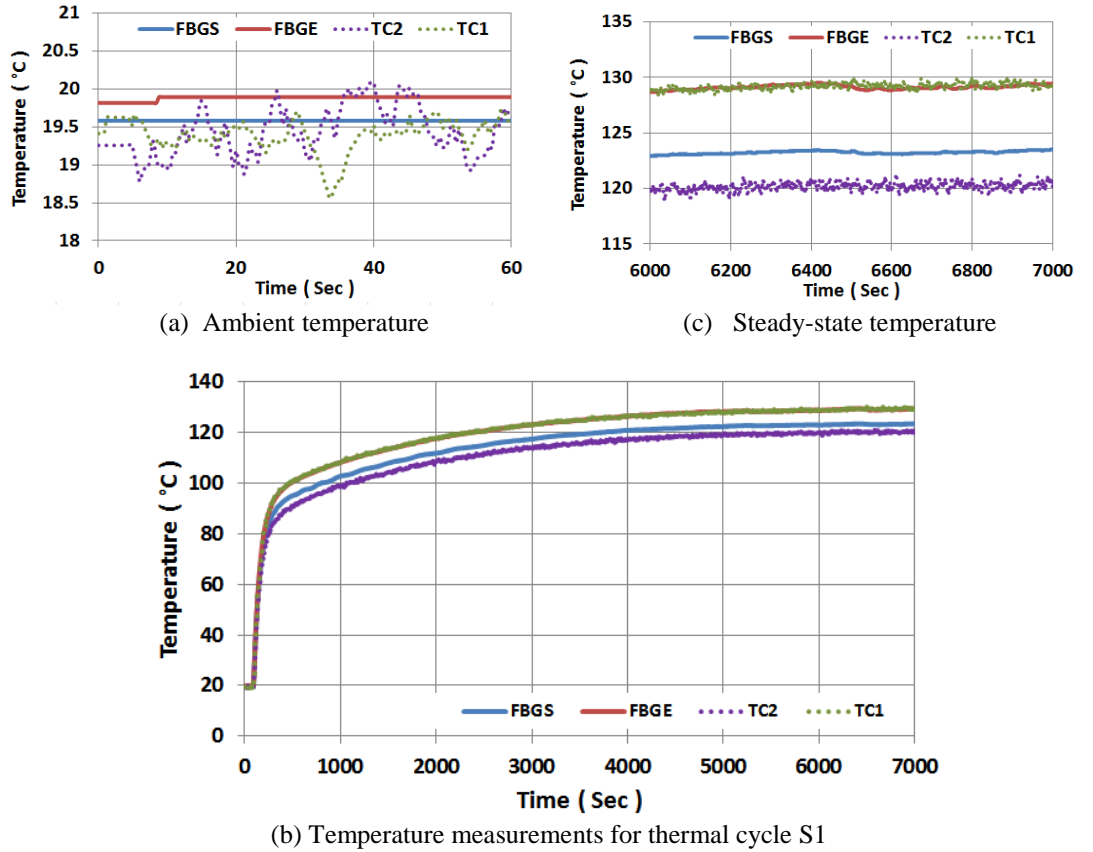


Fig. 15: Thermal measurement for a continuous thermal cycle

Fig. 16 shows the measured thermal dynamic response curves of the stator wound test coil under an applied intermittent periodic duty cycle S3 60%. It can be observed that the four thermal sensors report closely similar profiles. The measured data however show different temperature gradients with the highest temperature reported by FBGE and TC1, which indicate the coil hot spot position in these conditions. When the test coil is de-energised the temperature decreases and the difference between individual sensors' thermal measurements is significantly reduced. The obtained FBG measurements are seen to exhibit good repeatability in monitoring the examined cyclic thermal behaviour.

To explore the embedded thermal sensing behaviour in the presence of a current carrying coil in the neighboring slots, another coil was wound into the stator core and placed in the slots next to those containing the test coil with FBG and TC sensors. A continuous cycle S1 test was then performed on the instrumented test coil while keeping the adjacent coil current at zero value. Once steady-state thermal conditions were achieved the adjacent coil is energised with an identical current level for a period of ≈ 10 mins to investigate its thermal influence on FBG thermal records in the test coil. The FBGS and FBGE measurements and their respective difference are shown in Fig. 17. The thermal measurement difference in steady-state conditions when only the test coil is excited is measured as ≈ 6 °C. Once the adjacent coil is energised (≈ 150 sec) the measurement difference starts decreasing, with the FBGS reading clearly more affected by the heat generated by the adjacent coil than that of FBGE. The FBG thermal readings difference reduces to ≈ 2 °C at the point the adjacent coil is de-energised (≈ 650 sec), after which it starts rising back to its original level. The reported results demonstrate that the wound coil embedded distributed FBG thermal sensing can provide high resolution information on the coil thermal conditions.

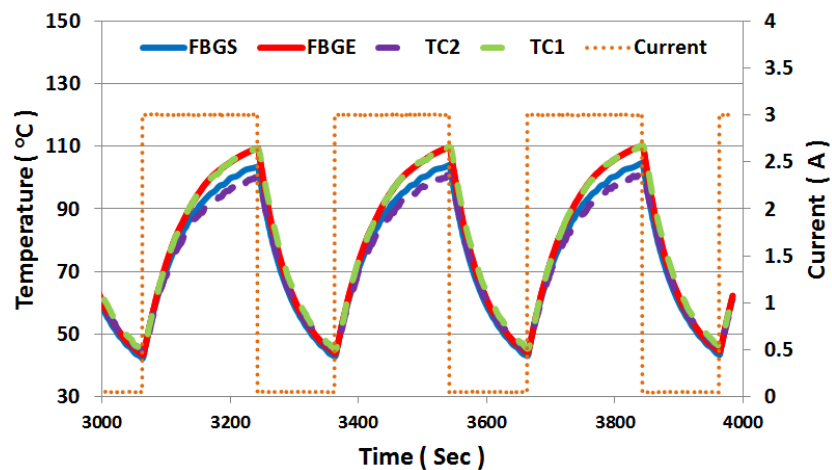


Fig. 16: Thermal measurements for an intermittent periodic thermal cycle

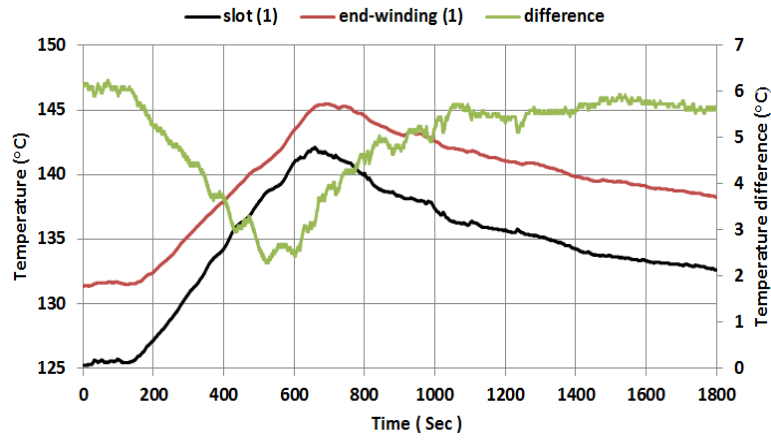
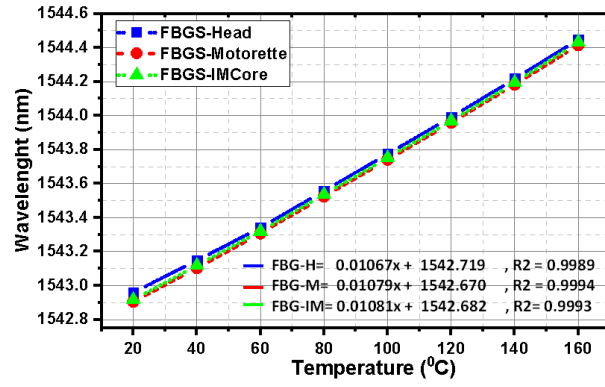


Fig. 17: External thermal excitation measurements effects

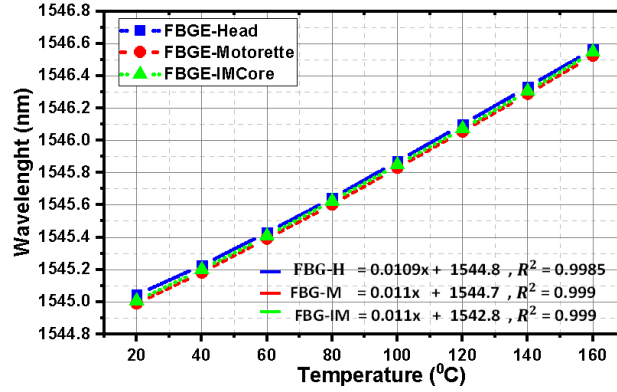
3) *In-situ FBG sensors characterisation*

The results of characterisation tests of the FBG sensing system embedded in the motorette and in the stator core are reported in this section. The test data provides an assessment of how the random wound coil implanted FBG sensing system may be affected by the process of sensor packaging and its embedding into the coil structure. For this purpose an identical calibration procedure was performed on the free FBG heads before these were packaged with PEEK capillary and on after embedment the stand-alone and the stator core wound test coils. The obtained results of free FBG head are compared with those achieved by performing an identical test procedure on the packaged sensors embedded within stand-alone (motorette in Fig. 10) and stator core wound (IM core in Fig 14.) test coils. The calibration tests were performed in the temperature range of 20 to 160 °C in a rising sequence of 20 °C steps. At each step the temperature was held constant for a time period sufficient to ensure the thermal equilibrium is achieved before thermal measurements were taken. The FBG wavelength and the chamber temperature values were recorded at each evaluated thermal equilibrium in the investigated temperature range.

The linearity and temperature sensitivity measured in calibration tests for free FBGs and packaged and embedded FBGS and FBGE sensors are shown in Fig. 18a and Fig. 18b respectively. The measured data indicate a reasonable linearity of coil embedded packaged FBG sensors, both having the correlation coefficient measured value higher than ≈ 0.999 . Furthermore, the average temperature sensitivity coefficients calculated from the slope of the FBGS and FBGE calibration test data linear fits are in the ranges of 10.67 to 10.81 pm/°C and 10.95 to 11.02 pm/°C, respectively. These values are fit within the theoretical calculated temperature sensitivity range of a bare FBG in section II. The calibration results suggest that the procedure of FBG head packaging and insertion into a random wound coil geometry centre positions has a negligible effect on the sensor temperature sensitivity.



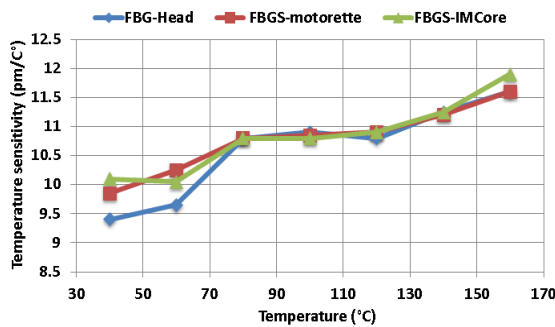
(a) FBGS wavelength and temperature characteristics



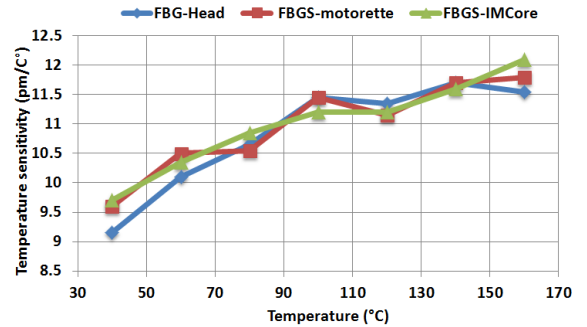
(b) FBGE wavelength and temperature characteristics

Fig. 18: FBG sensing system wavelengths - temperature characteristics

To further evaluate the embedded FBG sensor characteristics, the influence of the installation induced on the average temperature sensitivity is examined. Fig. 19 shows the comparison of the average temperature sensitivity measured in thermal tests. The coil embedded sensors are seen to manifest a closely similar pm/°C profile to that of a free FBG head in the examined temperature range. The FBG thermal measurement sensitivity increases with the monitored temperature increase from a value lower than ≈ 10 pm/°C to ≈ 12 pm/°C. This is a typical behaviour of FBG sensors caused by the nonlinearity of the thermo-optic coefficient of the optic fibre [14]. The measured data however illustrate the importance of appropriate calibration of the coil embedded FBG sensors.



(a) FBGS



(b) FBGE

Fig. 19: (a) FBGS measured temperature sensitivity; (b) FBGE measured temperature sensitivity

D. In-situ multiplexed FBG temperature sensor performance for distributed thermal monitoring

This section evaluates the sensing implication and performance of in-situ FBG temperature sensor based on multiplexing feature of FBG technology for internal distributed thermal monitoring in random wound coils. The in-situ sensing performance was examined under even/uneven thermal stress distribution in the examined coil systems. First the multiplexing feature was used to create an internal sensing network within a single current carrying coil system, and the feature use then extended to produce a single internal thermal sensing network covering a multi coil system.

1) Single-coil test system results

This test coil system consists of a single prototype coil wound of class H enamelled copper wire, typically used in conventional low voltage machinery. The packaged array sensor illustrated in Fig. 2b was placed in the centre of the coil structure to be in near proximity of thermal hot spots of interest; this was achieved by first winding half the coil turns before placing the sensor package in its centre and winding the remainder of the coil turns. The resulting array sensor installation effectively takes the shape of a single turn

centred in the test coil's assembly. The array's four FBG heads were distributed within the coil structure so that two are placed in the coil sides (FBG2, FBG4) and the remaining two in the coil ends (FBG1, FBG3), as shown in Fig. 20. Fig. 20 also shows a cross-section of the test coil to illustrate further the FBG sensor location within the test coil structure. The test coil was fixed to a support plate for the purpose of experimental work. The described test system provides an effective tool for evaluating embedded distributed sensing performance in a typical wound coil geometry, including coil side and end segments.

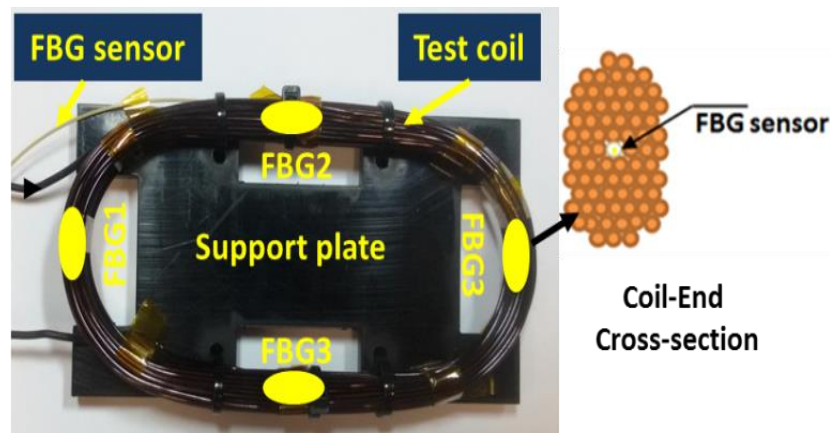


Fig. 20: Single-coil test system

a) *FBG array sensor performance under static and dynamic conditions and uniform thermal stress*

The distributed thermal monitoring performance of the single coil embedded FBG array sensor was evaluated in static and dynamic thermal tests. To enable the assessment of steady-state thermal monitoring performance, the embedded coil was first injected with a 3A DC current giving ≈ 4.2 W power loss dissipated as heat. Fig. 21 shows the temperature measurement obtained by the four FBGs from ambient temperature, including a detailed view of steady-state thermal measurements for clarity. Individual FBG measurements obtained in different coil locations are seen to exhibit close internal temperature readings that are within ≈ 1.5 °C. While the power loss induced by the coil resistance is relatively small at ≈ 4.2 W, it generates coil internal hotspot temperatures of ≈ 76 °C. This is expected as the induced heat is dissipated from the coil to the surrounding ambient by convection, which is an inherently slow heat transfer process. The average internal coil temperature measured at steady-state is ≈ 75.5 °C.

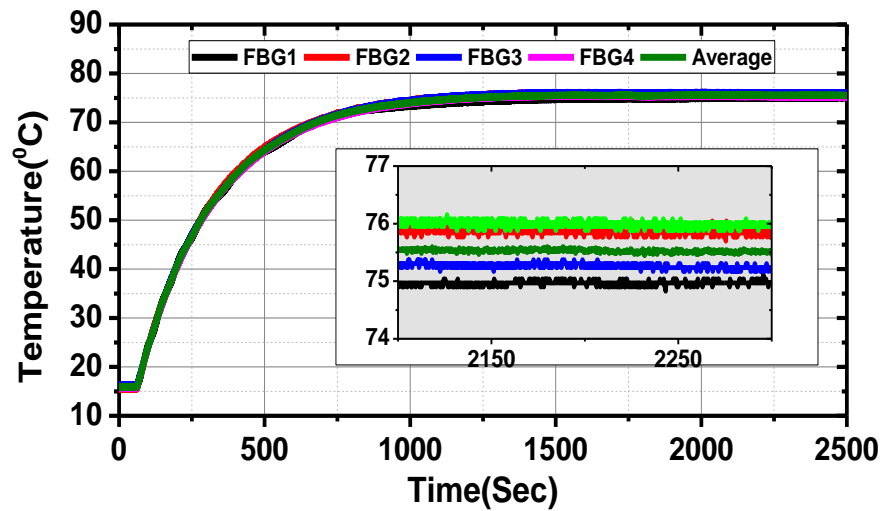


Fig. 21: FBG array thermal measurements in steady state conditions

The dynamic thermal monitoring performance of the FBG array sensing system was assessed in an intermittent periodic duty cycle, performed by appropriate modulation of the coil excitation current. A sequence of identical thermal cycles was applied by regular switching of the DC current level from zero to constant 6 A. The total applied periodic thermal cycle duration is 10 mins, including a 4 min period of increasing thermal stress (i.e. constant 6A current flow) followed by a 6 min cooling period (i.e. zero current flow). This provides a representative dynamic thermal profile that is within the thermal rating of the examined coil design. The data measured in the dynamic test are shown in Fig. 22. The applied periodic duty cycle is reported by the embedded array sensor to induce an internal temperature cycle in the range of ≈ 44 to ≈ 138 °C within the tested coil. The transient

thermal profiles recorded by individual FBGs are seen to be in close agreement and show good repeatability. The obtained results clearly demonstrate the capability of effective multi-point internal thermal sensing for on-line thermal monitoring using the proposed FBG array sensor.

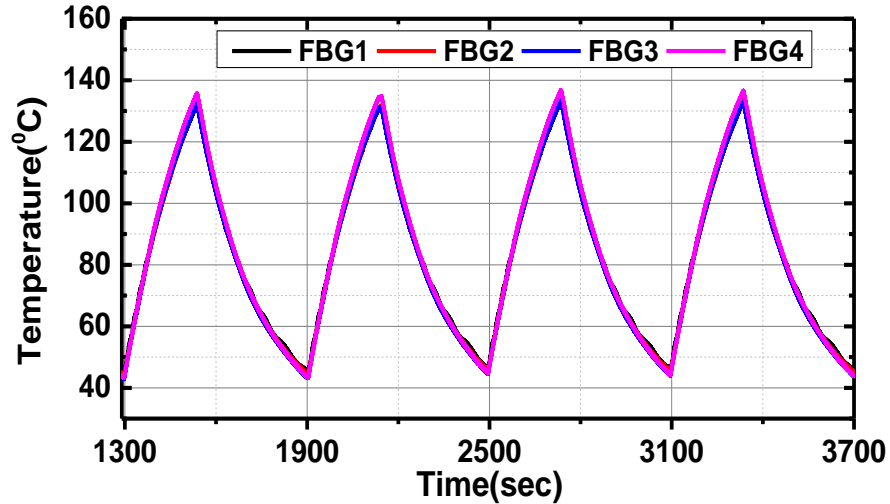


Fig. 22: FBG array thermal measurements in transient conditions

b) FBG array sensor performance under non-uniform thermal stress

A particularly attractive feature of distributed thermal monitoring is the capability of identification of excessive localised thermal stress within the coil structure which in practical applications can often be an early sign of a possible degradation process. Acquiring a single localised thermal reading of the entire coil's internal temperature will not be adequate for providing full information about the coil thermal state in such condition, as the position of the excessive thermal stress induced hot spot is difficult to predict and could be anywhere within the coil structure. Distributed internal thermal sensing can, in principle, provide an adequate solution as it delivers multi-point thermal measurement in different locations within the coil structure. To examine the embedded distributed thermal monitoring performance in a localised high thermal stress operating scenario an additional, external coil was wound around a section of the test coil where FBG4 sensing head is positioned, as illustrated in Fig. 23. The external coil was energised with a constant DC current of 10 A in the tests to provide localised increased thermal stress in the main test coil embedded with the FBG array sensor. The main coil was first excited with a DC current of 3 A in the tests and once the thermal steady-state was reached the external coil was energised to provide additional localised stress. This procedure results in unequal thermal conditions within the main coil structure as the external coil induced heat will be unevenly dissipated in the tested coil.

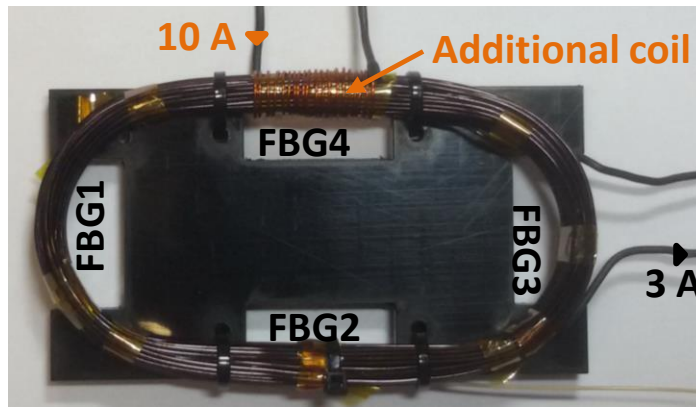


Fig. 23: Illustration of external coil use for localised high thermal stress

Fig. 24 shows the array sensor thermal measurements obtained in the performed test. The first 75 sec in the plot represent the temperature readings before the external coil is excited. The four FBGs exhibit a closely similar transient profile in this period. Once the external coil is excited there is an obvious change in the distributed readings, where FBG4 records the highest temperature ($\approx 128.6^\circ\text{C}$) and FBG2 the lowest ($\approx 117.6^\circ\text{C}$), while FBG1 and FBG3 report very similar readings (≈ 122.7 and $\approx 121.6^\circ\text{C}$). The recorded differences between FBG head readings correspond to their distribution in the test coil structure. A difference of $\approx 10^\circ\text{C}$ between the point of highest and lowest thermal stress in the coil was reported by the embedded array sensor, illustrating the advantages in recognition of localised hot spots of high thermal stress by using distributed thermal sensing based on FBG technology. Fig. 25 shows the thermal images of the test coil before and after the external thermal excitation. The image recorded before the excitation in Fig. 25.a shows almost identical temperature gradient on the test coil surface, which confirms the results obtained in Fig. 21. The thermal image recorded after the external thermal excitation was applied shows an induced hot spot on the left side of the test coil propagating towards coil ends. This image confirms the thermal measurements obtained by the distributed FBG sensors embedded in the test coil.

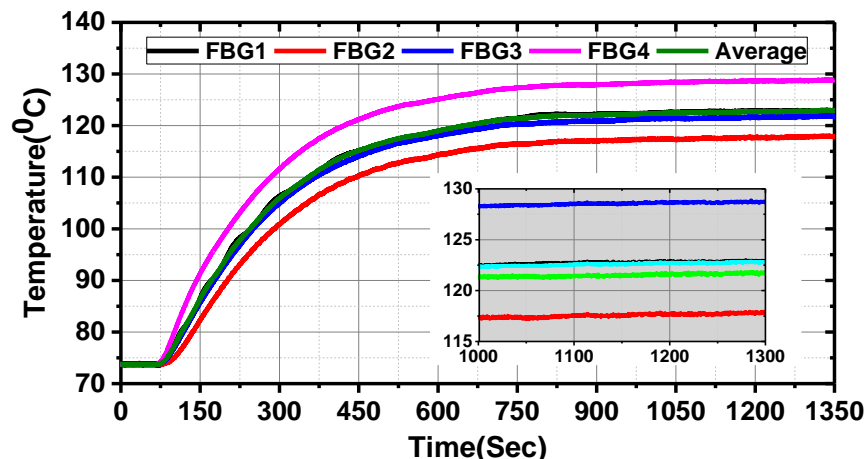


Fig. 24: Thermal measurements under non-uniform thermal stress

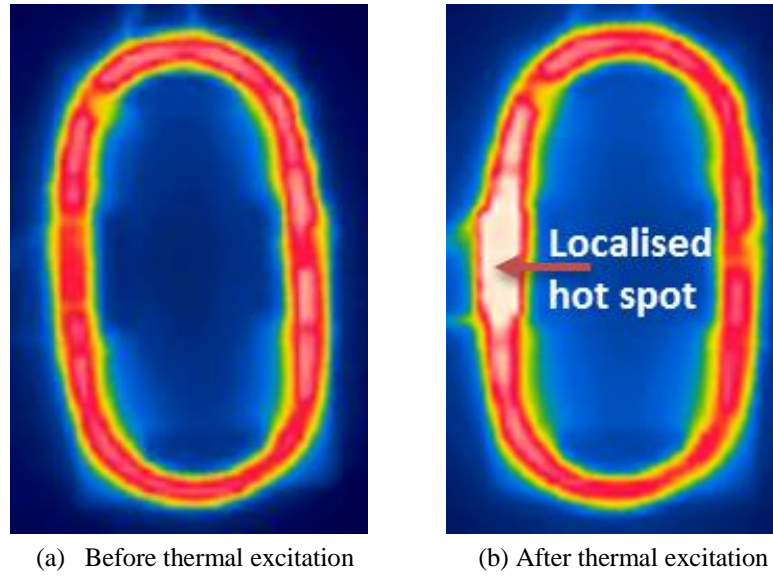


Fig. 25: Thermal images under non-uniform thermal stress

2) Multi-coil test system results

The purpose of this test system is to evaluate the proposed in-situ thermal sensing multiplexing design use for distributed internal thermal monitoring in multi-coil systems such as those that would be encountered in practical electrical machine windings. The multi-coil test system, shown in Fig. 26, is built by winding three coils on the winding machine and then mounting these on a purpose built steel core to emulate the general environment representative of electric coil exploitation conditions in a typical machine magnetic core.

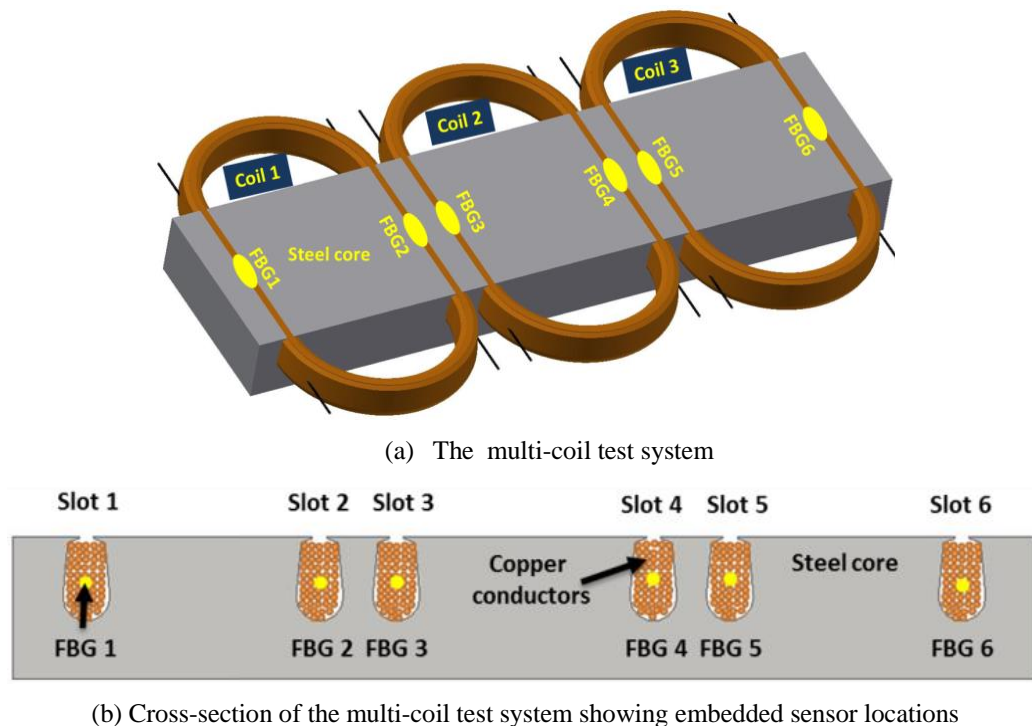


Fig. 26: Multi-coil test system

The core contains six slots, which are designed to house the three random wound coils sides. Each coil was wound of 115 turns of a single strand of 24 AWG class H insulated copper wire. The turn number and the slot geometry were designed to yield a coil slot packing factor of $\approx 43\%$, which is a typical value for electric machine applications. The FBG array temperature sensor with six 5 mm FBG heads shown in Fig. 2c was embedded in the multi-coil test system. The distance between individual FBGs was designed to match the dimensions of the multi-coil test system and enable an FBG to be embedded in the axial centre length position in each of its six slot sections (FBG1-6 in Fig. 26.a). The array sensor is embedded in the cross sectional centre point position of each of the three coils comprising the test system as shown in Fig. 26b; this ensures the sensors are in close proximity to individual coil thermal hot spot points of interest.

a) FBG array sensor performance under static and dynamic conditions and even thermal excitation

The aim of this test is to illustrate and assess the performance of the FBG array thermal sensor embedded in the multi-coil system under static and dynamic thermal conditions. Three test coils comprising the multi-coil test system were thus connected in series to ensure that the same current flows through each coil, so that the power losses in each coil and hence the induced generated heat are equal.

A DC power supply was used to energise the test system with a 1.5 A DC current. The resulting thermal excitation was monitored in each coil side by the embedded sensing array. The monitored temperatures in each coil were recorded for a 10000 second period until the thermal steady-state was achieved, as shown in Fig. 27. The measurements indicate that the thermal time constant of the coil system is considerable; this is due to the nature of its slow cooling heat transfer mode (i.e. convection). The obtained dynamic temperature measurements show that the array sensor individual sensing points placed in separate slots report closely similar thermal profiles, as would generally be expected for the examined test conditions. The average steady-state temperature in the final 100 seconds of measurements in Fig. 27 is $\approx 90^\circ\text{C}$, as seen in the detailed view inset in the figure. The difference between individual sensor steady-state measurements is seen to be in the order of up to $\approx 2.5^\circ\text{C}$ and is largely induced by different location in the test system structure, resulting in exposure to slightly different thermal conditions as imposed by the structure of the examined system. The obtained experimental data demonstrate that the proposed in-situ sensor array is capable of achieving effective distributed sensing of internal multi-coil conditions.

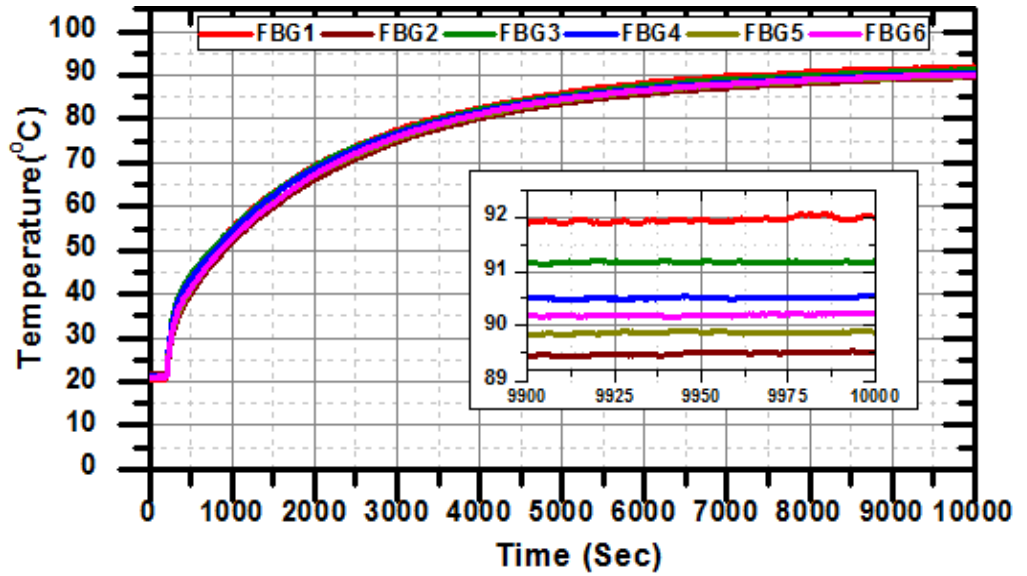


Fig. 27: Measured dynamic temperature by the in-situ FBG array sensor under even thermal excitation

Fig. 28 shows the obtained dynamic thermal measurements by the array sensor under an intermittent periodic duty cycle. A sequence of identical duty cycles was applied to the multi-coil system by performing an appropriate modulation of the DC current. The total applied periodic thermal cycle duration is 5 mins, with duration factor of 20 % to induce a dynamic thermal profile that is within the thermal rating of the coil. The thermal profiles recorded by the FBG heads in the multi-coil system hot spots are seen to be in close agreement, with a maximum temperature difference between individual sensor readings of ≈ 5 °C; the measured coil hot spot temperature is seen to range from ≈ 58 to ≈ 118 °C within the applied duty cycle. The obtained measurements demonstrate the capability of the reported in-situ FBG array sensor design to facilitate on-line tracking the internal thermal hot spots in a multi-coil system structure.

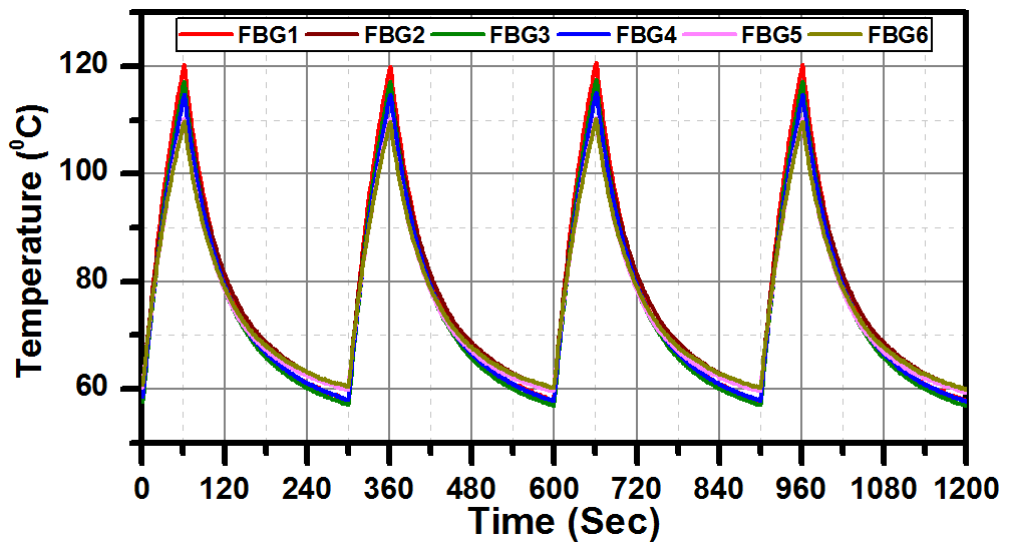


Fig. 28: FBG array thermal measurements in transient conditions

b) FBG array sensor performance under uneven thermal excitation

This test was performed to assess the performance of the FBG sensing system for distributed thermal sensing in a multi-coil system under uneven thermal excitation. In this test each coil is connected to a separate DC power supply and an equal 1.5 A DC excitation current first injected in each coil. When the thermal equilibrium was reached in all coils a 3 % individual coil excitation current imbalance was applied as follows: after recording the steady-state temperatures induced by 1.5 A DC current for 5 min, the current in coil1 was increased by 3 % to 1.55 A and the current in coil3 was reduced by 3 % to 1.45 A, while the coil2 current was kept at 1.5 A; thermal reading were taken in imbalanced excitation current conditions for a 10 min period. After the 10 min period has elapsed the current in coil1 is reduced to 1.45 A and in coil3 increased to 1.55 A and thermal measurement taken for a further 10 min period; the current in coil2 is kept at constant 1.5 A DC. This test case generally replicates the current flow condition in electrical machine windings operating in unbalanced supply, where individual phase/coil current can considerably differ resulting in unevenly distributed winding temperatures.

Fig. 29 shows the measured dynamic temperatures changes by the FBG array sensor during the test. Fig. 30 shows the corresponding thermal images recorded at even thermal excitation (i.e all coils injected with 1.5 A) and at uneven thermal excitation (i.e coil1-1.55A, coil2-1.5A and coil3-1.45). The experimental data clearly demonstrate the high sensitivity of the proposed embedded sensor design, which unambiguously registered coil internal thermal changes due a minor excitation current change of ≈ 50 mA. The thermal camera obtained temperature readings shown in Fig. 30 however did not detect this thermal variation and cannot clearly distinguish the distributed thermal conditions. The thermal traces in Fig 29 are the measured temperatures subtracted by the steady-state temperature at 1.5 A excitation. The FBG pairs in each coil recorded similar temperature change profiles, which clearly follow the excitation current magnitude variation, i.e. the supply current increase and decrease, in each individual coil. However, at steady-state the FBG pairs embedded in individual coils report slightly different thermal readings: this can be explained by different individual sensor positions in the steel core, resulting in slightly different practical thermal conditions. The FBG sensors reporting lower readings are those adjacent to the mid test coil (i.e. coil2 in Fig. 26a) and hence their readings are affected by the heat produced by this nearby coil.

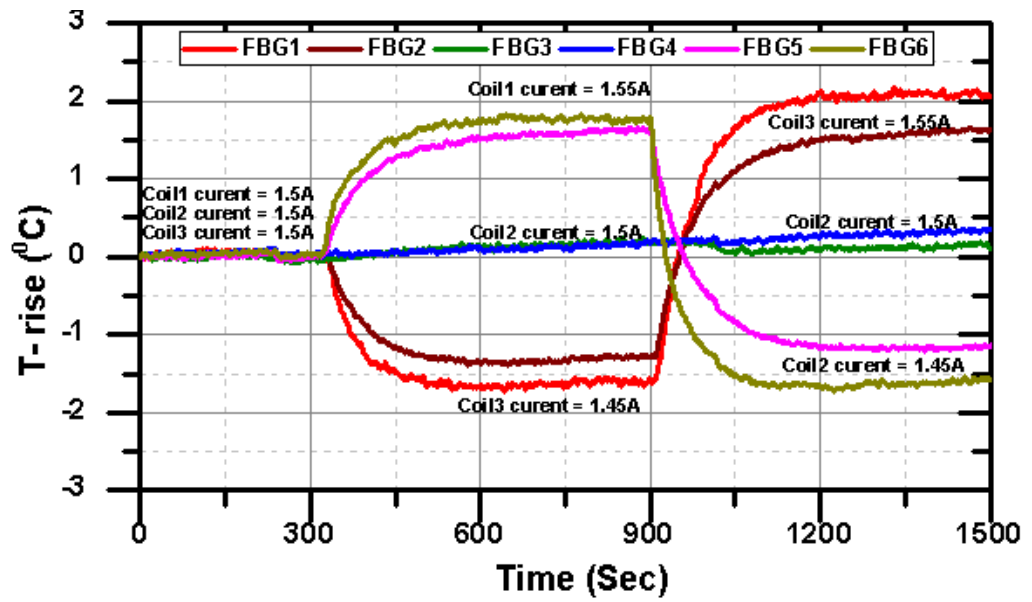


Fig. 29: Measured dynamic temperature by the in-situ FBG array sensor under uneven thermal stress

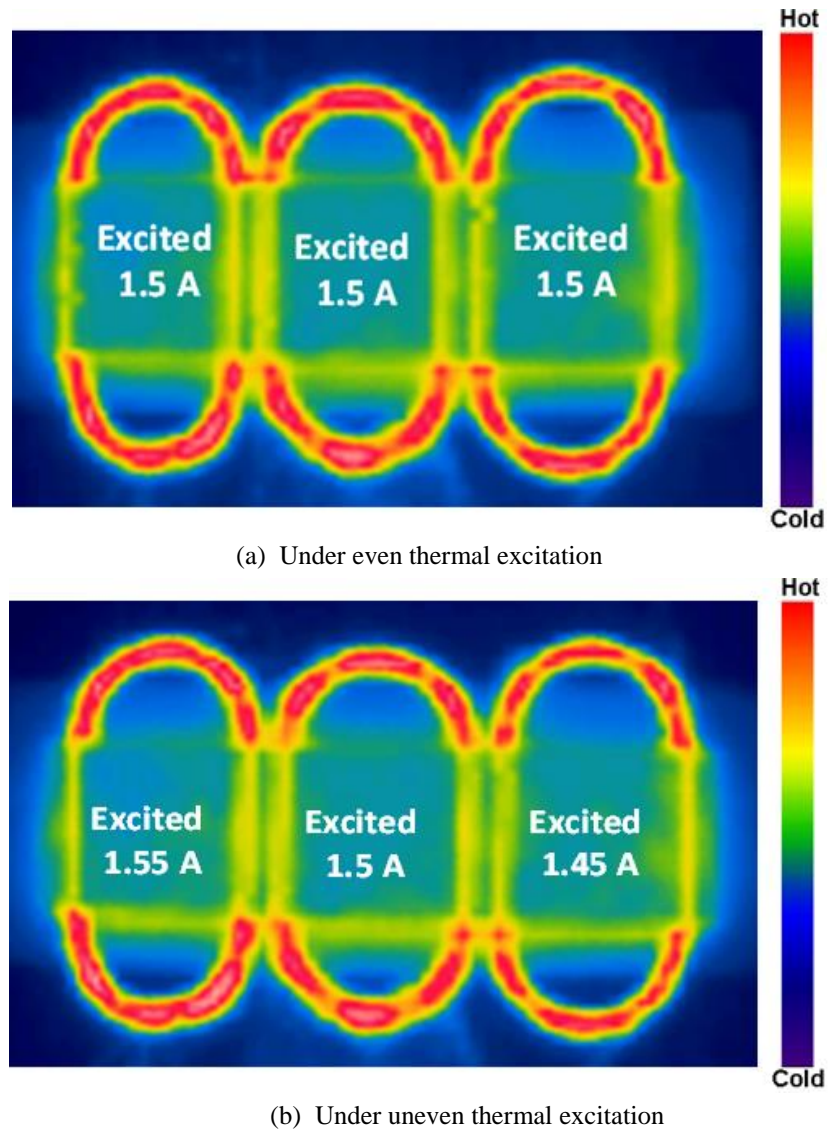


Fig. 30: Thermal images of the tested multi-coil system

V. CONCLUSIONS

This paper reports a detailed investigation of the design and installation procedures and operational capabilities of FBG sensor enabled thermal hot spot temperature sensing in random wound coils such as used in electric machinery. The potential of the embedded FBG package to enable thermal hot spot temperature monitoring is first examined in a range of experiments on a test coil under controlled static and dynamic thermal conditions. The reported results demonstrate that the presented FBG sensor design can reliably measure hot spot thermal conditions in a random wound electric coil and provide a useful precursor to informing further applications in wound components of operational electric machinery.

The current carrying coil embedded thermal monitoring performance is evaluated in a number of static and dynamic thermal experiments on a prototype test coil system in a stand-alone environment and when wound into a stator core structure. The coil embedded FBG sensor performance is validated by conventional TC sensors and is shown to have a strong potential to provide a flexible and EMI immune hot spot thermal monitoring solution that delivers improved fidelity information on the coil thermal conditions.

This work also reports a performance assessment of an embedded sensing system aimed at distributed internal monitoring of thermal conditions in electric machine wound coils. The proposed embedded sensing hardware was found to provide satisfactory performance in monitoring coil internal thermal conditions under typical steady-state and transient thermal cycles: the system has significant potential to facilitate effective recognition of multiple localised points of thermal stress in the wound coil structure. The proposed design provides a versatile platform for further application of wound coil embedded distributed thermal sensing systems and their integration for real-time thermal management in electrical machinery.

REFERENCES

- [1] M. Rosu, P. Zhou, D. Lin, D. M. Ionel, M. Popescu, F. Blaabjerg, *et al.*, *Multiphysics Simulation by Design for Electrical Machines, Power Electronics and Drives*: John Wiley & Sons, 2017.
- [2] Stone, Greg C. "General principles of winding failure repair and rewinding." In *Electrical insulation for rotating machines: design, evaluation, aging, testing, and repair*, pp. 129-135. Wiley, 2004.
- [3] H. Zhang, "Online Thermal Monitoring Models for Induction Machines," in *IEEE Transactions on Energy Conversion*, vol. 30, no. 4, pp. 1279-1287, Dec. 2015.
- [4] P. Tavner, LI Ran and J. Penman, "Condition monitoring of rotating electrical machines," *IET Power and Energy Series*, 2008.
- [5] IEEE Recommended Practice for General Principles of Temperature Measurement as Applied to Electrical Apparatus," in *IEEE Std 119-1974* , vol., no., pp.0_1-, 1975

- [6] Hoffmann, Lars, Mathias S. Muller, Sebastian Kramer, Matthias Giebel, Gunther Schwotzer, and Torsten Wieduwilt. "Applications of fibre optic temperature measurement." *In Proceedings of the Estonian Academy of Sciences: Engineering*, vol. 13, no. 4, pp. 363-379. Estonian Academy Publishers, 2007.
- [7] Martelli, Cicero, Erlon Vagner da Silva, Kleiton de Moraes Souza, Felipe Mezzadri, Jonas Somenzi, Marcos Crespim, Hypolito José Kalinowski, and Jean Carlos Cordoza da Silva. "Temperature sensing in a 175MW power generator." *In OFS2012 22nd International Conference on Optical Fiber Sensors*, vol. 8421, p. 84212F, 2012.
- [8] K. Sousa, A. Hafner, M Crespim, V. Oliveira, H. Kalinoski and J. Silva, "Fiber Bragg grating sensing applications in temperature monitoring of three-phase induction motors," *Microwave & Optoelectronics Conference (IMOC)*, 2011 SBMO/IEEE, 2011.
- [9] D. S. Vilchis-Rodriguez, S. Djurović, P. Kung, M. I. Comanici and A. C. Smith, "Investigation of induction generator wide band vibration monitoring using fibre Bragg grating accelerometers," *2014 International Conference on Electrical Machines (ICEM)*, Berlin, 2014, pp. 1772-1778.
- [10] Willsch, M., T. Bosselmann, M. Villnow, and W. Ecke. "Fiber optical sensor trends in the energy field." *In OFS2012 22nd International Conference on Optical Fiber Sensors*, vol. 8421, p. 84210R, 2012.
- [11] A. D. Kersey, M. A. Davis, H. J. Patrick, M. LeBlanc, K. P. Koo, C. G. Askins, M. A. Putnam, and E. J. Friebele, "Fiber grating sensors." *Journal of lightwave technology* 15, no. 8 (1997): 1442-1463.
- [12] N. M. Theune et al., "Investigation of stator coil and lead temperatures on high voltage inside large power generators via use of fiber Bragg gratings," *SENSORS, 2002 IEEE*, Orlando, FL, USA, 2002, pp. 1603-1607 vol.2.
- [13] P. Wang, J. Liu, F. Song and H. Zhao, "Quasi-distributed temperature measurement for stator bars in large generator via use of Fiber Bragg Gratings," *Proceedings of 2011 6th International Forum on Strategic Technology*, Harbin, Heilongjiang, 2011, pp. 810-813.
- [14] Willsch, M., T. Bosselmann, and M. Villnow. "Fiber optic sensor solutions for increase of efficiency and availability of electric power generators." (*EWOFs'10*) *Fourth European Workshop on Optical Fibre Sensors*, vol. 7653, p. 756337, Sep. 2010.
- [15] IEEE Standard Test Procedure for Thermal Evaluation of Systems of Insulating Materials for Random-Wound AC Electric Machinery," *in IEEE Std 117-2015 (Revision of IEEE Std 117-1974)*, vol., no., pp.1-34, 6 May 2016
- [16] Rao, Yun-Jiang, "In-fibre Bragg grating sensors," *Measurement science and technology* 8, no.4, p. 355, Apr. 1997.
- [17] M. Reddy, S. Kamineni, and V. Rao Pachava, "Characterization of encapsulating materials for fiber bragg grating-based temperature sensors." *Fiber and Integrated Optics* 33, no. 4, pp 325-335, Jul. 2014.
- [18] A. D. Kersey et al., "Fiber grating sensors," *in Journal of Lightwave Technology*, vol. 15, no. 8, pp. 1442-1463, Aug. 1997.
- [19] SmartFibres, "Our Technology," Available: <https://www.smartfibres.com/technology>
- [20] D. Barrera, V. Finazzi, J. Villatoro, S. Sales and V. Pruneri, "Packaged Optical Sensors Based on Regenerated Fiber Bragg Gratings for High Temperature Applications," *in IEEE Sensors Journal*, vol. 12, no. 1, pp. 107-112, Jan. 2012.
- [21] International Electrotechnical Commission, "IEC 60034-1:2010 Rotating electrical machines - Part 1: Rating and performance," IEC, 2010.

4.3 Paper 2:

FBG Thermal Sensing Features for Hot Spot Monitoring in Random Wound Electric Machine Coils

A. Mohammed, *Student Member, IEEE*, S. Djurović, *Member, IEEE*

Abstract—This paper investigates the key design and operational features of embedded Fibre Bragg Grating (FBG) sensing for thermal hot spot monitoring in random wound coils such as used in low voltage electrical machines. To this end thermal experiments are performed on test wound coils embedded with FBG sensors to examine the vital application features of embedded sensor design, such as the sensor packaging material choice, in-situ calibration, sensitivity to vibration and thermal response time. Measurement error rates are examined and quantified in representative practical tests. The reported results enable a much improved understanding of the performance implications of embedded FBG sensor design features and the attainable in-situ hot spot thermal monitoring performance in random wound coils.

Index Terms—FBG thermal sensor, embedded sensing, random wound coils, winding thermal hot spot monitoring.

I. INTRODUCTION

ELECTRIC machines have found many uses in modern industrial systems. A significant proportion are employed in low voltage applications for which they are almost invariably designed with random wound electric coils due to the benefit of reduced manufacturing cost [1]. Random wound coil design however imposes a penalty of inferior coil endurance to electro-thermal stresses experienced during machine operation and therefore a potential increased risk of premature failure if the coils are operated outside their rated performance envelope. Exposure to undesired, but frequent in practical applications, thermal or electrical overloads is of particular concern as it can result in rapid insulation breakdown [2]. Real-time monitoring of internal temperature in random wound coils, where thermal hot spots are located, is thus of utmost importance; this can enable understanding of coils' operational integrity and ultimately that of a machine or a wider industrial process they facilitate, with an underlying aim to help reduce maintenance and downtime cost [3].

Random wound coil thermal hot spots are typically localised in close proximity to the coil centre [3, 4]. From a thermal monitoring perspective, this location is challenging to effectively access. Conventional thermal monitoring techniques for electric machine wound components, such as thermocouples or resistance temperature detectors, impose significant application constraints in coil embedded hot spot sensing applications due to sensor electrical conductivity, size and sensitivity to electromagnetic interference (EMI) [5,6]. An attractive alternative has emerged with advances in Fiber Bragg Grating (FBG) sensing technology, which provides critical features such as EMI immunity, small size, multiplexing and general resistivity to harsh environments [7]. These attributes make FBG sensors a strong candidate for embedded sensing solutions in confined high EMI environments such as found within electric coils and machines. Recent literature demonstrates the feasibility of electric machine embedded thermal and mechanical monitoring using FBG sensors [5-12]. In [6,7] the advantages of using FBG thermal sensing technology in low voltage induction motors were demonstrated by using multiplexed FBGs to measure winding surface thermal dynamic change. However, where thermal monitoring of wound components is concerned, the reported literature is constrained to metallic packaged FBG sensor application in large form wound coil structures or on the outer surface of random wound coils and not in the proximity of coil embedded hot spots that are of critical interest in low voltage machinery. The reported positioning, packaging and installation techniques can impose significant limitations in efficacy of thermal monitoring in low voltage machinery and therefore require further investigation; the reported sensing is largely away from critical winding thermal hot spots and utilises surface bonded metallic packaging in a strong magnetic field environment and is therefore susceptible to undesirable mechanical and thermal stress that may cause inaccurate readings and sensor displacement. Embedded FBG sensing for internal thermal monitoring of low voltage random wound machine components has not been much researched. The authors demonstrate the fundamental feasibility of FBG thermal sensing for hot spot thermal monitoring of wound coils in [13,14]. However the features and performance potential of this technique are not fully understood and further investigation is required to understand the practical implications of embedded sensor design and positioning on its operational capability.

FBGs respond to both mechanical and thermal excitation. In order to achieve an exclusively thermal monitoring capability in a wound coil embedded position an FBG sensor needs to be isolated from mechanical stress inherent to machine coils. An operative

solution can be obtained by inserting the FBG head within a capillary of mechanically rigid material and placing this package in the middle of the coil during the winding process [13,14]. However measurement reliability is strongly influenced by factors such as sensor calibration, packaging and installation methods, all of which impose specific requirements in this application and can have considerable impact on sensing accuracy and sensitivity [15,16]. Measurement accuracy is essential in thermal monitoring of electric machinery, as inaccurate readings can give an incorrect indication of the wound component thermal stress and aging process. For satisfactory accuracy to be achieved the error sources need to be identified, evaluated and accounted for in the sensing process. Consequently, three vital application aspects of random wound coil embedded FBG hot spot monitoring are examined in this study:

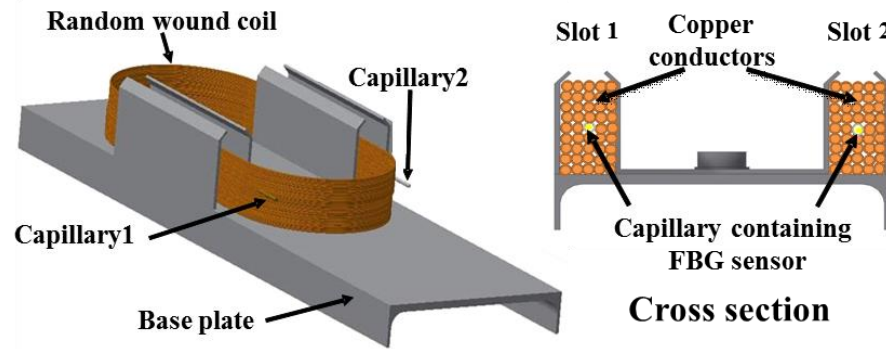
- The effect of thermal sensor installation process on its calibration characteristic and in-situ measurement error.
- The embedded FBG thermal sensor sensitivity to vibration.
- The influence of sensor packaging material choice on the attainable in-situ thermal monitoring response time.

To this end the paper reports a series of real-time thermal measurement experiments performed by a number of packaged FBG sensors operated by a commercial interrogator system. The examined FBGs were embedded in motorette test-rigs or prototype coils installed into a commercial low voltage motor structure. The motorette rigs are designed according to the IEEE 177 standard [17]. The study examines the performance implications of both metallic and non-metallic packaging use, giving more focus to the latter as a preferred choice for this type of application. The underlying aim of this work is to increase the understanding of the influence of embedded sensor design features on attainable in-situ hot spot thermal monitoring performance, with a view to underpinning the acceptance and effective application of this technique in operational device embedded sensing applications.

II. TEST SYSTEM DESCRIPTION

Experimental work was largely performed on random wound coil and slot assemblies (i.e. motorettes) designed according to relevant IEEE standards [17]. The test coils were wound using 0.56 mm^2 (24AWG) class F insulated copper wire with 80 turns to represent a typical low voltage random wound element. The coils were manufactured on a purpose

made bobbin using a winding rig and wound at low speed to increase wire tension and yield a typical packing factor of $\approx 40\%$. Where appropriate the coils were mounted on motorette rigs in tests; test coils, their manufacture and mounting are shown in Fig. 1.



(a) Motorette rig with an FBG embedded test coil



(b) Winding bobbin



(c) Test random wound coil

Fig. 1: Test coil design, manufacture and the IEEE motorette rig

The target sensing point in this work is the thermal hot spot located in the middle of the coil structure. The bare sensing fibre is fragile and cannot be effectively inserted or wound into the coil architecture due to constraints imposed by the coil construction and the associated mechanical stress. For this reason the sensor package is designed by inserting the FBG sensing head in a capillary made of rigid material [13,14]. This protects the sensing fibre from undesirable mechanical excitation and yields a predominantly thermal excitation sensitive structure. To maximise the embedded sensing package contact with the surrounding 0.56 mm^2 conductors a closely similar capillary outer diameter of 0.8 mm was used for the packaging; the capillary inner diameter is 0.6 mm . This dimension choice yields a very narrow capillary wall of 0.1 mm which is desirable to enhance the sensor time response by reducing the packaging thermal resistance. However this also imposes considerable concern regarding the ability of the capillary to mechanically resist the strain imposed by the coil conductors. The fibre outer diameter is 0.125 mm resulting in a narrow air gap between the capillary and the FBG sensing head it surrounds. The capillary length is chosen to match that of the coil side in this work. The capillary thus encloses the fibre section containing the FBG sensing head, while the rest of the fibre is protected with

Teflon tubing, as shown in Fig.2. Single and array FBG sensors imprinted in double coated polyimide fibre are used in this research as their thermal rating suits the application in conventional low voltage machine coils that are typically class F insulated to withstand temperatures up to 160 °C [18]. The Bragg wavelengths of the used FBG heads were distributed in the range of 1530-1560 nm. The FBG heads length was 5 mm and their average reflectivity and bandwidth 81 % and 0.33 nm, respectively.

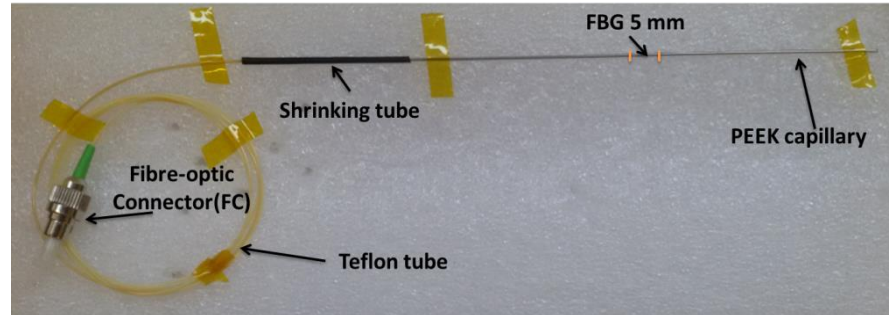


Fig. 2: FBG thermal sensor design for hot spot temperature monitoring

To ensure the sensor is positioned in the coil centre the packaging capillary is first embedded within the coil structure as shown in Fig. 1.a. This is achieved by winding half of coil turns before fitting the capillary and then winding the rest of the coil. Once the coil is completed and mounted on the motorette frame the FBG sensing fibre is loosely inserted into the capillary; the embedded sensor's positioning is illustrated in the coil cross section sketch in Fig 1.a. This process enables in-situ hot spot sensing and offers an advantage of avoiding the undesirable exposure of the fragile sensing fibre to mechanical stress during the wind process. Another key practical advantage is that the installed sensing fibre is made accessible for replacement or re-calibration, which is not the case with conventional temperature sensors [19].

The desired thermal conditions were achieved in experiments by exposing the test coils to thermal excitation in a controlled thermal chamber or energising them with controlled DC current using a programmable DC power supply. The dynamic measurement of FBG sensors was performed using a commercial multi-channel Smart Fibres SmartScan04 interrogator.

III. IN-SITU MEASUREMENT ERROR

The possible error in embedded FBG temperature measurement due to in-situ sensor placement is examined in this section. The sensor installation procedure can pre-strain the sensor and thus potentially significantly alter its calibration characteristic due to FBG thermo-mechanical cross sensitivity. The installed sensor calibration process is impractical

as it would involve the calibration of the entire coil/machine geometry within a controlled thermal process. The in-situ sensor's response is thus usually interpreted based on the sensor calibration characteristic obtained before it is embedded into the monitored structure [7,11]; however this pre-embedment characteristic can considerably differ to that of an in-situ sensor. The quantification of possible in-situ thermal measurement error induced by the installation procedure is key to understanding the attainable thermal monitoring accuracy in typical wound coil installations.

The installation induced mechanical strain in in-situ FBG temperature sensor will result in a shift of the peak Bragg wavelength (λ_B) in the pre-embedment obtained calibrated thermal characteristic. However, it has been shown that the FBG thermal sensor nature, its interrogation and calibration units (FBG sensing system) can also present a source of peak λ_B shift [16]. The discrimination between the λ_B shift caused by the FBG sensing system and that caused by any installation imposed strain is important to quantify the error induced by the latter effect. This is illustrated in Fig. 3, where the central line represents the actual FBG reflected peak λ_B corresponding to a specific measured temperature; area A denotes the possible peak λ_B measurement error margin caused by the inherent FBG sensing system inaccuracy while area B represents the possible additional error due to the installation process induced mechanical excitation of the sensor package. To determine the error boundaries of area B the boundaries of area A must first be identified. The experimental work reported in this section is thus divided into two stages. First, the measurement error of the peak λ_B and hence the temperature measurement error (boundaries of area A) due to the used FBG sensing system is determined. The peak λ_B and hence the temperature measurement error due to in-situ mechanical stress (boundaries of area B) is then quantified.

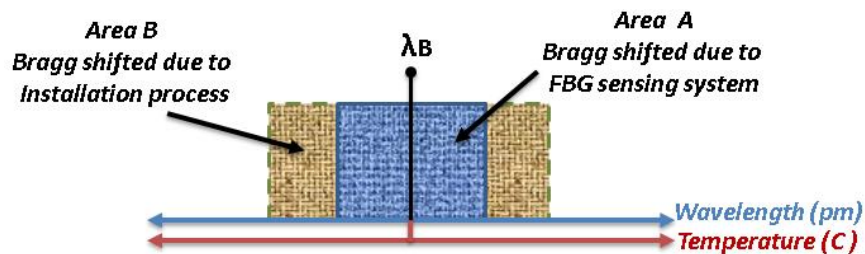


Fig. 3: Possible error margins for coil embedded FBG sensor measurements

For this study a series of experiments were carried out on a sample size of four FBGs to ensure the results are representative of variations encountered in a typical commercial sensing fibre design. In stage one, the FBG heads were inserted in individual ceramic capillaries fixed to a ceramic support plate using Kapton tape to enable FBG calibration in

an unstrained packaged environment. The ceramic capillaries were chosen due to their low thermal expansion, to reduce any packaging thermal expansion (mechanical deformation) effects on the obtained measurements. The ceramic plate with FBG sensors was placed in a controlled thermal chamber, as illustrated in Fig. 4. The FBG heads were exposed to four identical thermal cycles. In each cycle the temperature was increased in steps of 20 °C from 40 to 180 °C and the reflected peak λ_B of the four FBGs recorded at each temperature increment after the thermal equilibrium was reached. The thermal accuracy of the thermal chamber and the Fluke thermometer type K are ± 0.5 °C and ± 0.1 °C, respectively. Theoretically, these uncertainties could cause FBG Bragg wavelength shift deviation of $\approx \pm 5$ pm by the thermal chamber and 1pm by the Fluke thermometer.

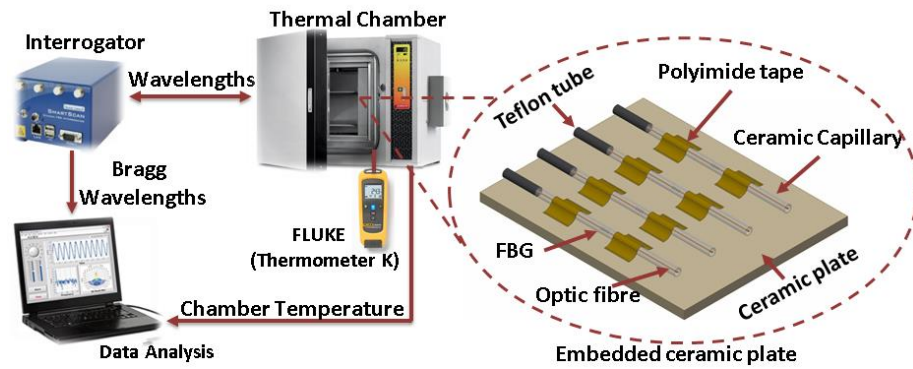


Fig. 4: FBG sensor pre-embedment calibration process

From the obtained measurements the average peak λ_B were calculated at each steady-state temperature increment for the four examined FBG heads. For illustration purposes Fig. 5 shows the measured and averaged data for a single FBG head; other tested FBGs manifested closely similar deviation levels. The data show good linearity with an average measured correction factor coefficient of 0.9991. The inset detailed view shows individual measurements taken at 120 °C to illustrate the typical deviation in the measured peak λ_B for the applied thermal cycles. The obtained data were analysed to determine the wavelength standard deviation (WSD) and the resulting temperature standard deviation (TSD) of the examined FBG sensing heads due to the FBG sensing system. These values define the error boundaries of area A in Fig. 3. The TSD was obtained by multiplying the WSD with the measured temperature sensitivity of each tested FBG. The temperature sensitivity is acquired from the tests as the slope of the linear fit curve of the mean measured values. The maximum measured WSD was calculated to be 5.42 pm; this gives a maximum TSD, i.e. the maximum FBG sensing system induced error of ≈ 0.5 °C. Pre-embedment calibration fit curves (PEFC) were also calculated for the examined FBG heads based on the averaged measured λ_B .

In the second stage of testing the FBG heads were inserted into four capillaries embedded in slot section centres of two IEEE motorette test coils (one FBG per coil side). The sensor installation procedure followed the principles described in section II. Four different capillary materials were used to provide different sensor package mechanical stiffness properties: copper, polyetheretherketone (PEEK), stainless-steel and aluminum. The embedded packaged sensors were calibrated in-situ by exposing entire motorette coils to the identical thermal cycle to that used to calibrate FBGs pre-embedment (i.e. 40-180 °C range in steps of 20 °C). For in-situ calibration purposes the reflected peak λ_B were recorded for the four motorette embedded FBG sensors at each temperature increment and from these the average in-situ calibration fit curves of embedded FBG sensors (EFC).

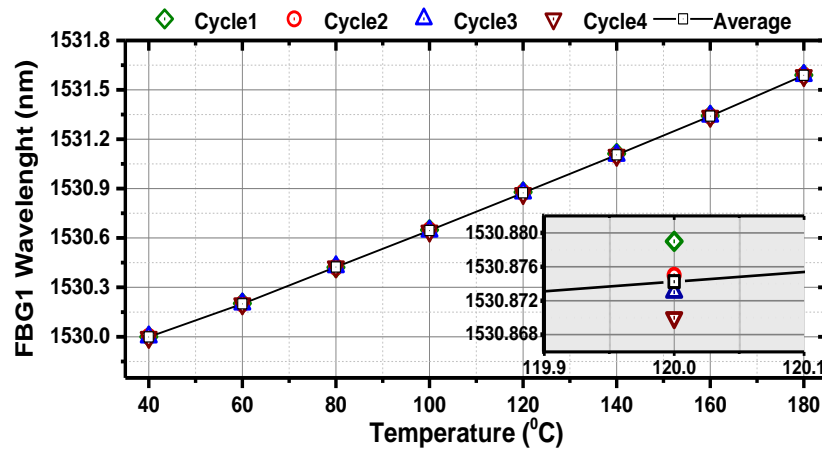


Fig. 5: Measured Bragg wavelength for a single FBG head

To evaluate the measurement error induced in the sensor thermal response due to the installation process, the measured average reflected peak λ_B at each temperature increment for the embedded FBGs were converted to thermal readings using the obtained PEFC and EFC. The resulting temperatures were compared to a reference temperature provided by the commercial thermal chamber's proprietary thermal measurement system and the absolute error calculated and plotted in Fig. 6. The results clearly show that the application of PEFC for interpretation of in-situ thermal measurement results in a general measurement error increase. This illustrates the effect of unavoidable pre-stressing of the sensor during installation on its hot spot thermal monitoring performance. The error magnitude is seen to vary between FBG packages made of different materials due to different mechanical properties and consequently different amount of stress imposed on the sensor as a result of the installation procedure; the maximum measured error was ≈ 1.4 °C and is associated with PEEK packaging which has the lowest hardness coefficient of the four examined materials and is thus inherently more flexible than the other tested capillaries. The error obtained in stage two tests (≈ 1.4 °C) represents the joint error

boundaries of areas A and B in Fig. 3, which clearly increase the error margins of area A ($\approx 0.5^\circ\text{C}$) determined in stage one tests by $\approx 0.9^\circ\text{C}$. The maximum error measured when using EFC for interpretation of in-situ temperature readings is $\approx 0.55^\circ\text{C}$. This is mainly caused by the FBG sensing system and confirms the error rates obtained in stage one tests.

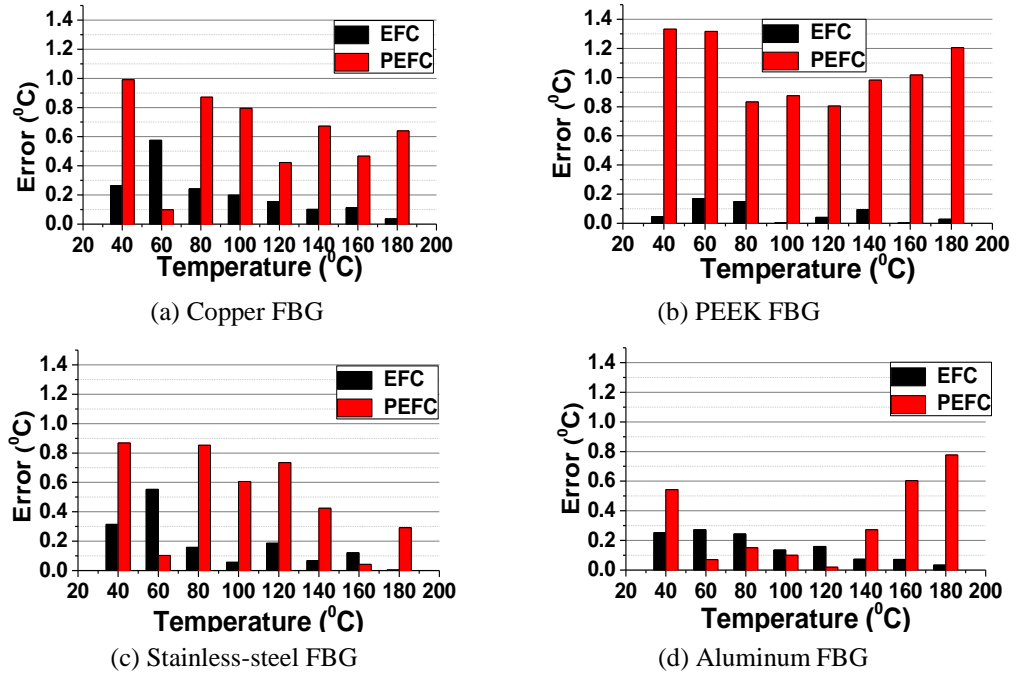


Fig. 6: In-situ measurement error using EFC and PEFC calibration curves for motorette coils

The error rates reported in Fig. 6 were obtained for sensors embedded into motorette coils. However, in practical electric machine applications of random wound coils there may be additional mechanical stress on the sensor package due to the insertion process of the coil's conductors within the iron core/slot geometry. To examine these effects a test coil was wound into a stripped stator core of commercial low voltage squirrel cage induction motor as shown in Fig. 7. The coil dimensions and turns number (117 turns) were chosen to be identical to the commercial motor winding design. Two capillaries were embedded into slot centres during the wind process, one made from PEEK and the other from aluminium, relating to the largest and smallest error observed in Fig. 6 tests.

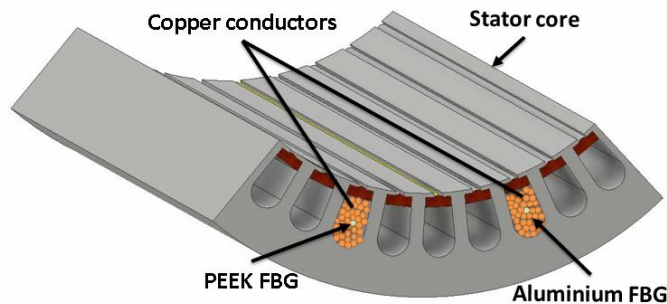


Fig. 7: Embedded stator slots cross-sections with FBG temperature sensor

To obtain the in-situ calibration characteristic of wound coil embedded sensors the entire stator core was placed in the thermal chamber where it was exposed to the identical calibration procedure to that performed on pre-embedment and motorette embedded FBGs. The core embedded sensor in-situ calibration fit curve (CEFC) was obtained from the wavelengths recorded in the calibration thermal cycle. Once the CEFC fit curve was acquired the measured average peak λ_B at each temperature increment for the coil embedded FBGs were converted to temperature readings using the obtained PEFC and CEFC and compared to the chamber thermal reading at each increment. Fig. 8 presents the measured error at each temperature increment. The error is seen to be more strongly pronounced between the two fit curves for the PEEK packaged FBG sensor; this is due to the in-situ PEEK packaged FBG being more likely to pre-stress during installation compared to the more rigid aluminum packaged FBG. The results in Figs. 6 and 8 are generally consistent and show that, while some error is induced by applying the pre-embedment calibration curve for in situ measurement, this is relatively small in magnitude even when using non-metallic packaging materials such as PEEK that has inferior mechanical proprieties when compared to metallic capillaries but is preferable for this application.

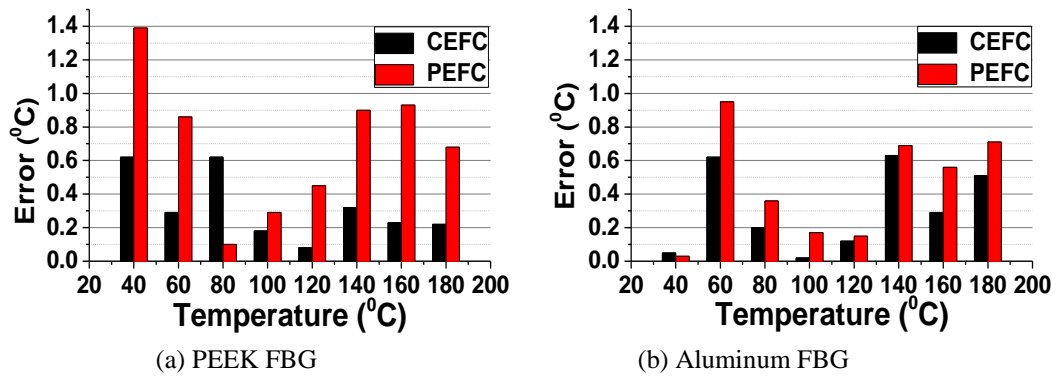


Fig. 8: In-situ measurement error using CEFC and PEFC calibration curves for stator core embedded coils

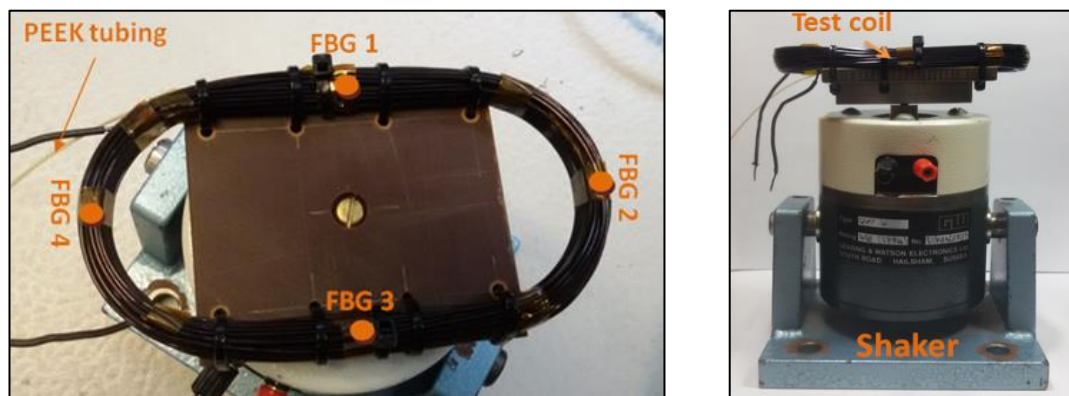
IV. INFLUENCE OF VIBRATION ON HOT-SPOT EMBEDDED SENSOR PERFORMANCE

This section examines the influence of vibration levels typical for random wound coils in electrical machinery on in-situ FBG thermal measurement. A concern when utilising FBG thermal sensing is its inherent sensitivity to any existing mechanical stress and vibration which may excite the sensor and give rise to undesirable error [16, 20]. The coil embedded thermal sensor is designed by placing the sensing fibre within a packaging capillary; while this provides a significant level of immunity to wound coil structure imposed mechanical stress it also results in a relatively loosely positioned fibre within the packaging air gap. In this space the fibre can displace when exposed to vibration, causing micro bending in the

FBG sensor head and thus imposing an undesirable error in thermal measurements. The significance of these effects is quantified in representative experiments in this section.

A sensor array containing four FBG heads was used in this study. The array was packaged in a PEEK capillary and placed in the centre of a test coil. This enabled the examination of multiple hot spot thermal sensing points located in different sections of the coil. PEEK was chosen as packaging material for this test since its flexibility combined with its non-metallic properties make it an attractive option for embedded distributed thermal sensing in wound coils as the sensor package can conform to the coil shape. The inherent PEEK flexibility could however pose challenges in a high vibration environment and requires careful assessment.

Fig. 9a shows the array embedded test coil, with two sensing points designed to be located in the coil slot sections (FBG1 and FBG3) and the remaining two in the end-winding sections (FBG2 and FBG4). To examine the influence of vibration on in-situ thermal monitoring performance the tested coil was mounted on a commercial shaker as shown in Fig. 9.b. A purpose designed dielectric board (TUFNOL) was built to enable the test coil to be mounted on the shaker. TUFNOL was chosen for its high mechanical strength and low thermal heat capacity. The board was dimensioned to allow the sides of the test coil to be fixed while leaving the coil ends free. This emulates coil positioning within electrical machines, where end-windings are typically exposed and thus subjected to greater mechanical stress than the coil slot sections contained within the rigid iron core [17]. The shaker mounted instrumented test coil was used to perform a range of experiments using the set up shown in Fig. 10. The shaker was excited by a function generator and an amplifier to expose the coil to a desired vibration magnitude and frequency. A DC power supply was used to thermally excite the test coil and achieve a desired operating temperature.



(a) FBG array embedded test coil

(b) Shaker mounted test coil

Fig. 9: Random wound test coil embedded with an FBG array

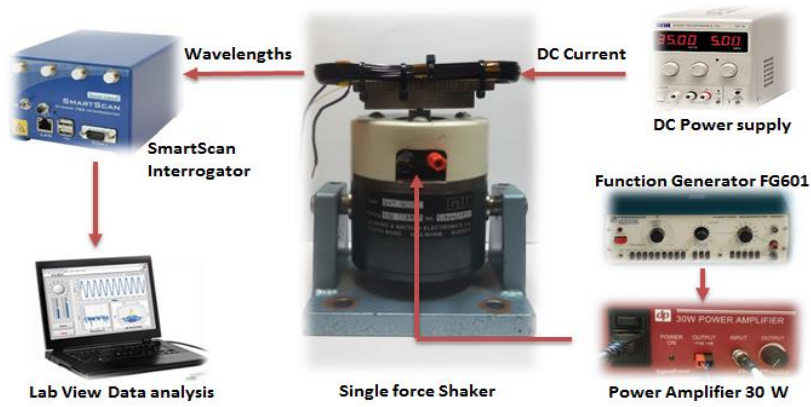


Fig. 10: Experimental system setup for vibration sensitivity test

The test coil was subjected to different vibration conditions in experiments adjusting both the frequency and displacement of the vibration signal. The IEEE 117 standard [17] specifies vibration characteristics to apply mechanical stress representative of operational conditions on a test coil as supply frequency vibration with a peak-to-peak (pk-pk) displacement of ≈ 0.2 mm at ambient temperature. To broaden the relevance of this study and assess a wide range of operating conditions encountered within electrical machines the test vibration conditions were extended to three different frequencies of oscillating motion and three different displacement levels. The following vibration frequencies were examined: the supply frequency (50 Hz) according to [17]; double supply frequency (100 Hz) which is a known frequency component under electrical unbalance/fault conditions in electric machinery [8]; 25 Hz to illustrate a typical low supply frequency operating scenario in an inverter driven machine. The considered pk-pk displacement levels are: 0.2 mm, 0.6 mm and 1.5 mm. The displacement values higher than those prescribed by the IEEE standard were chosen to emulate high vibration conditions that can occur under mechanical and/or electrical fault.

The test coil in-situ thermal measurements obtained in ambient temperature (≈ 23 °C degrees, no current in the test coil) experiments at 100, 50 and 25 Hz vibration frequencies are shown in Fig. 11, respectively. In each constant frequency vibration test thermal measurements were taken for the first 100 sec with no shaker excitation, i.e. no applied vibration. In the subsequent three 100 sec periods the shaker is excited and used to apply three different increasing pk-pk displacement values: 0.2 mm (Level-1 region in Fig. 11), 0.6 mm (Level-2 region in Fig. 11) and 1.5 mm (Level-3 region in Fig. 11). The experimental data indicate that no significant influence of applied vibration can be observed in the obtained in-situ FBG thermal measurements. While minute vibration induced measurement deviations exist, in general the four FBG sensing points provide steady temperature measurement under the considered vibration levels.

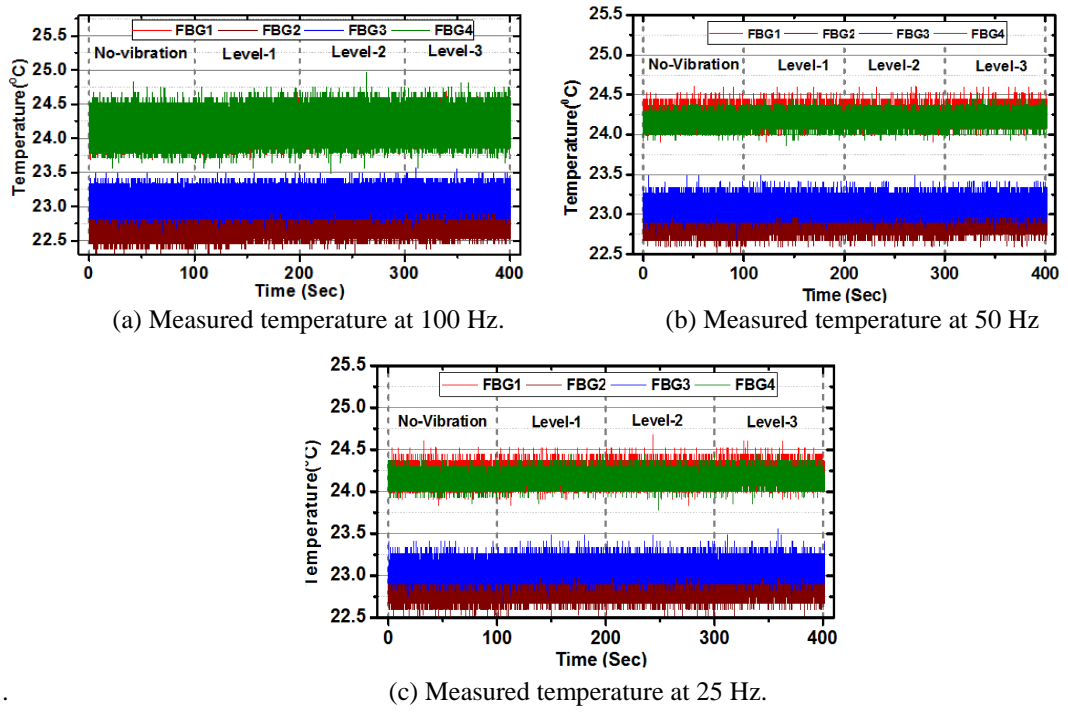


Fig. 11: Test coil embedded FBG array sensor in-situ thermal hot spot measurements under mechanical excitation

To consider operating scenarios pertinent to electric machine embedded coil operation additional tests were performed at a higher temperature representative of thermal conditions encountered in current carrying low voltage winding practical applications. For this purpose the test coil was excited with a DC current of 3.5 A to yield a steady-state coil hot spot temperature of ≈ 100 °C. The temperature was first measured for 100 seconds with no vibration imposed on the test coil in the tests; the shaker was then excited at 50 Hz and the pk-pk displacement increased in successive 100 sec periods from 0.2 mm to 0.6 mm and finally 1.5 mm (Level-1, Level-2 and Level-3 in Fig. 12, respectively). The recorded thermal traces in Fig. 12 report closely similar thermal trends. In contrast to the obtained thermal data of identical vibration conditions at ambient temperature (Fig. 11b) there is a clear decrease in the measured temperature with the increase in the vibration magnitude. This phenomenon can be explained by the vibration induced changes in the coil heat transfer mechanism. During the first 100 sec where no vibration was applied the generated heat within the static coil is dissipated to the surrounding air largely by natural convection. However, once the coil is exposed to vibration the dominant heat transfer mechanism becomes that of forced convection due to the movement of the coil. As would be expected, the increase in the displacement magnitude is seen to enhance the coil heat transfer and result in a faster decrease in measured temperature, as demonstrated by the in-situ readings in Fig. 12; with the increase in vibration magnitude the gradient of the obtained thermal measurement clearly increases.

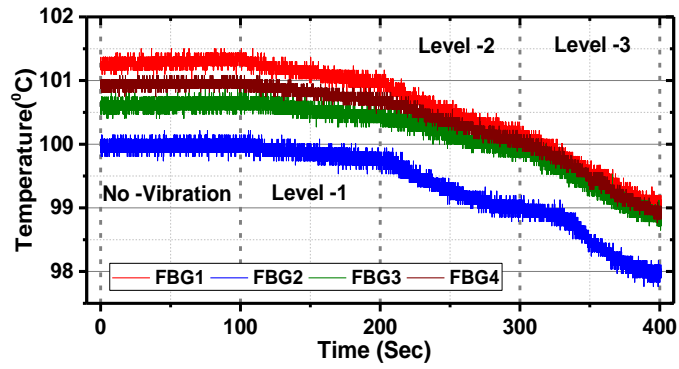


Fig. 12: Hot spot temperature at 50 Hz for a thermally excited coil

To further validate these observations and eliminate the possibility of FBG sensor measurement induced error a type K thermocouple (TC) was attached to the surface of the test coil. The TC output was synchronously recorded with that of FBG sensors to allow direct correlation of the trends observed in in-situ FBG measurements with a conventional TC system. A test was then performed where at first no vibration was imposed on the current carrying test coil; after 60 sec the coil was exposed to constant vibration at 50 Hz with a 1.5 mm pk-pk displacement. The test was designed to confirm that the temperature decrease trends observed in Fig. 12 will eventually cease as they are not caused by an FBG measurement error due to coil vibration. In terms of heat transfer, the temperature drop in the test coil due to forced convection should eventually reach a steady-state, hence the test was run for an extended period of time and both FBG and TC measurements synchronously taken for cross validation purposes, as shown in Fig. 13. The data show that the thermal transient due to forced convection expires after ≈ 15 mins. This confirms that the temperature change trends are due to coil movement caused forced convection and that there is no perceivable error in the in-situ FBG thermal measurement in the current carrying test coil under vibration. The FBG array reported thermal trends are confirmed by those obtained synchronously by the coil surface mounted TC sensor. The TC readings were ≈ 2.5 °C lower than those obtained by the FBG array, clearly demonstrating the advantage of measuring temperature in the coil center rather than on its surface.

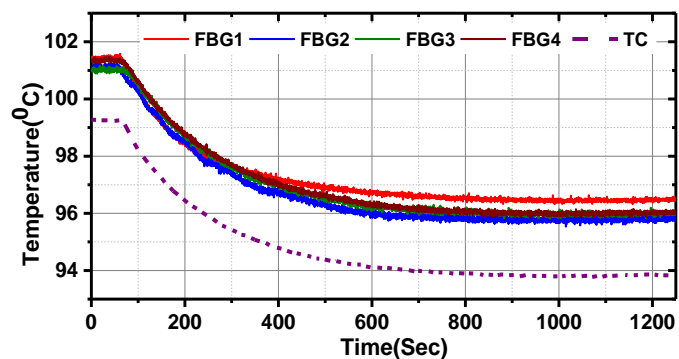


Fig. 13: Measured temperature at 50 Hz with a 1.5 mm pk-pk displacement

V. ASSESSMENT OF PACKAGING MATERIAL INFLUENCE ON DYNAMIC THERMAL RESPONSE

The attainment of coil hot-spot steady-state temperature measurement with a satisfactory level of accuracy is not sufficient for thermal monitoring applications in operational devices. In practice, electric machine coils are frequently subjected to transient thermal stress under healthy and faulty operating conditions. The response rate is therefore a critical feature in real-time monitoring of coil temperature, since a critical insulation breakdown characteristic of fault occurrence and the accompanying significant thermal stress can be fast occurring processes [21-23]. Any thermal sensing delay in response to monitored temperature change in these conditions can compromise the recognition of the breakdown process and therefore needs to be understood. The FBG sensor head size is in micrometers and thus provides low heat capacity and a fast thermal response [24]. However, the physical dimensions and characteristics of the FBG sensor packaging strongly influence its heat-transfer performance. While in the examined thermal sensor packaging methodology the packaging capillary narrow wall inherently presents a relatively low thermal resistance, the thermal resistivity of the capillary material will have a considerable impact on the attainable thermal response time of the packaged sensor. It is therefore key to examine the impact of the narrow wall packaging thermal properties on in-situ FBG sensor response. To this end, the operational implications of the use of a range of packaging materials with different thermal and electrical properties, and the attainable in-situ monitoring performance under various thermal transients is quantified in thermal model studies and practical tests in this section.

The tested capillaries are made of different materials and designed with identical dimensions to enable direct performance comparison: the capillary outer diameter is 0.8 mm and its wall thickness 0.1 mm. The selection of studied materials was made based on thermal, electrical and mechanical (i.e. the suitability for use in the coil insertion process) properties, and ultimately market availability in target size. It is generally desirable for embedded sensor packaging to be electrically non-conductive due to the risks imposed by use of conductive elements within a current carrying coil. However, electrically conductive metals normally possess good thermal conductivity and are mechanically rigid, and hence carry significant potential for providing high thermal conductivity packaging solutions and are thus included in this study. Performance of FBG sensors with packaging capillaries made of the following six materials, grouped according to electrical conductivity capability, was assessed:

- Electrically conductive packaging: Copper, Brass, Aluminium and Stainless steel.
- Electrically non-conductive packaging: PEEK and Teflon.

The individual capillary thermal properties including thermal conductivity, thermal specific heat, density and thermal diffusivity are given in Table I. The thermal diffusivity values in particular provide a measure of the heat transfer rate within the packaging material.

TABLE I
TESTED CAPILLARIES THERMAL PROPERTIES

Material	Thermal conductivity W/(m.K)	Thermal specific heat J/(Kg.k)	Density Kg/m ³	Thermal Diffusivity m ² /s
PEEK	0.173	1300	1300	1.02367E-07
Teflon	0.23	1400	1800	9.12698E-08
Copper	400	397	8913	0.000113043
Aluminium	205	990	2712	7.63535E-05
Brass	120	402	8470	3.52429E-05
Stainless steel	17	500	7800	4.35897E-06

To enable further understanding of the packaging material thermal properties influence on sensor performance a 2D finite element thermal model of the packaged FBG temperature sensors were developed using the ABAQUS software platform. Individual finite element analysis (FEA) transient thermal models were developed of the packaged sensor geometry for each investigated packaging material. Fig. 14 shows the packaged sensor FEA model with the FBG sensing head assumed to be centred within the packaging capillary. The FBG sensing fibres used in this work have the outer diameter of 0.125 mm. The resulting radial air gap length between the capillary's inner surface and the fibre's outer surface is thus 0.237 mm. In principle, the heat flow within the packaged FBG sensor occurs by conduction through the packaging capillary wall and convection through the capillary air-gap containing the sensing fibre. However, the capillary air-gap is very small and provides an extremely limited space for air movement; in addition, the air within

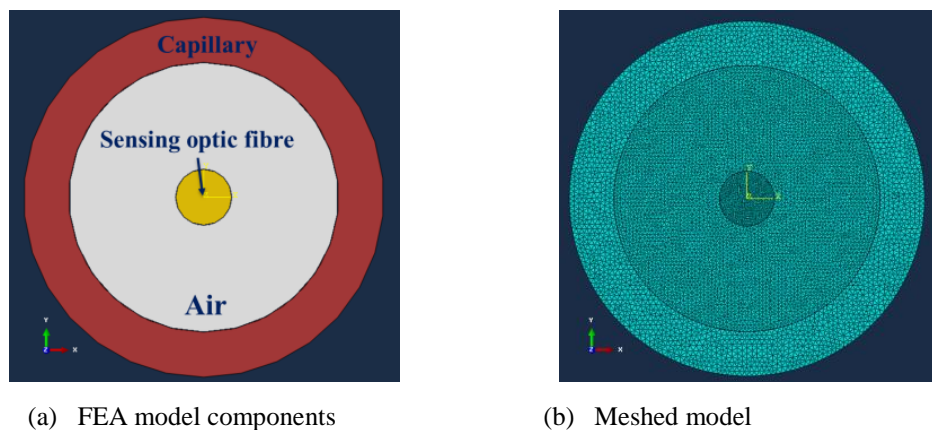


Fig. 14: Thermal FEA model of the FBG sensor package

the sensor package is almost static in this application and thus minimises the circulating convection heat [25]. Consequently and for the purpose of simplicity the heat transfer process in the air-gap is modelled as occurring through conduction.

The FEA model was used to simulate sensor transient response to a typical instantaneous step temperature rise at the packaging surface of 80 °C. This was achieved by defining the initial model components temperature to be 20 °C and setting the packaging capillary outer surface as a boundary condition at 100 °C. An identical thermal transient was modelled for each investigated FBG design. The dynamic temperature results obtained at the output surface of the sensing optical fibre are shown in Fig.15. The data show a clear delay in response of FBG sensors with PEEK and Teflon capillaries when compared to those with metallic packaging; for clarity, a detailed view of the fast response obtained by sensors with metallic packaging is inset in Fig 15. The copper, aluminium and brass packaged sensors show a closely similar response reaching the steady-state within ≈ 6 ms and are closely followed by the stainless steel packaged sensor reaching the measured 100 °C in ≈ 12 ms. PEEK and Teflon packaged sensors however require ≈ 180 ms to reach steady-state. The obtained model results confirm the general thermal behaviour trends suggested by the diffusivity values presented in Table I.

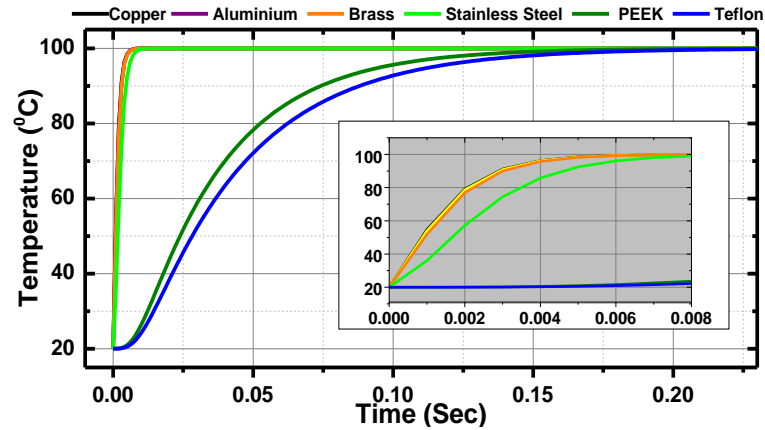


Fig. 15: Simulated transient thermal response of different package FBGs

In order to ascertain the performance and limitations of the examined FBG sensor designs a series of controlled thermal transient tests were performed. Six FBG sensors with different packaging materials were built for this purpose by first embedding different material capillaries in hot spot positions within three motorette test coils and then inserting the calibrated FBG sensing heads. The sensor installation procedure described in section II was adhered to with significant attention paid to building approximately identical test coils. This was to ensure closely similar thermal conditions between individual coils carrying

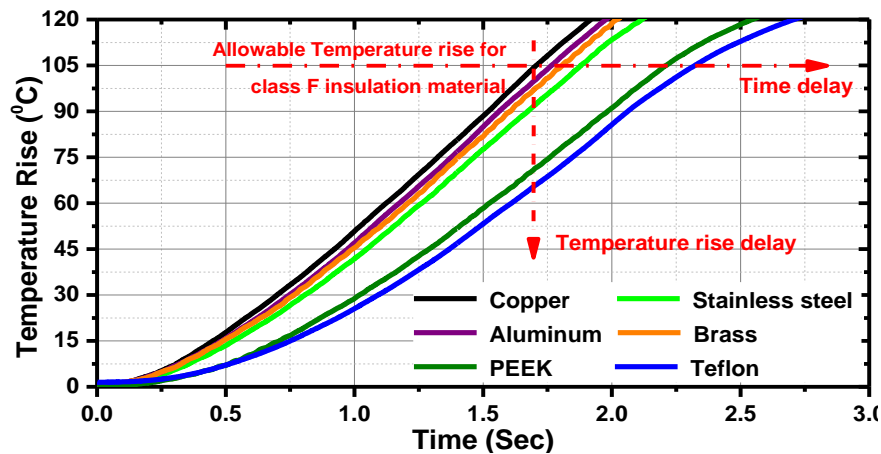
different FBG sensors and thus enable direct correlation of the obtained results. The test coils were exposed to a range of controlled thermal transients using a DC power supply to inject the required current into the coil conductors. The thermal response obtained from the six tested in-situ sensors was synchronously measured in the tests.

A number of different thermal transients were achieved by controlling the magnitude and duration of the applied DC current. The applied transient magnitude was chosen based on the permissible temperature rise/thermal ratings for class F insulation. NEMA standards specify the maximum allowable temperature rise above the ambient temperature of 40 °C for electrical machines class F insulation material to be 105 °C [18]. Based on this the transient thermal tests were designed to ensure a thermal rise of at least 105 °C. Sensor behaviour was examined in four different temperature average rise rates achieved by appropriate control of the coil excitation current, namely: ≈ 55.4 °C /s, ≈ 28.5 °C /s, ≈ 13.5 °C /s and ≈ 3.7 °C /s.

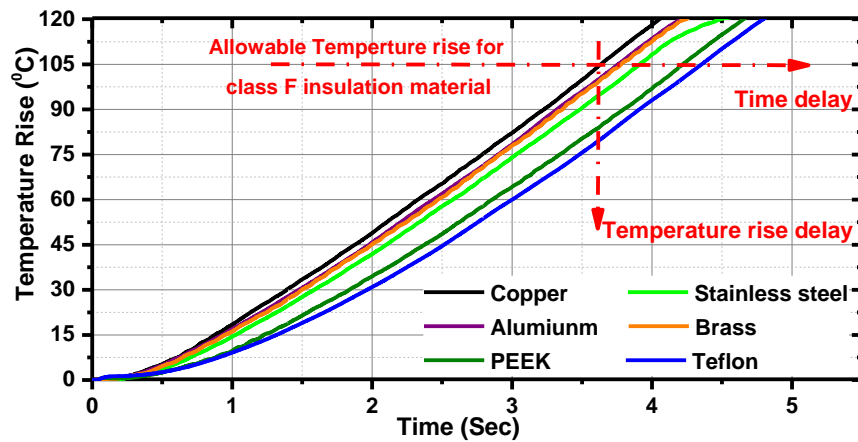
Figs. 16a-c show the temperature rise measured synchronously by the six packaged FBG sensors during the four examined thermal transient tests, respectively. In general, as would be expected based on the data in Table I, the thermal response of the metallic packaged FBGs is seen to be faster than that recorded with non-metallic packaged sensors. The measured transient profiles exhibit general trends that are closely similar to those obtained by the FEA thermal model study. The permissible temperature rise limit for class F insulation is indicated in the graphs by a horizontal dot-dash arrow which also indicates the sensing time delay of individual sensors; a vertical dot-dash arrow is used to indicate the sensed temperature rise delay between different packages.

The results for the fastest considered temperature change rate in Fig 16.a show a significant delay in response between different sensors. The copper packaged sensor reaches the permissible temperature rise for class F insulation ≈ 500 ms earlier than PEEK and Teflon packaged sensors. At the time instant in which the copper packaged FBG reports a hot spot thermal rise rate of 105 °C the PEEK and Teflon packaged FBGs report thermal rise readings of ≈ 71.8 and ≈ 66.4 °C respectively. The brass and aluminium packaged FBG readings on the other hand are only a few ms delayed in comparison to the fast copper packaged sensor measurement. At the thermal rise rate limit point of 105 °C these differ by less than 10 °C from the copper packaged FBG measurement, with the aluminium packaged sensor measuring ≈ 100.9 °C and the brass packaged sensor ≈ 98.9 °C. The stainless steel packed FBG manifests a slower response than other metallic packaged sensors but is still significantly faster than non-conductive packaged FBGs.

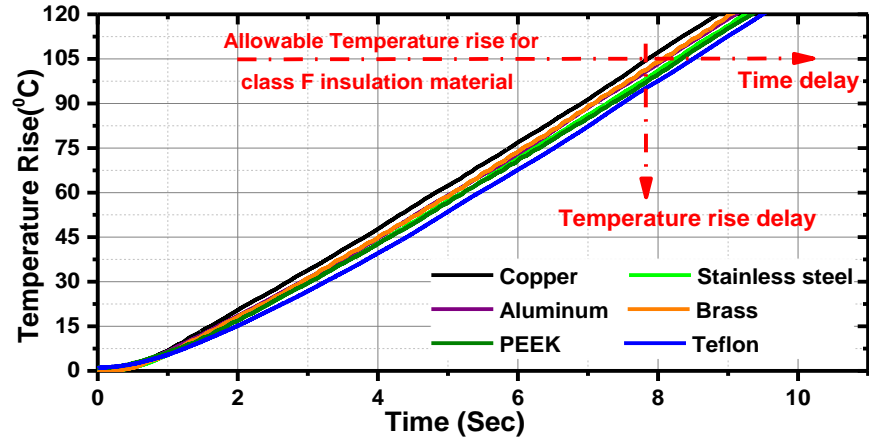
As the temperature rise rate is reduced the temperature measurements reported by different packaging FBGs start showing a more uniform behaviour. The results in Fig. 16b obtained for a reduced thermal rise rate of ≈ 28.5 °C /s show that the brass and aluminium packaged FBGs perform at response times close to those obtained by copper. However, the non-conductive material packaged FBGs still manifest a significantly slower response time in comparison to their metallic material packaged counterparts. As an illustration, the thermal reading error at permissible rise rate between copper and PEEK packaged FBGs reduces to ≈ 22 °C and due to the slower rise rate of the examined thermal transient the delay time rises to ≈ 600 ms. Similar trends continue with further reduction in the thermal rise rate as illustrated by data in Figs. 16c-d, where at temperature rise rate of 13.5 °C /s this difference is reduced to ≈ 8 °C while the delay time is ≈ 1480 ms. For the measurements at the slowest examined rise rate of 3.6 °C /s in Fig. 16d the temperature rise reported by the six packaged FBGs is overlapping with negligible difference between individual thermal readings.



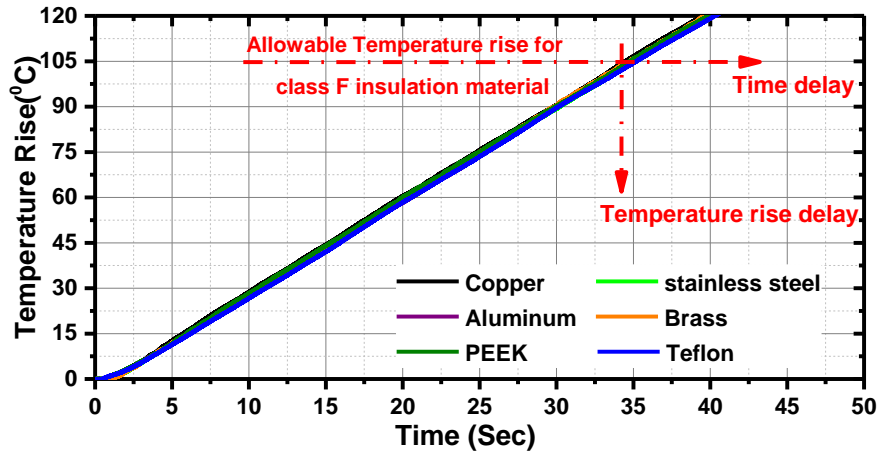
(a) Thermal measurements at average rise rate of ≈ 55.4 °C /s



(b) Thermal measurements at average rise rate of ≈ 28.5 °C /s



(c) Thermal measurements at average rise rate of ≈ 13.5 °C /s



(d) Thermal measurements at average rise rate of ≈ 3.7 °C /s

Fig. 16: In-situ temperature rise measurements for thermal transient tests

VI. CONCLUSIONS

This paper investigated the design and operational features of FBG sensor use for thermal hot spot monitoring in random wound coils such as used in low voltage electric machinery. Prototype coils were used as test vehicles for examining and understanding the coil embedded FBG sensing key application aspects that directly influence measurement error.

The obtained results quantify the effect of unavoidable pre-stressing of the sensing package during its installation into the coil structure on the sensor pre-calibrated thermal characteristic. The reported data show that the use of sensor thermal calibration characteristic obtained prior to coil embedment to interpret in-situ hot spot measurements yields a measurement error that has been experimentally quantified and shown to be smaller than ≈ 1 °C. This error rate is deemed acceptable for electrical machine coil thermal monitoring in most practical applications [17, 19]. Crucially, the presented results show that in-situ calibration of coil embedded FBG sensors is not a requirement for their effective utilisation. This is an important implication for embedded FBG sensing use in

windings contained in electric machine geometries that are typically large and would pose prohibitive limitations to in-situ calibration.

The reported experimental findings demonstrate that in-situ FBG thermal sensing performance remains largely unaffected by the vibration levels representative of those acting on random wound coils in low voltage electrical machinery. This further confirms the practical application potential of the examined FBG enabled hot spot thermal monitoring approach.

The influence of packaged sensor design on its in-situ response time was studied in a range of representative transient tests to establish the practically attainable on-line monitoring performance. It was found that, despite the sensor package thickness being very small, the thermal properties of the packaging material largely determine the sensor thermal response. The performance of a number of packaging materials was examined, showing that electrically conductive packaging generally provides faster thermal response compared to non-conductive packaging. The application of non-conductive packaging is however preferable within the current carrying coil structure, as conductive packaging use could pose challenges related to electric fault immunity. It was shown that for the thermal rise rates encountered in electric machinery that are generally relatively low [22, 26] the non-conductive packaging can provide an effective thermal monitoring solution.

The reported findings significantly increase the understanding of design and operational features of FBG sensing for in-situ hot spot thermal monitoring in low voltage random wound coils, required to underpin a wider acceptance and application of this sensing technique in operating machinery.

REFERENCE

- [1] A. Mesrobian and J. H. Holdrege, "Random wound versus form wound on low voltage synchronous generators," *37th Annual Conference on Petroleum and Chemical Industry*, Houston, TX, USA, 1990, pp. 185-190.
- [2] G. C. Stone, E. A. Boulter, I. Culbert and H. Dhirani, "Electrical insulation for rotating machines- design, evaluation, aging, testing, and repair," in *IEEE El. Ins. Mag.*, vol. 20, no. 3, pp. 65, June 2004.
- [3] H. Zhang, "Online Thermal Monitoring Models for Induction Machines," in *IEEE Transactions on Energy Conversion*, vol. 30, no. 4, pp. 1279-1287, Dec. 2015.
- [4] M. Kirouac, M. Bergeron, J. Cros, P. Viarouge, "Thermal Slot Model for Random Wound Electrical Machines Using Statistical Approach," in *International Journal of Advanced Research in Electrical, Electronics and Instrumentation Engineering*, Vol. 5/3, March 2016.
- [5] N. M. Theune *et al.*, "Investigation of stator coil and lead temperatures on high voltage inside large power generators via use of fiber Bragg gratings," *SENSORS, 2002 IEEE*, Orlando, FL, USA, 2002, pp. 1603-1607 vol.2.
- [6] N. Haramoni, A. S. Paterno, A. Goedtel, G. R. Soares, J. C. C. Silva and H. J. Kalinowski, "Hybrid Wavelength-Time-Domain Interrogation System for Multiplexed Fiber Bragg Sensors Using a Strain-Tuned Erbium-Doped Fiber Laser," in *IEEE Sensors Journal*, vol. 8, no. 7, pp. 1061-1066, July 2008.

- [7] K. d. M. Sousa, A. A. Hafner, H. J. Kalinowski and J. C. C. da Silva, "Determination of Temperature Dynamics and Mechanical and Stator Losses Relationships in a Three-Phase Induction Motor Using Fiber Bragg Grating Sensors," in *IEEE Sensors Journal*, vol. 12, no. 10, pp. 3054-61, Oct. 2012.
- [8] D. S. Vilchis-Rodriguez, S. Djurović, P. Kung, M. I. Comanici and A. C. Smith, "Investigation of induction generator wide band vibration monitoring using fibre Bragg grating accelerometers," *2014 International Conference on Electrical Machines (ICEM)*, Berlin, 2014, pp. 1772-1778.
- [9] J. M. Corres, J. Bravo, F. J. Arregui and I. R. Matias, "Unbalance and harmonics detection in induction motors using an optical fiber sensor," in *IEEE Sensors Journal*, vol. 6, no. 3, pp. 605-612, June 2006.
- [10] K. M. Sousa, U. J. Dreyer, C. Martelli and J. C. Cardozo da Silva, "Dynamic Eccentricity Induced in Induction Motor Detected by Optical Fiber Bragg Grating Strain Sensors," in *IEEE Sensors Journal*, vol. 16, no. 12, pp. 4786-4792, June 15, 2016.
- [11] M. M. Werneck, R. C. Da Silva Barros Allil and B. A. Ribeiro, "Calibration and operation of a fibre Bragg grating temperature sensing system in a grid-connected hydrogenerator," in *IET Science, Measurement & Technology*, vol. 7, no. 1, pp. 59-68, January 2013.
- [12] R. Pomorski Linessio, K. d. M. Sousa, T. da Silva, C. A. Bavastrri, P. F. d. C. Antunes and J. C. Cardozo da Silva, "Induction Motors Vibration Monitoring Using a Biaxial Optical Fiber Accelerometer," in *IEEE Sensors Journal*, vol. 16, no. 22, pp. 8075-8082, Nov. 15, 2016.
- [13] A. Mohammad, S. Djurović, "Evaluation of fiber-optic sensing performance for embedded thermal monitoring of electric machinery wound components," *2016 5th Mediterranean Conference on Embedded Computing (MECO)*, Bar, 2016, pp. 72-76.
- [14] A. Mohammed, S. Djurović, A. C. Smith and K. Tshiloz, "FBG sensing for hot spot thermal monitoring in electric machinery random wound components," *2016 XXII International Conference on Electrical Machines (ICEM)*, Lausanne, Switzerland, 2016, pp. 2266-2272.
- [15] Y. Zhang et al., "Comparison of Metal-Packaged and Adhesive-Packaged Fiber Bragg Grating Sensors," in *IEEE Sensors Journal*, vol. 16, no. 15, pp. 5958-5963, Aug. 1, 2016.
- [16] Possetti, G. R. C., et al "Metrological evaluation of optical fiber grating-based sensors: an approach towards the standardization." In *IEEE Journal of Lightwave Technology* 30.8 (2012): 1042-1052.
- [17] "IEEE Standard Test Procedure for Thermal Evaluation of Systems of Insulating Materials for Random-Wound AC Electric Machinery," in *IEEE Std 117-2015 (Revision of IEEE Std 117-1974)*, pp.1-34, 2016.
- [18] IEEE Guide for AC Motor Protection," in *IEEE Std C37.96-2012 (Revision of IEEE Std C37.96-2000)*, vol., no., pp.1-160, Feb. 20 2013.
- [19] "IEEE Recommended Practice for General Principles of Temperature Measurement as Applied to Electrical Apparatus," in *IEEE Std 119-1974*.
- [20] Li, Y., Wen, C., Sun, Y., Feng, Y. and Zhang, H., 2014. Capillary encapsulating of fiber Bragg grating and the associated sensing model. *Optics Communications*, 333, pp.92-98.
- [21] R. M. Tallam, T. G. Habetler and R. G. Harley, "Experimental testing of a neural-network-based turn-fault detection scheme for induction machines under accelerated insulation failure conditions," *Diagnostics for Electric Machines, Power Electronics and Drives conference*, 2003. pp. 58-62.
- [22] Staton, Dave, and Livio Susnjic. "Induction motors thermal analysis." *Strojarstvo* 51, no. 6 (2009): 623-631.
- [23] M. Sumislawska, K. N. Gyftakis, D. F. Kavanagh, M. McCulloch, K. J. Burnham and D. A. Howey, "The impact of thermal degradation on electrical machine winding insulation," *2015 IEEE 10th International Symposium on Diagnostics for Electrical Machines, Power Electronics and Drives (SDEMPED)*, Guarda, 2015, pp. 232-238.
- [24] W. Chen et al., "Performance assessment of FBG temperature sensors for laser ablation of tumors," *2015 IEEE International Symposium on Medical Measurements and Applications (MeMeA) Proceedings*, Turin, 2015, pp. 324-328. Pfundstein, M. et al, "Insulating materials: principles, materials, applications", DETAIL Practice, Architektur-Dokumentation GmbH & Co., Munich, 2008.
- [25] M. G. Melero, M. F. Cabanas, C. Rojas, G. A. Orcajo, J. M. Cano and J. Solares, "Study of an induction motor working under stator winding inter-turn short circuit condition," *4th IEEE International Symposium on Diagnostics for Electric Machines, Power Electronics and Drives, 2003. SDEMPED 2003.*, Atlanta, GA, USA, 2003, pp. 52-57.

Chapter 5: *On-line Low Voltage Stator Winding Internal Temperature Monitoring Using In-situ FBG Thermal Sensing System*

5.1 Introduction

This chapter examines the use of the in-situ FBG thermal sensing system proposed and examined using the prototype random wound coil systems in **Chapter 4** for on-line stator winding internal thermal monitoring in LVEMs. The chapter reports the embedment, operation, sensing performance and use of the FBG thermal sensor design in an grid/inverter driven IM. It consists of two papers written up in paper-style format. The second author contribution to both papers is performing a technical and academic writing review and technical guidance during this work.

Paper 1: the content of this paper has been published in *IEEE Transactions on Energy Conversion* [17]. The main contributions of this paper are:

- It reports a validated novel scheme for on-line internal temperature measurement in a low voltage random wound machine stator winding using electrically non-conductive and electromagnetic interference immune FBG sensing technology embedded in close proximity to hot spots of interest.
- It provides a thermal analysis of the examined IM motor stator windings' hot spots that enables an enhanced understanding of actual motor thermal conditions during on-line operation and could be used for enhancing the utilisation and protection of electric motors in future industrial applications.

Paper 2: The content of this paper was submitted to *IET Electric Power Applications*. The main contribution of this paper is:

- It reports a validated thermal sensing network based on the multiplexing feature of FBGST for distributed hot spot monitoring of LVEM stator winding.
- The thermal sensing network was used to monitor and evaluate the examined IM thermal condition and capacity under uniform and uneven degraded cooling system capability.

5.2 Paper 1:

Stator Winding Internal Thermal Monitoring and Analysis Using in-situ FBG Sensing Technology

A. Mohammed, *Student Member, IEEE*, S. Djurović, *Member, IEEE*

Abstract—This paper reports a novel thermal monitoring scheme for on-line internal temperature measurement in low voltage random wound machine stator windings. The scheme is based on utilising electrically non-conductive and electromagnetic interference immune fibre optic sensing technology embedded in close proximity of hot spots of interest to create a robust thermal monitoring system within the machine windings. The key design and implementation features of the proposed system are presented and applied on a prototype mains-fed induction motor. The on-line thermal monitoring performance is examined in a number of typical continuous and periodic running duty tests, as defined by the relevant IEC standards for rating and performance of rotating electrical machines. It is shown that the presented scheme has the potential to provide competent on-line measurement of critical machine thermal hot spots. Furthermore, the proposed scheme underpins a higher fidelity understanding of the distribution and propagation of winding thermal stress, demonstrated by the experimental analysis reported in the paper.

Index Terms—Induction motor, on-line thermal monitoring, internal stator winding temperature, FBG sensor.

I. INTRODUCTION

LOW voltage random wound electrical machines (LVEMs) are currently finding increased use in novel, safety critical energy conversion system applications, such as those in aerospace, electric vehicle and offshore wind industries [1-3]. These industrial applications impose increasingly higher requirements for reliability and performance of the employed electrical machines. As thermal stress is the major contributor to lifetime and performance reduction of LVEMs and reliable understanding of machine thermal conditions a precursor to achieving more effective machine exploitation, the area of machine thermal monitoring and analysis is receiving increased attention [4-7]. Development and application of improved thermal monitoring techniques that can enable performance advances through increased awareness of operational stresses and enhanced thermal management is highly relevant in this respect [8-9].

Thermal stress such as that occurring in overheating or cycling transients degrades the integrity of the winding organic insulation material, the machine component most susceptible to thermal stress. This results in its accelerated thermal aging: the ensuing insulation deterioration eventually leads to machine failure [10]. Thermal monitoring is thus a fundamental requirement for machine protection and enhancement of its reliability [11]. This is particularly pertinent where the internal thermal stress conditions in windings are concerned, as these are invariably the points of highest temperature within the machine: winding thermal hot spots are in slot centres and end-windings interior, their distribution depending on machine design and cooling arrangements. The allowable temperature in windings is defined by the thermal limits within which their insulation material retains its mechanical and electrical integrity to enable fault-free machine operation [12, 13]. The relevant standards identify machine insulation classes by their maximum allowable operating temperature while in service [14]: for a given insulation class, the maximum allowable temperature is defined as the sum of the ambient temperature (max 40 °C), the permissible temperature rise (i.e the difference between ambient temperature and the final elevated temperature) and the hot spot allowance temperature, as illustrated in Fig. 1. The hot spot allowance temperature provides a thermal safety margin for the temperature of the winding interior; this is typically the point of highest temperature in the winding which is usually challenging to directly measure or estimate due to limitations of the available measurement methods [15]. Accurate knowledge of winding hotspot temperature of an in-service machine would enable cooling system control directly related to hot spot temperature and thus machine lifetime extension through hot spot regulation. This would also enable performance improvements through controlled overloads or identification of overly conservative ratings, and be used for correction of temperature dependent machine model parameters to increase automation performance [4,7].

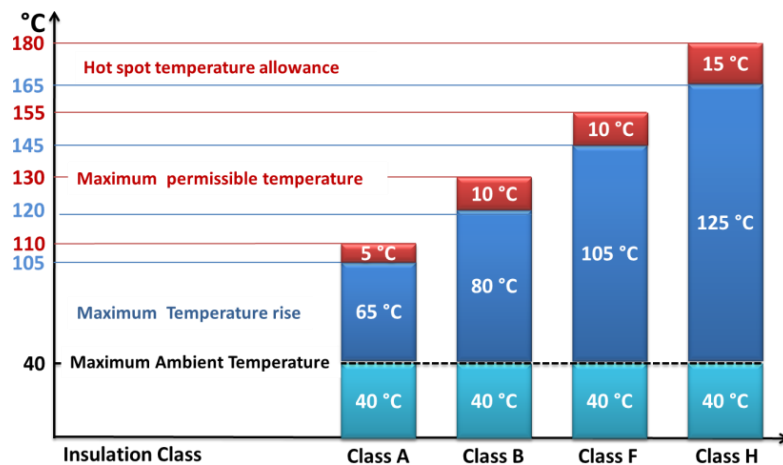


Fig. 1: Thermal limits for insulation classes A, B, C and F [14]

The current practice for monitoring winding thermal conditions is based on employing temperature estimation techniques or embedded thermal sensors [16]. The former are generally established using a thermal model-based or a parameter-based temperature estimator [17-19]. Assessing winding temperature using a parameter-based temperature estimator is achieved by estimating on-line the winding electrical resistance and hence its temperature [18]. However, this cannot provide a full thermal image of the winding nor its hot spots and yields only the average winding temperature, while also being limited in accurate tracking of thermal change during fast transient conditions [10]. Hot spot on-line monitoring using thermal model-based estimators such as finite element (FE) or lumped network models imposes considerable constraints: the FE models are computationally demanding and therefore not effective in on-line applications, while lumped network thermal models impose complexity in appropriate evaluation of model parameters including parameter dependency on thermal conditions [18-19].

Winding thermal hot spot monitoring using conventional sensing techniques such as thermocouples (TCs) or resistance temperature detectors (RTDs) can be limited for safety critical applications, primarily due to inherent use of electrically conductive material in the sensor structure: this poses a risk to the winding and the sensing system integrity, as any direct contact between the sensor and the winding can allow high current flow. Insulating these sensors with appropriate packaging can minimise this risk. This however considerably increases the sensor structure size, which can be impractical where the machine geometries of interest for monitoring such as the slot areas are concerned, and can compromise vital design parameters [20]. As a consequence of the constraints imposed by the winding construction and the sensor structure and its wiring, the sensing points in which TC and RTD sensors are applied in LVEMs are typically on end-windings and more rarely on winding surface of the slot section, and not in the winding centre where the highest temperature is located [21-22]. Further general constraints to more effective RTD and TC application in safety critical electrical machinery are imposed by their intrinsic low electromagnetic interference (EMI) immunity and low resistance to harsh environmental conditions and long term deployment [23].

The existing thermal monitoring techniques are limited in safe and accurate monitoring of the highest temperature points in LVEMs. The availability of reliable thermal monitoring tools, able to accurately track winding hotspot temperatures in all possible operating conditions will be essential in meeting the desired LVEM improved efficacy usage targets in future system critical transport and industrial sectors applications. A

thermal sensing alternative is provided by recent advances in fibre-optic Fibre Bragg Grating (FBG) sensing technology, whose inherent robustness, flexibility, long lifetime, electrical/EMI immunity, multiplexing and small size make it an attractive candidate for improving embedded thermal monitoring solutions for machine wound components [24]. The FBG sensor cost is currently comparable to cost of TC and RTD sensors conventionally used in electric machine applications, but the required FBG interrogator systems are costly. However, FBG sensing features can provide a number of attractive monitoring and performance improvements in electric machines that would be very challenging to deliver by alternative sensing or design approaches. In addition, the inherently multi-physical and multiplexing nature of FBG sensing systems has the potential to provide a sizeable considerable reduction of the overall monitoring system size and cost [25-27]. Despite its current relatively high cost, this sensing technology has already found use in aerospace and wind industries where its features have contributed to development of more effective monitoring systems [28-30]. The use of these sensors for hot spot monitoring in in-service LVEMs presents an attractive opportunity but still remains largely unexplored.

The interest in applying FBG sensors in electric machinery for mechanical and thermal measurements has been increasing recently [31-35]. FBG sensors are now identified as a suitable thermal monitoring technique for thermal cycle testing of bars and coils of large rotating machines, as specified by the IEEE 1310-2012 standard [36]. The general FBG potential for thermal monitoring internal to machine structure is assessed in [24, 32-33] for low and high power machinery. The reported literature however focuses on large form wound winding structures [24, 32] and winding surface [33] thermal monitoring in LVEMs, and does not consider coil embedded hot spot locations that are of critical interest. In addition, the FBG thermal sensor packaging designs used in reported studies utilise conductive materials such as stainless steel and aluminium which can impose operational challenges in safety critical machine applications. Advances have recently been made in understanding the optimal features of random wound coil embedded FBG thermal sensors use for in-situ monitoring of hot spot temperature [37-40]. This was however done only on prototype IEEE motorette systems and its application and performance in operating machines is yet to be examined.

This study reports an in-situ FBG thermal sensing technique for on-line thermal monitoring of the stator winding internal temperature in widely used random wound squirrel cage induction motors. The proposed technique enables adequate real-time

monitoring of stator winding hot spot temperatures, in locations that are largely beyond effective reach of conventional thermal monitoring in practical machine applications. The reported scheme is evaluated on a commercial totally enclosed fan cooled (TEFC) induction machine design. The test motor was rewound for the purpose of proposed scheme application and then operated in mains supplied conditions under dynamic thermal cycles defined by the relevant IEC standard [23]. The obtained measurements are cross-correlated with predictions from a representative FE thermal model [41-44] to further investigate the potential and performance of the presented scheme. The proposed system's on-line monitoring performance was found to deliver an acceptable indication of the winding hot spot temperatures in a range of typical dynamic operating regimes.

II. THERMAL HOT SPOT IDENTIFICATION

This study focuses on the development of a winding hot spot in-situ thermal monitoring system as a means of improving the attainable on-line thermal monitoring. In addition to sensing technique improvement, an essential element in providing enhanced monitoring is the reliable identification of sensor placement points. These ideally need to be in, or close to, positions of highest temperature in wound components to ensure the monitoring system reports the maximum existing thermal stress. To this end, and for illustration purposes, the hot spot locations in the investigated commercial TEFC motor were first examined using thermal simulation.

A. Thermal model study

The studied motor specification is presented in Table I. A thermal model of the test motor was developed using the Motor-CAD software package for thermal analysis [41]. Motor-CAD provides a specialised tool for design and analysis of thermal aspects in electrical machines [42-44]; its machine thermal models are based on an analytical lumped parameter thermal network enhanced with numerical 2D FE analysis for steady-state solutions. The integrated FE analysis provides increased detail on conduction heat transfer in various components in the motor, which allows the prediction of hot spot temperatures in the machine structure. The test motor thermal model in Motor-CAD was developed using detailed geometry/design data and material properties of the examined motor. The motor losses required for model development were obtained based on the procedure prescribed by the IEEE 112 standard [45]. The model was tuned using DC power, locked rotor and load tests [41,44, 46].

TABLE. I: TEST MOTOR SPECIFICATION

<i>TEFC Motor Data</i>	
Rated Power / Voltage / Current	0.55 kW / 400 V / 1.6A
Efficiency	66 %, IE1
Rated speed	1380 rpm
Pole number	4
Cooling method	IC 41
Slot number stator / rotor	24 / 30
Insulation class	F
Temperature rise class	B
Duty cycle type rating	S1
Frame / Core axial length	130 / 80 mm
Housing diameter	110 mm
Design standard	IEC 60034

Development of a representative winding thermal model for random wound electrical machines is challenging due to the random distribution of winding conductors in the slot and end-winding portions. For the purpose of winding thermal model development its structure can be divided into three portions: the non-drive end end-winding, the slot winding and the drive end end-winding. For the slot winding portion a thermal slot model representation that allows the conductors to be arbitrarily positioned in the slot and considers other slot components such as slot liner, wedges and impregnation is used in this work. Fig. 2 shows the details of the slot thermal model for the examined TEFC motor. The end-windings model is more complex as their structure is inherently random and the heat convection of the external end-winding surface plays a significant role. In this study an end-winding portion is modelled as a single thermal component based on its available shape and volume data.

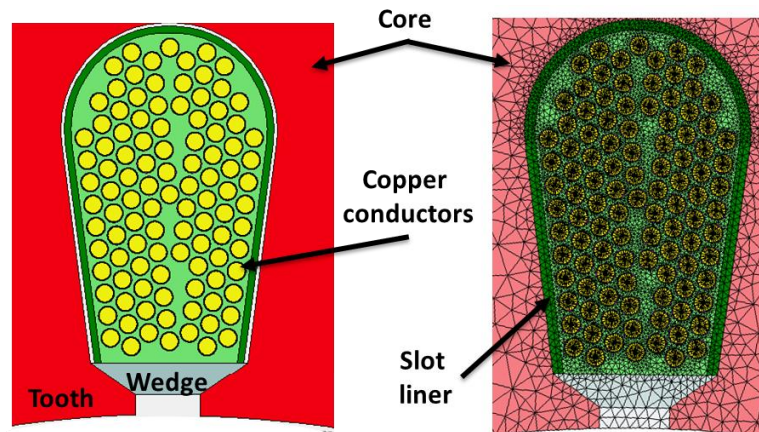


Fig. 2: Stator slot thermal model

To enhance the thermal prediction of the end and slot winding portions the total stator winding loss was divided between portions based on their length [41]:

$$P_{slot} = P_s * \frac{(2 \times \text{stator axial length})}{(2 \times \text{stator axial length} + \text{Ewd length})}, \quad (1)$$

$$P_{Ewd} = P_s * \frac{(Ewd\ length)}{(2 \times stator\ axial\ length + Ewd\ length)}, \quad (2)$$

where: P_s is the total stator winding copper loss, P_{slot} and P_{Ewd} are the copper loss in the slot and end-winding portions respectively, *stator axial length* represents the coil axial length in the slot portion and the *Ewd length* represents the coil ends length in the drive end (DE) and non-drive end (NDE) end-windings. The total calculated end-winding loss is evenly divided between DE and NDE end-windings.

Figs. 3 and 4 show the predicted winding steady-state temperature of the examined TEFC motor at no-load and full-load conditions. Fig. 3 shows the temperature distribution of the winding slot section. This is presented for one slot only as, for the sake of the model study, all slots are assumed to have identical conductor distribution and the calculated slot copper loss from (1) is evenly distributed between individual stator slots. As is generally expected, the predicted slot winding portion hot spot temperature is located in the centre of the slot. The predicted slot hot spot temperature increases from $\approx 65.5^\circ\text{C}$ at no-load to $\approx 92.6^\circ\text{C}$ at full-load. The predicted difference between the maximum and minimum temperature within the slot section is $\approx 4.5^\circ\text{C}$ at no-load increasing to $\approx 8^\circ\text{C}$ at full-load. The bottom of the slot is the coolest part of the slot section, as it is highly affected by the stator iron yoke.

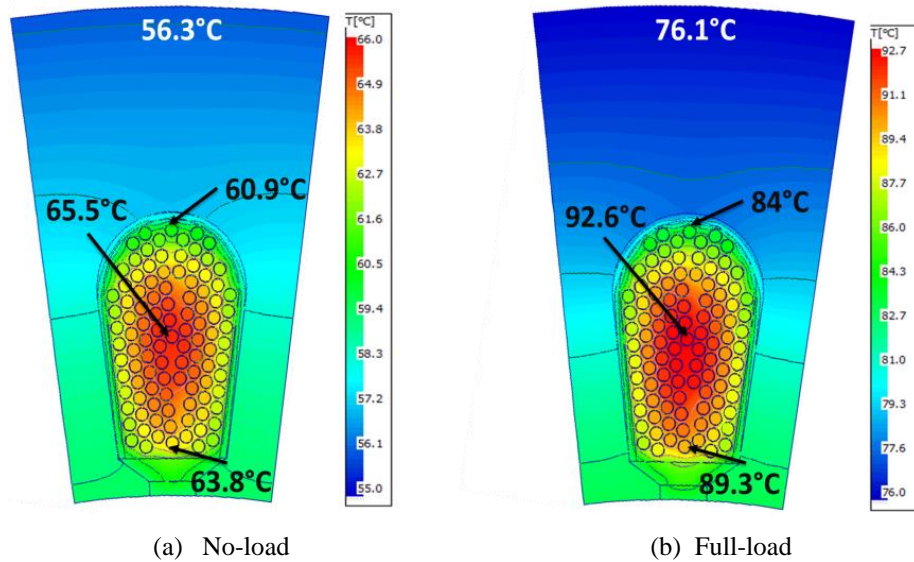
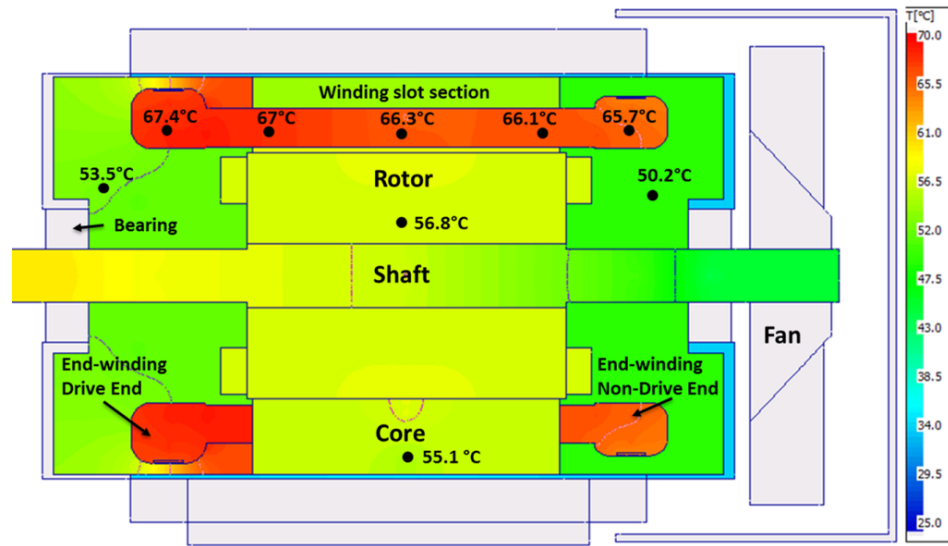


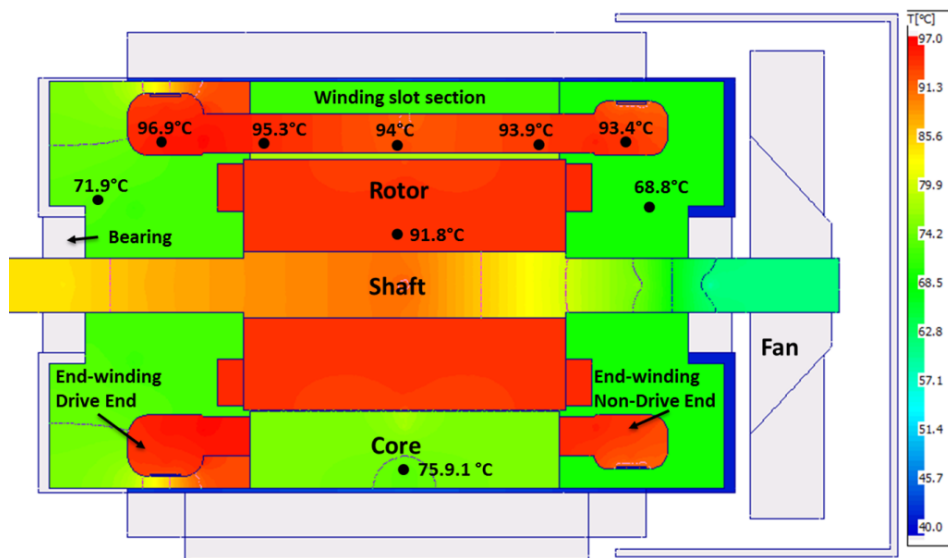
Fig.3: Predicted steady-state temperature gradient of the slot section

The predicted temperature gradients in the axial cross section of the examined TEFC motor at no-load and full-load conditions are shown in Fig. 4. It is apparent that the motor winding temperature gradually increases with distance from the cooling fan, as is normally anticipated. For the examined motor design the hottest temperature in the axial cross

section was predicted in the DE end-winding at $\approx 67.4^\circ\text{C}$ and $\approx 96.9^\circ\text{C}$ at no-load and full-load conditions, respectively. The predicted temperatures in DE end-winding were $\approx 1.7^\circ\text{C}$ and $\approx 3.5^\circ\text{C}$ higher than in NDE end-windings at no-load and full-load conditions, respectively. For the slot axial section, the hottest location is displaced towards the core drive end, as is generally expected for a non-drive end fan cooled machine. The maximum and minimum predicted temperatures in the slot axial section are $\approx 67^\circ\text{C}$ and $\approx 66.1^\circ\text{C}$ at no-load and $\approx 95.3^\circ\text{C}$ and $\approx 93.9^\circ\text{C}$ at full-load. This results in a maximum temperature difference along the slot axial length section of $\approx 1.4^\circ\text{C}$. The axial thermal change effects in the slot section are seen not to be considerable, as would be expected of the examined relatively small size machine design. However, this thermal difference is highly dependent on and varies with motor thermal design and size.



(a) No-load



(b) Full-load

Fig. 4: Predicted axial thermal gradient in the test motor

B. Thermal monitoring point requirements

The thermal model predictions clearly show that, as is generally expected, the highest hot spot temperature in the examined motor is in its DE end-windings followed by that in the centre of the winding slot portions. Monitoring only the highest thermal hot spot located in the DE end-windings however does not provide sufficient understanding of the existing thermal conditions in the motor. This stems from the fact that the end-winding portions combine the coils of all phase windings into a single thermal component. In abnormal operating conditions, such as for example a supply or other inherent electrical unbalance, different current levels can exist in different phase windings resulting in unevenly distributed copper loss across phases and thus an uneven temperature between individual phase windings. The temperature measured in the end-windings is the average temperature of the separate phase winding coils comprising it, and does not enable the understanding of existing thermal conditions in individual phases, which may in this case exceed the temperature levels observed in the end-winding. The same is valid for operation under electric fault conditions such as inter-turn faults, where high current and therefore thermal stress can typically be localised within a few turns of a single, faulty, phase winding. It is evident that monitoring the slot hotspot temperature in these conditions can provide more accurate information on the actual thermal status of individual phase windings. However, monitoring only the slot portion hot spot thermal conditions would ignore the temperature rise in the DE end-winding due to its slow cooling process caused by its distance from the cooling fan and would therefore not be appropriate. The optimum solution is therefore to design the thermal monitoring system to observe both end-winding and slot portion hot spots in all machine operating conditions; this requires thermal sensors that are suitable for effective application in a variety of slot and end-winding centre positions within the motor geometry.

III. FBG SENSING PRINCIPLES AND IN-SITU MONITORING SYSTEM DESIGN

A. FBG temperature sensor operating principles

FBGs are the periodic gratings on the optical fibre core that result in a periodic modulation of its refractive index when exposed to an interference pattern of laser light [47]. The wavelengths reflected by the FBG structure will alter with the variation in the strain and/or temperature it is exposed to, thus enabling the fibre structure to act as a strain and thermal excitation sensitive element. With appropriate design [37-40] this phenomenon enables the grating fibre to be utilised as an exclusively mechanical or a

thermal sensor. The reflected FBG wavelength is known as the Bragg (i.e. centre) wavelength, λ_B , and is defined by [47]:

$$\lambda_B = 2 \Lambda n_{eff} \quad (3)$$

where: Λ is the grating period (i.e. the spacing between successive gratings) and n_{eff} is the effective fibre core refractive index. A change in the fibre temperature and/or strain will give rise to a change in n_{eff} and Λ , and consequently result in an alteration of the reflected wavelength. The reflected Bragg wavelength relative rate of change can be defined in terms of the existing thermal and/or mechanical excitation as [48]:

$$\Delta\lambda_B = \overbrace{2\lambda_B \left(\Lambda \frac{dn_{eff}}{d\varepsilon} + n_{ef} \frac{d\Lambda}{d\varepsilon} \right)}^A \Delta\varepsilon + \overbrace{2\lambda_B \left(\Lambda \frac{dn_{eff}}{dT} + n_{ef} \frac{d\Lambda}{dT} \right)}^B \Delta T \quad (4)$$

where: ε is strain and T is temperature. Term A in (4) represents Bragg wavelength shift caused by the strain induced elastic-optic effect, while term B describes the temperature change induced wavelength shift that arises due to thermo-optic and thermal expansion effects [47]. The reflected wavelength variation due to temperature change only can be expressed in terms of the fibre thermal characteristics as [49]:

$$\Delta\lambda_B = \lambda_B (\alpha + \xi) \Delta T \quad (5)$$

where: α is the fibre thermal expansion coefficient ($\approx 0.55 \times 10^{-6}/^\circ\text{C}$) and ξ is the fibre thermo-optic coefficient ($\approx 6.67 \times 10^{-6}/^\circ\text{C}$) [47]. For a standard bare FBG with the Bragg wavelength of 1550 nm operating at ambient temperature the fibre thermal sensitivity is $\approx 11 \text{ pm}/^\circ\text{C}$ [48].

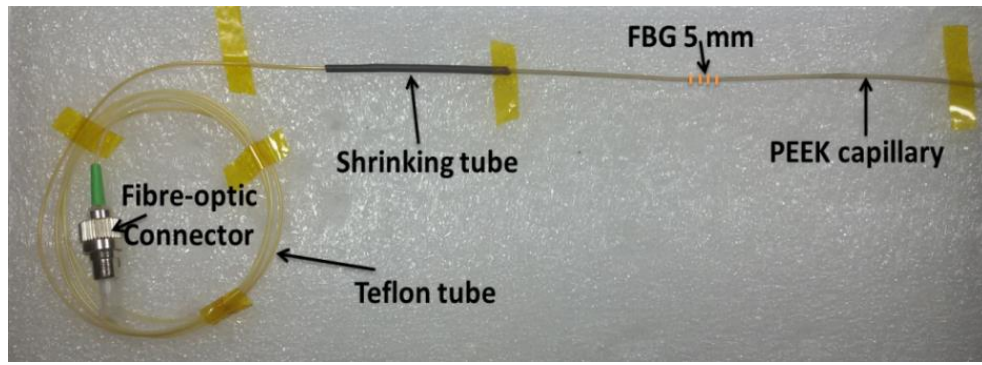
B. In-situ FBG temperature sensor design

The target sensing application in this study is internal thermal monitoring within a random wound stator winding structure in a class F insulated electrical machine, in direct proximity to the winding thermal hot spots located in the coil centre. The primary design constraints of the thermal sensing system, arising from its application within a current carrying coil, are the desirability for the sensing element to be electrically non-conductive and EMI immune with a size sufficiently small to enable seamless sensor implantation in the target hot spot position between individual current carrying conductors, without significant disturbance of the designed motor slot fill factor. In addition, the sensing element has to be capable to operate in and withstand the thermal environment characteristic of the examined conventional class F insulated machine design.

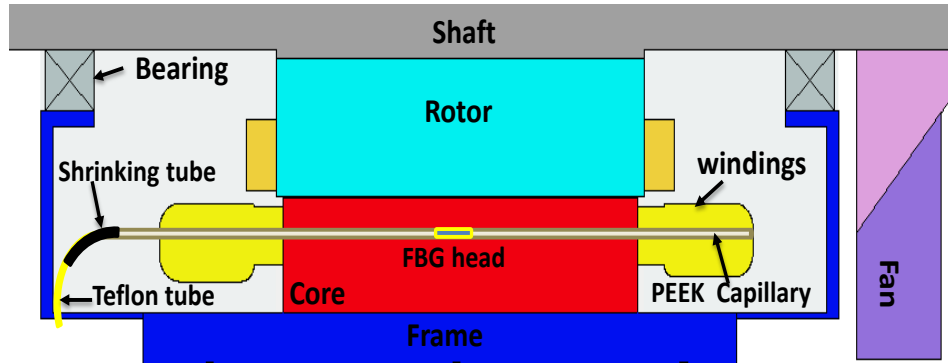
FBG sensing fibres are inherently immune to EMI, non-conductive and typically manufactured in diameter sizes of a few micro meters. An individual fibre is extremely fragile and requires suitable packaging to protect its mechanical integrity. Another important role of packaging in exclusively thermal sensing applications is to isolate the sensing fibre from mechanical excitation and ensure a sensor design that is only temperature sensitive [37]. To satisfy the said design constraints a Polyetheretherketon (PEEK) capillary is used in this work to package the FBG sensing heads. PEEK was chosen due to its dielectric and mechanical properties; it has a thermal conductivity of 0.173 W/m.k and can withstand operating temperatures in excess of ≈ 250 °C [38].

Fig. 5a shows the in-situ FBG temperature sensor design used in this work. The probe length is 1.5 m and it contains a single 5 mm FBG head imprinted in a polyimide coated fibre. The FBG head bandwidth is ≈ 0.3 nm and its reflectivity $\approx 88\%$. A section of the sensing fibre containing the FBG head is packaged in a PEEK capillary while the remainder of the optic cable is tubed in Teflon for protective purposes. The outer diameter of the utilised PEEK capillary was chosen as 0.8 mm. This was done to provide a relatively close match to the 0.56 mm diameter size of the examined stator winding's copper wire and therefore facilitate easier placement and more effective thermal sensing performance of the sensor package within the random wound stator winding structure [37,40]. The PEEK capillary wall thickness was chosen to be 0.1 mm to yield a low conduction thermal resistance and hence enhance the sensor response [40].

The PEEK capillary length is chosen to house the entire fibre section containing the FBG sensing head that is implanted in the winding slot region. The sensing head is installed at the centre point of the stator stack length for this study, as illustrated in Fig. 5b. The sensing fibre is kept loose within packaging. This design allows for positioning of the FBG sensing head at any desired point along the axial length of the winding slot section. As the purpose of this study is to examine the performance of the proposed monitoring scheme and considering the size of the commercial test machine imposes relatively minor thermal differences in the slot axial direction, the FBG head was placed in the centre of the core axial length as shown in Fig. 5b. The packaged sensors in the end-winding sections were embedded in the end-winding section cross-sectional centre point. This enabled practical monitoring of internal temperature of different winding sections (i.e. slot and end winding hot spots). Combined with the multiplexing feature of FBG sensors this design can allow different distributed thermal configurations to be established: a single fibre with multiple FBGs can monitor the axial length of the winding including slot and end-winding sections.



(a) Sensing probe design



(b) In- situ FBG sensor installation

Fig. 5: FBG sensor for in-situ hot spot temperature monitoring

C. In-situ FBG temperature sensor calibration

The interpretation of the FBG sensor reflected Bragg wavelength to temperature readings first requires a sensor calibration test to obtain the required temperature-wavelength fit curve [40]. The experimental setup for calibration of the described FBG sensor design is shown in Fig. 6. A controlled thermal chamber was used to expose the sensors to a desired, controlled, steady-state thermal excitation level. The reference temperature within the thermal chamber was read by the chamber proprietary thermal sensors and a type K TC sensor placed inside the chamber in close proximity to the FBG sensors under calibration. The FBG sensors were illuminated by a commercial SmartScan interrogator system enabling dynamic measurement of reflected wavelengths.

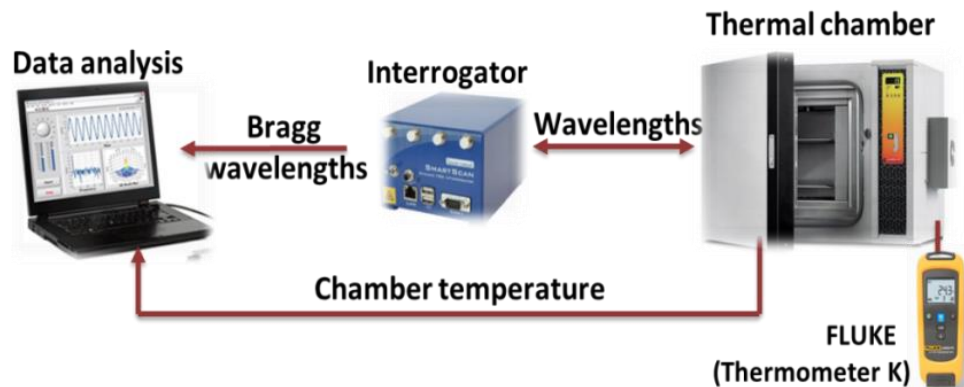


Fig. 6: Experimental system for FBG sensor calibration tests

Calibration tests were performed in the temperature range of 20 to 160 °C to match the rated thermal range of the class F insulated motor windings. The temperature was regulated by the chamber controller in the tests in a rising sequence of 20 °C steps. At each step the temperature was held constant for a time period sufficient to ensure the thermal equilibrium is achieved before thermal measurements were taken. The FBG reflected wavelength and the chamber temperature were recorded at each evaluated thermal equilibrium in the investigated temperature range. The calibration test data for the four FBG sensors used in this work are presented in Fig. 7 and show a close-to-linear temperature-wavelength dependency. A second order polynomial fit curve was calculated from the obtained data for each FBG to enable accurate conversion of the monitored reflected wavelength shift to temperature readings in further tests [39].

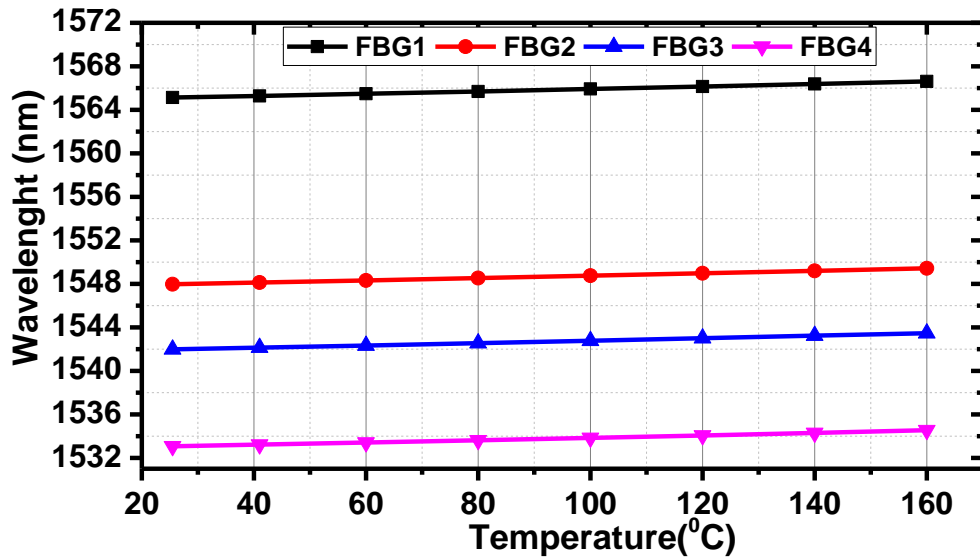


Fig. 7: Sensor calibration test data

IV. INDUCTION MACHINE HOT SPOT MONITORING SYSTEM EXPERIMENTAL TEST RIG DESCRIPTION

This section describes the design and implementation of the winding hot spot monitoring experimental system. The proposed on-line monitoring scheme was established by installing a number of FBG probe designs discussed in section III into the test induction machine specified in Table I. For the purpose of embedding the sensors in the target positions, the motor stator winding was stripped and rewound.

Fig. 8 illustrates the embedded thermal sensor locations in the test machine. These were chosen to include both slot and end-winding portion hot spots of the stator windings, as discussed in section II. To this end, three FBG sensors were embedded between copper conductors in the slot centre of three different slots, each slot containing a different phase

winding (one FBG fitted per phase, referred to as FBG-SA, FBG-SB and FBG-SC in further text, respectively), as illustrated in Fig. 8a. The three FBGs were pitched by 8 slots to enable a uniform thermal sensing distribution within the examined motor geometry, as shown in Fig. 8b. An additional, fourth, FBG sensor (FBG-DE in further text) was embedded in the motor drive end end-winding section, shown in Fig 8c.

To ensure the installed sensors are approximately positioned in the coil centre the following installation procedure was followed [37-40]. First the packaging capillaries were embedded within the slot structure during the rewind process. This was achieved by winding half of a relevant coil section and inserting it in its respective slot/end winding position, before fitting the packaging capillary in the coil centre location and winding the remainder of the coil. Once the winding process was completed and the windings impregnated (dip impregnation) the FBG sensing fibres were loosely inserted into the installed PEEK capillaries. This process enables in-situ hot spot sensing in positions of interest and offers an advantage of avoiding the undesirable exposure of the fragile sensing fibre to mechanical stress during the wind and impregnation process. Another key practical advantage is that the sensing fibre is made accessible for replacement, re-positioning and/or re-calibration, which is not the case with conventional thermal sensors [50].

To benchmark the in-situ FBG sensing thermal system performance a number of type K thermocouples were embedded in the stator windings as shown in Fig. 8. Two TCs were embedded in the end-windings: one in the drive end (TC-DE) to benchmark the FBG-DE performance and the other in the non-drive end (TC-NDE) to validate the obtained results. Another two TCs were embedded between the coil surface and the slot wall insulation, one in the bottom of the slot (TC-SB) and the other in the top of the slot under the slot wedge (TC-ST). The TCs positions were chosen in accordance with the IEC 60034-1 standard [23].

The test rig used to examine the on-line performance of the proposed in-situ thermal monitoring system is illustrated in Fig. 9. The rig contains the prototype FBG sensor embedded induction motor coupled to a PMDC load machine whose armature current is regulated using a controllable resistive load bank. The induction motor was supplied directly from the grid via a variable transformer in the tests. Its currents were measured using LEM-LA25 Hall effect current transducers whose output was monitored via an NI 9205 DAQ and conditioned on a personal computer in a LabView VI routine. TC outputs were acquired and conditioned by a thermocouple input module NI9211 DAQ. The FBG sensors were illuminated by a commercial multi-channel Smart Fibres SmartScan04

interrogator unit; the monitored FBG wavelengths were processed using the LabView based SmartSoft software [30].

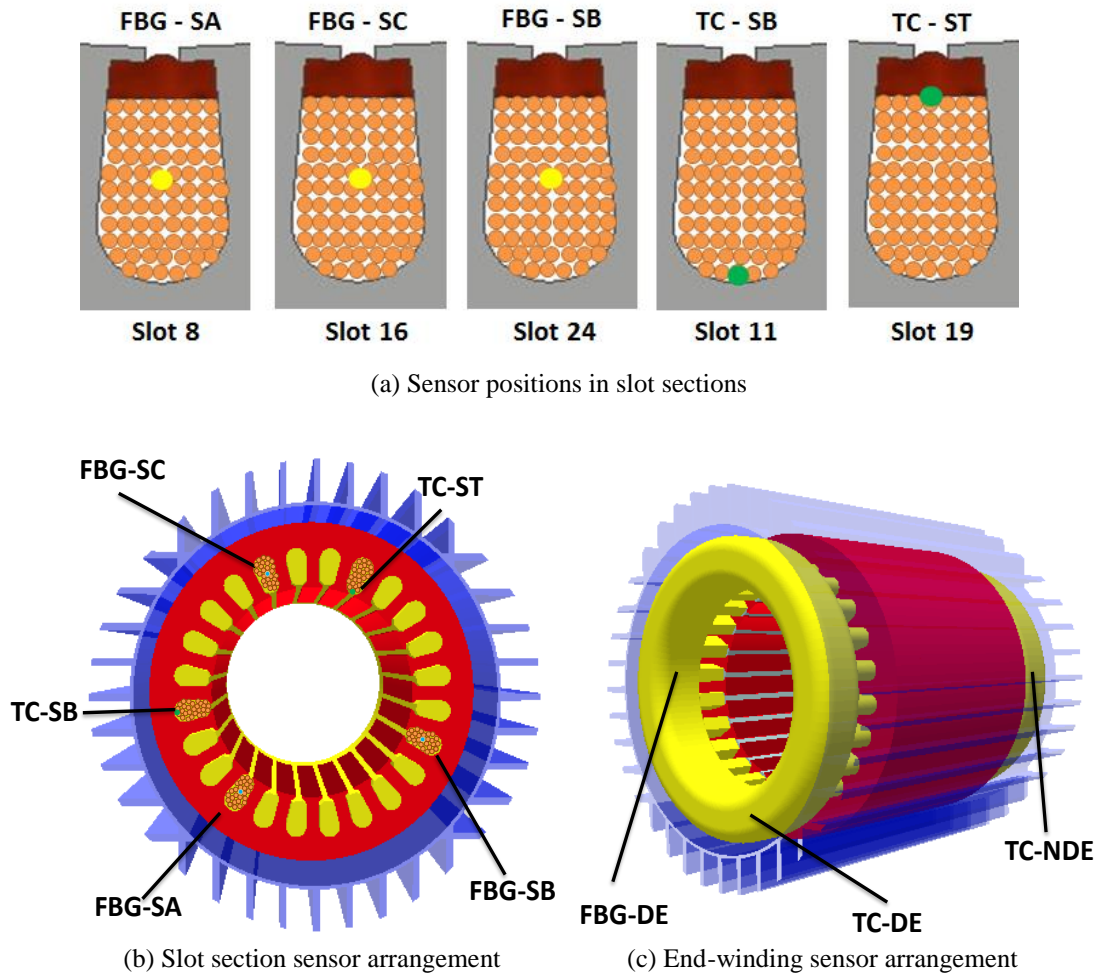


Fig.8: Temperature sensor positions in the tested motor

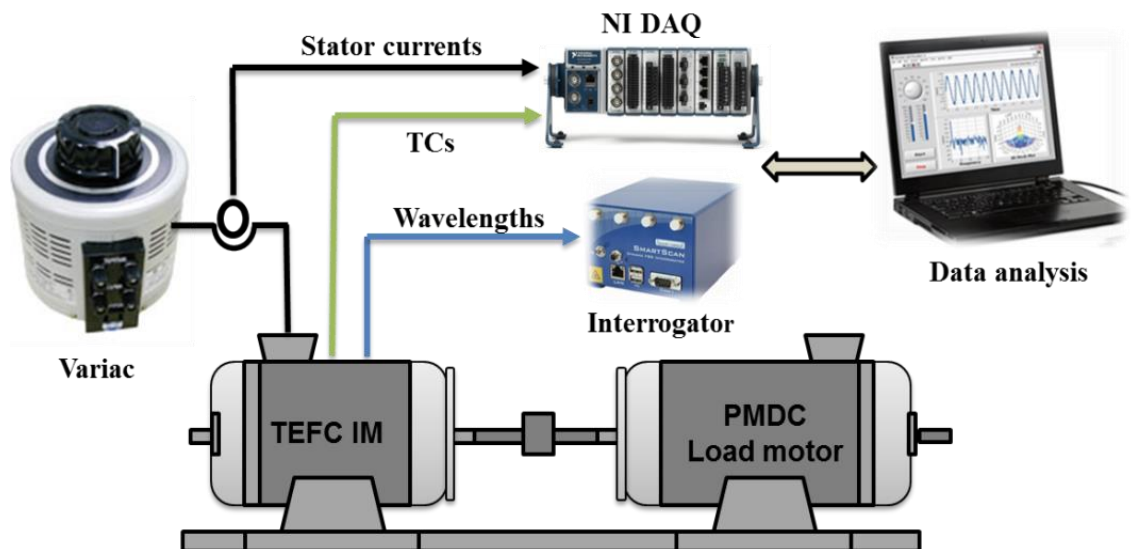


Fig. 9: Experimental test rig for TEFC on-line temperature monitoring

V. EXPERIMENTAL RESULTS

The on-line hot spot monitoring performance of the proposed in-situ FBG sensing system was evaluated in extensive thermal tests on the prototype FBG embedded motor. This section presents the winding internal thermal readings obtained in a range of typical dynamic thermal cycle tests performed on the laboratory test rig. The applied thermal cycles were defined based on the IEC 60034-1 standard for rating and performance of rotating machines [23]. The thermal characteristics of the examined motor design have been considered in order to enhance the interpretation of the obtained measurements.

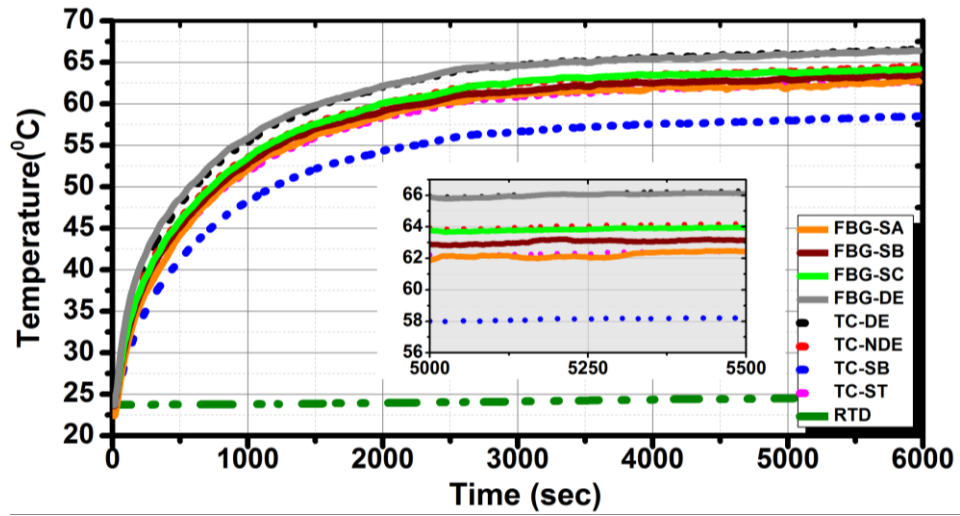
A. Continuous running duty operation

A significant proportion of TEFC induction motors in modern industrial applications are S1 duty rated. The S1 duty rating specifies continuous machine operation under a constant load, maintained for a time period sufficient to allow the machine to reach a thermal equilibrium within its nominal rating [23].

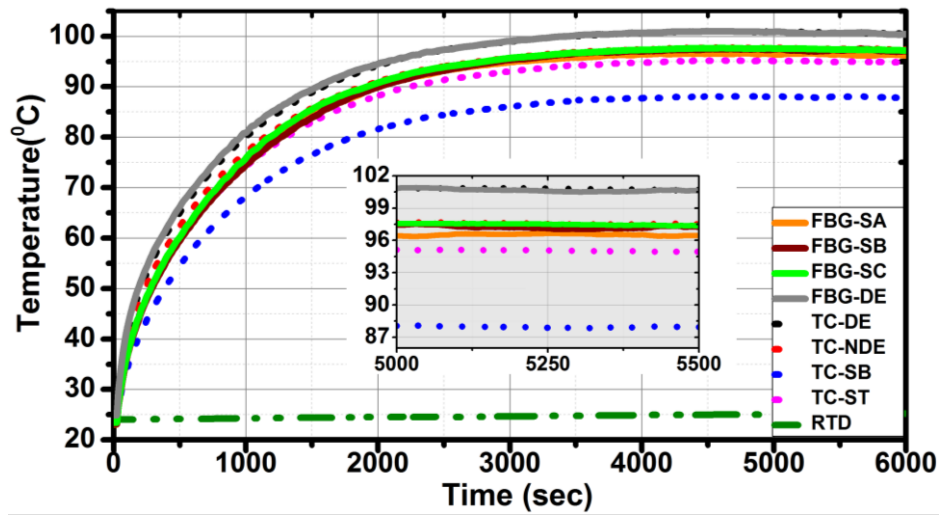
The proposed monitoring system's performance was first examined for test motor operation in a number of S1 continuous duty cycles. To this end a series of S1 cycles at different load levels were applied on the test motor, ranging from no-load to nominal load in increments of 25% (i.e. 0%, 25%, 50%, 75% and 100% load). The thermal measurements obtained by in-situ FBG and TC sensors at 0% and 100% load S1 duty cycles are shown in Fig. 10 for illustrative purposes. The winding temperature rise measured at thermal equilibrium for all considered S1 duty cycles is shown in Fig. 11; this was calculated by averaging the winding temperature measurement referred to the measured ambient temperature during a 15 min steady-state period of each examined duty cycle. The ambient temperature was measured by an RTD sensor connected to an RTD input module NI 9217 DAQ. The RTD was placed at shaft height and at one meter distance from the motor as prescribed in [23]. The ambient temperature measured in the tests is shown in Fig. 10 for illustration purposes.

A variety of information about the FBG sensing system performance and the motor thermal characteristics can be extracted from the presented measurements. Firstly, it is evident from Fig. 10 that the average internal winding temperature exhibits a relatively large increase of ≈ 34 °C, from ≈ 64 °C at no-load to ≈ 98 °C at full-load. This can be explained by the examined motor's standard efficiency class (IE1) design, expected to exhibit a significant increase in losses, and stator winding loss in particular, with increase in load [51]. The thermal rise is further enhanced by the relative degradation of the cooling

process (shaft mounted fan) due to a relatively significant rotor speed reduction at full-load, resulting from the large nominal slip ($\approx 8\%$) of the tested motor design.



(a) No-load measured winding temperature



(b) Full-load measured winding temperature

Fig. 10: Stator winding temperature measured by in situ FBG and TC sensors during running duty cycle S1 operation: (a) no-load. (b) full-load

The maximum winding temperatures are recorded at full-load: $\approx 100^\circ\text{C}$ in the drive end end-winding measured by FBG-DE and confirmed by TC-DE, and an average of $\approx 96^\circ\text{C}$ in the slot section measured by FBG-SA, FBG-SB and FBG-SC. These hot spot readings are $\approx 50^\circ\text{C}$ below the maximum allowable temperature of the examined motor (155°C). The readings conform to the class F insulation and class B temperature rise ratings of the investigated motor design, commonly used by manufacturers to lengthen the insulation life by lowering winding temperature at rated load [52]. This is illustrated in Fig. 11 by the measured hot spot temperature rise at full-load of $\approx 75^\circ\text{C}$, $\approx 5^\circ\text{C}$ lower than the permissible temperature rise of class B rated motors of 80°C . The temperature rise measured for no-load to 50% load conditions is approximately half of that observed for full-load operation, as is expected for an IE1 class motor [51].

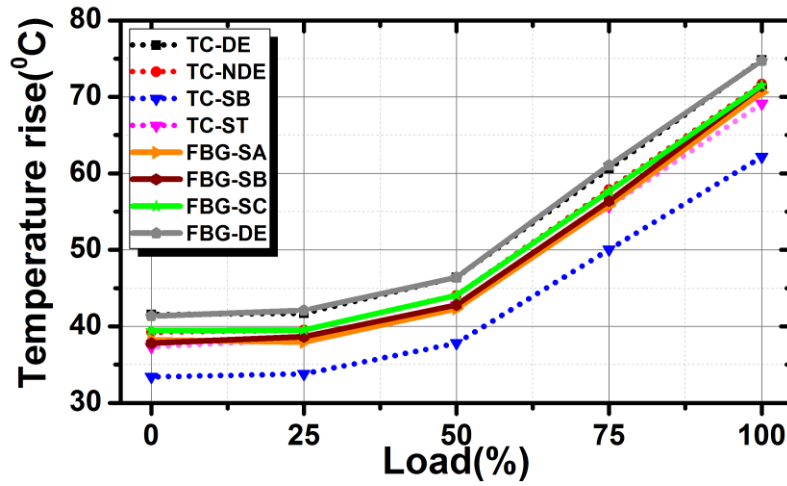


Fig. 11: Measured S1 duty cycle steady-state temperature rise versus load

The data in Fig. 10 and 11 allow for another important observation relating to the increase in the difference between thermal readings reported by sensors embedded at different locations with the change in motor load. The difference between the drive end end-winding temperature (FBG-DE, TC-DE) and the slot bottom temperature (TC-SB) for example is seen to increase from $\approx 7^\circ\text{C}$ at no-load to $\approx 13^\circ\text{C}$ at full-load. This clearly demonstrates the importance of thermal sensing in appropriate locations for accurate tracking of the highest stator winding temperature. The FBG hot spot thermal measurements and those obtained by TC sensors are seen to be in good agreement with the tuned thermal model predictions shown in Figs. 3 and 4. As expected, the FBGs placed in the slot centre report higher thermal readings when compared to the TCs placed in contact with coil slot section surface. At no-load, the TC sensors installed on the top (TC-ST in Fig. 8) and the bottom of the coil slot section (TC-SB in Fig. 8) report a temperature that is $\approx 0.9^\circ\text{C}$ and $\approx 3.6^\circ\text{C}$ lower than that recorded by the FBGs in the slot centre, respectively. The difference between the TC-SB and TC-ST sensor readings and those of slot centre placed FBGs increases with load and is measured as $\approx 9^\circ\text{C}$ and $\approx 2^\circ\text{C}$ at full-load, respectively.

The temperatures within the slot area measured by FBGs in the slot centre and TCs at slot top and bottom (TC-SB and TC-ST), and predicted by the FE thermal model in Fig. 4 are shown in Fig. 12 for the lowest and the highest measured temperature gradient (i.e. for 0% and 100% load). The data indicate that the temperature gradient within the slot area increases with load for the investigated motor design. The heat generated within the slot increases with the square of the winding current which in turn rises with load; the heat dissipation path in the slot area on the other hand is largely defined by the slot fill factor, winding impregnation and the slot liner design. Therefore, for operation at full-load the

heat generation rate within the slot increases considerably with respect to the attainable slot heat dissipation rate, resulting in a large temperature gradient and a high thermal hot spot in the slot centre. The observed difference between thermal measurements in the slot hot spot point (i.e. centre) and the slot top and bottom points is seen to change with load and is an artefact of the heat dissipation process. The slot bottom is affected by the proximity of the core yoke which exhibits a largely load independent loss mechanism and therefore provides a relatively effective cooling path between the slot conductors and the ambient. Conversely, the top of the slot is affected by the air gap and rotor temperatures which generally increase with load [52]. This is demonstrated by the difference between the thermal readings in the slot top and bottom positions, which increases from $\approx 3.5^\circ\text{C}$ at no-load to $\approx 7^\circ\text{C}$ at full-load. The experimental data in Fig. 12 clearly illustrate the advantage of thermal sensing in the slot centre position, where the highest thermal stress within the slot area is located.

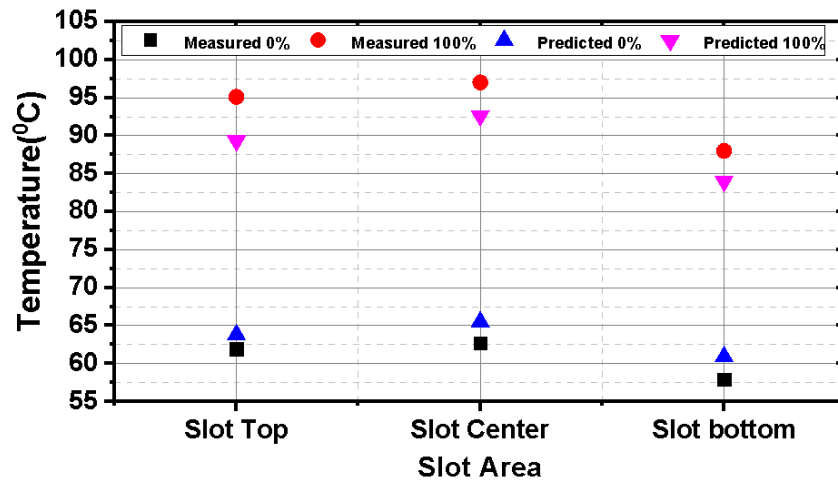


Fig. 12: Temperature gradients measured within the slot area

The drive end end-winding temperature was measured to be $\approx 2.2^\circ\text{C}$ higher at no-load and $\approx 3.6^\circ\text{C}$ higher at full-load, than the slot hot spot temperature (FBG-SA, FBG-SB, FBG-SC). This difference arises due to the slow end-winding cooling process, largely based on convective heat transfer; the distance between the motor drive end and its cooling fan is another influencing factor, as it results in the air inflow reaching the end cap being significantly hotter than that at the cooling fan. It is interesting to observe that the measured ambient temperature increases by up to $\approx 3^\circ\text{C}$ in performed tests as a result of the heat dissipated in the surrounding ambient by the tested induction motor as well as its load motor with the resistance bank. The observed thermal increase can be higher in applications where the surrounding ambient consists of heat sources in close proximity to the motor that can be drawn back by the cooling air inlets and increase the motor temperature [52].

B. Periodic running duty operation

In many industrial applications TEFC motors are operated in variable-load periodic duties. These dynamic operating conditions can pose a risk of giving rise to motor internal temperatures increase beyond permissible levels and thus endanger its integrity. The current industrial thermal protection systems for electric motors used to prevent overheating in these conditions are not fully effective [16]. It is challenging for existing thermal relays to accurately determine the motor's thermal characteristic under different operating conditions as they are mostly designed based on a single thermal time constant. As a result these are often too conservative, resulting in unnecessary stoppage, or alternatively can incorrectly interpret existing thermal conditions and consequently fail to react, resulting in significant overheating [18]. For effective utilisation and protection of motors operated in periodic running duty applications the accuracy of internal winding temperature monitoring is essential.

This section examines the proposed system's performance when used for on-line thermal monitoring of the test motor operating under intermittent periodic duty S3 and continuous–operating periodic duty S6, as defined by IEC 60034-1 [23]. The applied cycles' period and duration factor were controlled to ensure that the motor's highest hot spot temperature rise rate reaches but does not exceed the maximum permissible temperature rise rate for its design class.

1) Duty type S3 - intermittent periodic duty

The S3 duty type is identified as a sequence of identical duty cycles, each including a time of operation at constant load and a time de-energised and at rest, where the starting current is such that it does not significantly affect the temperature rise [23]. An S3 23% cyclic duration factor was applied to the examined motor for the purpose of this test; this was achieved by periodically applying 125% of rated load for a duration of 3 min followed by a 10 min de-energised period. The dynamic thermal measurements obtained by the embedded FBG and TC sensors are shown in Fig. 13. The maximum temperature is recorded at completion of the constant load period and is measured in the drive end end-winding at $\approx 106\text{ }^{\circ}\text{C}$, which is equal to the sum of the measured motor temperature rise of $\approx 80\text{ }^{\circ}\text{C}$ and the measured ambient temperature of $\approx 26\text{ }^{\circ}\text{C}$. The embedded thermal sensors report different temperature rates of change in heating and cooling conditions. The FBG sensors embedded in the slot centre show higher thermal readings and lower heating thermal time constants when compared to those obtained by TC sensors attached to the coil surface. In the examined S3 duty type the test motor is periodically de-energised for a

period of time after a period of over loading. A sufficient cooling period duration is therefore highly desirable in this duty, to prevent the motor from overheating when starting up in the following cycle. Things are further complicated by the fact that the TEFC motor cooling characteristic significantly changes based on whether it is energised: the cooling mechanism changes from forced and natural convection heat transfer in an energised motor, to only natural convection heat transfer in a de-energised motor. The latter heat transfer mechanism is slower and thus results in a larger cooling thermal time constant, as observed in the hot spot thermal measurements in Fig. 13. Accurate tracking of hot spot winding temperature is thus essential to reliably identify the time required for the motor to cool down to a temperature sufficiently low to allow its safe and effective re-energisation.

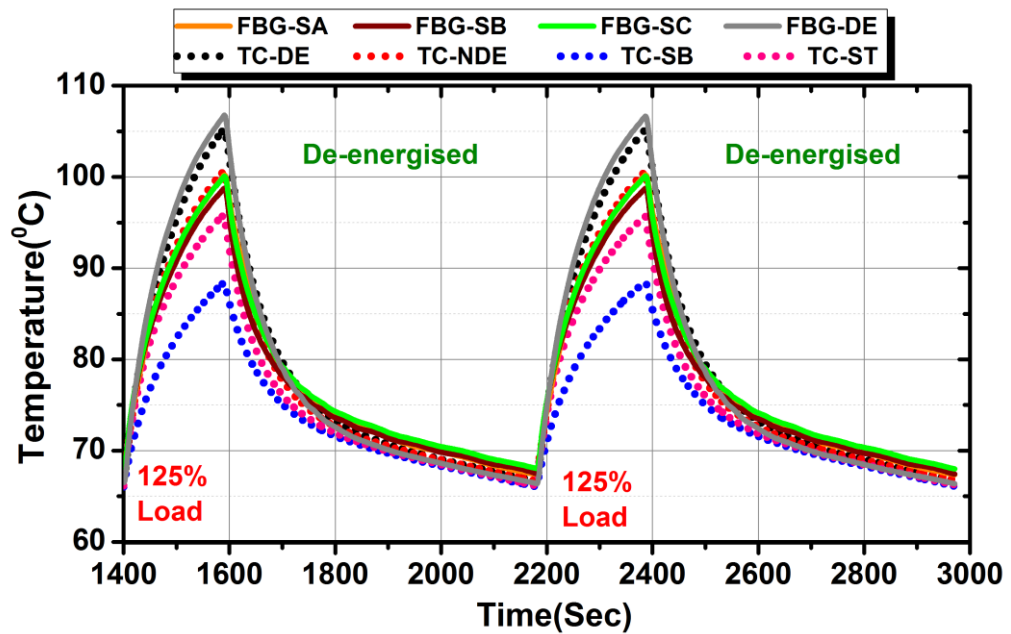


Fig. 13: Measured temperature under intermittent duty cycle S3

2) Duty type S6 - continuous operation periodic duty

The continuous operating periodic duty type S6 is specified as a sequence of identical duty cycles: each cycle consists of a period of operation at constant load and a period of operation at no-load; at no time is the motor de-energised, at rest or reaches a thermal equilibrium [23]. In this experiment, an S6 duty type with a period of 20 min and a cyclic duration factor of 50% was applied to the test motor. In each cycle the motor is loaded at 125 % of rated load for a 10 min period and then run under no-load for the remainder of the cycle. The recorded temperature readings obtained by the embedded FBG and TC sensors are shown in Fig. 14. The highest temperature was measured to be ≈ 100 °C in the drive end end-winding. The ambient temperature was measured as ≈ 25.2 °C during the experiment. The studied S6 cycle could therefore be deemed to be safe to apply on the

examined motor as the highest measured temperature is lower than the permissible temperature for the motor insulation class and the highest measured thermal rise rate ($\approx 75^\circ\text{C}$) is lower than the designed class B temperature rise. However, a small increase in the examined cyclic duration factor can result in temperature rise beyond that permissible for the tested motor design.

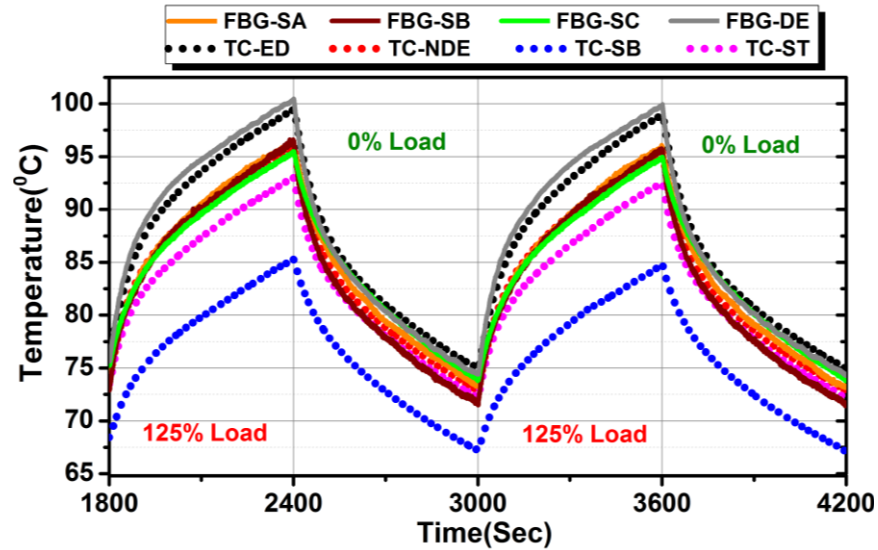


Fig. 14: Measured temperature under continuous operation duty cycle S6

3) Discussion

The presented thermal dynamic profiles demonstrate the capability of the in-situ FBG sensing system to provide effective on-line tracking of internal winding temperature in typical periodic running duty applications. The obtained winding hot spot measurements clearly show the different heating and cooling time constants and report a noticeable difference between individual measurements during the examined duty cycles. Therefore, relying on the average winding temperature in these conditions, such as would be provided by a resistance estimator technique, is not adequate to fully protect the motor from overheating, as the difference between average winding temperature and a localised hot spot can be high. This clearly illustrates the limitations in motor thermal protection by conventional thermal relays based on single time constant recognition and the advantages that the proposed monitoring scheme can provide in this regard.

VI. CONCLUSION

The paper reports a new and robust technique for on-line thermal hot spot monitoring in low voltage machinery random wound windings using FBG sensing technology. The proposed scheme has been implemented and its performance examined and validated on a mains-fed TEFC squirrel cage motor.

The proposed scheme utilises electrically non-conductive and EMI immune, power passive, fibre optic sensors that are particularly suitable for embedded application in random wound coils in a variety of machine sizes, ratings and applications. The reported in-situ monitoring network design enables sensor in-situ accessibility for replacement, repositioning or recalibration which is not possible with conventional sensing techniques, and provides a versatile and safety critical monitoring platform that can be expanded to achieve further embedded distributed thermal sensing capability.

The reported scheme was applied to perform thermal measurements on a prototype mains-fed induction motor operating in a number of continuous and periodic running duty cycles identified by the IEC standards. Where possible, the measured temperatures were cross correlated with measurements obtained by conventional TC sensors and with temperatures predicted by a thermal model of the test motor, which was initially used to inform the general thermal monitoring scheme design. The obtained experimental data illustrate the advantages of the proposed in-situ sensing scheme in delivering robust and effective on-line thermal sensing in thermal hot spot positions internal to the winding structure, where the highest thermal stress within the slot and end-winding areas is located.

The reported thermal analysis enables an enhanced understanding of actual motor thermal conditions during on-line operation and could be used for enhancing the utilisation and protection of electric motors in future safety critical industrial applications. A particularly pertinent condition in this regard is motor operation in different dynamic cycles such as those examined in this work, where the proposed technique clearly reports different hot-spot thermal time constants and illustrates the limitations of motor monitoring and protection systems based on application of a pre-defined single thermal time constant. Furthermore, the accurate tracking of the actual winding hot spot temperature is essential to identify the required time of motor de-loading to enable sufficient cooling in dynamic duty cycles, where any inaccuracies in thermal monitoring will either lead to a reduction of motor effective operation time or, more critically, a reduction of its life time through thermal overload.

The reported study demonstrates the potential of the proposed in-situ thermal sensing scheme to enable monitoring and recognition of winding thermal conditions in arbitrary internal positions, thus enabling a much improved awareness of key thermal parameters in operating low voltage induction machinery that would be exceptionally challenging and impractical to achieve with conventional monitoring techniques.

REFERENCES

- [1] W. Cao, B. C. Mecrow, G. J. Atkinson, J. W. Bennett and D. J. Atkinson, "Overview of Electric Motor Technologies Used for More Electric Aircraft (MEA)," in *IEEE Transactions on Industrial Electronics*, vol. 59, no. 9, pp. 3523-3531, Sept. 2012.
- [2] K. Fischer, F. Besnard and L. Bertling, "Reliability-Centered Maintenance for Wind Turbines Based on Statistical Analysis and Practical Experience," in *IEEE Transactions on Energy Conversion*, vol. 27, no. 1, pp. 184-195, March 2012.
- [3] J. de Santiago et al., "Electrical Motor Drivelines in Commercial All-Electric Vehicles: A Review," in *IEEE Transactions on Vehicular Technology*, vol. 61, no. 2, pp. 475-484, Feb. 2012.
- [4] M. O. Sonnaillon, G. Bisheimer, C. D. Angelo and G. O. García, "Online Sensorless Induction Motor Temperature Monitoring," in *IEEE Transactions on Energy Conversion*, vol. 25, no. 2, pp. 273-280, 2010.
- [5] Popov, Nikola Z., Slobodan N. Vukosavic, and Emil Levi. "Motor temperature monitoring based on impedance estimation at PWM frequencies." *IEEE Transactions on Energy Conversion* 29.1 (2014): 215-223.
- [6] Milić, Saša D., Aleksandar D. Žigić, and Milan M. Ponjavić. "Online temperature monitoring, fault detection, and a novel heat run test of a water-cooled rotor of a hydrogenerator." *IEEE Transactions on Energy Conversion* 28.3 (2013): 698-706.
- [7] H. Zhang, "Online Thermal Monitoring Models for Induction Machines," in *IEEE Trans. on En. Conv.*, vol. 30/4, pp. 1279-87, 2015.
- [8] Electric Machines roadmap," Advanced Propulsion Centre, UK Automotive Council, 2017.
- [9] S. Rogers, S. Boyd, "Overview of the DOE VTO Electric Drive Technologies R&D Program," US Department of Energy Vehicle Technologies Office, June 2016.
- [10] Siddique, Arfat, G. S. Yadava, and Bhim Singh. "A review of stator fault monitoring techniques of induction motors." *IEEE transactions on energy conversion* 20.1 (2005): 106-114.
- [11] Sang-Bin Lee, T. G. Habetler, R. G. Harley and D. J. Gritter, "An evaluation of model-based stator resistance estimation for induction motor stator winding temperature monitoring," in *IEEE Transactions on Energy Conversion*, vol. 17, no. 1, pp. 7-15, Mar 2002
- [12] Austin H. Bonnett" Operating Temperature Considerations and Performance Characteristics for IEEE 841 Motors," in *IEEE Transactions on Industry Applications*, vol. 37, no. 1, July/august 2001.
- [13] Hey, Jonathan, et al. "Online monitoring of electromagnetic losses in an electric motor indirectly through temperature measurement." *IEEE Transactions on Energy Conversion* 31.4 (2016): 1347-1355.
- [14] NEMA Motor-Generator Standard, MG-1-2014.
- [15] D. Reimert, "Protective relaying for power generation systems," CRC press, 2005, ch 16, sec 10, pp 497-498.
- [16] M. A. Valenzuela and P. Reyes, "Simple and Reliable Model for the Thermal Protection of Variable-Speed Self-Ventilated Induction Motor Drives," in *IEEE Transactions on Industry Applications*, vol. 46, no. 2, pp. 770-778, March-April 2010.
- [17] Z. Gao, T. G. Habetler, R. G. Harley and R. S. Colby, "A Sensorless Adaptive Stator Winding Temperature Estimator for Mains-Fed Induction Machines With Continuous-Operation Periodic Duty Cycles," in *IEEE Transactions on Industry Applications*, vol. 44, no. 5, pp. 1533-1542, Sept.-Oct. 2008.
- [18] P. Zhang, B. Lu and T. G. Habetler, "An Active Stator Temperature Estimation Technique for Thermal Protection of Inverter-Fed Induction Motors With Considerations of Impaired Cooling Detection," in *IEEE Transactions on Industry Applications*, vol. 46/5, pp. 1873-81, 2010.
- [19] Z. Lazarevic, R. Radosavljevic and P. Osmokrovic, "A novel approach for temperature estimation in squirrel-cage induction motor without sensors," in *IEEE Transactions on Instrumentation and Measurement*, vol. 48, no. 3, pp. 753-757, Jun 1999.
- [20] P. Tavner, Li Ran and J. Penman, "Condition monitoring of rotating electrical machines," *IET Power and Energy Series*, 2008.
- [21] P. B. Reddy, A. M. El-Refaie, K. K. Huh, J. K. Tangudu and T. M. Jahns, "Comparison of Interior and Surface PM Machines Equipped With Fractional-Slot Concentrated Windings for Hybrid

- Traction Applications," in *IEEE Transactions on Energy Conversion*, vol. 27, no. 3, pp. 593-602, Sept. 2012.
- [22] N. Z. Popov and S. N. Vukosavic, "Estimator of the Rotor Temperature of Induction Machine Based on Terminal Voltages and Currents," in *IEEE Transactions on Energy Conversion*, vol. 32, no. 1, pp. 155-163, March 2017.
 - [23] IEC 60034-1:2010, Rotating electrical machines - Part 1: Rating and performance.
 - [24] N. M. Theune et al., "Investigation of stator coil and lead temperatures on high voltage inside large power generators via use of fiber Bragg gratings," *Proceedings of IEEE Sensors*, 2002, pp. 1603-1607 vol1.2.
 - [25] F. Marignetti et al., "Fiber Bragg Grating Sensor for Electric Field Measurement in the End Windings of High-Voltage Electric Machines," in *IEEE Transactions on Industrial Electronics*, vol. 63, no. 5, pp. 2796-2802, May 2016.
 - [26] Vilchis-Rodriguez, D. S., S. Djurović, P. Kung, M. I. Comanici, and A. C. Smith. "Investigation of induction generator wide band vibration monitoring using fibre Bragg grating accelerometers." In *Electrical Machines (ICEM)*, 2014 International Conference on, pp. 1772-1778. IEEE, 2014.
 - [27] K. M. Sousa, U. J. Dreyer, C. Martelli and J. C. Cardozo da Silva, "Dynamic Eccentricity Induced in Induction Motor Detected by Optical Fiber Bragg Grating Strain Sensors," in *IEEE Sensors Journal*, vol. 16, no. 12, pp. 4786-4792, June15, 2016.
 - [28] Ecke, Wolfgang, and Kerstin Schröder. "Fiber Bragg grating sensor system for operational load monitoring of wind turbine blades." *Proc. SPIE*. Vol. 6933. 2008.
 - [29] Gao, Zhiyuan, et al. "Active monitoring and vibration control of smart structure aircraft based on FBG sensors and PZT actuators." *Aerospace Science and Technology* 63 (2017): 101-109.
 - [30] Smartfibres.com. (2017). Smart Fibres | Pioneering Optical Fibre Sensing. [online] Available at: <http://www.smartfibres.com>.
 - [31] N. Haramoni, A. S. Paterno, J. C. C. Silva and H. J. Kalinowski, "Hybrid Wavelength-Time-Domain Interrogation System for Multiplexed Fiber Bragg Sensors Using a Strain-Tuned Erbium-Doped Fiber Laser," in *IEEE Sensors Journal*, vol. 8, no. 7, pp. 1061-1066, July 2008.
 - [32] Werneck, Marcelo Martins, Regina Célia da Silva Barros Allil, and Bessie A. Ribeiro. "Calibration and operation of a fibre Bragg grating temperature sensing system in a grid-connected hydrogenerator." *IET Science, Measurement & Technology* 7.1 (2013): 59-68.
 - [33] K. d. M. Sousa, A. A. Hafner, H. J. Kalinowski and J. C. C. da Silva, "Determination of Temperature Dynamics and Mechanical and Stator Losses Relationships in a Three-Phase Induction Motor Using Fiber Bragg Grating Sensors," in *IEEE Sensors Journal*, vol. 12, no. 10, pp. 3054-61, Oct. 2012.
 - [34] J. M. Corres, J. Bravo, F. J. Arregui and I. R. Matias, "Unbalance and harmonics detection in induction motors using an optical fiber sensor," in *IEEE Sensors Journal*, vol. 6, no. 3, pp. 605-612, June 2006.
 - [35] R. Pomorski Linessio, K. d. M. Sousa, T. da Silva, C. A. Bavastri, P. F. d. C. Antunes and J. C. Cardozo da Silva, "Induction Motors Vibration Monitoring Using a Biaxial Optical Fiber Accelerometer," in *IEEE Sensors Journal*, vol. 16, no. 22, pp. 8075-8082, Nov.15, 2016.
 - [36] IEEE Recommended Practice for Thermal Cycle Testing of Form-Wound Stator Bars and Coils for Large Rotating Machines - Redline," in *IEEE Std 1310-2012 (Revision of IEEE Std 1310-1996) - Redline*, vol., no., pp.1-58, May 21 2012.
 - [37] A. Mohammad, S. Djurović, "Evaluation of fiber-optic sensing performance for embedded thermal monitoring of electric machinery wound components," 2016 5th Mediterranean Conference on Embedded Computing (MECO), Bar, 2016, pp. 72-76.
 - [38] A. Mohammed, S. Djurović, A. C. Smith and K. Tshiloz, "FBG sensing for hot spot thermal monitoring in electric machinery random wound components," 2016 XXII Int. Conference on Electrical Machines (ICEM), Lausanne, Switzerland, 2016, pp. 2266-2272.
 - [39] A. Mohammed and S. Djurović, "FBG array sensor use for distributed internal thermal monitoring in low voltage random wound coils," 2017 6th Mediterranean Conf. on Emb. Comp. (MECO), Bar, 2017, pp. 1-4.
 - [40] A. Mohammed and S. Djurović, "FBG Thermal Sensing Features for Hot Spot Monitoring in Random Wound Electric Machine Coils," in *IEEE Sensors Journal*, vol. 17, no. 10, pp. 3058-3067, May15, 2017.

- [41] Motor Design. (2017). Motor-CAD Software by Motor Design - EMag, Therm and Lab. [online] Available at: <https://www.motor-design.com/motor-cad-software>.
- [42] D. A. Staton and A. Cavagnino, "Stator winding thermal conductivity evaluation: an industrial production assessment," in *IEEE Transactions on Industrial Electronics*, vol. 52, no. 5, pp. 3509-3516, Oct. 2016.
- [43] D. A. Staton and A. Cavagnino, "winding design for minimum power loss and low cost ," in *IEEE Transactions on Industrial Electronics*, vol. 55, no. 10, pp. 3509-3516, Oct. 2015.
- [44] D. Staton, A. Boglietti and A. Cavagnino, "Solving the More Difficult Aspects of Electric Motor Thermal Analysis in Small and Medium Size Industrial Induction Motors," in *IEEE Transactions on Energy Conversion*, vol. 20, no. 3, pp. 620-628, Sept. 2005
- [45] IEEE Standard Test Procedure for Polyphase Induction Motors and Generators," in *IEEE Std 112-2004 (Revision of IEEE Std 112-1996)* , vol., no., pp.0_1-79, 2004.
- [46] A. Boglietti, A. Cavagnino, M. Lazzari and A. Pastorelli, "A simplified thermal model for variable speed self-cooled industrial induction motor," *Conference Record of the 2002 IEEE Industry Applications Conference. 37th IAS Annual Meeting (Cat. No.02CH37344)*, Pittsburgh, PA, USA, 2002, pp. 723-730 vol.2
- [47] Rao, Yun-Jiang, "In-fibre Bragg grating sensors," *Measurement science and technology* 8.4 (1997): 355.
- [48] M. Reddy, S. Kamineni, and V. Rao Pachava, "Characterization of encapsulating materials for fiber bragg grating-based temperature sensors." *Fiber and Integrated Optics* 33, no. 4 (2014): 325-335.
- [49] A.D. Kersey, M.A. Davis, H.J. Patrick, M. Leblane. "Fiber grating sensors." *Journal of lightwave technology* 15.8 (1997): 1442-1463.
- [50] "IEEE Recommended Practice for General Principles of Temperature Measurement as Applied to Electrical Apparatus," in *IEEE Std 119-1974*.
- [51] F. J. T. E. Ferreira, B. Lepretre and A. T. de Almeida, "Comparison of Protection Requirements in IE2-, IE3-, and IE4-Class Motors," in *IEEE Transactions on Industry Applications*, vol. 52, no. 4, pp. 3603-3610, July-Aug. 2016.
- [52] Austin H. Bonnett" Operating Temperature Considerations and Performance Characteristics for IEEE 841 Motors," in *IEEE Transactions on Industry Applications*, vol. 37, no. 1, July/august 2001

5.3 Paper 2:

Multiplexing FBG Thermal Sensing in Stator Windings Interior for Distributed Thermal Monitoring in In-service Electric Machines

A. Mohammed, *Student Member, IEEE*, S. Djurović, *Member, IEEE*

Abstract—This paper reports a distributed thermal sensing system for stator winding internal thermal conditions monitoring in operating low voltage electric machines (LVEMs). To achieve multiple thermal sensing points distributed radially in the interior of the stator windings structure, the proposed sensing system utilises the multiplexing feature of FBG sensing technology coupled with flexible and non-conductive sensing fibre packaging. The proposed technique enables distributed temperature monitoring with much reduced sensing volume, weight and wiring, including a key advantage of ease of in-situ sensing points repositioning post-installation. System performance was evaluated in tests on a purpose built inverter driven totally enclosed fan cooled induction machine (TEFC-IM). In addition, its potential use for thermal capacity monitoring and evaluation of the examined TEFC-IM design under deteriorated cooling capability is evaluated. The results demonstrate that the proposed sensing system is effective in providing radial peak temperatures distribution of the stator windings in operating machines under normal and abnormal operating conditions.

Index Terms—Internal distributed thermal sensing, winding temperature gradient, multiplexed FBG, TEFC-motors, cooling system capability.

I. INTRODUCTION

ON-LINE thermal monitoring and management of LVEMs are increasingly sought after. This is due to the fact that thermal status of these machines has direct impact on their performance and lifetime and is particularly pertinent where LVEMs at the core of modern and future safety critical applications, such as in traction and aerospace systems for example, are concerned [1-3]. Modern LVEMs are largely designed to provide high power density. However, increasing the power is often associated with the increase in losses and hence the dissipated heat. As consequence, the machine heat density is also increased, which almost invariably leads to higher temperature gradients within the machine structure and higher hotspot to average temperature difference [4]. The increased thermal density issue is further highlighted by the fact that most modern LVEMs are driven by power electronic converters in a wide range of speed/frequency. This can introduce additional

sources of thermal excitation due to converter harmonics, and result in a considerable increase in machine losses such as core and winding ac loss (skin and proximity losses) due to high operating speed and frequency [5-7].

The integrity of the stator winding insulation system due to thermal stresses in modern LVEMs is thus a point of concern [8]. Consequently, insulation system thermal capability improvement has been widely investigated [8-9]. In addition, novel cooling system designs have also been researched and proposed in an attempt to improve machine heat dissipation capability [10-11]. However, the insulation system thermal capability is limited by the used insulation material properties, while the proposed cooling systems usually require complex manufacturing and size and cost increase. LVEM thermal monitoring techniques that can enable distributed temperature monitoring within the machine structure and provide advanced thermal status information, in particular within the interior of the stator winding, are thus of particular interest for achieving improved machine protection and thermal management [2, 12]. Effective on-line monitoring of the winding internal temperature could also enable development of intelligent machine exploitation management systems, such as optimal overload control through better awareness of proximity to thermal limits, but also be used to enable recognition of early stages of failure, enabling remedial action to be undertaken before a catastrophic fault occurs [1,13].

Conventional techniques for on-line thermal condition monitoring of LVEMs stator windings impose considerable limitations in provision of winding thermal status awareness. Temperature estimation techniques (resistance-based estimator) only provide average winding temperature and not hot spot temperature nor temperature gradient [14-15]. Direct measurements using conventional thermal sensors (i.e. resistance temperature detectors (RTDs) or thermocouples (TCs)) can in principle provide localised winding temperature if sensors are appropriately distributed in the winding structure. However, these sensors are principally suboptimal for embedded distributed sensing solutions due to their volume and wiring lead bulk constraints; furthermore, they are limited for thermal hot spot monitoring in current carrying coils due to lack of EMI immunity and use of electrically conductive material in their structure [16-17].

The multiplexing feature of fibre optic Fibre Bragg Grating (FBG) sensors can provide multi-point sensing capability in a single flexible fibre and thus presents an attractive proposition for provision of LVEM stator winding embedded distributed sensing applications. This is enhanced by other FBG features such as small size and inherent non-conductivity and EMI immunity [18-19]. The applications of FBG temperature sensors in

LVEMs have recently received attention in number of studies including author's previous work [12, 20, 21]. The use of FBG multiplexing feature for distributed thermal sensing in LVEMs was reported in [20] and [21]. However, these studies do not consider winding sensing locations identified by relevant electric machines standards such as IEC 60034-1[22] and the associated key hotspots of interest. In addition, the reported distributed sensing designs may pose challenges in long term exploitation, since the FBG sensing heads with metallic packaging were bonded in the slot openings above the slot wedges, which is a strongly mechanically and magnetically excited area. The application of sensing thermal networks design proposed in [20] and [21] can thus be deemed limited for in-situ, winding embedded thermal monitoring, as these were conceived for surface sensing away from standard sensing locations for winding monitoring. The authors' recent work [12], reported the use of FBGs for LVEM winding internal temperature monitoring, where a number of separate in-situ single FBG temperature sensors were applied for on-line hot spot monitoring in a grid connected induction machine. The authors have recently reported a proof of principle study examining and prototyping implementation of in-situ thermal sensing arrays utilizing FBG multiplexing feature in standalone random wound test coils aimed at underpinning further exploration of development and application of these solutions for operating in-service machines [23-25].

This study designs, implements and tests a distributed thermal sensing system based on FBG multiplexing feature for on-line internal distributed winding thermal monitoring in operational LVEMs. The proposed embedded thermal sensing system is aimed at enabling much improved awareness of winding thermal conditions in LVEMs with reduced distributed sensing system requirements (i.e. wiring, installation and acquisition). A design of FBG thermal sensing array for radially distributed thermal monitoring of winding internal structure is first reported. Radial thermal sensing distribution in winding slot section is considered for the purposes of this study, since the heat generated in LVEMs is largely radially removed by conduction through the stator core and convection thorough the frame. The designed FBG array was embedded into and its performance tested on an inverter driven commercial TEFC-IM design. A series of experimental tests were conducted on the proposed sensing array design under normal and abnormal test motor thermal operating conditions. In addition to extensive testing in healthy conditions the sensing system performance was examined under TEFC-IM deteriorated cooling capability as in these conditions thermal levels within the machine structure can be unevenly distributed and thus in principle readily recognised by the embedded sensing array. To

evaluate this, the efficacy of the proposed distributed sensing system in monitoring the examined IM thermal capacity limit in a range of different deteriorated cooling system conditions was examined.

II. TEFC-MOTOR DESIGN COOLING CAPABILITY

The effect of cooling system performance on machine temperature distribution and its thermal capacity is used in this study to examine the proposed thermal sensing system performance and use. A complete or partial failure of the cooling system can give rise to uniform or uneven temperature [14,15,17]. This section discusses the operating conditions that cause variation in the cooling system performance in TEFC machines.

In TEFC-motor designs the rotor speed, available frame surface and cowling conditions are the parameters vital for effective cooling system performance. With regards the rotor speed, variable-speed operating conditions can cause cooling system performance deterioration, when operation at slower speeds [14]. The frame surface and cowling conditions can cause deterioration in the cooling system performance through [15]: blockage of cowling air inlets due to dirt, thus reducing the cooling air flow rate over the frame; coverage of frame fins and surface with built-up dust or other materials, resulting in reduction of the natural-convection cooling mode capability; and contamination, where dirt and dust build-up in windings and stator core laminations, resulting in reduction of heat dissipation based on conduction cooling mode capability. Fig. 1 shows images of deteriorated cooling system capability reported in TEFC IMs operating in paper, pulp and steel industries [14, 15]. In these applications the motors are likely to have layers of contamination over the housing and cowling where more than 50 % of air inlets can be blocked due to contamination [26]. In such condition the motor winding can be overheated even with motors operating well below nominal condition.

Critically, the deterioration of the cooling system condition generally cannot be detected or evaluated by conventional thermal protection systems [27]. For example, motor thermal overload relays are based on simplified thermal models and current measurements, which are insensitive to cooling capability variation. More importantly, these thermal models cannot accurately follow the variation of motor thermal characteristics [28]. An effective on-line distributed thermal monitoring capability in TEFC machines could therefore enable improved protection of key components under deteriorating cooling system capability.

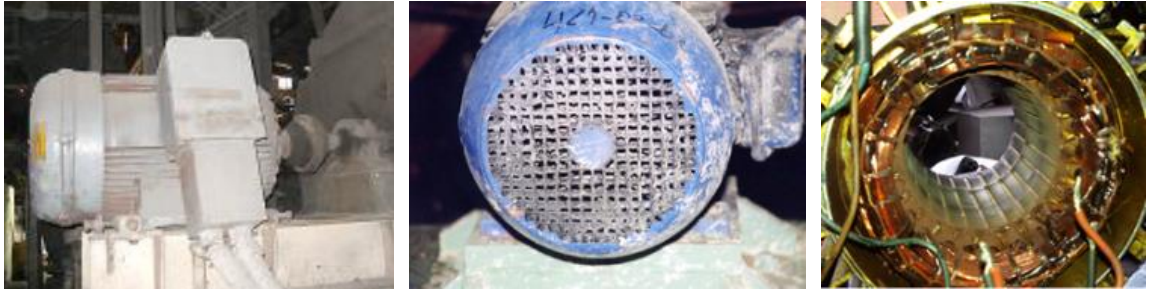


Fig. 1: Reported cases of deteriorated cooling system capability in TEFC machines operating in paper machine and pulp industries [14,15]

III. SENSING SYSTEM DESIGN AND TEST SETUP DESCRIPTION

This study employs multiple FBG sensing head multiplexing on a single fibre strand to facilitate in-situ distributed internal thermal sensing in TEFC-IM stator windings. An FBG sensing array design for monitoring radial internal thermal distribution in random wound stator windings is prototyped. The array sensor was installed in and its performance evaluated on an inverter driven laboratory induction motor.

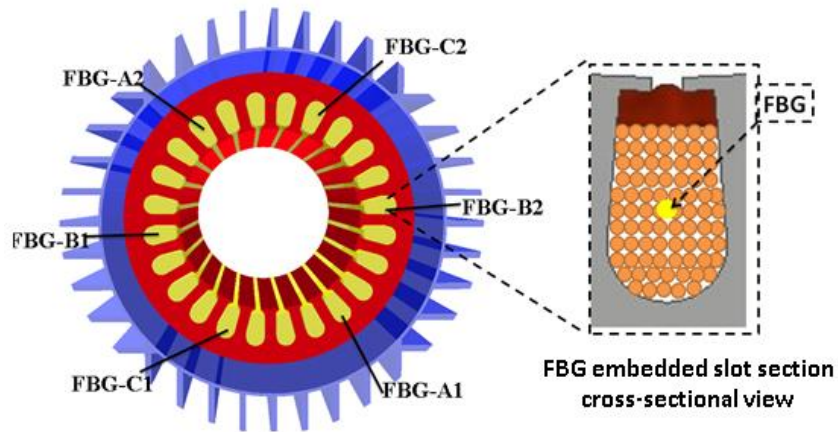
A. FBG thermal sensing array design for stator winding internal temperature radial distribution monitoring

The test motor examined in this work is a 0.55 kW, 415 V, 4 pole, 24 slot, class F, three-phase squirrel cage induction motor driven by a commercial drive in open-loop control mode. The motor stator was rewound to enable installation of an FBG sensor array to facilitate thermal monitoring of multiple hot spots internal to stator winding in a radial spatial distribution pattern. To this end, an array sensor containing six 5 mm FBG heads imprinted in bend insensitive polyamide fibre was designed; the bend insensitive fibre is used to enable optimal installation and placement flexibility, i.e. sensor fibre bending at minimal radius with less light losses. This is an important feature for the examined application, since it enables the sensing fibre to be accurately threaded through the desired configuration within the winding structure. This is further enhanced by the used flexible packaging design utilising PEEK capillary in the slot section; the rest of the fibre structure was packaged in Teflon tube for protective purposes. The technical methods used for packaging, calibration and embedding FBG sensors in the random wound stator winding followed the principles reported in author's previous work [12, 18, 23-25]. The winding was rewound to be installed with a PEEK capillary routed in the winding through the desired slot center positions which was then used to house the thermal array sensor. The array was designed to enable the positioning of individual thermal sensing FBG heads so they are located in the axial length mid position of respective winding slot sections.

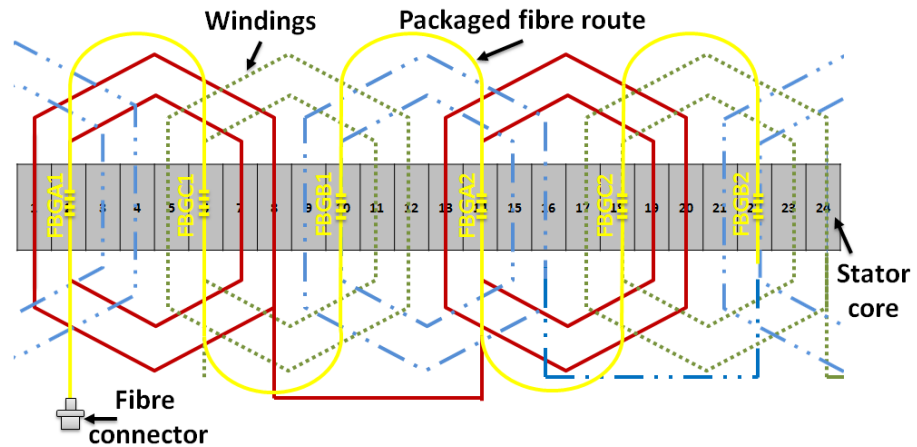
Fig. 2 illustrates: the FBG temperature array probe design (Fig. 2a), the designed radial distribution of thermal sensing points (Fig. 2b) and the embedded array sensor path within the examined TEFC-IM windings (Fig. 2c). The fibre array probe diameter including the packaging is 0.8 mm and its length is 2.3 m. The probe was designed to ensure individual FBG heads are embedded between copper conductors in the slot centre of six different slots, to enable radially distributed winding thermal hot spots monitoring; 2 FBGs are fitted per phase winding, referred to as FBG-A1 and FBG-A2 for phase A, FBG-B1 and FBG-B2, and FBG-C1 and FBG-C2 for phase B and C in further text, respectively. The spatial separation between adjacent radially distributed FBG heads was set to three slot pitches to enable uniform radial thermal sensing distribution within the examined motor geometry.



(a) FBG array design for radial distributed thermal sensing in TEFC-IM



(b) FBG sensing locations in the examined motor stator winding



(c) FBG array route within the TEFC-IM windings

Fig. 2: FBG array for distributed radial thermal sensing in TEFC-IM

B. Experimental test setup

Fig. 3 illustrates the general schematic diagram of the test system setup used in this study. The examined TEFC-IM was operated using a commercial three-phase drive system (Parker 890 SDD). In the tests, the TEFC-IM was driven using an open-loop (constant V/f) control strategy. To enable experimental emulation of desired load conditions the TEFC-IM was coupled to 0.75 kW permanent-magnet DC load machine in the tests. The FBG array thermal sensor embedded in the test motor was illuminated using tunable broadband light spectrum provided by a commercial multi-channel interrogator unit (SmartFibres SmartScan04) and monitored wavelengths processed using its proprietary LabView routine (SmartSoft). The test motor power, voltage and current signals were monitored using a three-phase power analyser (Norma D6000). For real-time three-phase current measurements Hall effect current transducers (LEM-LA25) whose outputs were acquired by an NI 9205 DAQ module and conditioned via a LabView VI routine were used. A FLIR TG-165 thermal camera was used to monitor the test machine frame surface temperature. A digital anemometer (Testo 405i) was also used to measure the air velocity along the frame axial length.

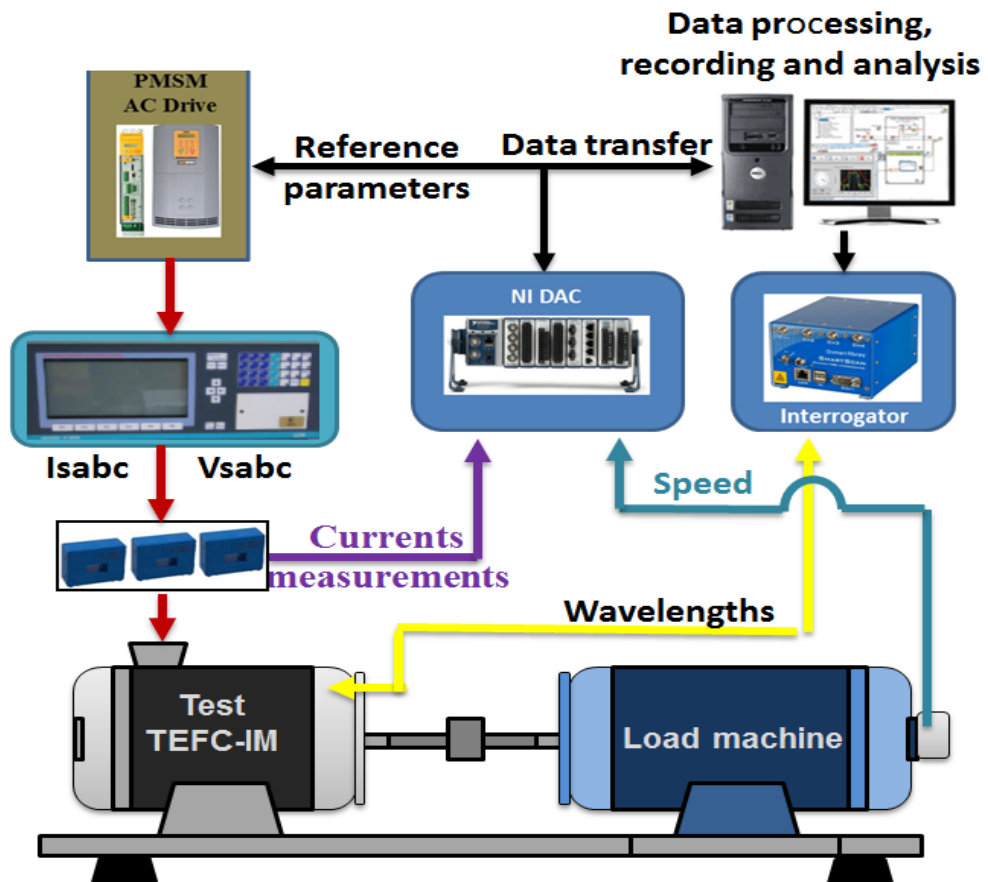


Fig. 3: Schematic diagram of the experimental test rig

IV. EXPERIMENTAL RESULTS AND DISCUSSION

The performance of the proposed thermal sensing system was first assessed in tests on the examined TEFC-IM operating in healthy conditions. Its potential for condition monitoring and thermal management purposes was then examined through: monitoring the test motor windings thermal status under even and uneven thermal conditions, and monitoring and evaluating the test motor thermal capacity limit under deteriorated cooling system performance. To enable this analysis a series of tests were undertaken in healthy and evenly/unevenly reduced cooling system capability conditions. For experiments in healthy conditions the test motor was operated at rated frequency and different load levels with the aim to test the sensor efficacy in enabling determination of the motor thermal/cooling status at nominal conditions. The experiments emulating cooling system even and uneven deterioration included testing under: partial coverage of motor frame, air inlet obstruction and variable-speed operation including the low speed region.

A. Performance evaluation in healthy conditions

In this section, the performance of the sensor array system embedded in TEFC-IM for radial thermal monitoring was examined in healthy condition (healthy cooling system). The examination was conducted by applying three an IEC-60034-1 standard defined S1 duty cycle at base frequency (50Hz) but with different load conditions (0 %, 50 % and 100 % load). The thermal measurements obtained from the sensor array (FBG heads) in tests at all applied duty cycles are shown in Fig. 4.

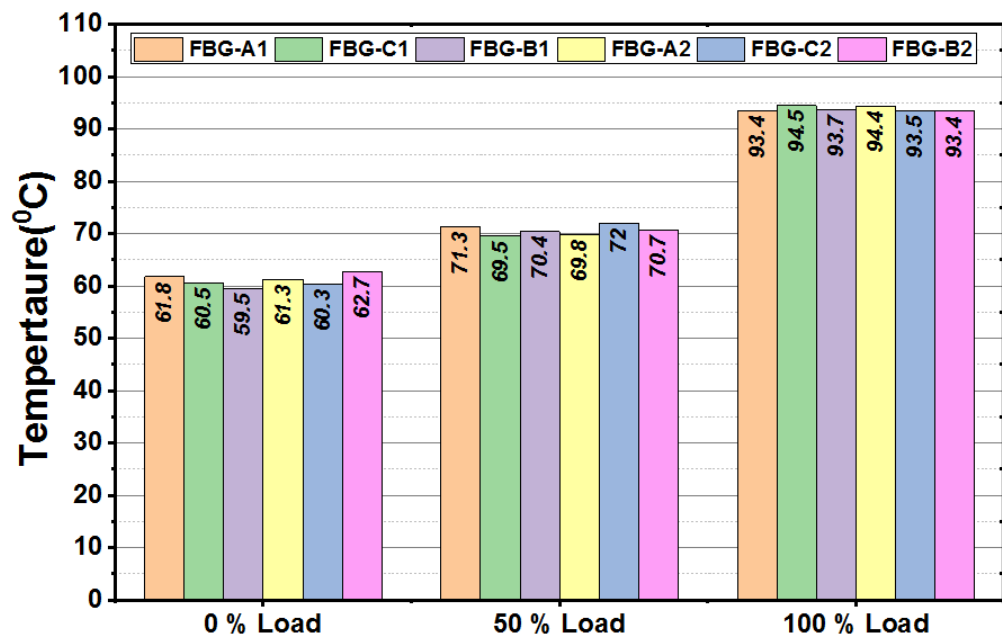


Fig. 4 Measured radial temperature distribution for different load conditions

In Fig. 4 the column heights correspond to steady-state measured temperatures by each FBG head in the array for each examined S1 cycle. The data show almost equal measured temperatures at each load condition, thus illustrating, as expected, the nearly even distribution of the radial thermal excitation levels measured in the examined motor windings under healthy conditions. The measured hot spot temperature difference at each examined load is within ≈ 3 °C. The monitored temperatures are seen to increase with load, corresponding to the expected temperature rise in the winding internal temperature with load rise: for the test motor this is seen to increase from an average of ≈ 61 °C at 0%-load to an average of ≈ 71 °C and ≈ 93.4 °C at 50%-load and 100%-load, respectively. This temperature rise level is typical for an IE1 efficiency class motor design with a class F insulation system (155 °C) and a class B temperature rise (80 °C).

As a further performance illustration Fig. 5 shows the thermal dynamic measurements obtained by the in-situ FBG array for an applied S1 duty cycle with 100%-load. The thermal measurements obtained by all array FBG heads are seen to exhibit closely similar temperature profiles typical of the S1 thermal cycle [22]. However, a low level variation in the magnitude of thermal measurements obtained by the array individual FBG sensors was observed in the dynamic measurements. It was found upon inspection that each pair of FBG heads fitted in the same phase winding reported measurements varying in an identical manner. This is illustrated in Fig. 6 showing a detailed y-axis view for 1000 seconds of the measured temperature profiles: Fig. 6a presents the temperatures measured by FBG-A1 and FBG-A2 in phase A, while Figs. 6b and c show measurements by FBG-B1 and FBG-B2 in phase B, and FBG-C1 and FBG-C2 in phase C. The closely identical low level variation of FBG pairs installed in the same phase can be explained by FBG sensing head locations: these are all situated in the centre of respective slots and between copper conductors which enhances their sensitivity to the variation in the copper loss and thus its induced heat. Copper loss induced heat is largely driven by the phase current and will thus vary with the variation in the current rms level. This is confirmed by superposing the synchronously taken phase current rms value measurement onto the corresponding thermal measurements in Fig. 6: the observed low level variation in FBG reported thermal measurement is seen to clearly follow the variation trends in the associated phase current rms value. These results clearly demonstrate the high sensitivity of the reported array sensor design to tracking distributed internal thermal conditions variation in the stator winding.

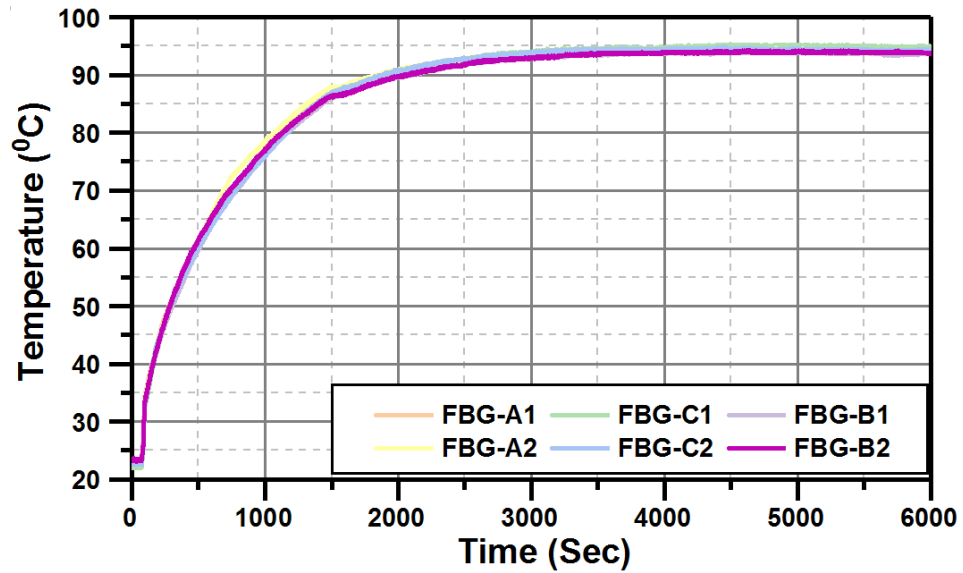


Fig. 5: Measured temperatures at 50Hz and 100% load

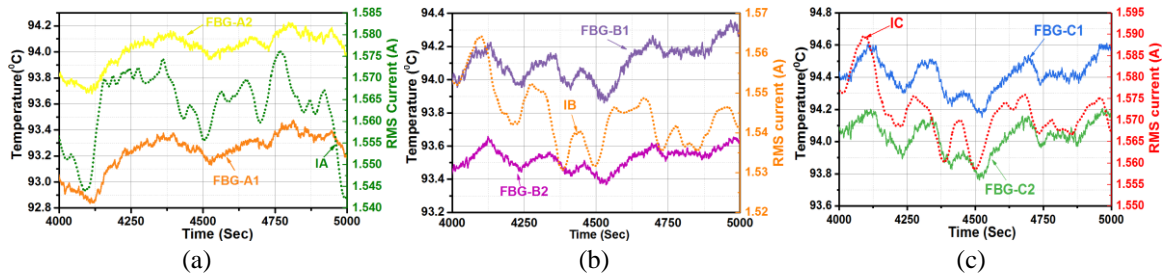


Fig. 6: Measured temperatures and phase currents at 50Hz in 100% load

To enable understanding of the cooling system performance in the examined TEFC-IM at optimum conditions and facilitate further analysis of sensing array and motor operation in deteriorated cooling capability conditions, the cooling air velocity was measured at 0%-load and nominal frequency along the test TEFC-IM axial length. At 0%-load condition the rotor rotates at maximum speed (\approx synchronous speed) and hence its cooling performance is at maximum. Fig. 7 shows the measured cooling air velocity obtained by the digital anemometer. The air velocity was measured at five points along the frame axial length and the results shown in Fig. 7. The air velocity is seen to be largely reduced along the frame as cooling air travels away from the cooling fan: the velocity reduces from ≈ 6 m/s at the cowling exit to ≈ 1.7 m/s at the drive-end cap centre. The air velocity measured at the frame axial length centre point is ≈ 2.8 m/s, which corresponds to the FBG heads location in the winding slot section axial length and will thus be used in further analysis as a reference for performance comparison under different examined cooling conditions.

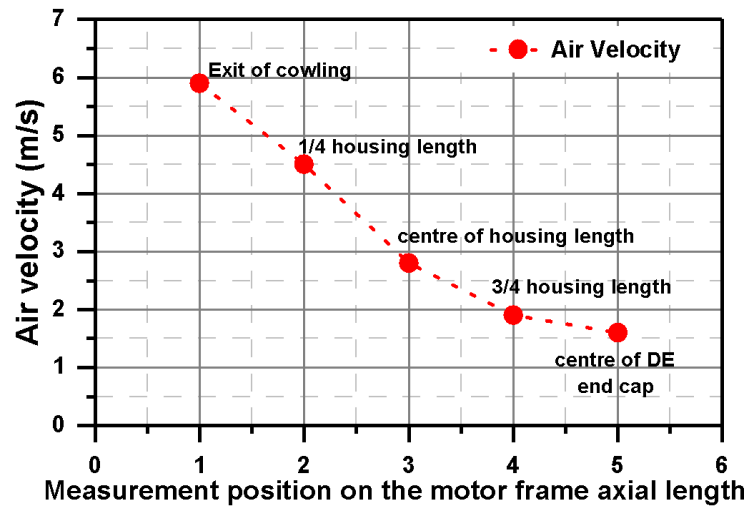


Fig. 7: Measured air velocity along the axial length of the TEFC-IM

B. FBG array monitoring performance under uneven winding heat dissipation caused by obstructed frame conditions

In this section, the proposed sensing system monitoring capability to provide information on the stator windings internal temperature in uneven windings heat dissipation conditions is examined. To introduce uneven radial heat dissipation in the test TEFC-IM its frame was partially coated. The applied partial coating deteriorates the cooling process in the coated section by forcing the cooling air to change direction and blocking its flow between the affected fins, reducing/eliminating the forced convection cooling process; the coating also introduces an additional layer between the frame surface and ambient, reducing the convection cooling process. The partial coating was practically achieved by applying appropriately dimensioned sponge segments between frame fins in the desired area. Fig. 8 shows a photograph of the coated upper frame side of the test motor; both upper and left frame sides were separately coated in tests to enable practical emulation of uneven heat dissipation in two different locations.



Fig. 8: Test motor with coated upper frame

Fig. 9 a and b shows the measured temperature rise in the winding interior obtained by the FBG array sensor in separate tests with only upper or only left frame section coated. The tests were performed at optimal cooling capability (0%-load, base frequency). The measurements show that the partly deteriorated heat dissipation results in a modulation of the winding temperature spatial distribution. The FBG heads in the array measured different levels of temperature rise, indicating a redistribution of winding hot spots. The FBGs located under the coated frame area measured higher temperature rise than other array FBGs: when upper frame side was coated the FBG-C2 and FBG-A2 recorded a temperature rise of ≈ 5.6 °C (refer to Fig. 2b for FBGs locations) while in coated left frame side test FBG-B1 reported the highest temperature rise of ≈ 6.6 °C.

The presented data demonstrate effective array sensor performance in partially obstructed frame conditions that compromise motor cooling, giving rise to thermal hot spots redistribution: this is clearly reported by the embedded array sensor. To enable further improvements in clarity of interpretation of obtained measurements Fig. 10 presents a visualisation of the measured stator temperature distributed gradient. The visualisation is based on a simple representative radial cross-section model of the examined TEFC-IM stator. The measured array FBGs temperatures are the inputs for the model. Fig 10.a shows an obvious hot spot induced in the upper side of the stator when the upper frame side is coated, while in Fig. 10b the hot spot is moved to the left side where the coating is applied. These results show how straightforward the requirements for effective interpretation of obtained measurements for diagnostic purposes are, indicating a considerable potential of the proposed sensing method to be applied in advanced electric motor condition monitoring applications.

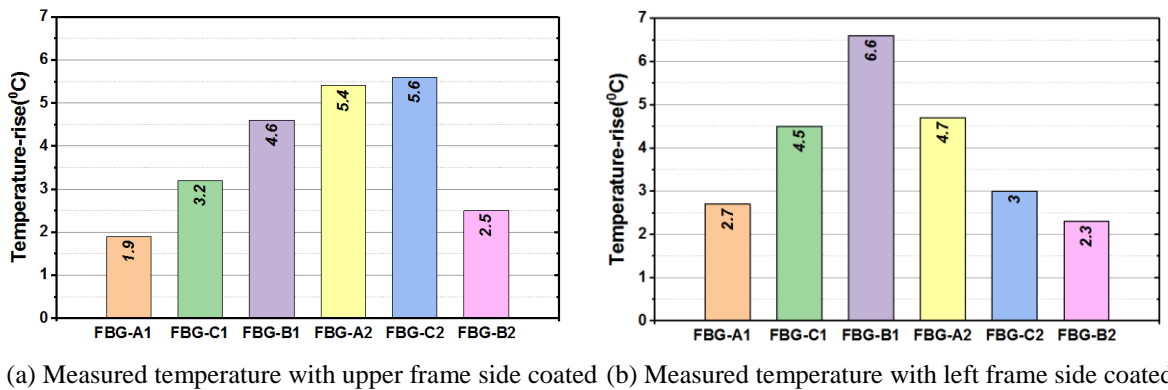


Fig. 9: Measured radial temperature in coated frame tests

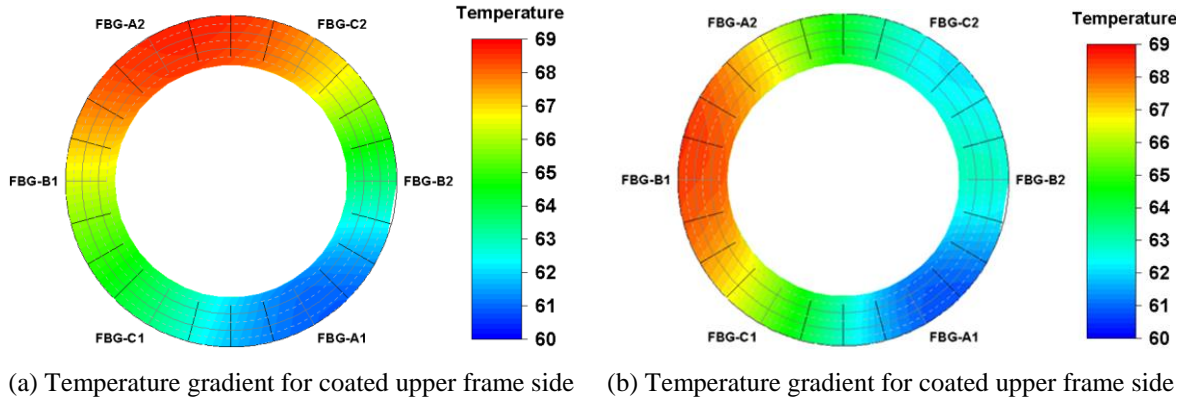


Fig. 10: Measured temperature rise in coated frame tests

C. FBG array monitoring performance under transient and uneven winding heat dissipation caused by obstructed cooling air flow

Further investigation was carried out to examine the radially distributed in-situ FBG sensing performance for condition monitoring purposes in transient and uneven heat dissipation conditions. To this end, a part of the cooling air flow exiting the cowling towards the fins was separately blocked in a chosen side section (upper, left, right). To enable array sensor performance evaluation in challenging transient conditions the blockage tests were performed during machine thermal transient from ambient to no-load thermal steady state. Fig.11 shows the cooling air blockage locations with respect to the FBG sensor locations. The air flow blockage was achieved by blocking the air exiting the cowling and entering the related fins area with appropriately shaped cardboard sections. This enabled practical emulation of uneven cooling air distribution on the frame surface and thus uneven frame cooling.

To examine system performance during cooling air flow blockage the upper, right and left side of the test motor housing were blocked in sequence during ≈ 3000 secs of thermal transient operation. The obtained thermal measurements are shown in Fig. 12. The first 650 seconds of results show the thermal measurements when frame upper side was blocked (see Fig. 11a): here FBG-C2 and FBG-A2 show the highest temperature readings as they are closest to the blockage area. Identical trends are observed in the other two blockage scenarios: when the right frame side air flow was blocked FBG-B2 and FBG-A1 reported a sudden rise in temperature while that measured by FBG-C2 and FBG-A2 drops; during left side air blockage FBG-B1 and FBG C1 recorded a temperature rise while other sensors show a drop in temperature. The experimental results illustrate high sensitivity of the in-situ array sensor to thermal variation of the winding internal temperature caused by uneven frame cooling in thermal transient conditions.

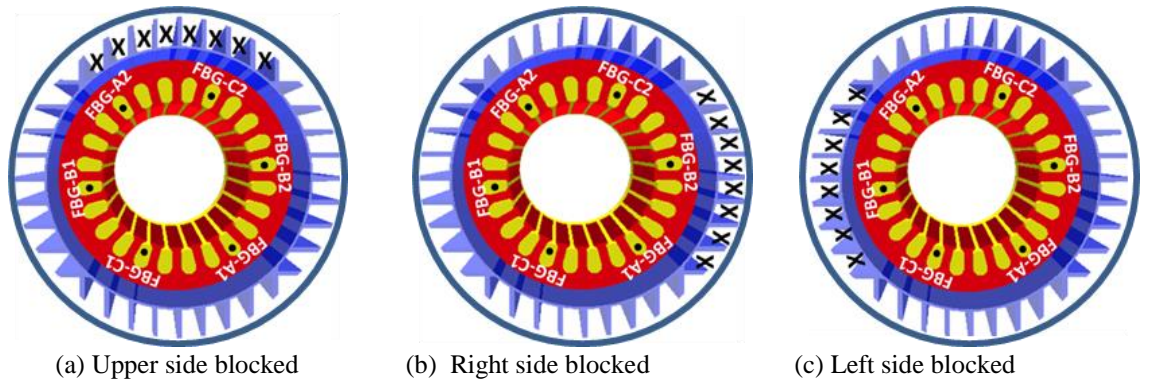


Fig. 11: Emulated cooling air blockage areas

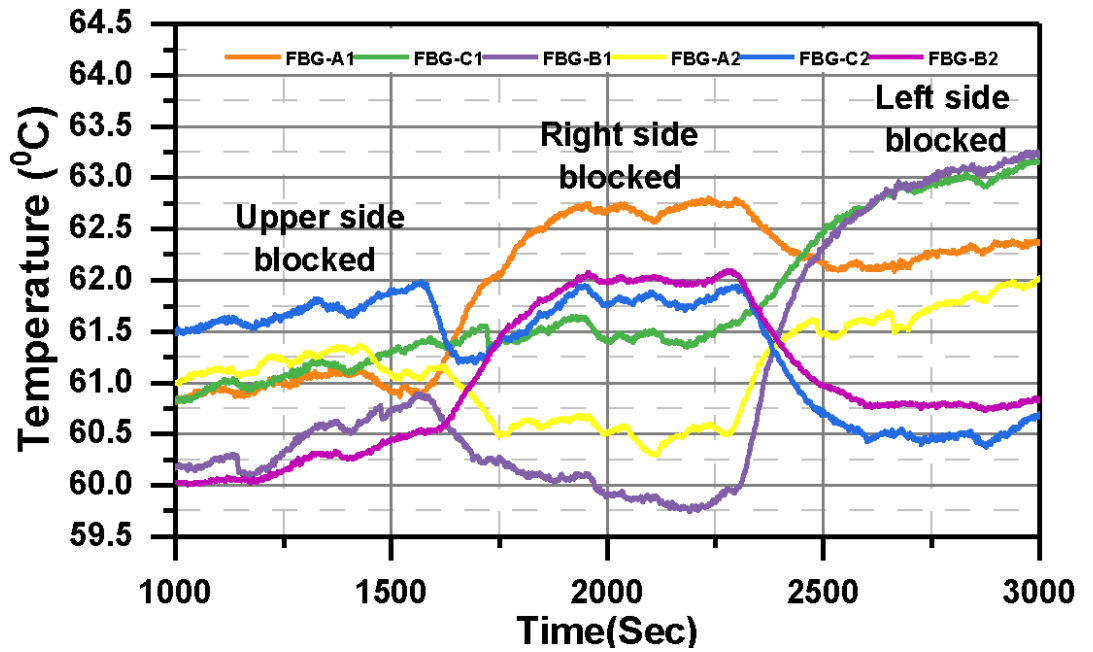


Fig. 12: Measured hot spot temperature during uneven frame cooling

D. FBG array monitoring performance under even deteriorated cooling capability caused by obstructed cowling air inlets

A partial or a full obstruction of cowling air inlets can in practical use lead to deterioration of cooling system performance. This reduces or prevents the cooling air from flowing between housing fins, which in turn reduces the heat transfer to the surrounding ambient and hence increases the internal winding temperature. Cowling air inlets obstruction is a common problem in some industrial applications such as paper and pulp industries [26, 29]. This section presents winding internal temperature measurements obtained under different scenarios of cowling inlets obstruction on the test TEFC-IM.

50% and 100% obstruction of cowling inlets was achieved by application of appropriately sized Kapton sheets. Fig. 13 shows the examined obstruction cases. The tests were performed at 0%-load conditions (1.2 Arms stator current) to ensure the test motor is

protected from destructive overheating. During testing the TEFC-IM was first operated in healthy conditions until the thermal equilibrium was reached, and the cowling inlets were then fully or partly obstructed.

Fig. 14a presents the temperature rise measured by the winding array sensor for 50% inlet coverage localized in the inner cowling area. Fig. 14b presents the measured temperature rise for total inlet obstruction. The obtained results indicate that cowling inlets obstruction can cause a considerable and uniform temperature rise in the interior of TEFC-IM windings. The temperature rise level is seen to be determined by the scale of the existing obstruction: the measured average temperature rise for a 50% obstruction is ≈ 6 °C, but rises sevenfold to ≈ 42 °C in case of a 100% obstruction. This is due to the fact that the cooling air flow velocity and thus the air flow rate are air-inlet cross-section area dependent. The three-phase stator currents were also monitored during the examined obstruction tests. This is to investigate whether there is any currents variation due to deteriorated cooling capability caused by obstructed cowling air inlets. From the obtained current measurements there were no clear changes in the currents for 50% obstruction. A small reduction in the currents during 100% obstruction test was observed however, which can be explained due to the increase in the phase resistance resulting from the high winding temperature rise caused by 100% obstruction, as shown in Fig. 14b.

To further assess this relationship, the cooling air flow velocity between frame fins at the center of the housing that corresponds to the FBG heads location in the winding slot section axial length was measured in tests and is stated in Fig. 13. The air velocity measured at the center of the housing in healthy condition (≈ 2.8 m/s, refer to Fig. 7) was found to reduce by ≈ 25 % in 50% obstruction case and by ≈ 97 % for 100 % obstruction. The measured winding temperature rise in the performed tests is thus expected to considerably increase in both magnitude and rate of change at higher load conditions, where the heat generation to dissipation rate ratio is inherently higher.

To illustrate the importance of axial sensing position in these operating conditions for effective monitoring of thermal excitation the frame thermal profile was monitored during the 100 % obstruction test using a thermal camera. The camera was used to take thermal images of the motor (left housing side profile) once in each successive 5 min period since fault application, including healthy condition. For brevity Fig. 15 shows the obtained thermal images with ≈ 13 °C temperature rise difference at the center of the frame to illustrate thermal excitation propagation caused by cowling obstruction; the temperature value measured in the frame centre is shown in the top right corner in the images.

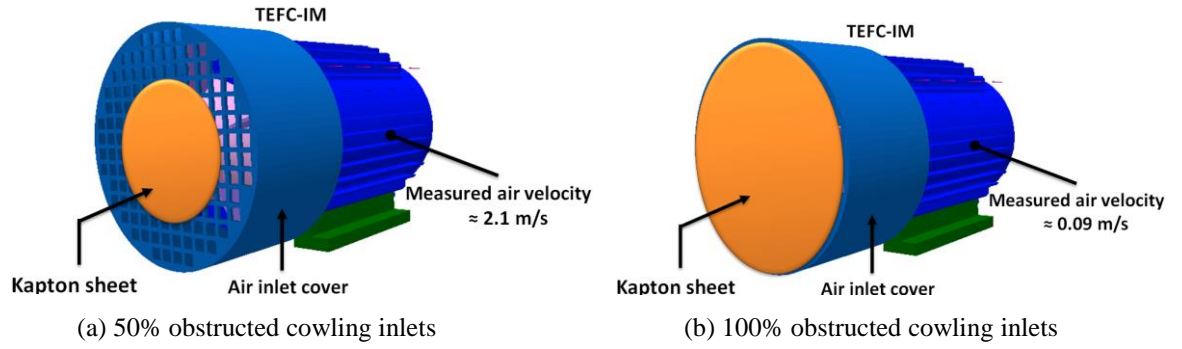


Fig. 13: Examined TEFC-IM cowling obstruction scenarios

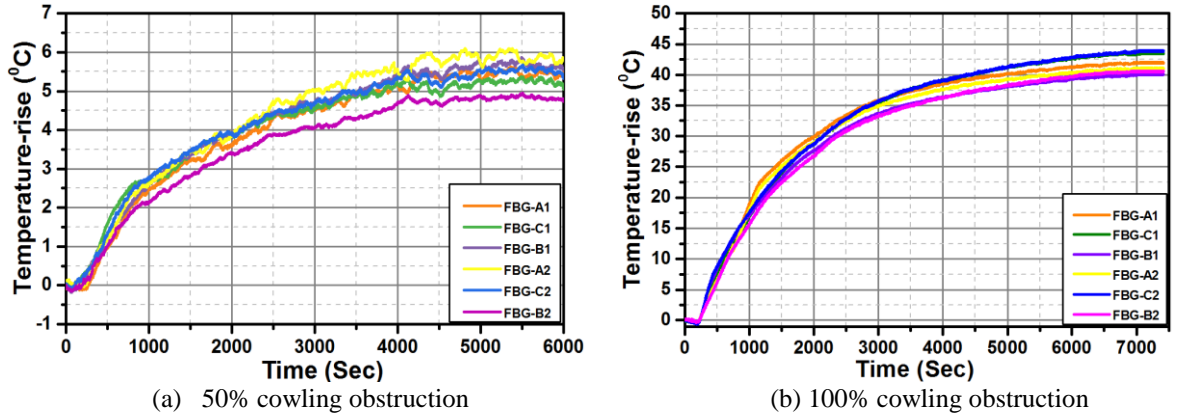


Fig. 14 Thermal measurements under obstructed air inlets

In Fig. 15a the motor was healthy and the Kapton sheet was not applied to the cowling. It can be seen that the cowling remains cooler than the motor frame, and that the frame surface temperature gradually rises towards the drive end-cap. Figs. 15b and c, taken after 100% obstruction of inlets was performed show the gradual motor frame temperature increase and hot spot generation in the frame centre, illustrated by the white area denoted by the white x in the thermal images; the cowling temperature is seen to gradually increase

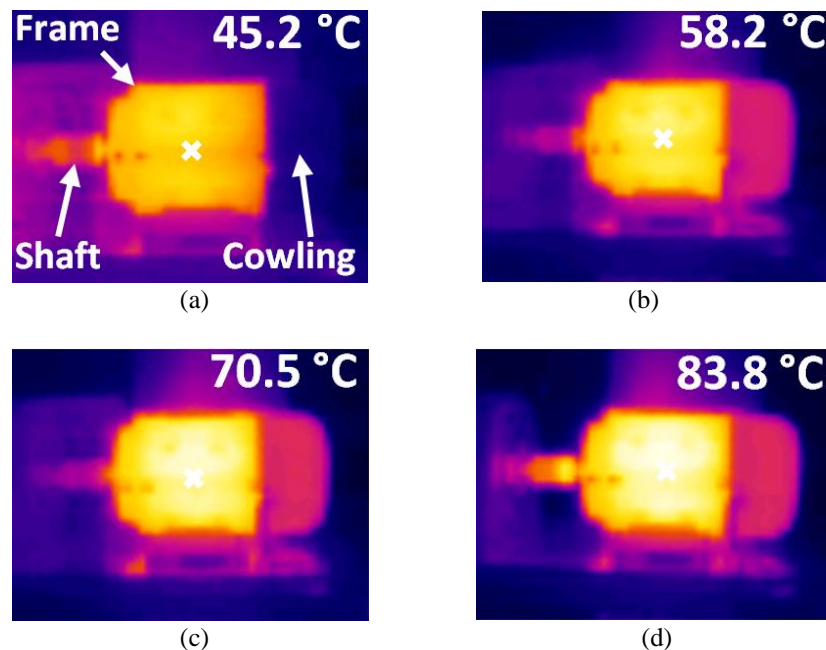


Fig. 15: Thermal images before and during 100% cowling air inlets obstruction

as well. Fig. 15d shows the thermal conditions once thermal equilibrium with full blockage is reached: the hot spot area in the frame surface centre has now become prominent with the highest temperature measured by the thermal camera of $\approx 83.8^\circ\text{C}$, which presents a $\approx 38^\circ\text{C}$ temperature rise from healthy. The obtained thermal images illustrate that machine axial centre length is the most sensitive to deteriorated cooling air flow rate in the examined machine design, further justifying the design decisions made for individual array FBG sensor positioning, as detailed in section III A.

E. FBG array use for thermal capacity monitoring and evaluation under reduced and compromised cooling system performance

This section evaluates the array sensor application for thermal capacity evaluation in variable-speed operation, including compromised cooling system performance scenarios. The cooling capability of TEFC-motors can considerably decrease in variable-speed operation involving slower speed conditions, as the cooling air velocity over the motor housing is much reduced. As consequence, the capability of dissipating the heat from the motor structure to the surrounding ambient is deteriorated. It is thus important to observe the motor heat generation and dissipation, and the resulting temperature rise in its components under such conditions. A general approach used to prevent winding overheating and thus insulation system degradation or failure in TEFC-motor designs under variable-speed operation, is to apply a large safety factor by either derating or over sizing the motor [30]. However, reliable on-line monitoring of the winding temperature and in particular the internal winding hot spot temperature can enable identification of permissible load conditions at any speed/cooling condition and thus ensure reliable awareness of thermal stress and retention of winding integrity.

To evaluate the potential of array sensor use to this end, a series of S1 duty cycles were applied to the TEFC-IM drive run at different supply frequencies (50, 40, 30, 20 Hz) in the constant V/f control operating range. To assess the performance in most relevant, highest thermal excitation level, conditions, for each assessed duty cycle/operating frequency the load torque was kept at constant nominal value. This resulted in a constant slip speed of 120 rpm and rated speeds of (1380, 1080, 780 and 480 rpm), as shown in the examined torque-speed characteristics illustrated in Fig. 16. In each evaluated test cycle the motor was operated from ambient to steady-state temperature.

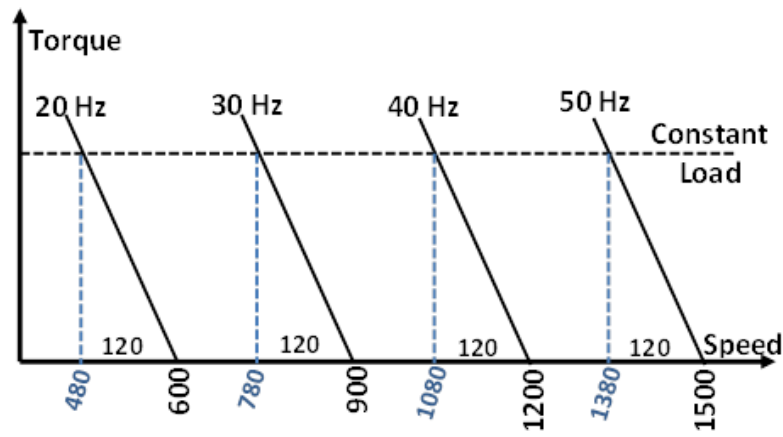


Fig. 16: Examine torque-speed characteristics in constant V/f control

The internal winding temperature measurements obtained using the radial monitoring array in all preformed tests are summarized in Fig. 17 and Fig. 18. Fig. 17 shows the measured radial temperature rise above ambient ($\approx 23^\circ\text{C}$) for all applied S1 conditions. The FBG array reported winding temperature rise radial distribution is seen to be almost uniform for all considered operating points. This is because the deterioration in cooling system performance with speed reduction is evenly applied to the entire motor structure. The internal winding temperature is seen to clearly increase with reduction of the rotor speed and the consequent reduction in the cooling system ability: at 50 Hz/1380rpm the winding internal temperature rise is $\approx 71^\circ\text{C}$, increasing with operating speed reduction to $\approx 83^\circ\text{C}$, $\approx 94^\circ\text{C}$ and $\approx 108^\circ\text{C}$ at 40Hz/1080rpm, 30Hz/780rpm and 20Hz/480rpm, respectively. The winding temperature rise in the examined motor has an approximately linear relationship with speed reduction, with an average slope of $\approx 12^\circ\text{C}$. This is illustrated in Fig. 18, which presents the FBG array average temperature measured for all examined cases.

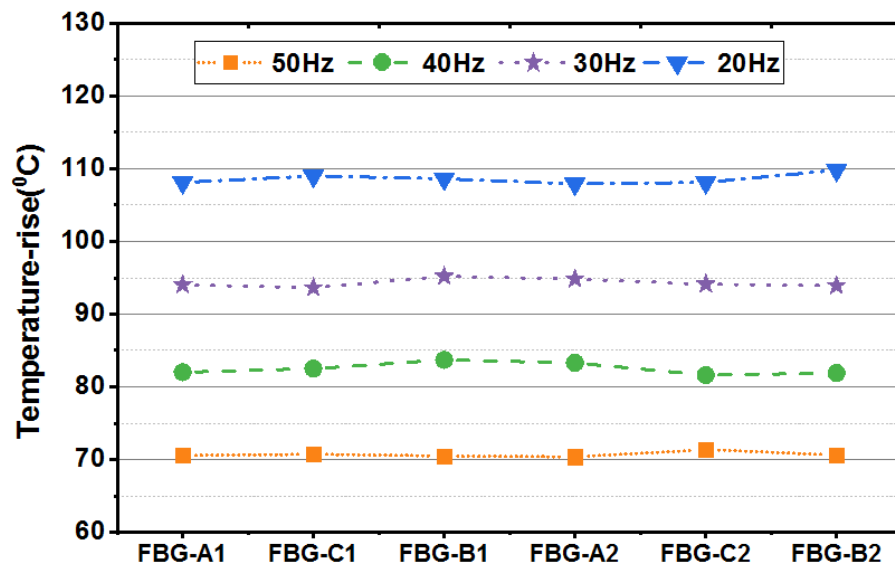


Fig. 17: Measured temperature-rise distribution at different frequency

Although torque derating was not implemented in reduced speed tests, the examined motor is seen to still be thermally capable of delivering nominal torque at all assessed reduced speed/frequency levels without exceeding the thermal limits of its insulation system. At low speed condition (480 rpm) the in-situ FBG array measures the average hot spot temperature of $\approx 131\text{ }^{\circ}\text{C}$, which is $\approx 23\text{ }^{\circ}\text{C}$ lower than the thermal limit of the examined machine insulation class ($155\text{ }^{\circ}\text{C}$). Even though the allowable maximum ambient temperature ($40\text{ }^{\circ}\text{C}$) is considered the motor can still deliver nominal torque without degrading the winding insulation [31], indicating that load derating for its usage in the examined operating range is not an absolute requirement; this awareness is made possible by the proposed in situ FBG thermal sensing array.

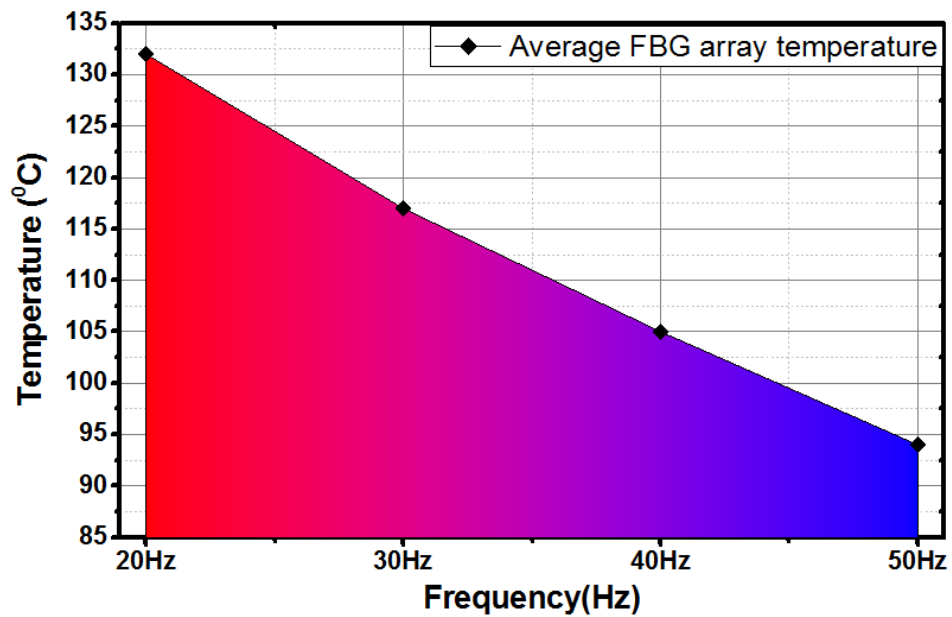


Fig. 18: Measured radial average temperature distribution at different supply frequency

V. CONCLUSIONS

Advanced monitoring techniques that can facilitate enhanced awareness of LVEM windings' thermal conditions are increasingly sought after. This paper reports a study of FBG sensing technology multiplexing feature use for enabling distributed in-situ thermal condition monitoring within LVEMs stator winding interior. An FBG array with multiple thermal sensing points was designed and embedded into the stator winding of a commercial inverter driven induction machine. The reported sensor design and application enable distributed temperature monitoring with much reduced sensing volume, weight and wiring, including the key operational advantages of in-situ sensing points repositioning ease post-installation, and accuracy of sensing point placement within the winding geometry.

The FBG array sensor thermal monitoring performance and usage for evaluating motor thermal capacity were experimentally examined in laboratory tests under different thermal conditions, including healthy motor operation and operation with even and uneven under cooling system deterioration. The obtained measurements demonstrate effective performance of the proposed sensor design and its ability to facilitate advanced understanding of windings thermal status and temperature distribution trends under various cooling system conditions.

The reported thermal sensing system has an attractive capability of conforming to an arbitrary winding geometry, which, when coupled with FBG inherent features of EMI immunity and multiplexing, presents unparalleled practical application potential for development of winding embedded 2D and 3D smart thermal monitoring schemes.

REFERENCE

- [1] Y. Yang et al. "Thermal management of electric machines" IET Electrical Systems in Transportation, pp. 104-116, 2017.
- [2] H. Zhang, "Online thermal monitoring models for induction machines," *IEEE Transactions on Energy Conversion*, vol. 30, pp. 1279-1287, 2015.
- [3] F. Ahmed and N. C. Kar, "Analysis of End-Winding Thermal Effects in a Totally Enclosed Fan-Cooled Induction Motor With a Die Cast Copper Rotor," *IEEE Transactions on Industry Applications*, vol. 53, pp. 3098-3109, 2017.
- [4] Nerg, Janne, Marko Rilla, and Juha Pyrhonen. "Thermal analysis of radial-flux electrical machines with a high power density." *IEEE Transactions on industrial electronics* 55.10 (2008): 3543-3554.
- [5] De Almeida, Aníbal T., Fernando JTE Ferreira, and Dick Both. "Technical and economical considerations in the application of variable-speed drives with electric motor systems." *IEEE Transactions on Industry Applications* 41.1 (2005): 188-199.
- [6] A. Boglietti *et al.*, "Electrical Machine Topologies: Hottest Topics in the Electrical Machine Research Community," in *IEEE Industrial Electronics Magazine*, vol. 8, no. 2, pp. 18-30, June 2014.
- [7] M. Malekpour, B. T. Phung and E. Ambikairajah, "Online technique for insulation assessment of induction motor stator windings under different load conditions," in *IEEE Transactions on Dielectrics and Electrical Insulation*, vol. 24, no. 1, pp. 349-358, Feb. 2017.
- [8] A. T. T. Hoang and Y. V. V. Serdyuk and S. M. M. Gubanski, "Electrical characterization of a new enamel insulation," *IEEE Transactions on Dielectrics and Electrical Insulation*, Vol. 21, No 3, pp. 1291-1301, 2014.
- [9] Iosif, Vadim, et al. "Assessment and improvements of inorganic insulation for high temperature low voltage motors." *IEEE Transactions on Dielectrics and Electrical Insulation*, 23.5 (2016): 2534-2542.
- [10] G. Zhu, Y. Zhu, W. Tong, X. Han and J. Zhu, "Double-Circulatory Thermal Analyses of a Water-Cooled Permanent Magnet Motor Based on a Modified Model," in *IEEE Transactions on Magnetics*, vol. 54, no. 3, pp. 1-4, March 2018.
- [11] J. Zeng, X. Sun and Z. Qian, "Thermal simulation of an oil-cooled permanent magnet synchronous motor," *2017 IEEE International Electric Machines and Drives Conference (IEMDC)*, Miami, FL, 2017, pp. 1-7.
- [12] A. Mohammed, and S. Djurovic. "Stator Winding Internal Thermal Stress Monitoring and Analysis Using in-situ FBG Sensing Technology." *IEEE Transactions on Energy Conversion*, vol. 30, (2018).
- [13] N. R. Devi, D. V. S. S. Siva Sarma and P. V. Ramana Rao, "Diagnosis and classification of stator winding insulation faults on a three-phase induction motor using wavelet and MNN," in *IEEE Transactions on Dielectrics and Electrical Insulation*, vol. 23, no. 5, pp. 2543-2555, October 2016.

- [14] M. A. Valenzuela and P. Reyes, "Simple and Reliable Model for the Thermal Protection of Variable-Speed Self-Ventilated Induction Motor Drives," in *IEEE Transactions on Industry Applications*, vol. 46, no. 2, pp. 770-778, March-april 2010.
- [15] Zhang, Pinjia, et al. "Impaired-cooling-condition detection using DC-signal injection for soft-starter-connected induction motors." *IEEE Transactions on Industrial Electronics* 56.11 (2009): 4642-4650.
- [16] G. C. Stone, "Condition monitoring and diagnostics of motor and stator windings – A review," in *IEEE Transactions on Dielectrics and Electrical Insulation*, vol. 20, no. 6, pp. 2073-2080, December 2013
- [17] M. J. Picazo-Ródenas, J. Antonino-Daviu, V. Climente-Alarcon, R. Royo-Pastor, and A. Mota-Villar, "Combination of noninvasive approaches for general assessment of induction motors," *IEEE Transactions on Industry Applications*, vol. 51, pp. 2172-2180, 2015.
- [18] A. Mohammed and S. Djurović, "FBG Thermal Sensing Features for Hot Spot Monitoring in Random Wound Electric Machine Coils," in *IEEE Sensors Journal*, vol. 17, no. 10, pp. 3058-3067, May15, 2017.
- [19] G. Ma, C. Li, R. Mu, J. Jiang and Y. Luo, "Fiber bragg grating sensor for hydrogen detection in power transformers," in *IEEE Transactions on Dielectrics and Electrical Insulation*, vol. 21, no. 1, pp. 380-385, February 2014.
- [20] K. d. M. Sousa, A. A. Hafner, H. J. Kalinowski and J. C. C. da Silva, "Determination of Temperature Dynamics and Mechanical and Stator Losses Relationships in a Three-Phase Induction Motor Using Fiber Bragg Grating Sensors," in *IEEE Sensors Journal*, vol. 12, no. 10, pp. 3054-61, Oct. 2012.
- [21] Fabian, Matthias, et al. "Comprehensive Monitoring of Electrical Machine Parameters Using an Integrated Fiber Bragg Grating-Based Sensor System." *Journal of Lightwave Technology* 36.4 (2018): 1046-1051.
- [22] IEC 60034-1:2010, Rotating electrical machines - Part 1: Rating and performance.
- [23] A. Mohammed, and S. Djurović. "A study of distributed embedded thermal monitoring in electric coils based on FBG sensor multiplexing." *Microprocessors and Microsystems* 62 (2018): 102-109.
- [24] K. Tshiloz, A. C. Smith, A. Mohammed, S. Djurović and T. Feehally, "Real-time insulation lifetime monitoring for motor windings," *2016 XXII International Conference on Electrical Machines (ICEM)*, Lausanne, 2016, pp. 2335-2340.
- [25] A. Mohammed and S. Djurović, "A Feasibility Study of Embedded FBG Thermal Sensing Use for Monitoring Electrical Fault Induced Thermal Excitation in Random Wound Coils," *9th IET international Conference on Power Electronics, Machines and Drives (PEMD)*, 2018.
- [26] O. Shield, "Effects of Pulp on Electric Motors," Available: www.orangeshield.com/docs/TAPPI-Pulp-Report.pdf
- [27] R. M. Tallam et al., "A Survey of Methods for Detection of Stator-Related Faults in Induction Machines," in *IEEE Transactions on Industry Applications*, vol. 43, no. 4, pp. 920-933, July-aug. 2007
- [28] Sang-Bin Lee and T. G. Habetler, "A remote and sensorless thermal protection scheme for small line-connected ac machines," in *IEEE Transactions on Industry Applications*, vol. 39, no. 5, pp. 1323-1332, Sept.-Oct. 2003.
- [29] Albers, Timothy, and Austin H. Bonnett. "Motor temperature considerations for pulp and paper mill applications." *Pulp and Paper Industry Technical Conference, 2002. Conference Record of the 2002 Annual.* IEEE, 2002.
- [30] Austin H. Bonnett" Operating Temperature Considerations and Performance Characteristics for IEEE 841 Motors," in *IEEE Transactions on Industry Applications*, vol. 37, no. 1, July/august 2001.
- [31] NEMA Motor-Generator Standard. MG-1-2014.

Chapter 6: *Winding Fault Detection and Diagnosis Based on Fault Induced Thermal Signature Monitoring*

6.1 Introduction

This chapter reports the use of the in-situ FBG thermal sensing system (examined in **Chapter 4** and **Chapter 5**) for winding fault diagnosis. Winding fault is a common in LVEMs, and can result in catastrophic damage and extended downtime for maintenance as discussed in **Chapter 2**. Its diagnosis is thus important and particularly at incipient stages where reliable diagnosis remains a challenge.

The chapter consists of two papers. The second author contribution to both papers is performing a technical and academic writing review and technical guidance during this work. The third author contribution to paper number 1 is the assistance in the experimental work of conducting ITSCF tests.

Paper 1: the content of this paper has been published in *IEEE Transactions on Industrial Electronics* [57]. The main contributions of this paper are:

- An experimentally validated novel study on on-line detection of incipient stator short circuit faults in an inverter driven random wound IM, based on in-situ monitoring of windings' fault thermal signature using a slot embedded FBG temperature sensor.
- A new analysis of IM winding thermal and electrical characteristics at the onset of inter-turn faults that enables better understanding of fault diagnostic requirements and provides a general map for determining winding fault induced thermal signatures under different operating conditions.

Paper 2: The content of this paper has not been submitted. The main contribution of this paper is:

- It proposes an optimised stator winding thermal monitoring scheme, based on an end-winding embedded FBG thermal sensing ring for stator winding uniform and localised overheating condition monitoring. This is key for enabling stator winding protection, health monitoring and fault diagnostics. The proposed thermal sensing scheme was examined for winding fault diagnosis in PMSMs with stranded winding configuration.

6.2 Paper 1:

Stator Winding Fault Thermal Signature Monitoring and Analysis by In-situ FBG Sensors

A. Mohammed, *Student Member, IEEE*, Juan I Melecio, S. Djurović, *Member, IEEE*

Abstract—Winding short circuit faults are recognised as one of most frequent electric machine failure modes. Effective on-line diagnosis of these is vital but remains a challenging task, in particular at the incipient fault stage. This research reports a novel technique for on-line detection of incipient stator short circuit faults in random wound electrical machines based on in-situ monitoring of winding thermal signatures using electrically non-conductive and electromagnetic interference immune Fibre Bragg Grating (FBG) temperature sensors. The presented method employs distributed thermal monitoring, based on the FBG multiplexing feature, in a variety of points within windings, in proximity to thermal hot spots of interest that arise from the fault. The ability of the proposed method to enable fault diagnosis through identification of fault induced localised thermal excitation is validated in steady-state and transient operating conditions on a purpose built inverter driven induction machine test facility. The results demonstrate the capability of unambiguous detection of inter-turn faults, including a single shorted turn. Furthermore, the winding thermal and electrical characteristics at the onset of the inter-turn fault are examined and correlated enabling better understanding of fault diagnostic requirements.

Index Terms—Inter-turn fault detection, inverter driven induction motor, in-situ thermal monitoring, FBG sensor.

I. INTRODUCTION

Winding short circuit faults are one of most commonly occurring faults in electrical machines, especially in those utilising random wound winding configurations. Short circuit related faults are reported to account for ≈ 30 -40% of total machine failures [1,2]. The main cause of these is insulation material breakdown, occurring as a result of a combination of stresses (thermal, electrical, mechanical and environmental) acting on windings during their operating life [1]. This insulation breakdown results in an inter-turn short circuit fault (ITSCF) which in turn gives rise to further excessive thermal excitation in windings and ultimately leads to their failure. In-service detection of incipient stage ITSCF is thus vital as it could enable prevention of critical damage and reduction of the associated repair costs and production losses.

Research on stator winding ITSCF detection has received significant attention and a range of diagnostic techniques has been suggested in literature [1-9]. These in general rely on non-invasive on-line monitoring and analysis of electrical and/or electromagnetic quantities such as stator current, voltage, impedance or flux. The reported techniques can however impose significant drawbacks in diagnostic capability and are particularly limited in effective recognition of early fault stages; for instance, minor changes in operating conditions such as load variation, supply unbalance and inherent asymmetry, in particular at non-stationary conditions, can greatly affect their diagnostic performance [1,10]. Additional drawbacks are posed by the challenges of fault location and fault severity diagnosis [10]. To overcome these, advanced processing of diagnostic signals is required, further complicating the implementation of the diagnostic process [3].

Thermal monitoring methods for ITSCF detection have not been widely investigated, mainly due to unavailability of adequate in-situ winding thermal sensing technology and the lack of understanding of fault induced thermal stress propagation. A few studies examine ITSCF diagnosis using thermographic analysis, where thermal imaging is used to monitor the machine frame in order to observe thermal hot spots induced by winding faults internal to machine structure [11-13]. While this approach does not allow fast recognition of in-situ fault effects and hence rapid and timely diagnosis, nor the recognition of incipient fault stages, it has been used to detect ITSCF in induction machines (IMs) with fault severity of 16% and above [11-13].

The duration of the transition period from the instant of ITSCF onset to that of machine breakdown is still not fully understood [4,7,9]. A model study in [8] has shown that an ITSCF in a 15 kW IM could develop to phase-to-ground fault in less than 5 seconds. However, the model reported in [8] assumed that there is no heat transfer from the faulty coil to the ambient, which may not be the case in a practical fault scenario. [14-16] report experimental studies of realistic, practical inter-turn fault conditions in IMs rated at 3.7 kW, 2.2 kW and 11 kW, respectively. The three studies recorded different transition times from the incipient inter-turn fault stage to phase-to-ground fault: in [14], the IM takes about 20 seconds to breakdown, while in [15] the recorded breakdown time was 5.5 hours and in [16] 15 minutes. While there are many complex factors depending on machine's design, rating and operating conditions that determine the fault transition period, it can generally be concluded that the short circuit fault propagation time is challenging to evaluate and can vary from seconds, to hours [14-16] or even days and months [4, 7]. However, the excessive winding thermal hot spots induced by this type of fault and their

propagation can be considered the main factor that characterises this transition. This localised excess heat is rapidly induced in the shorted turns and thus, if monitored appropriately, could be used as an effective diagnostic tool. In fact, knowledge of the fault induced thermal excitation can be used not only for fault detection, but can also help estimate the time to reach critical insulation breakdown temperatures of the adjacent healthy turns, which is crucial to determine the time available for corrective action to be applied. Such diagnostic knowledge would be highly valuable in critical electrical machine applications such as in air and ground electric vehicles or offshore wind generation.

This paper reports a proof of concept study of a new technique for on-line detection of ITSCFs in random wound electrical machines based on winding in-situ thermal signature monitoring using coil embedded Fibre Bragg Grating (FBG) temperature sensors. FBG sensing technology provides a number of advantages over electrical machine conventional sensing technologies, making it an attractive candidate for facilitating operative condition monitoring solutions. FBG sensors are characterised by inherent electromagnetic interference (EMI) immunity, robustness, multiplexing, small size and multi-physical sensing features [17,24]. From the machine application point of view, FBG sensing is an invasive monitoring technique, thus the cost and complexity of installation could potentially be considered as one of its drawbacks. In principle the FBG monitoring system architecture follows the general structure of commercial condition monitoring systems used for electrical machines/drive trains, requiring a suite of dedicated sensors and a hardware device to enable interpretation, monitoring and analysis of sensed diagnostic signals [25]. The FBG sensor cost is currently comparable to cost of conventional thermal sensors used in electric machine applications, but the required FBG interrogator systems remain relatively costly. FBG sensing technology has already found use in aerospace and wind industries where its features have contributed to development of more effective monitoring systems [25-27]. The application of FBG thermal sensors in electric machines has recently been examined and techniques developed and validated that enable effective FBG thermal sensing application within random wound windings [20-24].

In this work a series of experimental tests were carried out to examine the potential of using targeted, in-situ, FBG enabled thermal monitoring for diagnosis of ITSCF with a particular focus on the critical, incipient fault stages. To this end, a number of FBG temperature sensors were embedded in points of interest of an inverter driven test induction machine stator windings. The test machine was rewound to enable the installation of in-situ sensors and its windings modified to facilitate practical emulation of

an ITSCF. The diagnostic potential of in-situ monitored ITSCF thermal signature was examined in steady-state and transient operating conditions and shown to be superior to that provided by conventional current signature analysis; the method enables effective diagnosis of early stage ITSCF (i.e. single turn), as well as fault severity diagnosis and fault location identification. In addition, the electrical and thermal characteristics of stator windings during an inter-turn fault event are examined and correlated and it was shown that clearer understanding of these can significantly contribute to fault diagnostic reliability.

II. ANALYSIS OF ITSCF ELECTRO-THERMAL FEATURES

Winding faults almost invariably propagate from an ITSCF, when insulation breaks down between two adjacent turns of the same coil; the direct electrical contact between these causes a high circulating current, which gives rise to localised excessive heat in the faulty winding part, i.e. in the shorted turns [2-3]. The resulting high temperature in turn degrades the insulation of neighbouring healthy turns, thus involving more turns in the fault as a consequence. If the ITSCF is not detected and remedied in its early stages, this process propagates and deteriorates the surrounding healthy winding insulation [4-5], initiating further fault expansion and leading to more significant, phase-to-phase or phase-to-ground faults, and ultimately machine failure. Detecting the fault in the incipient stage is therefore key in avoiding potentially catastrophic damage to operating machines. The electro-thermal features of an ITSCF are analysed in this section as an enabler to understanding the requirements and challenges of its diagnosis based on thermal and/or electrical signal analysis.

A. *Electrical characteristics of inter-turn fault*

The electrical circuit diagram in Fig. 1 illustrates a three-phase stator winding under the ITSCF condition assumed in phase A. The ITSCF modifies the faulty phase into two separate electrical circuits: one formed by the healthy winding portion and the other by the winding conductors encompassed by fault. The resistances and inductances of the healthy and faulty circuits depend on the faulty, N_F , to healthy, N_H , turns number ratio, μ , where $\mu = N_F \setminus N_H$ [7].

The two circuits are electrically independent and magnetically coupled and are established as follows: when the ITSCF occurs, the shorted turns physically act as a shorted coil placed in the machine main magnetic field path, as illustrated in Fig.2a. An electromotive force (EMF) (E_{a2}) is thus induced in these driving a fault current (I_{a2}) [8].

Due to Lenz's law, the fault current establishes a flux opposing that of the main field, consequently reducing it along the faulty coils, and in turn reducing E_{a2} . Another effect reducing E_{a2} is the main magnetomotive force (MMF) reduction due to fault induced reduction of ampere/turns in the faulty phase [8-9]. As illustrated in Figs. 2a-b, the faulty turn current, I_{a2} , is in opposite direction to healthy winding portion current, I_{a1} , and is determined by the impedance of the short circuited turns and E_{a2} [5]. I_{a2} can thus vary significantly and is challenging to determine; recent studies have reported it possible for it to be up to 12 times the magnitude of machine rated current [6]. I_{a1} on the other hand is mainly affected by the phase impedance which varies with μ .

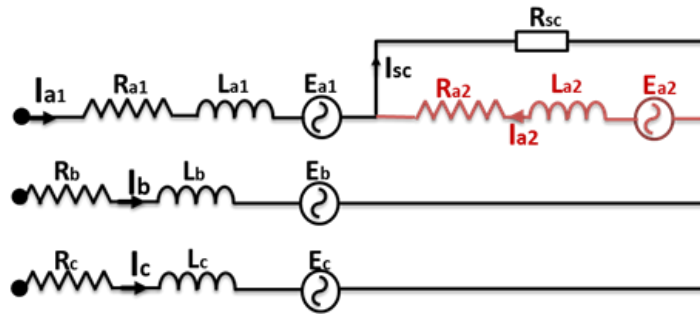


Fig. 1: IM stator winding under inter-turn fault

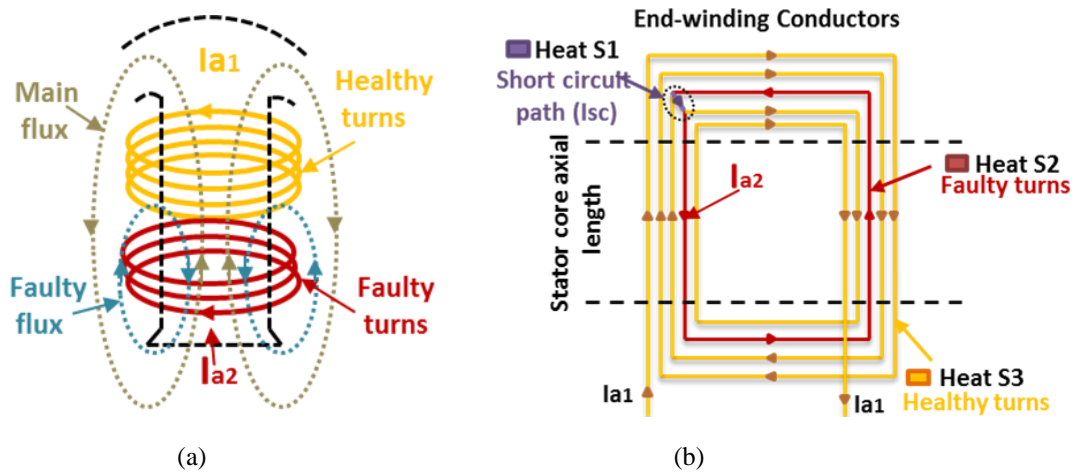


Fig. 2: A winding coil with inter-turn fault

ITSCF detection using electrical or magnetic signals generally depends on identifying effects caused by two distinct electro-magnetic features of an ITSCF event [28]: the first is the air-gap field distortion caused by shorted turns and the consequent MMF reduction, while the second is the fault induced phase impedance asymmetry giving rise to phase currents imbalance. However, in an ITSCF low severity events encompass a single or a few turns, which characterise the fault incipient stage, these effects are typically insignificant. This illustrates the inherent complexity of incipient ITSCF detection using electro-magnetic signature analysis.

B. Thermal characteristics of inter-turn fault

1) Inter-turn fault induced heat thermal analysis

In healthy conditions, the heat generated in the stator winding is a result of the ohmic losses, determined by winding current and resistance and dissipated as heat to the surrounding ambient. In a conventional balanced machine, the ohmic losses induced by each stator phase winding are, in general, almost equal. This results in an even generation and dissipation of heat in the winding, and hence an even temperature distribution. In ITSCF conditions, due to the high fault current circulating in the shorted turns, a faulty coil will generate higher ohmic loss compared to healthy coils. This will result in a localised thermal hot spot in the winding where the fault is occurring. Therefore, understanding the thermal behaviour of the faulty coil is key to understanding the thermal monitoring requirements for fault diagnostic purposes.

The ITSCF starts when local insulation breakdown occurs between two adjacent turns in a coil. This breakdown can occur at any location in the coil structure, i.e. in the coil sides (slot section) or in the coil ends (end-winding section). At the breakdown location a high short circuit current (I_{sc}) flows between the shorted turns, that is generally equal to the sum of the phase current and the shorted turns' current [8], illustrated in Fig. 1. The I_{sc} and the contact resistance (R_{sc}) between shorted turns' generate heat at the contact location in the faulty coil, denoted as heat source 1 (Heat S1). The second source of heat (Heat S2) induced in the faulty coil arises due to high current (I_{a2}) in the shorted turns and their resistance (R_{a2}); Heat S2 acts along the shorted turn length and hence along the faulty coil structure. The healthy turn's resistance (R_{a1}) and current (I_{a1}) determine a third source of heat (Heat S3). Table I summarises the calculation of heat loss components in a coil under healthy and ITSCF conditions.

Table. I : Heat loss calculation in healthy and faulty coils

Healthy coil	$\text{Heat} = (I_{\text{phase}})^2 \times R_{\text{Coil}}$	(1)
Faulty coil	$\text{Heat S1} = (I_{sc})^2 \times R_{sc}$	(2)
	$\text{Heat S2} = (I_{a2})^2 \times R_{a2}, \quad R_{a2} = \mu R_{\text{Coil}}$	(3)
	$\text{Heat S3} = (I_{a1})^2 \times R_{a1}, \quad R_{a1} = (1 - \mu)R_{\text{Coil}}$	(4)

The heat loss in the faulty coil is seen to be defined by a range of quantities, such as I_{a1} , I_{a2} , I_{sc} , and μ . These will vary with fault severity and operating condition variation, e.g. fault propagation and changes in motor load and/or speed/frequency. As the fault induced heat loss largely determines the fault induced thermal signature, the thermal signature of a

faulty coil will also vary with fault severity and load and speed variation. In general, as the winding fault propagates (i.e. fault severity is increased) the number of shorted turns N_F , and hence μ , increases: this leads to increase of the shorted turns induced voltage E_{a2} , and consequently the shorted turns current I_{a2} . The faulty coil healthy turns N_H are consequently reduced, resulting in a reduction of the healthy turn's resistance R_{a1} . The reduction in R_{a1} increases the phase current I_{a1} and hence the loss in the healthy coils of the faulty phase. At high fault severities this can result in an uneven temperature distribution between winding phases and increased thermal stress in the healthy part of the winding. On the other hand, with load variation (i.e. load increase) the winding operating temperature increases due to increase in the phase current I_{a1} and the heat loss it generates. Consequently, R_{a2} and R_{a1} will also increase due to copper electric resistance temperature dependency. The change in these resistances will yield a change in corresponding currents, I_{a1} and I_{a2} , and the associated fault induced heat losses. Finally, variable speed operation such as is applied under variable frequency drive motor control, can directly affect the shorted turn induced voltage E_{a2} . The variation in E_{a2} with speed variation will lead to variation in I_{a2} and hence in fault induced heat. In summary, understanding the heat losses dependence on fault severity and machine operating conditions is valuable for thermal signature based diagnostics. In this respect, identification of consistent thermal signature variation patterns with fault and load variation would underpin consistent thermal signature based winding fault diagnosis for an arbitrary machine design and operating condition.

2) *Inter-turn fault induced heat monitoring requirement*

From the point of in-situ thermal monitoring and instrumentation for winding fault diagnostic purposes, Heat S1 is extremely challenging to monitor as it can occur at any point of the winding structure. In addition, the fault contact resistance R_{sc} can be assumed very small and is hence generally not expected to be the dominant component of thermal excitation originating from a fault event. Heat S2 generated by I_{a2} is generally expected to produce a more significant contribution to total fault induced thermal excitation, and therefore a more significant detriment to winding health, and the neighboring healthy turns in particular. The resulting excess Heat S2 acts in the shorted turns along the coil length (see Fig. 2b). While monitoring end winding temperature is common and specified in thermal management standards of electrical machines [29], the end windings generally act as a single thermal component combining all coil ends and thus any temperature measurement in these largely yields an average temperature reading of all coil ends temperatures. Monitoring thermal changes induced at outset of an ITSCF event in end-

windings would therefore not be effective for diagnostic purposes. Monitoring thermal excitation in any of the faulty coil sides would on the other hand enable the measurement of fault induced thermal excitation, as this is localised within the slot section and acts along the core axial length; this approach would facilitate in-situ thermal monitoring enabled ITSCF fault diagnosis.

In the slot section, the fault can occur at any position, thus understanding the sensing placement in the slot cross-section that yields optimal performance is key. From the heat transfer point of view, the slot centre has the highest sensitivity to any thermal variation in the slot area. This is due to the fact that the heat in the slot transfers from conductors towards slot walls, to the adjacent teeth and core yoke. However, as result of the slow heat transfer process between the winding and the stator core structure surrounding it due to the presence of the slot liner, a temperature gradient is generated in the slot section with highest temperature in the slot centre. Therefore, in case where any additional heat source is induced in the heat transfer path between the slot centre (hot spot) and slot walls, such as in case of an ITSCF, will slow the heat transfer rate from the slot centre and hence increase its temperature. Consequently, enabling thermal monitoring in the slot section hot spot location would provide the most effective means to detect fault induced thermal variation, short of installing in-situ sensors to cover the entirety of the slot cross sectional area which would be prohibitive in practical applications. Furthermore, locating the thermal sensor in the slot centre between the copper conductors ensures it is positioned at an optimal point in terms of distance from all possible fault locations in the slot winding and therefore yields optimal recognition response of the fault thermal signature assuming use of a single sensor. In addition to this, for healthy motor operation, monitoring of winding thermal hot spots is key to understanding efficacy of machine utilisation and can enable development of winding life estimation routines [30]. A single thermal sensing point in the slot centre hot spot location would therefore enable recognition of the ITSCF thermal signature.

To understand thermal behaviour in a single slot section Table II defines the heat loss under healthy and faulty conditions. The total heat loss in the slot section under fault conditions can be calculated based on the current in the healthy and faulty turns and the conductor electrical resistance per core axial length ($R_{\text{slot-axial length}}$). Based on the above analysis, the ability to measure even small excursions in winding slot section temperature can enable the detection of possible problems in the winding due to faults at an early stage. Therefore, this study reports an in-situ thermal sensing scheme to enable monitoring of slot section hotspots that originate from winding fault, and therefore its diagnosis.

Table II: : Heat calculation in the slot section

Heat in healthy condition	$I_{phase}^2 \times R_{slot-axial\ length} \times N_H$	(4)
Heat in faulty condition	$I_{a2}^2 \times R_{slot-axial\ length} \times N_F$	(5)
	$I_{a1}^2 \times R_{slot-axial\ length} \times N_H$	(6)

III. EXPERIMENTAL TEST RIG DESCRIPTION

The proposed stator winding fault on-line diagnostic technique based on the in-situ thermal signature was established by installing a number of FBG probes into a 0.55kW /three phase cage rotor IM. The examined motor specifications are provided in table III.

Table. III: Test Motor specification

<i>Examined IM Data</i>	
Rated Power / Voltage / Current	0.55 kW / 400 V / 1.6A
Efficiency, Efficiency class	66 %, IE1
Rated speed / Pole number	1380 rpm / 4
Magnetisation current	1.1A
Cooling method	IC 41
Slot number stator / rotor	24 / 30
Insulation class/ Temperature rise class	F / B
Duty cycle type rating	S1

The stator was rewound to enable sensor installation in target positions and ITSCF experimental emulation. Windings were modified to allow emulation of a range of single or multiple turn faults by tapping specific phase A winding points, as shown in Fig. 3. The test motor phase windings consist of 4 series connected coils, each with 105 turns of 24 AWG enamelled copper wire. The fault location is arbitrarily chosen to be in coil 2 of phase A. The practically examined ITSCF severities defined as percentage ratio of winding shorted and effective turns are presented in Table IV. The maximum examined fault severity is 2.38% as this study focuses on detection of incipient stages of ITSCFs.

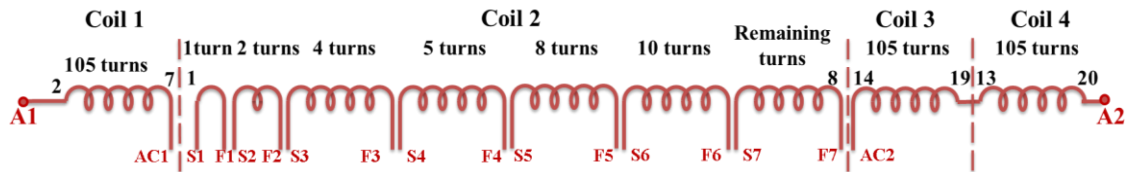


Fig. 3: Modified stator phase for winding ITSCF emulation

Table IV: Investigated inter-turn fault severity

Turns	1	2	3	4	5	8	10
Severity %	0.23	0.47	0.71	0.95	1.19	1.9	2.38

Fig. 4 illustrates the embedded thermal sensor locations in the test machine. Based on the thermal sensing requirements for ITSCF detection discussed in section II.B, at least one in-situ thermal sensor per coil is required to cater for the diagnosis of the entire winding. However, the aim of this feasibility study is to demonstrate the viability of in-situ FBG thermal sensing concept for ITSCF detection: to this end, an array FBG sensor containing 4 FBG heads was embedded and distributed in four known healthy and faulty slots, Fig.4a. The in-situ sensor was designed following the principles put forward in [22-24]: the individual FBG head length is 5 mm, imprinted in bend insensitive polyimide single mode fibre with average bandwidth of ≈ 0.34 nm, reflectivity of $\approx 80\%$ and sensitivity of ≈ 12 pm/ $^{\circ}\text{C}$. The central Bragg wavelengths of each FBG head are 1554.684, 1549.962, 1544.930 and 1539.881 nm, respectively. The FBG heads are packaged in a polyetheretherketone (PEEK) capillary to eliminate external mechanical excitation, while the remainder of the optic cable is tubed in Teflon for protective purposes. PEEK is electrically non-conductive and EMI immune and can withstand operating temperatures in excess of ≈ 250 $^{\circ}\text{C}$. The utilised sensor design has been shown to provide reliable measurement with measurement error lower than 1 $^{\circ}\text{C}$ [24].

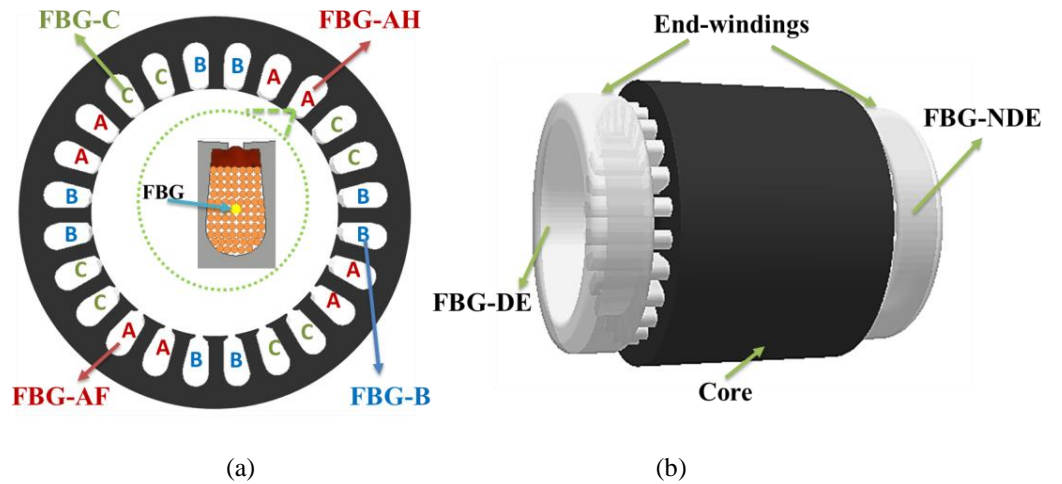
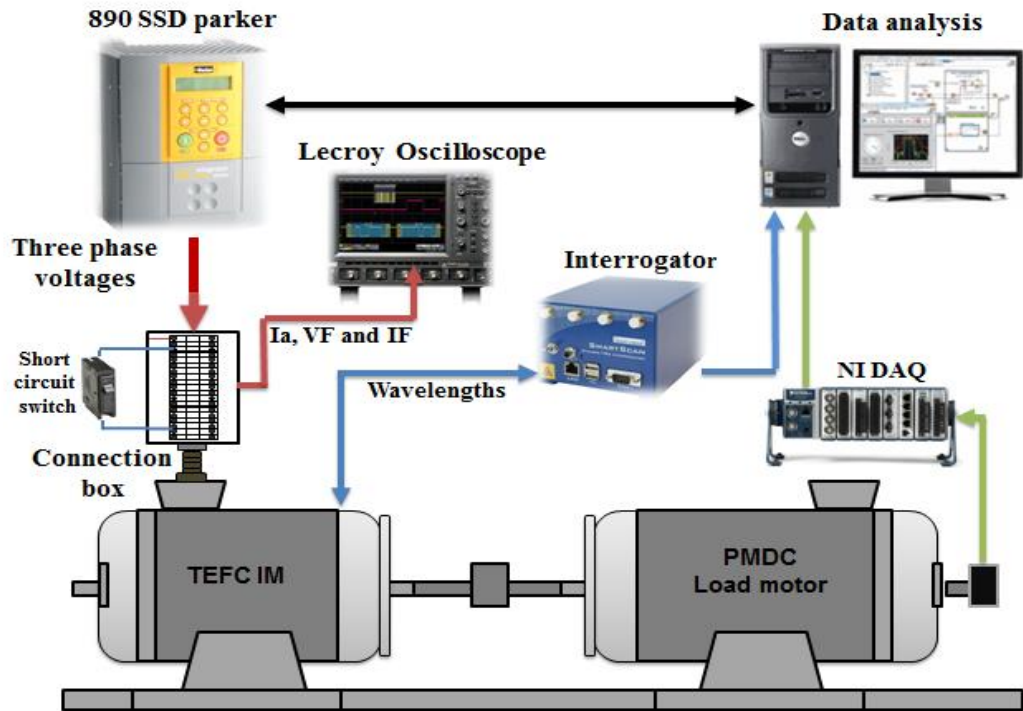


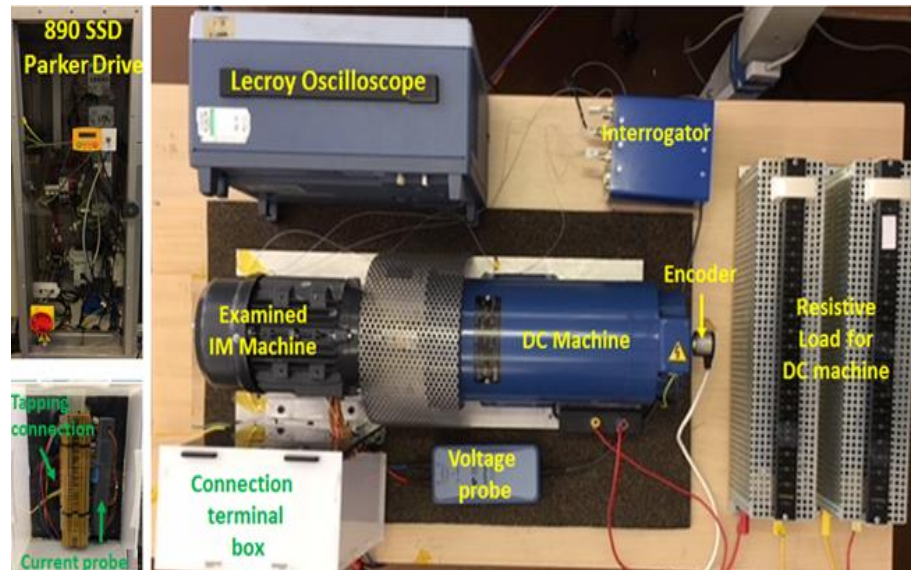
Fig.4: Test motor thermal sensor positions. (a) FBG sensor locations in slot sections. (b) FBG locations in end-winding sections

Each FBG head was placed between copper conductors in the slot centre, following installation principles in [22-24]. The FBGs were positioned to enable thermal monitoring of an emulated fault location and a uniform thermal sensing distribution within the examined motor geometry. Two FBG heads were thus installed in slots containing phase

A coils, one (FBG-AH) in the slot containing a healthy coil side and the other in the slot that contains the faulty coil side (FBG-AF). The two remaining FBG heads (FBG-B and FBG-C) were installed in slots containing coils of healthy phases B and C, respectively. In addition to the FBG array sensor two single FBG sensors were installed to monitor the end-windings: one was embedded in the drive-end winding (FBG-DE) and another in the non-drive end winding (FBG-NDE), Fig. 4b.



(a) Experimental test rig configuration



(b) Photograph of the test rig

Fig. 5: Experimental test-rig setup

The performance of the proposed scheme was examined in experiments on a laboratory test-rig. Fig. 5a gives the schematic diagram of the test rig configuration and Fig. 5b shows a photograph of the actual test rig. The prototype FBG instrumented IM was coupled to a PMDC load machine whose armature current was regulated using a controllable resistive load bank. The IM was supplied by a three-phase Parker SSD890 AC drive operating in open-loop (V/f) control mode. The phase A current and the shorted turns circulating current and voltage were monitored by LeCroy CP150 current probes and a LeCroy ADP300 voltage probe in the tests. Instantaneous currents and voltage were synchronously recorded using a LeCroy 434 digital oscilloscope. The FBG sensors were illuminated using a broadband light source provided by a commercial multi-channel (SmartScan04) interrogator unit. The monitored FBG wavelengths were processed using the LabVIEW based SmartSoft software.

IV. EXPERIMENTAL RESULTS AND DISCUSSION

An experimental study undertaken to evaluate the application of the proposed in-situ thermal monitoring scheme for incipient ITSCF diagnostics on the inverted driven IM test rig is reported in this section. The study also includes an analysis of electro-thermal characteristics of the test motor operating in early stages of ITSCF. The signature of fault severities ranging from a single to ten shorted turns is examined under steady-state and transient thermal conditions at different operating frequencies in V/f control mode.

A. Fault thermal signature in steady-state conditions

1) Base frequency conditions

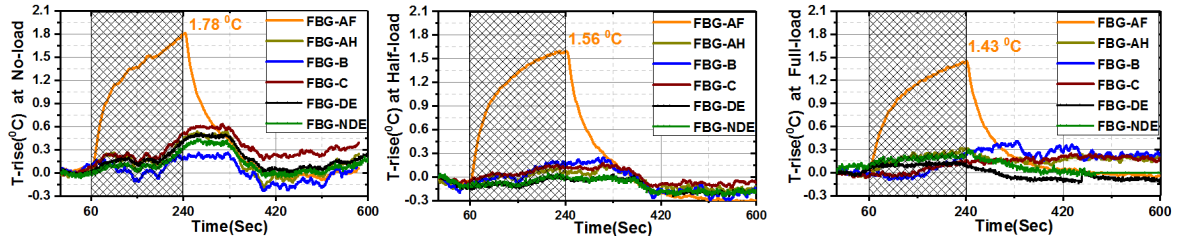
This section studies the efficacy of fault diagnosis in steady-state thermal conditions: to this end an ITSCF was emulated in the test machine after thermal equilibrium for a chosen operating point was reached. Fault severities of 1, 2, 3, 4, 5, 8 and 10 shorted turns were examined, as summarised in Table IV. For each considered fault case, tests were undertaken at a nominal supply frequency of 50 Hz and at no-load, half-load and full-load conditions.

a) Test procedure description: the test procedure applied for each fault case and load condition involved waiting for the thermal equilibrium to first be achieved and then performing the following procedure: healthy winding hot spot temperatures at thermal equilibrium were first monitored for 60 sec. A short-circuit fault was then induced and maintained for a period of 180 sec within which thermal readings were taken. Finally, the fault was removed and thermal readings taken during the cool down period and return to

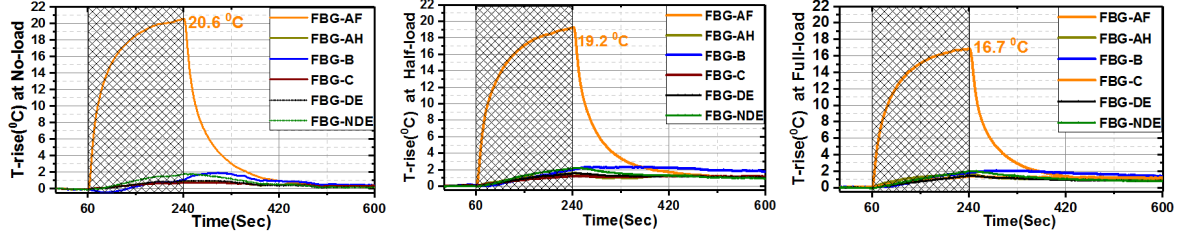
healthy winding thermal equilibrium. To practically emulate short circuit fault conditions as close as possible to those of an actual fault but without damaging the machine, the faulty turns were directly shorted in experiments using an electrical switch for fault tests of up to and including 5 shorted turns. Here the tapping leads and the switch resistance act as current limiters. In the tests involving 8 and 10 shorted turns however, an additional resistance was added to limit the faulty current to 8 A in order to protect the motor. The 8 A short circuit current limit was set based on undertaking offline DC thermal excitation tests to rated thermal limits of the tested motor.

b) In-situ thermal signature monitoring performance: for the sake of brevity, only the thermal measurements obtained by FBG sensors in 1, 5 and 10 shorted turn tests are shown in Fig. 6. To clearly illustrate the observed thermal changes, the recorded thermal rise with respect to the healthy thermal steady-state is presented. The data demonstrate that the in-situ FBG sensor (FBG-AF) in the faulty coil slot is able to instantaneously measure the additional thermal excitation arising from an ITSCF. A temperature rise of 1.8 °C is recorded at the lowest case of fault severity (single turn) and around 28.5 °C at the highest examined fault severity (10 shorted turns). The other FBG sensors embedded in the healthy slots and in the end-windings report insignificant thermal rise rates in comparison, as they are located away from the fault induced localised thermal stress, as discussed in section II.B.2. The ITSCF thermal signature is seen to be clearly distinguishable from the fault onset. The presented results highlight the high sensitivity of in-situ FBG sensors and their capability of registering thermal variations as small as ≈ 0.2 °C between measurements under different load conditions, as observed in the single turn shorted fault case.

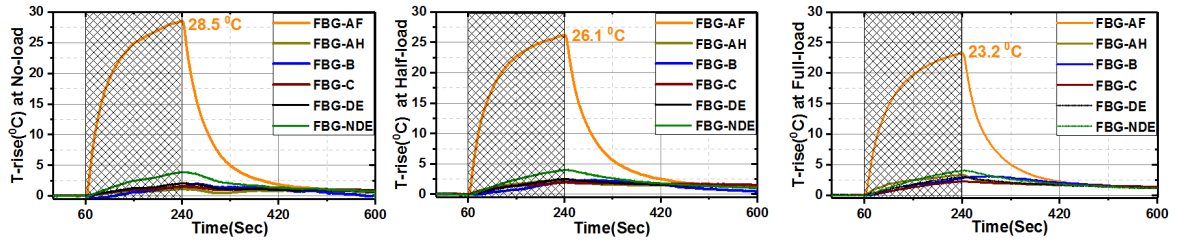
The experimental data in Fig. 6 clearly demonstrates the capability of the proposed in-situ thermal monitoring scheme for detection of stator winding ITSCFs. It should be noted that the reported measurements were taken under constrained fault conditions in order to avoid test equipment damage. In a practical ITSCF scenario however the fault currents will be higher and hence the fault thermal signature expected to be even more obvious. As an illustration, considering a 1 turn fault in the examined motor with an assumed fault current of 12 times the rated current [6]: this will generate ≈ 3.6 W of heat loss in the winding slot section containing a faulty coil side, according to Eq. (5) in table II ($R_{slot-axial\ length}$ in the examined machine is $\approx 0.01 \Omega @ 25$ °C). This is higher than the heat loss of ≈ 3.2 W produced by a 5 shorted turns fault with an imposed 8 A fault current limit. It can thus be expected in a practical single short turn fault scenario to observe a temperature rise ≈ 20 °C or more higher than was measured by the FBG-AF in the 5 shorted turns fault case.



(a) Measured temperature rise with single turn short circuit fault



(b) Measured temperature rise with five turn short circuited



(c) Measured temperature rise with ten turn short circuited

Fig. 6: Measured temperature rise profiles under ITSCF condition

c) *Thermal signature analysis:* to enable understanding of diagnostic potential the experimental results for fault thermal signature in Fig. 6 are examined with respect to fault severity and load dependency. The measured temperature rise and its rate of change reported by FBG-AF are seen to be significantly more affected by fault severity than by loading. On the other hand, it is interesting to observe that the amount of heat generated in the winding slot section containing a faulty coil side is reduced when the load increases, as evidenced by the measured temperature rise profiles for each considered ITSCF case summarised in Fig. 7. The examined fault severities are seen to exhibit a closely similar

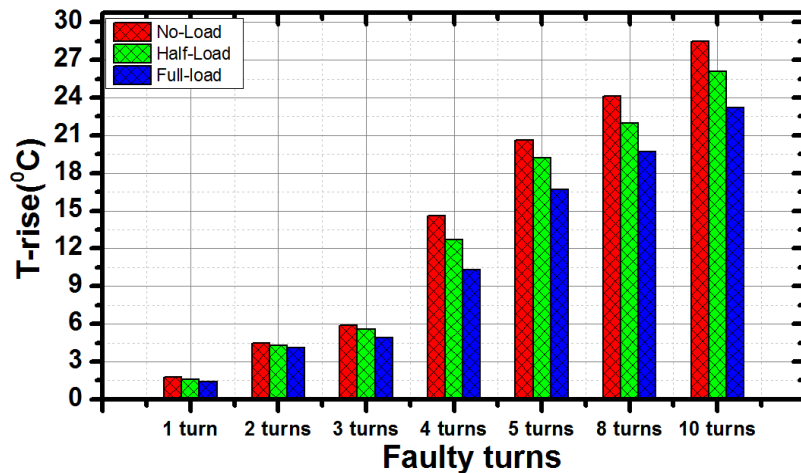
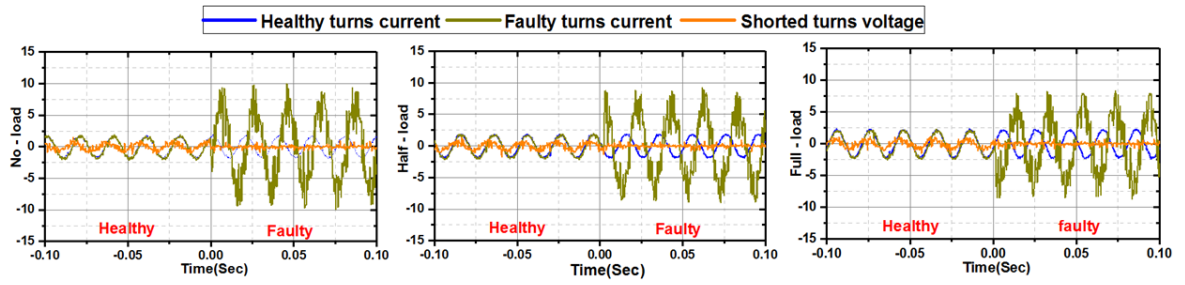


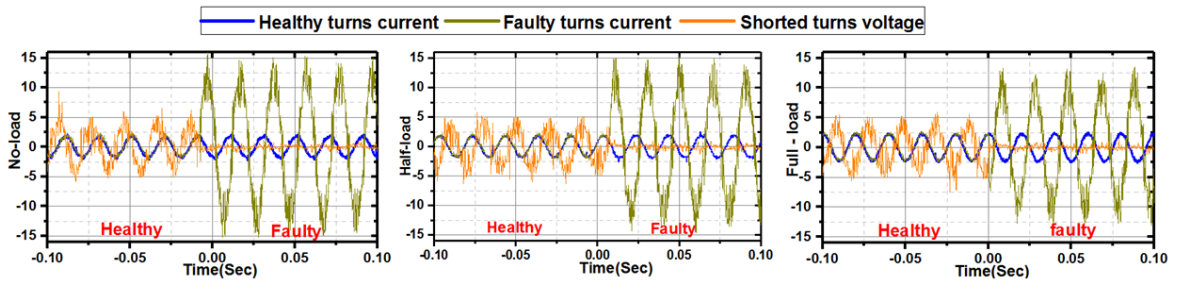
Fig. 7: Measured fault induced temperature rise in steady-state conditions

profile of thermal signature rise with load. The observed temperature rise presents a clear fault detection index, while the difference in thermal signature magnitude (i.e. column height in Fig. 7) provides a diagnostic index for fault mapping.

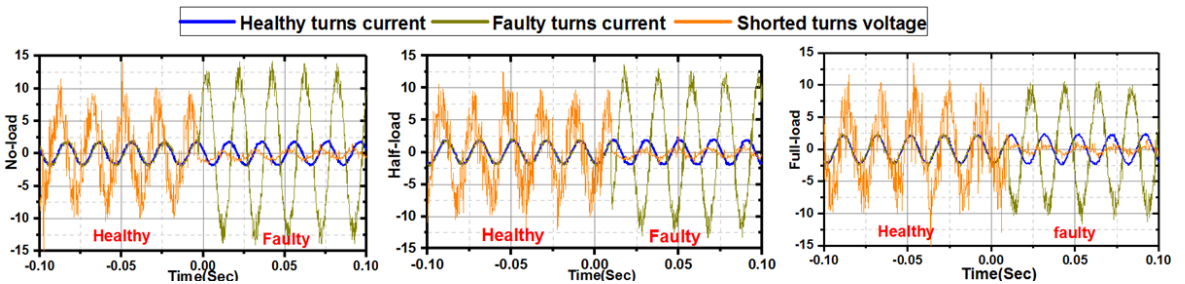
To obtain understanding of observed fault thermal signature trends shown in Fig.6 and Fig. 7 with respect to fault severity and load dependency, the winding electro-thermal characteristics and the resulting fault induced heat loss were analysed. For this purpose, the currents in the healthy and faulty turns and the shorted turns voltage signals were synchronously measured for each fault case. For illustration purpose, Fig. 8 shows the obtained measurements in 1, 5 and 10 shorted turn cases at different load conditions. The graphs show measurements in healthy conditions followed by a fault period. The measured shorted turn current (dark green trace) exhibits a sizable rise with fault application, with little noticeable change in healthy turns current (blue trace). Current levels of ≈ 1.6 A, ≈ 1.3 A and ≈ 1.1 A were recorded for healthy operation under full-, half- and no-load conditions, respectively. The shorted turns' current is seen to be phase shifted to the.



(a) Measured currents in healthy and faulty turns, induced voltage in shorted turns in case of 1 shorted turn.



(b) Measured currents in healthy and faulty turns, induced voltage in shorted turns in case of 5 shorted turn.



(c) Measured currents in healthy and faulty turns, induced voltage in shorted turns in case of 10 shorted turn.

Fig. 8: Measured currents in healthy and faulty turns, induced voltage in shorted turns

current in healthy turns and acts to reduce the shorted turns voltage induced in the shorted turns (orange trace) during a fault event. These measurements confirm the analysis of ITSCF electrical characteristics provided in section II. A

The rms values of the measured shorted turns current were used to determine the fault induced heat loss in the slot section for each fault condition, using Eq. (5) in table II. The $R_{\text{slot-axial length}}$ value was corrected for each load condition based on the measured winding operating temperature as follows: no-load resistance $\approx 0.011\Omega$ @ 65°C , half-load resistance $\approx 0.012\Omega$ @ 74°C and full-load resistance $\approx 0.013\Omega$ @ 97°C . The measured shorted turns' current values along with the associated fault induced heat loss for all examined fault cases and loads are shown in table V. The presented data show an increase in the shorted turns current and fault induced heat loss with fault propagation and their clear decrease with load increase; for the shorted turn current this trend is apparent in measurements shown in Fig. 8. The calculated fault induced heat loss behaviour can be directly linked to and clarifies the measured thermal signature profiles in Fig. 6 and Fig. 7, since these thermal profiles are determined by the amount of heat loss induced in the slot due to fault presence.

The increase in the fault induced heat loss and hence fault induced thermal signature rise with fault severity can be explained as follows: as severity increases more shorted turns are involved in the fault, resulting in an increase of the shorted turn induced voltage. This in turn leads to an increase in the shorted turn current and hence the associated heat loss and thermal signature increase as shown in table V and Fig. 7, respectively. On the other hand, the decrease in fault induced heat loss (table V) and the corresponding thermal signature (Fig. 7) with load increase can be explained by associated electro-thermal effects. Fundamentally, the shorted turns' current magnitude is determined by the values of shorted turn induced voltage and resistance. A load increase also increases the drawn phase current and hence winding loss and operating temperature, resulting in healthy and faulty turns' resistance increase. The shorted turn resistance increase resulting from load rise will thus act to limit the shorted turns' current which consequently decreases with load increase, as shown in table V. This decrease is amplified to an extent by the minor decrease observed in the measured shorted turns' voltage with load increase. While, in general, the shorted turn resistance increase would be expected to result in a heat loss increase in shorted turns, this loss is predominantly influenced by the more substantial shorted turn current reduction. To illustrate this, Fig. 9 shows the calculated fault induced heat loss in the slot section for a 10 shorted turn fault case versus load along with the measured shorted turns'

current and $R_{\text{slot-axial length}}$. The data in Fig. 9 show that $R_{\text{slot-axial length}}$ is increased with load from $\approx 0.011 \Omega$ at no-load to $\approx 0.013 \Omega$ at full-load due to operating temperature increase. The shorted turn current is consequently reduced from about $\approx 7.9 \text{ A}$ to $\approx 6.7 \text{ A}$. Crucially, the fault induced heat loss reduces from $\approx 7.2 \text{ W}$ at no-load to $\approx 5.8 \text{ W}$ at full-load. In general, for an arbitrary number of shorted turns, the total shorted turns resistance increase due to load rise induced temperature increase is directly proportional to the number of turns shorted. This explains the difference in no-load to full-load temperature rise trends with fault severity observed in Fig. 7 and the heat calculations in table V.

Table V: Shorted turns current and heat loss components for all fault cases

Shorted turns number	Shorted turns current	Heat loss	Shorted turns current	Heat loss	Shorted turns current	Heat loss
	No-load		Half-load		Full-load	
	A	W	A	W	A	W
1	5	0.2885	4.7	0.26347	4.34	0.24279
2	7	1.13092	6.6	1.03908	6	0.92808
3	6.15	1.30941	5.7	1.16252	5.23	1.05774
4	8.3	3.17996	7.9	2.97746	7.3	2.74763
5	7.9	3.60106	7.5	3.35447	7.1	3.24892
8	7.8	5.61675	7.35	5.15461	6.75	4.69841
10	7.9	7.20211	7.38	6.49597	6.71	5.80361

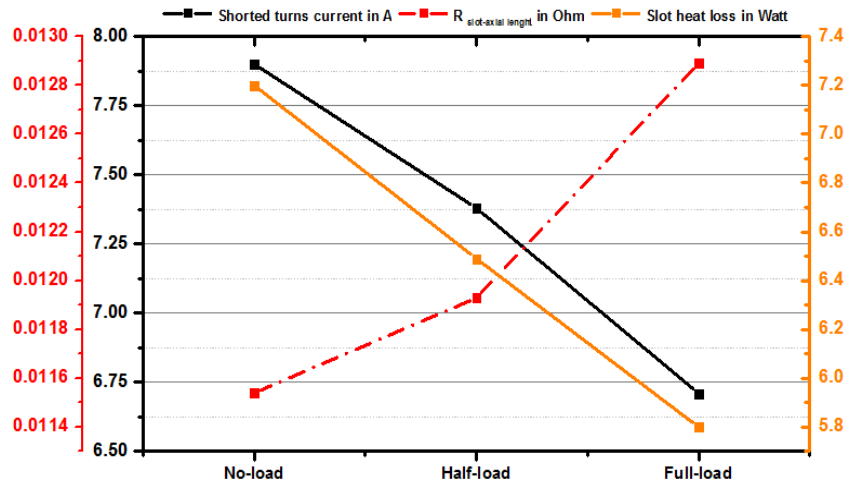


Fig. 9: Fault induced heat loss, shorted turn current and resistance variation with load, 10 turns shorted fault

To examine the actual thermal stress related to thermal rise recordings in Fig. 7, the corresponding temperature measurements are shown in Fig. 10. It should be noted that the examined machine is an IE1 standard efficiency class design, meaning that it produces relatively high losses that significantly increase with loading. The relationship between loading and losses for IE1 design class is quadratic, and can be equally applied to the relationship between loading and temperature [31]; this is evident in the thermal measurements trends in Fig. 10, where the difference between no-load and full-load winding temperature is $\approx 35^\circ \text{C}$. Although the temperature rise measured due to fault at no-load is higher than at full-load (Fig. 7), the winding thermal excitation is higher during

fault at full-load (Fig. 10) due to the high operating temperature of $\approx 97^{\circ}\text{C}$. However, in machines with higher efficiency classes, e.g. IE3 or IE4, this thermal behaviour can differ and higher thermal stress due to ITSCF may occur at no-load conditions.

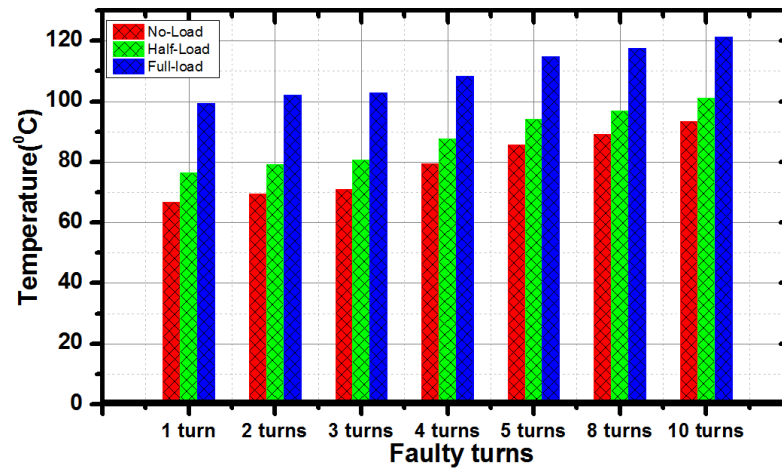


Fig. 10: ITSCF temperature measurement in steady state conditions

2) Motor current signature analysis comparison

To illustrate the diagnostic potential of the proposed in-situ FBG thermal monitoring for ITSCF detection, this section presents the diagnostic signatures obtained from applying motor current signature analysis (MCSA) on the examined machine. MCSA is a widely proposed technique for winding fault detection in electrical machines and is based on identifying fault specific changes in the stator current signal [1,3,5]. However, the manifestation of winding fault specific spectral signature in the stator current is reported to be largely machine design dependent and is still not fully understood or consistently interpreted [31-32].

The IM currents measured in fault tests were therefore examined for the presence of known MCSA diagnostic components. It was found that high severity ITSCF can lead to the generation of slot harmonic components in the current spectrum, despite the examined machine geometry not being expected to produce a slot harmonic signature in healthy operating conditions [32]; no other spectral changes arising from ITSCF presence could be identified. The ITSCF induced spectral changes were observed at lower and upper principal slot harmonic frequencies. The measured spectral narrow bands containing the observed fault signatures are shown in Fig. 11. At no-load condition, the lower and upper principal slot harmonics frequencies in the examined machine are at ≈ 694 Hz and ≈ 794 Hz, while at full-load condition these are ≈ 640 and ≈ 740 Hz. The presence of increased severity ITSCF is seen to give rise to a modest increase of component magnitudes at slot harmonic frequencies; however, the lower severity faults ranging from a single to 3 shorted turns do not produce any MCSA diagnostic signature and thus cannot be diagnosed by this

technique for the examined machine. Furthermore, the fault signatures of higher severity faults are not considerable nor very clearly pronounced and would be challenging to employ for diagnostic purposes.

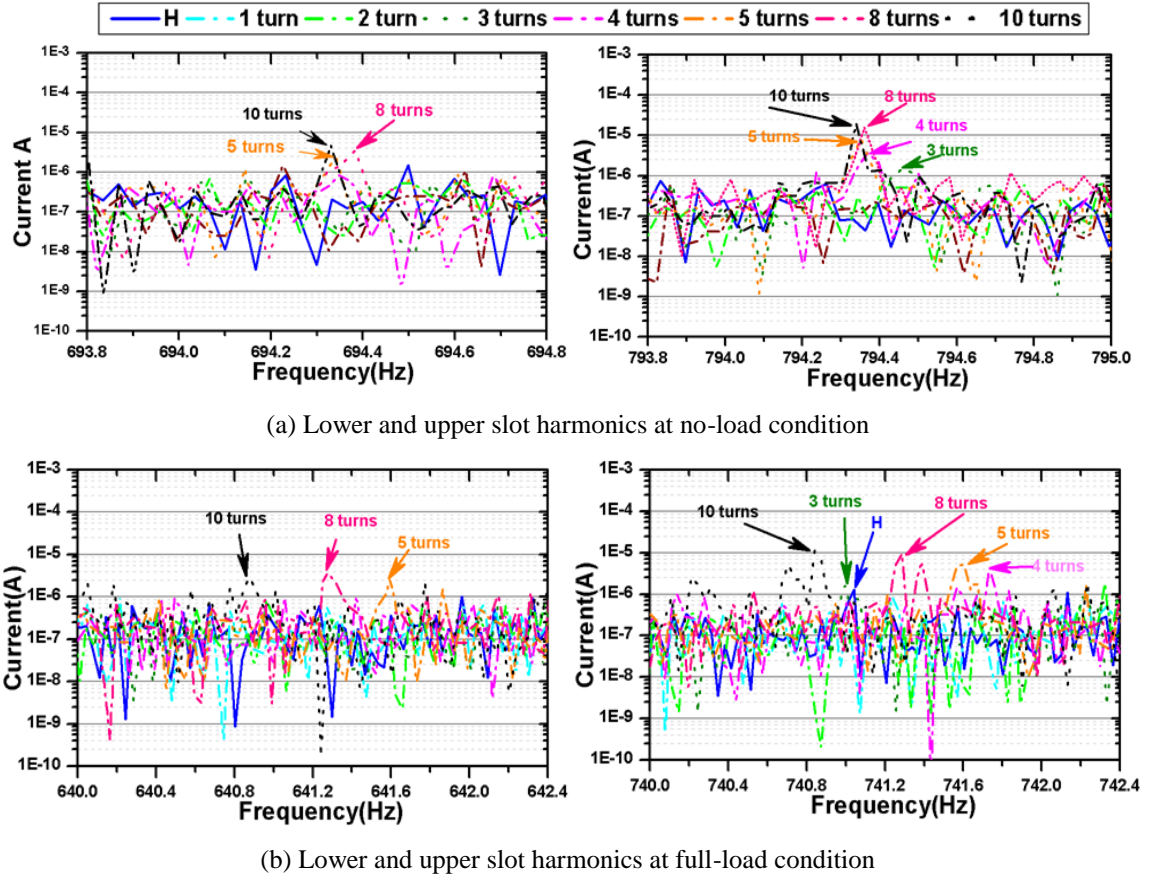


Fig. 11: Measured MCSA ITSCF signature

Further examination of presented spectral narrow bands reveals that the slot harmonics components exhibit a noticeable decrease in magnitude with load increase, while the general expectation would be the opposite. However, this observation can be explained by the electro-thermal interaction characteristics of the motor winding in an ITSCF event, provided in section IV. A.1. The observed reduction can be linked to the fault current reduction with load caused by electro-magnetic and thermal effects, as discussed in table IV. It can be thus concluded that the MCSA is incapable of detection of an ITSCF involving a few turns in the test machine, which typically represents incipient fault stages that are of highest diagnostic interest. To the contrary, the in-situ thermal monitoring signature in Figs. 6-7 enables clear diagnosis of each of the analysed ITSCF scenarios. In addition, the in-situ thermal monitoring can be used to enhance the efficacy of MCSA and facilitate better understanding of the spectral components behaviour used for diagnostic purposes.

3) *V/f control operating frequency change*

ITSCF thermal signature recognition is examined in this section for the *V/f* controlled test machine operation at a range of different supply frequencies. The following five different operating points were assessed: 50 (base frequency) 40, 30, 20 and 10 Hz. A 5 shorted turn fault was experimentally tested under each of these frequencies. This is for the reason that the 5 turn fault emulation within non-destructive fault current limit constraints on the available laboratory system can be assumed approximately equivalent in terms of resulting thermal excitation to a practical single turn fault scenario, as discussed in section IV.A. The tests were performed following an identical procedure to that described in section IV.1.A. Tests were executed under no-load conditions in order to avoid overheating the examined motor winding due to the natural degradation of the cooling capability at low frequency operation for this motor design class. The thermal measurements obtained by FBG-FA are summarised in Fig. 12. Fig. 12 columns are divided into two areas: the blue area represents the healthy winding hot spot at thermal equilibrium for each operating frequency, while the red area is the measured hot spot temperature rise caused by the fault.

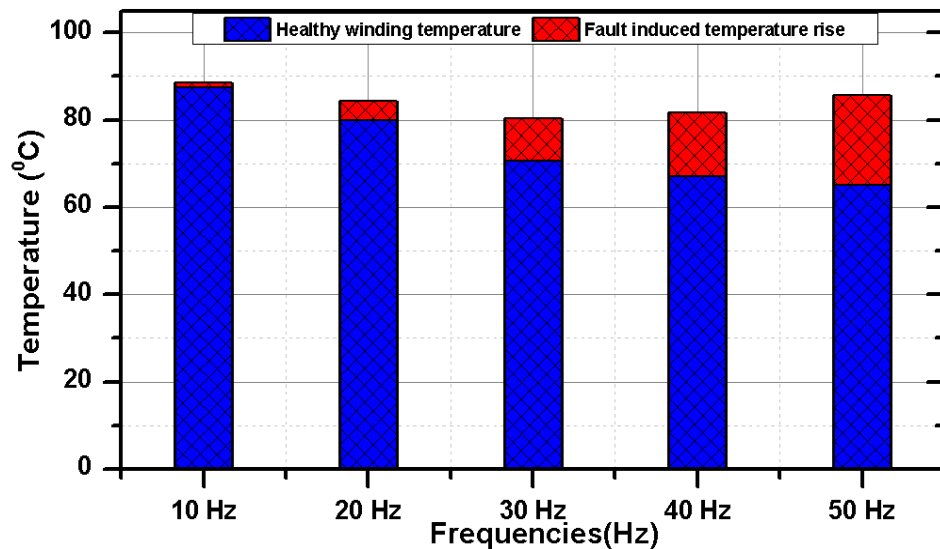


Fig. 12: FBG-AF measurements for different operating frequencies

The results show that as the operating frequency is reduced, the fault induced thermal stress reduces as well, while the healthy, i.e. operational, thermal excitation increases. The *V/f* controlled IM drive operating factor that causes this behaviour is the operating speed. The operating speed reduces with supply frequency reduction; this reduces the machine cooling system capability, as at reduced speeds the motor becomes predominantly cooled by natural rather than forced convection. This cooling performance degradation with speed reduction yields an increase of the healthy winding temperature, seen to rise in the measured data from 65 °C at 50 Hz to 87.4 °C at 10 Hz. Conversely, the ITSCF induced

thermal rise is seen to reduce with operating frequency reduction, from 20.6 °C at 50 Hz to 1.2 °C at 10 Hz. This is largely due to the decrease of the induced shorted turn's voltage as result of reduction of the speed, but is further amplified by the winding temperature increase resulting in shorted turn resistance increase and thus fault current reduction. Most importantly, the data show that the same ITSCF condition can produce different thermal excitation levels at different operating frequencies due to winding electro-thermal characteristics at fault outset; the fault induced thermal stress is more significant at 10 and 50 Hz than at 20, 30 and 40 Hz in the examined system.

B. Fault thermal signature in transient conditions

This section examines the detection of an ITSCFs thermal signature in transient conditions. Transient conditions impose challenges, as during these, stator current can increase to many times more than its steady-state value. The healthy winding temperature rise and its rate of change under such thermal transients could affect the diagnostic performance of the in-situ FBG sensing system. To evaluate diagnostic performance in this respect a cycling transient at 50 Hz is applied on the test machine under healthy and ITSCF conditions.

The examined thermal transient involved application of an S6 cycle to the test machine based on the IEC 60034-1 standard [29]. In this cycle, the motor was tested with a 125% load for 4 min followed by 6 min of no load operation. The cycle was controlled to keep the winding temperature rise above the ambient lower than the permissible temperature rise (80 °C, class B) for the examined motor. Once thermal equilibrium was reached under the applied cycle, a 5 shorted turns fault was introduced; two 60 sec fault instances were examined within a single cycle, one within the cycle heating period and the other in the cycle cooling period. Fig. 13 shows the two applied cycle measurement without and with the inter-turn fault. In the heating period, the fault was applied at the instant of loading (i.e. heating period start), which is assumed to be the most difficult instant to distinguish healthy and faulty thermal profiles as all sensors inherently record temperature rise. The fault in the cooling period was applied at the period midpoint. In healthy conditions, the FBG-AF is seen to report a thermal profile closely similar to those read by other sensors. From the outset of fault however, the FBG-AF readings show an extreme temperature rise in both the heating and cooling period fault instances. This originates from additional, fault induced, rise in thermal loss in the slot and follows the principles discussed in section IV but now in dynamic conditions: upon removal of fault this additional thermal loss is removed and the measured temperature seen to gradually return to its healthy cycle form

after a cool down period. Monitoring the discussed fault induced thermal rise can enable unambiguous fault diagnosis. Thermal signature based fault detection is more straightforward in the cooling period, as all sensors report a temperature decrease while the sensor in the faulty slot reports a temperature rise. In the heating transient, the in-situ sensor shows high sensitivity in recognition of fault induced thermal stress. The experimental data demonstrate the capability of incipient ITSCF thermal fault signature recognition by the proposed in-situ thermal monitoring scheme in transient conditions.

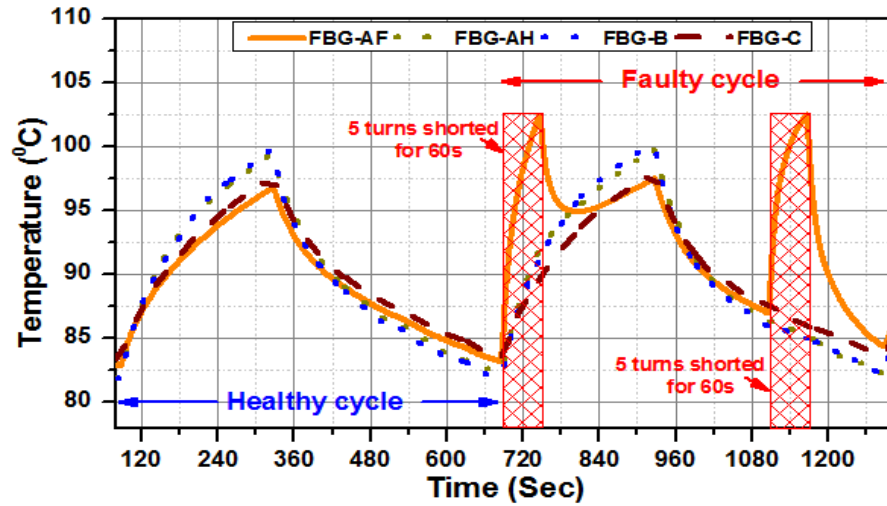


Fig. 13: Thermal measurements in dynamic conditions, 5 turns shorted fault

C. Fault severity trending

The breakdown of the winding is the final stage of an ITSCF, and is typically reached after a series of stages of fault propagation [6]. Effectively monitoring the fault propagation stages to extract knowledge of machine operational status is an underlying requirement for useful diagnostic systems. It has been shown in the previous sections that different ITSCF severities generate different levels of thermal stress and hence, different levels of fault thermal signature, which can be used as an indicator of the fault propagation stage.

In this section experimental work was performed in order to investigate the capability of the in-situ FBG sensor to recognise the ITSCF propagation stages. A test was performed to emulate an ITSCF propagation scenario comprising five distinct stages, starting with a single turn fault and increasing to 5 shorted turns fault in steps of one turn fault. Each fault stage was maintained for a period of 60 seconds in the test before introducing the following fault stage. The test commences after the thermal equilibrium of the winding was reached in no-load conditions. Fig. 14 shows the measured temperature profiles obtained by the four FBGs for the applied fault scenario. The measurements demonstrate that the proposed in-situ thermal monitoring system is able to provide clear recognition of fault

status and its propagation signature: at each fault stage the FBG-AF reports a different, distinct temperature level. The faulty coil side hot spot temperature increases with fault propagation from $\approx 67.5^{\circ}\text{C}$ at healthy conditions to reach $\approx 88^{\circ}\text{C}$ at 5 turn fault stage. Another attractive advantage of the proposed diagnostic technique is that it does not require complex real-time algorithms for interpretation of fault signature such as needed with electro-magnetic signal signature analysis techniques [3].

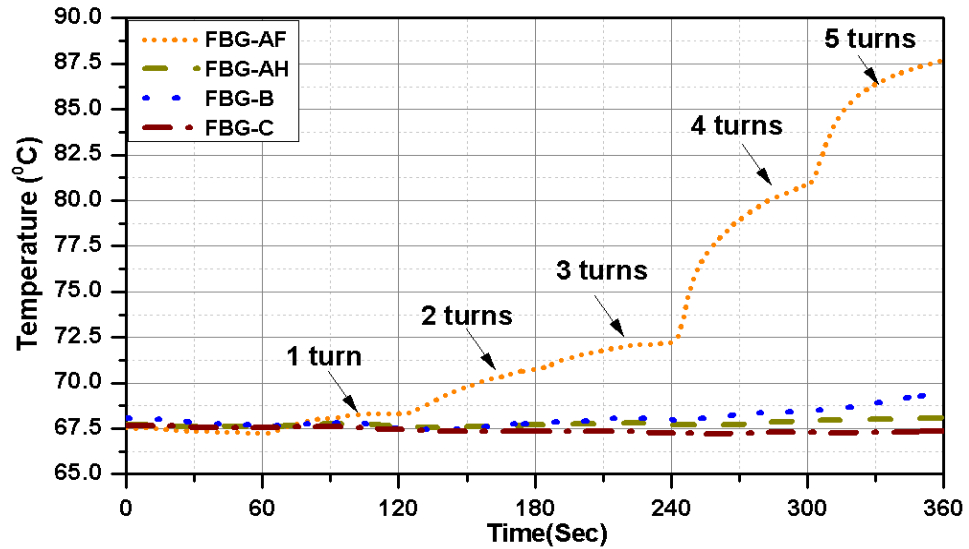


Fig. 14: Measured temperature profile under fault propagation

V. CONCLUSION

This research reports a new technique for ITSCF on-line diagnosis in random wound machines based on fully EMI immune FBG sensor in-situ monitoring of winding internal thermal excitation. The proposed scheme is implemented and its performance validated on an inverter driven induction motor. The study focuses on the detection of the early stages of an ITSCF, where other techniques largely present limited success.

The reported findings demonstrate that the presented scheme can provide reliable diagnosis of ITSCFs including: detection of an ITSCF at its earliest stages (i.e. single turn), fault severity diagnosis, and a straightforward identification of fault location. The winding in-situ thermal sensing network required to underpin this diagnosis can readily be achieved utilising FBG multiplexing features in a single fibre array sensor. The results and analysis in this paper enable full understanding of the FBG monitoring principles required for practical establishment of such a scheme.

The proposed in-situ FBG thermal sensing for ITSCF detection provides advantages over existing diagnostic techniques in steady-state and in particular in transient conditions, as no complex real-time processing is required for fault signature diagnostic interpretation.

Finally, it is shown that improved understanding of the interaction between the electrical and thermal characteristics of faulty windings can significantly contribute to understanding ITSCF effects and diagnostic features. The manifestation of the observed fault induced thermal phenomena is generally expected to be dependent on machine design class.

REFERENCES

- [1] S. Grubic, J. M. Aller, B. Lu and T. G. Habetler, "A Survey on Testing and Monitoring Methods for Stator Insulation Systems of Low-Voltage Induction Machines Focusing on Turn Insulation Problems," in *IEEE Trans. on Ind. Electronics*, vol. 55, no. 12, pp. 4127-4136, Dec. 2008.
- [2] G. N. Surya, Z. J. Khan, M. S. Ballal and H. M. Suryawanshi, "A Simplified Frequency-Domain Detection of Stator Turn Fault in Squirrel-Cage Induction Motors Using an Observer Coil Technique," in *IEEE Trans. on Ind. Electronics*, vol. 64, no. 2, pp. 1495-1506, 2017.
- [3] A. Gandhi, T. Corrigan and L. Parsa, "Recent Advances in Modeling and Online Detection of Stator Interturn Faults in Electrical Motors," in *IEEE Transactions on Industrial Electronics*, vol.58, pp.1564-75, 2011.
- [4] F. Çıra, M. Arkan, B. Gümüş and T. Goktas, "Analysis of stator inter-turn short-circuit fault signatures for inverter-fed permanent magnet synchronous motors," *IECON 2016 - 42nd Annual Conference of the IEEE Industrial Electronics Society*, Florence, 2016, pp. 1453-1457.
- [5] Dorrell, David G., and Khanyisani Makhoba. "Detection of Inter-turn Stator Faults in Induction Motors Using Short Term Averaging of Forwards and Backwards Rotating Stator Current Phasors for Fast Prognostics." *IEEE Transactions on Magnetics* (2017).
- [6] Park, Jun-Kyu, and Jin Hur. "Detection of inter-turn and dynamic eccentricity faults using stator current frequency pattern in IPM-type BLDC motors." *IEEE Trans. on Ind. Elec.* 63.3 (2016): 1771-1780.
- [7] V. Nguyen; J. Seshadrinath; D. Wang; S. Nadarajan; V. Vaiyapuri, "Model-Based Diagnosis and RUL Estimation of Induction Machines under Inter-Turn Fault," in *IEEE Transactions on Industry Applications*, 2017, vol. PP, no. 99, pp. 1-1.
- [8] C. Gerada et al., "The results do mesh," in *IEEE Industry Applications Magazine*, vol. 13, no. 2, pp. 62-72, March-April 2007.
- [9] G. M. Joksimovic and J. Penman, "The detection of inter-turn short circuits in the stator windings of operating motors," in *IEEE Transactions on Industrial Electronics*, vol. 47, pp. 1078-84, Oct 2000.
- [10] Riera-Guasp, Martin, Jose A. Antonino-Daviu, and Gérard-André Capolino. "Advances in electrical machine, power electronic, and drive condition monitoring and fault detection: state of the art." *IEEE Transactions on Industrial Electronics* 62.3 (2015): 1746-1759.
- [11] Singh, Gurmeet, T. Ch Anil Kumar, and V. N. A. Naikan. "Induction motor inter turn fault detection using infrared thermographic analysis." *Infrared Physics & Technology* 77 (2016): 277-282.
- [12] Glowacz, Adam, and Zygfryd Glowacz. "Diagnosis of the three-phase induction motor using thermal imaging." *Infrared Physics & Technology* 81 (2017): 7-16.
- [13] Garcia-Ramirez, Armando Guadalupe, et al. "Fault detection in induction motors and the impact on the kinematic chain through thermographic analysis." *Elec. Pow. Systems Research* 114 (2014): 1-9.
- [14] R. M. Tallam, T. G. Habetler and R. G. Harley, "Experimental testing of a neural-network-based turn-fault detection scheme for induction machines under accelerated insulation failure conditions," *4th IEEE International Symposium on Diagnostics for Electric Machines, Power Electronics and Drives, 2003. SDEMPED 2003.*, 2003, pp. 58-62.
- [15] M. G. Melero et al., "Study of an induction motor working under stator winding inter-turn short circuit condition," *4th IEEE International Symposium on Diagnostics for Electric Machines, Power Electronics and Drives, 2003. SDEMPED 2003.*, 2003, pp. 52-57.
- [16] W. T. Thomson, "On-line MCSA to diagnose shorted turns in low voltage stator windings of 3-phase induction motors prior to failure," *IEMDC 2001. IEEE International Electric Machines and Drives Conference*, Cambridge, MA, 2001, pp. 891-898.
- [17] F. Marignetti et al., "Fiber Bragg Grating Sensor for Electric Field Measurement in the End Windings of High-Voltage Electric Machines," in *IEEE Trans. on Ind. Elec.*, vol. 63 no. 5, pp. 2796-2802, May 2016.

- [18] J. M. Corres, J. Bravo, F. J. Arregui and I. R. Matias, "Unbalance and harmonics detection in induction motors using an optical fiber sensor," in *IEEE Sensors Journal*, vol. 6, no. 3, pp. 605-612, June 2006
- [19] Fabian, M., Ams, M., Gerada, C., Sun, T., Grattan, K. T. V, "Vibration measurement of electrical machines using integrated fibre Bragg gratings." *Proc. SPIE 9634, Int. Conf. on Optical Fibre Sensors*, 2015.
- [20] Leite, Reinaldo Corrêa, et al. "Analysis of Thermo-Mechanical Stress in Fiber Bragg Grating used for Generator Rotor Temperature Monitoring." *Journal of Microwaves, Optoelectronics and Electromagnetic Applications (JMoe)* 16.2 (2017): 445-459.
- [21] K. d. M. Sousa, A. A. Hafner and J. C. C. da Silva, "Determination of Temperature Dynamics and Mechanical and Stator Losses Relationships in a Three-Phase Induction Motor Using Fiber Bragg Grating Sensors," in *IEEE Sensors Journal*, vol. 12, no. 10, pp. 3054-61, Oct. 2012.
- [22] A. Mohammad and S. Djurović, "FBG array sensor use for distributed internal thermal monitoring in low voltage random wound coils." *Embedded Computing (MECO), 2017 6th Mediterranean Conference on*. IEEE, 2017, pp. 1-4.
- [23] A. Mohammed, S. Djurović, "Stator Winding Internal Thermal Stress Monitoring and Analysis Using in-situ FBG Sensing Technology," in *IEEE Transactions on Energy Conversion*, 2018.
- [24] A. Mohammed and S. Djurović, "FBG Thermal Sensing Features for Hot Spot Monitoring in Random Wound Electric Machine Coils," in *IEEE Sensors Journal*, vol. 17, no. 10, pp. 3058-67, May15, 15 2017.
- [25] Smartfibres.com. (2017). *Smart Fibres / Pioneering Optical Fibre Sensing*. [online] Available at: <http://www.smartfibres.com>
- [26] Gao, Zhiyuan, et al. "Active monitoring and vibration control of smart structure aircraft based on FBG sensors and PZT actuators." *Aerospace Science and Technology* 63 (2017): 101-109.
- [27] Ecke, Wolfgang, and Kerstin Schröder. "Fiber Bragg grating sensor system for operational load monitoring of wind turbine blades." *Proc. SPIE*. Vol. 6933. 2008.
- [28] Tavner, P. J. "Review of condition monitoring of rotating electrical machines." *IET Electric Power Applications* 2.4 (2008): 215-247.
- [29] IEC 60034-1:2010, Rotating electrical machines - Part 1: Rating and performance.
- [30] F. J. T. E. Ferreira, B. Leprettre and A. T. de Almeida, "Comparison of Protection Requirements in IE2-, IE3-, and IE4-Class Motors," in *IEEE Trans. on Ind. App.*, vol. 52, no. 4, pp. 3603-3610, 2016.
- [31] Ishida, Muneaki, and Koji Iwata. "A new slip frequency detector of an induction motor utilizing rotor slot harmonics." *IEEE Transactions on Industry Applications* 3 (1984): 575-582.
- [32] Nandi, S., et al., "Performance analysis of a three-phase induction motor under mixed eccentricity condition." *Energy Conversion, IEEE Transactions on* 17.3 (2002): 392-399.

6.3 Paper 2:

FBG Thermal Sensing Ring Scheme for Stator Winding Condition Monitoring in PMSMs

A. Mohammed, *Student Member, IEEE*, S. Djurović, *Member, IEEE*

Abstract—This paper proposes a random wound stator winding thermal monitoring scheme utilizing an end-winding embedded, ring shaped, Fibre Bragg Grating (FBG) thermal sensing array. The scheme enables in-situ measurement of winding distributed thermal conditions, which is key to attaining their effective health diagnosis and protection. It is designed to provide a thermal sensing point per each individual end-winding coil-end span and thus enable monitoring of the entire winding structure. This was achieved by utilizing the multiplexing feature of FBG thermal sensing in a ring shaped sensor array geometry inserted into the end-winding assembly to ensure desired in-situ placement of separate sensing elements. The reported scheme was implemented on an inverter driven permanent magnet (PM) synchronous motor and its performance examined in laboratory tests under healthy and faulted winding conditions. The obtained results demonstrate the capability of effective monitoring of healthy windings' distributed thermal status. It also demonstrates unambiguous identification of localised overheating originating from an incipient winding fault, providing operative monitoring functionality that is largely unattainable by conventional thermal sensing techniques. Finally, the proposed scheme also enables straightforward advanced graphical visualization of the windings' thermal status and hence a more effective diagnostic interpretation of thermal data to extract knowledge on locations of increased thermal stress.

Index Terms—localised temperature monitoring, end-winding, FBG technology, PMSM, winding fault, thermal monitoring.

I. INTRODUCTION

DUE to high efficiency and power density and a wide operating range, permanent magnet synchronous machines (PMSMs) have become the preferred rotating electric machine choice in a number of applications, ranging from modern electric vehicles to military, medical, factory automation, aerospace and wind energy systems [1-4]. As PMSMs are often enabling components in these systems, their integrity and availability is critical not solely regarding the related maintenance costs when failed, but also due to the fact that their failure can generally lead to system shutdown and undesirable associated issues [4].

The stator winding is one of the most frequently failing PMSM components [5]. Its failures are invariably related to the insulation system degradation resulting from various operational stresses while in service [6]. Winding faults generally lead to excessive damage and thus motor and system shutdown and extended downtime for maintenance. They are particularly critical in PMSMs due to the risk of PM demagnetization by the fault induced excessive heat, and the demagnetizing magnetic field driven by fault current [7].

PMSM winding fault diagnosis has received considerable attention [2, 5, 8-11]. The reported diagnostic methods generally rely on non-invasive monitoring and spectral analysis of electrical and/or electromagnetic quantities, as widely explored in induction machines. However, these impose considerable limitations in diagnostic reliability and fidelity in PMSMs due to the challenge in identification of reliable and consistent fault spectral signatures [5]

Thermal aging caused by overheating is the main contributor to the winding insulation system degradation process and thus winding fault. The insulation system is designed to operate to a permissible temperature limit [6]. There are however many practical operating conditions in which stator windings of electric machines can be uniformly or locally overheated such as: running overloading, transient overloading (cycling), unbalanced supply, inverter driven harmonics, partly or fully degraded cooling capability, and high ambient temperature [12]. The consequence of uniform or localised winding overheating is the degradation of their insulation system. This eventually leads to insulation breakdown between winding adjacent turns, causing the Inter-Turn Short Circuit Fault condition (ITSCF). The ITSCF is generally considered a winding fault incipient stage. At this stage, localized overheating in the winding faulted section is generated due to the high current circulating in the shorted turns [12]. Consequently, an early stage winding fault can also constitute a cause of localized overheating, which accelerates the degradation process of the neighboring healthy turns' insulation system and thus propagates the fault to more advanced stages characterized by increased heat loss [13].

In light of the above, the realization of an effective winding thermal monitoring scheme capable of distributed monitoring of winding thermal conditions including uniform and localized overheating is significant for multiple reasons: it could ensure full protection of windings from uniform or localised overheating under normal and abnormal conditions and thus extend insulation lifetime and mitigate winding faults, it could enable advanced fault diagnostic capability by appropriately monitoring incipient winding fault induced localized thermal excitation, and it could provide enhanced motor thermal management

through improved awareness of proximity to thermal design limits.

The machine winding conventional on-line thermal monitoring techniques are not fully effective in accessing and measuring localized winding thermal hot-spots in normal and abnormal conditions. Thermal estimation based monitoring techniques, such as a resistance based-temperature estimator (model-based or injected signal-based), only provide winding average temperature [14]. Thermal model-based temperature estimator techniques such as those embedded in modern thermal protection relay microprocessors are limited by applied model complexity and the challenge in accurately determining its thermal parameters. In addition, prediction of localised heat caused by abnormal conditions using thermal models requires practically inaccessible parameters such as short circuit current during winding faults or cooling air speed during deteriorated cooling capability in air-cooled machines [6]. The alternative is provided by thermal sensing techniques conventionally used in electric machine windings such as thermocouple (TC) or resistance temperature detectors (RTD) [15]; these however impose considerable limitations in practical application due to the ideally required number of sensing points for winding distributed thermal sensing and the installation complexity caused by sensor bulk and wiring. In addition, their inherently conductive structure and sensitivity to electromagnetic interference largely limit their embedment in direct contact with winding conductors [12, 14].

An alternative on-line winding thermal monitoring technique based on the use of Fibre Bragg Grating (FBG) sensing technology has recently been reported [16-19]. A FBG is a microstructure inscribed in an optical fibre which behaves like a non-conductive and electromagnetically immune sensing element and thus presents an attractive prospect for in-situ winding sensing application [16]. Multiplexing and multi-physical sensing are additional key aspects of FBG technology: these features facilitate development of targeted distributed embedded sensing schemes and enable an ‘all-in-one’ sensing system design for advanced electric machine monitoring applications [18]. FBG sensor application for on-line stator winding interior thermal monitoring in random wound machines has been reported in authors’ recent works [16, 19]. In [16] authors reported the use of a new in-situ FBG temperature sensor for healthy random wound stator winding hot spot monitoring, which is fundamental for understanding winding insulation system degradation. [19] reported a proof of concept study of winding fault induced thermal signature monitoring in induction machines based on slot embedded in-situ FBG sensing configuration.

This paper reports a new FBG thermal sensing scheme for healthy and faulty stator winding condition monitoring aimed at enhancing wider acceptance of FBG thermal

sensing application in electrical machines by enabling easier implementation and interpretation of this technology. The proposed scheme thus considers key practical application aspects, such as sensing optimization, installation and measurement interpretation. To this end a 2D-thermal sensing ring design (2D-TSR) embedded in the end-winding section of a random wound stator winding is proposed that can enable improved awareness of winding thermal status under different operating conditions by allowing for effective monitoring of distributed thermal conditions in its entire structure. The reported 2D-TSR scheme's performance was examined in tests on an inverter driven PMSM in healthy and faulted winding conditions. The obtained thermal measurements demonstrate the scheme's capability to map the thermal status of the examined PMSM winding in a wide range of healthy operating conditions. In addition, it is shown that the 2D-TSR is effective in monitoring localized thermal excitation such as that arising from winding fault. This allows for recognition and localization of fault events through observation of their thermal signature as evidenced on the examined commercial PMSM design, which are typically challenging for winding fault diagnostics [5]. Finally, an effective graphical presentation of 2D-TSR distributed thermal measurements is proposed that enables straightforward understanding of the winding thermal status and its operational diagnosis in both healthy and fault conditions.

II. PROPOSED 2D-TSR SENSING SCHEME PRINCIPALS

End-windings in random wound stator winding design consist of combined coil-ends of all stator coils. These coil-ends can generally either be uniformly or locally thermally stressed in operation. Fig.1 illustrates different overheating scenarios in a simplified schematic diagram of a three-phase random wound winding configuration containing two coils per phase (green, orange and black coils).

Uniform overheating can be caused by operating conditions such as transient or running overloads, fully reduced cooling capability and a high ambient temperature. In such conditions all coil-ends are uniformly overheated, as indicated by the blue dashed rectangle in Fig.1. From thermal protection and monitoring prospective, a single thermal sensor attached to the end-winding structure at any point could ensure effective monitoring and detection of such overheating conditions.

Localised overheating can be caused by conditions such as unbalanced phase currents, partially deteriorated cooling capability and incipient winding fault. Unbalanced three phase winding currents result in uneven individual phase temperatures, where one phase

winding can be hotter than others, as illustrated in Fig. 1 by the red dashed rectangle on the coils shown in black. To monitor the unbalanced currents induced localized overheating a single thermal sensing point per phase in the end-winding would be required. A partially deteriorated cooling system can cause a partial reduction in the heat dissipation capability from stator coils to ambient, resulting in overheating the stator coils whose heat dissipation pathway is affected by the cooling deterioration; this is illustrated in Fig.1 by the brown dashed rectangle showing an assumed overheated winding section due to deteriorated cooling capability. Under this condition at least one sensing point per affected area would be required to ensure registering of localised heat. Early stages of short circuit fault can also cause localised heat in the faulted turns, illustrated in Fig .1 by the purple dashed rectangle highlighting an assumed faulted coil. From thermal monitoring point of view, one sensing point for each stator coil-end would be required to ensure measurement of thermal excitation resulting from an arbitrary ITSCF case.

From the sensing requirement analysis for different overheating scenarios discussed above, it can be concluded that a single thermal sensing element per every individual coil-end span in the end-winding structure is sufficient to ensure thermal monitoring of the entire stator winding, as illustrated in Fig.1. The end-winding is conventionally instrumented with a number of thermal sensing elements (generally three sensing elements, one per phase) [20-21]. However only three thermal sensing points in the end-winding can readily miss out localised overheating, thus they are not sufficient to provide full protection and effective monitoring of the entire stator winding, as demonstrated by a large number of operating machines that despite being instrumented in this manner have failed in-service as

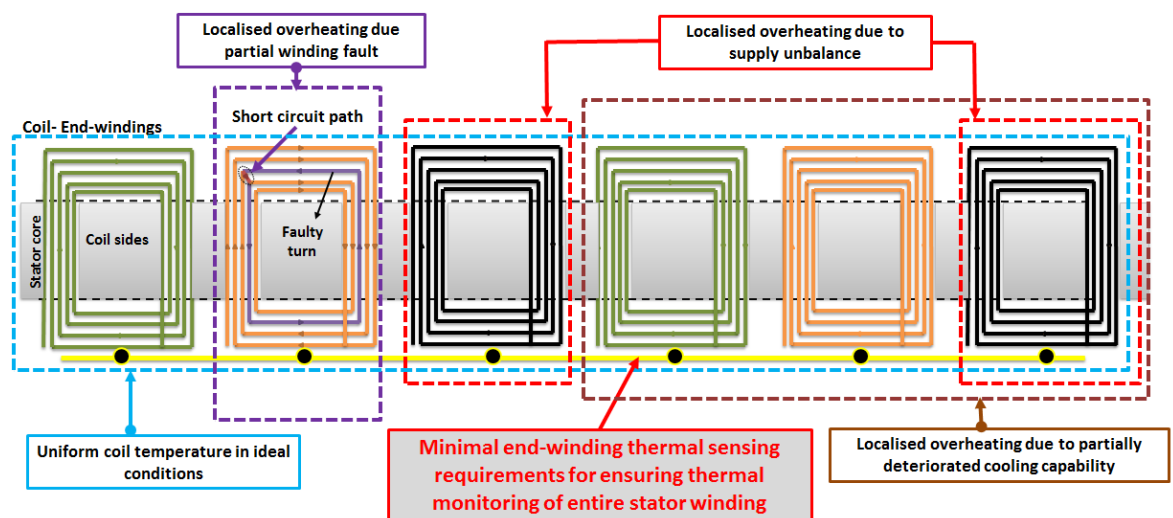


Fig. 1: A simple schematic diagram of three-phase stator winding highlighting different overheating scenarios

result of insulation breakdown [21-22]. In general, the short circuit fault thermal condition is the most critical in terms of winding overheating. This is due to the fact that the level of fault induced heat can be excessive and have a rapid rate of change, and its location in the winding structure is unpredictable. A thermal monitoring technique capable of registering winding fault induced localized heat can therefore be expected to be capable of monitoring other possible winding overheating conditions. This paper therefore examines and evaluates the proposed thermal sensing scheme under ITSCF conditions.

III. TEST RIG SETUP DESCRIPTION

The proposed 2D-TSR application for stator winding thermal monitoring under healthy and faulty conditions was experimentally investigated in tests on a commercial PMSM. The 2D-TSR was designed and prototyped to conform to the examined PMSM stator winding configuration. This section describes the used experimental including: the test PMSM, its winding configuration modified for fault emulation, the 2D-TSR design and embedment, and the test rig system setup.

A. The examined PMSM description

The examined machine is a commercially available 5.5 kW 3-phase, 400 V, 6 pole, PMSM by Lafert. Its specifications are shown in Table I and its stator winding configuration in Fig. 2. The stator winding is of concentric and stranded design; each phase contains six series connected coils, where each coil is wound with six parallel strands of 23.5 AWG enameled copper wire. Since sensing points of interest in this study are located in the end-windings, the coil-ends arrangement in the drive end-winding section (DE-winding) of the test machine is shown in Fig. 3. The coil-ends are distributed in three layers (one layer per phase): phase C coil-ends are in the bottom layer close to the frame bore surface, the mid layer coil-ends belong to phase B, while the top layer facing the air-gap are phase A coil-ends. The three layers are insulated from each other by phase insulation.

Table. I : PMSM motor specification

PMSM data	Standard: IEC 60034
Voltage / Current / Frequency	400 V / 11.5A / 75 Hz
Power/ Torque / Speed	5.5 kW / 35 Nm / 1500 rpm
Pole number / Rotor configuration	6 / Surface mounted magnet
Insulation class / Temperature rise class/Duty cycle type rating	F / B / S1

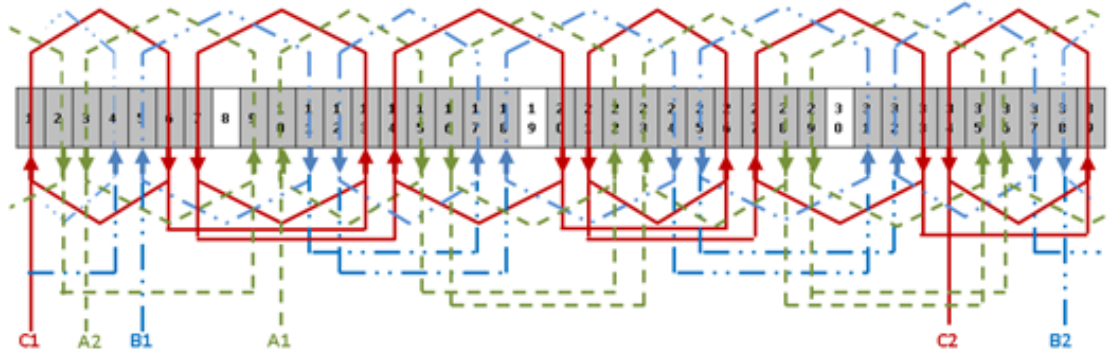


Fig. 2: PMSM stator winding configuration

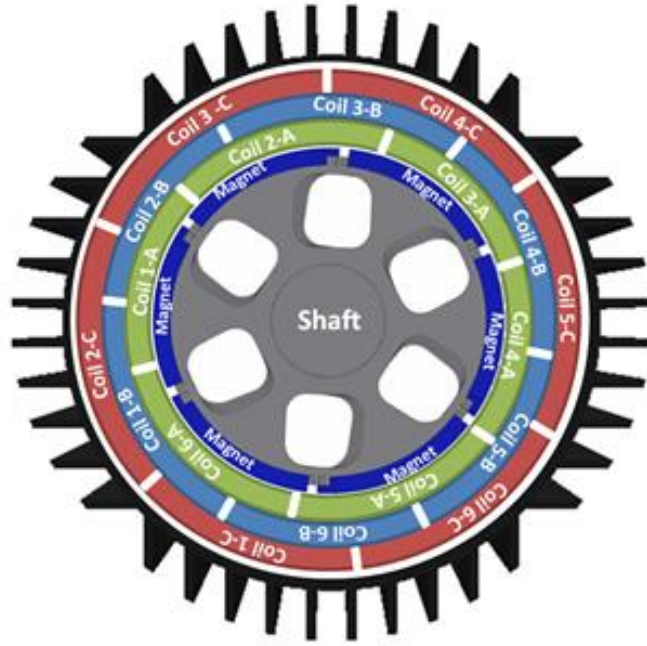


Fig. 3 Three phase coil-ends arrangement in DE-winding

B. 2D-TSR design and installation

Based on the coil-ends arrangement in the targeted DE-winding shown in Fig. 3 and the proposed sensing requirements of having one thermal sensing point per each individual coil-end span, two FBG thermal sensing arrays, A and B, were designed and developed as shown in Fig. 4a. The two arrays form the 2D-TSR; each consists of six 5 mm FBG heads imprinted in a bend insensitive single mode polyamide fibre. The FBG arrays were packaged in PEEK capillaries to protect the fragile fibres and eliminate any mechanical excitation effects during measurement [16]. Individual array FBG heads were spaced to enable sensing point positioning in target DE-winding structure locations, as shown in Fig. 4b. Array-A was embedded between the coil-ends of phases A and B and array-B between phase B and phase C coils-ends. The FBG heads' positions are coded as shown in Fig. 4b, starting from the bottom of DE-winding in clockwise direction (array-A sensing heads with

odd numbers and those belonging to array-B with even numbers). This provides an optimised 2D-TSR design having sensing locations (i.e. FBG heads) radially distributed with an ≈ 30 degree separation between adjacent points: this layout ensures at least one sensing point for each coil-end span: (for example, FBG 1 monitors coil5-A and coil6-B, FBG2 monitors coil1-C and coil6-B, etc.).

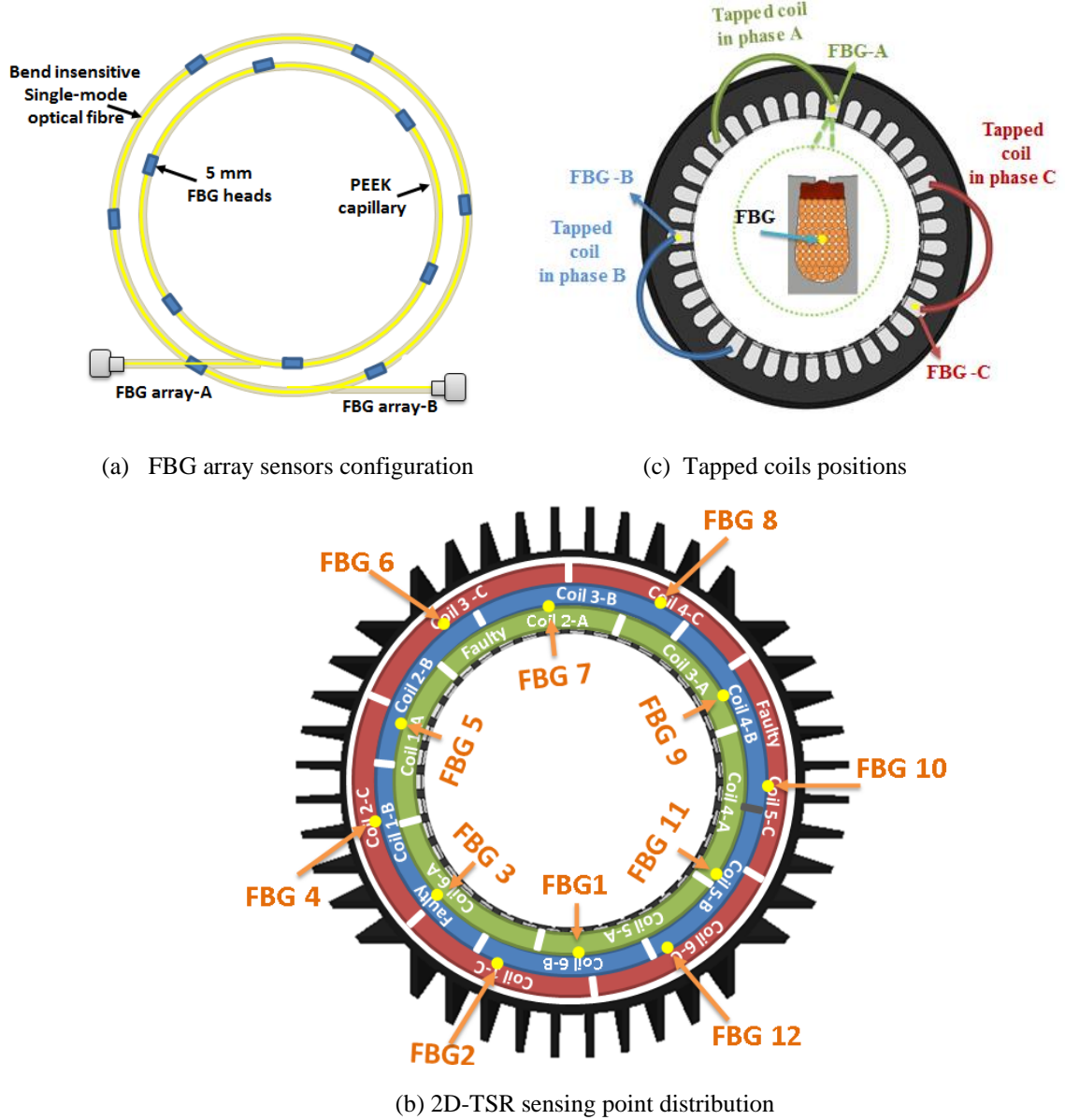


Fig. 4 2D-TSR design and location in the examined PMSM windings

Additionally, three FBG temperature sensors were embedded between conductors in centres of three different slots, one per phase (FBG-A, FBG-B and FBG-C). These sensors are located in slots that contain a side of the coil tapped for fault emulation as detailed in section III.C; their locations are shown in Fig. 4c. The purpose of these is-situ slot sensors is to enable comparison of fault induced thermal signature monitored in end-windings investigated in this study and slot sections (reported in [19]).

To enable FBG sensors installation and winding fault emulation the stator was rewound. The 2D-TSR embedment in the DE-winding was achieved as follows: once the winding coils were fully inserted in stator slots and secured by the slot top insulation liner and wedges, the PEEK capillaries were embedded between targeted coil-ends; the end-windings were then tied and the winding impregnated. Finally, the FBG arrays were inserted in appropriate PEEK capillaries. For the FBG installation in the winding slot section the procedure described in authors' previous work was followed [19].

C. Winding Modification for fault emulation

To evaluate the proposed 2D-TSR capability to monitor localised thermal excitation, such as arising at outset of ITSCFs, and hence fault diagnostic capability, the windings were modified during rewinding to include tapplings in specific coils for fault emulation. ITSCFs emulation in three different coils was enabled, one in each phase.

The examined PMSM is designed with a stranded winding configuration: each of the six series connected coils forming a phase winding contains 138 turns, and is made up of six parallel strands having 23 turns each, as illustrated in Fig. 5 for phase B winding. For fault emulation purpose, one strand in the targeted coil per phase was modified with tapplings to enable emulation of ITSCF scenarios involving 2, 5 or 10 shorted turns providing fault severity of 0.24 %, 0.6 % and 1.2 %, respectively. Fig. 5 shows the tapped turns in coil1 of phase B. Identical tapplings were applied to phases A and C; this was done in phase A coil2 and phase C coil5 to enable physically different fault locations in the examined winding structure. Figs. 4b and c illustrate the tapped coils locations.

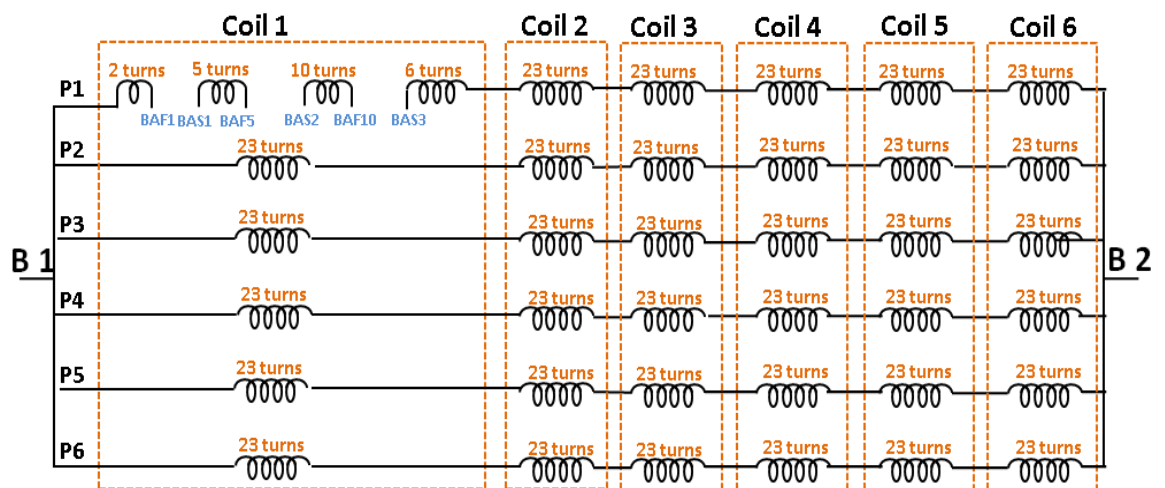


Fig. 5: Modified phase B winding configuration

D. Laboratory test system

A test rig was built to enable operating the PMSM under healthy and faulty conditions and facilitate on-line thermal monitoring performance assessment of the installed FBG 2D-TSR. The rig layout is illustrated in Fig.6. The test PMSM instrumented with the 2D-TSR system was operated in closed-loop vector control using a 7.5 kW (Parker 890SSD) drive, which was automated via DSE Lite software package. To enable operation in loaded conditions the PMSM was coupled to a DC machine controlled by a Parker 590SSD DC drive. The in-situ FBG 2D-TSR and slot sensors were interrogated by a commercial interrogator unit (SmartScan) at a sampling rate of 10 Hz. LeCroy CP150 current and ADP300 voltage probes operated by a LeCroy 434 digital oscilloscope were used for on-line measurement of relevant currents and voltages, including those in the faulted coil.

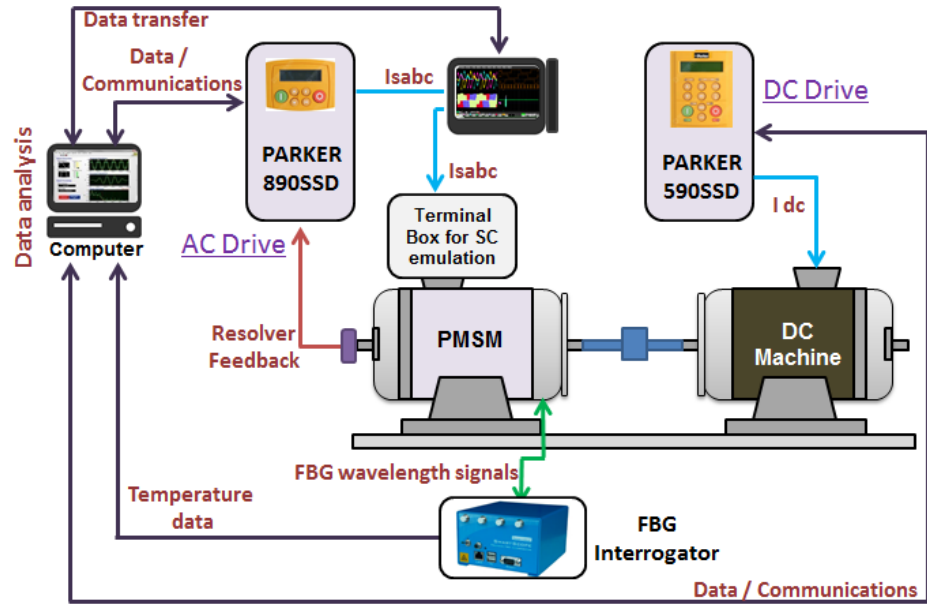


Fig. 6 Test-rig setup

IV. EXPERIMENTAL RESULTS AND DISCUSSION

Experimental tests were conducted to evaluate the performance of the proposed in-situ 2D-TSR design for healthy winding thermal condition monitoring, and examine its capability to enable detection and diagnosis of early stage winding fault. This section presents the obtained experimental results and discusses the findings.

A. Healthy winding condition monitoring evaluation

To practically emulate a range of different winding thermal conditions during healthy PMSM operation a series of IEC 60034-1 standard defined S1 duty cycles were applied on the test motor at different speed and load levels [20].

1) Evaluation of 2D-TSR performance and winding thermal statue under different load conditions

Three S1 duty cycles were applied to the PMSM at constant speed (full-speed (FS), 100 % speed =1500 rpm) and at three different load levels: no-load (NL, 0 % load), half-load (HL, 50 % load) and full-load (FL, 100 % load). Fig. 7 shows the steady-state thermal measurements obtained by the 2D-TSR for the three applied S1 duty cycles. The 2D-TSR thermal measurements are presented in a spatially distributed thermal web form which enables enhanced physical interpretation of the obtained localized thermal conditions and their straight forward correlation to the actual winding/machine geometry. The web radial lines represent the reference directions of the thermal sensing points (i.e. FBG heads locations in DE-winding) with respect to the reference point in the cross-sectional centre of the machine geometry (refer to Fig. 4b). The web concentric circles represent constant temperature gradients shown for illustration purposes in 10 °C steps.

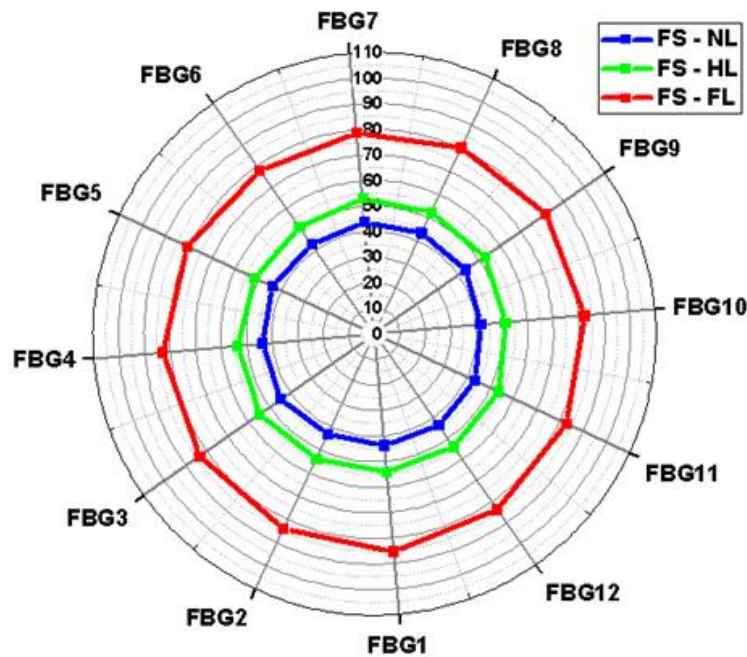


Fig. 7: Thermal web measurements at rated speed and different load conditions

The blue, green and red quasi-circular patterns plotted in the thermal web in Fig. 7 are the temperatures measured by the 2D-TSR's 12 FBG heads in NL, HL and FL conditions, respectively. Individual dots in the plotted thermal patterns correspond to the actual steady-state measured temperatures by corresponding individual 2D-TSR FBG heads. The presented distributed thermal measurements are manifested in an almost uniform circular shape, thus illustrating, as expected, the nearly even distribution of the radial temperature levels measured in the examined motor windings in healthy conditions: a temperature

difference between 2D-TSR FBG heads of up to ≈ 3.5 °C was measured at steady-state. It can also be observed that the measured thermal patterns radius increases with load, reflecting the rise in the monitored end-winding internal thermal hot spots due to loss increase with load; for the examined PMSM this is seen to increase from an average of ≈ 42 °C at NL to ≈ 53 °C at HL and ≈ 80 °C at FL (temperatures obtained by averaging the respective radii of corresponding thermal patterns).

2) Evaluation of 2D-TSR performance and winding thermal status under different speed conditions

In this test, the PMSM was exposed to a series of S1 duty cycles at three different speed levels: low-speed (LS, 25%, 375 rpm), half-speed (HS, 50 %, 750 rpm) and FS examined in the previous section. Each speed level was applied at three different load levels (NL, HL and FL) giving nine test S1 duty cycles in total. The test motor is a totally enclosed rotor fan cooled design where cooling capability is operating speed dependent. The winding's internal thermal status is thus expected to vary considerably with speed variation. This change is generally expected to be further enhanced by the fact that some of machine loss components such as core and mechanical losses are also speed dependent.

Fig. 8 shows the obtained thermal webs for all examined S1 duty cycles. The presented thermal measurements demonstrate the variation in the winding internal temperature due to variation in the PMSM speed and thus the variation in speed dependent loss components magnitude and cooling capability. The degradation in the cooling capability and thus winding heat dissipation with reduction of operating speed is most apparent when FL condition is considered. The average radius of the FL thermal web patterns (red) is seen to increase from ≈ 80 °C at FS-FL to ≈ 89 °C at HS-FL and further to ≈ 101 °C at LS-FL. The expected general reduction in loss components such as core iron loss and mechanical loss with speed is seen to be insufficient to compensate the reduction in cooling capability and maintain the winding's temperature at constant level. In contrast, the radii of the thermal patterns at HL (green) show a slight decrease of ≈ 4 °C with speed reduction from FS-HL to LS-HL, illustrating that the winding's internal temperature decreases with speed reduction at HL conditions. This decrease is further magnified at NL, where the average temperature reduces from ≈ 43 °C at FS-NL to ≈ 31 °C at LS-NL. This thermal behaviour can be explained by the decrease in loss components (iron and friction) with speed reduction that can offset the speed reduction caused decrease in winding heat dissipation to the ambient: the rate of heat generated within the test motor to heat dissipated is maintained at an almost constant level at HL and decreased at NL.

The obtained and presented thermal measurements illustrate the efficacy of the proposed 2D-TSR to monitor and map the stator winding thermal dynamics under different operating conditions.

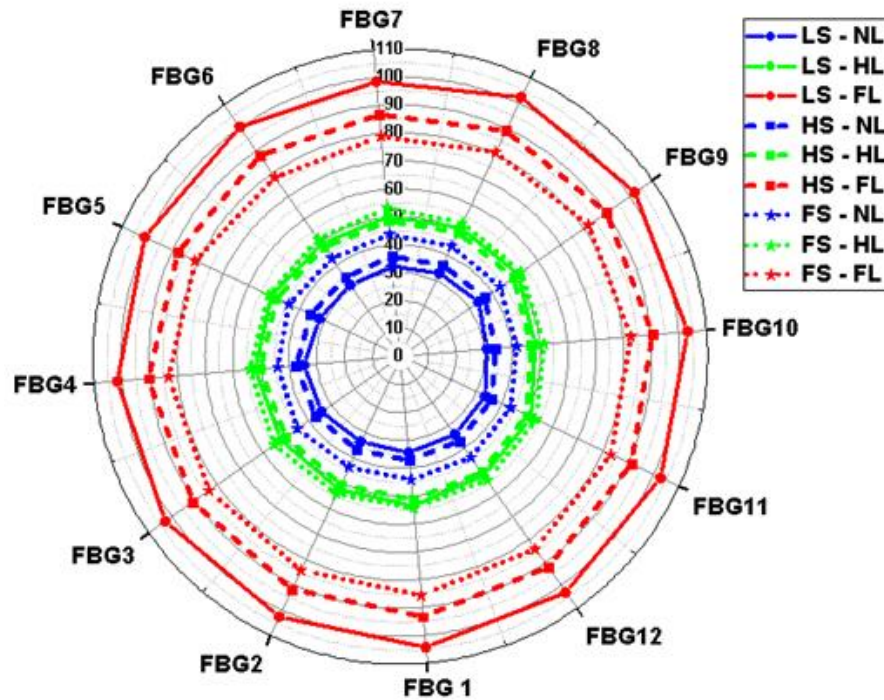


Fig. 8: Thermal web measurements at different speed/load conditions

B. Localised thermal excitation monitoring for ITSCF diagnosis

This section examines the 2D-TSR application for incipient ITSCF diagnosis in experiments involving various faulty operating conditions. The ITSCF induced thermal signature was monitored and analysed for different fault severity and location.

1) Fault test procedure

The test procedure applied for each experimentally examined fault condition involved waiting for the thermal equilibrium to first be achieved for healthy machine operating at the examined operating point; a short-circuit fault then is induced and maintained for a 60s period. To practically emulate short circuit fault conditions without permanently damaging test machine windings, the circulating current in the shorted turns was limited at a maximum of 15 A at rated conditions ($\approx 130\%$ of rated current) using an external resistance connected in series with the short circuit path. The short circuit current limit was set based on undertaking offline DC thermal excitation tests.

2) ITSCF thermal signature monitoring

To practically examine the 2D-TSR capability to detect ITSCF induced localised heat

loss (i.e. fault thermal signature) ITSCFs were induced in coil2-A with 2, 5 and 10 shorted turns cases (2TA, 5TA and 10TA) at rated conditions (FS and FL), following the procedure described in the previous section. Fig. 9 shows the obtained 2D-TSR measurements at the end of fault period.

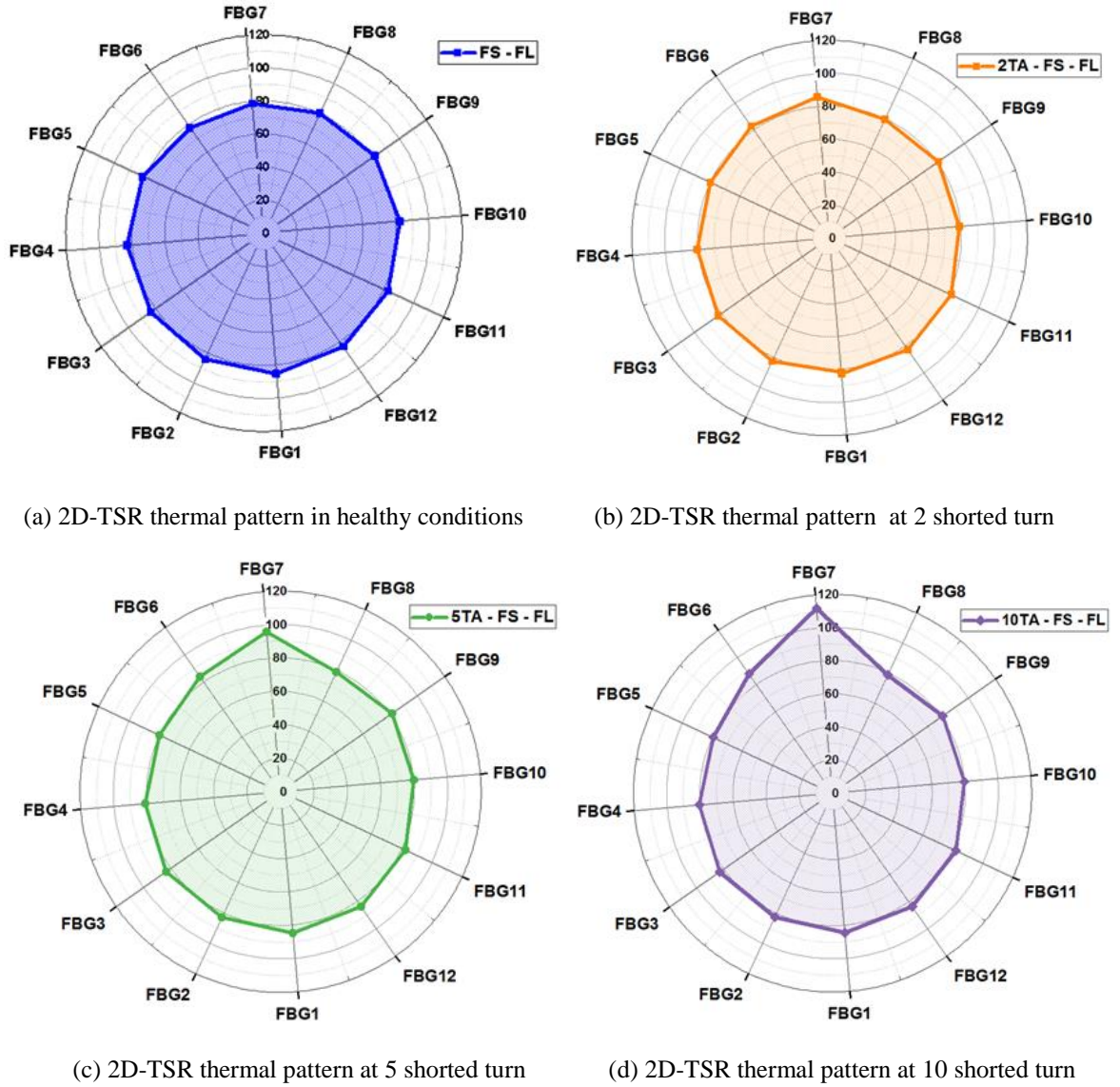


Fig.9: 2D-TSR induced thermal patterns for ITSCF diagnosis in phase A

Fig. 9a shows the 2D-TSR reported thermal pattern in healthy conditions, seen to be manifested as an almost uniform quasi-circular shape with an average radius of ≈ 79 °C, as discussed in Section IV.A. However, with ITSCF presence the observed quasi-circular thermal pattern alters, reporting temperature level increase in the direction of FBG6 and FBG7. This trend is magnified with fault severity increase, as seen in the measurements shown in Figs. 9b-d for 2, 5 and 10 shorted turns cases, respectively. The 2D-TSR FBG6 and FBG7 were capable of registering the ITSCF induced heat in coil2-A, since these FBG heads are located close to the faulty coil (refer to Fig. 4b). However, FBG7 recorded a

relatively higher temperature when compared to FBG6; this is because in this fault case FBG7 is the sensing head in direct contact with the faulted coil. FBG7 measures temperatures of ≈ 85 , ≈ 96.8 and ≈ 112.2 °C in 2, 5 and 10 shorted turns tests, which corresponds to ≈ 6 , ≈ 17.8 and ≈ 33.2 °C temperature rise above the healthy winding operating temperature of ≈ 79 °C at the examined condition. The presented experimental data demonstrate the ability of the proposed in-situ 2D-TSR design for incipient ITSCF detection with the capability for fault severity diagnosis. The 2D-TSR observed thermal patterns also show the capability of fault location identification within the winding structure, which is further investigated in the following section.

3) Thermal signature monitoring for fault location diagnosis

This section examines the 2D-TSR potential to enable advanced diagnostic capability, focusing on fault location diagnosis. To this end, a number of ITSCFs were induced in different locations within the examined PMSM winding structure. Faults were separately induced in phase A, B and C and in locations discussed in section III.C at all examined fault severities and at rated operating conditions. Fig. 10 shows the measured thermal patterns for all examined fault cases.

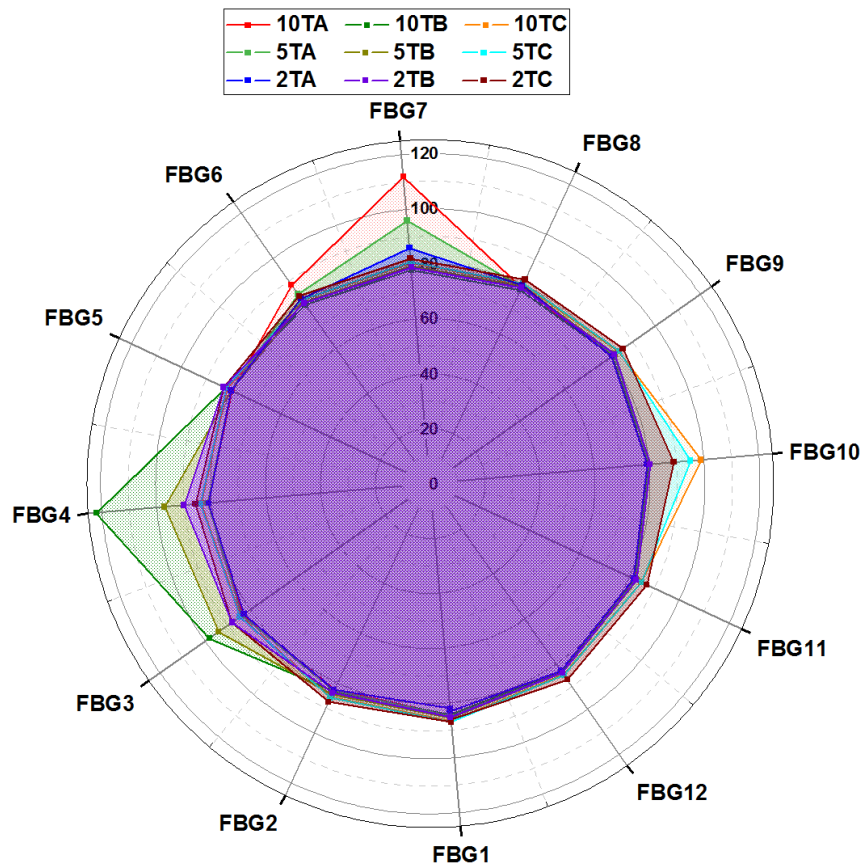


Fig. 10: Thermal web measurements at different fault locations

The measured thermal patterns in Fig. 10 show the 2D-TSR design's ability to facilitate effective identification of fault physical location within the winding structure. In addition, the results demonstrate the schemes capability to also identify the faulty coil and thus the faulty phase. This can be illustrated by considering, for example, the measurements obtained for the coil2-A fault case along with the arrangement of the coil-ends and FBG heads in the end-winding area close to the fault location (refer to Fig. 4b). The coil-ends located in this section of the end-winding belong to: coil2-A, coil3-B, coil3-C and coil4-C, and are monitored by FBG6, FBG7 and FBG8. In case fault occurs in one of the above coils, the temperature rise levels measured simultaneously by the three co-located FBG heads can enable identification of the faulty coil and phase: when fault occurs in coil2-A FBG7 is expected to show higher temperature rise than FBG6 and FBG8, which is clearly reported in the corresponding measurements shown in Fig 10. Similarly, if a fault occurs in coil3-B, FBG7 and FBG8 are expected to show higher temperature rise and when fault occurs in coil3-C or coil4-C FBG6 and FBG8 are expected to show higher temperature rise, respectively. The same principles can be applied to faults in other end-winding sections in order to enable location diagnosis.

The measurements in Fig. 10 indicated that the 2D-TSR measured fault thermal signature magnitudes are different for identical fault severity present at different locations. For example, FBG4 measures a temperature of ≈ 122 °C for a 10 shorted turns fault induced in coil1-B (10TB), whereas FBG7 and FBG10 measure ≈ 111.8 and ≈ 98 °C for the same fault level emulated in coil2-A (10TA) and coil5-C (10TC), respectively. This can be explained by the nature of the phase coil-ends arrangement in the test motor end-winding (refer to Fig. 3) and the nature of radial heat dissipation in the test motor design: phase B coil-ends are located between phases A and C coil-ends; individual phases are mutually separated by phase insulation. This arrangement reduces the dissipation rate of the fault induced heat from phase B at the outset of an ITSCF. Thus in case of an ITSCF in phase B 2D-TSR registered the highest temperature level for all examined fault severities, which was measured by FBG4. When an ITSCF was induced in phase C the 2D-TSR registered the lowest temperature rise levels, measured by FBG10. This is because phase C is located close to the frame bore surface allowing faster dissipation of fault induced heat. In the case of an ITSCF induced in phase A, the measured temperature rise levels were lower than those observed for fault in phase B and higher than those measured for phase C fault, since phase A coil-ends location (at the air-gap) imposes slower heat dissipation than in case of Phase C fault but still provides a degree of cooling due to air flow in the air gap.

It can be concluded that fault in phase-B can be considered the most critical ITSCF location in the examined motor winding in terms of the resulting thermal stress, and thus the fault magnitude and speed of development.

C. Fault thermal signature analysis under different load/speed conditions

Sections B examined the sensing performance of the proposed in-situ 2D-TSR for an ITSCF diagnosis including fault induced localised overheating detection and fault severity and location diagnosis. However, this assessment was conducted only at rated operating conditions (FS and FL). However, modern electric machines are largely inverter driven to operate in variable speed and load conditions. Therefore, this section examines the 2D-TSR diagnostic performance and the fault thermal signature behaviour under a wider range of load and speed conditions. The presented analysis also enables the identification of the examined PMSM critical operating points in ITSCF conditions.

1) Different load conditions

All ITSCF cases examined in section IV.B.3 under FL condition were examined here for operation in NL and HL conditions. The tests were performed in rated speed conditions (FS) to enable observation of the fault induced thermal signature and sensor performance with load variation only.

For illustration, Fig. 11 shows the obtained thermal measurements for the examined ITSCFs with 2, 5 and 10 shorted turns in coil5-C under NL, HL and FL, respectively. The presented thermal measurements are obtained by FBG10, which is the FBG head monitoring coil5-C. Fig. 11a shows the measured temperature rise (healthy to faulty) and Fig. 11b shows the actual measured temperature for each examined fault case. The data in Fig. 11a indicate that load variation does not result in a considerable variation in the fault induced heat and thus its thermal signature for a given constant fault severity level: the measured temperature rise level difference remains within ≈ 2 °C. However, it can be noted that there is a slight decrease in the fault induced thermal signature with load increase at high fault severity levels (5 and 10 shorted turns). This is because of the shorted turn's resistance temperature dependency. As the load increases, the winding operating temperature also increases due to increase in winding loss, as shown in Fig. 7. This increase results in an increase in the shorted turn's resistance, which acts to reduce the circulating shorted turn current and thus the fault induced heat.

The measurements in Fig. 11b illustrate that knowledge of the winding operating thermal status is key to understanding critical thermal conditions in fault presence. The fault

induced heat magnitude remains almost constant with load as seen in Fig. 11a. However, the winding temperature is considerably higher at high load and the thermal stress and resulting damaging effects of fault therefore expected to be more significant: the ITSCF neighboring healthy winding can be expected to thermally age faster at high load conditions and the fault to propagate relatively quicker.

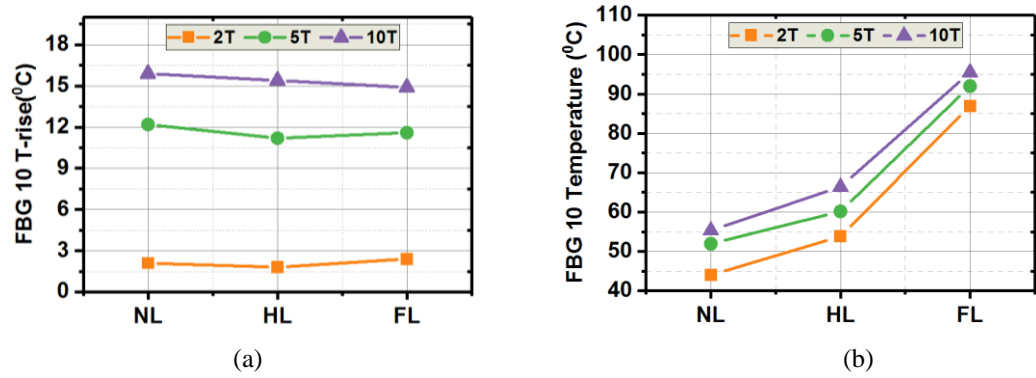


Fig. 11: Fault induced thermal signature behaviour at different load levels

2) Different speed conditions

The ITSCF cases examined in the previous section under FS are examined in this section under LS and HS. The tests were performed at constant load (FL) to examine the fault thermal signature variation exclusive to operating speed change. For illustration, Fig. 12 shows the thermal measurements for ITSCF in coil5-C, while Fig. 12a shows the corresponding measured temperature rise (healthy to faulty) and Fig. 12b the actual temperature measured by FBG10.

In contrast to the load variation impact on fault induced thermal signature, the speed variation results in a considerable change in the fault induced thermal signature. FBG10 recorded a temperature rise of ≈ 14.6 °C for the 10 shorted turns case at FS, which reduced to ≈ 8.2 °C and 2 °C at HS and LS, respectively. The obtained thermal measurements illustrate that fault induced heat detection is more challenging at lower speeds. The direct relationship between the operating speed and the fault induced thermal signature in the examined PMSM design is due to the shorted turns induced EMF voltage speed dependency. Since the shorted turns essentially act as a shorted coil placed in the rotor magnetic field, the reduction in rotor speed causes reduction in its back EMF and thus the circulating fault current, which in turn reduces the fault induced heat. This was confirmed by the shorted turns induced voltage and circulating currents measurements obtained during the tests. For illustration, Fig 13 shows the measured shorted turn induced current and voltage for the 10 shorted turns case in coil5-C under FS, HS and LS demonstrating their clear reduction with the reduction in operating speed.

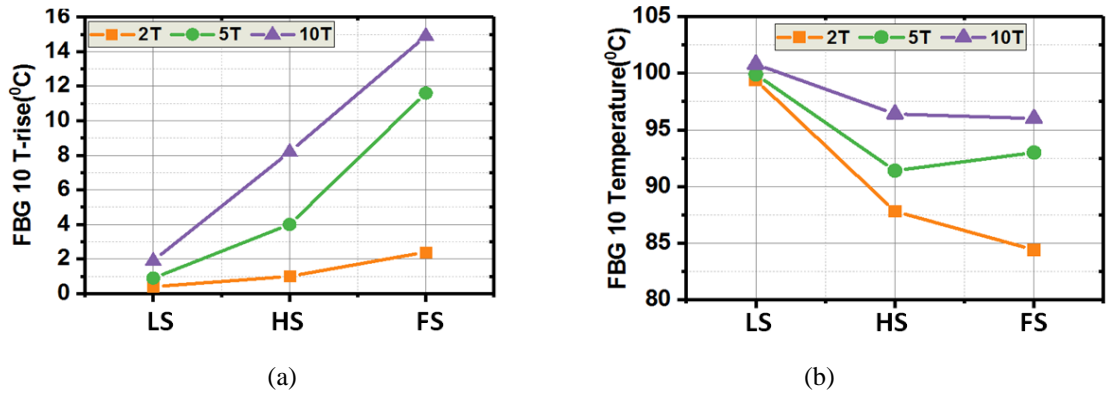


Fig. 12: Fault induced thermal signature behaviour at different speeds

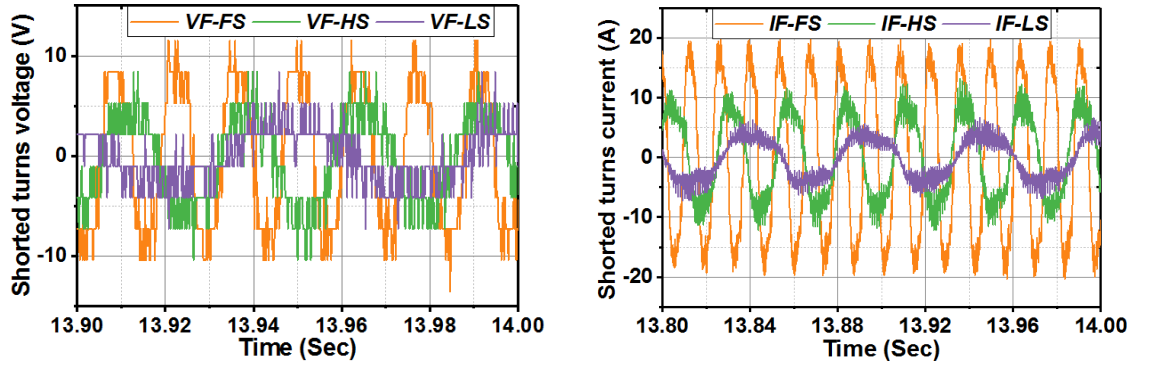


Fig. 13: Measured shorted turns induced voltage and current in coil5-C under different speed condition

In the examined PMSM design low speed operation at full load generally reduces the cooling capability and thus results in winding operating temperature increase, as shown in Fig. 8. Therefore, despite the fault induced temperature rise level largely reducing at lower speeds, the winding is still more thermally stressed in low speed operation conditions, as can be seen in Fig. 12b. This means that the time taken for the neighboring healthy turns' insulation system degradation at low speed can generally be expected to be smaller than at high speed, and the fault can thus propagate relatively faster in low speed conditions. However, it was discussed in Section IV.A.2 and shown in Fig 8 that the winding thermal characteristics of the test PMSM vary with different combination of speed and load operating conditions. Further examination was therefore conducted to evaluate the critical thermal conditions in fault presence under LS, HS and FS in HL and NL conditions. Fig. 14 shows the obtained temperature measurements by FBG10 for a 10 turn ITSCF in coil5-C at HL (Fig. 14a) and NL (Fig. 14.b). The obtained thermal measurements show an opposite trend to that obtained at FL (Fig. 12b). For lower load conditions the thermally critical operating point with fault is seen to be manifested at FS operation.

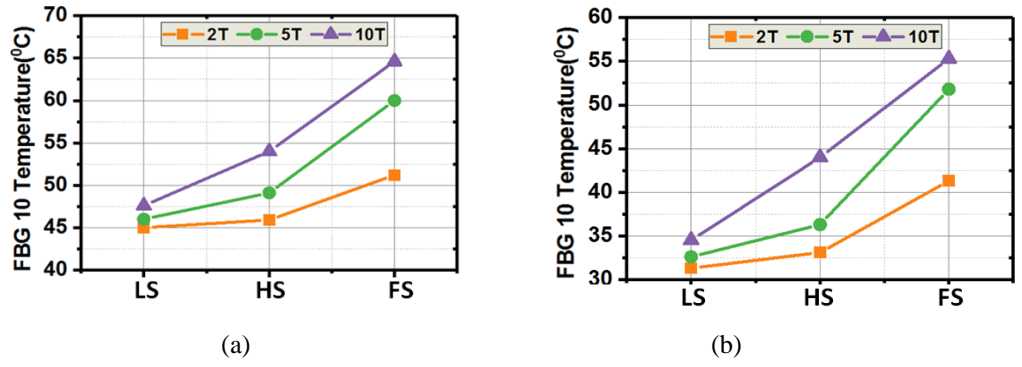


Fig. 14: Fault induced thermal signature behaviour at different speed/load

D. 2D-TSR thermal monitoring performance comparison with slot section embedded FBGs

In [19] the authors analysed the optimal thermal sensing position for monitoring ITSCF induced thermal signature in a random wound machine, which was reported to be in the slot section and in particular in the slot cross-section centre. In the same study it was also demonstrated that two thermal sensing points in the stator end-winding are not adequate to reliably detect localized heat arising from an arbitrarily located ITSCF. The proposed 2D-TSR design in this paper overcomes this as demonstrated in previous sections. However, the 2D-TSR detection of ITSCF signature can be affected by the nature of the end-winding structure and the 2D-TSR embedment (i.e. location between coil-ends surfaces). Therefore, this section compares the dynamic sensing performance of 2D-TSR with FBG sensors embedded in the slot section [19].

During the ITSCF tests performed in section IV.B.3 thermal measurements were synchronously recorded from both TSR and slot FBG sensors (discussed in section III.B) for each ITSCF case. Fig. 15 shows the FBG4 (on the 2D-TSR) and FBG-B (in slot) measurement when an ITSCF was induced in coil1-B for performance comparison purposes: Fig. 15 a, b and c show temperature rise measurements for 2, 5 and 10 turn ITSCFs, respectively. The results are divided into three sections on the time axis: the first 60s show measurements before fault is practically emulated, the following 60s show the fault induced temperature rise (fault period) and the remaining 180s the cooling period after fault was removed. The data show that slot section FBG responds slightly faster to fault than that in the 2D-TSR. In addition, the temperature rise level measured by the TSR FBG is seen to be lower than that measured by FBG-B. In the 2 shorted turns fault case the FBG4 registered temperature rise of ≈ 3.7 °C at the end of fault period while FBG-B registered ≈ 5.7 °C. For 5 and 10 shorted turn faults, FBG4 registered ≈ 16 °C and ≈ 46 °C whereas FBG-B registered ≈ 21 °C and ≈ 41 °C, respectively. Similar behavior was observed for fault experiments in other two phases.

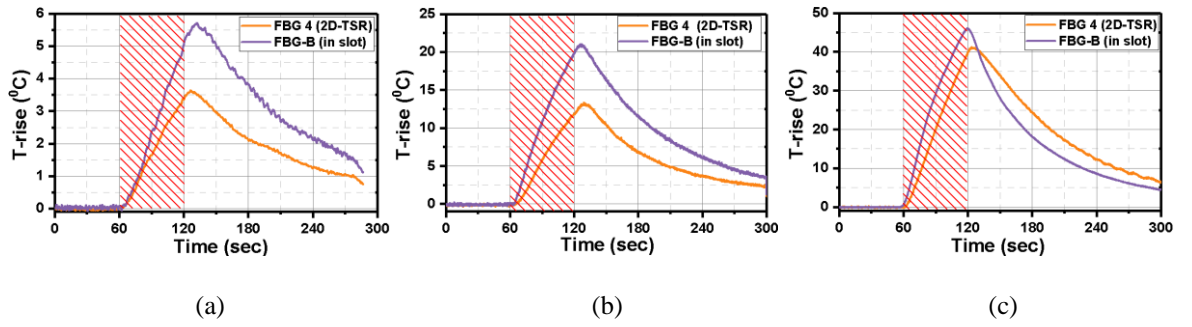


Fig. 15: Dynamic performance assessment of the 2D-TSR in comparison with FBG located in the winding slot section

E. 2D-TSR data visualisation

Effective interpretation of condition monitoring data is key in enabling its use for diagnostic decision making and maintenance management; this is particularly pertinent when performing diagnostics in critical systems with large number of monitored components. Availability of a CM data advanced graphical interface could enable effective and straightforward interpretation of monitored diagnostic signals and any fault signatures contained, and lead to improved reliability diagnosis. In addition, advanced CM data visualization could also enable easier simultaneous analysis of multiple components health condition and ensure unambiguous CM data communication between diagnostic engineers. To this end, this section proposes 2D-TSR thermal measurements graphical form aimed at enabling straightforward and rapid interpretation of winding health conditions.

Fig. 16 shows a 2D graphical representation of the examined PMSM end-winding radial thermal status measured by the 2D-TSR design. A contour heat-map graphical technique using OriginPro 2017 software was used to develop the 2D end-winding graphical representation. The twelve dots shown in the 2D graphical representation represent the FBG heads locations in the end-winding, as shown in Fig. 4b. The temperature gradient in the produced 2D thermal image is automatically interpolated by the OriginPro software based on the updated FBGs thermal data. Fig. 16 a-c show the 2D end-winding thermal representation when an ITSCF was induced in the coil1-B for all examined fault severity at rated conditions (FS and FL). A hot spot can be clearly seen in the location of the fault (refer to fault locations in Fig. 4c), measured by FBG4 and FBG3. The hot spot temperature level increases with the fault severity increase to $\approx 91^\circ\text{C}$ for 2 a turn ITSCF, and $\approx 98^\circ\text{C}$ and $\approx 123^\circ\text{C}$ for 5 and 10 ITSCF cases. In Fig. 16 e-f the 2D end-windings graphical model illustrates the end-winding thermal states when an ITSCF was induced in coil2-A. The hot spot is displayed to the top of the 2D model indicating both the fault presence and its location.

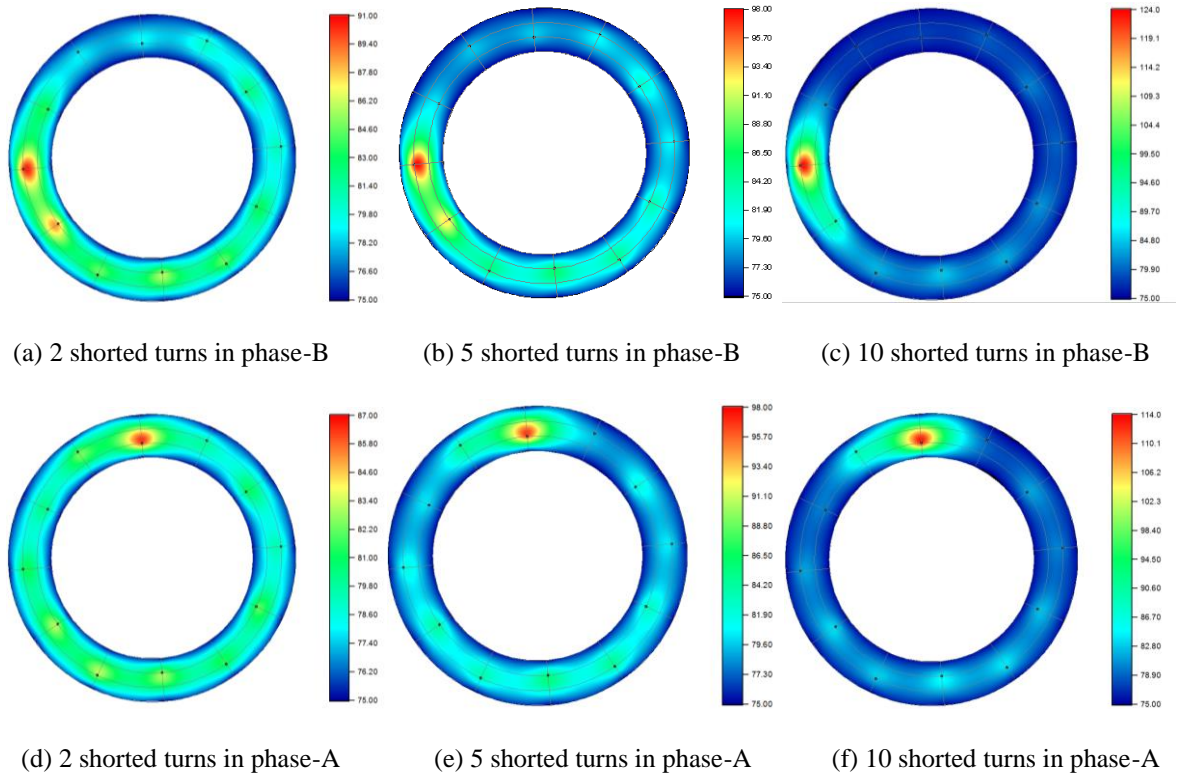


Fig. 16: End-winding thermal visualisation using 2D graphical representative

V. CONCLUSIONS

This paper reported a new thermal sensing configuration for stator winding on-line thermal and thus health condition diagnosis. The proposed sensing scheme is based on multiple thermal sensing points distributed within the stator end-winding section, practically achieved by designing a single fibre 2D-TSR inscribed with a number of FBG heads. The 2D-TSR was adapted to and installed in a commercial inverter driven PMSM and its performance examined in experiments under different healthy and faulty operating conditions.

The results demonstrate the efficacy of 2D-TSR design in effectively monitoring the test PMSM stator winding thermal status by registering both uniform thermal variation due to operating conditions variation, and localised thermal excitation such as induced by ITSCFs. The 2D-TSR is shown to enable unambiguous recognition and diagnosis of ITSCFs in PMSMs, which remains a challenging task for conventional diagnostic techniques. This includes fault severity trending from low fault level but also the capability of fault location diagnosis.

The reported 2D-TSR scheme enable inherent optimisation of distributed sensing points and can facilitate more straightforward sensor installation when compared to existing studies on FBG use for winding thermal monitoring. These improvements however come

at a penalty of a relatively minor reduction in sensing performance under fast thermal transient conditions, such as those generated in winding fault.

The paper also applies the proposed scheme to provide an analysis of winding fault induced thermal signature behaviour under a wide range of PMSM operating speeds and loads. The analysis demonstrates that load variation has no considerable impact on fault thermal signature which is shown to be largely determined by operating speed and considerably decreases with operating speed decrease. In addition, the overall impact of fault in the neighbouring healthy turns in terms of possible fault propagation time and level was also analysed to determine thermally critical fault operating conditions. This is largely ignored in literature and is not fully understood. For the examined motor design it was shown that the critical operating point in ITSCF conditions is defined by the both operating speed and load: at high loads the fault impact is higher at lower speed conditions (LS) while, in contrast, at low loads the fault critical condition is manifested at full speeds (FS).

Finally this work reports the utilization of advanced graphical presentation of 2D-TSR distributed thermal measurement for improved understanding and usability of condition monitoring data and enhanced winding health diagnosis.

REFERENCES

- [1] T. D. Kefalas and A. G. Kladas, "Thermal Investigation of Permanent-Magnet Synchronous Motor for Aerospace Applications," in *IEEE Transactions on Industrial Electronics*, vol. 61, no. 8, pp. 4404-4411, Aug. 2014.
- [2] H. Jeong, S. Moon and S. W. Kim, "An Early Stage Interturn Fault Diagnosis of PMSMs by Using Negative-Sequence Components," in *IEEE Transactions on Industrial Electronics*, vol. 64, no. 7, pp. 5701-5708, July 2017.
- [3] M. A. Parker, L. Ran and S. J. Finney, "Distributed Control of a Fault-Tolerant Modular Multilevel Inverter for Direct-Drive Wind Turbine Grid Interfacing," in *IEEE Transactions on Industrial Electronics*, vol. 60, no. 2, pp. 509-522, Feb. 2013.
- [4] S. K. Kommuri, M. Defoort, H. R. Karimi and K. C. Veluvolu, "A Robust Observer-Based Sensor Fault-Tolerant Control for PMSM in Electric Vehicles," in *IEEE Transactions on Industrial Electronics*, vol. 63, no. 12, pp. 7671-7681, Dec. 2016.
- [5] S. Choi *et al.*, "Fault Diagnosis Techniques for Permanent Magnet AC Machine and Drives-A Review of Current State of the Art," in *IEEE Transactions on Transportation Electrification*, vol. 4, no. 2, pp. 444-463, June 2018.
- [6] S. Grubic, J. M. Aller, B. Lu and T. G. Habetler, "A Survey on Testing and Monitoring Methods for Stator Insulation Systems of Low-Voltage Induction Machines Focusing on Turn Insulation Problems," in *IEEE Transactions on Industrial Electronics*, vol. 55, no. 12, pp. 4127-4136, Dec. 2008.
- [7] W. le Roux, R. G. Harley and T. G. Habetler, "Detecting Rotor Faults in Low Power Permanent Magnet Synchronous Machines," in *IEEE Transactions on Power Electronics*, vol. 22, no. 1, pp. 322-328, Jan. 2007.
- [8] M. A. Mazzeletti, G. R. Bossio, C. H. De Angelo and D. R. Espinoza-Trejo, "A Model-Based Strategy for Interturn Short-Circuit Fault Diagnosis in PMSM," in *IEEE Transactions on Industrial Electronics*, vol. 64, no. 9, pp. 7218-7228, Sept. 2017.
- [9] N. Leboeuf, T. Boileau, B. Nahid-Mobarakeh, N. Takorabet, F. Meibody-Tabar and G. Clerc, "Estimating Permanent-Magnet Motor Parameters Under Inter-Turn Fault Conditions," in *IEEE Transactions on Magnetics*, vol. 48, no. 2, pp. 963-966, Feb. 2012.

- [10] L. Romeral, J.C. Urresty, J.-R.R. Ruiz, and A.G. Espinosa, "Modeling of surface-mounted permanent magnet synchronous motors with stator winding interturn faults," *IEEE Trans. Ind. Electron.*, vol. 58, no. 5, pp. 1576-1585, May 2011.
- [11] R. T. Meyer, R. A. DeCarlo, S. C. Johnson and S. Pekarek, "Short-Circuit Fault Detection Observer Design in a PMSM," in *IEEE Transactions on Aerospace and Electronic Systems*, vol. 54, no. 6, pp. 3004-3017, Dec. 2018.
- [12] R. M. Tallam *et al.*, "A Survey of Methods for Detection of Stator-Related Faults in Induction Machines," in *IEEE Transactions on Industry Applications*, vol. 43, no. 4, pp. 920-933, July-aug. 2007.
- [13] D. C. Patel and M. C. Chandorkar, "Modeling and Analysis of Stator Interturn Fault Location Effects on Induction Machines," in *IEEE Transactions on Industrial Electronics*, vol. 61, no. 9, pp. 4552-4564, Sept. 2014.
- [14] S. D. Wilson, G. W. Jewell and P. G. Stewart, "Resistance estimation for temperature determination in PMSMs through signal injection," *IEEE International Conference on Electric Machines and Drives*, 2005., San Antonio, TX, 2005, pp. 735-740.
- [15] J. P. Bazzo, F. Mezzadri, E. V. da Silva, D. R. Pipa, C. Martelli and J. C. Cardozo da Silva, "Thermal Imaging of Hydroelectric Generator Stator Using a DTS System," in *IEEE Sensors Journal*, vol. 15, no. 11, pp. 6689-6696, Nov. 2015.
- [16] A. Mohammed and S. Djurović, "Stator Winding Internal Thermal Monitoring and Analysis Using In-Situ FBG Sensing Technology," in *IEEE Transactions on Energy Conversion*, vol. 33, no. 3, pp. 1508-1518, Sept. 2018.
- [17] K. D. M. Sousa, A. A. Hafner, H. J. Kalinowski, J. C. C. da Silva, "Determination of temperature dynamics and mechanical and stator losses relationships in a three-phase induction motor using fiber Bragg grating sensors", *IEEE Sens. J.*, vol. 12, no. 10, pp. 3054-3061, Oct. 2012.
- [18] Matthias Fabian, David Martin Hind, Chris Gerada, Tong Sun, and Kenneth T. V. Grattan, "Comprehensive Monitoring of Electrical Machine Parameters Using an Integrated Fiber Bragg Grating-Based Sensor System," *J. Lightwave Technol.* 36, 1046-1051 (2018)
- [19] A. Mohammed, Juan. Melecio, and S. Djurović, " Stator Winding Fault Thermal Signature Monitoring and Analysis by in-situ FBG Sensors," in *IEEE Transactions on industrial electronics*, 2018.
- [20] IEC 60034-1:2010, Rotating electrical machines - Part 1: Rating and performance.
- [21] P. J. Tavner, "Review of condition monitoring of rotating electrical machines," in *IET Electric Power Applications*, vol. 2, no. 4, pp. 215-247, July 2008.
- [22] IEEE Guide for AC Motor Protection," in *IEEE Std C37.96-2012 (Revision of IEEE Std C37.96-2000)* , vol., no., pp.1-160, 20 Feb. 2013.

Chapter 7: *FBG Sensing Application for Electric Machinery Rotary Components Condition Monitoring*

7.1 Introduction

Bearings and the rotor are vital components in rotating electric machinery, and their health status monitoring is thus of practical importance to ensure the reliability and availability of machine operation. Bearing and rotor failures account for more than half of overall EM failures [1, 58]. Development of improved monitoring and fault diagnostic techniques for these components is thus of particular interest [189].

Thermal and mechanical stresses are the main causes of bearing and rotor failures [38]. In addition, both bearing and rotor faults will produce thermal and mechanical excitation. Therefore, effective thermal and mechanical condition monitoring of these components is important for maintaining their integrity and enabling reliable understanding of their health status and diagnosis of impending faults. To this end, this chapter reports a feasibility study of examining the use of FBGST to enable on-line condition monitoring of bearing and rotor vital health parameters (i.e. operating temperature and strain). The underlying aim is to examine the potential of using a single FBG head embedded in bearing and rotor structures to infer information on their thermal and mechanical operating conditions. The main aim of this thesis is to examine the feasibility of FBG thermal sensing for LVEMs; the proof of principle study reported in this chapter on rotary component in-situ FBG sensing is done with a view to expertise development that can facilitate further areas of FBG technology application in rotating machines.

The chapter consists of one paper, which was submitted to *IEEE international electric machines and drive conference (IEMDC 2019)*. The second author contribution to both papers is performing a technical and academic writing review and technical guidance during this work. The main contributions of this paper are:

- The paper proposes a new method that enables simultaneous monitoring of thermal and mechanical operating condition of LVEM bearings and rotor structures using a single FBG sensor. The proposed method is underpinned by the FBG inherent thermal

mechanical cross-sensitivity feature and the inherent difference in mechanical and thermal domain dynamics of electric machines.

7.2 Paper 1:

A Feasibility Study of Simultaneous Thermal and Mechanical Fibre Optic Sensing for Electric Motor Rotary Components Condition Monitoring

A. Mohammed, *Student Member, IEEE*, S. Djurović, *Member, IEEE*

Abstract—This paper reports a feasibility study of Fibre Bragg Grating (FBG) sensing application for extracting simultaneous thermal and mechanical information on electric machinery rotary components for condition monitoring purposes. The underlying aim is to examine the potential of using a single FBG head embedded on bearings or the rotor structures to infer information on their thermal and mechanical operating conditions. To this end, experiments were undertaken on the FBG instrumented drive-end bearing and rotor cage of an operating squirrel cage induction motor. The paper demonstrated in details the in-situ FBG sensor design, its embedment and calibration with analysis of the obtained experimental measurements. It is shown that the obtained measurements contain simultaneous thermal and mechanical information that can enable understanding of the examined motor bearing and rotor thermal and mechanical operating conditions, providing a step forward towards enabling better understanding and wider adoption of this technique in electric motor monitoring applications.

Index Terms—Rotor, bearings, rotary components embedded sensing, condition monitoring, Fibre Bragg Grating sensors, thermal sensing, strain sensing.

I. INTRODUCTION

ELECTRIC machines are a core element of modern industrial applications. With ambitious global scale plans for electrification of transport and development of renewables the use of electric motors is set to further increase in the near future. This increased use will be closely followed by a step change in availability targets for electric motors, where, in addition to improved design, increased availability is largely expected to come from a step change in efficacy of condition monitoring and diagnostic techniques [1]. Bearings and rotor are the rotary components in the electric motors, which are vital elements for enabling the energy conversion process. It is well recognised that the motor's rotary components are prone to failure more frequently. Bearings are reported as the most failed components in electric motors, whilst rotor failures come as third after stator

winding failures [2]. The failure root causes of the bearings and rotor largely arise due to mechanical and thermal stresses imposed on their structure while in service [2, 3]. Generally, undetected failures in an electric motor's rotary components will result in loss of availability, often accompanied by irreversible damage and/or high maintenance cost. Therefore, electric motor rotary components structure monitoring is important to ensure their reliability and availability.

The common monitoring techniques applied for electrical motors are largely based on temperature monitoring, vibration analysis [4]. The bearings health monitoring is largely based on machine frame vibration analysis using accelerometers and/or temperature monitoring using conventional thermal sensors. This is because bearings, whether healthy or faulty, will inherently generate mechanical and thermal excitations [3]. However, both techniques need to overcome a range of challenges from the sensing perspective such as sensing point placement nearer to the actual bearing being monitored to extract exclusive, clear, and more reliable operating status indices, and EMI immunity challenges of currently used sensors where reliable measurements are required [5]. Due to the rotational motion of the rotor, the accessibility of rotor exclusive parameters is restricted. Embedding conventional sensors on the rotor structure is challenging due to the requirement of reliable signal transmission and complexity of installation due to size and wiring problems [6]. Therefore, the rotor condition monitoring and its faults diagnosis is largely based on rotor fault induced signature in other motor component signals such as stator currents [7, 8]. However, these techniques showed some diagnosis reliability limitations due to effect of the variation of operating conditions on fault signature and possibility of fault signature interference with other motor component fault signatures or those specific to device operation [9].

Fibre optic sensing has emerged as a promising alternative for electric motor condition monitoring: its application for machine mechanical and thermal monitoring [10-16] is attracting increased interest. FBG sensing technology, with its advanced features such as small size, EMI immunity, multiplexing, multi-physical sensing and sensing capability in rotary parts through fibre optic rotary joint (FORJ) device presents a promising proposition for enabling targeted in-situ monitoring of bearing and rotor multi physical operating conditions.

FBG sensing applications for electric motor bearings and rotor structure monitoring is only starting to be examined with very recent reports suggesting encouraging potential for this application [12-16]. For the rotor sensing application, the reported work is feasibility

study focused in temperature monitoring of surface mounted PM motor with limited information about sensor design implementation, FORJ adaption and result interpretation. For bearing sensing application, however, the work seems exclusively focused on strain monitoring and is largely performed on standalone bearing structures where sensing is performed within the bearing housing and not on the actual bearing geometry, with limited content [14] examining bearing structure in-situ application but not providing information of application technique nor full interpretation of obtained results. The available literature suggests that, the rotary component FBG sensing applications in electric machines have not been adequately researched. In particular the use of the FBG multi-physical sensing feature for simultaneous monitoring of multiple critical rotary component operational parameters was not investigated.

To this end, this work investigates the feasibility of FBG usage for simultaneous in-situ monitoring of both thermal and mechanical operating conditions of in-service squirrel cage induction motor (IM) bearing and rotor structure. For this purpose, the rotor cage and the drive end bearing of the test IM were instrumented with a number of FBG sensors operated by a commercial interrogator platform. The sensor design, application and calibration procedure are detailed in the study. While the sensors' calibration is performed for exclusively thermal excitation, its use for inferring information on both thermal and mechanical operating conditions of the monitored bearing and rotor structure is examined, underpinned by the apparent difference in mechanical and thermal domain dynamics of these structures. Experiments are undertaken for different mechanical and thermal operated conditions on a purpose built laboratory test-rig and the obtained data is analysed to examine its potential to provide useful multi domain information on bearing and rotor operating conditions. It is found that, the proposed method enables recognition of both thermal and mechanical operating conditions relevant to diagnostic purposes, thus providing a step forward in understanding of FBG technology usage potential to provide reduced cost yet improved robustness and fidelity alternative to conventional monitoring techniques in electric machinery.

II. OPERATING PRINCIPLES OF FIBRE BRAGG GRATING SENSOR

An FBGS is a short segment imprinted into a core of a single-mode optical fibre. It is formed longitudinally on the optical fibre core, in which a modulated periodic refractive index is formed in a fibre core when exposed to an interference pattern of ultraviolet laser light [1]. The basic operation principle of FBG sensing is to monitor the narrowband reflected wavelength after injecting broadband light into the optical fibre. The wavelengths

reflected by the FBG structure change with the variation in the temperature and strain it is exposed to. The base Bragg wavelength, λ_B , can be defined by [17]:

$$\lambda_B = 2 \Lambda n_{eff} \quad (1)$$

where: Λ is the FBG gratings pitch and n_{eff} is the effective index of the optic core. These parameters alter with the change in strain and/or temperature the FBGS is exposed to, in turn altering the reflected wavelength. The reflected λ_B relative rate of change due to changes in the FBG structure parameters can be defined in terms of the acting thermal and/or mechanical excitation as [17]:

$$\frac{\Delta\lambda_B}{\lambda_B} = k_\varepsilon \Delta\varepsilon + k_T \Delta T \quad (2)$$

$$\text{where: } k_\varepsilon = \left(\Lambda \frac{dn_{eff}}{d\varepsilon} + n_{eff} \frac{d\Lambda}{d\varepsilon} \right),$$

$$\text{and } k_T = \left(\Lambda \frac{dn_{eff}}{dT} + n_{eff} \frac{d\Lambda}{dT} \right)$$

In (2): $\Delta\lambda_B$ is the shift in the Bragg wavelength, $\Delta\varepsilon$ is the change in strain, ΔT is the change in temperature and k_ε and k_T are the FBG sensitivity factors to strain and temperature, respectively. k_ε signifies the Bragg wavelength shift caused by elastic-optic effect due to strain while k_T describes the Bragg wavelength variation due to thermo-optic and thermal expansion effects caused by temperature variation. A standard 1550 nm wavelength FBG has sensitivity to mechanical strain of $\approx 1.2 \text{ pm}/\mu\varepsilon$ and to thermal excitation of $\approx 12 \text{ pm}/^\circ\text{C}$ [1,17].

III. TEST SYSTEM DESCRIPTION

The feasibility of the in-situ simultaneous multi-physic sensing system based FBG for electric motor rotary components was examined on 0.55 kW squirrel cage IM. The examined IM specifications are shown in Table. I. The examined motor rotor and drive end bearing were instrumented with FBG sensors. The following sections describe the examined bearing and rotor structures, the FBG sensors and their instrumentation, calibration and the test-rig system.

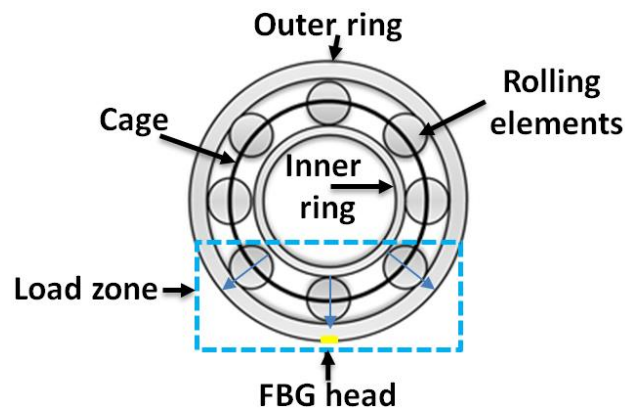
TABLE. I: TEST MOTOR SPECIFICATION

<i>TEFC Motor Data</i>	
Rated Power / Voltage / Current	0.55 kW / 400 V / 1.6A
Efficiency	66 %, IE1
Rated speed	1380 rpm
Pole number	4
Slot number stator / rotor	24 / 30
Insulation class/ Temperature rise class	F / B
Duty cycle type rating	S1
Bearings	NSK (NSK-6202Z)
Design standard	IEC 60034

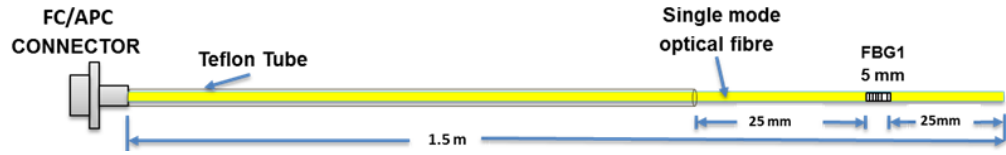
A. Bearing embedded FBG sensing system

The test IM uses NSK (NSK-6202Z) ball bearings. These are a single row radial ball bearing design containing eight balls, the spacing between which is maintained by means of a bearing cage. The balls spin between the outer and inner rings structure. Fig. 1a illustrates the examined bearing structure. A single FBG sensor (FBG-B) was embedded on the examined bearing. Fig 1b shows the schematic diagram of the used FBG probe; it is designed to carry a single 5mm head length (sensing area) imprinted in a 0.125 mm diameter bend insensitive single mode polyamide coated fibre.

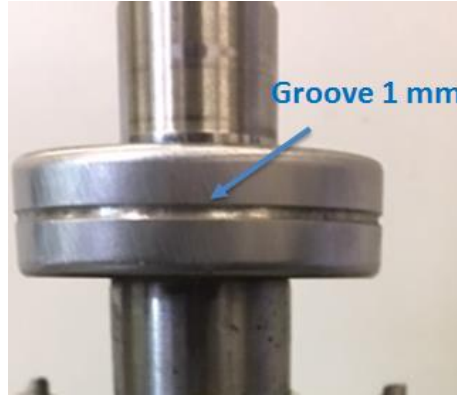
For the purpose of embedding the FBG sensor, the drive end bearing was disassembled and a 1 x 1 mm groove was machined on its surface in circumferential direction, as shown in Fig. 1c.1. The optical fibre containing the sensing FBG head was then embedded into the machined groove and bonded to the outer ring structure by means of strain gauge glue. Finally, the FBG instrumented bearing was assembled, mounted on the rotor shaft and installed into the end-cap housing, as shown in Fig. 1c.2. To maximise sensor exposure to excitation care was taken to position the sensing head in the bearing's load zone, as illustrated in Fig. 1a.



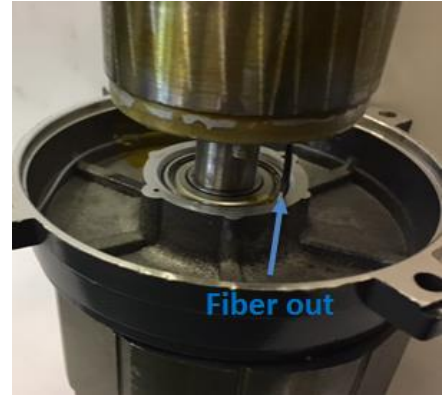
(a) Bearing structure and FBG head location



(b) Structure diagram of the used FBG probe



(1) Grooved bearing



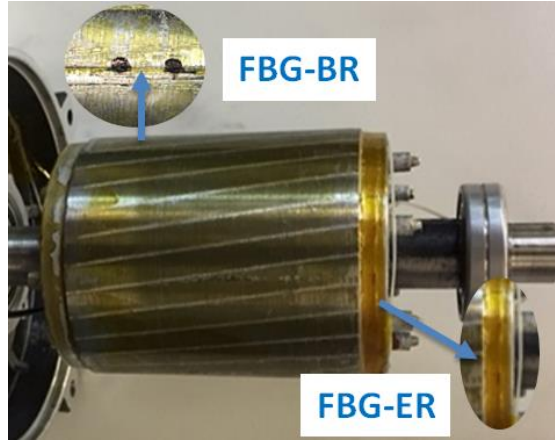
(2) End-cap housing installed bearing

(c) FBG sensor installation

Fig. 1: Bearing instrumentation with FBG sensing system

B. Rotor embedded FBG sensing system

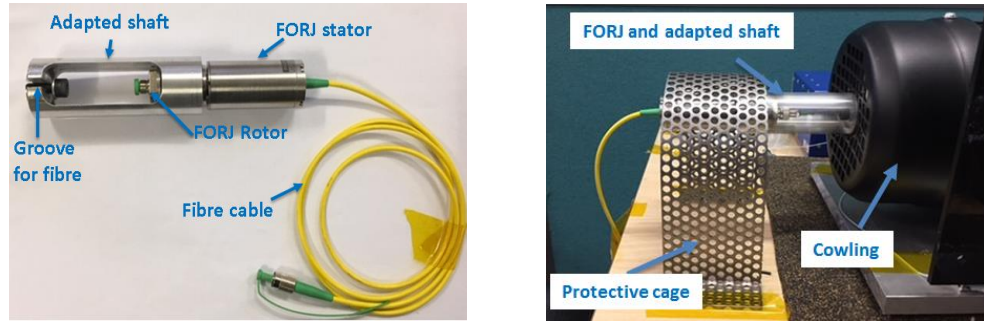
The examined squirrel cage rotor is made of aluminum cage with skewed 30 bars connected to two end-rings. For the research purpose, two FBG heads were bonded to the cage structure; one FBG (FBG-BR) was glued on the bar surface in the rotor slot tooth opening and the other was glued to the end-ring surface (FBG-ER), as shown in Fig. 2a. The FBG heads were imprinted in a bend insensitive single mode polyamide coated fibre. Fig. 2a illustrates the FBG array design embedded in the rotor cage; it consists of two 5 mm FBG heads with specified spatial separation to enable sensing embedment in the targeted positions. To enable communication with the FBG heads installed on the rotor structure while it rotates, a FORJ model (MJXA-FAP-155-28-FA) was adapted to the rotor to enable light transmission between the FBG array and the interrogation unit. Fig. 2c shows the FORJ adaption to the examined IM through the adapted shaft. The adapted shaft was designed to enable positioning of the FORJ rotor and its connection to the IM shaft using the machined hollow area to facilitate the FORJ and FBG array connectors coupling. The fiber was routed from the rotor cage to FORJ through a groove machined into the rotor shaft.



(a) Rotor structure and FBG head location



(b) FBG array design for rotor instrumentation



(c) FORJ adaption to the examined IM

Fig. 2: Rotor instrumentation with FBG sensing system

C. Embedded FBG thermal sensing system calibration

Once the embedded rotor, bearing and the end-cap structure was assembled, the FBG heads were thermally calibrated in-situ. This was achieved by inserting the entire structure in an industrial thermal chamber, as shown in Fig. 3. The whole structure was exposed to a series of static thermal excitation conditions in the examined bearing thermal operating range of 25 to 120 °C. The aim of the calibration tests is to determine the in-situ FBG sensors sensitivity to thermal excitation and thus the FBGs reflected wavelengths shift-temperature fit curves, which can facilitate in-situ temperature measurements and indirectly underpin recognition of in-situ strain measurements using the same sensing head. The discrimination between temperature and strain in the observed FBG wavelength shift in this application is based on: the intrinsic substantial excitation frequency difference, as governed by electric machine multi-physics, i.e. a relatively high excitation frequency for

mechanical excitation (strain) and a low excitation frequency for thermal excitation; the variation band width, which is limited for excitation arising from monitored strain due to the rigid bearing structure; and the inherent significant difference between FBG strain ($\approx 1.2 \text{ pm}/\mu\epsilon$) and temperature ($\approx 12 \text{ pm}/^\circ\text{C}$) sensitivity [17]. Once the FBG sensors were thermally calibrated the rotor was installed into the remainder of the examined IM geometry.

Mechanical calibration for absolute strain sensitivity determination in a rotary application is beyond the scope of this study; relative strain measurement is deemed sufficient to enable understanding of diagnostic related information. Calibrating the sensor behaviour under exclusively thermal excitation conditions however will facilitate the differentiation of in-service signatures arising from thermal excitation from those produced by mechanical excitation, which will inherently be simultaneously registered by the in-situ sensing head.

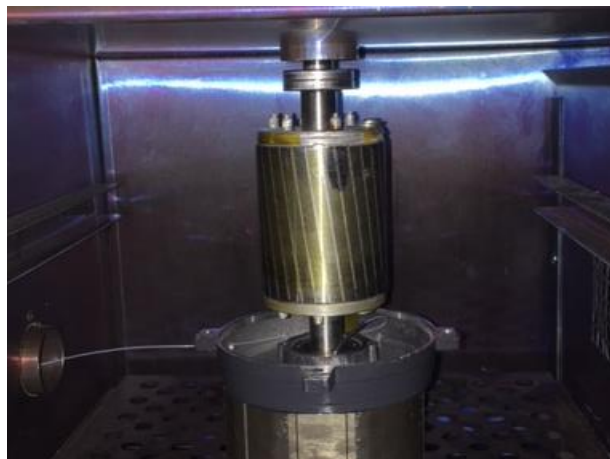


Fig. 3: Embedded FBG sensors thermal calibration

D. Test-rig system

Fig. 4 shows the schematic diagram of the test-rig system used in this study. The 0.55kW IM was driven by a commercial drive (Parker SDD890) operating in constant V/f control mode. For loading purposes, the IM was coupled to 0.75kW DC permanent-magnet machine whose armature current was controlled to achieve a desired operating point. The FBG sensors are interrogated by a SmatFibres SmartScan04 platform and processed using its proprietary LabView based SmartScan routine. The FBG array embedded in the rotor was connected to the interrogator through FORJ. The reflected Bragg wavelength from the installed FBG sensor was acquired at a frequency of 5 kHz. For validating purposes a thermal camera type (FLIR TG-165) was used to monitor the drive end-cap thermal profile thus its bearing temperature.

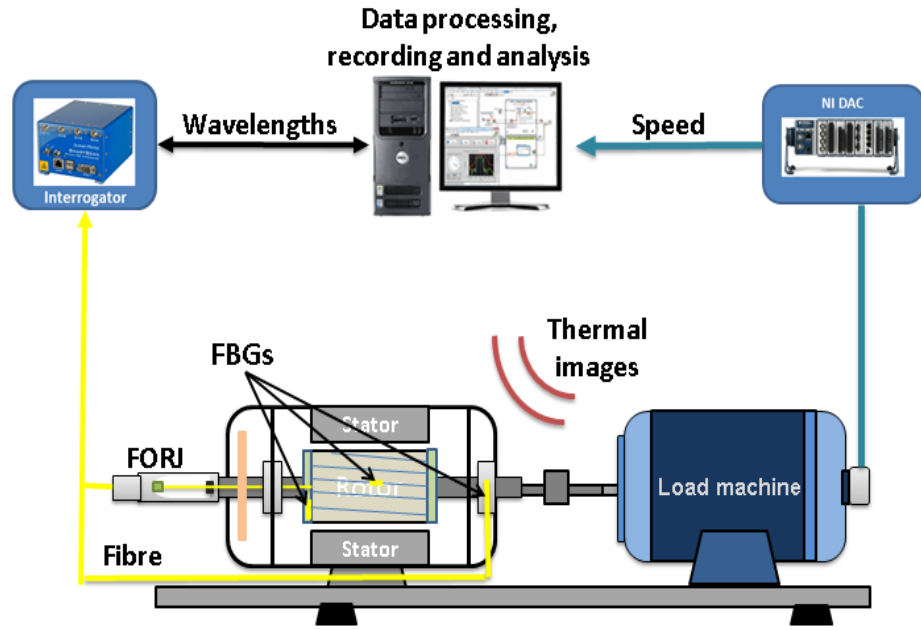


Fig. 4: Test-rig setup

IV. EXPERIMENTAL RESULTS AND DISCUSSION

This section reports the experimental tests undertaken on the IM laboratory test system and discusses the obtained measurements from the proposed in-situ FBG sensing. The examined IM was exposed to three standard healthy S1 duty cycles involving different loads (0% load, 50% load and 100% load). The aim of these applied cycles is to ascertain the efficacy of the proposed in-situ FBG sensing method in enabling simultaneous thermal and mechanical conditions monitoring on the examined bearing and rotor structure, since the applied cycles enable different trends and levels of thermal and mechanical excitation on the examined motor design. Loading induction machines will generally result in thermal excitation increase mostly due to associated current rise with load (1.1A @ 0% load, 1.3A @ 50% load and 1.6A @ 100 load, for the examined IM) and the resulting winding heat loss. In contrast, IM loading modifies the mechanical excitation speed related frequencies due to the rotor speed reduction with load (1488 rpm @ 0% load, 1440 rpm @ 50% load and 1380 rpm @ 100 load, for the examined IM). The following sections demonstrate and discuss the obtained measurements from the single FBG (FBG-B) embedded on the bearing and the FBG array (FBG-BR and FBG-ER) embedded on the rotor under the applied duty cycles.

A. Single embedded FBG bearing results

Fig. 5 shows the averaged FBG-B reflected Bragg wavelength measured in the tests and converted to thermal measurements using the thermal calibration test obtained fit curve as explained in section III.C. The bearing temperature profiles in Fig. 5 start at ambient

temperature ($\approx 27^\circ\text{C}$) until its steady-state thermal equilibrium is reached for the three applied S1 cycles. It can be seen that the bearing temperature rises with load increase as result of the overall motor loss increase. The FBG-B recorded a steady state-temperature of $\approx 46.6^\circ\text{C}$, $\approx 54.9^\circ\text{C}$ and $\approx 66.5^\circ\text{C}$ for 0%, 50% and 100% loads, respectively. To validate the obtained thermal measurements from the in-situ FBG-B thermal images were taken of the examined motor drive end-cap (which houses the examined bearing) when thermal steady-state was reached for each load condition. The thermal images are shown in Fig. 6; the temperature readings in the top of the images represent the measured values in the end-cap location denoted by the cursor on the image, which is located above the bearing location; thermal measurement in this position reflects the thermal condition existing in the bearings [18]. The obtained bearing temperatures from the thermal images show a close match to the obtained bearing temperatures from FBG-B. The observed minor difference between thermal camera and FBG sensor readings is expected, as FBG-B temperature readings are taken in-situ whilst thermal images provide only surface temperature.

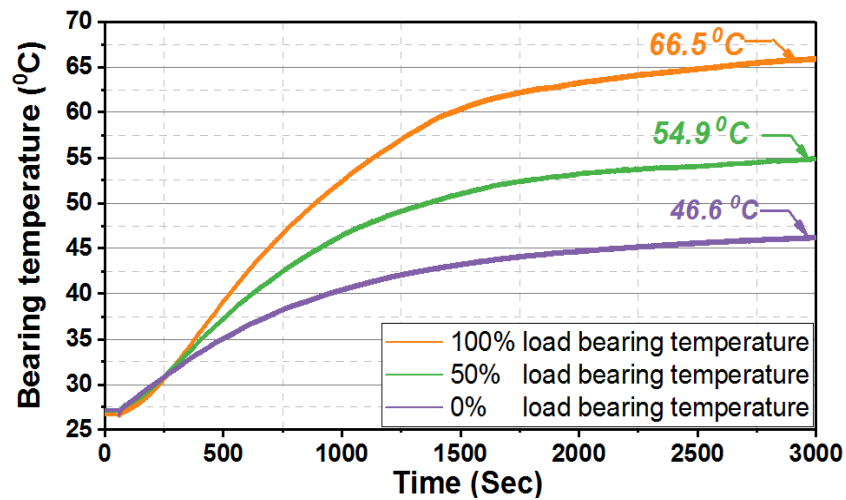


Fig. 5: Measured bearing temperature by FBG-B under different load condition

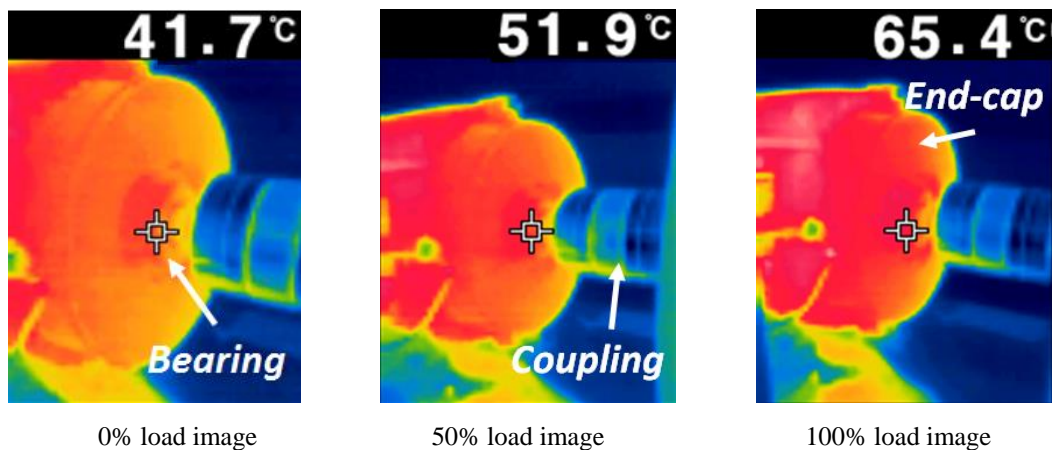
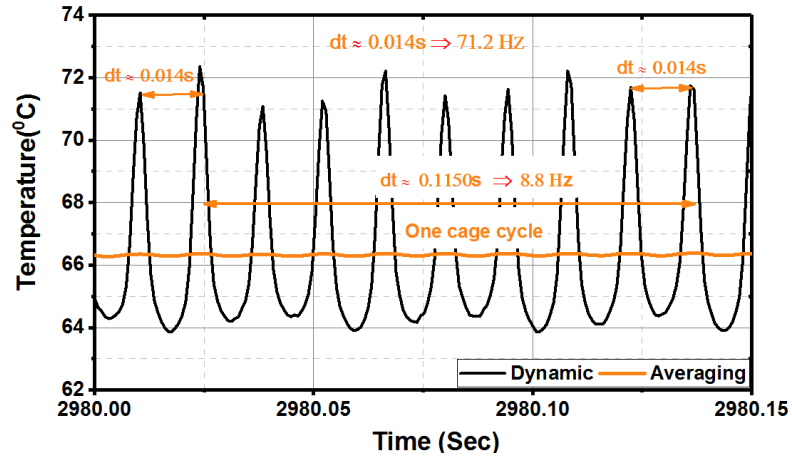
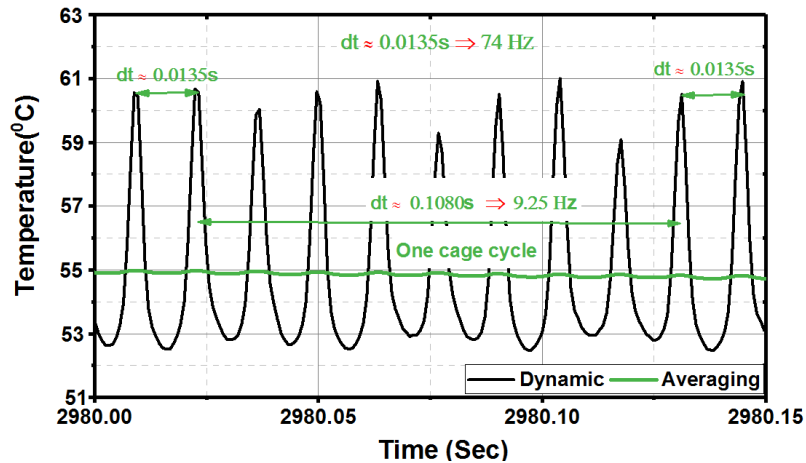


Fig. 6: End-cap obtained thermal images

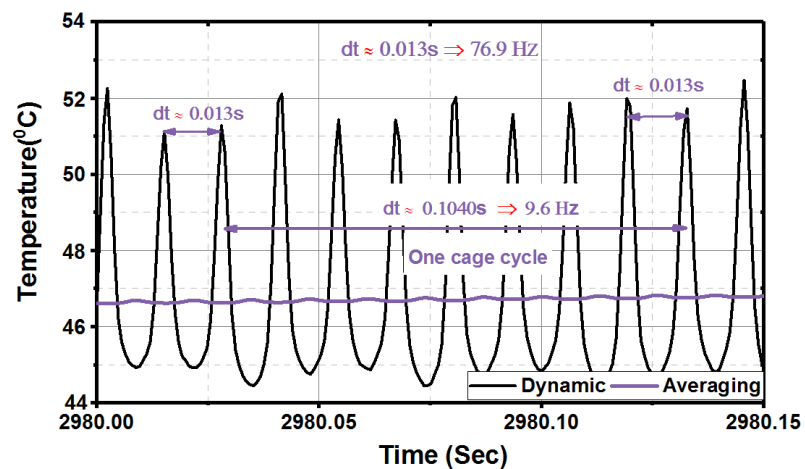
Fig.7 shows magnified plot of the bearing thermal equilibrium dynamic measurements obtained by FBG-B without averaging for the applied cycles; the black trace in the figures represents the dynamic temperature measurement while the orange, dark green and purple traces are the average temperature measurement plotted in Fig .5a, b and c for 0%, 50% and 100% load, respectively. It can be seen that the measured bearing temperature exhibits



(a) Detailed view of dynamic measurements taken at thermal equilibrium by FBG-B at 100% load



(b) Detailed view of dynamic measurements taken at thermal equilibrium by FBG-B at 50% load



(c) Detailed view of dynamic measurements taken at thermal equilibrium by FBG-B at 0% load

Fig. 7: Analysis of mechanical operating conditions related information

a magnitude variation of $\approx 8\text{ }^{\circ}\text{C}$ around the average value, manifested in a uniform pattern with a constant frequency for each load condition and a relatively uniform peak level. This variation can be explained by the mechanical excitation measured simultaneously with thermal excitation by the FBG-B sensing head: the observed constant frequency peaks in the dynamic measurement ripple are an artefact of the deformation induced in the bearing outer ring due to individual ball pass events, which is measured as in-situ strain variation by the FBG-B head each time a ball passes its position. These results show the high dynamic performance of the FBG to register such high frequency strain.

The nature of the observed dynamic thermal measurement variation and the information it contains on bearing operation was examined further: the measured peak frequency was found to be $\approx 71.2, 74, 76.9\text{ Hz}$, as shown in Fig.7 for 0%, 50% and 100% load, respectively. The measured frequencies closely match the test bearings manufacturer's specification of ball pass frequency value observed on the outer ring for the examined speeds (71.1 Hz @ 1380 rpm, 73.2 Hz @ 1440 rpm and 75.6 Hz @ 1488 rpm). The studied bearing is an eight ball design hence one full cycle of the rotating element, also known as the cage assembly rotational frequency, will generate nine successive uniformly distributed peak events at the examined constant rotational speeds; this yields a cycle frequency of $\approx 8.8, 9.25$ and 9.6 Hz from the FBG reported measurement, presenting a close match to the manufacturer's data sheet rotational frequency of the cage assembly value (8.77 Hz @ 1380 rpm, 9.15 Hz @ 1440 rpm and 9.45 Hz @ 1488 rpm).

To further examine the mechanical condition related information in the obtained dynamic measurements FFT analysis was applied on the collected thermal steady-state data. Fig. 8 gives the measured FFT spectras for the examined conditions in a frequency range of 0-250 Hz for illustrative purposes. The spectra are found to clearly report the harmonics of bearing outer ring ball pass frequencies and their multiples for each applied load/speed condition, i.e. $\approx 71.2\text{ Hz}$, $\approx 73.9\text{ Hz}$ and $\approx 76.6\text{ Hz}$ etc. The FFT thermal spectra also contain harmonic components of the IM fundamental rotational speed, i.e. $\approx 23\text{ Hz}$, $\approx 23.90\text{ Hz}$ and $\approx 24.81\text{ Hz}$ etc. These findings demonstrate that the reported data contain information on both the thermal status of the bearing and its mechanical excitation conditions.

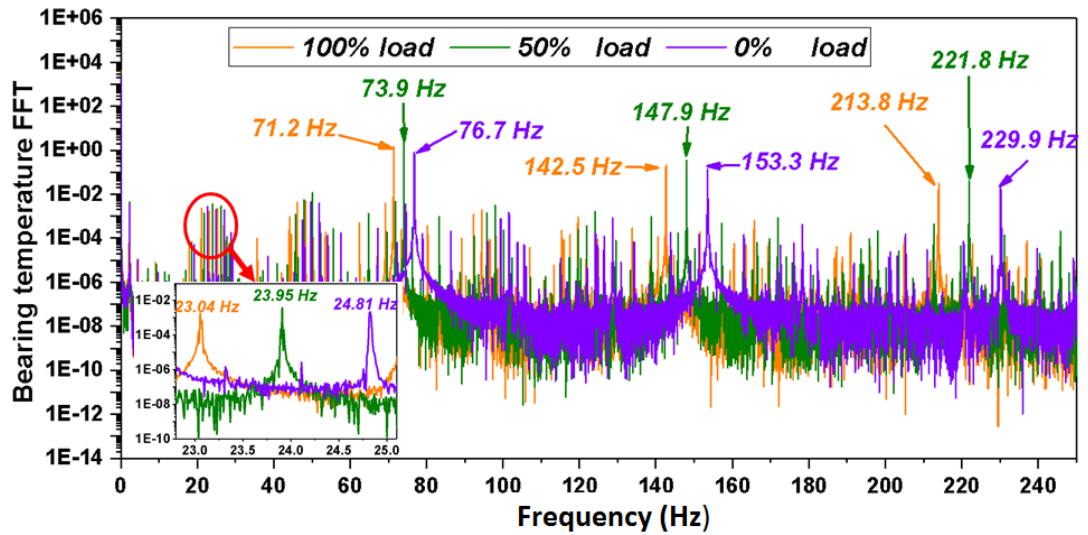


Fig. 8: FFT spectrum of thermal steady-state dynamic measurements

B. FBG array embedded rotor results

The reflected Bragg wavelengths from the FBG array embedded on the rotor cage were also simultaneously recorded with the FBG-B for all applied load cycles. The FBG array reflected wavelengths were converted to thermal measurements using the relevant fit curves obtained by thermal calibration test described in section III.C. Fig. 9 shows the rotor thermal measurements performed by FBG-BR and FBG-ER for all applied load cycles. The data show three rotor temperature profiles measured by the two array FBG heads, each profile matching a particular examined load condition. The measured rotor temperature profiles showed large increase in the rotor temperature rise level and its rate of change with load increase. This is due to the inherent increase in the rotor loss with load. It can also be observed that there is a steady-state temperature difference within $\approx 5^{\circ}\text{C}$ between temperatures measured by FBG-BR and FBG-ER, with the latter sensor recording the highest temperature level. The temperature difference can be largely caused by the FBG heads embedment on the rotor structure. Due to the limited space in the air-gap the FBG-BR was not protected from the air circulating in the air-gap, which can affect its temperature measurements. The FBG-ER on the other hand was isolated from air circulating by layers of Kapton tape as shown in Fig. 2b. The FBG array recorded an average rotor temperature of $\approx 56^{\circ}\text{C}$ @ 0% load, 69°C @ 50% load and 94°C @ 100% load. These temperatures are higher than the bearing temperature measured by FBG-B and the observed measurement difference is seen to show an increase with load (from $\approx 9.4^{\circ}\text{C}$ @ 0% load, 14.1°C @ 50% load and 27.5°C @ 100% load). The temperature difference increase is effectively due to rotor loss load dependency. The obtained results demonstrated the FBG sensing capability to provide thermal information on the examined squirrel cage rotor while in-service.

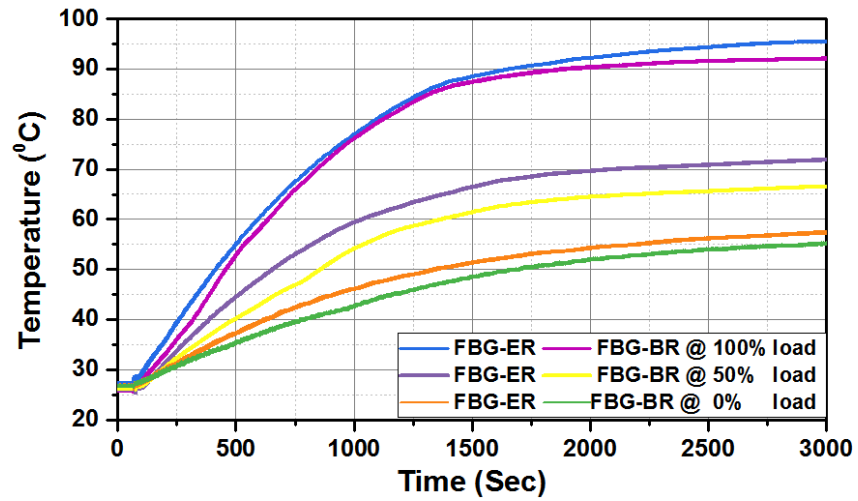


Fig. 9: Measured bearing temperature by FBG-B under different load condition

Further analysis was carried out on the obtained rotor thermal measurements to examine their feasibility of containing mechanical information. Fig. 10 shows a detailed view of one second period of the thermal measurements obtained by FBG-BR (Fig. 10a) and FBG-ER (Fig. 10b) at 100% load. From the zoom-in plot, it can be seen that both FBG heads exhibit a temperature variation of $\approx 0.3^{\circ}\text{C}$ in uniform pattern. The variation is within an acceptable level for electrical machine thermal measurements, however, due to its uniformity and its frequency that is related to rotor speed, it is believed it can be strain measured by the FBG simultaneously with the temperature measurements. Therefore, identical to the FFT analysis applied to the bearing dynamic thermal measurements, FFT analysis was also applied to the rotor thermal steady-state data. Fig. 11 gives the FFT spectrums for the examined 100% load conditions in a frequency range of 0-250 Hz for illustrative purposes. The spectra are found to clearly report the harmonics of IM fundamental rotational speed at 100% load, i.e. $\approx 23\text{Hz}$, $\approx 46\text{Hz}$, etc. In addition to the 4 Hz component, which matches the operating slip frequency. More detailed analysis is needed to ascertain the consistence of the strain related measurements in the rotor component in-situ FBG thermal measurement.

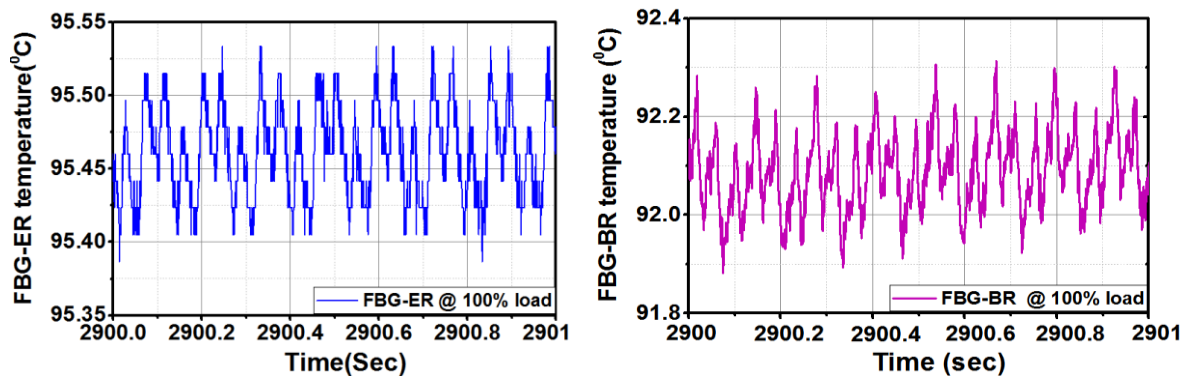


Fig. 10: FBG array analysis of mechanical operating conditions related information @ 100% load

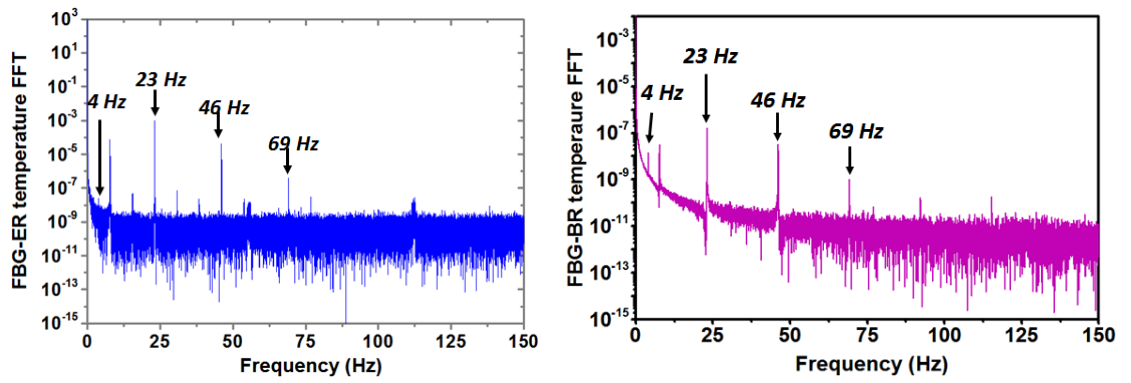


Fig. 11: FFT spectrum of array thermal steady-state dynamic measurements @ 100 load

V. CONCLUSIONS

This paper reported a feasibility study of simultaneous thermal-mechanical FBG sensing for electric motor rotary components condition monitoring application using a single FBG sensing head. To this end, experiments were undertaken on drive end bearing and rotor structures of IM were instrumented with FBGs.

The reported experimental findings demonstrate that in-situ FBG sensing on bearing and rotor structure of in-service electric machines can enable provision of information on their thermal and mechanical operating conditions. The simultaneous measurements of thermal and mechanical excitation are enabled by FBG inherent thermal and mechanical cross-sensitivity sensing while the differentiation of thermal from mechanical effects is enabled by exclusively thermal calibration of the in-situ sensor prior to its in-service application, in combination with the considerably different dynamics of these two domains inherent to electric machinery.

The obtained experimental results suggest that useful information on both bearing thermal and bearing mechanical operating conditions can be provided by the proposed monitoring technique based on using a single FBG sensing head embedded on the bearing outer ring. For the rotor, the obtained results demonstrated the efficacy of the FORJ with a simple insulation method and the in-situ FBG array to provide thermal information on the rotor structure while rotates with potential of provide some mechanical information.

While further research is required to investigate possible sensing embedment and positions with a more in-depth understanding of dynamic measurement contain information interpretation, the presented method proves the feasibility of the simultaneous thermo-mechanical sensing for rotary component based on use of a single FBG, The proposed method has the potential to provide a straightforward, low cost and fully EMI immune alternative to conventional accelerometer based frame vibration monitoring and

conventional thermal sensors for CM and diagnostic purposes, with the advantage of monitoring signatures of interest in-situ, in the proximity of stress and failure points.

REFERENCES

- [1] A. Mohammed, N. Sarma and S. Djurović, "Fibre optic monitoring of induction machine frame strain as a diagnostic tool," *2017 IEEE International Electric Machines and Drives Conference (IEMDC)*, Miami, FL, 2017, pp. 1-7.
- [2] P. Tavner, "Review of condition monitoring of rotating electrical machines," *Electric Power Applications, IET*, vol. 2, pp. 215-247, 2008.
- [3] H. Guo and L. Ruan, "Wireless power supply RF temperature monitoring system applied to the rotor of generators," *2011 International Conference on Electronics, Communications and Control (ICECC)*, Ningbo, 2011, pp. 593-596.
- [4] S. Nandi, H. A. Toliyat and X. Li, "Condition Monitoring and Fault Diagnosis of Electrical Motors—A Review," in *IEEE Transactions on Energy Conversion*, vol. 20, no. 4, pp. 719-729, Dec. 2005.
- [5] Hasib Alian, Shlomi Konforty, Uri Ben-Simon, Renata Klein, Moshe Tur and Jacob Bortman, "Using optical fiber sensors for health monitoring of rotational systems," in *International Conference Surveillance 9, 2017*
- [6] N. Z. Popov and S. N. Vukosavic, "Estimator of the Rotor Temperature of Induction Machine Based on Terminal Voltages and Currents," *IEEE Transactions on Energy Conversion*, vol. 32, pp. 155-163, 2017.
- [7] A. Naha, A. K. Samanta, A. Routray and A. K. Deb, "A Method for Detecting Half-Broken Rotor Bar in Lightly Loaded Induction Motors Using Current," in *IEEE Transactions on Instrumentation and Measurement*, vol. 65, no. 7, pp. 1614-1625, July 2016.
- [8] M. Eltabach, A. Charara, I. Zein and M. Sidahmed, "Detection of broken rotor bar of induction motors by spectral analysis of the electromagnetic torque using the Luenberger observer," *IECON'01. 27th Annual Conference of the IEEE Industrial Electronics Society (Cat. No.37243)*, Denver, CO, USA, 2001, pp. 658-663 vol.1.
- [9] F. Briz, M. W. Degner, P. Garcia and D. Bragado, "Broken Rotor Bar M. Benbouzid and G. B. Kliman, "What stator current processing-based technique to use for induction motor rotor faults diagnosis?," in *IEEE Transactions on Energy Conversion*, vol. 18, no. 2, pp. 238-244, June 2003.
- [10] Fabian, M., Ams, M., Gerada, C., Sun, T., Grattan, K. T. V., "Vibration measurement of electrical machines using integrated fibre Bragg gratings." *Proc. SPIE 9634, Int. Conf. on Optical Fibre Sensors*, 2015.
- [11] M. Fabian, D. M. Hind, C. Gerada, T. Sun, and K. T. Grattan, "Comprehensive monitoring of electrical machine parameters using an integrated fibre Bragg grating-based sensor system," *Journal of Lightwave Technology*, 2017.
- [12] K. M. Sousa, U. J. Dreyer, C. Martelli and J. C. Cardozo da Silva, "Dynamic Eccentricity Induced in Induction Motor Detected by Optical Fiber Bragg Grating Strain Sensors," in *IEEE Sensors Journal*, vol. 16, no. 12, pp. 4786-4792, June 15, 2016.
- [13] C. Hudon, C. Guddemi, S. Gingras, R. Leite, and L. Mydlarski, "Rotor temperature monitoring using fiber Bragg gratings," in *IEEE Electrical Insulation Conference (EIC)*, 2016, 2016, pp. 456-459.
- [14] Jones, Kevin, Chris Staveley, and Jean-Francois Vialla. "Condition monitoring of a subsea pump using fibre optic sensing." *23rd International Conference on Optical Fibre Sensors*. Vol. 9157. International Society for Optics and Photonics, 2014.
- [15] Wei, Peng, et al. "Fault diagnosis of the rolling bearing with optical fiber Bragg grating vibration sensor." *Optical Measurement Technology and Instrumentation*. Vol. 10155. International Society for Optics and Photonics, 2016.
- [16] Konforty, S., Khmel'nitsky, M., Kressel, I., Klein, R., Tur, M., & Bortman, J. Bearing health monitoring using optical fiber sensors. European Conference of The Prognostic and Health Management Society, 2016.
- [17] Rao, Yun-Jiang, "In-fibre Bragg grating sensors," *Measurement science and technology* 8.4 (1997).
- [18] Garcia-Ramirez, Armando Guadalupe, et al. "Fault detection in induction motors and the impact on the kinematic chain through thermographic analysis." *Electric Power Systems Research* 114 (2014): 1-9.

Chapter 8: *Conclusions and Recommendation for Future Research*

8.1 Conclusions

This PhD thesis describes the use of FBGST for LVEM thermal monitoring applications. The aim is to examine the possibility of overcoming considerable performance limitations in existing LVEM thermal monitoring techniques, as a step towards improving machine reliability, availability and in-service performance. The current LVEM thermal monitoring techniques are limited in providing effective thermal hot spot measurements, including sensing positioning accuracy, EMI sensitivity, sensor bulk and provision of distributed internal temperature measurement, and consequently usage for fault diagnosis. FBGST on the other hand offers unique features, making it a promising alternative for improved thermal sensing solutions in LVEMs. The interest in FBG sensing applications for EMs has been reported in very recent literature; however, LVEM FBG sensing applications for condition monitoring and fault diagnostic purposes have not been researched and require examination.

This research first reviewed the LVEM common failure modes, their existing thermal monitoring techniques and the FBGST. The first part of the review highlighted temperature as one of the root causes of common LVEM faults and their inherent signature. An effective in-situ temperature monitoring tool could therefore provide a powerful fault diagnostic instrument by registering fault induced thermal signature, and thus enabling the mitigation of fault occurrence or progression through ensuring that machine component temperature is within permissible limits.

Thermal monitoring in LVEM is largely focused on winding temperature. This is because the winding insulation system is the most vulnerable component to thermal stress and the hot spots are invariably located in the windings. Winding temperature monitoring is performed either by direct measurement, thermal models or application of resistance estimation techniques. These techniques have limitations in achieving reliable, effective and safe winding thermal monitoring: the resistance estimation techniques only provide winding average temperature and their measurement reliability is adversely affected by the operating conditions; thermal models are limited by the need for complex determination of

the model parameters and their updates with operating condition variation; and direct measurements are limited by conventional thermal sensors due to their inherent conductive structure, electromagnetic sensitivity, size and wiring.

The review of FBGST provided a background on this technology, its operating principles and its sensing features. FBG sensors' key features make them amenable to application in electromagnetic environments such as found in electric motors: they are suitable for sensing in the presence of electric and/or magnetic fields, in harsh and hazardous atmospheres and in compact diameters, with a low weight requirement. In addition, their inherent multiplexing and multi-sensing capability make them extremely capable for delivery of advanced, multifunctional and robust sensing schemes.

The sensing target in this research was the interior of a current carrying wound component. Therefore, the proposed FBG temperature sensor was loosely packaged within a PEEK capillary. PEEK has unique features, which make it a suitable choice for this application: it is electrically non-conductive and has a melting point temperature of $\approx 350^{\circ}\text{C}$. Its high mechanical strength ensures FBG sensor integrity, while its flexibility enables distributed temperature monitoring by facilitating sensor package routing to conform to the desired wound component shape. The purpose of leaving the FBG loose in a fine air-gap within the PEEK capillary is to mitigate as much as possible the FBG thermal-mechanical cross-sensitivity effect.

The packaged FBG temperature sensor was extensively examined on prototype wound coil systems. These allowed understanding of the implications of the sensor installation procedure, and its in-situ calibration, characteristics and performance in operating conditions representative of those encountered in actual LVEM to be evaluated. A number of single/multi wound coil systems embedded with FBG sensors were developed and examined under different controlled static and dynamic, uniform and uneven thermal excitation conditions using a range of different experimental systems. The obtained results provide an in-depth insight of the sensing aspects of the proposed system design for in-situ thermal sensing application in random wound electric coils.

The effect of mechanically stressing the in-situ FBG temperature sensor during installation process on the sensor pre-calibrated characteristics was quantified. It was shown that an error of up to $\approx 1^{\circ}\text{C}$ can result due to the installation process when pre-calibrated thermal fit curves are used. This illustrates that the use of pre-embedded sensor calibration is valid after embedment since the resulted measurement error is deemed acceptable for electric coil temperature measurements. The vibration effect on the sensor

measurement reliability was examined. Different vibration levels representative of those acting on random wound coils in LVEMs were investigated. It was demonstrated that the in-situ FBG sensor measurements remain largely unaffected by vibration. The influence of PEEK packaging choice design on sensor response time was also examined in a comparison study with other packaging materials reported in literature. It was shown that PEEK provides performance levels comparable to those attained by using electrically conductive packaging at thermal rise rates that can be encountered in EM.

Once the test coil embedded in-situ FBG application features were understood, the FBG sensing system performance was examined in operational LVEMs for on-line stator winding thermal monitoring and winding fault diagnosis. A 0.55kW IM and a 5.5kW PMSM were instrumented with different in-situ FBG sensing configurations. Experiments were performed on the test machines under a wide range of healthy and faulty conditions, including grid and inverter driven operation and various static and dynamic standard thermal cycles, but also with a full and partial cooling capability deterioration and with winding ITSCFs. The obtained results illustrate the advantages of the proposed in-situ sensing scheme in delivering effective on-line distributed thermal sensing in thermal hot spot positions internal to the winding structure, which are critical for winding insulation system ageing process. Different in-situ FBG network designs based on FBG multiplexing and the proposed packaging flexibility were embedded within the examined machines' winding enabling distributed sensing in the slot and end-winding sections. The reported system enables sensor in-situ accessibility for replacement, repositioning or recalibration which is not possible with conventional sensing.

The thesis also examined the use of the proposed FBG sensing system as a diagnostic tool for winding ITSCFs based on in-situ monitoring of fault induced thermal signature. The reported method employs distributed thermal monitoring in a variety of points within windings, in close proximity to thermal hot spots of interest that arise from fault. This enables detection of a single shorted turn fault, as well as winding fault severity trending, fault location and determination of fault critical thermal operating conditions; the scheme requires no complex real-time processing for fault signature diagnostic interpretation. Furthermore, the winding thermal and electrical parameters at the onset of ITSCF were analysed. This enables determination of the fault induced thermal signature critical parameters under a wide range of operating conditions. Some of the FBG sensing network measurements were presented in an advanced thermal web and graphical models, which facilitate their easy understanding and diagnostic interpretation.

Finally, the thesis reported a feasibility study of using FBGST for rotary components simultaneous thermal and mechanical monitoring condition. Drive-end bearing and the rotor cage bar/end-ring of the examined IM were instrumented with a single FBG sensor each. Relying on the FBGST mechanical–thermal cross-sensitivity and the thermal and mechanical frequencies inherent difference in EMs, simultaneous measurement of thermal and mechanical conditions was achieved with a single FBG sensing head.

8.2 Thesis contribution summary

This thesis reported a novel method of in-situ FBG thermal sensor design and use for LVEM thermal condition monitoring applications. A detailed examination of the sensor's key design and operational features for the target sensing application (hot spot monitoring in random wound electric machine coils) was performed through extensive experimental work. The reported thermal sensing technique is shown to enable on-line stator winding hot spots monitoring including end-winding and slot sections in operational LVEMs, which are fundamental for winding health operation and fault diagnosis. This method also enables distributed thermal monitoring aimed at much improved awareness of thermal conditions in LVEM with much reduced sensing volume, weight, and wiring, including a key advantage of ease of in-situ sensing points reposition post-installation.

A new winding fault diagnostic technique based on the proposed sensing system was also reported. The technique provides reliable fault diagnosis including low fault severity detection, fault severity tracking, and faulty coil/phase identification, while imposing no requirements for complex signal processing techniques. Analysis of the monitored fault induced thermal signature based on winding thermal and electrical characteristics at the onset of fault was reported, which enhanced the fault thermal signature understanding in variable operating conditions. Finally, LVEM's rotary components simultaneous thermal and mechanical condition monitoring using FBGST was demonstrated.

8.3 Recommendation for future research

A number of additional research points arose during this research that could be considered for further investigation.

- **Improved in-situ sensing response performance**

It would be appropriate if the in-situ FBG response time is investigated in more detail aiming for understanding and improving its thermal response. An investigation can be carried out for understanding the optimal packaging geometry (size and wall thickness)

corresponding to a specific winding gauge and slot geometry. Further research can be conducted for improving sensing response by exploring the possibility of filling the packaging narrow air-gap with appropriate highly thermally conductive filling material (e.g. mineral oil).

- **3D- thermal sensing tool for LVEM smart health monitoring**

The proposed design can be extended further to produce a 3D thermal sensing network tool for future LVEM condition monitoring and fault diagnosis. A 3D thermal sensing network embedded within the machine structure would significantly improve awareness of existing thermal conditions, leading to new research avenues for improving a number of LVEM utilisation aspects such as: the development of improved machine thermal protection systems by improved awareness of machine thermal conditions, improved condition monitoring/diagnostic solutions using fault induced thermal signature monitoring, control system integration with the 3D sensing network for real-time estimation of machine parameters (i.e. resistance) in all operating conditions and thus improvement of automation performance.

- **Winding insulation system lifetime prognosis**

The knowledge of the winding insulation system condition and lifetime estimation has recently received much increased research attention, in particular for wound LVEM in modern industrial applications – this is largely caused by the increasing stresses (i.e. thermal, mechanical, electrical and environment) imposed on the insulation system while in service. The reported sensing system can enable real-time distributed hotspot monitoring in LVEM stator windings: monitoring these is key for understanding the winding insulation system degradation process based on thermal aging. Therefore, research that develops insulation lifetime predication algorithms to be integrated with the in-situ hotspot sensing system is important.

- **Different fibre optic sensing families for LVEMs condition monitoring applications**

Optic fibre sensing technology is still experiencing rapid development, continuously resulting in new sensing technology and improvement of existing techniques. Recently, a novel interrogation technology known as optical frequency domain reflectometry that enables high spatial resolution (\approx mm) distributed measurement in any length of optical fibre to be used for thermal and mechanical sensing has been commercialised. In addition, the recent developments of fibre optic Raman technology can enable sensing spatial

resolution of 10 cm. Therefore, research investigating the application of these technologies in EMs may provide more advantages from sensing prospective, an in particular in the attainable spatial resolution.

- **All-in-one LVEM sensing system based FBGST**

The reported FBGST application for LVEMs in this thesis was mainly focused on thermal sensing for LVEM thermal condition monitoring. However, the FBGST application for LVEM condition monitoring can be extended using FBGST multi-physical sensing features, where different points (FBG heads) of a single fibre can be used as thermal and mechanical (i.e. strain, stress, vibration, magnetic field, force, electrical currents) sensors operating on a single interrogator device. In addition, FBGST inherent sensing sensitivity can enable a single FBG to perform simultaneous monitoring of two different physical quantities. Research on this can lead to development of an all-in-one sensing system for LVEMs condition monitoring and fault diagnosis with reduced cost and complexity but advanced monitoring and diagnostic functionality.

- **In-situ FBG sensor life time in EMs applications**

Generally, FBG sensors are commercially certified for a minimum 25 year lifetime in the telecommunications industry according to the Telcordia programme (consisting of a number of tests such as temperature cycling, high temperature storage and humidity testing etc.). In addition, this thesis has examined the influence of mechanical excitation (vibration) on the sensor performance on instrumented IEEE standard coil prototype systems that have been exposed to extensive acceleration levels using a commercial shaker and no detrimental performance effects could be identified over extended testing periods. However, undertaking a detailed examination of the reliability and robustness of FBG sensing application in electric machines to ascertain their longevity in device lifetime tests would be highly recommended.

References

- [1] P. Tavner, *Condition monitoring of rotating electrical machines* vol. 56: IET, 2008.
- [2] H. Henao, G.-A. Capolino, M. Fernandez-Cabanas, F. Filippetti, C. Bruzzese, E. Strangas, *et al.*, "Trends in fault diagnosis for electrical machines: A review of diagnostic techniques," *IEEE industrial electronics magazine*, vol. 8, pp. 31-42, 2014.
- [3] M. Riera-Guasp, J. A. Antonino-Daviu, and G. A. Capolino, "Advances in Electrical Machine, Power Electronic, and Drive Condition Monitoring and Fault Detection: State of the Art," *IEEE Transactions on Industrial Electronics*, vol. 62, pp. 1746-1759, 2015.
- [4] H. A. Toliyat, S. Nandi, S. Choi, and H. Meshgin-Kelk, *Electric machines: modeling, condition monitoring, and fault diagnosis*: CRC press, 2012.
- [5] W. Cao, B. C. Mecrow, G. J. Atkinson, J. W. Bennett, and D. J. Atkinson, "Overview of electric motor technologies used for more electric aircraft (MEA)," *IEEE Transactions on Industrial Electronics*, vol. 59, pp. 3523-3531, 2012.
- [6] J. De Santiago, H. Bernhoff, B. Ekergr ard, S. Eriksson, S. Ferhatovic, R. Waters, *et al.*, "Electrical motor drivelines in commercial all-electric vehicles: A review," *IEEE Transactions on vehicular technology*, vol. 61, pp. 475-484, 2012.
- [7] A. C. UK, "Electric Machines roadmap, Advanced Propulsion Centre," 2017.
- [8] J. Carroll, A. McDonald, and D. McMillan, "Reliability comparison of wind turbines with DFIG and PMG drive trains," *IEEE Transactions on Energy Conversion*, vol. 30, pp. 663-670, 2015.
- [9] N. Mehala, "Condition monitoring and fault diagnosis of induction motor using motor current signature analysis," *A Ph. D Thesis submitted to the Electrical Engineering Department, National Institute of Technology, Kurushetra, India*, 2010.
- [10] S. Grubic, J. M. Aller, B. Lu, and T. G. Habetler, "A survey on testing and monitoring methods for stator insulation systems of low-voltage induction machines focusing on turn insulation problems," *IEEE Transactions on Industrial Electronics*, vol. 55, pp. 4127-4136, 2008.
- [11] S. Nandi, H. A. Toliyat, and X. Li, "Condition monitoring and fault diagnosis of electrical motors—A review," *IEEE transactions on energy conversion*, vol. 20, pp. 719-729, 2005.
- [12] H. Zhang, "Online thermal monitoring models for induction machines," *IEEE Transactions on Energy Conversion*, vol. 30, pp. 1279-1287, 2015.
- [13] Y. Wu and H. Gao, "Induction-motor stator and rotor winding temperature estimation using signal injection method," *IEEE Transactions on Industry Applications*, vol. 42, pp. 1038-1044, 2006.

- [14] F. Ahmed and N. C. Kar, "Analysis of End-Winding Thermal Effects in a Totally Enclosed Fan-Cooled Induction Motor With a Die Cast Copper Rotor," *IEEE Transactions on Industry Applications*, vol. 53, pp. 3098-3109, 2017.
- [15] N. Z. Popov and S. N. Vukosavic, "Estimator of the Rotor Temperature of Induction Machine Based on Terminal Voltages and Currents," *IEEE Transactions on Energy Conversion*, vol. 32, pp. 155-163, 2017.
- [16] A. H. Bonnett and G. C. Soukup, "Cause and analysis of stator and rotor failures in three-phase squirrel-cage induction motors," *IEEE Transactions on Industry Applications*, vol. 28, pp. 921-937, 1992.
- [17] A. Mohammed and S. Djurovic, "Stator Winding Internal Thermal Monitoring and Analysis Using in-situ FBG Sensing Technology," *IEEE Transactions on Energy Conversion*, vol. 33, pp. 1508-1518, 2018.
- [18] M. O. Sonnaillon, G. Bisheimer, C. De Angelo, and G. O. García, "Online sensorless induction motor temperature monitoring," *IEEE transactions on Energy Conversion*, vol. 25, pp. 273-280, 2010.
- [19] Z. Lazarevic, R. Radosavljevic, and P. Osmokrovic, "A novel approach for temperature estimation in squirrel-cage induction motor without sensors," *IEEE Transactions on Instrumentation and Measurement*, vol. 48, pp. 753-757, 1999.
- [20] M. A. Valenzuela and P. Reyes, "Simple and reliable model for the thermal protection of variable-speed self-ventilated induction motor drives," *IEEE Transactions on Industry Applications*, vol. 46, pp. 770-778, 2010.
- [21] G. A. Capolino and A. Cavagnino, "New trends in electrical machines technology - Part I," *IEEE Transactions on Industrial Electronics*, vol. 61, pp. 4281-4285, 2014.
- [22] M. Rosu, P. Zhou, D. Lin, D. M. Ionel, M. Popescu, F. Blaabjerg, *et al.*, *Multiphysics Simulation by Design for Electrical Machines, Power Electronics and Drives*: John Wiley & Sons, 2017.
- [23] K. Fischer, F. Besnard, and L. Bertling, "Reliability-centered maintenance for wind turbines based on statistical analysis and practical experience," *IEEE Transactions on Energy Conversion*, vol. 27, pp. 184-195, 2012.
- [24] P. Chouinard, M. Denninger, and J.-S. Plante, "Reliable and lightweight primary flight control actuation using magneto-rheological clutches in slippage," in *Robotics and Automation (ICRA), 2015 IEEE International Conference on*, 2015, pp. 213-219.
- [25] P. Tavner, "Review of condition monitoring of rotating electrical machines," *IET Electric Power Applications*, vol. 2, pp. 215-247, 2008.
- [26] A. H. Bonnett, "Operating temperature considerations and performance characteristics for IEEE 841 motors," in *Petroleum and Chemical Industry Conference, 2000. Record of Conference Papers. Industry Applications Society 47th Annual*, 2000, pp. 77-89.
- [27] W. Zhou, T. G. Habetler, and R. G. Harley, "Bearing Condition Monitoring Methods for Electric Machines: A General Review," in *2007 IEEE International Symposium on Diagnostics for Electric Machines, Power Electronics and Drives*, 2007, pp. 3-6.
- [28] M. Eftekhari, M. Moallem, S. Sadri, and A. Shojaei, "Review of induction motor testing and monitoring methods for inter-turn stator winding faults," in *Electrical Engineering (ICEE), 2013 21st Iranian Conference on*, 2013, pp. 1-6.

- [29] W. L. Roux, R. G. Harley, and T. G. Habetler, "Detecting faults in rotors of PM drives," *IEEE Industry Applications Magazine*, vol. 14, pp. 23-31, 2008.
- [30] A. Boglietti, E. Carpaneto, M. Cossale, S. Vaschetto, M. Popescu, and D. A. Staton, "Stator winding thermal conductivity evaluation: An industrial production assessment," *IEEE Transactions on Industry Applications*, vol. 52, pp. 3893-3900, 2016.
- [31] Z. Gao, T. G. Habetler, R. G. Harley, and R. S. Colby, "A sensorless adaptive stator winding temperature estimator for mains-fed induction machines with continuous-operation periodic duty cycles," *IEEE transactions on industry applications*, vol. 44, pp. 1533-1542, 2008.
- [32] Y. Yang, B. Bilgin, M. Kasprzak, S. Nalakath, H. Sadek, M. Preindl, *et al.*, "Thermal management of electric machines," *IET Electrical Systems in Transportation*, vol. 7, pp. 104-116, 2017.
- [33] J. Pyrhonen, T. Jokinen, and V. Hrabovcova, *Design of rotating electrical machines*: John Wiley & Sons, 2013.
- [34] J. Hey, A. C. Malloy, R. Martinez-Botas, and M. Lampérth, "Online monitoring of electromagnetic losses in an electric motor indirectly through temperature measurement," *IEEE Transactions on Energy Conversion*, vol. 31, pp. 1347-1355, 2016.
- [35] R. Krishnan, *Permanent magnet synchronous and brushless DC motor drives*: CRC press, 2017.
- [36] M. A. Valenzuela and G. Ramirez, "Thermal models for online detection of pulp obstructing the cooling system of TEFC induction motors in pulp area," *IEEE Transactions on Industry Applications*, vol. 47, pp. 719-729, 2011.
- [37] Y. C. Chong, "Thermal analysis and air flow modelling of electrical machines," 2015.
- [38] W. Zhou, T. G. Habetler, and R. G. Harley, "Bearing condition monitoring methods for electric machines: A general review," in *Diagnostics for Electric Machines, Power Electronics and Drives, 2007. SDEMPED 2007. IEEE International Symposium on*, 2007, pp. 3-6.
- [39] P. de la Barrera and G. Bossio, "Stator core faults detection on induction motor drives using signal injection," in *Diagnostics for Electric Machines, Power Electronics & Drives (SDEMPED), 2011 IEEE International Symposium on*, 2011, pp. 98-104.
- [40] P. Zhang, B. Lu, and T. G. Habetler, "An active stator temperature estimation technique for thermal protection of inverter-fed induction motors with considerations of impaired cooling detection," *IEEE Transactions on Industry Applications*, vol. 46, pp. 1873-1881, 2010.
- [41] A. Siddique, G. Yadava, and B. Singh, "A review of stator fault monitoring techniques of induction motors," *IEEE transactions on energy conversion*, vol. 20, pp. 106-114, 2005.
- [42] L. Parsa and H. A. Toliyat, "Fault-Tolerant Interior-Permanent-Magnet Machines for Hybrid Electric Vehicle Applications," *IEEE Transactions on Vehicular Technology*, vol. 56, pp. 1546-1552, 2007.
- [43] N. M. Theune, M. Muller, H. Hertsch, J. Kaiser, M. Willsch, P. Krammer, *et al.*, "Investigation of stator coil and lead temperatures on high voltage inside large

power generators via use of fiber Bragg gratings," in *Sensors, 2002. Proceedings of IEEE*, 2002, pp. 1603-1607.

- [44] F. Marignetti, E. de Santis, S. Avino, G. Tomassi, A. Giorgini, P. Malara, *et al.*, "Fiber Bragg grating sensor for electric field measurement in the end windings of high-voltage electric machines," *IEEE Transactions on Industrial Electronics*, vol. 63, pp. 2796-2802, 2016.
- [45] D. Vilchis-Rodriguez, S. Djurović, P. Kung, M. Comanici, and A. Smith, "Investigation of induction generator wide band vibration monitoring using fibre Bragg grating accelerometers," in *Electrical Machines (ICEM), 2014 International Conference on*, 2014, pp. 1772-1778.
- [46] K. M. Sousa, U. J. Dreyer, C. Martelli, and J. C. C. da Silva, "Dynamic eccentricity induced in induction motor detected by optical fiber Bragg grating strain sensors," *IEEE Sensors Journal*, vol. 16, pp. 4786-4792, 2016.
- [47] Y. Wang, L. Liang, Y. Yuan, G. Xu, and F. Liu, "A two fiber bragg gratings sensing system to monitor the torque of rotating shaft," *Sensors*, vol. 16, p. 138, 2016.
- [48] A. Mohammed, S. Djurović, A. Smith, and K. Tshiloz, "FBG sensing for hot spot thermal monitoring in electric machinery random wound components," in *Electrical Machines (ICEM), 2016 XXII International Conference on*, 2016, pp. 2266-2272.
- [49] M. Fabian, D. Hind, C. Gerada, T. Sun, and K. T. Grattan, "Multi-parameter monitoring of electrical machines using integrated fibre Bragg gratings," in *25th International Conference on Optical Fiber Sensors*, 2017, pp. 103231I-103231I-4.
- [50] M. M. Werneck, R. C. d. S. B. Allil, and B. A. Ribeiro, "Calibration and operation of a fibre Bragg grating temperature sensing system in a grid-connected hydrogenerator," *IET Science, Measurement & Technology*, vol. 7, pp. 59-68, 2013.
- [51] K. de Moraes Sousa, A. A. Hafner, H. J. Kalinowski, and J. C. C. da Silva, "Determination of temperature dynamics and mechanical and stator losses relationships in a three-phase induction motor using fiber Bragg grating sensors," *IEEE Sensors Journal*, vol. 12, pp. 3054-3061, 2012.
- [52] D. Academy. (2018). *Journal format thesis submission*. Available: <https://www.bmh.manchester.ac.uk/doctoral-academy/your-phd/thesis-submission/alternative-format/>
- [53] A. Mohammad and S. Djurović, "Evaluation of fiber-optic sensing performance for embedded thermal monitoring of electric machinery wound components," in *Embedded Computing (MECO), 2016 5th Mediterranean Conference on*, 2016, pp. 72-76.
- [54] A. Mohammed and S. Djurović, "FBG array sensor use for distributed internal thermal monitoring in low voltage random wound coils," in *Embedded Computing (MECO), 2017 6th Mediterranean Conference on*, 2017, pp. 1-4.
- [55] A. Mohammed and S. Djurović, "A study of distributed embedded thermal monitoring in electric coils based on FBG sensor multiplexing," *Microprocessors and Microsystems*, vol. 62, pp. 102-109, 2018/10/01/ 2018.
- [56] A. Mohammed and S. Djurovic, "FBG Thermal Sensing Features for Hot Spot Monitoring in Random Wound Electric Machine Coils," *IEEE Sensors Journal*, 2017.

- [57] A. Mohammed, J. I. Melecio, and S. Djurovic, "Stator Winding Fault Thermal Signature Monitoring and Analysis by in situ FBG sensors," *IEEE Transactions on Industrial Electronics*, pp. 1-1, 2018.
- [58] "IEEE Recommended Practice for the Design of Reliable Industrial and Commercial Power Systems," *IEEE Std 493-2007 (Revision of IEEE Std 493-1997) - Redline*, pp. 1-426, 2007.
- [59] J. Cibulka, M. K. Ebbesen, G. Hovland, K. G. Robbersmyr, and M. R. Hansen, "A review on approaches for condition based maintenance in applications with induction machines located offshore," *Modeling, identification and control*, vol. 33, p. 69, 2012.
- [60] A. H. Bonnett, "Root cause AC motor failure analysis with a focus on shaft failures," *IEEE transactions on industry applications*, vol. 36, pp. 1435-1448, 2000.
- [61] R. M. Tallam, S. B. Lee, G. C. Stone, G. B. Kliman, J. Yoo, T. G. Habetler, *et al.*, "A survey of methods for detection of stator-related faults in induction machines," *IEEE Transactions on Industry Applications*, vol. 43, pp. 920-933, 2007.
- [62] N. E. m. Association, "NEMA Motor and Generatirs Standard," ed: NEMA, 2014.
- [63] ZhifuWang, Y. Jingzhe, Y. Huiping, and Z. Wei, "A review of Permanent Magnet Synchronous Motor fault diagnosis," in *2014 IEEE Conference and Expo Transportation Electrification Asia-Pacific (ITEC Asia-Pacific)*, 2014, pp. 1-5.
- [64] A. Guezmil, H. Berriri, R. Pusca, A. Sakly, R. Romary, and M. F. Mimouni, "Detecting inter-turn short-circuit fault in induction machine using high-order sliding mode observer: simulation and experimental verification," *Journal of Control, Automation and Electrical Systems*, vol. 28, pp. 532-540, 2017.
- [65] D. C. Patel and M. C. Chandorkar, "Modeling and Analysis of Stator Interturn Fault Location Effects on Induction Machines," *IEEE Transactions on Industrial Electronics*, vol. 61, pp. 4552-4564, 2014.
- [66] G. M. Joksimovic and J. Penman, "The detection of inter-turn short circuits in the stator windings of operating motors," *IEEE Transactions on Industrial Electronics*, vol. 47, pp. 1078-1084, 2000.
- [67] P. D. Howard W Penrose, CMRP, President, MotorDoc® LLC. (2017). *Electric Motor Repair and Reliability*. Available: <http://empoweringmotors.com/2017/06/05/electric-motor-repair-and-reliability/>
- [68] R. M. Tallam, T. G. Habetler, and R. G. Harley, "Experimental testing of a neural-network-based turn-fault detection scheme for induction machines under accelerated insulation failure conditions," in *Diagnostics for Electric Machines, Power Electronics and Drives, 2003. SDEMPED 2003. 4th IEEE International Symposium on*, 2003, pp. 58-62.
- [69] M. Melero, M. Cabanas, C. Rojas, G. Orcajo, J. Cano, and J. Solares, "Study of an induction motor working under stator winding inter-turn short circuit condition," in *Diagnostics for Electric Machines, Power Electronics and Drives, 2003. SDEMPED 2003. 4th IEEE International Symposium on*, 2003, pp. 52-57.
- [70] V. Nguyen, J. Seshadrinath, D. Wang, S. Nadarajan, and V. Vaiyapuri, "Model-Based Diagnosis and RUL Estimation of Induction Machines Under Interturn Fault," *IEEE Transactions on Industry Applications*, vol. 53, pp. 2690-2701, 2017.

- [71] T. e.-M. Authority. (1985). *Typical Failures in Three-Phase Stator Windings*. Available: <https://www.easa.com/resources/booklet/typical-failures-three-phase-stator-windings>
- [72] B. T. f. t. G. G. I. S. 1882. (2006). *Include generators and exciters in your outage inspections*. Available: <http://www.powermag.com/include-generators-and-exciters-in-your-outage-inspections/?pagenum=7>
- [73] J. R. R. Ruiz, J. A. Rosero, A. G. Espinosa, and L. Romeral, "Detection of Demagnetization Faults in Permanent-Magnet Synchronous Motors Under Nonstationary Conditions," *IEEE Transactions on Magnetics*, vol. 45, pp. 2961-2969, 2009.
- [74] Edvard. (2016). *When a 3-phase motor experience phase failure*. Available: <https://electrical-engineering-portal.com/when-3-phase-motor-run-when-one-phase-failure>
- [75] M. Kunli and W. Yunxin, "Fault diagnosis of rolling element bearing based on vibration frequency analysis," in *Measuring Technology and Mechatronics Automation (ICMTMA), 2011 Third International Conference on*, 2011, pp. 198-201.
- [76] A. C. Charlie R. Brooks , Ashok Choudury *Metallurgical Failure Analysis*: McGraw-Hill Inc.,US (1 Jan. 1992), 1992.
- [77] M. E. C. a. Forensics, "CAUSE AND CONTRIBUTING FACTORS OF FAILURE OF GEARED WIND TURBINES, Part 1," 2010.
- [78] W. Ost and P. De Baets, "Failure analysis of the deep groove ball bearings of an electric motor," *Engineering Failure Analysis*, vol. 12, pp. 772-783, 2005/10/01/2005.
- [79] "Report of Large Motor Reliability Survey of Industrial and Commercial Installations: Part 3," *IEEE Transactions on Industry Applications*, vol. IA-23, pp. 153-158, 1987.
- [80] P. F. Albrecht, J. C. Appiarius, R. M. McCoy, E. L. Owen, and D. K. Sharma, "Assessment of the Reliability of Motors in Utility Applications - Updated," *IEEE Power Engineering Review*, vol. PER-6, pp. 31-32, 1986.
- [81] O. V. Thorsen and M. Dalva, "A survey of faults on induction motors in offshore oil industry, petrochemical industry, gas terminals, and oil refineries," *IEEE Transactions on Industry Applications*, vol. 31, pp. 1186-1196, 1995.
- [82] M. Blodt, P. Granjon, B. Raison, and G. Rostaing, "Models for Bearing Damage Detection in Induction Motors Using Stator Current Monitoring," *IEEE Transactions on Industrial Electronics*, vol. 55, pp. 1813-1822, 2008.
- [83] Y. Han and Y. Song, "Condition monitoring techniques for electrical equipment-a literature survey," *IEEE Transactions on Power delivery*, vol. 18, pp. 4-13, 2003.
- [84] J. I. Melecio, A. Mohammed, and S. Djurović, "Towards embedded intelligence enabled autonomous condition monitoring systems for AC motor drives," in *2018 7th Mediterranean Conference on Embedded Computing (MECO)*, 2018, pp. 1-5.
- [85] M. D. Negrea, "Electromagnetic flux monitoring for detecting faults in electrical machines," 2006.
- [86] K. N. Gyftakis, D. V. Spyropoulos, J. C. Kappatou, and E. D. Mitronikas, "A Novel Approach for Broken Bar Fault Diagnosis in Induction Motors Through Torque

- Monitoring," *IEEE Transactions on Energy Conversion*, vol. 28, pp. 267-277, 2013.
- [87] S. F. Legowski, A. S. Ula, and A. M. Trzynadlowski, "Instantaneous power as a medium for the signature analysis of induction motors," *IEEE Transactions on Industry Applications*, vol. 32, pp. 904-909, 1996.
 - [88] G. Kliman and J. Stein, "Methods of motor current signature analysis," *Electric Machines and power systems*, vol. 20, pp. 463-474, 1992.
 - [89] A. M. Cardoso, S. Cruz, and D. Fonseca, "Inter-turn stator winding fault diagnosis in three-phase induction motors, by Park's vector approach," *IEEE Transactions on Energy Conversion*, vol. 14, pp. 595-598, 1999.
 - [90] H. Jeong, S. Moon, and S. W. Kim, "An Early Stage Interturn Fault Diagnosis of PMSMs by Using Negative-Sequence Components," *IEEE Transactions on Industrial Electronics*, vol. 64, pp. 5701-5708, 2017.
 - [91] M. E. H. Benbouzid, "A review of induction motors signature analysis as a medium for faults detection," *IEEE transactions on industrial electronics*, vol. 47, pp. 984-993, 2000.
 - [92] R. Yan, R. X. Gao, and X. Chen, "Wavelets for fault diagnosis of rotary machines: A review with applications," *Signal processing*, vol. 96, pp. 1-15, 2014.
 - [93] J. A. Antonino-Daviu, K. N. Gyftakis, R. Garcia-Hernandez, H. Razik, and A. J. M. Cardoso, "Comparative influence of adjacent and non-adjacent broken rotor bars on the induction motor diagnosis through MCSA and ZSC methods," in *Industrial Electronics Society, IECON 2015-41st Annual Conference of the IEEE*, 2015, pp. 001680-001685.
 - [94] A. Gandhi, T. Corrigan, and L. Parsa, "Recent advances in modeling and online detection of stator interturn faults in electrical motors," *IEEE Transactions on Industrial Electronics*, vol. 58, pp. 1564-1575, 2011.
 - [95] "IEEE Standard Test Procedure for Thermal Evaluation of Systems of Insulating Materials for Random-Wound AC Electric Machinery - Redline," *IEEE Std 117-2015 (Revision of IEEE Std 117-1974) - Redline*, pp. 1-75, 2016.
 - [96] W. R. Finley, M. M. Hodowanec, and W. G. Holter, "An analytical approach to solving motor vibration problems," in *Industry Applications Society 46th Annual Petroleum and Chemical Technical Conference (Cat.No. 99CH37000)*, 1999, pp. 217-232.
 - [97] B. Li, M.-Y. Chow, Y. Tipsuwan, and J. C. Hung, "Neural-network-based motor rolling bearing fault diagnosis," *IEEE transactions on industrial electronics*, vol. 47, pp. 1060-1069, 2000.
 - [98] V. Bicego, E. Lucon, C. Rinaldi, and R. Crudele, "Failure analysis of a generator rotor with a deep crack detected during operation: fractographic and fracture mechanics approach," *Nuclear engineering and design*, vol. 188, pp. 173-183, 1999.
 - [99] S. Djurović, D. S. Vilchis-Rodriguez, and A. C. Smith, "Investigation of wound rotor induction machine vibration signal under stator electrical fault conditions," *The Journal of Engineering*, vol. 2014, pp. 248-258, 2014.
 - [100] P. Tchakoua, R. Wamkeue, M. Ouhrrouche, F. Slaoui-Hasnaoui, T. A. Tameghe, and G. Ekemb, "Wind turbine condition monitoring: State-of-the-art review, new trends, and future challenges," *Energies*, vol. 7, pp. 2595-2630, 2014.

- [101] F. P. G. Márquez, A. M. Tobias, J. M. P. Pérez, and M. Papaelias, "Condition monitoring of wind turbines: Techniques and methods," *Renewable Energy*, vol. 46, pp. 169-178, 2012.
- [102] S.-B. Lee, T. G. Habetler, R. G. Harley, and D. J. Gritter, "An evaluation of model-based stator resistance estimation for induction motor stator winding temperature monitoring," *IEEE Transactions on energy conversion*, vol. 17, pp. 7-15, 2002.
- [103] P. Zhang, B. Lu, and T. G. Habetler, "A remote and sensorless stator winding resistance estimation method for thermal protection of soft-starter-connected induction machines," *IEEE Transactions on Industrial Electronics*, vol. 55, pp. 3611-3618, 2008.
- [104] R. Beguenane and M. E. H. Benbouzid, "Induction motors thermal monitoring by means of rotor resistance identification," *IEEE Transactions on Energy conversion*, vol. 14, pp. 566-570, 1999.
- [105] P. Mellor, D. Roberts, and D. Turner, "Lumped parameter thermal model for electrical machines of TEFC design," in *IEE Proceedings B (Electric Power Applications)*, 1991, pp. 205-218.
- [106] I. E. Commission, "IEC 60034-1:2010 Rotating electrical machines - Part 1: Rating and performance," ed: IEC, 2010.
- [107] "IEEE Standard Test Procedure for Polyphase Induction Motors and Generators," *IEEE Std 112-2004 (Revision of IEEE Std 112-1996)*, pp. 1-83, 2004.
- [108] P. B. Reddy, A. M. El-Refaie, K.-K. Huh, J. K. Tangudu, and T. M. Jahns, "Comparison of interior and surface PM machines equipped with fractional-slot concentrated windings for hybrid traction applications," *IEEE Transactions on Energy Conversion*, vol. 27, pp. 593-602, 2012.
- [109] "IEEE Recommended Practice for General Principles of Temperature Measurement as Applied to Electrical Apparatus," *IEEE Std 119-1974*, p. 0_1, 1975.
- [110] S. P. Panchangam and V. Naikan, "Reliability analysis of temperature sensor system," *International Journal of Reliability, Quality and Safety Engineering*, vol. 20, p. 1350003, 2013.
- [111] M. J. Picazo-Ródenas, J. Antonino-Daviu, V. Climente-Alarcon, R. Royo-Pastor, and A. Mota-Villar, "Combination of noninvasive approaches for general assessment of induction motors," *IEEE Transactions on Industry Applications*, vol. 51, pp. 2172-2180, 2015.
- [112] G. Singh, T. C. A. Kumar, and V. Naikan, "Induction motor inter turn fault detection using infrared thermographic analysis," *Infrared Physics & Technology*, vol. 77, pp. 277-282, 2016.
- [113] A. G. Garcia-Ramirez, L. A. Morales-Hernandez, R. A. Osornio-Rios, J. P. Benitez-Rangel, A. Garcia-Perez, and R. de Jesus Romero-Troncoso, "Fault detection in induction motors and the impact on the kinematic chain through thermographic analysis," *Electric Power Systems Research*, vol. 114, pp. 1-9, 2014.
- [114] X. Liang, "Temperature estimation and vibration monitoring for induction motors," in *Electrical Power and Energy Conference (EPEC), 2017 IEEE*, 2017, pp. 1-6.
- [115] T. G. Habetler, F. Profumo, G. Griva, M. Pastorelli, and A. Bettini, "Stator resistance tuning in a stator-flux field-oriented drive using an instantaneous hybrid flux estimator," *IEEE Transactions on Power Electronics*, vol. 13, pp. 125-133, 1998.

- [116] H. Kubota and K. Matsuse, "Speed sensorless field-oriented control of induction motor with rotor resistance adaptation," *IEEE Transactions on Industry Applications*, vol. 30, pp. 1219-1224, 1994.
- [117] M. J. Duran and J. Fernandez, "Lumped-parameter thermal model for induction machines," *IEEE transactions on Energy Conversion*, vol. 19, pp. 791-792, 2004.
- [118] J. Doolan Fernandes, F. E. Carvalho Souza, G. G. Cipriano Maniçoba, A. O. Salazar, and J. A. de Paiva, "Wireless monitoring of induction machine rotor physical variables," *Sensors*, vol. 17, p. 2660, 2017.
- [119] R. J. Brighton and P. N. Ranade, "Why overload relays do not always protect motors," *IEEE Transactions on Industry Applications*, pp. 691-697, 1982.
- [120] A. Boglietti, A. Cavagnino, M. Lazzari, and M. Pastorelli, "A simplified thermal model for variable-speed self-cooled industrial induction motor," *IEEE Transactions on Industry Applications*, vol. 39, pp. 945-952, 2003.
- [121] M. M. Werneck, R. Allil, B. Ribeiro, and F. de Nazaré, "A guide to fiber bragg grating sensors," *Current Trends in Short-and Long-Period Fibre Gratings; InTech: Rijeka, Croatia*, pp. 1-24, 2013.
- [122] K. Hill, Y. Fujii, D. C. Johnson, and B. Kawasaki, "Photosensitivity in optical fiber waveguides: Application to reflection filter fabrication," *Applied physics letters*, vol. 32, pp. 647-649, 1978.
- [123] G. Meltz, W. W. Morey, and W. Glenn, "Formation of Bragg gratings in optical fibers by a transverse holographic method," *Optics letters*, vol. 14, pp. 823-825, 1989.
- [124] M. Kreuzer, "Strain measurement with fiber Bragg grating sensors," *HBM, Darmstadt, S2338-1.0 e*, 2006.
- [125] A. D. Kersey, M. A. Davis, H. J. Patrick, M. LeBlanc, K. P. Koo, C. G. Askins, *et al.*, "Fiber grating sensors," *Journal of Lightwave Technology*, vol. 15, pp. 1442-1463, Aug 1997.
- [126] G. R. Store, "Global Fiber Bragg Grating Sensors Sales Market Report 2018," 2018.
- [127] Y. J. Rao, "In-fibre Bragg grating sensors," *Measurement Science and Technology*, vol. 8, pp. 355-375, Apr 1997.
- [128] D. Arora, J. Prakash, H. Singh, and A. Wason, "Reflectivity and Bragg's wavelength in FBG," *International Journal of Engineering*, vol. 5, pp. 341-9, 2011.
- [129] A. Othonos and K. Kalli, *Fiber Bragg gratings: fundamentals and applications in telecommunications and sensing*: Artech House, 1999.
- [130] K. O. Hill and G. Meltz, "Fiber Bragg grating technology fundamentals and overview," *Journal of lightwave technology*, vol. 15, pp. 1263-1276, 1997.
- [131] K. O. Hill, B. Malo, F. Bilodeau, D. Johnson, and J. Albert, "Bragg gratings fabricated in monomode photosensitive optical fiber by UV exposure through a phase mask," *Applied Physics Letters*, vol. 62, pp. 1035-1037, 1993.
- [132] D. Kang, S. Park, C. Hong, and C. Kim, "The signal characteristics of reflected spectra of fiber Bragg grating sensors with strain gradients and grating lengths," *NDT & E International*, vol. 38, pp. 712-718, 2005.

- [133] A. Kersey, T. Berkoff, and W. Morey, "High-resolution fibre-grating based strain sensor with interferometric wavelength-shift detection," *Electronics Letters*, vol. 28, pp. 236-238, 1992.
- [134] A. Othonos, K. Kalli, D. Pureur, and A. Mugnier, "Fibre bragg gratings," in *Wavelength Filters in Fibre Optics*, ed: Springer, 2006, pp. 189-269.
- [135] C. Doyle, "Fibre Bragg Grating Sensors-An Introduction to Bragg gratings and interrogation techniques," *Smart Fibres Ltd*, pp. 1-5, 2003.
- [136] SmartFibres. (2018). *Our Technology*. Available: <https://www.smartfibres.com/technology>
- [137] HBM. (2018). *Optical sensors based on Fiber Bragg Gratings (FBG)*. Available: <https://www.hbm.com/en/1629/fiber-bragg-grating-technology-explained/>
- [138] W. W. Morey, G. Meltz, and W. H. Glenn, "Fiber optic Bragg grating sensors," in *OE/FIBERS'89*, 1990, pp. 98-107.
- [139] A. Mohammed and S. Djurović, "FBG array sensor use for distributed internal thermal monitoring in low voltage random wound coils," in *2017 6th Mediterranean Conference on Embedded Computing (MECO)*, 2017, pp. 1-4.
- [140] S. Ugale and V. Mishra, "Fiber Bragg grating modeling, characterization and optimization with different index profiles," *International Journal of Engineering Science and Technology*, vol. 2, pp. 4463-4468, 2010.
- [141] W. Li, Y.-W. Li, X.-D. Han, and G.-Q. Yu, "The study of enhancing temperature sensitivity for FBG temperature sensor," in *Machine Learning and Cybernetics, 2009 International Conference on*, 2009, pp. 2746-2749.
- [142] Z. Zhou and J. Ou, "Techniques of temperature compensation for FBG strain sensors used in long-term structural monitoring," in *Microtechnologies for the New Millennium 2005*, 2005, pp. 167-172.
- [143] D. Barrera, V. Finazzi, J. Villatoro, S. Sales, and V. Pruneri, "Packaged optical sensors based on regenerated fiber Bragg gratings for high temperature applications," *IEEE Sensors Journal*, vol. 12, pp. 107-112, 2012.
- [144] A. Azhari, R. Liang, and E. Toyserkani, "A novel fibre Bragg grating sensor packaging design for ultra-high temperature sensing in harsh environments," *Measurement Science and Technology*, vol. 25, p. 075104, 2014.
- [145] Y. Zhang, L. Zhu, F. Luo, M. Dong, R. Yang, W. He, *et al.*, "Comparison of metal-packaged and adhesive-packaged fiber Bragg grating sensors," *IEEE Sensors Journal*, vol. 16, pp. 5958-5963, 2016.
- [146] M. Fabian, D. M. Hind, C. Gerada, T. Sun, and K. T. Grattan, "Comprehensive monitoring of electrical machine parameters using an integrated fibre Bragg grating-based sensor system," *Journal of Lightwave Technology*, 2017.
- [147] Y. Zhang, D. Feng, Z. Liu, Z. Guo, X. Dong, K. Chiang, *et al.*, "High-sensitivity pressure sensor using a shielded polymer-coated fiber Bragg grating," *IEEE Photonics Technology Letters*, vol. 13, pp. 618-619, 2001.
- [148] F.-f. Tian, J.-w. Cong, B.-f. Yun, and Y.-p. Cui, "A fiber Bragg grating current sensor with temperature compensation," *Optoelectronics Letters*, vol. 5, pp. 347-351, 2009.

- [149] M. L. Filograno, M. Pisco, A. Catalano, E. Forte, M. Aiello, C. Cavaliere, *et al.*, "Triaxial Fiber Optic Magnetic Field Sensor for Magnetic Resonance Imaging," *Journal of Lightwave Technology*, vol. 35, pp. 3924-3933, 2017.
- [150] L. Hoffmann, M. S. Müller, S. Krämer, M. Giebel, G. Schwotzer, and T. Wieduwilt, "Applications of fibre optic temperature measurement," *Proc. Estonian Acad. Sci. Eng.*, vol. 13, pp. 363-378, 2007.
- [151] J.-H. Lee, S.-G. Kim, H.-J. Park, and M. Song, "Investigation of Fiber Bragg Grating temperature sensor for applications in electric power systems," in *Properties and applications of Dielectric Materials, 2006. 8th International Conference on*, 2006, pp. 431-434.
- [152] C. Hudon, C. Guddemi, S. Gingras, R. Leite, and L. Mydlarski, "Rotor temperature monitoring using fiber Bragg gratings," in *IEEE Electrical Insulation Conference (EIC), 2016*, 2016, pp. 456-459.
- [153] Y.-J. Rao, "Recent progress in applications of in-fibre Bragg grating sensors," *Optics and lasers in Engineering*, vol. 31, pp. 297-324, 1999.
- [154] C. Hudon, M. Lévesque, M. Essalihi, and C. Millet, "Investigation of rotor hotspot temperature using Fiber Bragg Gratings," in *Electrical Insulation Conference (EIC), 2017 IEEE*, 2017, pp. 313-316.
- [155] A. Singh, S. Berggren, Y. Zhu, M. Han, and H. Huang, "Simultaneous strain and temperature measurement using a single fiber Bragg grating embedded in a composite laminate," *Smart Materials and Structures*, vol. 26, p. 115025, 2017.
- [156] P. Wang, J. Liu, F. Song, and H. Zhao, "Quasi-distributed temperature measurement for stator bars in large generator via use of Fiber Bragg Gratings," in *Strategic Technology (IFOST), 2011 6th International Forum on*, 2011, pp. 810-813.
- [157] Z. Gao, X. Zhu, Y. Fang, and H. Zhang, "Active monitoring and vibration control of smart structure aircraft based on FBG sensors and PZT actuators," *Aerospace Science and Technology*, vol. 63, pp. 101-109, 2017.
- [158] W. Ecke and K. Schröder, "Fiber Bragg grating sensor system for operational load monitoring of wind turbine blades," in *Smart Sensor Phenomena, Technology, Networks, and Systems 2008*, 2008, p. 69330I.
- [159] M. Optics, "Sensing Solutions."
- [160] FBGS. *FIBER BRAGG GRATING (FBG) SENSOR PRINCIPLE*. Available: <https://www.fbgs.com/technology/fbg-principle/>
- [161] N. INSTRUMENTS. (2018). *PXI Universal Input Module*. Available: <http://www.ni.com/en-gb/support/model.pxie-4844.html>
- [162] K. d. M. Sousa, A. A. Hafner, M. Crespin, J. Somenzi, V. d. Oliveira, H. J. Kalinowski, *et al.*, "Fiber Bragg grating sensing applications in temperature monitoring of three-phase induction motors," in *2011 SBMO/IEEE MTT-S International Microwave and Optoelectronics Conference (IMOC 2011)*, 2011, pp. 862-866.
- [163] M. M. Werneck, R. C. Allil, and B. A. Ribeiro, "Fiber Bragg grating temperature sensing system for large air cooled hydrogenerators," in *Sensing Technology (ICST), 2011 Fifth International Conference on*, 2011, pp. 329-334.

- [164] C. Martelli, E. Silva, K. Sousa, F. Mezzadri, J. Somenzi, M. Crespin, *et al.*, "Temperature sensing in a 175MW power generator," in *OFS2012 22nd International Conference on Optical Fiber Sensors*, 2012, pp. 84212F-84212F.
- [165] K. de Moraes Sousa, A. A. Hafner, E. G. Carati, H. J. Kalinowski, and J. C. C. da Silva, "Validation of thermal and electrical model for induction motors using fiber Bragg gratings," *Measurement*, vol. 46, pp. 1781-1790, 2013.
- [166] R. C. Leite, V. Dmitriev, C. Hudon, S. Gingras, C. Guddemi, J. Piccard, *et al.*, "Analysis of Thermo-Mechanical Stress in Fiber Bragg Grating Used for Hydro-Generator Rotor Temperature Monitoring," *Journal of Microwaves, Optoelectronics and Electromagnetic Applications*, vol. 16, pp. 445-459, 2017.
- [167] M. Willsch, "Fiber optical sensors in power generation," in *Third Asia Pacific Optical Sensors Conference*, 2012, p. 835137.
- [168] J. Weidner, "Direct Measurement of Copper Conductor Temperature at Generator Windings with Fibre Bragg Grating (FBG) Sensors," *SC AI Rotating Machines, Contribution PSI Q*, vol. 1, 2012.
- [169] F. Mezzadri, J. P. Bazzo, C. Martelli, E. V. Silva, and J. C. C. da Silva, "200 MW hydroelectric generator stator surface temperature monitoring using a DTS system," in *24th International Conference on Optical Fibre Sensors*, 2015, p. 963442.
- [170] J. W. Snow, "An Overview of Fibre Optic Rotary Joint Technology and Recent Advances," *IFAC Proceedings Volumes*, vol. 31, pp. 77-81, 1998.
- [171] M. Fabian, D. M. Hind, C. Gerada, T. Sun, and K. T. Grattan, "Comprehensive Monitoring of Electrical Machine Parameters Using an Integrated Fiber Bragg Grating-Based Sensor System," *Journal of Lightwave Technology*, vol. 36, pp. 1046-1051, 2018.
- [172] C. Faria, M. Dos, and S. F. Luis, "SYSTEM AND METHOD FOR MONITORING MACHINE CONDITION AND FORCE MEASUREMENT IN A STATOR OF AN ELECTRICAL MACHINE," ed: US Patent 20,170,089,776, 2017.
- [173] K. M. Sousa, I. B. V. da Costa, E. S. Maciel, J. E. Rocha, C. Martelli, and J. C. C. da Silva, "Broken Bar Fault Detection in Induction Motor by Using Optical Fiber Strain Sensors," *IEEE Sensors Journal*, vol. 17, pp. 3669-3676, 2017.
- [174] R. P. Linessio, K. d. M. Sousa, T. d. Silva, C. A. Bavastri, P. F. d. C. Antunes, and J. C. C. d. Silva, "Induction Motors Vibration Monitoring Using a Biaxial Optical Fiber Accelerometer," *IEEE Sensors Journal*, vol. 16, pp. 8075-8082, 2016.
- [175] M. Fabian, J. B. Bartolo, M. Ams, C. Gerada, T. Sun, and K. Grattan, "Vibration measurement of electrical machines using integrated fibre Bragg gratings," in *24th International Conference on Optical Fibre Sensors*, 2015, p. 963417.
- [176] P. Kung, L. Wang, and M. I. Comanici, "Stator end winding vibration and temperature rise monitoring," in *2011 Electrical Insulation Conference (EIC)*. 2011, pp. 10-14.
- [177] M. Sasic, H. Jiang, and G. Stone, "Requirements for fiber optic sensors for stator endwinding vibration monitoring," in *Condition Monitoring and Diagnosis (CMD), 2012 International Conference on*, 2012, pp. 118-121.
- [178] J. P. Fracaroli, J. B. Rosolem, E. K. Tomiyama, C. Floridia, R. S. Penze, R. Peres, *et al.*, "Development and field trial of a FBG-based magnetic sensor for large hydrogenerators," in *SPIE Commercial+ Scientific Sensing and Imaging*, 2016, pp. 98520L-98520L-6.

- [179] M. D. Limited. (2017). *Motor-CAD Thermal*. Available: <https://www.motor-design.com/motor-cad-software/therm/>
- [180] A. Boglietti, A. Cavagnino, and D. A. Staton, "TEFC induction motors thermal models: a parameter sensitivity analysis," *IEEE Transactions on Industry Applications*, vol. 41, pp. 756-763, 2005.
- [181] P. T. Limited. (2018). *PEEK Tubing*. Available: <http://www.polyflon.co.uk/products/fluoropolymer-tubing/peek-tubing>
- [182] ZEUS. (2018). *PEEK Insulated Wire*. Available: <https://www.zeusinc.com/products/insulated-wire/peek-insulated-wire>
- [183] FIBERCORE. (2018). *Polymide coated SM Fiber*. Available: https://www.newport.com/medias/sys_master/images/images/hf4/haa/8797241901086/Polyimide-Coated-SM-Fiber.pdf
- [184] ArGrating. (2018). *Optical fiber makes sense for future*. Available: <http://www.atgrating.com/en/>
- [185] Princetel. *Fibre Optic Rotary Joint*. Available: http://www.princetel.com/forj_mjx.asp
- [186] G. M. Flockhart, R. R. Maier, J. S. Barton, W. N. MacPherson, J. D. Jones, K. E. Chisholm, *et al.*, "Quadratic behavior of fiber Bragg grating temperature coefficients," *Applied optics*, vol. 43, pp. 2744-2751, 2004.
- [187] TEC MOTORS. (2018). *TECA Aluminium Motor*. Available: <http://www.tecmotors.co.uk/products/motors/three-phase/teca-aluminium-motors>
- [188] F. INSTRUMENTS. (2018). *FLIR TG165*. Available: <http://www.flir.co.uk/instruments/tg165/>
- [189] M. D. Prieto, G. Cirrincione, A. G. Espinosa, J. A. Ortega, and H. Henao, "Bearing Fault Detection by a Novel Condition-Monitoring Scheme Based on Statistical-Time Features and Neural Networks," *IEEE Transactions on Industrial Electronics*, vol. 60, pp. 3398-3407, 2013.